GRINDING OF ADVANCED CERAMIC MATERIALS EXPERIMENTAL AND THEORETICAL INVESTIGATION INTO CRACK INITIATION AND PROPAGATION

Amin Abdul-Wahab Mokbel
(BSc. Industrial Engineering)

Thesis submitted for the Degree of
Doctor of Philosophy

Department of Mechanical and Manufacturing Engineering
University of Glamorgan, Wales, UK
March 1997

ABSTRACT

Advanced ceramic materials are assuming increasing industrial importance because of their special properties. However, the extreme hardness and brittleness of these materials make their machining efficiency low. The difficulty arises from shaping ceramics whilst conserving their surface integrity, strength and high quality surface finish. Manufacturing processes such as grinding with diamond bonded wheels present one solution. The use of a diamond grinding wheel on the surface of ceramics, creates a complex system of elastic/plastic deformation, and subsequent cracking. For ceramic materials such as silicon nitride, two types of damage can occur; firstly surface damage in the form of machining marks which cause stress concentrations and surface cracks and secondly sub-surface cracking. These problems caused a major delay in the utilisation of these materials in the aeronautics industry. This research was aimed at providing a better understanding of the grinding process and parameters involved in machining ceramic component.

An extensive preliminary study was carried out to understand the behaviour of advanced ceramic material during grinding. The effect of very high infeed and grinding wheel parameters were studied as an initial investigation. A system for on line detection of grinding wheel surface condition during grinding was developed during this research. Acoustic emission AE technique to monitor the wheel condition was also investigated during the experimental work.

The grinding machine used is a commercially available machine with a stiffness coefficient of 18.5 N/μm. The machine was modified to accommodate a higher feed rate. The purpose of using this machine was to investigate how a commercial machine would grind hard material such as advanced ceramics and what the effect would be on the process of crack initiation and propagation during grinding. The effect of different grinding wheel and machine tool parameters on crack initiation and propagation was investigated and represent the main concern of this research. Experimental design using modified L_{27} orthogonal array was used. The response of the surface roughness, fracture strength, AE spectral amplitude, grinding forces, grinding energy, crack size, sub-surface cracks distance from the ground surface, depth of surface damage due to different grinding wheel and machine parameters used in the fractional factorial array were all investigated.

Three basic types of cracks that were found to occur after the passage of an abrasive grain on the surface of ceramics materials were identified. These are radial, median and lateral cracks. Only radial cracks and machine marks are visible on the surface, median and lateral cracks (parallel to the surface) are formed below the affected zone and thus not visible. The load of an individual grain and its shape on the grinding wheel surface were found to have an influence on the crack initiation and propagation. Higher damage depth on the ground surface was measured when the grain size increased or was extremely sharp. Median cracks were found to be at a deeper location from the ground surface (2-15 μm) compared with lateral cracks. The dimensions and depth of median cracks beneath a ground surface was found to increase when the levels of grinding wheel grit size, wheel bond hardness, depth of cut and table feed were increased. However, locations of lateral cracks were found not to be affected when these

parameters increased and found to occur at 2-4 μm below the surface. The median cracks were located close to the ground surface at low table feed rates compared with deeper location when the table feed rate increased.

A correlation between AE, SEM and 3D data and the ground surface condition was carried out. The condition of the ground surface whether smooth or rough was identified and linked with AE signals. The link between these observations show that an increase in percentage of surface fracture is accompanied by low-amplitude long-duration events which can be assumed as the characteristic of brittle mode grinding. This observation was confirmed by the SEM and the 3D observations. Higher AE spectral amplitude was found to be associated with smooth ground surfaces. However, sub-surface median cracks were found for this condition. This correlation was the first reported attempt to link different experimental measurements and parameters.

Different artificial cracks were initiated on ceramic specimen surfaces in both longitudinal and transverse directions using v-shaped discs. This method of initiating cracks is more realistic than that produced by a single diamond scratch. The very random nature of diamond grit shape, size and location on the surface of the wheel would alter the characteristics of a crack initiated in a real grinding process. This technique used for creating an artificial crack is the first reported attempt hitherto. The groove generation mechanism observed using SEM was almost brittle when the depth of scratch increased. At larger groove depths, a deeper locations of sub-surface median cracks were found. Grinding processes were then carried out on these cracks to investigate their propagation. The AE spectral amplitude was found to be higher for specimens ground with artificial cracks compared with specimens ground without artificial cracks. The sub-surface cracks initiated due to grinding specimens with artificial cracks were found to be at deeper locations than to those for ceramic specimens ground without artificial cracks. The effect of remaining damage depths on the ground surface on the fracture strength were also studied. Increasing the diamond grinding wheel grit sizes, wheel bond hardness and table feed were found to be the most influential factors that increase the propagation distance of the artificial cracks during grinding.

A computer model based on finite element analysis package was used to study the behaviour of the ceramics in grinding. This package was used to establish a theoretical model which was validated using experimental results. Normal and tangential grinding forces from experimental work were used as input to the FE model. These forces were chosen to indicate different wheel and machine parameters. The model simulates the process of grinding by applying these forces on the surface of the ceramic specimen to study the crack initiation, propagation and their distance from the ground surface. A complete simulation for the grinding process was made including removal of material during the process.

ACKNOWLEDGEMENTS

The author would like to thank DR T. M. A. Maksoud for his guidance and supervision. His generously given support have been invaluable during this research. Thanks are also due to DR J. Morgan (University of Bristol) for the supervision and support given to this research.

Acknowledgements are to Sana'a University (Yemen) for the assistance given during this research.

A very grateful thanks to Professor J. Ward (Head of Mechanical and Manufacturing Engineering) for the support given to this research.

Many thanks also go to DR R. Kingdom (Faculty of Technology Study) for his assistance. Technical support from the technician staff in Department of Mechanical and Manufacturing Engineering is appreciated and particular gratitude for their invaluable assistance.

Finally, and not least, the author would like to acknowledge the support and encouragement of his family over past years.

MEMORANDUM

The accompanying dissertation "Grinding of advanced ceramic materials experimental and theoretical investigation into crack initiation and propagation" is submitted in support of an application for the Degree of Doctor of Philosophy at the University of Glamorgan.

The work has not been submitted for any other degree in this University, nor for an award of a Degree or Diploma of any other Institution.

The dissertation is based on independent work by the candidate, all contributions from others being acknowledged in the dissertation itself.

I hereby declare that the above statements are true.

Signed .....

A. A. Mokbel

CONTENTS

FIGURES

TABLES

1.0. INTRODUCTION

The requirement for materials capable of operating in extreme condition of increasing severity has led to a growing interest in advanced ceramics materials. The attractive properties of ceramics including high hardness, high thermal resistance and chemical inertness make them desirable in high performance applications. This has meant them occupying positions traditionally reserved for metals and alloys. The properties of these materials cause problems during the machining process.

These very properties also make ceramics difficult and restrictive to shape. They also put a great demand on machining them accurately without adversely affecting their inherent properties. Manufacturing processes such as grinding with diamond bonded wheels present one, nevertheless difficult, solution. The difficulty arises from shaping ceramics whilst conserving its surface integrity, its strength and high quality surface finish.

1.1. Preliminary Investigations

Extensive preliminary investigations have been carried out in this research to understand the behaviour of advanced ceramic materials during grinding. The different research phases which were carried out during this research are shown in Figure 1.

1.1.1. Grinding of Ceramic Materials

The main objective of this research was to study the initiation and propagation of cracks in the grinding of ceramic materials. In order to study this, a comprehensive study has to be made of the different parameters that may affect the mechanics of the grinding operation itself. These parameters are, the diamond grinding wheel bond type, grit size, high infeed effects and wheel surface topography.

1.1.1.1. Diamond Grinding Wheel Bond Type

Three diamond grinding wheels with different bond were used in the preliminary investigation. Material strength and surface roughness characteristics and the effects of grinding attributes on the resultant surface finish were investigated. Experimental design with Taguchi L_9 orthogonal array was used. The results from the experiments were translated into their respective signal to noise ratios (S/N) of larger is better for strength analysis and smaller is better for surface roughness analysis. This work produced a refereed paper and shown on the published work section.

1.1.1.2. Very High Table Infeed

Grinding using diamond wheel is one major contributor to shaping and forming ceramic. In order to avoid any strength degradation, critical surface defects must not be generated on the ground component. This will require reducing the loading of the grinding wheel diamond grits during the grinding process. High loading of the grits is thought to alter the mechanics of material removal in a deteriorating manner.

Using a high speed grinding wheel means the introduction of a very large number of diamond grits to the arc of cut in a very short time. This large number of grits would mean a much smaller loading on each grit, hence altering the removal of material characteristics. In this research, an attempt was made to simulate the same effect but through altering the infeed of the ceramic component. Very high infeed (32767 mm/min) was used in association with a shallow depth of cut. The simulation was applied to two types of ceramics, Sialon 101 and 201. The result of the surface finish, surface topography and fracture strength of the ground components were then compared to conventionally ground component. This work produced a refereed paper and shown on the published work section.

1.1.2. Grinding Wheel Condition

Grinding wheel conditions were investigated during this research. A system for detection of the grinding wheel condition was developed. An acoustic emission (AE)

technique was also used to monitor the wheel condition at different grinding/truing speed ratios during the main experimental work of this research.

1.1.2.1. Grinding Wheel Topography

Spatial distribution of sharp cutting edges on the surface of grinding wheels has an important effect on the characteristics of the ground components. Random protrusion of sharp edges can result in a combination of randomly distributed grinding forces. A well dressed and trued wheel is essential for monitoring and control of the grinding process. A system for on line detection of grinding wheel condition during grinding has been developed.

The system is used to detect in-process changes of grinding wheel surface topography by using a flapper nozzle arrangement. A pressure transducer was fixed on the flapper nozzle as shown in Figure 12. The flapper nozzle was located at a certain distance from the grinding wheel, this distance was predetermined to ensure an effective response from the transducer. When the wheel was running and an air supply is connected to the flapper nozzle a static pressure Ps was obtained. The optimum distance of the flapper nozzle from the grinding wheel surface determined by calibration. External triggering of the data acquisition system was provided to include more accurate assessment of the wheel surface irrespective of the wheel speed. An experimental study of different dressing depths and grinding variables and their effect on the grinding wheel topography has also been investigated. This work produced a refereed paper and shown on the published work section.

1.1.2.2. Grinding Wheel Condition Monitoring by Using AE Technique

The aim of this part was to monitor the diamond grinding wheel condition by using AE technique. This was achieved by imprinting the grinding wheel surface profile on mild steel specimens after different grinding wheel/truing speed ratios and directions. An acoustic emission (AE) sensor was attached on the mild steel specimens during one grinding pass. The raw AE signals were then analysed using FFT methods.

The surface roughness of these specimens were measured. These results were then compared with the AE signals.

The variations in both AE spectral amplitude and surface roughness was found to reflect the wheel surface condition. Imprinting the grinding wheel surface profile on mild steel specimens with small surface roughness values was found to be associated with high AE spectral amplitude. However, the rough surfaces were associated with low AE spectral amplitude. The AE technique was found to be more accurate and can cope with higher grinding wheel speeds due to the higher sampling frequency used.

1.2. Main Experimental and Theoretical Investigation

Crack initiation and propagation during grinding of advanced ceramic materials have been investigated experimentally and theoretically. Experimental results were validated using a FE model. The objective of this investigation was to produce comprehensive research into the crack generation in advanced ceramics due to grinding process.

Acoustic emission technique (AE) was used to study the grinding wheel condition, crack initiation and propagation during the grinding process and during the three point bending test of ground ceramic. The raw signals of AE generated from the grinding zone were stored using a digital oscilloscope and then transferred to PC as ASCII files to analyse the signal using a fast Fourier transform (FFT) method. The machining marks and radial cracks on the surface have been measured using SEM, optical microscopy inspection and 3D surface topography. Stylus of Talysurf with tip radius of less than 1.2 μm was also used to measure the damage depth on the ground surface (R_{max}).

A non-contacting laser based system for surface wave velocity measurement to detect the sub-surface cracks of ground ceramic has been tried in the University of Nottingham; the system based on measuring the surface acoustic wave velocity at frequency close to 100 MHz. At this frequency the wave length is approximately 50 μm

in ceramics. The penetration depth of the surface wave is also comparable to the wave length. In order to study the sub-surface cracks of the ground ceramic specimens using this system, the specimens should have a very small surface roughness (0.1 μm). This means that another process should be carried out after the grinding. It is predicted that this particular method will be improved so that rougher surfaces can be accommodated and the sub-surface damage then obtained. The system failed to detect any results. The reasons for this was the closeness of the cracks to the surface.

Ultrasonic equipment with a 100 MHz sampling rate has also been tried as a non destructive test (NDT) to detect the sub-surface micro-cracks (Ultrasonic Science Inc. in Fleet). It was very difficult to detect micro-cracks that are very close to the surface. Some cracks with estimated size of 20 μm have been detected using the same equipment for unground specimens (sintering process damage), these cracks were found at a depth of 500-1000 μm from the surface. Micro-focus X-ray equipment has also been tried to detect the internal micro-cracks, but none were detected. In this research the distance of the sub-surface cracks from the ground surface was measured after the bending test of the ground specimens.

Hitherto, there is no practical possibility of measuring the sub-surface cracks' locations, which are presumably in the layers near the ground surface. The cracks which were to be detected in this research was very close to the ground surface (2-15 μm) and this depth was found to depend on the wheel and machine parameters.

1.2.1. Effect of Grinding Wheel and Machine Tool Parameters on the Ground Ceramic Component

The effect of different levels of diamond grinding wheel grit size (D46, D76 and D126) at different levels of depth of cut (20 to 500 μm), grinding wheel speed (20 to 32 m/s) and grinding wheel condition (-0.3 to +0.6) on the ground ceramic were investigated. The response of the surface roughness, fracture strength, AE spectral amplitude, grinding forces, grinding energy, crack size, sub-surface cracks distance from the ground surface, depth of surface damage due to different grinding wheel and machine parameters used in the fractional factorial array were all investigated.

The results obtained in this research should be looked at in the light of two points. The first is the limitations on the machine used. The machine is a commercially available machine that was modified to accommodate a higher feed rate. One of the main aims was to investigate how this machine would grind hard material such as advanced ceramics and what the effect would be on the process of crack initiation and propagation during grinding. The second point, is the analytical "Taguchi" technique used. Although Taguchi's method is a well established and recognised, it also has its own limitations. In the author's opinion, the limitations of the Taguchi's technique is that interpretation of the results is not a straight forward matter. Some false trends can be concluded from graphical results if the reader is not fully familiar with the technique. When a large array, such as the L_{27}, used in this research, is operative, one should be very careful when considering the weight importance of each parameter involved. A conclusion may not be obvious from looking at one isolated figure.

1.2.2. Correlation of Acoustic Emission (AE), Scanning Electron Microscopy (SEM) and 3D Topography Data to Investigate the Ground Ceramic Condition

The AE signals generated from the grinding zone were analysed and linked with the ground surface condition identified by both SEM and 3D surface topography. The sub-surface condition of the ground specimens was investigated following three point bending tests. This is the first reported attempt to link the following experimental measurements and parameters:

- ◊ AE spectral amplitude and frequency.
- ◊ Time between AE event and RMS_{Volt}.
- ◊ Surface condition of ground ceramic, from SEM and 3D surface topography.
- ◊ Sub-surface condition of ground ceramic after the bending test, from SEM.

The grinding process can be considered as series of micro-cutting operations due to the huge number of grains on the grinding wheel surface. Each grain on the surface has its own AE event during the material removal process. The AE events of the

grains change rapidly especially during ceramic grinding. The grinding wheel rotates at high speed and a higher frequency on the contact zone occurs. A higher sampling frequency rate of the AE sensor should be used to cope with this situation. In this research a sensor attached to the workpiece with a frequency sensitivity up to 1.25 MHz.

The state of the ground ceramic surface (whether smooth or rough) was recognised from the AE signals. The results indicate that an increase in percentage of surface fracture is accompanied by low-amplitude long-duration events which can be assumed as the characteristic of brittle mode grinding. This observation was confirmed by the SEM and the 3D observations. Higher AE spectral amplitude was found to be associated with smooth ground surface. However, sub-surface median cracks were found for this condition.

1.2.3. Evaluation of Surface and Sub-Surface Cracks of Ground Ceramic

Ceramic materials possess very low fracture toughness values compared with metals and alloys. This means that they are very sensitive to cracks and other damage. The major form of damage usually occurs as surface and sub-surface cracks. Different crack types were produced due to the grinding process. These cracks can be classified in two forms, visible radial cracks and the machining marks found on the ground surface. The second type are median and lateral cracks and formed below the affected grinding zone and thus not visible. The hidden lateral and median cracks are, however, just as responsible for chip formation as the visible radial cracks. The energy introduced in the layers close to the surface invariably leads to the formation of these cracks.

The most influential factors found that initiate cracks on the ground surfaces were the grinding wheel condition and the increase in grinding wheel grit size (D46 to D126). The propagation distance of surface cracks were found to be larger when the wheel grit size increased at low table feed levels and small levels of depth of cut. A blunt grits and fine grit size were found to initiate sub-surface median cracks. The propagation of these median cracks were found to be of larger size when harder bond grinding wheels were used. At higher table feeds, sub-surface median cracks were

initiated at deeper depths beneath the ground surface. The propagation distance of these cracks in the sub-surface were found to increase when the depth of cut was increased.

Median and lateral cracks were found to be initiated in the sub-surface at layers very close to the ground surface. Below this layer, tensile stresses may occur which could initiate this type of sub-surface micro crack. This phenomena was observed in the FE model when the grinding process was simulated. The animation option of solved FE model shows that loading and unloading of the grinding forces on the ceramic FE model creates this type of cracks. It was also observed that sub-surface median micro cracks were initiated at the weaker element of the ceramic component under the compressive layer on the surface.

The sub-surface cracks were investigated after the bending test on the ground specimens. The size of these cracks and their depth from the ground surface were measured using SEM. The experimental observations showed that, median cracks were at a deeper distance from the ground surface compared with lateral cracks. The depth of median cracks from the ground surface was observed to increase (2-15 μm) with increasing the depth of cut and when the grinding wheel was blunt. Lateral cracks were found under a thin layer with a thickness of (2-4 μm). It is believed that they were created due to residual stresses. The depth of the lateral cracks from the ground surface were not found to be affected by increasing the depth of grinding cut.

1.2.4. Artificial Cracks Creation

The author believes that the use of a v-shaped disc would be more realistic than producing an artificial crack with a single diamond scratch. This technique used for creating an artificial crack is the first reported attempt hitherto. Previous research performed a scratch test using a single-diamond point at fixed depth of cut.

The very random nature of diamond grit shape, size and location on the surface of the wheel would alter the characteristics of a crack initiated in a real grinding process. For this particular reason, to simulate real grinding, artificial cracks were initiated on the surface of the ceramic specimens by using a diamond v-shape edge disc.

The disc has the same grit size as those used for the grinding wheels. It was chosen such that the characteristics of the crack initiated would be the same as that produced during a real grinding situation. The crack would be produced such that the effect of crack initiation on the surrounding area will also be simulated.

Grinding process were carried out on these artificial cracks to investigate their propagation. An AE sensor was attached on the ceramic specimens during the scratch test and the grinding process. The AE signals generated during ceramic specimens ground with and without artificial cracks were then compared. 3D surface topography was used to measure the artificial crack depths and their propagation. Scanning electron microscopy (SEM) was used to study the surface and the sub-surface section after the bending test. Although some research has been carried out in this area, most of these lacks the investigation of crack behaviour during grinding of advanced ceramic materials. This is the first reported attempt to link the induced crack indenter grit size to the actual size of diamond grits in the grinding wheel.

1.2.5. Experimental Verification of FE Model

A computer model based on finite element I-DEAS (Integrated Design Engineering Analysis Software), was used to study the behaviour of ceramic in grinding. The model simulates the process of grinding by applying a randomly distributed tangential and normal forces on the ceramic specimen.

The finite element model divides the structure into a grid of elements that form a model of the ceramic specimen. The model was then applied in such a way that zones of different deformation schemes could be identified. These were then used to simulate the process of crack initiation. By eliminating the grid elements where cracks appear, a further investigation into crack growth was then made. Cracks were found to be initiated on the surface due to the tensile action of the grinding forces on the surface of the ceramic FE model. Sub-surface cracks were also observed under the compressed layer due to the compressive behaviour of the grinding forces on the ground surface. The distance of these cracks from the ground surface depend on the mechanical properties of the ceramic material, the ratio of normal to tangential forces per grit and

their direction. This work produced a refereed paper and shown on the published work section.

The cracks were observed to be initiated when the grinding wheel condition changes. This was simulated by varying both normal and tangential grinding forces. Surface cracks were initiated when the wheel condition is sharp. This was simulated by applying high values of normal forces and low values of tangential forces. Sub-surface cracks were observed to initiate when the values of tangential force increased compared with normal forces. The propagation of these cracks in depth was indicated by values of stresses which are expected around a crack growth. The crack tip lies at a zone of tensile residual stress.

The compressive layer on the ground surface was associated with the formation of sub-surface crack. This phenomenon was observed when D46 grit size of diamond grinding wheel used in both experimental and simulation model. The higher compressive residual stress on the surface greatly increase the resistance to crack initiation on the ground surface. However, when a surface flaw is already present, the compressive stress effectively closes the mouth of the crack. Below this compressive layer, the cracks were observed on the sub-surface.

1.3. Research Aims

A fundamental knowledge base is needed for optimising the grinding process of ceramics and for the prevention of strength degradation. It is important that the mechanics of grinding of ceramic materials be understood in order to decrease the possibility of crack initiation and growth. This research was directed in these areas;

- **Primarily Study**

To investigate the effect of different parameters that may affect the mechanics of the grinding of ceramic material as preliminary investigation. These parameters are:

◊ Different levels of grinding wheel grit size and bond type hardness (resin, vitrified and cast iron).

◊ Effect of high infeed grinding.

◊ Monitoring diamond grinding wheels surface condition using AE technique.

◊ One objective of the primarily study was to develop a new system to monitor the grinding wheel condition using flapper nozzle arrangement.

♦ Main Experimental and Theoretical Investigation

• Effect of Different levels of Grinding Wheel and Machine Tool Parameters on the Ground Ceramic Component

Major experimental study was designed to investigate selected range of wheel and machine tool parameters. One of the objective was to monitoring the ceramic specimens during grinding and to investigate the following:

◊ The fracture strength.

◊ Surface roughness.

◊ AE spectral amplitude.

◊ Grinding forces.

◊ Grinding energy.

◊ Crack size of ground component.

• Correlation of Acoustic Emission (AE), Scanning Electron Microscopy (SEM) and 3D Topography Data to Investigate the Ground Ceramic Condition

◊ To analyse the raw AE signals and link the main characteristics such as spectral amplitude, frequency and time between AE events with the SEM and 3D topography to investigate the ground ceramic condition.

- **Evaluation of Surface and Sub-Surface Micro-Cracks**

The main objective of this part was to investigate the most influential factors that initiate surface and sub-surface cracks on the ground ceramic component. The effect of different levels of wheel and machine parameters on the surface damage depth, the sub-surface median cracks size and their depth beneath the ground surface was one of the main aims of this research.

- **Artificial Cracks Creation**

To initiate different depths of artificial cracks on the surface of ceramic specimens using v-shape disc have the same grit size of those used in the grinding wheel. The author believes this method of crack production was more accurate in simulating the crack initiation due the grinding process compared with single diamond scratch method. This part was carried out in two parts. Artificial cracks creation and grinding specimens with artificial cracks. AE sensor was attached to the ceramic specimens during these tests. The aims of this part was to investigate the following:

◊ Effect of increasing the groove depth on the generation of AE signals, surrounding area of the groove surface and the affected zone underneath the groove.

◊ Comparison of the AE signals generated from ceramic specimens ground with and without artificial cracks initiated on their surfaces.

◊ Effect of different wheel and machine parameters on the propagation of these artificial cracks and their effect on the fracture strength.

- **Experimental Verification of FE Model**

◊ Developing a FE model and using it to validate the experimental results. FE results were compared with the experimental results of the surface and sub-surface cracks measured by using SEM.

2.0. LITERATURE SURVEY

An extensive literature survey was carried out in all areas related to this research. The behaviour of ceramic materials during the grinding process, crack initiation and propagation, and grinding wheel condition of previous studies were reported.

2.1. Grinding of Advanced Ceramic Materials

Ceramic components of high surface finish and strength qualities are increasingly in demand for different industrial applications. The successful application of the new engineering materials is to some extent dependent upon overcoming the problems of machining them economically and accurately without affecting their advantageous properties. These properties are tempered by associated low fracture strength. Grinding using different bond materials and grit size diamond wheel is one major contributor to shaping and forming ceramic. In order to avoid any strength degradation, critical surface defects must not be generated or they should be minimised on the ground component.

Grinding is a metal-cutting process using tools with multiple cutting edges provided by randomly bonded abrasive grits which remove material at high speed Boothroyd [1]. The abrasive grains are generally of irregular shape with each grain acting as a small cutting tool containing a large negative rake angle. The grinding process is an interaction between an abrasive grit and workpiece in the contact zone. The result of the interaction being the extraction of a chip of workpiece material. The amount of energy required to produce the chip is of importance as this is a measure of process efficiency. In practice however, this occurs under a great deal of intrinsic discontinuities in grit and bond material breakdown during grinding Metzger [2].

The grinding process differs from the cutting process because of three frictional interactions Ernst and Merchant [3];

- The chip-bond interaction.
- The bond-work interaction.

- The cutting geometry of the abrasive constantly changes in the grinding process.

The optimal grinding process attempts to minimise these interactions and to maximise the abrasive/workpiece interaction. Precise grinding of ceramic is an output of a large number of variables. The parameters influencing the grinding process described by Spur, G. et al [4] is shown in Figure 2. The influence of the grinding process on workpiece and grinding wheel is shown in Figure 3. Cracks and residual stresses were produced on the workpiece due to the grinding process. The grinding wheel also affected by the grinding process that change the condition of the grains on the surface as shown in Figure 3.

The grinding process can be sectioned into creep-feed and speed-stroke grinding. These techniques are differentiated by grinding parameters and mechanics of material removal. Speed-stroke grinding is markedly more efficient in grinding time and energy. Grinding forces and energy are important to any grinding operation. For brittle materials, the specific grinding energy is much lower and the ratio of normal to tangential forces is much higher than for ductile materials Pai, D.M., et al [5]. As in the case of metals, the specific grinding energy varies inversely with the mean undeformed chip thickness as long as the volume between wheel and workpiece is sufficient to accommodate the chips produced. Otherwise, there is an increase in specific grinding energy due to lack of chip storage space. The particular influence of the lack of chip storage space on grinding energy per unit volume depends upon the details of the chip storage problem pertaining Pai, D.M., et al [5]. Specific energy relates to the interaction of the abrasive grit and the workpiece is given by,

$$U = \frac{Ft \,.\, Vs}{W \,.\, V_W \,.\, d} \qquad (J/mm^3) \tag{2.1}$$

where; F_t = Tangential force
V_s = Peripheral wheel speed
W = Grinding width
V_w = Workpiece velocity
d = Depth of cut

The volumetric material removal rate Q_w is defined as

$$Q_w = d \cdot V_w \cdot W \quad (mm^3/s) \tag{2.2}$$

The volumetric material removal rate per unit width Q'_w is defined as :

$$Q'_w = d \cdot V_w \quad (mm^2/s) \tag{2.3}$$

The power consumed during the interaction of the abrasive grit and the workpiece is given by;

$$P = F_t \cdot V_s \tag{2.4}$$

The grinding of brittle materials, such as advanced ceramics, by removing material from the surface of the component in a brittle fracture mode leaves residual stresses and micro-cracks which reduces the component strength and fatigue life. Accordingly, a fracture mode of material removal is preferred from the perspective of efficiency. Unfortunately, the finished surface obtained through a fracture mode of chip formation (deformed chip thickness) is also highly fragmented, and the strength after grinding is significantly lower than that obtained by a plastic flow mode of chip formation.

For ceramics materials, the plastic flow region is very small and the fracture process plays a predominant role in chip formation. This phenomena was observed during the bending test of the ceramic specimens during this research. Ceramics have the disadvantage of brittleness with little elongation at failure. To eliminate or minimise such micro-cracks in grinding of ceramics materials should be removed by plastic flow of chip formation.

A review of the literature reveals a considerable research effort devoted to the grinding of advanced ceramic. Inasaki [6] and [7] presented a comprehensive literature review on surface grinding of advanced ceramic materials. They concluded that the

material removal process by ceramic grinding is primarily due to the micro-brittle fracture of the material. They also concluded that creep feed grinding, characterised by large depths of cut and excessively slow workpiece is not necessarily adequate for high-efficiency grinding of ceramic materials.

The higher grinding forces, in particular, involves serious problems in achieving a high machining accuracy, and conventional pendulum grinding with higher workpiece speed is more desirable, Inasaki [6]. From the view point of ground surface quality, however, the above suggested condition has some adverse effect; i.e., an increase of the surface roughness, formation of micro-cracks, and chipping on the workpiece surface.

Inasaki [7] also proposed that it is especially important to distinctly divide the process into two stages; roughing and finishing. A high workpiece speed and a small depth of cut are suggested for roughing process to keep the grinding force small and suppress the increase of the grinding force with time. On the other hand, the workpiece speed should be kept relatively low in the finishing process to remove the damaged surface layer without forming a new damaged layer. This suggestion is not a practical solution because new cracks underneath the new ground layers were found in this research.

Morgan, J. E. and Hooper, R., [8], investigated the effect of grinding forces generated at the diamond/specimen interface change with changing grinding parameters during the grinding of PSSN (Pressureless Sintered Silicon Nitride). They concluded that the diamond grinding of ceramics is a complex process involving the operation of a number of mechanisms ranging from repeated brittle fracture, through sub-surface cracking, to purely plastic grooving. The relative magnitudes of which are dependent on the external operating conditions and micro mechanisms of the materials.

Inasaki [9] showed that the effect of speed-stroke grinding featured by the large cross-sectional area of active cutting edges is quite efficient in decreasing the grinding force and the grinding time. However, the surface roughness and depth of cracks have increased. Malkin [10] carried out several grinding experiments on glass material. It

was observed that the specific grinding energy needed in the fracture mode is about an order of magnitude lower than that needed for the plastic flow of chip formation. Micro-structure effects on grinding of alumna and glass ceramics was investigated by Marshall et al [11]. They mentioned that the microstructures were found to exert a deep influence on the machinability. In particular, the controlling toughness variable is that which refers to small cracks, not that conventionally measured in a large scale fracture specimen.

The effects of the grinding process upon grinding accuracy of advanced ceramics was investigated by Yui, A., et al [12]. They mentioned that the grindability of advanced ceramics is mainly affected more by the fracture toughness than by the hardness of the ground materials. They also observed that the surface characteristics of ground ceramics are affected by grinding condition. They observed that the higher the table feed rate and the larger the grinding depth of cut is set, the higher the grinding temperature occurred.

The mechanisms of material removal in the precision grinding of ceramics have been studied by Subramanian and Ramanath [13]. A set of experiments were carried in their study. From the results obtained they showed that the precision grinding of ceramics using diamond abrasive always occurs with a combination of a brittle fracture and plastic deformation. The precision grinding of ceramics can be used to preferentially promote brittle fracture or plastic deformation, by the proper selection of the grinding 'process parameters' and the grinding 'system variables'.

Lutz, G. [14], compared the chip formation properties of ceramic materials with those of metal, with brittle fracture being a characteristic grinding feature of ceramics. He mentioned that, the stress peaks in the vicinity of the crack are neutralised by means of the measures of specific normal forces. Crack propagation under load will - after a certain length of time- lead to breakage of the component without prior warning as soon as the critical stress intensity is exceeded. This phenomena was observed during the bending test during this research. An acoustic emission sensor was attached on the ground ceramic specimens to monitor and study the signals before the specimens fail.

For some specimens cracks propagated in a very short time 20 to 60 μs before fracture occurred as shown in Figures 194 and 195.

The effect of high grinding wheel speed on the strength of ground ceramic was investigated by Kovach, J. A. et al [15]. They used a relatively coarse (120 grit) brazed diamond wheel at wheel speeds up to 178 m/s and material removal rates up to 11 mm^2/s. They showed that the grinding forces decreased considerably with increased wheel speed and/or reduced material removal rate and that a tendency towards improved surface finish is developed as wheel speed is increased.

Kovach, J. A. et al [15] also found that increasing wheel speed, while operating at a relatively low material removal rate, can dramatically reduce surface fragmentation. They explained that this behaviour stems from the fact that the unit grit load is reduced significantly by increasing wheel speeds. They concluded that although extensive modulus of rupture MOR testing is yet to be performed, these results suggest that a transition from a `brittle fracture` mode of grinding to a low damage `ductile` grinding mode can be achieved by increasing wheel speed or decreasing the material removal rates.

It has been reported that successful grinding of ceramic materials can be achieved using a very high grinding wheel speed reaching 50,000 rpm Kovach et al [15]. The effect of this very high speed is to introduce a very large number of diamond grits to the arc of cut in a very short time. This large number of grits would mean a much smaller loading on each grit, hence altering the removal of material characteristics. In this research the maximum grinding wheel speed of 40 m/s can be achieved. An attempt was made to simulate the same technique but through altering the infeed of the ceramic component Maksoud and Mokbel [16]. Very high infeeds up to 32767 mm/min were used in association with a shallow depth of cut. The simulation was applied to two types of ceramics, Sialon 101 and 201. The result of the surface finish, surface topography and fracture strength of the ground components were then compared to a conventionally ground component. This is explained in section 7.2.2.

2.1.1. Material Removal Mode

The material removal mechanisms in grinding of ceramics have been discussed by Zhang, Bi. [17]. He used single-point diamond and diamond wheels, and SEM to investigate the grinding mode of ceramic materials. He found that material pulverisation was discovered on the surface layer of ground ceramic. Based on this study, he concluded that:

- Powder regime rather than ductile regime was observed in single point test.
- Powder regime appears to result from pulverisation induced by a complex stress state.
- The pulverisation material is loosely connected in comparison to the bulk material.
- It can be re-compacted by hydrostatic compressive stress in the contact region at the interface of abrasive grain and workpiece.
- The larger an abrasive grain is, the more powder regime it generates.
- Material flows sideways in signal-point grinding process, causing pile-ups. The coefficient of pile-ups increases as the depth of cut decreases.

Micro grinding apparatus to achieve ductile regime grinding of brittle materials was described by Bifano et al [18]. They mentioned that all materials, regardless of their hardness or brittleness, will undergo a transition from a brittle machining regime to a ductile machining regime if the grinding infeed rate is made small enough. They suggested that the grit depth of cut for ductile mode grinding of silicon carbide ceramic should be about 0.2 μm or less; above this value the grinding mode changes from a ductile to a brittle mechanism.

Below this threshold depth of cut, the energy required to propagate cracks is larger than the energy required for plastic yielding. Bifano et al [18] also observed, that a change in grinding infeed rate from 75 nm/rev to 1.5 nm/rev resulted in a transition from 99% surface fracture to 5% surface fracture, using SEM. Very high infeed up to 32767 mm/min used in association with a shallow depth of cut was investigated by

Maksoud and Mokbel [16]. SEM observations show a smooth ground surface at very shallow depth of cut.

Bifano et al [18] concluded that a ductile regime grinding of brittle materials requires a stiff structural loop, real-time control of the grinding infeed, relative isolation from environment disturbances, and state-of-the-art wheel truing techniques. They also concluded that the brittle material will undergo plastic rather fracture if the depth of machining is small enough.

Three dimensional form grinding with a rigidity and numerical control function of machining centre was used by Nakagawa et al [19]. High toughness and grinding ratio of cast iron bond diamond grinding wheel was used. They achieved a maximum stroke removal rate of 2000 mm^3/min in high feed rate grinding of silicon nitride material. From their study, grinding forces were very high (250 N/mm) in spite of using an in-process dressing tool in creep feed grinding. In this research at higher depths of cut, cast iron bonded diamond grinding wheels produced higher ground strength, low grinding forces and good surface roughness, but at low depths of cut the opposite was observed. This may be due to the variation in the wheel/workpiece stiffness when the depth of cut was increased.

Previous studies on grinding of advanced ceramic materials [10,17,21,22] have shown that when an abrasive grain passes through the grinding zone Figure 4, material is initially plowed aside at a shallow grain depth of cut (undeformed chip thickness), or at the beginning of cuts taken by individual abrasive grains, followed by flow-type chip formation.

When the grain depth of cut becomes sufficiently large for lateral cracking, the removal mechanism will be chipping (ductile) or brittle mode. Akbari et al [20], stated that when fracture occurs, the specific grinding energy is much less than with flow-type chip formation, but the finished surface is highly fragmented and the strength after grinding is lower.

2.1.2. Effect of Grit Depth on Strength of Ground Ceramic

The effect of grit depth of cut on the flexural strength of ground hot pressed silicon nitride has been investigated by Mayer et al [21]. They used an expression to estimate the grit depth of cut h_{max};

$$h_{max} = \sqrt{(4v_w / v_c C\Gamma)(\sqrt{a_e / d_s})} \qquad (2.5)$$

where; h_{max} = Grit depth of cut (maximum undeformed chip thickness)
C = Number of active cutting points per unit area of the wheel periphery (grit surface density)
Γ = Ratio of chip width to average undeformed chip thickness
v_c = Wheel peripheral speed
v_w = Workpiece speed
a_e = Wheel depth of cut
d_s = Wheel diameter

They observed that, the effect of h_{max} on the flexural strength appeared to be true regardless whether h_{max} is varied by varying wheel grit size or the machine parameters of the workpiece speed and depth of cut. They advise that the conclusion is based on a limited number of experiments;

- The controlling factors influencing flexural strength of ground HPSN appear to be grind direction and wheel grit depth of cut, h_{max}.
- The wheel grit depth of cut, h_{max}, has little or no effect on flexural strength when the direction of grind is longitudinal, i.e. when the grinding direction is parallel to the applied tensile stress. For transverse; when the grinding direction is perpendicular to the applied tensile stress, the flexural strength drops off when the wheel grit depth of cut, h_{max}, is increased beyond a critical value, $h_{max.crit.}$. For HPSN $h_{max.crit}$ appears to be about 0.16 microns. In this research three levels of diamond grinding wheel grit size were used. The results obtained in the up-cut grinding show that small grit size D46 produced higher fracture strength of ground silicon nitride material compared with D76 and D126 diamond grinding wheel grit size.

A concept for maximum strength grinding of hot pressed silicon nitride was presented by Mayer et al [22] based on the relationship of flexural strength versus wheel grit depth of cut. They showed that maximum strength in the ground ceramic is achieved when the wheel grit depth of cut is equal to or less than a critical value of grit depth of cut. They also showed that conventional grinders can provide maximum strength grinding of structural ceramics.

However, ductile-regime grinding of ceramic material could improve the strength of ground ceramic. This can be achieved if there are certain principles regarding machine accuracy, machine stiffness, real-time feedback control of position, critical depth of cut, the wheel bond type, grit size and the condition of the wheel surface, that have to be considered and adapted.

Under conditions where the wheel periphery is sharp, grinding forces are relatively low and the roughness of the ground component is the main cause for strength deterioration Takaki and Liu [23]. Wheel sharpness can be dictated by the truing speed ratio and has significant influence on the induced damage. The individual grits on the diamond grinding wheel interact with the workpiece as a series of micro-cutting tools. The shape of these cutting edges is dictated by one pass imprint on a mild steel specimen prior to the grinding and must influence the strength of ground ceramic. There exists a point of minimum damage as the dressing speed ratio (speed of grinding wheel/speed of truing wheel) is increased from .35 to 1. Maximum damage is induced with a wheel periphery which is extremely sharp, Takaki and Liu [23]. These results are in agreement with the results obtained from this research. This was observed mainly when the wheel periphery was extremely sharp, the fracture strength of ground ceramic was reduced. The effects of different levels of grinding wheel/truing speed ratios, and directions, on the grits' condition of the grinding wheel surface were investigated.

Takaki and Liu [23] concluded that, the deterioration of strength is related to the level of cracking produced. Factors affecting cracking length can be approximated using indentation;

$$C_o = \{ A[(E/H)] / K_c] . (\cos B)^{2/3} P\}^{1/2} \qquad (2.6)$$

Where; C_o = Radial crack size
A = Constant
E = Elastic modulus
H = Hardness
K_c = Fracture toughness
2B = Included angle of the indenter
and P = Load

Takaki and Liu [23] also concluded that the strength of ground specimens vary with the elastic modulus of the bond material of diamond grinding wheel used. Resin bond wheels have the lowest modulus and induce the lowest level of damage in a ceramic workpiece.

In this research resin, vitrified and cast iron diamond grinding wheels having different elastic modulus of the bond material were used. The effects of this range of grinding wheel bond material changed when the depth of cut increased. A soft material such as resin bond, can produce a higher strength of ground ceramic than metallic bond until a certain depth of cut. Once the depth of cut is increased, the metallic bond can achieve a higher strength of ground strength than resin bond. Wheel sharpness has been investigated with varying the truing/grinding speed ratios. These ratios increased from -0.3 to 0.6, which indicated a significant influence on the strength of ground ceramic.

The influence of surface roughness and phase transforms produced due to grinding on the strength of zirconia was investigated by Tanaka et al [24]. They mentioned that the surface roughness as a result of the grinding operation changes the structure in the deformed surface layer which influence the mechanical properties of zirconia. The bending strength σ_b of ground specimens is presented as a function of both the volume of martensitic transformed phase and the roughness of the surface.
The bending strength σ_b of the ground specimen is assumed to be;

$$\sigma_b = \sigma_0 (1 + \epsilon_{m+r} + \Upsilon) \quad (2.7)$$

$$\epsilon_{m+r} = 1.71 (V_m - 1.3) / 100 \quad (2.8)$$

$$\Upsilon = - 0.55 (R_{max} - 0.1) / 100 \quad (2.9)$$

Where; σ_0 = The original bending strength of the specimen.
V_m = The volumetric percentage of monoclinic phase.
R_{max} = Maximum surface roughness of the ground specimen.

They observed that the bending strength decreased as much as 2-5% because of an increase in surface roughness. These results show that the maximum damage on the ground surface R_{max} reduced the strength of ground zirconia. In this research R_{max} was measured and compared with the fracture strength of the ground silicon nitride. The damage depth on the ground surface was also measured by three dimension surface topography. The results show that the damage depth on the ground surface was found to affect on the fracture strength of ground silicon nitride.

2.1.3. Sub-surface Evaluation of Ground Ceramic

Sub-surface cracks can be a function of several factors including material properties, grinding conditions, grinding wheel parameter and grinding wheel truing and dressing conditions. Lawn [25] reported that the brittleness, which is defined as the ratio of hardness to toughness H/K_c of a material was a governing factor affecting the penetration depth of sub-surface damage. Lawns and Evans [26] proposed a critical condition for the initiation of sub-surface damage;

$$C_{min} = \xi (K_c / H)^2 \qquad (2.10)$$

Where ξ is a dimensionless constant. The above critical condition by Lawn and Evans was extended to a grinding situation by Bifano et al [18]. They presented a model to correlate the critical grit depth of cut with material properties. The model is described by a simple power-law equation;

$$dc = 0.15 (E / H) (K_c / H)^2 \qquad (2.11)$$

An analytical model for the prediction of sub-surface damage of ceramics subjected to grinding was described by Zhang and Howes [27]. The model correlates

sub-surface damage to the type of workpiece material and grinding parameters. The penetration depth of sub-surface damage δ was given by;

$$\delta = (200\, h_{max})^{1/\log(\lambda\,(H/Kc))} \qquad (2.12)$$

Where; λ = Constant (10^{-2} $m^{1/2}$)
h_{max} = The maximum grit depth of cut was given in equation (2.5).
H = Material hardness.
E = Elastic modulus.
and Kc = Fracture toughness of the material.

Zhang and Howes [27] identified two types of sub-surface damage as a result of grinding of silicon nitride, alumina and silicon carbide. Diamond grinding wheels with various grit size were used. This damage was identified into powder regime in the superficial layer, and voids in the sub-surface of ground ceramics. Clustered voids were induced in the less brittle materials, while scattered voids occurred in all the ceramic materials tested.

In this research, surface and sub-surface micro cracks were observed. Radial cracks and machining marks were found in the ground ceramic surface. The cracks depths on the ground surface were noticed to be dependant on the grit size of the diamond grinding wheel used. The higher damage depth on the surface, the smaller fracture strength of ground ceramic was produced. Median and lateral hidden micro cracks were found in the sub-surface. The size of these cracks and their distance from the ground surface were found to be affected by different levels of wheel and machine parameters. Lateral cracks were very close to the surface, e.g. 2-4 μm and median cracks 2-15 μm from the ground surface.

2.2. Damage in Grinding of Ceramic Materials

Ceramic materials posses very low fracture toughness values compared with metals and alloys. This means they are very sensitive to cracks and other mechanical failures. Grinding of brittle materials such as advanced ceramics is normally carried out

by removing material from the surface of the component mostly in a brittle fracture mode leaving residual stresses and micro cracks which reduce the component strength and fatigue life.

2.2.1. Crack Initiation and Propagation

The mechanics of crack initiation and propagation beneath a moving sharp indenter was investigated by Conway and Kirchner [32]. The stresses generated beneath the indenter for selected horizontal -to- vertical load were used in conjunction with an appropriate fracture mechanics solution to predict the propagation depth of 'penny' cracks.

The failure model assumed that median opening cracks are adequately modelled as embedded penny cracks. The penny cracks are assumed to initiate on the boundary of plastically deformed and locally shear cracked zone extending a distance Z_0 beneath the surface and propagate to a final distance C as shown in the figure below.

Lawn and Swan [33] showed that the maximum propagation depth of a penny crack can be obtained by defining the stress intensity factor given by Shi [34];

$$K_I = [2 / (\pi c)^{1/2}] \int_{Z_0}^{c} \frac{r\sigma\phi\ (r)\, dr}{(C^2 - r^2)^{0.5}} \qquad (2.13)$$

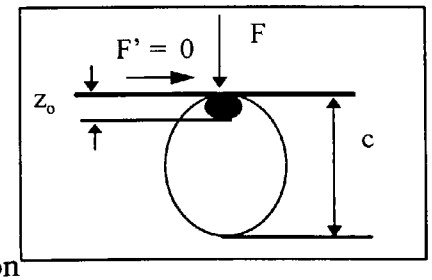

Where; K_I = Stress intensity factor
C = Final distance of the propagation of the deformed zone
$\sigma\phi$ = Out-of-plane hoop stress distribution
θ,ϕ and r = Polar co-ordinates

The out-of-plane hoop stress for the plane $\phi = 0$ directly beneath the indenter ($\theta = 0$) given as;

$$\sigma_\phi = \frac{FQ}{8\pi r^2} \qquad (2.14)$$

Where; F = Vertical load
r = Distance beneath the indenter
Q = Factor represent the increase in out-of-plane hoop stress for a corresponding increase in horizontal-to-vertical load ratio.

Substitution of equation (2.14) to equation (2.15) and integrating gives;

$$K_I = \frac{0.02\ F\ Q}{(C^{0.5} Z_0)} \qquad (2.15)$$

Introducing the mode I crack opening critical stress intensity factor K_{IC}, an expression for the maximum propagation depth of the penny crack was obtained as;

$$C = \frac{0.02\ F\ Q^2}{K_{IC} Z_0} \qquad (2.16)$$

From the result of this model used by Conway et al [32], the depth of damage increased with an increase of tangential force i.e. increased Q, for the plane perpendicular to the plane of motion of the tool. The tangential force does not affect the out-of-plane hoop stress (Q = 1) indicating that the penny cracks will propagate to greater length in the plane of motion of the tool.

In a multi-grinding study, Mecholsky et al [35] have shown that glass specimens fractured by stress applied perpendicular to the grinding direction, fail at lower stresses than those in which the applied stresses are parallel to the grinding direction. This result showed that cracks in the plane of motion of the grinding wheel are deeper than those perpendicular to this plane.

Single-point diamond grinding in hot-pressed silicon nitride was described by Kirchner [36]. He analysed the variation of crack length induced as a result of vertical loading under a moving indenter. Two different load/crack size relationships were given indicating that the distinct mechanisms are dictating the crack response to loading

which is a result of residual stress effects. When a surface is loaded perpendicularly by a sharp point, the yield stress is exceeded in the region directly under the point and the material is irreversibly deformed. Lawn and Swain, [33] integrated a standard fracture mechanics equation to obtain the following equation for the stress intensity factor;

$$K_I = \frac{(1 - 2\nu)^P}{2^{1/2}\ \pi^{5/2}\ Z_0\ c^{1/2}} \qquad (2.17)$$

Where;
ν = Poisson's ratio.
P = The vertical load.
Z_0 = The depth of irreversibly deformed zone.
c = The depth of median/radial cracks.

They assumed that the characteristics of the contact can be neglected and that the cracks propagate in response to the stress which varies inversely with the square of the distance from the contact. For a given material and indenter shape, this approach leads to;

$$P \alpha c^{1/2} \qquad (2.18)$$

The effect of residual crack opening stresses become a significant driving force for crack propagation only after a load value of 40 N is applied during single-point grinding in hot pressed silicon nitride.

A model for crack initiation of micro fracture beneath a sharp indenter has been investigated by Lawn, et al [26] by using a simple approximation for the tensile stress distribution in the elastic/plastic indentation field, in conjunction with the principle of geometrical similarity. Fracture mechanics procedures were applied to determine critical conditions for the growth of penny like "median cracks" from sub-surface flaws.

The maximum tensile stress occurs at the elastic/plastic interface σ_m, depth below the surface d, and the spatial extent over which the tensile component of the field, b act as shown below;

$$\sigma_m = \theta H \approx \text{const.}, \qquad (2.19)$$

$$b = \eta a = (\eta^2 / \alpha \pi H)^{0.5} P^{0.5} \qquad (2.20)$$

where; α and η = dimensionless factors

H = hardness

$$\sigma(r) = \sigma_m (1 - r/b) \qquad r \le b \qquad (2.21)$$

$$\sigma(r) = 0 \qquad r \ge b \qquad (2.22)$$

The aim of this model was to determine the loading conditions at which the "dominant flaw" becomes critical and by evaluating the stress intensity factor for exially symmetric penny crack as used by Shi [34];

$$K = [2 / (\pi c)^{0.5}] \int_0^c r \sigma(r) \, dr / (c^2 - r^2)^{0.5} \qquad (2.23)$$

Where; K = Stress intensity factor
C = Final distance of the deformation
r = Polar co-ordinates
$\sigma(r)$ = Out-of-plane hoop stress distribution

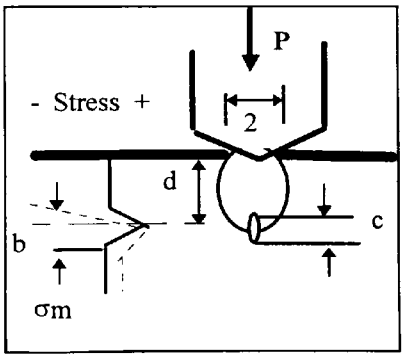

Substitution of Equation (2.21) and (2.22) into Equation (2.23).

$$K = 2 \sigma_m (c/\pi)^{0.5} [1 - 0.5 (1 - b^2/c^2)^{0.5} - 0.5 (c/b) \sin^{-1} (b/c)] \qquad c \ge b \qquad (2.24)$$

$$K = 2\sigma_m (c/\pi)^{0.5} (1 - c/4b), \qquad c \le b \qquad (2.25)$$

The model showed that the crack initiation will depend to a large extent on the starting flaw type. In the absence of a large flaw, the indentation will expand until a suitable intermediate flaw is encountered and taken to threshold before being engulfed within the plastic zone. The indentation variables are obtained by;

$$C = (1.767 / \theta^2)(K_c / H)^2 \tag{2.26}$$

$$P = (54.47\ \alpha / \eta^2\ \theta^4)(K_c / H)^3\ K_c \tag{2.27}$$

Where; C = Crack size
K_c = Critical stress intensity factor
H = Hardness
α and η = Dimensionless factors

The micro mechanics of failure emanating from machining-induced cracks in brittle materials was investigated by Marshall et al [37]. The crack response was described by a relation between applied stress and the equilibrium crack size;

$$\sigma_a = [K_c / \pi\ \Omega\ c)^{1/2}][\ 1-\chi_r\ P / K_c\ c^{3/2}] \tag{2.28}$$

$$\chi_r = (E / H)^{1/2} \tag{2.29}$$

Where; K_c = Stress intensity factor
Ω = Crack geometry parameter
c = Crack size
ξ = Dimensionless constant depend on the indenter geometry
E = Elastic modulus
H = Hardness of material

The failure condition is defined by the maximum of c_m and σ_m in the σ_a function,

$$c_m = (4\chi_r\ P / K_c)^{2/3} = 4^{3/2}\ c_0 \tag{2.30}$$

$$\sigma_m = 3\ K_c / 4\ (\pi\ \Omega\ c_m)^{1/2} \tag{2.31}$$

The above failure condition is produced by stable equilibrium crack growth from c_0 to c_m. This behaviour contrasts with the response of ideal, free cracks, where crack instability is achieved at a critical applied stress level without precursor extension. The existence of stable crack extension according to equation (2.28) occurs in a wide variety of ceramic materials. The strength of these materials depend on its properties and contact load.

Initiation and propagation of median as well as lateral cracks are considered to greatly contribute to the material removal rate in grinding process. A schematic representation of opening crack formation is shown in Figure 5, Lawn et al [33]. A sequence and sub-sequence crack propagation was summarised as follows:

- The sharp point of the indenter produces a brittle deformation zone
- At some threshold, a deformation - induced flow suddenly develops into a small crack, termed median crack.
- An increase in the load causes further, steady growth of the median crack
- Upon unloading, the median crack begins to close
- Upon complete removal, the lateral openings continue their extension, toward the specimen surface and may accordingly lead to chipping

The types of cracks formed in ground ceramic is shown in Figure 6, median cracks (longitudinal cracks) are running parallel to the grinding direction and perpendicular to the surface, Hakulinen et al [38]. These cracks result from the high tensile stresses at the bottom of the grinding groove. Radial cracks extend radially from the grinding groove. They are located perpendicular to the grinding direction and the surface but not as deep as the median cracks.

Malkin and Ritter [10] presented a critical review and evaluation of the grinding mechanisms for ceramic materials and their influence on the finished surface and mechanical properties. Median/radial cracks are associated with strength degradation, lateral cracks are assumed to be mainly responsible for material removal in erosion and abrasion. They developed fracture mechanics models for lateral cracks, assuming that

the volume removed by grit (indenter) under a normal load P_n is proportional to the dimensions of the lateral crack and the length of travel L, the volume removal V_i for one grit was obtained as;

$$V_i = \alpha_I \frac{P_n^{9/8}}{K_c^{1/2} H^{5/8}} (E/H)^{4/5} L \qquad (2.32)$$

Where;
α = material-independent constant.
P = normal load
E = elastic modulus
H = hardness
L = length of travel
K_c = fracture toughness

Summing the contribution of all the abrasive points, the total volumetric removal V with a normal load P would follow a relationship of the form;

$$V = \alpha \frac{P^{9/8}}{K_c^{1/2} H^{5/8}} (E/H)^{4/5} L \qquad (2.33)$$

For abrasion with linear scratching motion as in Figure 6, it seems likely that strength impairing median cracks should be generated mainly parallel to the direction of motion, Conway et al [32]. Median cracks on ground surfaces have been found both parallel and perpendicular to the direction of motion, Rice et al [39].

Malkin et al [10] found their expressions in equations (2.32 and 2.33) correlate reasonably well with some data for grinding of various ceramics they examined. However, the removal rates per unit width in their experiments showed at least one to two orders of magnitude smaller than for typical grinding practice mainly because of abnormally low workpiece feed velocities.

A major source of damage occurring during ceramic grinding can result from heat generated in the grinding zone Maksoud et al [40]. The heat generated can have a

deleterious effect on the ground surface as a result of high repetitive thermal stresses within the component. The effects of increasing the diamond wheel grit size and number of dressing passes on the residual stress field have been studied by Maksoud et al [41] using x-ray diffraction technique. They determined that the crack tip lies outside the residually stressed region for the wheel parameters investigated. They concluded that the evidence of crack tip location being in a compressively stressed region is inconclusive due to the inaccuracy of the residual stress profile determination.

A model for micro-crack initiation and propagation beneath hertzian contacts in polycrystalline ceramics was described by Lawn et al [42]. Unlike the well defined classical cone fracture that occurs in the weak tensile region outside the surface contact in homogeneous brittle solids, the fault micro crack damage in polycrystalline ceramics is distributed within a sub-surface shear compression zone below the contact. They determined the scale of individual damage events by characteristic micro-structure dimensions of the material. They discussed the threshold conditions for the initiation of micro-cracks and subsequent propagation. The cracks were observed to be in the size of the grain size of the material structure. They assumed that these micro-cracks propagate along constrained grain boundaries or other weak interfaces in predominantly extension mode i.e. mode I.

- Contact fracture mechanics under a single point diamond grinding differ in certain respects to the static indenter tests. The difference is the presence of horizontal loading arising in single point grinding tests. If the presence of a horizontal load has little effect on the crack size induced in ceramics, then static indentation tests will be relevant to single point grinding test. If however, horizontal loading does influence the crack dimensions during a contact event, via either the elastic loading or the residual plastic loading, then the level of this influence must be understood in order to predict the level of damage under single point grinding.

- Single-point diamond grinding with normal and tangential force components exist is more accurate than a static indenter test. This is because the damage can then vary with different grinding parameters such as depth of cut, wheel speed, grit size,.. etc.

Moreover response of machining cracks may also occur by the interaction of residual stresses from grinding grooves in the neighbourhood of active grits. This is the reason which led the author to believe that a finite element scheme which models the micro structure of the specimen under a single diamond grit is more true to the real situation.

- A v-shape edge disc was used in this research to initiate different depth of cracks (grooves) on the surface of ceramic specimens. The normal and tangential forces were stored along with AE signals simultaneously. A grinding process was then carried out on the specimens with and without cracks on the surface. The raw signals of AE for both crack initiation and during grinding were stored using a digital oscilloscope and then transferred to a PC as ASCII files in order to analyse the signal using a fast Fourier transform (FFT) method.

Two principal crack systems have been identified from the plastic zone; median/radial cracks and lateral cracks. The behaviour of both types of cracks is affected by residual stresses from the non uniform plastic deformation in elastic/plastic material.

2.2.1.1. Median / Radial Crack

Indentation fracture analysis begins with some knowledge of the stress fields through which the cracks evolve. Marshall et al [37], separated the stresses set up during the indentation process into two parts:

- The residual component, which is generated through mismatch between the plastically and elasticity deformation zones and which remains when the indenter is unloaded.
- The elastic component, which is generated during indentation and is removed when the indenter is removed.

The driving force for fracture has its origin in the residual component of the elastic/plastic field which is initiated by wedge-link action during loading, and may continue to propagate during unloading due to residual tensile stresses acting on the

crack tip. This is assuming that an equilibrium condition exists between the elastic loading and crack dimension. Also, it is assumed that the crack dimension is sufficiently large compared with the plastic zone radius, so that the elastic crack opening stress can be considered as a point source located at the crack centre. The condition for equilibrium growth of the cracks is obtained by equating the net stress intensity factor, to the critical stress intensity value.

The stress intensity associated with the residual crack opening stress (K_r) arising from plastic deformation, for an ideal penny-shaped crack, of radius (C), under a wedge opening component of the indenter load (P), is given by Marshall et al [43].

$$K_r = X_r \cdot P / C^{3/2} \qquad (2.34)$$

Where; X_r = dimensionless indenter/specimen constant, which is function of indenter angle, contact friction, and free surface effects.

A similar expression can be derived for the stress intensity associated with elastic component (K_e),

$$K_c = X_e \cdot P / C^{3/2} \qquad (2.35)$$

The condition for equilibrium growth of the cracks is obtained by equating the net stress intensity factor, (K) to the critical stress intensity value (K_c) for the system in Figure 7.

$$K_e + K_r = K_c \qquad (2.36)$$

Combining equation (2.35), (2.36)

$$K_c = X_e \cdot P/C^{3/2} + X_r \cdot P/C^{3/2} \qquad (2.37)$$

2.2.1.2. Lateral Crack

Lateral cracks are observed to initiate and propagate by residual stresses only as the indenting load is removed. The mechanics of lateral crack propagation in a sharp-indenter contact field was described by Marshall et al [44]. The fracture associated with elastic/plastic contact on brittle surface is of two basic types, 'median/radial' and 'lateral'. The mechanics of lateral crack propagation in a sharp-indenter contact field was described by Lawn, et al [45]. Lateral cracks are observed to initiate near the base of the plastic deformation zone below the contact and spread out laterally on a plane closely parallel to the specimen surface, Marshall et al [37].

In accordance with the indentation fracture mechanics approach, a stress intensity factor is sought for the configuration of Figure 7, in terms of contact load and crack size. The contact at load P leads to a crack of characteristic radius c, at depth h below the surface. The plastic zone supports the indenter, included angles 2° (not shown), over the characteristic radius a, and extends outward to a radius b. The stress intensity factor is calculated as;

$$K = [A / 2\pi (1 - \upsilon^2)]^{1/2} P_r / h^{3/2} \qquad (2.38)$$

Where; A = dimensionless geometrical constant.
ν = Poisson's ratio.

For the dimensionless constant A two specific lateral/radial configurations were considered;

i - laterals >> radials $\quad A = 3 (1 - \nu^2) / 4\pi \qquad (2.39)$

ii - laterals < radials $\quad A = 3/4 \qquad (2.40)$

The mechanical characteristics of the central deformation zone was considered by Marshall et al [37], and an expression for the equilibrium crack size as a function of applied load is obtained and setting $K = K_c$;

$$C^{L} = \{(\xi_L / A^{1/2}) Cot\psi)^{5/6} [(E/H)^{3/4} / K_c H^{1/4}]\}^{1/2} P^{5/8} \quad (2.41)$$

Where; ξ_L = Dimensionless constants, independent of the material/indenter system
ψ = Dimensionless factor
E = Young's modules.
H = Hardness.
P = Peak indentation load.

Evolution of a new cracking pattern of 'ortho-lateral' cracks which originate at the intact corners of the Vickers indentation after specimen-failure in brittle materials has been observed by Padture [46]. The new cracking pattern running orthogonal to the classic-lateral cracks and parallel to the new fracture surface. He also observed that, in some instances, post failure extension of the classic-lateral cracks toward the surface.

Three basic types of cracks that can occur after the passage of an abrasive grain on the surface of ceramics materials were observed in this research as shown in Figure 8. Only radial cracks and machine marks are visible on the surface, median and lateral cracks (parallel to the surface) are formed below the affected zone and thus not visible. The hidden lateral and median crack are, however, just as responsible for chips formation as the visible radial cracks. The energy introduced in the layers close to the surface invariably leads to the formation of the three types of cracks mentioned above. In this research AE was used to monitor the mode of material removal. Smooth and/or rough ground surface were identified by analysing AE signal energy amplitude and compared with SEM observations.

2.3. Experimental Detection of Micro Cracks

Crack measurement techniques are of growing importance in production engineering because cracks influence the static as well as the fatigue strength of a component. Cracks in or beneath a machined ceramic surface may severely damage a component Tonshoff et al [47]. Available methods of crack detection are;

◊ **Dye Penetration Inspection**

It is a physical-chemical non-destructive inspection procedure designed to detect and expose discontinuities in engineering materials. The penetrate applied has to be allowed a sufficient time to enter the surface discontinuities. It is applicable only if the defects reach the surface of the part. This means that this method cannot be used to detect sub-surface discontinuities that are not open to the exposed surface of the test part.

◊ **Ultrasonic Testing With Surface-sensitive Waves**

The surface and near-surface zones of components are zones of restricted accessibility for non-destructive methods using ultrasonic volume waves. The waves from ultrasonic equipment are calibrated to give an indication of any change of the frequency reflected as existing sub-surface damage.

◊ **Photo Acoustic and Acoustic Microscopy**

Surface and sub-surface characterisation of a component can be detected by photo acoustic microscopy. A local thermal temperature-rise is produced at the surface, preferably by an amplitude-modulated laser beam. The absorbed laser energy penetrates a certain distance into the solid as given by:

$$\delta = (2\,X / W)^{0.5} \qquad (2.42)$$

Where; X = The thermal diffusivity
W = The modulation frequency of the laser beam

The sound amplitude depends on the thermal and optical properties of the surface such as thermal diffusivity, thermal conductivity, thermal expansion and optical absorption within the penetration length.

An extensive literature survey about AE revealed that different sources of transient AE signals can be distinguished. Invariably, these sources are fast stress changes at specific locations. Stress pulses can be described in the time domain by their

rise time, duration, and level. The properties of such signals are strongly related to the chosen size of the sampling time window. Kanai et al [48] used an acoustic microscope as a non contact measurement. They mentioned that the results of AE measurements of cracking of glass are shown at frequencies up to 100 MHz. They suggest that sensors with a much broader band will provide additional information about the process.

◊ Three Dimension Surface Topography

Zygo's New View 100 3D Imaging surface structure analyser was used in this research. It is a scanning white-light interferometer that uses frequency domain analysis (FDA) to generate quantitative 3D images of surfaces. FDA is a mathematical method for processing complex interferograms in term of phases and spatial frequency. For a well-balanced interferometer with a single-frequency source, the normalised intensity varies as;

$$I = 0.5\ (1+\cos(\varphi)) \qquad (2.43)$$

$$\varphi = L\ .\ k + \varphi_o \qquad (2.44)$$

$$k = 2\pi / \lambda \qquad (2.45)$$

Where
φ = The interferometric phase.
L = the optical path difference (OPD)
λ = The source wavelength
φ_o = Constant phase offset characteristic of the interferometer and the material properties of the mirrors
k = The wave number or spatial frequency of the source light.

The idea behind FDA is looking at the interference phase, not the original intensity data measured by the detector. Distance is calculated by determining L, which is the slope of the above equation showing the rate of changing of interferometric phase with spatial frequency. In this research the following tests were carried out;

- The surface roughness of ground specimens was measured. The equipment used in this research was "Rank Taylor Hobson" Talysurf 5. The stylus tip radius of less than 1.2 μm has a variable inductance transducer which is connected to an electronic unit.

The signal is electronically processed, and can be displayed graphically or numerically as a roughness average, Ra value.

- SEM was used to inspect the surface and sub-surface damage of the ground specimens after the three point bending test. SEM was also used to study the mode of material removal. This instrument proved crucial to this research.

- Zygo's New View 100 3D Imaging surface structure analyser was used to measure the depth of surface damage by generating quantitative 3D images of surfaces. It was used to measure the depth of radial cracks and machining marks on the ground surface.

- A three point bend test was used as a destructive test to study the strength of ground specimens at different levels of grinding wheel and machine parameters.

- Ultrasonic equipment with 100 MHz sampling rate has been tried as NDT to detect sub-surface micro-cracks (Ultrasonic Science Inc. in Fleet) as shown in Figure 9. It was very difficult to detect the very closed micro-cracks to the ground surface. Some cracks with an estimated size of 20 μm have been detected. Using the same equipment for unground specimens (sintering process damage), a crack at a depth of 500-1000 μm from the surface was detected.

- Micro-focus X-ray equipment has also been tried to detect the internal micro-cracks. The system failed to produce any results. The reason for this was the closeness of the cracks to the surface.

Hitherto, there is no practical possibility of measuring the cracks' depth, which are presumably in the layers near the ground surface. The cracks which were to be detected in this research were found to be very close to the ground surface (2-15 μm) and this depth depends on the wheel and machine parameters. The sub-surface crack was investigated after the bending tests of the ground surface. The dimensions of these cracks and their depths from the ground surface were measured using SEM.

3.0. ACOUSTIC EMISSION TECHNIQUE

3.1. Introduction

Acoustic emission is a passive non destructive testing technique that detects the stress wave emissions from deformation and fracture processes within a material. Industrial applications of AE include monitoring loaded components such as pressure vessels and piping, weld monitoring through to grinding. The acoustic emission (AE) generated during machining processes has proven to contain information which is strongly related to the efficiency of the process and condition of its components. AE waves travel to the surface of the solid, where they can be detected by a piezoelectric transducer.

Research over the last several years has established the effectiveness of acoustic emission based sensing methodologies for machine tool condition monitoring and process analysis. AE technique has not yet become a common practice to monitor workpiece condition and surface integrity of advanced ceramics during grinding process.

3.2. Fundamentals of Acoustic Emission

Acoustic emission or stress wave emission is the phenomena of transient elastic wave generation due to a rapid release of strain energy caused by a structural alteration in a solid material. Generally, these structural alterations are the results of either internally generated or externally applied mechanical or thermal stresses. Numerous mechanisms have been proposed and confirmed as sources of AE. A partial listing of reported sources include movement of dislocations and grain boundaries, formation and growth of twins, generation and propagation of cracks, fracture of brittle inclusions and surface films, fire breakage and delimitation in composites, phase transformations, micro seismic and seismic activity in geological materials etc.

The phenomenon of AE was scientifically investigated in 1948. However, the first clearly documented and serious investigation of AE was made in 1950 at the Technical University of Munich. The first successful application of AE technique to a practical problem, was achieved in the establishment of integrity assurance of fibre wound rocket-motor cases. Monitoring AE during proof-tests predicted the burst pressures of test vessels to within ten percent of actual values. Since then, the applications of AE techniques in the nuclear, chemical, petroleum and aerospace industry have increased rapidly.

3.2.1. Acoustic Emission Types and Characteristics

Traditionally, the AE signals have been classified into two different types, continuous type and burst type. The difference between these two types is in the average repetition rate. The burst emission signal consist of pulses detectable from background noise and well enough separated in time so that there is not a lot of overlap. If resolution of individual pulses is not possible then the emission is called continuous emission.

The mechanics of acoustic emission, whether continuous or burst, rely upon the release of energy at a continuous source such as dislocation motion or burst source such as crack advance. The released energy propagates as a stress wave to a free surface which then oscillates, producing either a pressure on a piezoelectric type transducer or interfering with an optical deflection measuring device. In each case, the pressure or deflection reading is transformed to a voltage time output.

The amplitude of continuous emission is usually lower than that of burst emission. Generally, the amplitude of an acoustic emission process will have some correlation with the volume of the region producing it. Since continuous emission is a superposition of many bursts, the volume of each region producing a burst is necessarily small. Therefore, the amplitude of each burst and thus the continuous emission is low.

3.2.2. Choice of Parameters

The type of emission, whether it is burst or continuous is the first consideration for deciding the choice of the parameters for further analysis. For continuous wave emissions, amplitude and frequency analyses are more meaningful. For burst type emissions, ring down counting and energy analysis are useful. Amplitude and rate parameters are most easily measured and have been more widely used. In grinding process continuous AE signals were generated. Amplitude and frequency analysis were selected in this research.

3.3. Grinding and Acoustic Emission

Acoustic emission sensing techniques have been under development for the last thirty years for application in materials science and aerospace engine testing. The use of AE for the monitoring of the grinding process is a relatively young technology. In the last ten years a flurry of technical papers from Germany, Japan and the US have attempted to correlate the AE signal to chatter Inasaki [50], dressing control Inasaki [51], contact detection Dornfeld [52], burn detection Koenig [53], ductile/brittle mode transition Bifano [54] and differing wheel wear phenomenon Hundt et al [55].

Grinding is the most popular method that is used to machine ceramic materials using diamond grinding wheels. Each grain on the diamond grinding wheel surface can be considered as a micro-cutting tool and has its own AE event. The conditions of the grains on the wheel surface change rapidly due to the grinding of hard material such as silicon nitride material. This will effect on the AE events of the individual grains that reflect the efficiency of the material removal or damage may occur. Therefore, it is of paramount importance that such damage be detected at the early stages of machining in order to avoid catastrophic failures. These grains remove the material from the ceramic surface at high speed. Sensors should, therefore, be used with a high bandwidth to be compatible with the high grain contact frequencies of several hundred KHz.

Webster et al [56] showed that, AE signals is a useful tool for controlling the grinding process and the AE is prior to grinding forces for detecting wheel/workpiece

contact as start of cycle. They also showed that normal force/AE ratio shows a good correlation with cross-lay surface roughness and can detect grinding wheel burn. They concluded that the technique they used requires further development for real-time crack detection and control.

The predominant parameter studied in previous AE research is the root mean square RMS filtered signal AE_{rms}. Although they contain much information of interest, due to their inherent averaging operations AE_{rms} signals are to some degree insensitive to impulsive events that may occur during a grinding cycle. An additional but less published parameter used by Liu [57] is kurtosis, which is much more useful for identifying spontaneous events within the raw AE signal. Liu [57] has built an analogue kurtosis meter to investigate a narrow bandwidth in order to achieve the best signal to noise ratio (SNR) from the grinding process. Dornfeld [58] and Inasaki [51] have introduced fluid coupling as a method to minimise acoustic path variations during chatter investigations. In this investigation a stream of grinding fluid was directed at an area of interest to give a constant SNR.

Webster et al [56] has used a recursive least square filter RLS to separate the tonal part (distortions of strain waves that propagate from the grinding zone to the sensor) from the stochastic part (from grinding). The RLS filter is an innovative means of recovering a signal which has been substantially altered in transmission. This method is different from conventional techniques in that it does not require the system which produces the distortions to have properties which remain constant in time.

The physical coupling of the AE sensor to the part being ground is crucial for obtaining a high SNR. Dornfeld [58] has shown that mechanical sensor contact in close proximity to the grinding zone is extremely effective. However, since the grinding zone is not constant and moves relative to the workpiece, the signal measured by a fixed sensor will vary in amplitude.

Typically, AE monitoring of machining or grinding operations requires a long signal transmission path. In order to detect abnormal conditions, it is important to

prevent the attenuation and distortion of AE signals on the way to the transducer. This is especially true in high speed cutting. Here, noise levels are very high and it is most important to minimise the attenuation of AE signals on the way to the transducer. Such attenuation of signal consists of the material attenuation and the interface attenuation. Though the attenuation in wave guides is not negligible, a great part of the attenuation is caused by the interfaces. Many types of interfaces actually exist; e.g. at joints by adhesives or by bolts, at interference fitting joints, and at joints buffered bearing.

The band pass cut-off frequencies are often based upon experimental tests. Koenig [53], states that he has conducted many experiments collecting data over different frequency ranges and with different band widths to establish the best correlation with various parameters. This empirical approach of band passing can be time consuming and may result in the loss of important data by rejecting a wide range of frequencies within the raw AE signal.

Hundt et al [55] have carried out studies in measuring AE during the grinding process and in a frequency range up to 3.5 MHz. Single grain experiments shows different wear phenomena to be readily distinguishable by their individual AE signature at these frequencies as shown in Figure 10. The high grain contact frequency of the real process, however, produces strongly overlapping AE signals. A strategy was developed to separate and to describe several different AE sources. Their correlation to physical events is the object to further research [55].

3.4. Crack Initiation and Propagation Monitoring Using AE Technique

In material removal processes, AE signals are due to either fracture or plastic flow. Because elastic waves propagate with frequencies from 100 KHz to 2 MHz, well above most structural natural frequencies, machine vibration will not influence the AE signals. Acoustic emissions are therefore ideal for characterising the material removal activity.

In materials testing, noise level is very low since tests are carried out under the best possible conditions. On the other hand, machining and grinding are made in the shop site where levels of high noise are common. Sometimes strong AE signals are generated even in normal cutting or grinding. These create an interference with the AE detecting system. One of the most difficult problems in applying AE techniques to machining processes is the sampling of the signals in the rough shop environment. Due to the low signal energy, the sensors must be very sensitive.

Frequency discrimination is among the most commonly used techniques for differentiating between damage related events and other sources, such as vibrations. These latter events, although high in intensity, usually occur at frequencies below 100 KHz. On the other hand, damage events such as crack growth, typically have high acoustic amplitudes in the frequency region between 100 KHz and 1 MHz. Frequency analysis of raw AE signals using fast Fourier transform method was conducted to investigate the crack initiation and propagation during the experiments in this research. A pre-amplifier was used to capture the signals between 100 KHz to 1.2 MHz, then signals were stored using a digital oscilloscope for further analysis.

Critical defect sizes in brittle materials are among the smallest of all materials of the order of 1 μm to 50 μm depending upon the application and the material. For polycrystalline the critical defect size is in the order of grain size. In silicon nitride structural materials, the critical defects are silicon inclusions of around 25 μm in size, measured using ultrasonic by Evans et al [59]. This defect of silicon nitride was detected in this research for unground ceramic (sintering damage) using 100 MHz acoustic microscopy at a depth of 500 to 1000 μm from the unground surface of the silicon nitride material.

The main AE sources in grinding are shown in Figure 11. The single grain pulse is a combination of the impact of the grain on the workpiece, of the wear phenomena, and of the fracture of the workpiece material (e.g. indentation cracking). Particular emphasis was placed on obtaining the spectrum of the signals. The spectrum was important because the grinding process and the growth of cracks is a nearly stochastic

process, hence one of the main reasons for this statistical approach. The statistical approach was pursued in the hope of being able to characterise certain parameters of the grinding process, and hence, any uncharacteristic behaviour could be attributed to certain phenomena such as cracking or mode of material removal.

The removal of material of ceramic materials is governed by brittle and ductile grinding modes simultaneously. Cracks associated with the brittle fracture occurred. If the characteristic frequency ranges of crack formation or propagation during grinding process was known, e.g. 600-800 KHz, this characteristic frequency range could be used to band pass the AE raw signals using a band pass filter. The process of detection of crack formation or propagation may become possible. A similar approach has been successfully carried out by Eda et al [60], for the detection of thermal grinding cracks of hardened steel.

A method for detecting grinding cracks during the grinding process has not yet been full developed. If such a method were available, a workpiece with grinding cracks could be rejected, or the grinding conditions would be changed so that cracks were not produced or minimised on the ground workpiece. Therefore under certain controlled conditions, it is possible to machine brittle materials using ductile mode grinding, in which material is removed by plastic flow, leaving a crack-free surface.

On the other hand, in a flexible manufacturing system which requires a high level of manufacturing automation, in-process monitoring is a key factor, since reliable information about the state of the process is required for feedback controllers to function effectively. Among the different methods for in-process monitoring, acoustic emission signal analysis has proven to be an effective technique in metal cutting, tool wear and tool breakage, as well as crack growth and chipping of ceramics.

Eda et al [60] successfully used band pass frequency approach to detect grinding cracks in-process. They performed grinding tests under abusive conditions to hardened steel, with the aim of detecting grinding cracks in-process by acoustic emission signals. The signals were analysed and compared with the signals produced before the grinding

cracks were formed. Acoustic emissions between 600-800 KHz were detected when grinding cracks were formed, but were not detected when grinding cracks were not formed. By utilising this relationship, it becomes possible to detect grinding cracks in-process.

Eda et al [60] stated that since the acoustic emissions caused by grinding cracks are mixed with those produced by the grinding process itself, it is impossible to distinguish them first by looking at the signal. But when the AE signal was passed through the characteristic frequency range of crack formation 0.6-0.8 MHz band-pass filter a number of large grinding cracks formed during grinding operations were detected in-process.

The energy introduced in the layers close to the surface of ground ceramic always leads to the formation of different crack types. These cracks may be created on the surface or in the sub-surface at a few microns from the ground surface. In this research it was assumed that every single grain contact generates a stress pulse in the workpiece and has its own AE event. Bond materials and abrasive grains issue different signals when fractured Hundt et al [55].

The energy of breaking atomic bonds during the material removal can be related to the energy changes generates in the form of stress wave or acoustic emission. A crack of longer size may generate a stress wave of higher amplitude. Malen and Bolin [61] calculated theoretically the amount of the stress amplitude during plastic deformation and crack propagation. According to this theory, the stress wave amplitude at time t for crack propagation can be expressed as;

$$\sigma (r , t) = \mu\delta\int_s \mu_z \, ds \qquad (3.1)$$

Where
μ_z = The crack opening displacement
μ = Shear modulus
s = Crack surface
δ = Wave propagation factor

For the specific case of crack extension in brittle material, Diei and Dornfeld [62], used the above equation and they obtained the relationship;

$$\sigma\,(r\,,\,t) = E_1\, a^{\beta/2}\,(a\Delta)^{1/2}\, fA\Delta \qquad (3.2)$$

Where; E_1 = Material and geometrical-dependant constant.
a = Crack length.
A = Crack area.
β = Constant, depends on the boundary conditions.

In a similar attempt, Desai and Gerberich [63] proved that the stress wave amplitude (σ) is proportional to both stress intensity (σ_0) and incremental area swept out by the advanced crack ($A\Delta$);

$$\sigma = \xi\, \sigma_0\, A\Delta \qquad (3.3)$$

Where; ξ = Material and geometry dependent constant depends on the specimen size and the crack length.

These theoretical calculations are in good agreement with the result of this work. Increasing the grain depth of cut causes more cracking and surface damage which generates high-amplitude stress wave containing more AE energy. The results obtained by other researchers also indicate that AE amplitude and energy increase when there is more material cracking. Dalgleish et al [64], observed, during a study of the fracture toughness of alumina, that the number of AE events depends on the amount of sub-critical cracks growth. They also studied the amplitude distribution of AE signals and found that low-amplitude and short duration events were generated when the fracture was characterised by grain boundary flow, but high amplitude events were the result of a catastrophic failure. In this research, however, the results only indicate that an increase in percentage of surface fracture is accompanied by low-amplitude long-duration events which can be assumed as the characteristic of brittle mode grinding. This was observed when coarse wheel grit sizes were used. Higher AE spectral amplitude was observed when a smooth ground surface was produced. However,

underneath this surface, sub-surface cracks were found. This was observed when small grit sizes were used. This could be due to the higher friction contact between small grit size and workpiece was occurred at high levels of grinding depth of cut.

Cuthrell [65] suggested that a distinct peak at higher amplitude could be a characteristic curve shape for the fracture of the brittle material during low speed drilling and scratching tests of different hydrogen embrittled ceramics. Konsztowicz [66] reported that low energy initial cracking within the glass phase of both zirconia and alumina during thermal shock is of short duration.

3.5. Acoustic Emission Instrumentation

An acoustic emission system uses a pre-amplifier connected to a transducer. The pre-amplifier consists of a low noise input stage, band pass filters and a low impedance output stage. These pre-amplifiers are designed to have a relatively flat frequency response between about 20 KHz and 2 MHz without the band pass filters. An AE system usually includes post amplifiers and signal processors of various kinds. This allows the use of signal processors with fixed input ranges of thresholds in conjunction with fixed gain amplifiers. More specialised equipment often associated with a system include transient recorders, spectrum analysers, tape recorders, distribution analysers and special discrimination circuits. Recently, microprocessor based systems have become commercially available. These systems are capable of performing all the standard methods of single channel analysis as well as performing source location for two to eight AE channels.

Based upon the above AE instrumentation it is possible to extract information about the nature of the AE signals. However, reliable structural integrity evaluation in real time can be achieved by involved instrumentation hardware. As a result, a great deal of interest has arisen lately in the application of expert systems in conjunction with both acoustic emission and operational monitoring data to maximise the utilisation of large amounts of information available from operating plants and structures.

3.5.1. AE Transducer

A transducer is a device that generates an electrical signal where it is stimulated by AE waves. Most transducers used in conventional AE systems are piezoelectric crystals and have been developed for high sensitivity at frequencies in the range of 50 KHz-1 MHz. Their response is relatively of narrow band and resonant type. However, broad band transducers are also available, whose frequency response band-width is extended up to 2 MHz. A transducer is the most critical component of any AE measuring system. As a result, if any meaningful source characterisation is to be carried out, the response of the transducer should be extremely satisfactory.

Piezo-electric transducer sensor physical acoustic [94] model S9225 with a broad band sensitivity of 1.2 MHz was used in this research. The transducer dispatched electrical signals which were amplified by a nominal gain of 40-60 dB from the pre-amplifier physical acoustic model 1220A. The transducer and the pre-amplifier are powered by their own power supply. The amplifier also filter the signal and reject the signal outside the range of 100 KHz to 1.2 MHz. Subsequently, the signals were captured and digitised by digital storage oscilloscope 'gould 450'. It had the ability to sample at a rate of 100 mega samples/sec. In this test sample frequency was selected to be twice the sensor frequency.

3.5.2. Detection Threshold

The detection threshold, sometimes called sensitivity of an AE transducer is defined as the minimum level of the signal amplitude that can be detected above the background noise. Since the incoming signal cannot be intensified and the noise cannot be reduced by signal averaging as the signal is changing with time, it is important that the transducer and preamplifier combination generate the minimum of background electronic noise.

3.6. Calibration of AE Sensor

Transducer calibration must be carried out in absolute units of displacement if it is to be correlated with dynamic phenomenon. It is also necessary to calibrate the frequency response of the transducer. The following are some methods used often for calibration of AE sensors.

◊ **Face to Face Transducers Calibration**

A pre-calibrated sensor is used as a transmitter. A known voltage signal at different frequencies is fed to this as input. The sensor to be calibrated is coupled with the transmitter face to face and the output voltage signal is measured to obtain the frequency response of the transducer. This is the conventional ultrasonic method and generally used for transducers commercially available today.

◊ **Pencil Lead Breakage**

This method was developed through experimentation by Arved Nielsen and is sometimes called the Nielsen lead break method. A 2H pencil lead 0.5 mm diameter is usually utilised. The lead feed button is pressed repeatedly to extend a definite length of lead and then it is made to break against an even surface to which the AE transducer to be calibrated is coupled. To obtain repeatable constant AE source, the lead is broken at a fixed distance from the sensor, maintaining the same length and angle of contact of the lead with the surface.

◊ **Helium Jet**

A helium jet is also used sometimes as a source with a broad band random signal characteristic. A drop ball test and spark impulse are other types used for the calibration of AE transducers.

Though these calibration methods are sufficient in providing a record of the displacements of a point on the surface of the object being examined by the sensor, there are fundamental problems encountered during calibration, which need understanding for effective application of these methods, Eitzen and Breckenridge [67].

The frequency response of the AE sensor used in this research was calibrated using face to face method.

3.7. AE Signal Processing

There are several ways to process the AE signal. Most of them measure the characteristics of the individual burst emission and all of them can give useful information in an AE experiment. The main aim of the signal processing and display is to identify the character and significance of the event. The following are the more common ways by which signals are processed.

- Ring Down Counting Analysis.
- Energy Analysis.
- Amplitude Distribution Analysis.
- Frequency Analysis.

These methods of analysis are further discussed below.

3.7.1. Ring Down Counting (RDC) Analysis

Most acoustic emission signals have been found to be of relatively short duration (0 ~1 msec), reach maximum amplitude early in the signal and decay nearly exponentially to the level of background noise.

Ring down counting (RDC) is one of the easiest and most reliable methods of analysing AE signal. The principle of RDC is to count the number of times a threshold voltage is crossed by oscillating transducer output caused by acoustic emission. Advantages claimed by RDC are that the count obtained from a given event increases with signal amplitude and there is consequently some weight in favour of events of larger energy. Secondly RDC automatically improves noise rejection. However, results obtained by this analysis are strongly influenced by the geometry of the specimen, the properties of the transducer and its coupling to the specimen, the precise detection threshold and the performance of amplifiers and filters. Therefore, there are difficulties in the use of this approach for fundamental studies. It is commonly assumed by Harris et al [68], that sensor output can be modelled;

$$V = V_i \sin(2\pi ft) \exp\{-t/\iota\} \quad (3.4)$$

where; V = Output voltage of sensor
t = Time
V_i = Initial signal amplitude
f = Resonant frequency of the transducer
and; ι = Decay time of the envelope which is a function of ultrasound attenuation in the structure and in the transducer.

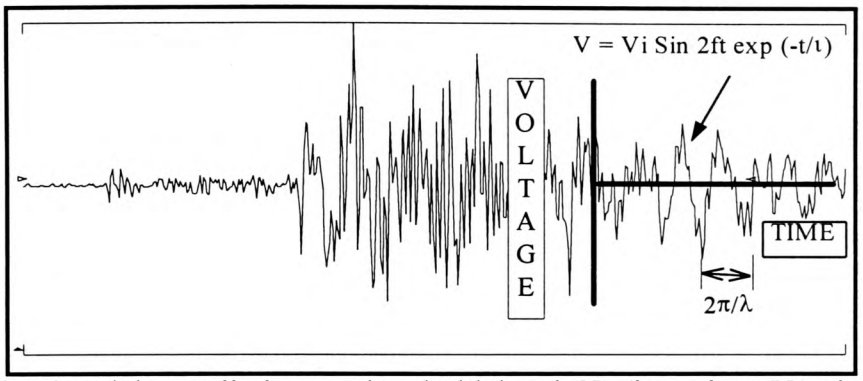

If this signal is applied to a threshold level V_t (less than V_i) the number of threshold crossings registered for the emission event is:

$$N = f \iota \ln \{V_i/V_t\} \quad (3.5)$$

The important features of the AE signals are the average repetition rate of the signals, the individual burst of amplitude, the energy of the burst and the frequency content. Other important characteristics include the signal rise time, decay constant and signal length.

3.7.2. Energy Analysis

Direct energy analysis can be achieved by digitising and integrating the wave form signal in accordance to the equation below or by designing a device to perform the integration electronically. The energy of the AE burst is defined by the equation, Evans and Lintzer [69];

$$E = 1/R \int_{te} V^2(t)\, dt \quad (3.6)$$

Where; V (t) = The time dependent voltage
R = The impedance of the measuring circuit.
$_{te}$ = Event duration.

The energy is usually measured after amplification of 80-100 dB. The commonly measured root mean square voltage (RMS) is closely related to the energy rate. It has been shown that energy analysis has an advantage in signifying high amplitude events for which the RDC may fail to register the proper relative magnitudes.

3.7.3. Amplitude Distribution Analysis

Amplitude distribution analysis is very useful in characterising the AE generated from a material. Amplitude relates to energy. Therefore, it is simpler to discern the physical meaning from this kind of signal processing. Most measurements of amplitude distributions reported to date have used the peak voltage of acoustic emission burst as the amplitude parameter.

Two Functions are generally used to describe the distribution of peak amplitudes Pollock [70]. First $n(V_i)$, function of emission population whose amplitude exceeds V_i, second $m(V_i)$, function of emission population whose amplitudes fall between V_i and $V_i + \Delta V_i$. These two functions are related as follows;

$$m(V_i) = d_n (V_i) / dV_i \qquad (3.7)$$

It may be noted that $n(V_i)$ is a monotonically decreasing function whereas $m(V_i)$ may show peaks if there is a tendency for emission amplitudes to cluster around particular energy values with the detection range. It is reported that the experimental data often approximates to power-law distribution of the form;

$$n(V_i) = (V_i/V_o)^{-b} \qquad (3.8)$$

Where; V_o = The lowest detectable amplitude
b = Characterises the amplitude distribution.

3.7.4. Frequency Analysis

The most common method of the determination of the frequency content of AE signals is to measure their power spectrum. Both frequency spectral analysis and auto-correlation analysis have been employed as in Ono et al [71]. Since the predominant frequency present in the power spectrum is inversely proportional to the duration of dynamic event, these measurements can provide information on the time scale of an AE process. This in turn may be used to characterise the evolution of the dynamic source event. In this research the continuous AE raw signals were analysed and displayed as frequency and spectral amplitude.

3.7.4.1. Basic Principles of Frequency Analysis

The basic principle of frequency analysis have been treated in several textbooks of random signal analysis, Bendat [72]. Namely, the signal at the source can be represented in the time domain as x(t), while the observed signal after undergoing detection and amplification is y(t). The effect of the system represented by $h(\tau)$ and is defined as the system impulse response when $x(t) = \delta(t)$. This is shown in the figure below. The frequency response function H(f) where f is the frequency is given by the Fourier transform:

$$H(f) = \int_0^\infty h(\tau)\, e^{-i2\pi f\tau}\, d\tau \qquad (3.9)$$

$$= h(f)\, e^{-i\theta(f)} \qquad (3.10)$$

With the gain factor;

$$H(f) = [H^2{}_R(f) + H^2{}_I(f)] \qquad (3.11)$$

and the phase factor;

$$\theta(f) = \tan^{-1}[H_I(f)/H_R(f)] \qquad (3.12)$$

Where HR (f) and HI (f) are the real imaginary parts of the function H(f) and I = $\sqrt{-1}$.

In the time domain, y(t) is calculated from the convolution integral.

$$y(t) = \int_0^{\infty} h(\tau)\, x(t - \tau)\, d\tau \qquad (3.13)$$

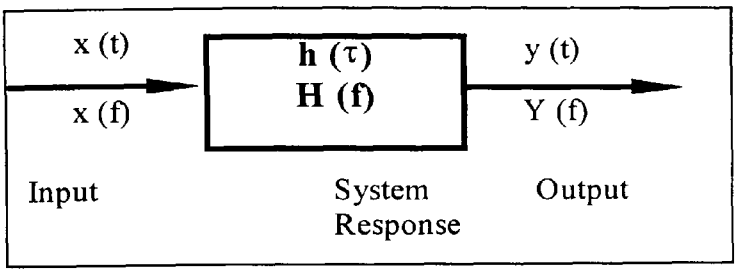

If the response of the system is linear, then, in the frequency domain; y(f) = H(f) X(f)

Where Y(f) and X(f) are the Fourier Transform of the output and input signals respectively. By performing a spectral analysis on the detected and amplified signals Y(f) obtained Bendat [72]. In acoustic emission studies, only the power spectrum S_y is obtained, or

$$S_y = \int_{-\infty}^{\infty} R_{yy}(\tau) \cos 2\pi f\tau d\tau \qquad (3.14)$$

With $R_{yy}(\tau)$ the auto-correlation function;

$$R_{yy}(\tau) = \lim_{T \to \infty} 1/T \int x(t)\, x(t + \tau)\, d\tau. \qquad (3.15)$$

3.7.4.2. Sampling Theorem

If the highest frequency component in a signal is F_{max}, then the signal should be sampled at the rate of at least 2 F_{max} for the samples to describe the signal completely;

$$F_s > 2\, F_{max} \qquad (3.16)$$

Where F_s is the sampling frequency or rate. Thus, if there is a maximum frequency component in an analogue signal of 4 KHz, then to preserve or capture all the information in the signal it should be sampled at 8 KHz or more.

Sampling at less than the rate specified by the sampling theorem leads to a folding over or 'aliasing' of 'image' frequencies into the desired frequency band so that the original signal cannot be recovered if we were to convert the sample data back to analogue. An important point to remember is that a signal often has significant energy outside of the highest frequency of interest and / or contains noise, which invariably has a wide band width. Thus, the sampling theorem will be violated if the signal or noise outside the band of interest is not removed. In practise, this is achieved by first passing the signal through an analogue anti-liasing filter.

4. GRINDING WHEEL TOPOGRAPHY

4.1. Introduction

There are many variables in the grinding process and the majority of these variables influence the final strength of the ground component. One of the most significant variables is the type of grinding wheel used. The choice of grinding wheel specifications such as material type (in the case of conventional wheels) and bond type and grit size (in case of diamond grinding wheels) is very important for successful grinding operation. The influence of the grinding process on workpiece and grinding wheel is shown in Figure 3.

4.2. Grinding Wheels and Grinding of Ceramic Materials

The condition of the grits or sharp edges on the periphery of a grinding wheel has a major influence, not only on the damage induced in a ground specimen, but also on the surface finish and the required tolerance, especially during the grinding of brittle materials.

McEachron and Lorence [73], investigated the interaction of different type of super abrasives. They concluded that diamond grinding wheels are more effective for the grinding of ceramic materials. Diamond wheels slowed the lower crystal wear and give a higher grinding ratio compared to other grinding wheels such as cubic boron nitride wheels (CBN). Wortendyke [74], summarised the influential factors with respect to diamond wheels in grinding of ceramic as follows;

- Abrasive's brittleness: A high degree of brittleness leads not only to lower tensile stresses but also to lower grinding ratios and a decreased chip-removing capacity.
- Grit size: Finer grains lead to both diminished tensile stresses with lower grinding ratios and to decreased chip-removing capacity.
- Bond type:

- Resin bond is elastic and thus able to absorb vibration in the grinding zone. For grinding ceramic material, resin bonds are most frequently used.

- Sintered metal bond where the grains are strongly bonded; the grinding wheel is very rigid. A high grinding ratio and a good chip-removing capacity can be achieved. However, it must be pointed out that increased normal grinding forces are produced.

- Ceramic bond: The well-known advantage of the potential high porous content of grinding wheels with this bond also has a positive influence on the machining of ceramics, since it leads to an increased movement of coolant through the grinding zone.

- Electroplated bond: This type of bond is occasionally used for ceramic materials that are easier to grind, such as aluminium oxide ceramics.

Guide lines for diamond wheel selection for grinding ceramic were investigated by Pung, R. [108]. He presented data on the performance of vitrified bonded wheels compared to resin bonded diamond wheels. The objective of his study was to determine if correlation could be found between grindability and some measurable physical properties of the ceramic materials.

Abrasive surface topography is normally assessed by considering the wheel specification together with the superimposed dressing condition. High efficiency and high performance grinding can be expected by using a diamond grinding wheel because of its strong bonding force to hold cutting edges. But in grinding of advanced ceramics, attrition wear of cutting edges can be caused very easily. Therefore truing and dressing must be operated frequently.

Truing as defined by King [83], is a process of regeneration of the desired surface wheel geometry and its attainment reduces runout and prevents cutting force changes during a complete wheel revolution. This helps reduce any eccentricity remaining after the hub mounting and avoids excessive vibration. In some cases it also prevents chatter during the grinding process.

Dressing is the regeneration of a desired surface condition on a grinding wheel, by either opening or closing up a wheel surface and to remove grinding debris from the

surface. The amount of dressing must be carefully monitored since excessive dressing of the wheel may cause bond material to be abraded and premature loss of grits may occur.

Grinding performance depends on the dressed condition of the wheel which is characterised by the protrusion heights of abrasive grains Syoji et al, [82]. Small protrusion height for example, means small chip pockets and leads to a contact between the bond components and the workpiece, resulting in an increase of grinding forces and heat generation. This may cause strength deterioration through the initiation of sub-surface cracking of ground ceramic materials.

4.3. Dressers Types

Dressing tools are of many various forms and are specified for certain applications. The effect of dresser type on the surface topography of a grinding wheel was investigated by Matsui [75]. He used two types of diamond dresser and studied their effects. One effect was the transferability of dresser profile onto the grinding wheel working surface, and the other was the sharpness of grain cutting edges formed by dressing.

Single and multi-point diamond dressing tools are used extensively to true and dress conventional aluminium oxide and silicon carbide wheels, and also to true cubic boron nitride (CBN) grinding wheels. The diamond creates a surface with sharp cutting edges.

The range of grinding wheel periphery conditions achievable with a diamond tool is limited, almost certainly requiring a further dressing operation using another material. Shafto [76], stated that using a diamond dresser for dressing diamond wheels produces a blunted peripheral grit conditions which affect the grinding operation condition. Also, in term of losing diamond grits as well as reducing the life, of the diamond dresser will be more costly.

Conventional abrasive stick dressers are also used either hand held or mechanically fed. Inasaki [77], analysed the effect of both a silicon carbide abrasive stick, and a silicon carbide brake truing device on the subsequent performance of a resin diamond grinding wheel when grinding a silicon nitride workpiece. He found that the time necessary to achieve a fully dressed wheel was a function of abrasive grain loading in the dressing operation, and the grain load can be used to uniquely describe the dressing efficiency, independent of the dressing method of condition used.

Taketo et al [78], compared the dressing efficiency of a resin bond glass fibre stick to conventional silicon carbide and aluminium oxide abrasive. It was found that the glass fibre dresser reduced the grinding forces and achieved greater grinding ratios than the abrasive silicon carbide and aluminium oxide materials.

Steel dressing devices are used to true and dress diamond grinding wheels. Notter and Bailey [79] have shown that low wheel speeds (10-20 m/s) are most efficient in the dressing operation. Rezeai [80], has investigated the various dressing methods used such as; continuous dressing, intermittent dress, or pulse dress. Continuous dress processes are usually used on conventional aluminium oxide, and silicon carbide wheels in creep feed grinding operations, where the peripheral condition alters rapidly. Intermittent and pulse dressing are processes when dressing occurs non-continuously. The wheel is allowed to wear via attrition, generating a wear flat to a point before the resultant grinding operation becomes unacceptable. Pulse dressing was introduced in diamond roll dressing of conventional wheels since the spark-out operation was found to cause blunting of the abrasive grits, in a grinding wheel.

The performance of a new 'cooltip' dresser has been evaluated during this research, Maksoud and Mokbel [81]. The dresser is used to dress alumna wheels (WA60KV), with a view that it may replace the more expensive single point diamond dresser. It is expected that this new dresser will open the way for the production of a whole range of new dressers designed specifically to suit different types of grinding wheels.

In this research, the truing and dressing process was carried out by using a rotary tool dresser at different dresser/grinding wheel speed ratios. An aluminium oxide truing wheel driven by servomotor was used in this investigation. The wheel condition was studied by grinding one pass on a mild steel specimen.

4.4. Grinding Wheel Condition Monitoring Technique

Conditioning of the wheel is a periodical correction to the wheel face to achieve truing or dressing or both to restore wheel performance. Scott et al [84] analysed the wear of conventional grinding wheels by noting their condition after different grinding tests. They also used random process analysis to investigate the effect of single point diamond dressing on conventional abrasive grinding wheels. It was shown that single point diamond shape and cross feed affects the distribution of profile heights.

Syoji et al, [82] investigated the mechanism and the phenomenon in the operations of truing and dressing of diamond wheels. They described a new three-dimensional technique which used scanning electron microscopy SEM to measure the diamond grit height, and discussed the influence of the protrusion height on grinding performance.

An optical sensor system based on laser triangulation was introduced by Tonshoff [85] to measure macro and micro geometrical quantities of the grinding wheel. The system can be used to take measurements of the grinding wheel roughness up to a cutting speed of 30 m/s. The results obtained by Tonshoff [85] were influenced by the turbulence of the coolant around the grinding wheel. Various measuring techniques were used to characterise the peripheral condition of the grinding wheel;

◊ Visual Methods

Light microscopy and electron microscopy are visual tests for the grinding wheel surface condition. The limitation of light microscopy is that the small depth of field makes it difficult to capture peaks and valleys on the grinding wheel surface, Thomas [86]. One of the problems with visual methods of wheel analysis is that they do

not easily lend themselves to quantitative analysis. Also, they require removal of the wheel from the spindle in most cases with the consequence of losing production time.

◊ **Stylus Methods**

By drawing a stylus across the surface of a grinding wheel at constant speed, the variation of its vertical displacement with time will represent the variation of height of the surface with horizontal displacement, Bhateja [87] and Davies [88]. This method is very difficult to be applied on-line. It is also not directly applicable to diamond grinding wheels, since the stylus may wear due to the hardness of the diamond grits.

◊ **Monitoring of Grinding Wheel Loading**

This is an indirect method for identifying the condition of a wheel. The method uses a measure of the grinding forces or power, (usually using a dynamometer) to reflect the condition of the wheel surface. High tangential forces usually indicate a higher percentage of wear flat area.

◊ **Imprint of Grinding Wheel Profiles**

The surface of a dressed grinding wheel can be checked by taking an imprint of the grinding wheel envelop profile (GWEP) on a mild steel workpiece, Maksoud et al [89]. It is not clear whether this method actually measures grain density or cutting-point density, a comparison was made of various stylus and taper print measurement on identical wheels dressed in the same way, Verkerk [90]. However most of these analyses are based on models which rely on the grinding groove being the exact replication of the grit size and distribution.

◊ **Acoustic Emission (AE) Technique**

An acoustic emission technique for monitoring the grinding wheel condition was investigated by Dornfeld and Cai [91]. They analysed the signals of AE generated from the surface grinding to measure wear-related loading of the grinding wheel and sparkout between the wheel and the work surface. They showed that the AE energy increases with the combined effects of wheel wear and loading. They also showed that this signal energy is a function of the undeformed chip thickness and that the signal

accuracy detects work/wheel contact and sparkout with a higher sensitivity than force measurement.

A system for monitoring grinding wheel condition using an AE sensor was developed by Matsumoto et al [103]. An AE sensor integrated CBN wheel was developed to define the tool life of the wheel. The detected AE signals are sent by wireless to the receiver outside of the grinding wheel. The system can detect the contact between the CBN wheel and the dresser. They also showed that when the chatter vibration occurs, a remarkable peak was observed in power spectrum of enveloped AE signals.

The structure-born sound emitted during the grinding process (AE) is especially suitable for such monitoring. The AE signal from the grinding, dressing and sharpening processes is not subject to temperature drift and is ultrasensitive under precision machining conditions, Konig and Klumpen [104]. As an indirect process parameter, the AE signal is characterised by much shorter response times as compared to machining forces or motor currents. They explained some AE applications for tool life monitoring, dressing fault diagnosis and sharpening process control. The AE_{rms} levels changed with the wheel condition they mentioned [104]. Dornfeld [111] has correlated the burn to AE spectral amplitude. He showed the burned workpieces to have higher AE spectral amplitude compared with unburned specimens.

A method of contact detection of dressing super-abrasive grinding wheels by using an acoustic emission sensor was described by Tonshoff and Heuer [105]. The sensor was placed next to the dressing tool. At the moment of contact between dresser and grinding wheel, the amplitude of the acoustic emission signal changes and so allows the detection of the first contact. They concluded that the success of this method is dependent on the noise which is produced by the dressing spindle.

4.5. Parameters for Characterisation of the Wheel Surface

A number of parameters have been identified to assess the condition of a grinding wheel surface. These parameters provide information on the height

distribution of the profile such as the centre-line-average (Ra), peak-to-valley height (Rt), etc. More comprehensive statistical parameters to describe the distribution of surface irregularities such as the probability density function (p.d.f) and the integral of p.d.f yield the cumulative distribution function (c.d.f) which is a useful parameter in specifying surface roughness.

The most universal of these is the Central-Line-Average (Ra) which is defined as the arithmetical average of the departures of the profile above and below the reference line throughout the prescribed sampling length.

A FORTRAN program has been written for these parameters to study the grinding wheel surface topography.

$$R_a = \frac{\sum_{i=1}^{k-1} f_i (y_i - Y)}{N} \qquad (4.1)$$

Where; $(y_i - Y)$ = Height from centre line

f_i = Frequency of height value

k-1 = Number of frequencies

and N = Total frequency $= \sum_{i=1}^{k-1} f_i$

Root mean square (RMS) is an alternative parameter which does have statistical significance. It is also known as standard deviation roughness (σ), derived from the variance (σ^2) of deviation from the centre line;

$$\sigma^2 = S_1 = \frac{\sum_{i=1}^{k-1} f_i (y_i - Y)^2}{(N-1)} \qquad (4.2)$$

Coefficient of Skewness;

$$S_2 = \frac{\sum_{i=1}^{k-1} f_i (y_i - Y)^3}{(N-1)(S_1)^3} \qquad (4.3)$$

Coefficient of kurtosis;

$$S_3 = \frac{\sum_{i=1}^{k-1} f_i (y_i - Y)^4}{(N-1)(S_1)^4} - 3 \qquad (4.4)$$

A system of measurement and analysis of conventional and diamond grinding wheels at truing and dressing has been developed in this research. The system is used to detect in-process changes of grinding wheel surface topography by using a flapper nozzle arrangement. A number of parameters have been identified to assess the condition of a grinding wheel surface. These parameters provide information on the height distribution of the profile such as the centre-line-average (Ra), peak-to-valley height (Rt), Kurtosis, Skewness, etc.

4.6. Grinding Wheel Condition Monitoring Using Flapper Nozzle Arrangement

Spatial distribution of sharp cutting edges on the surface of grinding wheels has an important effect on the characteristics of the ground components. Random protrusion of sharp edges can result in a combination of randomly distributed grinding forces. A well dressed and trued wheel is essential for monitoring and control of the grinding process. A system for on line detection of grinding wheel condition during grinding has been developed.

The system is used to detect in-process changes of grinding wheel surface topography by using a flapper nozzle arrangement. External triggering of the data acquisition system was provide to include more accurate assessment of the wheel

surface irrespective of the wheel speed. An experimental study of different dressing depths and grinding variables and their effect on the grinding wheel topography has also been investigated.

Description of the system, calibration, signals processing and digitisation techniques are explained in detail in chapter 5. Figure 12 shows a diagram of the instrumentation layout used for this technique of measurement and analysis. The flapper nozzle was located at a certain distance from the grinding wheel, this distance was predetermined to ensure an effective response from the transducer. When the wheel was running and an air supply is connected to the flapper nozzle a static pressure Ps was obtained, as shown in Figure 13. The optimum distance of the flapper nozzle from the grinding wheel surface can be determined by calibration. The arrangement was designed to have an on line link to a software program to give an immediate indication of;

- Truing condition of the wheel
- How much is removed from the wheel
- Dressing condition of the wheel as indicated by centre line average, root mean square, coefficient of Skewness and kurtosis, etc.

4.6.1. Experimental Results

Fine and coarse surface diamond grinding wheels were used to represent the range of wheels available. Dressing conditions for fine wheels are listed in Table 1. A truing and dressing process was carried out by using an aluminium oxide truing wheel driven by a servomotor at different grinding wheel and truing speed ratios. The different speed ratios gave different grit distributions on the surface of the wheel, which had a direct effect on surface integrity of the ground specimen. The depth of dresser was monitored using a linear variable differential transducer (LVDT).

An indication of the amount of actual material removed from the wheel periphery can be seen in Figure 15, where four dressing passes were taken. The

difference in nozzle/wheel distance between dress pass numbers 0 and pass 4 can be clearly seen. The figure also shows the runout section on the periphery of the wheel. The vertical axis on this figure shows the calibrated values of distance, extracted from the voltage values. Figures 16 and 17 show the method by which the dressing information, shown in Figure 17, was extracted from the flapper nozzle raw output, shown in Figure 16. This shows that a separation of truing and dressing information can easily be obtained by filtering out the low frequency content of the signal shown in Figure 16, the high frequency content of the signal obtained. The high frequency content of the signal is shown in Figure 17. This signal is used to indicate the wheel surface condition.

The truing of the wheel is quantified and indicated in Figure 16 and was obtained from the low frequency content of raw signal. Figure 18 shows the raw results of the flapper nozzle output voltages taken from the wheel rotates manually after being dressed with different dressing depth values. The figure shows the variation of the signal characteristics (represented by its RMS values) at different dressing conditions. The figure shows that the nozzle is responsive to changes in the range of 3-12 μm.

Figure 19 shows compiled results of several experiments. The aim of this set of experiments was to establish a direct relationship between the variation of RMS output signals from the transducer on the nozzle and the real Ra variation of the wheel surface. The Ra variation was obtained using a Talysurf. The Talysurf was used to measure the grinding wheel envelope profile (GWEP) on a mild steel specimen. An imprint of GWEP was taken on the specimen by one pass grinding.

The depth of cut was made so that it was higher than the maximum peak to valley distance on the wheel surface, in this case 50 μm depth of cut was taken as shown in Table 2. The parameters varied on this set of experiments were depth of cut during grinding and depth of dress on the wheel. Figure 19 was compiled from these parameters variations because both depth of cut and depth of dress can vary the wheel surface condition to different extents and the experiment was set to determine whether the nozzle can pick up any variation of the wheel surface, however small. The relation

extracted from the results shows that the R_a of the wheel relates to the RMS output of the nozzle by;

$$R_a = - 0.015694 (RMS)^2 + 0.475433 (RMS) + 1.133 \qquad (4.5)$$

This relation can be used as a calibration law for the flapper nozzle. This calibration relation will differ slightly with different transducers but it can be supplied with the nozzle. It is also advisable that each application should have its own calibration as explained in chapter 5. Table 3 shows a complete set of results which can be obtained from the written software. The results were obtained from a coarse wheel being used at a number of dressing passes. On each pass an effect on the wheel surface topography was obtained by the nozzle.

It can be concluded that in-process detection of diamond grinding wheel dressing and truing in both roundness and wheel flatness conditions by using a flapper nozzle arrangement is newly developed. The system design was used successfully and the results of experimental investigation of the system were reliable and accurate. The system can show how much is removed from the wheel and the truing condition. Statistical roughness of the grinding wheel surface condition and other surface profile parameters were analysed at different dressing and grinding condition depths.

4.7. Monitoring of the Grinding Wheel Condition Using AE Technique

Imprint of grinding wheel profile technique was used in this research by taking one grinding pass on a mild steel specimen. Different levels of truing and grinding wheel speed ratios and directions were investigated for three bond types of diamond wheel with three grit sizes each. An acoustic emission sensor with high frequency sampling of 1.25 MHz was attached on a mild steel specimen to monitor the wheel condition. The raw AE signals were then analysed using fast Fourier transform FFT. The AE spectral amplitude of different grinding wheel conditions represented by grinding wheel/truing speed ratios were then compared with the surface roughness of ground mild steel.

Figures 23 to 26 show the variations of the AE spectral amplitude and the surface roughness of one grinding pass imprint of the grinding profile envelop on mild steel specimens. It can be observed that low surface roughness (Ra $\approx$ 0.6 μm) was associated with high AE spectral amplitude as shown in Figures 23 and 24. This may be due to the higher friction on the contact between the grinding wheel and the workpiece. This could also be because the grinding wheel is blunt. These figures can give an indication about the wheel condition by observing the variations of the surface roughness and the AE spectral amplitude. The variations in both AE spectral amplitude and surface roughness shown are at different grinding wheel conditions for the same grinding wheel grit size and different bond type.

Figure 25 shows the variation of the surface roughness at different grinding wheel conditions of resin bonded grinding wheel with D76 grit size. The variations of both the surface roughness and the AE spectral amplitude can give a good picture which represents the grinding wheel surface condition. At wheel/truing speed ratio 0.5, it can be observed that the wheel was extremely sharp. This was represented by the surface roughness (Ra = 1.151 μm) of the grinding wheel profile envelop imprint. At this speed ratio where the wheel is rough, low AE spectral amplitude can be seen. This can be compared with speed ratio o.6 in the same figure to observe the difference. It can also be observed that at high surface roughness (Ra $\approx$ 1.3 μm) low AE spectral amplitude signals were generated as shown in Figure 26. This phenomena could also be because the grinding wheel surface was sharp and low interaction occurred between the grinding wheel and the workpiece.

From the above observations it can be suggested that the low surface roughness of grinding profile envelop imprint on mild steel specimens was associated with a higher AE spectral amplitude. Cast iron and vitrified bonded grinding wheels with the same grit size D46 produced smooth surface roughness, generated higher AE spectral amplitude as shown in Figures 23 and 24. Coarse resin bonded diamond grinding wheel with D126 grit size produced higher surface roughness and associated with low AE spectral amplitude generated from the wheel/workpiece contact as shown in Figure 26.

The aim of this part was to monitor the diamond grinding wheel condition by using the AE technique. This was achieved by imprinting the grinding wheel surface profile on mild steel specimens and measuring their surface roughness Ra. These results were then compared with the AE signals generated during the test. The figures mentioned above for different grit size, bond type and conditions indicate that the AE technique could be a useful tool to monitor the grinding wheel condition during the grinding process. This technique may be more accurate and can cope with the higher grinding wheel speeds due to the higher sampling frequency rate of the AE sensor used.

5. MACHINE TOOLS AND INSTRUMENTATION

This chapter describes the equipment and instruments used. The grinding equipment system and instrumentation were built to cover all the necessary areas in this research. Both speed-stroke and creep feed grinding as well as the grinding wheel topography measurements, acoustic emission monitoring with suitable data acquisition system were developed.

5.1. Grinding Machine

The equipment used in this research is a non- purpose built machine tool Jones and Shipman 'Fig 540' surface grinder of stiffness coefficient 18.5 N/μm as shown in Figure 27. An NC table feed controller and a more accurate control box for varying the grinding wheel speed were connected to the machine. It was modified to be applicable for speed-stroke grinding as well as creep feed grinding applications.

The table feed was driven by an AC servomoter using an NC control system, developed by Rexroth Ltd TRAN-01 (Indramat). The system allows continuously variable speed and the ability to reverse the motor direction. The depth of cut is monitored using a linear variable differential transducer LVDT, which gave digital readout. The output voltage of the LVDT transducer was calibrated and the conversion factor was m = 0.169 mv/μm.

5.1.1. Grinding Forces Measurements

A Kistler dynamometer (925A) piezoelectric transducer mounted on the table is used to measure the vertical and horizontal forces transmitted from the grinding wheel to the specimen as shown in Figure 27.

The output signal from the dynamometer was connected to two Kistler charge amplifiers to convert electrical charge signals into proportional signal, they consisted of twelve ranges, calibrated in mechanical units per volt and adjustment of the transducer sensitivity was made. The amplifier's charge can be driven to ± 10V, and they were set

at 50 N/Volts. This means the computer can be used to measure a maximum force of up to 500 N. The amplifiers were connected to an A/D card and the forces displayed on a PC screen using MAC software for windows [93].

External triggering facility for the grinding forces was used to trigger the data acquisition system when fast feeds were used (32767 mm/min). The data were then collected and analysed via specially written software capable of calculating and displaying the grinding forces.

5.1.2. Truing and Dressing the Grinding Wheel

Truing and dressing processes were carried out using an aluminium oxide truing wheel driven by a servomotor at different grinding wheel/truing speed ratios. It was mounted on a spindle which was allowed to rotate via two angular contact bearings, and was fixed on a dynamometer to monitor the dressing force. The truing wheel is driven by an AC servomoter as shown in Figure 29. A tachometer and stroboscope were used to adjust both truing wheel and grinding wheel speed to have different speed ratios. These ratios gave different grit distribution conditions on the surface of the wheel, which was found to affect the surface integrity of the ground specimen.

The surface of a dressed grinding wheel was then checked by taking an imprint of the grinding wheel envelop profile GWEP on a mild steel workpiece. An AE sensor was attached to the workpiece during the imprint grinding pass. The raw signals were then stored and analysed using a fast Fourier transform FFT for three different bond types of diamond grinding wheel, each with three grit sizes. These were carried out for different grinding and truing wheel speed ratios from -0.3 to 0.6.

5.1.3. Very High Infeed Set Up

The majority of today's grinding machines still employ conventional table speed. There is little information available on the effect of fast feed rates on strength and surface finish of ground ceramic component. The aim of this part of this research is to specifically seek information on the effect of high feed rates on ceramic grinding.

Purpose built very high spindle speed grinders of 50,000 rpm are very expensive. A cheaper alternative is to simulate the effect of the high spindle speed through increasing the feed rate, keeping similar relative tangential velocity between the wheel and the workpiece. This simulation is not complete because of the effect of diamond grits loading would not be the same. However, this effect was partially negated by using higher concentration diamond grits.

Although the higher concentration of diamond grits could improve the surface finish, the simulation is still not completely accurate because the chip pockets would still be different. The experiment was conducted using two types of ceramics, Sialon 101 and 201. The grinding process was based on a single pass in up cut direction. Because of the very high feed rates involved, a soft bond material was chosen for the diamond grinding wheel to minimise the possibility of cracks initiation at the edge of the specimens. A resin CDA 55N diamond grinding wheel with 140/170 mesh size with 75% concentration was chosen to give freer cutting action.

A speed stroke sub-table system with a numerically controlled servomotor was used to supply the higher feed rates. A photocell circuit was used in conjunction with data acquisition to allow for external triggering of grinding forces signals at the very high feed rate of 32767 mm/min as shown in Figure 27.

5.2. Grinding Wheel Topography Monitoring System

A system for on line detection of grinding wheel condition during grinding has been developed during this research. The system is used to detect in-process changes of grinding wheel surface topography by using a flapper nozzle arrangement as shown in Figure 12. External triggering of the data acquisition system was provided to include more accurate assessment of the wheel surface irrespective of the wheel speed.

The principle of the flapper nozzle was to use a high response miniature transducer (XCQ-093) to capture the variation of static pressure when the air issuing

from the nozzle impinges on the wheel surface. The miniature pressure transducer has a range of up to 500 psi with 20 mv/psi sensitivity.

The flapper nozzle was located at a certain distance from the grinding wheel, this distance was predetermined to ensure an effective response from the transducer. When the wheel was running and an air supply is connected to the flapper nozzle a variable static pressure Ps was obtained, as shown in Figure 13. The optimum distance of the flapper nozzle from the grinding wheel surface can be determined by calibration.

5.2.1. Calibration of the Flapper Nozzle/Grinding Wheel Distance

The calibration was made by taking the signal from the transducer at a location away from a solid surface, as shown in Figure 14. The location of the nozzle edge was changed until there was no change in the transducer output static pressure value. As the supply pressure changes, the transducer output static pressure also changes. The supply pressure was varied between 2 and 6 bars and Figure 20 shows the calibration curves at different supply pressures. From this curve, the distance of the nozzle from the wheel surface can be obtained. This distance ensures optimum response from the transducer. As the grinding wheel diameter reduces, the location can be readjusted accordingly. A calibration constant can also be extracted from this curve to convert pressure values to distance values. The fluctuation in the static pressure values correspond to different grit surface roughness heights. The output signal from the miniature transducer is linked to a data acquisition system.

5.2.2. Signal Processing of the Transducer Output

The raw signal from the transducer was first converted from voltages to micrometers by multiplying it by the calibration pressure constant taken from Figure 19. A software program was written (simulating a digital filter) to separate the low frequency signal information of less than 1 KHz. This signal was later used to indicate the truing condition of the wheel by calculating its RMS value. Also, by filtering out the high frequency information, the dressing condition can be obtained by calculating the RMS of the high frequency signal.

5.2.3. Digitisation Technique of the Raw Signals

The purpose of the flapper nozzle was to give an accurate picture of the wheel surface topography. In order to do this, the process of digitisation of the signal was designed so that a controllable distance between data points can easily be obtained. A space-wise digitisation procedure was followed. This was achieved by using two external triggers. The first external trigger was used to flag the point of starting digitising the signal on the surface of the wheel. A time delay facility in the software allowed the shifting of the starting point by a few microns at each wheel revolution. The second external trigger consisted of an opto-switch and a slotted disc.

The disc was divided into 180 slots which gave a trigger signal every two-degrees of rotation of the wheel. An electronic circuit was used to obtain further 10 triggers every two degrees. This meant that 1800 points at each revolution could be obtained. The 1800 points were spaced automatically to cover a full wheel circumference irrespective of the wheel speed. Controlling the delay time on each revolution allowed a very precise coverage of the wheel surface by the transducer signal as shown in Figure 12. A software program was then used to convert the separated high frequency signal to calculate the wheel surface parameters. These parameters are centre line average, root mean square, Skewness, kurtosis, etc.

5.2.4. Aerodynamic Interference Effects on the Transducer Output

Since the signals depend on the aerodynamic behaviour of a jet issuing from a flapper nozzle, the effect of air flow induced by the wheel rotation was investigated. A Pitot-tube connected to a micro manometer was used to measure the air flow around the circumference of the wheel for two types of grinding wheels rotating at different wheel speeds. The air speed around wheels with high and low porosity at different grinding wheel speed is shown in Figures 21 and 22. The speed of air output from the flapper nozzle was also measured for different nozzle/wheel distances. The air output from flapper nozzle was shown to be strong enough to avoid any interference from the air carried by the wheel rotation.

5.3. Acoustic Emission Technique Set Up

The main objective of this research was to investigate the initiation and propagation of cracks during the grinding of ceramic. The mode of material removal due to different levels of wheel and machine tool parameters was also investigated.

5.3.1. Data Acquisition Set Up

Acoustic emissions signals were picked up by using a piezo-electric transducer sensor, a physical acoustic [94] model S9225 with a broad band sensitivity of 1.2 MHz. The sensor was attached to the workpiece surface using pure petroleum jelly (Vaseline) as shown in Figure 32. The transducer dispatched electrical signals which were amplified by a nominal gain of 40-60 dB pre-amplifier, physical acoustic model 1220A. The transducer and the pre-amplifier are powered by their own power supply. The amplifier also filtered the signal outside range of 100 KHz to 1.2 MHz. The signals were then captured and digitised by digital storage oscilloscope, 'gould 450'. The oscilloscope had the ability to sample at a rate of 100 mega samples/sec. In this test sample frequency was selected to be twice the sensor frequency. The frequency response of the AE sensor was calibrated using the face to face method [110].

The stored data in the oscilloscope was then transferred directly to a personal computer via serial interface port as ASCII files using procomm package for further processing. Once the data was transferred to the computer, the data were then prepared by using word for windows to convert these ASCII files to text files to be suitable for analysis using fast Fourier transform FFT.

Based on the sampling theorem which states that a signal should be sampled at twice the maximum frequency of the source, the setting on the oscilloscope was of 20 μs/div., which gave a sampling frequency of 2.5 MHz and a signal duration of 200μs. The oscilloscope's functions were being explored to gain optimum use of the facilities available for the application e.g. sampling, repetitive capture, storage, cursor measurements etc. A few preliminary tests were carried out to ensure worthiness of the captured signal and aimed at optimising the sample storage.

From the specifications of the oscilloscope, the record length is 500 points (the time window on the oscilloscope has 10 divisions), if a setting of 20 μs/div is chosen then, the total time duration of captured signals 200 μs. 500 points were sampled over the duration, giving a sampling frequency of 2.5 MHz.

By using the pre-trigger mode, it allowed a section of the trace to occur before the trigger point could be acquired. The pre-trigger could be set anywhere between 0% and 100% of the time window. The pre-trigger setting showed good potential for use in this investigation, because it actually allowed the user to see what the wave form looked like before a high amplitude trigger event

The trigger delay allowed the capture of a trace following both the specified trigger and a specified delay. From the preliminary experiments it was observed that in normal capture mode with no delay or pre-trig settings, contact of the wheel and workpiece was triggering the acquisition and the recorded wave would be of that contact, so by making use of the pre-trigger, say 100 μs, a wave can be captured from where the wheel position is, a 100 μs after the trigger.

The raw signals transferred to the computer as ASCII files contained a set of numbers which were proportional to the amplitude (Volts). From the specification of the digital oscilloscope, the number is representative of 8 bits and 30 levels per division. In this case to convert these raw signals to volts, the signals should be divided by 30 and multiplied by the volts per division setting on the oscilloscope, as shown below;

$$V = (b / 30) Vs \qquad (5.1)$$

Where; V = The value in volts.
b = The numbers of the raw AE signals from the ASCII file
Vs = The volts per division setting on the oscilloscope.

Once the sequence is in volts the FFT is applied to 512 values, which yields transform in a series of complex numbers. The absolute values of the complex numbers are deduced to represent the amplitude spectral densities which are used with the

frequency as an indicator to investigate the crack initiation and propagation during grinding and bending tests of ground specimens. The mode of material removal was also investigated. Crack initiation on the ground ceramic components were characterised by comparatively higher spectral amplitudes in the 0.1-1 MHz frequency range. The grinding mode occurred during the material removal also characterised by the spectral amplitude. Low spectral amplitude AE in all the frequency range monitored means brittle fracture occurred at that time. These signals were compared with SEM observations on the surface and sub-surface of ground ceramic components.

5.4. Destructive and Non-Destructive Tests Used

Destructive and non-destructive inspections were carried out on the ground ceramic. Surface and sub-surface cracks were investigated carefully by the following techniques;

◊ **Surface Roughness**

The equipment used in this research was a "Rank Taylor Hobson" Talysurf 5 [95] which relies on stylus readings travelling across the ground surface of ceramic specimens. The stylus tip has a radius of less than 1.2 μm and has a variable inductance transducer which is connected to an electronic unit. The signal is electronically processed, and can be displayed graphically or numerically as a roughness average Ra value.

◊ **Scanning Electron Microscope (SEM)**

A scanning electron microscope SEM was used extensively in this research to inspect the surface and sub-surface damages of the ground specimens. SEM is also used to indicate the mode of material removal whether brittle or ductile. The ground ceramic specimens were coated with a very thin conducting layer of gold before the test was carried out. The SEM equipment used was STEREOSCAN 260 [96].

◊ **Three Dimensional Surface Topography**

A Zygo's New View 100 3D imaging surface structure analyser was used in this research [97] to measure the depth of cracks on the ground surface. It is a scanning

white-light interferometer that uses frequency domain analysis (FDA) to generate quantitative 3D images of surfaces. FDA is a mathematical method for processing complex interferograms in term of phases and spatial frequency.

The instrument includes appropriate optics for imaging an object surface and a reference surface together onto a solid-state imaging array, resulting in an interference intensity pattern that can be read electronically into a digital computer. Interferograms for each pixels or image points in the field of view are generated simultaneously by scanning the object in a direction approximately perpendicular to the surface illuminated by the interferometer, while recording detector data in digital memory.

◊ **Fracture Strength**

The fracture strength of the ground ceramic is varied due to different process parameters. In this investigation a bending tester "JJ M30K" [98] was used. The load was applied at a constant rate of 15 KN/min. Once the sample failed, the peak load at the point of failure was used to determine fracture strength and to estimate the crack size of the ground ceramic. An acoustic emission sensor was attached on specimens ground with and without cracks initiated on their surface as shown in Figure 33. Triggering level and delay time for the AE signals before the specimens fracture were recorded for further analysis.

• **Grinding Wheels Used**

Three diamond grinding wheels with three grit size each were used [99].

• Resin bonded diamond grinding wheel with grit size range D126 (BS 120/150), D76 (BS 200/240) and D46 (BS 350/400) with 50 concentration, 2.2 carats per cubic centimetre.

• Metal (Cast Iron) bonded diamond grinding wheel with grit size range D126 (BS 120/150), D76 (BS 200/240) and D46 (BS 350/400) with 50 concentration, 2.2 carats per cubic centimetre.

• Vitrified bonded diamond grinding wheel with grit size range D126 (BS 120/150), D76 (BS 200/240) and D46 (BS 350/400) with 25 concentration, 1.1 carats per cubic centimetre.

6. FINITE ELEMENT (FE) TECHNIQUE

6.1. Introduction

A computer model based on a finite element (FE) package was used to study the behaviour of ceramic in grinding. This package is being used to establish a theoretical model which was validated using the experimental results. This model was used to study crack initiation and propagation during grinding at different levels of grinding wheel and machine parameters. Normal and tangential grinding forces from experimental work were used as input to the FE model. These forces resulted from different wheel and machine parameters. The cracks initiated on the surface and sub-surface were then compared with those observed in the experimental work using SEM. The model simulates the process of grinding by applying these forces on the surface of the ceramic specimen.

The finite element model was used to divide the structure into a grid of elements (0.5-300 μm) that form a model of ceramic specimen. The model was then applied in such a way that zones of different deformation schemes can be identified. These were then used to simulate the process of crack initiation. By eliminating the grid elements where cracks appear, a further investigation into crack growth was then made. This model is the first reported attempt to include crack initiation and propagation in theoretical modelling of ceramic materials during grinding process.

6.2. Residual Stresses and Crack Initiation and Propagation

Grinding processes which remove material mechanically, introduce cracks on the surface and the sub-surface of ceramic materials. This damage is usually in the form of residual stresses, both compressive and tensile, surface and sub-surface cracks which have a major influence on the mechanical properties and integrity of the ceramic materials Johnson-Walls [112]. Residual stresses on ground ceramic surface have been detected using several methods. X-ray diffraction technique was used by Scott, J. [113].

Due to the relatively small amount of plastic deformation occurring in ceramic material when ground, the level of stresses is small.

The effect of increasing the diamond wheel grit size and number of dressing passes on the residual stress was investigated by Scott, J. [113]. In this research, a hole-drill technique to measure the residual stresses at different depths from the ground surface was tried. This process was unsuccessful because of the difficulty of controlling the depth of a blind hole using laser equipment. Also, an attempt was made using diamond tip drills, but it was also unsuccessful due to the difficulty in obtaining the required shape of the diamond drill tip.

The principle of this method is based upon the fact that when a small hole is drilled in a plate the residual stress in areas outside are partially relaxed. Residual stress that existed in the drilled area can then be determined by measuring the amount of stress relaxation that takes place in the area surrounding the drilled hole. In this method, a special purpose strain gauge rosette is attached to the component at the point of interest, and then a small hole is produced into the component through the centre of the rosette. The method is very successful for materials such as mild steel because the holes can be accurately drilled and positioned. Theoretical FE was used to study the residual stresses and their depth from ground surface. This was compared with previous experimental results analysed by using x-ray diffraction technique from previous studies obtained by Scott, J. [113].

6.3. FE Model Setting

The model is two-dimensional in nature, the boundary condition is in the form of nodal forces and restraints. This study considers the effect of normal and tangential forces as they are the main components that cause damage in grinding of ceramic. The ceramic specimen was divided into a number of elements (0.5-300 μm), the boundary conditions used to simulate the physical restraints in grinding is shown in Figure 35. The normal and tangential forces applied on the ceramic specimen assuming that, the

grits are uniformly distributed in space or volume of abrasive section of the grinding wheel. The force per grit is repeated for the next nodes as the loading moves from one location to the next.

The variations in the values of forces emits from the particular nature of radial distribution of diamond in the grinding wheel bond material and from changes of size of grits during grinding. Sharp and blunt grit were simulated at different ratios, high normal force and small tangential force may cause a mechanical type of damage whilst small normal force and high tangential force which may cause a thermal type of damage.

An assumption was made that all the forces are transferred through the grits only and all the grits in the grinding zone are in direct contact with the workpiece. The analysis of material removal assumes that the normal force per active grain exceeds the minimum threshold value that causes cracks. Critical values for the threshold loads cracks compared with average normal loads per grits in grinding was used to predict whether a fracture or flow mechanism may prevail.

6.4. Simulation of the Grinding Process

An attempt was made to simulate the grinding process at different machining parameters using finite element analysis, to study micro structural behaviour of the ceramic materials due to the grit/workpiece interface during grinding. A finite element computer package "IDEAS" solve linear static installed on DEC-station is used for this purpose [102]. A grid of different size elements is used to form a model of the ceramic specimen. Beneath a grit the grid elements were reduced in size to the order of magnitude of one diamond grit. The stiffness matrix solved for unknown displacements, given the known forces and boundary conditions. From the displacements at the nodes the stresses in each element can then be calculated. The simulation procedure consists of three phases as shown in Figure 34, which are;

◊ **Pre-Processing**

In pre-processing, the geometry of the model is initially defined either in solid modelling or it can be defined directly in a geometry modelled FE program. After the model has been defined, mesh creation is used to subdivide the ceramic specimen. Load and boundary conditions are then applied in order to simulate the actual conditions required for predictions. The material properties of ceramic such as modulus of elasticity, Poisons ratio and mass density were then selected before solving the model.

◊ **Input Parameters**

Randomly distributed normal and tangential forces per grit have been applied on ceramic workpieces. These forces represent different wheel and machine parameters resulted from the experiments. The calculation of the grinding forces per grain is explained in appendix A1. A series of simulation models of different cases to study different parametric effects was carried out. Different conditions simulated in this model can be identified as:

- Simulation of the grinding actions for a general case.
- Simulation of the grinding actions with very sharp abrasive grits.
- Simulation of the grinding actions with dulled abrasive grits.
- Simulation of the effect of tensile and compression grinding forces and their influence on the initiation and propagation of surface and sub-surface cracks.

6.5. Solving the FE Model

The second stage in FE processing is solving the model. Wide ranges of result can be obtained such as displacement, stresses, strains, strain energy, etc. The theoretical background of the model solving is explained in appendix A1.

◊ **Post-Processing**

After the model was analysed, the results of the analysis can then be displayed as deformed geometry, contour, shaded image, etc.

◊ **Output Results**

The results which can be obtained from the simulation model are displacement, stress, strain and strain energy. These results were then used to predict zones of material failure, cracks initiation and residual stresses combination. The accuracy of the resulting solution depend on the assumptions made for loads and boundary conditions and the accuracy of the element dimension used for the problem.

7. EXPERIMENTAL PROCEDURE AND RESULTS

7.1. Introduction

Extensive experimental work was carried out to understand the crack initiation and propagation due to grinding of advanced ceramic materials. The experimental work can be separated into two distinct sections.

1. A preliminary investigation to study different variables that could have an influence on the behaviour of advanced ceramic materials during grinding process. The preliminary investigated variables are:

A) Effect of different levels of grinding wheel bond type with the same grit size and machining parameters on the surface roughness and the strength of ground ceramic component. Experimental design with an L_9 orthogonal array was used in this part. The results from these experiments were translated into their respective signal to noise ratio (S/N) of larger is better for strength analysis and smaller is better for surface roughness.

B) Effect of very high infeed on the ground strength of ceramic component. The grinding forces, the surface roughness, the fracture strength were analysed. The estimated crack size was compared with the surface roughness and fracture strength at both conventional and very high infeed grinding.

2. A main experimental investigation into crack initiation and propagation of ground ceramic component. This part was carried out in two stages:

I. Grinding specimens without artificial cracks initiated on their surface. This was one of the main aims in this research. A fractional factorial experimental design technique was used to investigate different levels of grinding wheel and machining parameters. The relationship to surface roughness, fracture strength, AE spectral amplitude, grinding forces, grinding energy, crack size, sub-surface cracks distance from the ground surface, depth of surface damage due to different levels of grinding

wheel and machining parameters used in the fractional factorial array were all investigated. A correlation between AE signals and SEM and 3D surface topography observations of ground ceramic condition was carried out. Surface and sub-surface cracks of the ground ceramic due to different wheel and machine parameters was investigated.

II. Grinding specimens with artificial cracks initiated on their surface. The experimental study was carried out in two sections. Cracks were initiated on the surface of the ceramic specimen using v-shape edge disc at different groove depths. The second part was to study the propagation of these artificial cracks during normal grinding, at different grinding passes. The effect of different levels of grinding wheel and machining parameters on the crack initiation and propagation during grinding process of ceramic materials was also investigated.

Surface and sub-surface cracks initiated and propagated due to different levels of grinding wheel and machining parameters were validated by using FE mode designed for this purpose. The grinding forces obtained due to these levels were used in the FE model. The model was described in chapter 6.

The experimental work was carried out in different stages. This chapter describes the various experimental procedures used and results obtained.

7.2. Preliminary Investigation

A preliminary investigation was carried out to understand the behaviour of advanced ceramic material during grinding. Diamond grinding wheel bond type and machining parameters were investigated in the preliminary investigation. Resin, vitrified and cast iron bond diamond grinding wheels were used. The effect of very high infeed and the grinding wheel condition were studied as a preliminary investigation. The experimental procedures, equipment, instruments and calibrations used in the preliminary investigation are explained in chapter 5. The experimental procedures and techniques used in the major experimental work is explained in section 7.3.

7.2.1. Effect of Wheel and Machine Parameters

There are many variables which affect the control of the grinding process and the majority influence the final strength of the material. One of the most significant variables is the type of grinding wheel used. The effect of wheel/machine on the strength and integrity of Sialon 101 and 201 was carried out to identify the optimum machining parameters with respect to wheel type, feed rate and depth of cut, and grinding wheel speed. The three types of grinding wheel investigated were metal, vitrified, and resin bonded grinding wheels of equivalent mesh size.

The nature of the tests were a designed experiment consisting of four grinding passes at varying machining parameters. The normal and tangential forces produced during each pass was recorded as a control factor. The techniques used to specify material condition were a measure of the ground surface roughness and a three point bending test to evaluate the strength of ceramic component after grinding.

The condition of the grinding wheel surface was examined at intermittent stages throughout the experiment by producing cutting envelopes of the grinding wheel periphery prior to and subsequent to grinding. Analysis of surface roughness characteristics and the effect of grinding attributes on the resultant surface finish of ceramics specimens were investigated. Figure 45 shows that the effect of wheel type on surface finish is most distinct. The decline in surface quality with variation in wheel bond composition suggests that optimum surface characteristics are achieved using grinding wheels of high stiffness with good grit retention properties.

The low resilience of resin bonds however, mean that the extremities achievable are relatively low in comparison to either the metal or vitrified wheels. This is because the resin bond has low Young's modulus value compared with the other bonds. Some evidence of this was observed from the cutting envelopes produced which were designed to determine the relative sharpness of the wheels subsequent to dressing.

Analysis of material strength was investigated. Figure 46 shows that the decline in material strength becomes appreciable above 20 m/s wheel speed beyond which a marked fall in performance occurs. This could be attributed to an increase in sub-surface cracking, which is a usually associated with the onset of a micro-brittle fracture regime.

Results suggest that vitrified wheel produced better material properties. The experiments also suggest that for a creep-feed grinding there is little compromise in the selection of machine attributes. Optimum surface roughness is achieved with a metal bonded wheel, at 6 mm/s feed rate, 250 μm depth of cut, and peripheral wheel speed between 30-40 m/s. With vitrified wheel however, optimum strength is achieved at low wheel speed 20 m/s, low feed rate 1.0 mm/s, at maximum 250 μm depth of cut. The conditions necessary for best surface finish and material strength have been found at extremes. Subsequently no obvious single solution exists to achieve both optimum surface finish and material strength. Also, it was found that isolation of one attributes is impossible.

The effect of stiff grinding wheel such as metal bond diamond wheel gives better surface roughness but with low strength. This could be due to an increase in sub-surface cracking. Variation in strength properties with depth of cut was similarly dramatic above 250 μm. Observance of force measurement shows that increased depth of cut was accompanied with significant increase in normal force.

7.2.2. Effect of Very High Infeed

The effect of very high speed grinding is to introduce a very large number of diamond grits to the arc of cut in a very short time. This large number of grits would mean a much smaller loading on each grit. Hence altering the removal of material characteristics. In this research, an attempt was made to simulate the same technique but through altering the infeed of the ceramic component. Very high infeed (32767 mm/min) was used in association with a shallow depth of cut.

This simulation is not complete because of the effect of diamond grits loading would not be the same. However, this effect was partially negated by using higher concentration diamond grits. Although the higher concentration of diamond grits could improve the surface finish, the simulation is still not completely accurate due to the chip pockets would still be different. The simulation was applied to two types of ceramics, Sialon 101 and 201. The result of the surface finish, surface topography and fracture strength of the ground components were then compared to a conventionally ground component.

Figure 47 and 48 show the normal and tangential grinding forces. These forces were measured at two depths of cut 20 μm and 100 μm over a range of feed rates. The first feed rate represents the conventional feed rate that usually associated with the grinding of advanced ceramics. The range of the feed rates between 5762 mm/min and 32767 mm/min is extremely high feed not usual in conventional grinding. As was expected, the normal forces are higher than tangential forces with ratio range of 2.5 to 4.5. This ratio was kept constant even at different depths of cut.

The increase in both tangential and normal forces with increasing feed rate can be explained by the fact that the number of abrasive grit acting in the grinding zone per unit time has increased. Both Sialon 101 and 201 behaved exactly in the same manner under the load. This is because both materials can operates in an environment where temperatures exceeds 1000°c. The high feed rate creates higher temperatures in the grinding zone. Although the temperature was not measured, but observations of the associated spark confirm this.

The increase in depth of cut from 20 μm to 100 μm greatly affect the grinding forces measured. The effect of increasing depth of cut is more influential than that of increasing the feed rate. This is may be due to the increase in material removal rate. The surface roughness characteristics and the effect of both depth of cut and feed rate on the resultant surface finish was also investigated. Figure 49 shows the surface roughness measured in microns against the variation in feed rate and depth of cut for both Sialon 101 and 201. The surface finish of the unground component was also measured for

comparison purpose. As shown in the figure at conventional feed rate of 60 mm/min, the surface roughness parameters has a value of 1.1 on average for both materials and at different depth of cuts. This value was reduced further as the feed rate increased. This indicates a better surface quality with higher feed rates. However, the results seem to indicate a lesser effect as the feed rate increase beyond 19000 mm/min. This may indicate that the feed rate effect reduces beyond specific range. Also it was noticed that the depth of cut increase has a lesser influence on the surface roughness as compared to the feed rate. Photographs taken by scanning electron microscope confirmed these conclusions.

The effect of higher feed rates on fracture strength was a major concern of this research. The reduction in fracture strength of the ground component is a serious concern as it will affect the usefulness of the process. Also the fracture strength will shed a light on the mechanics of material removal as a direct results of boosting the feed rates. Figure 50 shows the effect of the process on the fracture strength of the ground ceramic components. The figure also shows the fracture strength of the unground component. The figure shows that the increase of feed rate from 60 mm/min to 5762 mm/min does not seem to have changed the strength. However, as the feed rate increased further a marked increase in the fracture strength can be seen. Also it was noticed that as the feed rate further increased, the effect on the strength was reduced.

Figure 51 shows the crack size against table feed at different depth of cut. From this figure the crack size increases with increasing depth of cut. The effect of very high infeed on the crack size was calculated. The crack size decreased with increasing the table feed as shown in Figure 51. The effect of very high infeed on the surface roughness, fracture strength and crack size at depth of cut of 30 and 100 μm is shown in Figures 52 and 53. These figures may indicate that the high infeed could have an influence on the surface roughness, which could affect on the fracture strength and the crack size of the ground ceramic.

The data indicates, as it did with the effect on surface finish, an asymptotic tendency at higher values. This may seem to indicate an optimum value for the feed rate

beyond which the improvement in either surface finish or fracture strength is reduced. The general improvement in surface finish and in fracture strength may be due to the change noticed in the material removal mechanism. A bias towards plastic deformation was noticed as the feed rate increased. This were particularly noted from the scanning electronic microscope examination. In general the 20 μm depth of cut gave better results than that of 100 μm at higher feed rates.

The research made studied the effect of remarkably increased feed rates in the grinding of advanced ceramics materials. It is hoped by this to introduce a cheaper alternative to very high spindle grinders. The feed rates of the ceramic components were increased through an alternative feed mechanism. The process indicates a higher fracture strength and better surface finish as compared to conventional feed rates. There seem to be an optimum value of feed rate around 19000 mm/min that gives a remarked improvement in surface quality and in strength. Beyond this value the improvement is minimal.

7.3. Main Experimental Procedures and Results

7.3.1. Grinding Wheel Condition

Grinding wheel condition was the first stage in the experimental work. The grinding wheel is directly over the truing wheel and adjusted to set the grinding wheel and truing depth of cut. This depth is set according to the grinding wheel grit size and set at either 25, 50 and 75 μm. A linear variable differential transducer (LVDT) was used to set this depth. Different levels of grinding wheel and truing wheel speed ratios were set at either -0.3, -0.4, -0.5, +0.3, +0.4, or +0.6. These ratios refer to the truing wheel speed divided by the grinding wheel periphery speed. Negative values represent that the wheel rotate in the opposite directions, and positive values to the wheels rotating in the same direction.

Once the test rig was set, a grinding profile was taken to ascertain the relative sharpness of the grinding wheel, the cutting envelope of the grinding wheel was taken

before and subsequent to each grinding operation. This was achieved by taking an imprint of the grinding wheel envelope profile GWEP on a mild steel specimen and measuring the surface roughness of the specimen using Talysurf. Truing and dressing process was carried out by using an aluminium oxide truing wheel driven by a servomotor at different truing/grinding wheel speed ratios.

A tachometer and stroboscope were used to adjust the wheel speed to choose different speed ratios of truing and grinding wheel. These ratios gave different grit and their distribution conditions on the wheel surface, which could affect the surface integrity of the ground specimen. Surface roughness of a one pass grinding imprint on mild steel specimens was measured before and after each grinding wheel/truing speed ratio. An AE sensor was attached to the mild steel specimen during this test. The raw signals then stored and analysed to compare the AE spectral amplitude with the surface roughness of mild steel specimens. This was carried out for different levels of grinding type, grit size and grinding wheel/truing wheels speed ratios as shown in Figures 23 to 26. These figures show low AE spectral amplitude when the grains are sharp, and higher when the grains are not sharp. This was indicated by the surface roughness of grinding wheel envelope profile GWEP. More details were explained in chapter 4.

One pass grinding on a mild steel specimens at 20-50 μm depth of cut and 2 mm/s table feed after different grinding/truing wheel speed ratios showed that the wheels did not need any more dressing. This was observed during measuring the surface roughness of wheel imprint on the steel specimens after the truing of the grinding wheel. The depth of one pass grinding cut was set according to the grinding wheel grit size used.

The main purpose of varying the condition and distribution of the grits on the wheel surface was to investigate their influence on surface and sub-surface cracks of ground ceramic. The different levels of speed ratios are produced different sharpness of the grains on the grinding wheel surface. The load of an individual grit as well as its shape can influence on the crack initiation and its propagation. Higher damage depth on the ground surface was observed when the grain is extremely sharp. The depth of

surface damage was measured by using 3D surface topography. Blunt grit condition was found to have an influence on the initiation of sub-surface cracks. This was observed by using SEM after the bending test.

7.3.2. Grinding Operation

Once the grinding wheel was ready for the test, a ceramic specimen was fixed on a special fixture bolted straight onto a Kistler dynamometer. The specimen on the fixture was adjusted to be flat by using LVDT to achieve the same depth of cut along the specimen. Before adjusting the depth of cut the grinding wheel was rotated by hand until it touched the ceramic specimen. Depth of cut was also adjusted by using the LVDT. The wheel speed was adjusted by using a speed control box and using a tachometer and stroboscope to achieve an accurate wheel speed. An NC controller was used to control the table feed from 1 mm/min to 32767 mm/min.

When the above settings were achieved, an AE sensor was then fixed on the surface of the specimen and the grinding process was carried out as shown in Figure 32. AE signals were recorded when they reached a certain level. Triggering level was carefully selected to record the highest AE event on a digital oscilloscope window. Normal and tangential grinding forces were measured via Kistler dynamometers connected to a data acquisition system. MAC program for windows was used to monitor and save the grinding forces. These forces were recorded on a PC simultaneously with the AE signals on the digital oscilloscope. The AE signals saved in the digital oscilloscope were then transferred to PC as ASCII files using a special program. The raw data were then sorted using word for window as text files to be analysed using the FFT method. Once the grinding was carried out the LVDT was used to measure the actual depth of cut.

The AE signals from each of the experiments were detected using a piezoelectric transducer described in chapter 5. The noise generated by the peripheral sources such as machine vibration and wheel rotation were easily omitted by using high-pass filter with cut off frequency outside the range of 100 KHz to 1200 KHz. Triggering level was set at 4 volts for a scratch test and 8 volts during grinding. This

setting was selected after observing the background noise level. The data processing time window was set at 200 μs for the data of all experiments.

After the grinding process was carried out the ceramic specimens were then inspected by using a Talysurf for surface roughness R_a and R_{max}. Three dimension surface topography was used to measure the depth of surface damages. The surface cracks, the mode of material removal and sub-surface cracks of ground specimens were then inspected by using scanning electron microscopy SEM.

The three point bending test was used to measure the strength of the ground ceramic samples. The technique used for the fracture strength analysis is explained in appendix 2. An AE sensor was attached on the specimen during this test to investigate the propagation of cracks before the failure of ground specimens occurred as shown in Figure 33. After the bending test, sub-surface cracks were then inspected. The sub-surface cracks located very close to the ground surface were inspected by using SEM. The type, size and the depth of these cracks from the ground surface were carefully investigated.

Ceramic materials used in this investigation were Sialon 101 and 201 with dimensions of 3 x 3 x 50 and 3.5 x 4.5 x 50. Different levels of grinding wheel and machine tool parameters were used to investigate the crack initiation and propagation of advanced ceramic material due to grinding process, these levels are;

- Seven levels of grinding wheel conditions represented by grinding wheel/truing speed ratios and directions (ranging from -0.3 to 0.6).
- Seven levels of grinding wheel speed (ranging from 20 to 32 m/s).
- Seven levels of depth of cut (ranging from 20 to 500 μm).
- Three levels of table feed rate (ranging from 2 to 7 mm/s).
- Three levels of grinding wheel bond type (resin, vitrified and cast iron).
- Three levels of grinding wheel grit size (D46, D76 and D126).
- Seven levels of artificial crack depths (ranging from 10 to 120 μm used only in the second experimental part of this research).

7.3.3 Limitation on Machine and Experimental Technique

The results obtained by using the experimental technique should be looked at in the light of two major points. The first is the limitations on the machine used. The machine is a commercially available machine that was modified to accommodate a higher feed rate. Using this machine would have both advantages and disadvantages. One of the main advantages was to investigate how a commercial machine would grind hard material such as advanced ceramics and what the effect would be on the process of crack initiation and propagation during grinding. The disadvantages could include the limitation associated with the difficulty of adjusting depth of cut less than 20 μm and grinding wheel speed restrained to a 32 m/s . In addition, the loop stiffness of the machine and the combined workpiece/grinding wheel stiffness were far less than what could be achieved using purpose built machines. However, the machine set up is reasonable over the average range of the studied variables. Accuracy however, deteriorate near to the variable extremities. This problem manifest itself in the repeatability of some results.

Second area of concern, is the analytical "Taguchi" technique used. Although Taguchi's method is a well established and recognised, it also has its own limitations. In the author's opinion, the limitations of the Taguchi's technique is that interpretation of the results is not a straight forward matter. Some false trends can be concluded from graphical results if the reader is not fully familiar with the technique. When a large array, such as the L_{27}, used in this research, is operative, one should be very careful when considering the weight importance of each parameter involved. A conclusion may not be obvious from looking at one isolated figure. A full understanding to the variance analysis associated with Taguchi's technique (see Appendix 3) is vital to the drawing of conclusions from the figures. Having said this, however, the alternative to Taguchi's technique would have meant the run of a systematic set of experiments of enormous magnitude involving excessive time. In order to match an L_{27} of Taguchi's means a set of over 9,000 experiments. In addition, these would also require a global look at the figures to overcome the problem of variable interactions.

It must be emphasised, however, that in the results discussed in the next section "points" on graphs may represent grinding under a number of different conditions -as defined by the Taguchi array- and simple comparison of graphical results should be treated with caution.

The range of parameters of both the grinding wheel and machine tool were selected from the preliminary investigation. The same parameter range was used to grind specimens with and without artificial cracks initiated on their surface. The fractional factorial experimental technique was used. The details of the experimental technique are illustrated in appendix 3 and the experimental array is shown in Table 5. A modified L_{27} orthogonal array was used for grinding specimens with and without artificial cracks created on their surface. This modified array was selected to cover the range of selected parameters. L_{27} Without modification would not have covered the full range of parameters involved. Modification of L_{27} array was explained in appendix 3.

In classical statistical experimental design, significance test, such as F ratio, play an important role. These are used to determine if a particular factor should be included in the model. In the Taguchi method, F ratios are calculated to determine the relative importance of the various control factors in relation to the error variance. Statistical significance tests are not used because a level must be chosen for every control factor regardless of whether that factor is significant or not. Thus, for each factor the best level is chosen depending upon the associated cost and benefit.

Analysis of an orthogonal array is performed by averaging the response variables i.e., fracture strength, associated with each factor and level. Effect of the factor in the first column of the array shown in Figure A3.5 is the average of response variable associated with experiments 1 to 3, 10 to 12 and 19 to 21 for level 1. The effect of the same factor at level 2 is the average of experiment 4 to 6 and the same method applied for other levels. Analysis of variance techniques was applied to orthogonal arrays to give an indication of significance of changing of the factor -depth of cut- on response variable (fracture strength). The degree of freedom associated with a complete orthogonal array is defined as one less than the total number of experiments. For

example, L_{27} array has 26 degree of freedom available. The number of degrees of freedom of the error (pooled error) should be about one-half the total number of degrees of freedom. The number of replications used in this research for specimens ground without artificial cracks was four. The response of different output results (i.e. fracture strength) obtained due to the different factors (i.e. depth of cut) and levels (seven setting depths of cut) were then analysed. The output results from different levels of wheel and machine parameters are;

- Fracture strength of ground specimens.
- Surface roughness R_a & $R_{max.}$
- Acoustic emission spectral amplitude.
- Crack initiation and propagation AE observations.
- Grinding forces.
- Specific grinding energy.
- Estimation of the crack size of ground ceramic components.
- Surface and Sub-Surface Damage Evaluation.
- Depth of the cracks on the ground surface using 3D surface topography.
- Depth, type and size of sub-surface cracks using SEM.

Experimental work to investigate the crack initiation and propagation was carried out simultaneously in two sections. The first part was to grind specimens without artificial cracks initiated on their surface. The second part was to grind specimens with artificial cracks initiated on their surface. The experimental work for both parts was carried out with the same grinding wheel and machine tool parameters. One of the aims of these experiments was to monitor the ceramic specimens ground with and without artificial cracks and identify the effect of their presence on the AE spectral amplitude, time and frequency, and also to compare the AE signals with surface and sub-surface cracks due to different levels of wheel and machine parameters. Grinding specimens without artificial cracks initiated on their surface will be discussed now. The specimens ground with artificial cracks will be discussed later.

7.4. Grinding of Advanced Ceramic Materials

The response of fracture strength, surface roughness, AE spectral amplitude, grinding forces, specific grinding energy, and crack size due to different levels of grinding wheel and machine tool parameters will be analysed in this section.

7.4.1. Analysis of Fracture Strength of the Ground Ceramic Component

The effect of different levels of grinding wheel and machine parameters on the fracture strength of ground ceramic is shown in Figures 54 to 67. These figures show the effect of different levels of wheel grit size (D46, D76 and D126), bond type (resin, vitrified and cast iron), wheel condition (grinding wheel/truing speed ratios of -0.3, -0.4, -0.5, +0.3, +0.4, +0.5 and +0.6), depth of cut (from 20 to 500 μm), wheel speed (from 20 to 32 m/s) and table feed (from 2 to 7 mm/s).

The spread shown in all figures indicate a very good repeatability of the experimental points. However, the reader should not look at the spread over only one single graph as this will not reflect the true indication for the figure. For example, Figure 58, for the graph of table feed of 2 mm/s, the range of the fracture strength is between 150 to 550 MPa, whilst the spread only occurs around 50 MPa. The reason for this is that the first point on the graph represent an average value of all the grit size used at table feed of 2 mm/s. The second and the third points represent a grit size of D46, the fourth and the fifth points represent a grit size of D76 and the last two points represent D126 grit size at this table feed. This is the reason why the spread is as shown. The two horizontal dashed lines represent the width of the spread for a single grit sizes. For the clarity of the figures, the author preferred not to put this type of horizontal lines in all the figures.

The effect of different factors and their levels on the fracture strength achieved will be compared with other results obtained. These results are the surface roughness, AE spectral amplitude, grinding forces, specific grinding energy, crack size, dimensions and type of surface and sub-surface cracks and their depth from the ground surface. These results could give an indication of the most influential factors that affect the

strength of ground ceramic. Successful grinding of ceramic must be associated with higher fracture strength of ground component.

The effect of different levels of diamond grinding wheel grit size and depth of cut on the fracture strength is shown in Figure 54. This figure shows that small grit size can achieve a better strength compared with coarse grit size. At a depth of cut of 52 μm, the strength achieved by D46, D76 and D126 wheels grit size are 569.6, 322.1 and 196.1 MPa respectively. The surface roughness of these specimens was found to affect the strength of ground ceramic. The surface roughness produced by these grit size are 0.68, 1.124 and 1.486 μm and shown in Figure 68. The fracture strength of the ground specimens was found to be reduced with increasing the depth of cut for the same grit size and different wheel bond used. At depth of cut of 52 μm, resin bonded wheel with D46 grit size was used. The fracture strength was found to be 569.6 MPa and the surface roughness of 0.68 μm. At higher depth of cut of 300 μm, stiff grinding wheel (cast iron) with the same grit size (D46) was used. The fracture strength was found to be 437.8 MPa and a smoother surface roughness of 0.591 μm compared with resin wheel. This was due to the initiation of the sub-surface median cracks underneath a solid (crack-free) layer and will be discussed later. Rough ground surfaces were found when D126 grit size was used. At depth of cut of 52 μm, a cast iron bonded wheel with D126 grit size was used, the fracture strength was found to be 196.1 MPa with a surface roughness of 1.486 μm. At higher depth of cut of 300 μm, vitrified bonded wheel with the same grit size (D126) was used. A higher surface roughness value (1.592 μm) and strength (203.75 MPa) was found compared with the cast iron wheel at lower depth of cut.

The grinding wheel grit size shown in Figure 54 represented different levels of grinding wheel bond type. The grinding wheel bond types of each grit size is shown in Figure 55. This figure shows the effect of the hardness of the grinding wheel bond type at different depths of cut on the fracture strength for different grit sizes. It can be seen that, resin bonded grinding wheels with three grit sizes achieved better strength compared with cast iron and vitrified bond. This could be due to the resin bond being a soft material when compared with a stiff wheel such as cast iron bond type which hold

the grits very firmly and generate higher grinding forces. The effect of different levels of bond types and grit sizes of the grinding wheel on the fracture strength of ground ceramic component is shown in Figure 56. Resin bonded grinding wheels with all the grit sizes used produced higher ground strength as shown in this figure.

The variation of the fracture strength due to different levels of table feed and depth of cut is shown in Figure 58. It can be observed that at slow table feed 2 mm/s a higher fracture strength of the ground specimens was produced at small levels of depth of cut and small diamond grinding wheels grit size used. However, the strength of ground ceramic deteriorate when both depth of cut or wheel grit size increase. At faster table feed 7 mm/s, low fracture strength was obtained at a small depth of cut and improved with a large depth of cut as shown in Figure 58. The variations on the strength shown in this figure due to the different grit sizes used at these levels of table feed. This mean that the effect of grit size out weighs the effect of depth of cut.

Figure 58, the first point shown (25 μm depth of cut), represents the average value of the fracture strength at each table feed for the three different grit sizes used. The spread of the results shown in this figure shows the effect of a range of different wheel grit sizes (D46 to D126) at different levels of table feed and depth of cut on the strength of ground ceramic material. The averaging point was selected at 25 μm which is the actual minimum depth of cut, of four repeated experiments, that can be achieved on the machine used. The fracture strength against depth of cut averaged over different levels of table feed, grit size and bond type is shown in Figure 59. These averaged values represented the response of fracture strength associated with several experiments carried out for individual levels of depth of grinding cut. Analysis of variance (ANOVA) shown in Table 6 has been constructed to illustrate the significance of grinding wheel and machine parameters on the strength of ground ceramic. It can be seen from this table that only the wheel grit size significantly influences the component strength at a confidence level of 95%, whilst the grinding wheel bond type does not.

The effect of different levels of grinding wheel grit size and grinding wheel speed on the fracture strength can be seen in Figure 60. The bond types of each grit size

and their influence on the fracture strength is shown in Figure 61. The spread of the results shown in this figure was affected by the grit size of each grinding wheel bond type used. From these figures, the strength of ground specimens using D46 grit size produced better ground strength in the range of 342.8 to 569.6 MPa at all grinding wheel speed levels compared with D126 grit size in the range of 169.7 to 381.8 MPa. The reduction in the fracture strength using a resin bonded grinding wheel (326.2 MPa) shown in Figure 61 was due to the changes in the grit size used. The grit sizes of this bond can be identified from Figure 60.

The effect of different levels of table feed and grinding wheel speed on the fracture strength of ground components is shown in Figure 62. From this figure, at slow table feed (2 mm/s) the fracture strength of ground ceramic varied at different levels of wheel speed. This was due to different grinding wheel grit sizes used as shown in this figure. The fracture strength against grinding wheel speed averaged over different levels of table feed is shown in Figure 63. The fracture strength is thus mainly affected by the grit size used. The strength of ground ceramic was found to be improved by reducing the diamond grinding wheel grit size. A strength of 569.6 MPa is associated with D46 grit size used as the grit size increases to D76 the strength reduced to a level around 322.1 MPa and at D126 grit size the strength further reduced to 196.1 MPa, at 52 μm depth of cut. When bond type changes from cast iron to vitrified to resin, the strength of ground ceramic component was found to improved. This was observed over all the grit sizes used of these wheel bond types.

Resin bonded grinding wheels with small grit size were found to improve the strength of ground ceramic. It was found that the wheel condition has an influence on the ground strength obtained. Sharp grains on the grinding wheel surface of coarse grit size was found to be associated with reduction in the strength of ground ceramic. The condition and distribution of the grits on the grinding wheel surface have an influence on surface and sub-surface cracks of ground ceramic. Different levels of grinding wheel condition, represented by truing wheel to grinding wheel speed ratios, means different sharpness of grains on the grinding wheel surface. The load of an individual grit as well

as its shape can influence the crack initiation and propagation. A higher depth of damage on the ground surface was observed when the grains were extremely sharp.

The effect of the grinding wheel condition represented by these ratios on the fracture strength of ground component at different levels of grinding wheel grit size is shown in Figure 64. The fracture strength was found to decrease when the grits on the wheel surface are extremely sharp. At ratios of +0.4 and +0.6, the fracture strength of specimens ground using D126 wheel grit size was found to be 381.8 and 169.71 MPa. The surface roughness of these specimens was found to be 1.3616 and 1.596 μm as shown in Figure 78. At the same speed ratios, the fracture strength of specimens ground using a wheel with small grit size (D46) was found to be 501.71 and 354.3 MPa. The surface roughness of these specimens was found to be 0.5674 and 0.755 μm as shown in Figures 64 and 78. The fracture strength against grinding wheel conditions for different levels of bond type is shown in Figure 65. This figure shows that the grinding wheel/truing speed ratio of -0.4 which produced uniform and reduced sharpness of grits, can improve the strength of the ground ceramic. The effect of different levels of grinding wheel condition and table feed on the fracture strength is shown in Figure 66. The highest fracture strength was found to be achieved at -0.4 and +0.4 speed ratios over different levels of averaged table feed as shown in Figure 67.

7.4.2. Analysis of Surface Roughness of the Ground Ceramic Component

The surface roughness produced due to different levels of grinding wheel and machine parameters have an influence on the strength of ground ceramic component. The effect of surface roughness is shown in Figures 68 to 81. These parameters are the diamond grinding wheel grit size, the wheel bond type, grinding wheel conditions, grinding wheel speed, depth of cut and table feed.

The effect of different levels of grinding wheel grit size and depth of cut on the surface roughness is shown in Figure 68. It can be seen from this figure that the smaller the grit size the better the surface roughness (0.567 μm). The figure also shows that the surface roughness slightly improved with increasing the depth of cut. This may be due to the change in the grits condition on the grinding wheel surface that could occur for

higher levels of depth of cut. This change was found to reduce the strength of the ground specimens due to the formation of sub-surface cracks. Higher depths of cut may also cause an increase in the heat flow in the grinding zone which may tend to reduce the degree of brittleness of the ceramic specimen and may improve the surface roughness. The sparks emitted due to the heat generated from the grinding zone increased at the higher depth of cut.

The surface roughness produced due to different wheel grit size can be compared with the ground strength at the same machining parameters. The surface roughness can give an indication of the strength of ground component as shown in Figures 54 and 68. Small diamond grinding wheel grit size (D46) was found to produce smooth ground surfaces over all other machining parameters. These were found to be in the range of 0.5674 to 0.7596 μm. The fracture strength achieved was found in the range of 437.6 to 569.6 MPa. Median diamond grinding wheel grit size (D76) was found to produce ground surfaces in the range of 0.8296 to 1.1984 μm. The fracture strength achieved for this case was found in the range of 290 to 383.8 MPa. Coarse diamond grinding wheel grit size (D126) was found to produce rough ground surfaces in the range of 1.179 - 1.596 μm. The fracture strength achieved here, was found in the range of 169.7 to 332 MPa.

The effect of the bond types of the diamond grinding wheel on the surface roughness at different levels of depth of cut is shown in Figure 69. The results indicated that resin bonded grinding wheels may achieve better surface roughness at small levels of depth of cut compared with cast iron bonded grinding wheels, but this effect may change with increasing depth of cut. The variations in the surface roughness shown in this figure was due to the wheel bond type used with different levels of wheel grit size.

The effect of diamond grinding wheel bond type with different grit size on the surface roughness is shown in Figures 70 and 71. Figure 70 shows resin diamond grinding wheel creates improved surface roughness values (0.7, 0.98, 1.3 μm) compared with vitrified (0.62, 1.17, 1.607 μm) and cast iron (0.65, 1.124, 1.509 μm) averaged values at different machining parameters for D46, D76 and D126 grinding

wheels grit size. This figure can be compared with the effect of this grit size on the strength achieved and shown in Figure 56. It can be seen that resin bond produced higher fracture strength values (503.5, 335.7 and 315.86 MPa) compared with vitrified (438.9, 322.6 and 240.6 MPa) and cast iron bonded grinding wheels (419.85, 276.24 and 239.1 MPa) averaged values at different machine tool parameters for D46, D76 and D126 grinding wheels grit size respectively. Small values of surface roughness produced by cast iron and vitrified bonded wheels with D46 grit sizes was associated with less fracture strength values compared with resin bonded wheel with the same grit size. This was due to the increase of sub-surface median cracks when harder bonded wheel was used.

The effect of different levels of table feed and depth of cut on the surface roughness is shown in Figure 72. At a table feed of 2 mm/s, the surface roughness increased with increased depth of cut. The increase in surface roughness values was associated with a reduction in the strength of ground ceramic as shown in Figure 58. At a feed rate of 7 mm/s, the surface roughness also has the same indication. The grinding wheel grit sizes used at each table feed shown in these figures should be noted. The surface roughness against depth of cut averaged over different levels of table feed is shown in Figure 73. This figure represents the averaging response of surface roughness associated with table feed levels at different levels of depth of cut. These results represent the average of different experiments of individual levels. The scatter in this figure was due to the change on the grits sizes and their conditions on the grinding wheel surface at higher depths of cut.

From the above figures, it was found that a smooth surface was produced when small grit sizes were used. The increase in surface roughness was also found to reduce the strength of ground ceramic component. This can be seen from Figures 54 and 68. Applying analysis of variance technique to resulting surface roughness data is shown in Table 7. It can be seen that all the levels of grinding wheel and machine parameters have significance influence on the surface roughness at confidence levels of 95% and 99%. The effect of different levels of grinding wheel grit size and grinding wheel speed on the surface roughness is shown in Figure 74. The grinding wheel speed seems to

have little or no effect on the surface roughness. This may be due to the range examined was only from 20 to 32 m/s. This range represent the wheel speed levels that can be achieved on the grinding machine. The effect of the grinding wheel bond type of these grit sizes is shown in Figure 75.

The effect of table feed at different levels of grinding wheel speed on the surface roughness is shown in Figure 76. From this figure, it can be seen that, at 2 mm/s table feed the surface roughness increased with increasing of both the grinding wheel speed and their diamond grit size. This figure can be compared with Figure 62 to indicate the effect of surface roughness produced on the ground strength at different levels of wheel speed and table feed. The surface roughness against wheel speed averaged over different levels of table feed is shown in Figure 77. This figure indicates that in this narrow range of wheel speed variation, the effect of table feed is some how suppressed to small variations.

The effect of grinding wheel condition on the surface roughness is shown in Figure 78. The surface roughness values shown in this figure were produced at different levels of grinding wheel grit size. This figure shows that there is a distinct variation in surface roughness at different grinding wheel conditions due to the change on the protrusion height of the grits on the grinding wheel surface. These variations on the wheel surface conditions were found to affect the strength of ground ceramic as shown in Figure 64. At a grinding wheel/truing speed ratio of +0.6 a D46 grit size was used. The grain conditions were extremely sharp and a higher surface roughness was produced (0.755 μm). Low fracture strength was found to be 354.3 MPa. At the same grinding wheel/truing speed ratio (+0.6) with a D126 grit size, the grain condition on the wheel surface were found to be extremely sharp with a ground ceramic surface roughness of 1.596 μm. The fracture strength of ground ceramic was reduced to 169.7 MPa.

The condition of the grits on the grinding wheel surface could be affected by different hardness bond type that hold these grits. This could have an influence on the surface roughness as well as the strength of ground ceramic. The surface roughness

against the grinding wheel conditions of different levels of grinding wheel bond types is shown in Figure 79. The changes in the surface roughness due to different levels of wheel condition of different bond types was governed by the grit size of each bond. This can be compared with the effect of the grit size shown in Figure 78. The variation of the surface roughness due to different bond type and wheel condition shown in Figure 79 was found to have an influence on the strength of ground ceramic as shown in Figure 65.

The effect of different levels of table feed and grinding wheel conditions on the surface roughness is shown in Figures 80 and 81. At 2 mm/s table feed when +0.5 and +0.6 truing speed ratios were used, the highest surface roughness values were produced as shown in Figure 80. These results were obtained when vitrified bonded wheel with D126 grit size was used. This figure shows that the grits condition effects on the wheel surface are extremely influential. This reduced the strength of ground specimens at 2 mm/s as shown in Figure 66. The surface roughness against different levels of grinding wheel conditions averaged over different levels of table feed is shown in Figure 81. The figure shows the response of surface roughness due to different levels of table feed, grit size and bond type. At a speed ratio of +0.4, the highest quality of surface can be obtained. This average value represents the three diamond grinding wheel grit size used. This was found to produce a higher strength of ground ceramic specimens as shown in Figure 67.

Small grit size produced smooth ground surfaces and higher strength of ground ceramic. Production of smooth surfaces does not necessarily mean a higher percentage of ductile grinding mode occurred. However, underneath this smooth ground surfaces, lateral and median sub-surface cracks were located in a distance very close to the ground surface. This was observed particularly when stiff grinding wheels were used. This will be discussed later in this chapter.

7.4.3. AE Spectral Amplitude Generated from the Grinding Zone

Acoustic emission signals generated during the grinding process were recorded and analysed. An AE sensor was attached on the ceramic specimens during the grinding

process. In this section the variation on the spectral amplitude due to different levels of grinding wheel and machine parameters will be discussed. These signals will be compared with the response of some variables due to the grinding process, i.e. grinding forces, specific grinding energy and fracture strength. The effect of different levels of grinding wheel and machine parameters on the generation of the acoustic emission signals is shown in Figures 84 to 95.

The grinding wheel grit size, bond type and condition have an influence on the strength of ground ceramic component. The changes in the shape and condition of these micro-cutting grains during grinding process have an influence on the strength of ground ceramic. AE signals can give a fast response to the behaviour of the grains and the workpiece interaction. The AE spectral amplitude signals generated due to different levels of diamond grinding wheel grit size and depth of cut is shown in Figure 84. It can be seen that the AE amplitude generated due to every grit size increased with increasing depth of cut. This could be due to the higher friction contact between this grit size and workpiece when the depth of cut increased. This was found to affect the sub-surface condition of ground ceramic specimens. The bond type of each grit size is shown in Figure 85. This figure shows that cast iron bonded grinding wheel in some cases generate higher AE amplitude when the depth of cut increased.

The effect of different levels of table feed and depth of cut on the AE spectral amplitude is shown in Figure 86. The AE amplitude ratio increased (151 to 299) with increasing the depth of cut (25 to 443 μm). This can be seen from the AE spectral amplitude against depth of cut averaged over different levels of table feed shown in Figure 87. Higher AE amplitude ratio (299) was observed where the specific energy is lowest (54.9 J/mm^3). This can be seen in Figures 87 and 111. The reduction on the specific grinding energy and the increase in AE amplitude, shown in these figures was due to the increase in the depth of cut, which was found to be associated with an increase in the normal grinding forces (4.4 to 9.75 N/mm) and tangential forces (1.47 to 3.83 N/mm) as shown in Figure 99. The results obtained from these figures were found to be associated with reduction in the fracture strength of ground component as shown in Figure 59.

The AE spectral amplitude levels generated from the grinding zone at different grit size and grinding wheel speed is shown in Figure 88. The bond type of each grit size is shown in Figure 89. From these figures it can be seen that increasing the grinding wheel speed may slightly affect the AE spectral amplitude. This can be observed from these figures at 30 and 32 m/s. These changes were observed when small grinding wheel grit sizes were used.

The effect of different levels of table feed and grinding wheel speed on the AE spectral amplitude levels generated from the grinding zone is shown in Figures 90 and 91. From these figures it can be seen that the AE spectral amplitude in some points slightly increased with increasing the wheel speed and decreasing table feed as shown in Figure 90. The variations on these signals was due to the influence of other factors and levels of the grinding wheel parameters. These levels can be identified from Figures 88 and 89. The AE spectral amplitude against grinding wheel speed averaged over different levels of table feed is shown in Figure 91. These averaged values represented the response of AE spectral amplitude associated with several experiments carried out for individual levels of table feed, grit size and bond type.

The grinding wheel condition of different levels of diamond grit size and bond type have an influence on the ground ceramic. Different levels of grinding wheel condition represented by different wheel/truing speed ratios and direction were used. These ratios change the grains condition on the wheel surface. The AE signals was found to be varied with the changes of these grains. The AE spectral amplitude generated from the grinding zone at different levels of grit size and grinding wheel conditions is shown in Figure 92. This figure shows that D126 grit size does not have a significant effect on the AE spectral amplitude levels over most of the grinding/truing speed ratios. This was due to that the grains being sharp and producing a rough ground surface. This was found to increase the surface roughness values as shown in Figure 78 and reduce the fracture strength of ground ceramic specimens as shown in Figure 64. These figures show that, low AE spectral amplitude was due to a higher percentage of brittle fracture that reduced the strength of ground ceramic component.

The grinding wheel bond hardness which hold the grits on the wheel surface also changes the levels of AE spectral amplitude. This influence was investigated at different levels of grinding conditions. Figure 93 shows the AE amplitude levels for different bond type. The cast iron bonded grinding wheel generated a higher AE amplitude in most of the cases shown. This could be due to the levels of the AE signals being increased when stiff grinding wheel bond type was used. The effect of different levels of table feed and grinding wheel conditions on the AE spectral amplitude is shown in Figure 94. At low table feed of 2 mm/s, The AE amplitude does not change in most of the cases shown in this figure. This could be due to the rough ground surfaces produced at this table feed. The AE spectral amplitude against grinding wheel conditions averaged over different levels of table feed, grit size and bond type is shown in Figure 95.

7.4.4. Grinding Forces Generated from the Grinding Zone

The grinding forces generated during the experiments were measured using a dynamometer. These forces were stored with the AE signals simultaneously. The effect of different levels of grinding wheel and machine parameters on the grinding forces generated from the grinding zone is shown Figures 96 to 107.

Figure 96 shows the grinding forces at different levels of wheel grit size and depth of cut. Small grit size was observed to generate low grinding forces at small depth of cut. However, these forces increased with increasing the depth of cut. The increased grinding forces where found to be associated with a reduction in the ground strength as shown in Figure 54. The bond type of these grit size is shown in Figure 97. This figure shows that the hardness of the wheel bond type can affect the grinding forces generated at any depth of cut. Cast iron bonded grinding wheel generates higher grinding forces at low depth of cut. These forces decreased when the depth of cut increased. This could be due to the influence of this bond stiffness and workpiece interaction when the depth of grinding cut increased.

The grinding forces generated from the grinding zone due to different levels of table feed and depth of cut is shown in Figures 98 and 99. The normal grinding forces increased (4.4 to 9.75 N/mm) with the increasing in the depth of cut averaged over different levels of table feed, grit size and bond type as shown in Figure 99. Figure 98 shows that the levels of grinding forces were increased when the table feed increased from 2 to 7 mm/s. The grinding forces shown in this figure was found to have an influence on the strength of ground ceramic specimens as shown in Figure 58.

The grinding forces generated from the grinding zone due to different levels of diamond grinding wheel speed and grit size is shown in Figure 100. The variations on the levels of grinding forces can be observed over all the grit size to be reduced between 26 to 30 m/s. This variation may be due to the reduction in the load per grain at higher grinding wheel speed. The bond type of each grit size is shown in Figure 101.

The effect of different levels of table feed and grinding wheel speed on the generation of the grinding forces is shown in Figure 102. This figure shows that the levels of grinding forces were increased when the table feed was increased. This can be observed at almost every grinding wheel speed level. The grinding forces against grinding wheel speed averaged over different levels of table feed, grit size and bond type is shown in Figure 103.

The grains conditions of different grit size on the wheel surface have an influence on the grinding forces generated from the grinding zone as shown in Figure 104. The bond type of these grit sizes is shown in Figure 105. The changes in the grinding forces generated due to different diamond grit sizes were found to have a wide range at speed ratios -0.3, -0.4, -0.5 and +0.3 for all grit size shown in Figure 104. However, this variations was reduced at speed ratios of +0.4, +0.5 and +0.6 as shown in the same figure. The variations on these forces were due to the changes in the grain condition on the wheel surface. The condition of the grits on the wheel surface was found to have an influence on the strength of ground ceramic. Low strength of ground ceramic specimens in most of the cases shown were associated with larger grinding forces generated due to the grinding wheel surface condition (see Figures 64 and 104).

The effect of different levels of table feed and grinding wheels conditions on the grinding forces is shown in Figure 106. This figure shows that, at speed ratios of -0.3, -0.4 and -0.5 the variations in the levels of grinding forces have a wide range. This can be observed at all the levels of table feed shown. However, at speed ratios of +0.3, +0.4, +0.5 and +0.6 low variations of grinding forces levels can be observed at all the levels of table feed used. The grinding forces against grinding wheel conditions averaged over different levels of table feed, grit size and bond type is shown in Figure 107.

The grinding forces were found to increase when the depth of cut was increase. The ratio of normal forces to tangential forces was found to increase from 31.8 % to 39.3 % when the depth of cut was increased from 25 to 443 μm. The load of individual grain as well as its shape were found to have an influence on the crack initiation and its propagation in both surface and sub-surface of the ground ceramic. Higher damage depth on the ground surface was observed when the grain is extremely sharp. Blunt wheel surface condition was found to be associated with sub-surface median cracks. The increase in the grinding forces was found to be associated with an increase in the AE spectral amplitude averaged over different levels of table feed, grit size and bond type when the depth of cut increased. Higher values of grinding forces were observed when the table feed was increased.

During the monitoring of the grinding process, it was observed that the AE signal has a much quicker response than grinding force detection. AE technique is proved to be a good tool that can be used to trigger the grinding forces measurement channels, without losing data just prior to the trigger. The development of the normal and tangential grinding forces at the beginning of the cut were slow in comparison with the rise in AE amplitude.

7.4.5. Specific Grinding Energy Generated from the Grinding Zone

Grinding of advanced ceramic was associated with surface and sub-surface micro-cracks. The energy introduced in the layers close to the ground surface invariably leads to the formation of several types of cracks. The purpose of this part was to

investigate the influence of the grinding energy on the strength of ground ceramic component. It was also to correlate the specific grinding energy to the response of different variables i.e. AE signals, grinding forces, fracture strength and the location of sub-surface cracks from the ground surface.

The effect of different levels of diamond grinding wheel grit size and depth of cut on the specific grinding energy is shown in Figure 108. The bond types of these grit sizes are shown in Figure 109. The specific energy was found to decrease (586.5 to 72.5 J/mm^3) with the increase in depth of cut (25 to 443 μm). This phenomena could be due to that the percentage of the brittle grinding mode was increased when the depth of cut increased. The specific grinding energy shown in these figures was calculated from the tangential grinding forces obtained during the experimental work. Cast iron bonded grinding wheel was found to generate higher specific grinding energy at most of the conditions shown in Figure 109.

The effect of different levels of table feed and depth of cut on the specific grinding energy is shown in Figures 110. This figure shows that the specific energy decreased (726 J/mm^3 to 31.9 J/mm^3) at different levels of table feed when the depth of cut was increased. It can also be observed that, at a low table feed of 2 mm/s, the specific grinding energy was found to be slightly higher compared with other levels of table feed used when the depth of cut was increased.

The reduction on the specific grinding energy was found to be associated with increasing in the AE spectral amplitude shown in Figure 87. The increase in grinding forces shown in Figure 99 was found to be associated with a reduction in the ground strength as shown in Figure 59. These figures can be compared with the specific energy against depth of cut averaged over different levels of table feed, grit size and bond type and shown in Figure 111. The specific grinding energy showing in this figure was found to decrease from 446.6 to 54.9 J/mm^3 when the depth of cut was increased.

An indication of how significant the grinding wheel and machine parameters on the specific grinding energy can be obtained by applying analysis of variance

technique. The results are shown in Table 8. Analysis of variance technique to specific grinding energy data was applied to different levels of grinding wheel and machine tool parameters. ANOVA Table 8 indicates that both depth of cut and table feed significantly affect the level of specific grinding energy.

7.4.6. Analysis of Crack Size of Ground Ceramic

Crack size of ground ceramic was estimated from the fracture strength results. The crack size represent the total amount of cracking on the ground specimen tested. The effect of different levels of grinding wheel and machine parameters on the crack size was investigated in this section. The purpose of this part was to find the most influential factor that could minimise the size of the cracks initiated due to the grinding process. A similar technique utilised by Samuel [109], where a simple model which treats the inherent flaws as edge cracks and ignores residual stresses was used to estimate the crack size of ground ceramic. Taking a typical value of the fracture strength σ of ground ceramic and a fracture toughness K_{IC} leads to an estimated of crack size which can be calculated by;

$$E = \left(\frac{K_{IC}}{1.12\sigma}\right)^2 \frac{1}{\pi}$$

The basic idea is that crack propagation and associated failure occurs when the stress intensity factor (K_I) consistent with an edge crack, reach a critical value (K_{IC}). The value of the stress intensity factor was taken from the mechanical property of the ceramic material. Such a crack size was distributed on the ground specimen tested, and can not be detected by SEM as an isolated crack size. During the inspection of ground ceramic no such surface or sub-surface cracks size individually have been observed directly with the larger estimated size calculated using the above formula.

The effect of different levels of diamond grinding wheel grit size and depth of cut on the crack size is shown in Figure 112. Small grit size D46 at depth of cut of 443 μm has less crack size (68.8 μm) compared with D126 grit size (522 μm). This means a

higher strength was achieved when D46 was used compared with D126 grit size as shown in Figure 54.

Figure 113 shows that the cast iron bonded grinding wheel produced higher crack size in the low levels of depth of cut. The crack size reduced at higher depth of cut using cast iron bonded grinding wheel. This was due to the different grit sizes used in these conditions and shown Figure 112. Resin bonded grinding wheel produced low crack size in low levels of depth of cut compared with higher depth of cut. This is also due to the increase of the grit sizes of this bond type.

The effect of different levels of table feed and depth of cut on the crack size is shown in Figure 114. The crack size shown in this figure was affected by the grit size used on each level of table feed. Three levels of wheel grit sizes D46, D76 and D126 were used in each table feed level i.e. 2 mm/s. The response of the crack size against depth of cut averaged over different levels of table feed, grit size and bond type was found to increase with increasing the depth of cut as shown in Figure 115.

The effect of different levels of grit size and grinding wheel speed on the crack size is shown in Figure 116. Larger crack size can be seen at D126 grit size and vitrified bonded grinding wheel at speed of 30 and 32 m/s. This was due to the sharp grains on the wheel surface shown in Figure 120. The bond type of these grit sizes is shown in Figure 117. This figure shows that, cast iron bonded grinding wheel resulted in a larger crack size compared with resin bonded wheel in most of these cases. This was be due to the higher hardness of cast iron material that generates higher grinding forces.

The effect of different levels of table feed and grinding wheel speed on the crack size is shown in Figure 118. From this figure it can be observed that, the cracks size tend to reduce at table feeds of 5 and 7 mm/s when the grinding wheel speed increased. The crack size was observed to increase with increasing the grinding wheel speed at low table feed 2 mm/s. This could be due to the change in the grinding wheel condition that could generate higher grinding forces at low table feed. The crack size

against grinding wheel speed averaged over different levels of table feed is shown in Figure 119.

The grinding wheel condition was found to have an influence on the crack size of ground ceramic component. The effect of different levels of diamond grinding wheel grit size and their condition on the crack size is shown in Figure 120. The bond type of these grit sizes is shown in Figure 121. At +0.3 and -0.5 grinding wheel/truing speed ratios, the crack size increased over all the grit size used as shown in Figure 120. At +0.3 speed ratio, the crack sizes of 128 μm, 292.2 μm and 388.7 μm were estimated from the broken ground ceramic component when D46, D76 and D126 respectively were used. The range of the diamond grit sizes used at different conditions could reflect the variations of the grains on the wheel surface from blunt to extremely sharp which affect on the crack size. Larger crack size of 522 μm at +0.6 speed ratio was found when coarse and sharp D126 grit size was used. At +0.4 speed ratio, small cracks size can be seen over all the grit sizes used. The grit sizes and their conditions were found to have an influence on the fracture strength of ground ceramic component as shown in Figure 64. The strength of ground ceramic was found to reduce when the grit size sharpness was increased.

The effect of different levels of grinding wheel condition and table feed on the crack size is shown in Figure 122. It can be observed that the direction of the grinding wheel/truing speed ratio could have an influence on the grains condition. This in turn could have an affect on the size of the cracks. At speed ratios -0.3, -0.4 and -0.5, the crack size was found to increase with increasing the table feed from 2 to 7 mm/s. However, at speed ratios +0.3, +0.4, +0.5 and +0.6 the crack size seems to vary over all levels of table feed. This could be due to the influence of other parameters and levels such as grit size and bond type. The crack size variation against grinding wheel conditions averaged over different levels of table feed, grit size and bond type is shown in Figure 123. From this figure, at +0.3 and +0.6 grinding wheel/truing speed ratio, the largest crack size was found to be 269.6 and 260.5 μm.

The purpose of this part was to investigate the response of the total amount of cracking on the ground ceramic component due to different levels of grinding wheel and machine tool parameters. Increasing the levels of diamond grinding wheel bond, grit size and their sharpness condition was found to be the most influential factors on increasing the cracks size of ground ceramic. This was found when both the depth of cut and the table feed were increased.

7.5. Correlation of Acoustic Emission (AE), Scanning Electron Microscopy (SEM) and 3D Topography Data to Investigate the Ground Ceramic Condition

The grinding process can be considered as a series of micro-cutting operations by considering the action of each individual grain on the grinding wheel surface. Each grain on the surface has its own AE event during the material removal process. The AE events from successive grains change rapidly during grinding of ceramic. The grinding wheel rotates at high speed and a substantially higher frequency of grit interaction on the contact zone occurs. A higher sampling frequency rate of the AE sensor (1.2 MHz) was used to cope with this situation. For a certain shape of a grit (or grits), cracks were initiated on the ground component. Surface cracks were found when the grits on the wheel surface were extremely sharp and also when the diamond grinding wheel grit size was increased (D46 to D126). However, when the grits on the wheel surface were blunt, sub-surface cracks were also found. These sub-surface cracks were found when a smaller diamond wheel grit size (D46) was used and the depth of cut increased.

AE signals generated from the grinding zone were analysed and linked with the ground surface condition identified by both SEM and 3D surface topography. The sub-surface condition of the ground specimens was investigated following three point bending tests. At this stage, it should be emphasised that in Figures 124-138, part of the top surface of the specimens is seen at the top of the sub-surface photos. This is due to fitting of the specimen during photography, but may give the false impression of the existence of a glassy surface layer. The top layer identified by an arrow at all the figures is the rugged edge projection on the background. However, the ground surface of the specimens can be seen in the photo shows the ground surface damage. Figures 124 to

138 were chosen from a large set of results. The chosen group is a representative of the most effective parameters studied. This group of micrographs is subdivided according to grit size, wheel bond hardness and machining conditions as shown on each figure. These figures are the first reported attempt to link the following experimental measurements and parameters:

- AE spectral amplitude and frequency.
- Time between AE event and RMS_{Volt}.
- Surface condition of ground ceramic, from SEM and 3D surface topography.
- Sub-surface condition of ground ceramic after the bending test, from SEM.
- Sintering process damage (if found), from SEM.

The understanding of crack initiation and propagation during grinding of advanced ceramic material is the main objective of this section. The state of the ground ceramic surface (whether smooth or rough) was recognised from the AE signals. Brittle fracture was associated with low AE amplitude. This was observed when coarse grinding wheel grit size was used (D126). This type of grit was found to produce high surface roughness values and low strength of ground ceramic component. Higher AE energies were observed when smooth ground surfaces were produced using fine grinding wheel grit size (D46). However, in this case, sub-surface median and lateral cracks were also found which is considered to be the reason for the higher AE spectral amplitude generated. The contact friction between small grit sized wheels and the workpiece could also generate higher AE spectral amplitude at higher depths of cut. This situation was observed when a stiff grinding wheel with D46 grit size was used. The AE signals were compared with the depth of damage measured using 3D surface topography and SEM observation.

Rough ground surfaces and higher surface damage can be seen when diamond grinding wheels with coarse grit size were used. Figures 124 and 125 show the ground surface condition observed by both SEM and 3D topography when a cast iron bonded

grinding wheel with D126 grit size was used with various machining parameters. The AE signals generated from the grinding zone using D126 grit size are shown in the top of these figures. From these figures, low AE spectral amplitude ratio (145) can be seen at a frequency range of 0.2 to 0.3 MHz and 0.6 to 0.7 MHz. The time between each AE events is longer and possibly reflects the long distance of crack propagation on the ground surface as shown in Figures 124 and 125. This may give an indication that for these grinding conditions, a higher percentage of brittle cracking was generated. High surface cracking on the rough ground surface can be seen from SEM observations. Thus, there is a greater likelihood for material removal through a brittle fracture mode when cast iron bonded wheels are used, rather than when with coarse diamond grit size (D126) was used. The depth of damage on the ground surface was measured by 3D surface topography and found to be 17 and 18 μm. The sub-surface condition of these specimens were inspected after the three point bending test. Figure 125 show that the surface cracks initiated due to brittle grinding mode were propagated a long distance into the sub-surface section.

Figure 126 and 127 show rough ground surfaces produced by resin bonded grinding wheels with D126 grit size at different machining parameters. Low AE amplitude ratio (150) can be observed in both figures between a frequency range of 0.14 to 0.7 MHz. The time between each AE event is long, which could again signify a long distance of crack propagation. This time event was associated with a rough ground surface as can be seen from SEM photos. Higher depths of damage of 13 μm and 11 μm were measured. Deeper locations of median cracks were found as shown in Figures 126 and 128. The higher AE amplitude ratio (250) shown in Figure 128 was due to the initiation of sub-surface median cracks. This can be seen from SEM photos of the sub-surface section. The strength of ground ceramic specimens produced by using D126 grit size with different bonded diamond grinding wheels is lower and shown in Figures 54, 56, 57, 60 and 64.

In contrast to the above results, the next group of figures (129 to 132) show that a smooth ground surface was produced by using fine diamond grinding wheel grit size (D46). Figure 129 and 130 show a smooth ground surface produced by using a cast iron

bonded grinding wheel with D46 grit size. This is confirmed by the ground surface inspected and shown by SEM photos. The depth of maximum surface damage on the ground surface was measured to be 9 μm and 7 μm respectively. The maximum AE spectral amplitude ratio generated during the grinding process shown in these figures are higher (350-700). These AE amplitudes increased when the depth of cut increased.

The highest AE spectral amplitude values were found in a frequency range of 0.5 to 0.7 MHz. The time between each AE event is small. This could be due to small crack propagation distance formed when small diamond grinding wheel grit size was used. The location of sub-surface cracks (depth from the ground surface) and their dimensions were found to be affected by increasing the depth of cut. After the bending test, the sub-surface median cracks were inspected and found at 7 μm and 13 μm below the ground surface. The dimension of these cracks are 20 μm x 14 μm at 6 μm depth of cut and 55 μm x 30 μm at 288 μm depth of cut. This can be seen from SEM photo shown in Figures 129 and 130. These dimensions and locations were observed beneath a smooth ground surface when D46 cast iron bonded grinding wheel was used.

The higher AE amplitude and smooth ground surface produced and shown in Figures 129 and 130 can be compared with the low AE amplitude and rough ground surface shown in Figure 124 and 125. The ground surfaces produced in all of these figures were formed when a cast iron bonded grinding wheel with grit sizes D46 and D126 were used.

Resin and vitrified grinding wheels with the D46 grit size produced smooth ground surfaces as shown in Figures 131 and 132. This can be seen from the SEM micrograph. The depth of damage on the ground surface was measured for both conditions to be 6 μm. The Figures show that, the AE amplitude generated was higher than before. However, cast iron bonded wheels with the same grit size generate high AE amplitudes. Median and lateral cracks were inspected and found underneath the high quality surface finish ground ceramics. These cracks were found at depths of 8 to 9 μm from the ground surface as shown in Figure 132.

Figures 133 to 138 show different wheel bond type and machining conditions for a D76 grit size. The AE amplitude, surface damage depth and the fracture strength using D76 grit gave results intermediate to those observed for D46 and D126 diamond grinding wheels.

The correlation between AE, SEM and 3D observation is clearly shown. The group of Figures 124 to 138 can be linked to Figures 54, 56, 60 and 64 which relate to the fracture strength at these conditions. Fine grinding wheel grit size (D46) produced a higher ground strength and this strength decreased with increasing diamond grinding wheel grit size D76 to D126.

The AE events of long duration and low amplitude are of low energy, which is typical for micro-cracks developed within the material. The short duration suggests a short distance of crack propagation and was observed when D46 fine grit sizes were used. The small cracks initiated on the surface and sub-surface using D46 was found to be associated with higher ground strength when compared with D126 grit size ground specimens. The results obtained when coarse diamond grinding wheels grit size (D126) were used only indicate that an increase in percentage of surface fracture is accompanied by low-amplitude long-duration events which can be assumed to be characteristic of brittle mode grinding.

The AE event signals are more sensitive when smooth ground surfaces were produced as opposed to rough. Smooth surfaces of ground ceramic were associated with higher AE energy. However, rough ground surfaces were associated with low AE energy. The time between each AE event was observed to be very small when smooth surfaces were produced (as shown in Figures 129 to 132). However, rough surfaces of ground ceramic were associated with a longer period of time between each AE event (as shown in Figure 124 to 128). The signals of AE events containing more oscillations indicated a higher degree of cracking.

For the micro-crack initiation observed from the AE signals, the duration distribution is short but it increased with increasing grinding forces. At high grinding

forces, some components with a long duration were observed. These may be related to chipping or long distance of crack propagation. In some cases the AE spectral amplitude increased with increased depth of cut as shown in Figures 129 and 130. This phenomena can be explained in so far that when the AE amplitude increased, median sub-surface cracks were initiated with larger dimensions and locations underneath smooth surfaces. This could also occur at higher depths of cut when higher friction contact between fine grit size and workpiece occurs with increasing tangential forces. This could increase the heat generated in the grinding zone.

The energy released during the material removal of ceramic is responsible for the formation of radial cracks on the surface and median and lateral cracks in the sub-surface. The energy released varied with the different parameters used in the grinding process. Figures 129 to 132 show a good surface finish was achieved using fine grit size with different bond type. However, the sub-surface median cracks were especially prevalent when cast iron bonded diamond grinding wheels were used.

During the bending tests of the ground ceramic specimens, it was observed that the failure point was not necessarily in the centre of the broken specimens. The specimens were observed to be fractured at the weakest part of the ground specimens and this was identified to be where the sub-surface cracks were found. An AE sensor was used to monitor the signals of both ground and unground ceramic specimens during bending. It was found that there were not any prior changes in the AE signals of unground specimens before they fractured. However, for some of the specimens ground with and without artificial cracks, the AE signals gave a prior indication before fracture. This indication reflected that the cracks propagated for a very short time of 50 to 80 μs. These signals can be seen in Figures 194 and 195. SEM observations of the sub-surface sections were compared for these signals. The sub-surface cracks initiated due to the grinding process were compared with the sub-surface section of unground specimens (after the bending test) as shown in Figure 153. Median and lateral cracks found in the sub-surface of ground ceramic specimens were not found in the sub-surface of unground specimens after the three point bending test. This indicates that such cracks

were formed during the grinding process and were not initiated during the three point bending test.

7.6. Evaluation of Surface and Sub-Surface Cracks of Ground Ceramic

Grinding of silicon nitride materials was found to be associated with surface and sub-surface micro cracks. The effect of the range used in the experimental array of grinding wheel and machine parameters on the initiation and the propagation of these cracks was investigated. The propagation distance of the radial micro cracks and the machining marks on the ground surface were measured by using three dimension surface topography (3D) and R_{max} of a Talysurf. The sub-surface cracks were inspected after the bending test of ground ceramic specimens. The size of these cracks and their depth from the ground surface were measured.

7.6.1. Analysis of Surface Micro-Cracks of the Ground Ceramic

The surface damage depths on the ground surface were found to increase with increasing the diamond wheel grit size used as shown in Figures 139 and 140. These depth were measured by using 3D topography which gave more accurate results compared with the R_{max} reading obtained from the stylus of Talysuref.

The depths of surface damage due to different levels of grit size and depth of cut is shown in Figure 141. This figure shows that the depth of surface damage increased (from 5.3 to 18.7 μm) with increasing the diamond wheel grit size used (D46 to D126). At depth of cut of 68.6 μm shown in this figure, higher surface crack depth can be seen (18.3 μm). This was observed at low table feed of 2 mm/s and wheel speed of 22 m/s (see Figures 143 and 145). This condition was observed when D46 grit size resin bonded wheel was extremely sharp (see Figure 149). The effect of bond types of these grit size is shown in Figure 142. Cast iron bonded diamond grinding wheel (D126) produced a larger damage depth at small depth of cut as shown in Figure 142. However, the surface damage depth decreased with increasing depth of cut and reducing the wheel grit size (D126 to D46).

The surface damage depth produced due to different levels of table feed and depth of cut is shown in Figure 143. This figure shows that the damage depth at low table feed of 2 mm/s increased with increasing the depth of cut. A higher damage depth obtained may indicate a larger crack size of ground component. The sub-surface cracks depth from the ground surface at the same machining parameters is shown in Figure 158. This figure shows that the location of sub-surface median cracks were found to be very close to the ground surface at low table feed of 2 mm/s. These locations can also be seen to increase in most of the cases with increasing the table feed as shown in Figure 158.

From the above results, it can be observed that, a higher damage depth on the ground surface at low table feed was measured. However, the location of sub-surface crack depth was found to be at a very small depth from the ground surface (see Figure 158 and 143). The damage depth on the ground surface against depth of grinding cut averaged over different levels of table feed, grit size and bond type is shown in Figure 144. These averaged values represent the response of the damage depth on the ground surface associated with several experiments carried out for individual levels of depth of grinding cut.

The surface damage depth produced at different levels of diamond wheel grit size and grinding wheel speed is shown in Figure 145. Small depth of surface damage was found over all grinding wheel speed when smaller grit size was used. The bond type of this grit size is shown in Figure 146. The surface damage produced using a cast iron bonded grinding wheel decreased with increasing the grinding wheel speed as shown in Figure 146. Hard grinding wheel bond was found to produce smooth ground surface when the grinding wheel speed increased.

The effect of different levels of table feed and grinding wheel speed on the surface damage depth is shown in Figure 147. It can be observed from this figure that the damage depth on the surface was found to be higher at low table feed 2 mm/s. Low depth of sub-surface median cracks was found for the same machining parameters and is shown in Figure 162. Most of the locations of these cracks in the sub-surface were

found to be in a deeper depth from the ground surface when the table feeds were increased. The variations on these depths shown in this figure at 2 mm/s can be compared with the grinding forces at the same table feed shown in Figure 102. From these figures, the grinding forces seem to have an influence on the depth of these sub-surface cracks from the ground surface. The sub-surface cracks were found to be at a deeper locations when the grinding forces were increased.

Figure 149 shows the effect of different levels of grinding wheel conditions and diamond grinding wheel girt size on the surface damage depth. The surface damage depth on the ground surface was found to increase with increasing the grit size used. The bond type of these grit size can be recognised from Figure 150. At -0.5 speed ratio, D46 resin grit size was extremely sharp. Low fracture strength of 508.8 MPa was obtain for this condition. The effect of different levels of grinding wheel conditions and table feed on the surface damage depth is shown in Figure 151. Speed ratios of -0.3, +0.3 and +0.4 produced low variations of surface damage depth over all levels of table feed. The surface damage depth against grinding wheel condition averaged over different levels of table feed, grit size and bond type is shown in Figure 152. This averaged values represented the response of surface damage depth associated with several experiments carried out for individual levels of grinding wheel conditions. The strength of the ground ceramic specimens obtained for these conditions is shown in Figure 64.

7.6.2. Analysis of Sub-surface Micro-Cracks Location of Ground Ceramic

Median and lateral cracks were found to be initiated in the sub-surface at layers very close to the ground surface. Below this layer, tensile stresses may occur which could initiate this type of sub-surface micro crack. This phenomena was observed in the FE model when the grinding process was simulated. The animation option of solved FE model shows that loading and unloading of the grinding forces on the ceramic FE model creates this type of cracks. It was also observed that sub-surface median micro cracks were initiated at the weaker element of the ceramic component under the compressive layer on the surface. The size of the median cracks and their distance from the ground surface was shown to be dependant on the wheel and machine parameters simulated by the grinding forces obtained from experimental work.

The experimental observations showed that, median cracks were at a deeper distance from the ground surface compared with lateral cracks. The depth of median cracks from the ground surface was observed to increase (2-15 μm) with increasing the depth of cut and when the grinding wheel was blunt. Lateral cracks were found under a thin layer with a thickness of (2-4 μm). It is believed that they were created due to residual stresses [44]. The depth of the lateral cracks from the ground surface were not found to be affected by increasing the depth of grinding cut.

The sub-surface median and lateral cracks were measured after the three point bending test by using SEM. During the bending test of the ground ceramic specimens, it was observed that the failure point occurs where the sub-surface median cracks initiated due to the grinding process. The sub-surface cracks initiated due to the grinding process were compared with the sub-surface section of unground specimens after the bending test shown in Figure 153. Median and lateral cracks found in the sub-surface of ground ceramic specimens were not found in the sub-surface of unground specimens after the three point bending test. This may be due to the high hardness of the silicon nitride materials and prove that such cracks were not created due to the three point bending test.

The dimensions of sub-surface median crack created by resin bonded grinding wheel with D76 grit size was found to be 30 μm in length parallel to the grinding direction and 20 μm in height perpendicular to the ground surface as shown in Figure 154. The depth of median crack from the ground surface was measured to be 6 μm. Increasing the grit size of the resin bonded grinding wheel to D126 at depth of cut of 120 μm was found to increase the dimension and distance from the ground surface of the sub-surface median cracks. The size was measured to be 40 μm in height parallel to the grinding direction and 22 μm perpendicular to the ground surface. The distance of this median crack from the ground surface was measured to be 11 μm as shown in Figure 155.

The increase in the depth of cut at the same grinding wheel bond type and grit size was found to increase the dimensions and the locations of the sub-surface median cracks. Soft bonded diamond grinding wheel produced small sub-surface cracks dimensions and depth from the ground surface compared with stiff bonded grinding wheel type. The increase in the grinding wheel grit size of soft bonded grinding wheel was found to increase the dimension and depth from the ground surface of median sub-surface micro cracks.

The sub-surface micro-cracks depth from the ground surface initiated due to different levels of grinding wheel grit size and depth of cut is shown in Figure 156. The depth of these sub-surface cracks was found to be affected by increasing the depth of cut. The deeper location of median cracks was found to reduce the fracture strength of ground component. The figure shows that the distance of sub-surface cracks from the ground surface using D46 grit size is small (2 μm) at small depth of cut (52 μm). However, this distance increased to 6.5 μm with increasing the depth of cut to 181 μm. This could be due to rapid wear of grits on the wheel surface at higher depth of cut. This rapid wear increases the friction between the wheel and the workpiece affecting the sub-surface layers and initiating median cracks in the sub-surface. This was observed to be associated with higher AE spectral amplitude. Blunt coarse grit size D126 produced a farther distance of sub-surface crack location beneath the ground surface (11.5 μm) at depth of cut of 108 μm. At this condition, small depth of surface damage was measured (9 μm) as shown in Figure 141. This value was an average of several measurement of these cracks on both surface and sub-surface of this condition.

The hardness of the diamond grinding wheel bond type was found to affect the sub-surface condition of the ground ceramic. The bond type of these grit sizes is shown in Figure 157. This figure shows the sub-surface cracks distance from the ground specimens due to different levels of bond type and depth of cut. The sub-surface cracks distance due to resin bond wheel was found to be small at small depth of cut. This distance increased with increasing depth of cut. A deeper location of sub-surface median cracks were observed when blunt D126 grit size of resin bonded wheel was used. This can be seen at depth of cut of 108 and 181 μm and shown in Figure 157.

This can also be seen from the small surface roughness (Ra) values at the same depth of cut and shown in Figure 68.

The depth of sub-surface cracks from the ground surface due to different levels of table feed and depth of cut is shown in Figure 158. The median cracks were observed at small distances from the ground surface at low table feed 2 mm/s. It can also be seen that the location of sub-surface cracks from the ground surface increased with increasing the depth of cut over all table feed levels. The location depth of sub-surface cracks against depth of cut averaged over different levels of table feed is shown in Figure 159.

The depth of the sub-surface median cracks due to different levels of wheel grit size and grinding wheel speed is shown in Figure 160. The locations of the sub-surface cracks were found to be affected by the condition of the grit size used. The bond type of these grit sizes is shown in Figure 161. Stiff cast iron bonded grinding wheel was observed to initiate deeper sub-surface cracks compared with resin bonded wheel at most of the wheel speed levels used. This phenomena varies with increasing the wheel speed. The locations of sub-surface cracks shown on Figure 161 were affected by other factors such as the grinding wheel grit size, table feed, and depth of cut. The increase in the grinding forces in some cases was found to be associated with deeper locations of the sub-surface median cracks as shown in Figure 101 and 161.

The effect of different levels of grinding wheel speed and table feed on the depth of sub-surface cracks from the ground surface is shown in Figure 162. The depths of the sub-surface cracks were found to be at lower locations from the ground surface in some cases and varied when the grinding wheel speed was increased as shown in Figure 162. This was due to the effect of the levels of other parameters i.e., grit size and their condition. The variations on these depths shown in this figure at 2 mm/s could be compared with the grinding forces at the same table feed as shown in Figure 102. From these figures, the grinding forces in most of the cases have an influence on the depth of these sub-surface cracks from the ground surface. The response of the depth of sub-

surface cracks from the ground surface due to different levels of table feed, grit size and bond types at different levels of depth of cut is shown in Figure 163.

Figure 164 shows that the grinding wheel condition have an influence on the sub-surface crack locations of ground ceramic. At speed ratios of -0.3, -0.4 and -0.5, the depth of sub-surface cracks increased with increasing the wheel grit size. Small grit size D46 initiated sub-surface cracks at deeper depth (5.2, 5.4, 6.7 and 6.2 μm) at the rest of speed ratios levels (+0.3, +0.4, +0.5 and +0.6). These conditions were found to be associated with small values of surface damage as shown in Figure 149. This was due to the grits being extremely blunt at these speed ratios. Coarse grit size D126 was observed to be associated with higher damage on the surface when the grains condition on the wheel surface were sharp. However, sub-surface cracks were observed when D126 grit sizes were blunt on the wheel surface. The sub-surface cracks were found to be at deeper location from the ground surface. This was found to reduce the strength of ground ceramic component as shown in Figure 64. The effect of bond type of these grit sizes is shown in Figure 165. Stiff bond type initiates sub-surface cracks at deeper depth from the ground surface in most of the cases shown in this figures.

The effect of different levels of table feed and grinding wheel conditions on the location of sub-surface cracks is shown in Figure 166. Low table feed (2 mm/s) was associated with cracks in the sub-surface at small depth beneath the ground surface. This can be seen over most of speed ratios shown in this figure. However, these locations were observed in most of the cases shown in Figure 166 at a deeper depth when the table feeds were increased. The sub-surface cracks depth from the ground surface against grinding wheel condition averaged over different levels of table feed is shown in Figure 167. This figure represents the averaging response of the depth of sub-surface cracks from the ground surface at different levels of table feed, grit size and bond type.

7.7. Artificial Cracks Creation

One of the most significant contribution of this work, is the method by which artificial cracks were created on the ceramic specimens. Using single point diamond to

create artificial cracks has been used by several researchers [28, 30, 32, 36, and 42]. The author believes that creating an artificial crack using a single point diamond does not accurately simulate the process responsible for crack initiation during grinding. The very random nature of diamond grit shape, size and location on the surface of the wheel would alter the characteristics of a crack initiated in a real grinding process. For this particular reason, to simulate real grinding, artificial cracks were initiated on the surface of the ceramic specimens by using a diamond v-shape edge disc. The disc has the same grit size as those used for the grinding wheels. It was chosen such that the characteristics of the crack initiated would be the same as that produced during a real grinding situation. The crack would be produced such that the effect of crack initiation on the surrounding area will also be simulated.

The author believes that use of a v-shaped disc would be more realistic than producing an artificial crack with a single diamond scratch. This technique used for creating an artificial crack is the first reported attempt hitherto. Previous research performed a scratch test using a single-diamond point at fixed depth of cut.

Different artificial cracks depth were initiated on the surface of the ceramic specimens by v-shape edge discs. These cracks were initiated at different directions on the specimens surface as shown in Figure 31. Before initiating the crack on surface of the workpiece, an LVDT was used to make sure the workpiece was level to ensure uniformity of groove depth. The effect of initiation of artificial cracks on the surrounding area formed by v-shape disc is shown in Figure 170. For comparison, the scratch surface performed by single diamond can also be seen in the same figure. The difference between these types of scratch test can easily been seen. Increasing the artificial crack depth was found to increase the surface radial cracks on the surrounding of the groove surface produced by the v-shape disc shown. The affected area underneath the groove edge surface increased with increasing the depth of groove as shown in Figure 169. This figure shows the sub-surface at the end of the groove of unbroken specimens.

The AE signals for different groove depths were stored and then analysed using FFT as shown in Figure 168. Different levels of crack depth (grooves) have been created (10-120 μm) at 2000 rpm and 2 mm/s table feed. Higher AE spectral amplitude was observed when the depth of groove increased. This increase in amplitude was due to the long distance of crack propagation which occurred when the depth of scratch was increased. Larger groove depths produced, a deeper location of median cracks extending perpendicular to the surface. Shorter median cracks propagated when the depth of artificial cracks was small. During the grinding process, lateral cracks were found to propagate in the sub-surface more or less parallel to the grinding and groove surface direction. These cracks caused chipping in many situations thus exposing the fracture surface.

7.7.1. Grinding on Specimens with Artificial Cracks on their Surface

The purpose of this part of the work was to investigate the effect of different levels of grinding wheel and machine parameters on the propagation of artificial cracks initiated on the ceramic surface specimens. An AE sensor was attached on the surface of ceramic specimens during this test. The AE signals were triggered and analysed, and the surface and sub-surface damage of the ground specimens were then inspected.

The machining marks and the radial cracks on the surface were investigated using SEM, Talysurf and 3D surface topography. Sub-surface micro cracks were investigated after the bending test had been carried out. The size of sub-surface cracks and their depth from the ground surface were measured using SEM. Only a thin layer of the ground ceramic surface was found to be affected by the grinding parameters described. This could be due to the high hardness of the silicon nitride materials. When the depth of grinding cut was higher than the depth of artificial cracks, these cracks were found to disappear.

Experimental design with an L_{27} experimental orthogonal array was used. AE signals generated during grinding specimens with artificial cracks on the ceramic surface (GC) and without cracks (GN) are shown in Figures 82 and 83. The AE spectral amplitude ratio of specimens ground with artificial cracks is higher in the range of 210

to 440 compared with specimens ground without artificial cracks in the range of 150 to 300 as shown in Figures 87 and 181. These AE amplitude values have been generated from the grinding zone averaged over the range of the grinding wheel and machine tool parameters used during this test. The higher AE amplitude was due to the long propagation distance of the artificial cracks on both the surface and sub-surface of ground ceramic component.

Grinding was carried out on specimens with artificial cracks on their surface. AE signals were recorded and analysed for different grinding passes on specimens with artificial cracks initiated on their surface as shown in Figures 173 and 174. The ground specimens were then inspected using SEM as shown in Figures 171 and 172. The depth of surface damage was measured using three dimension surface topography as shown in Figures 176 and 177. Three point bending tests were then carried out to inspect the sub-surface section of these specimens. The fracture strength of specimens ground with different crack depths created on the surface in the range of less than, equal to and larger than the depth of cut was calculated. This was at different grinding wheel and machine parameters.

7.7.1.1. Quantitative Results of Artificial Crack Propagation

The depth of the artificial cracks on the ceramic surface were measured before and after the grinding process. The propagation distance of the artificial cracks due to different grinding wheel and machine tool parameters was then measured. A ceramic specimen was ground with an artificial crack depth of 25 μm and then with an actual depth of grinding cut of 13.5 μm using cast iron bonded grinding wheel with D76 grit size as shown in Figure 176. The remaining depth of the artificial crack was measured to be 22.5 μm. The propagation distance on the ground surface was found to be 11 μm. The ground surface plus artificial crack was also investigated by using SEM as shown in Figure 171. It can be seen in some areas of the ground surface, the artificial crack was "closed up" by a thin layer of material. This could be due to the influence of residual stresses. The propagation distance of the artificial crack with actual depth of 140 μm due to the grinding process using resin bond with D126 grit size was measured as shown in Figure 177. The actual depth of cut was 128.7 μm, the remaining depth of

artificial crack was measured to be 24.2 μm. The propagation distance on the ground surface was measured to be ≅13 μm. From these figures, it was found that the propagation distance of the artificial cracks on the ground surface increases when the grinding wheel grit size increased.

The influence of artificial cracks on the ground sub-surface layer was investigated. Median and lateral sub-surface cracks were found underneath the ground surface with artificial cracks as shown in Figure 172. The sub-surface cracks were found to be at a deeper locations, 45 μm from the ground surface. However, these locations were found to vary in some areas, in the range of 15 to 30 μm. The locations of these sub-surface cracks were found to be at a larger depth from the ground surface compared with those measured when ceramic specimens were ground without artificial cracks.

Different grinding passes were carried out on the artificial cracks in different grinding directions. The AE spectral amplitude generated from the grinding zone was monitored as shown in Figures 173 and 174. The ground surface was inspected by using SEM as shown in Figure 175. The AE spectral amplitude shown in Figures 173 and 174 was found to vary with the grinding direction. Four grinding passes in each experiment were monitored. The first grinding pass was selected to be up-cut grinding. Most of the material was removed in this grinding pass. The AE spectral amplitude was found to be higher when the second down-cut grinding pass cut was performed as compared with the first up-cut grinding pass. The higher AE spectral amplitude in the second down-cut grinding pass was due to the propagation of lateral cracks or to possible removal of the thin layer that covered these cracks. These cracks could be initiated after actual cutting by a grain and propagated due to residual stresses. Down-cut grinding was found to generate a higher AE spectral amplitude which could reflect the long propagation distance that the cracks initiated.

AE spectral amplitudes generated from the grinding process for specimens ground with artificial cracks initiated on their surface are shown in Figure 178 to 185. These figures show the effect of different levels of grinding wheel and machine

parameters on ground ceramic specimens with different levels of groove depth. These figures show that the AE amplitude generated during grinding the specimens with artificial cracks on the ceramic surface is higher than specimens ground without artificial cracks and shown in Figures 84 to 95. The variations in the AE spectral amplitude recorded during grinding of the specimens, with and without artificial cracks on the surface, was due to the propagation of these artificial cracks. This can also be observed when the depth of artificial cracks is larger than the depth of cut.

7.7.1.2. AE Spectral Amplitude Generated from Specimens Ground with Artificial Cracks on their Surface.

The effect of different levels of grinding wheel and machine parameters on the AE spectral amplitude, depth of surface damage, fracture strength of specimens ground with different levels of artificial cracks depth will be discussed in this section.

The effect of different levels of wheel grit size and depth of cut on the AE spectral amplitude is shown in Figure 178. The AE spectral amplitude was found to increase with increasing depth of cut. It can also be observed that the AE spectral amplitude increased when using diamond grinding wheels with smaller grit size. Figure 178 shows that fine grit size D46 generates higher AE spectral amplitude compared with D76 and D126 diamond grinding wheel grit size. The bond type of these grit size is shown in Figure 179. The spectral amplitude was found to be higher when specimens containing artificial cracks were ground, as shown in Figure 178. This figure could be compared with specimens ground without artificial cracks as shown in Figure 84. The increase in the AE spectral amplitude could reflect a longer propagation distance of these artificial cracks during the grinding process. These figures represent identical machining conditions, however, the actual depth of cut was not the same for both conditions.

The effect of different levels of table feed and depth of cut on the AE spectral amplitude is shown in Figure 180. At low table feed, 2 mm/s, the AE spectral amplitude does not change with depth of cut. However, the AE signals can be seen to vary at higher table feeds. The AE spectral amplitude against depth of cut averaged over

different levels of table feed is shown in Figure 181. The increase in the table feed was found to be associated with the increase in the AE spectral amplitude generated from the grinding zone. This could reflect a long propagation distance of the artificial cracks when they were ground at higher table feed. A similar situation to that when ceramic specimens were ground without artificial cracks. The sub-surface median cracks were found to be at a deep location from the ground surface and had large dimensions.

The variation of the AE spectral amplitude due to different levels of grinding wheel speed and wheel grit size is shown in Figure 182. The AE spectral amplitude was found to increase slightly with increasing grinding wheel speed. The bond type of these diamond grinding wheel grit sizes is shown in Figure 183. Low variations on the AE amplitude can be seen at most of the grinding wheel speed levels. This could be due to the small range of the grinding wheel speeds (20-32 m/s). The variations on the AE signals shown in Figure 184 at different levels of wheel speed and table feed was affected by the grit size and depth of artificial cracks. The increase in the grinding wheel speed averaged over different levels of table feed was found to increase the AE spectral amplitude generated from the grinding zone as shown in Figure 185. Averaged results were at different levels of grit size, bond type and artificial cracks depth. It can be observed from this figure that, at low levels of wheel speed, the AE spectral amplitude does not change. However, these amplitudes seem to slightly increase with higher levels of wheel speed.

7.7.1.3. Effect of Surface Damage Depth on the Strength of Ceramic Ground with Artificial Cracks Initiated on their Surface.

The effect of different levels of wheel grit size and depth of cut on the damage depth of specimens ground with artificial cracks is shown in Figure 186. Depth of artificial cracks and depth of grinding cut were changed relative to each other. This figure shows that the damage depth decreased with increasing the depth of cut. This meant that the artificial cracks were removed when the depth of cut exceeded that of the artificial cracks. The depth of surface damage measured with specimens ground with artificial cracks on their surface against depth of cut averaged over different levels of grit size, table feed and bond type is shown in Figure 187.

The depths of any remaining artificial cracks after the grinding process were measured. Figures 186 and 187 show higher damage depths which reflect the propagation distance of these cracks on the ground surface due to different diamond grinding wheel grit sizes used. The influence of the remaining artificial crack depths after the grinding process can be compared with the strength of ground ceramic shown in Figures 188 and 189.

D46 wheel grit size was used at a depth of cut of 21 μm, and the remaining artificial crack depth after the grinding process was measured to be 29 μm. Low fracture strength of the ceramic workpiece was obtained (249 MPa). At the same depth of cut a D76 wheel grit size was used. The depth of remaining artificial crack was measured to be 22 μm. This was found to improve the fracture strength of this workpiece (318 MPa). Increasing the depth of grinding cut was found to reduce the effect of the artificial cracks on the fracture strength of ceramic specimens. At a depth of cut of 470 μm a D46 grit size was used, the damage depth was measured to be 5.7 μm. Higher fracture strength of ground ceramic specimen was found (387.1 MPa). At the same depth of cut and D76 wheel grit size was used, the damage depth was measured to be 9 μm. A lower fracture strength of ground ceramic specimen was obtained (352.3 MPa) as shown in Figures 186 and 188. It can be concluded from this that, small grit size inhibits the propagation of cracks and strengthen the ground specimens especially at higher depth of cut.

Figure 188 shows that the strength of ground ceramic was observed to improve when the artificial cracks were removed. This was due to the absence of the influence of the artificial cracks propagation. This means that, the higher depth of cut allows the wheel to plough underneath the artificial crack and remove it before it can propagate. The effect of the grit size on the ground strength produced can also be observed. Small grit size was found to produce high ground strength which means small distance of cracks propagation occurred compared with coarse grit size. The strength of ground ceramic against depth of cut averaged over different levels of grit size for specimens ground with artificial cracks on the surface is shown in Figure 189. It can be seen that

the strength of ground specimens were improved when the influence of artificial cracks propagation was absent. This can be compared with the depth of damage that decreased with increasing the depth of cut shown in Figure 187.

The effect of different levels of table feed and depth of cut on the damage depth of specimens ground with artificial cracks created on their surface is shown in Figure 190. This figure shows that the depths of damage were observed to be at a small depth for a low table feed of 2 mm/s. It can also be observed that a long propagation distance was associated with an increase in the table feed. The influence of the remaining artificial cracks on the strength of ground ceramic is shown in Figure 191. The strength was found to improve when the influence of artificial crack was reduced.

The effect of different levels of grinding wheel speed and grinding wheel grit size on the damage depth is shown in Figure 192. This figure shows that coarse diamond grinding wheel grit size (D126) can increase the propagation of the artificial cracks. The influence of the remaining artificial cracks on the ground strength of ceramic is shown in Figure 193. This figure shows the changes in the strength of ground specimens at different grinding wheel speeds and grit sizes. Coarse grit sizes was found to produce low ground ceramic strength.

8.0. DISCUSSION

8.1. Introduction

This chapter discusses the results obtained in this research work in the light of previous work by other authors. Extensive experimental study was carried out for a better understanding of the material removal of ceramic during grinding process. The effect of different levels of grinding wheel and machine tool parameters on the ground specimens were investigated. These parameters are diamond grinding wheel grit size, bond type, grinding wheel condition, depth of cut, grinding wheel speed and table feed. Each parameter has different levels to cover selected ranges of grinding wheel and machine tool. The response of the fracture strength, surface roughness, AE spectral amplitude, grinding forces, specific grinding energy, crack size, depth of sub-surface damage from the ground surface and the depth of damage on the ground surface due to different levels of grinding wheel and machine tool parameters will be discussed.

8.2. Preliminary Investigation

The main objective of this part of the research was to study the initiation and propagation of cracks in the grinding of ceramic materials. In order to study this, a comprehensive preliminary study has to be made of the different parameters that may affect the mechanics of the grinding operation itself. These parameters are, the diamond grinding wheel condition, grinding wheel bond type and the effect of very high infeed.

8.2.1. AE Technique to Study Grinding Wheel Condition

Imprint of grinding wheel profile technique was used to study the grinding wheel surface condition. This was carried out by taking one grinding pass on a mild steel specimen. Different levels of truing and grinding wheel speed ratios and directions were investigated. An acoustic emission (AE) sensor with high frequency sampling was attached on the mild steel specimen to monitor the wheel condition. The AE spectral amplitude of different grinding wheel condition represented by different levels of grinding wheel/truing speed ratios were compared with the surface roughness of a ground mild steel.

As an indirect process parameter, the AE signal is characterised by much shorter response times as compared to machining forces or motor currents. Konig and Klumpen [104], explained some AE applications for tool life monitoring, dressing fault diagnosis and sharpening process control. They observed that the AE_{rms} levels changed with the wheel condition. The results obtained in this study (see Figures 23 to 26) show the variations of the AE spectral amplitude and the surface roughness for one grinding pass imprint of the grinding profile envelop on mild steel specimens. It can be observed that low surface roughness ($Ra \approx 0.6$ μm) was associated with high AE spectral amplitude (see Figures 23 and 24). This could be due to the higher friction contact between the grinding wheel and the workpiece. This also was due to blunt grinding wheel condition. These figures can give an indication about the wheel condition by observing the variations of the surface roughness and the AE spectral amplitude. The variations in both AE spectral amplitude and surface roughness shown are at different grinding wheel conditions for the same grinding wheel grit size and different bond type.

From the above observations, it can be suggested that the smooth surface roughness of grinding profile envelop imprint on mild steel specimens generates a higher AE spectral amplitude. Cast iron and vitrified bonded grinding wheels with the same grit size D46 produced smooth surface roughness and higher AE spectral amplitude was generated. Coarse resin bonded diamond grinding wheel with D126 grit size produced higher values of surface roughness. This was observed to be associated with low AE spectral amplitude. Dornfeld [91,111] has correlated the burn to AE spectral amplitude. He showed that the burned workpieces to have higher AE spectral amplitude compared with unburned specimens. They also showed that the AE energy increases with the combined effects of wheel wear and loading.

The aim of this part was to monitor the diamond grinding wheel condition by using AE technique. This was achieved by imprinting the grinding wheel surface profile on mild steel specimens after different grinding wheel/truing speed ratios and directions. The surface roughness of these specimens were then measured. These results were then compared with the AE signals generated during the test. Different grit size, bond type and conditions used in this test indicate that the AE technique was a useful

tool to monitor the grinding wheel condition during the grinding process. The AE technique could be more accurate and can cope with higher grinding wheel speeds due to the higher sampling frequency used.

8.2.2. Grinding Wheel Bond Type

Three diamond grinding wheels with different bond types were used in the preliminary investigation. Material strength and surface roughness characteristics and the effects of grinding attributes on the resultant surface finish were investigated. Experimental design with Taguchi L_9 orthogonal array was used. The results from the experiments were translated into their respective signal to noise ratios (S/N) of larger is better for strength analysis and smaller is better for surface roughness analysis.

The effect of using a stiff grinding wheel such as metal bond diamond wheel gives better surface roughness but with low strength. The low strength could be due to an increase in sub-surface cracking. Variation in strength properties with depth of cut was similarly dramatic above 250 μm (see Figures 45 and 46). The effect of the depth of cut to surface roughness suggests that better surface qualities are achievable at increased depth. This can be attributed to the relatively higher ratio of active cutting edges available. However, there would appear to be a limit to this performance to be able to effectively penetrate the workpiece beyond 250 μm. This could be attributed to the extended sliding length of active grits through the workpiece for which attrition wear becomes most appreciable.

The low resilience of resin bonds however, mean that the extremities achievable are relatively low in comparison to either the metal or vitrified wheels, this is because the resin bond has low Young's modulus value compared with the other bonds. Some evidence of this was observed from the cutting envelopes produced which were designed to determine the relative sharpness of the wheels subsequent to dressing.

8.2.3. Effect of Very High Infeed

The effect of very high wheel speed reaching 50,000 rpm is to introduce a very large number of diamond grits to the arc of cut in a very short time. This large number

of grits would mean a much smaller loading on each grit, hence altering the removal of material characteristics. In this research a maximum grinding wheel speed of 4000 rpm can be achieved. Increasing wheel speed, while operating at a relatively low material removal rate, can dramatically reduce surface fragmentation. This behaviour stems from the fact that the unit grit load is reduced significantly by increasing wheel speeds. Kovach et al [15] used very high grinding wheel speeds up to 178 m/s and material removal rates up to 11 mm^2/s. They showed that the grinding forces decreased considerably with increased wheel speed and/or reduced material removal rate and that a tendency towards improved surface finish is developed as wheel speed is increased. They concluded that although extensive modulus of rupture MOR testing is yet to be performed, their results suggest that a transition from a `brittle fracture` mode of grinding to a low damage `ductile` grinding mode can be achieved by increasing wheel speed and/or material removal rates.

An attempt was made to simulate the effect of very high grinding wheel speed through altering the infeed of the ceramic component Maksoud and Mokbel [16]. Very high infeed up to 32767 mm/min was used in association with a shallow depth of cut. This simulation is not complete because of the effect of diamond grits loading would not be the same. However, this effect was partially negated by using higher concentration diamond grits. The simulation, however, is still not completely accurate due to the different chip pockets size.

The range of the feed rates between 5762 mm/min and 32767 mm/min is extremely high feed, not usual in conventional grinding, was used in this research. The result of the surface finish, surface topography and fracture strength of the ground components, crack size were then compared to conventionally ground component. As was expected, the normal forces are higher than tangential forces with ratio range of 2.5 to 4.5 (see Figures 47 and 48). This ratio was kept constant even at different depths of cut. The increase in both tangential and normal forces with increasing feed rate can be explained by the fact that the number of abrasive grit acting in the grinding zone per unit time was increased. The effect of increasing depth of cut is more influential than that of increasing the feed rate on the grinding force. This could be due to the increase

in material removal rate. The crack size was found to increase with increasing depth of cut. The effect of very high infeed on the crack size was calculated and found to decrease with increasing high infeed (see Figures 52 and 53).

8.3. Main Experimental Investigation into the Effect of Grinding Wheel and Machine Tool Parameters on the Ground Ceramic Component

The effect of different levels of diamond grinding wheel grit size (D46, D76 and D126) at different levels of depth of cut (20 to 500 μm), grinding wheel speed (20 to 32 m/s) and grinding wheel condition (-0.3 to +0.6) on the ground ceramic will be discussed in this section.

The strength of ground ceramic due to different levels of grinding wheel and machine tool parameters were investigated. It was found that the strength of ground ceramic component improved (569.6 MPa) when D46 diamond grinding wheel grit sizes were used. The surface roughness produced was found to affect the strength of ground ceramic (see Figure 54 and 68). Rough ground surface (Ra = 1.486 μm) was found to be associated with low ground strength (203.7 MPa) of ceramic component. The reduction in the strength of ground ceramic was found to be associated with an increase in both AE spectral amplitude ratio (151 to 299) and normal grinding forces from 4.4 to 9.75 N/mm (see Figures 84 and 96). These figures showed both AE spectral amplitude and grinding forces were increased when depth of cut was increased (25 to 443 μm). The specific grinding energy at the same machining parameters was found to decrease (586.5 to 72.5 J/mm^3) with increasing the depth of cut. The reduction on the specific grinding energy and the increase in both AE spectral amplitude and grinding forces was found to be associated with an increase in the crack size (68.8 to 522 μm) when the depth of cut increased (see Figures 108 and 112). This could reflect a higher percentage of brittle grinding mode occurred at higher depth of cut of these conditions. The increasing in both wheel grit size and the depth of cut were found to be the most influential factor on the amount of cracking in the ground ceramic specimens.

The ground ceramic specimens were found to be associated with surface and sub-surface micro cracks. These cracks were the main reason for reducing the strength

of ground component. The sub-surface median cracks depth from the ground surface was found to be at a deeper location when small or blunt wheel grit sizes were used and depth of cut was increased (see Figure 156). The deeper location beneath the ground surface (13 μm) and large crack dimensions (55 x 30 μm) of these median cracks were found to be associated with low strength of ground ceramic component at this condition.

The most influential factor which affect the strength of the ground ceramic at different levels of grinding wheel speed was the grit size used. Higher ground strength was achieved by using fine grit size. The changes in the ground strength (569.6, 322.1 and 196.1 MPa) was found to be affected by the variations in the surface roughness (Ra) of 0.68, 1.124 and 1.486 μm of D46, D76 and D126 grit sizes respectively. At grinding wheel speed of 26 m/s and 32 m/s and D46 grit size, it can be observed that any slight change in the surface roughness influences the strength of ground ceramic (see Figures 60 and 74). The very small change in the surface roughness and higher reduction in the fracture strength was due to the formation of sub-surface median cracks.

A concept for maximum strength grinding of hot pressed silicon nitride was presented by Mayer et al [21,22] based on the relationship of fracture strength versus wheel grit depth of cut. They showed that maximum strength in the ground ceramic is achieved when the wheel grit depth of cut is equal to or less than a critical value of grit depth of cut. They observed that, the effect of grit depth of cut on the fracture strength appeared to be true regardless of whether the grit depth of cut is varied by varying wheel grit size or the machine parameters such as the workpiece speed and depth of cut. In this research three levels of diamond grinding wheel grit sizes were used. The results obtained in this research are in agreement with the results obtained by [21,22]. Small grit size D46 produced higher fracture strength of ground silicon nitride material compared with D126 diamond grinding wheel grit size.

The variations of the grinding forces generated from the grinding zone at different grinding wheel speed give an indication on the crack size of ground ceramic

(see Figures 100 and 116). These figures represent the same levels of grinding wheel grit size and wheel speed. The reduction in the strength of ground ceramic component was found to be associated with increasing both AE spectral amplitude and grinding forces at different grinding wheel speeds (see Figures 88 and 100). The crack size of ground component shown in Figure 116 was found to increase when the grinding forces increased.

Low surface damage depth on the ground surface was observed when D46 grit size was used. However, sub-surface cracks were found to be at deeper locations from the ground surface at most of these grinding wheel speeds (see Figure 145 and 160). The influence of maximum surface damage on the strength was investigated by Tanaka et al [25]. They mentioned that the surface roughness as a result of the grinding operation changes the structure in the deformed surface layer which influence the mechanical property of the ground material. They observed that the bending strength decreased with the increase in the maximum damage on the ground surface measured by using R_{max} of the Talysurf. The results they obtained is in agreement with this research. However, in this research, the damage depth on the ground surface was measured by both R_{max} of Talysurf and three dimension surface topography. The results show that when the surface damage depth on the ground surface increased from 5.3 to 11.7 μm, low strength of ground silicon nitride was decreased from 427.4 and 196.7 MPa for these conditions.

The diamond grains condition on the grinding wheel surface was found to have an influence on the strength of ground component. The surface roughness produced due to different levels of diamond wheel grit size and grinding wheel conditions was found to be affected by the wheel surface condition (see Figures 64 and 78). The variations in the grain conditions due to different speed ratios (+0.3 and +0.6) of D126 grit size was found to have an influence on both the surface roughness (Ra) produced (1.3616 and 1.596 μm) and fracture strength (381.8 and 170 MPa). It was found that when the grains on the wheels surface were extremely sharp, large amount of surface cracking was detected. However, blunt grains condition of the wheel surface was found to be associated with sub-surface median cracks underneath smooth ground ceramic surface.

The AE spectral amplitude and the grinding forces generated from the grinding zone were monitored. It was found that the changes in the grinding forces are due to the changes in the grinding wheel surface condition (see Figures 92 and 104). Higher grinding forces were found to be associated with stiff bonded grinding wheel and blunt wheel surface. The crack size of the ground ceramic specimens was found to increase with increasing the grinding force (see Figures 104 and 120).

The depth of sub-surface cracks from the ground surface was found to be affected by grinding wheel condition of different levels of grit size (see Figure 164). Small grit size D46 of the grinding wheel initiates sub-surface cracks at higher depth from the ground surface when the grinding wheel surface condition changed. At +0.5 speed ratio a deeper location of sub-surface crack was found. This was associated with an increase in both AE spectral amplitude and grinding forces (see Figure 92 and 104). A smoother ground surface was produced at +0.5 and D46 grit size, however, low ground strength was found (see Figure 78 and 64). A deeper surface damage depth was found to be associated with an increase in the crack size of the ground component over all the levels of the grinding wheel grit sizes and their conditions (see Figures 120 and 149). Cast iron bonded wheel with D46 grit size produced slightly less value of surface roughness (Ra = 0.65 μm) compared with the same grit size of resin bond wheel (Ra = 0.7 μm). However, low ground strength of 419.85 MPa was obtained when cast iron boned was used compared with 503.5 MPa when resin bond wheel was used with the same D46 grit size (see Figures 56 and 70). This was due to the formation of the sub-surface median cracks when stiff grinding wheel was used as shown in Figures 153.

The specific grinding energy due to different levels of grinding wheel bond type and depth of cut was found to decrease with increasing depth of cut. At these levels of depth of cut, cast iron bonded grinding wheels was found to generate higher specific grinding energy compared with vitrified and resin bonded wheels. The increase in the percentage of the brittle grinding mode during material removal was associated with the formation of surface cracks when soft bonded grinding wheels were used at higher depth of cut. A higher amount of sub-surface cracks were initiated when stiff and small

grit size grinding wheels were used. This was found when the depth of cut was increased and smooth ground surfaces were produced. Stiff grinding wheels with coarse grit size initiate surface cracks with long distance of crack propagation on the ground surface. This was observed at low depth of cut. The surface roughness produced due to different levels of wheel bond and depth of cut was found to affect the ground strength obtained. The harder the diamond grinding wheel bond used the larger the cracks size was found when the depth of cut increased (see Figures 55, 69, 113).

The grinding wheel sharpness was found to be dictated by the grinding wheel/truing speed ratio and has significant influence on the induced damage. The individual grits on diamond grinding wheel interact with the workpiece as a series of micro-cutting tools. The shape of these cutting edges was obtained by one pass imprint on a mild steel specimen prior to the grinding and was found to have an influence on the strength of ground ceramic. There exists a point of minimum damages as dressing speed ratio (speed of grinding wheel/speed of truing wheel) is increased from -0.3 to +0.6. Maximum damage is induced with a wheel periphery which is extremely sharp. At this condition, the roughness of the ground component is one of the main cause for strength deterioration of ground ceramic.

The deterioration of strength is related to the level of cracking produced. Factors affecting cracking length can be approximated using indentation Takaki and Liu [23];

$$C_o = \{ A [(E/H)] / K_c] . (\cos B)^{2/3} P\}^{1/2}$$

The strength of ground specimens varies with the elastic modulus of the bond material of diamond grinding wheel used. Resin bond wheels have the lowest modulus and found to induce the lowest level of damage in a ceramic workpiece.

Resin, vitrified and cast iron diamond grinding wheels having different elastic modulus of the bond material were investigated. The effect of this range of grinding wheel bond material changed when the depth of cut increased. A soft bond such as resin, can produce higher strength of ground ceramic than metallic bond at small levels

of depth of cut. The grit size of each bond used was found to be the most influential factor that affect the initiation and propagation of both surface and sub-surface cracks. The small grit sizes of the grinding wheel used can produce smooth ground surface with less cracking on the ground ceramic component. This was found to improve the strength of ground ceramic component. However, sub-surface cracks were detected.

The grinding wheel/truing speed ratios investigated were found to have different effects on the wheel conditions according to the hardness of the bond. Soft bond type such as resin could be removed easily during the truing and dressing operations and sharp grains can be produced easily on the wheel surface. However, sharp grains on the wheel surface of cast iron bonded wheels was produced at higher grinding/truing speed ratios. Higher amount of surface cracking was found to be associated when coarse or extremely sharp grits condition on the wheel surface were used. This is rough produced. Sub-surface median cracks were found when small or blunt grits condition on the wheel surface were used even when smooth ground surfaces were produced.

8.4. Correlation of Acoustic Emission (AE), Scanning Electron Microscopy (SEM) and 3D Topography Data to Investigate the Ground Ceramic Condition

An understanding of crack initiation and propagation during the grinding of advanced ceramic material is one of the main objectives of this research. Roughness / smoothness of the ground surface condition was investigated. Higher AE spectral amplitude was observed when small diamond grinding wheel grit size was used and smooth ground surfaces were produced. The surface roughness of these surfaces was found in the range of 0.567 to 0.759 μm. The higher AE amplitude may be due to the higher energy generated during the material removal and the higher quality surface finish achieved. The formation of sub-surface median cracks was associated with higher AE amplitude.

Lower AE spectral amplitudes were generated from the grinding zone when a coarse grinding wheel grit size was used. Rough ground surfaces were observed using SEM and found to have surface roughness (Ra) values in the range of 1.179 to 1.596

μm. This coincided with a higher percentage of brittle grinding. A higher amount of cracking was found on both surface and sub-surface of the ground ceramic. The propagation distance measured by 3D surface topography of ground surface cracks was found to increase (6 to 18 μm) when the wheel grit size increased. The AE signals were compared with SEM observations which confirmed these results (see Figures 124 to 138).

The phenomena responsible for generation of high amplitude AE signals when fine wheel grit sizes were used was due to the initiation of sub-surface cracks underneath a smooth ground surface. Increasing the depth of cut using cast iron bonded wheel with small grit size (D46) was found to increase the generation levels of AE spectral amplitude ratio from the grinding zone (350-700). The depth of sub-surface median cracks from the ground surface were increased from 7 to 13 μm. For the deeper sub-surface median cracks (13 μm), the dimensions of this crack was found to be larger 30 μm x 55 μm (see Figures 129 and 130).This was observed when the depth of cut was increased and a smooth ground surface with Ra of 0.597 μm was produced. The fracture strength of the specimen for these conditions was found to be 437.6 MPa. Resin bonded wheel with the same grit size (D46) produced a smooth surface with Ra of 0.6798 μm and a fracture strength of 569.6 MPa. This increase in strength is due to fewer sub-surface median cracks being initiated when resin bonded wheels were used compared with a cast iron bonded wheel with the same grit size.

AE is an excellent tool to indicate how the grain condition on the wheel surface has an influence on the type of cracks initiated on the ground ceramic. Different crack types were found on the ground ceramic component. A higher percentage of radial cracks and machining damage were found when a rough ground surface was produced and in particular when the grains on the grinding wheel surface were extremely sharp. Increasing the size of the grit size (D46 to D126) was also found to initiate this type of surface damage. Median and lateral sub-surface cracks were found when smooth ground surfaces were produced. These were found when the grains on the wheel surface were blunt. Small grit sizes and stiffer bonded wheels were also found to increase the amount of sub-surface median cracks when the depth of cut was increased.

The AE events of short duration and low amplitude are of low energy, which is typical for micro-cracks developed during the material removal. Short duration suggest a short distance of crack propagation, and this was observed when D46 fine grit size was used and produced smooth ground surfaces. At high grinding forces, some AE components of long duration were observed. This may be related to the long distance of crack propagation.

The highest AE spectral amplitude ratio of 300 to 700 generated when smooth ground surfaces were produced was found to be in a frequency range of 0.3 to 0.7 MHz. This amplitude ratio of 145 to 200 was observed in a frequency range of 0.1 to 0.8 MHz when rough ground surfaces were produced. Eda et al [60] used a band pass frequency approach to detect in process grinding cracks. They performed grinding tests to hardened steel under abusive conditions, with the aim of detecting in-process grinding cracks by acoustic emission signals. The signals were analysed and compared with the signals produced before the grinding cracks were formed. Acoustic emissions between 0.6-0.8 MHz were detected on crack formation when grinding. This was in agreement with the range of higher AE amplitude observed during this research and correlated with SEM and 3D surface topography inspection.

The energy introduced in the layers close to the surface of the ground ceramic could lead to the formation of different crack types. These cracks were created on the surface at low AE amplitude when rough ground surfaces were produced or in the sub-surface at a few microns from the ground surface component. This condition was found when smooth ground surfaces and higher AE amplitudes were produced. In this research it was assumed that every single grain contact generates a stress pulse in the workpiece and has its own AE event. The energy of breaking atomic bonds during material removal can be related to the energy changes generated in the form of a stress wave or acoustic emission. Malen and Bolin [61] theoretically calculated the magnitude of the stress amplitude during plastic deformation and crack propagation. A crack of longer size may generate a stress wave of higher amplitude (see Figures 129 and 130). These figures show an increase in the AE spectral amplitude due to the increase in the

sub-surface median cracks. At an AE amplitude ratio of 350, the dimensions of sub-surface median crack was 14 μm x 20 μm and at 7 μm beneath the ground surface as shown in Figure 129. Increasing the depth of cut was found to be associated with increasing AE spectral amplitude ratio (700), the location of sub-surface median cracks (13 μm) and the dimensions of these cracks (30 μm x 55 μm) were both increased.

The theoretical calculations [61] are in good agreement with the experimental result obtained in this work. Increasing bluntness or fine grain depth of cut causes more cracking on the sub-surface which in turn generates high-amplitude stress waves containing higher AE amplitude. The results obtained by other researchers also indicate that AE amplitude and energy increase when there is more material cracking. Dalgleish et al [64], observed that the number of AE events depends on the amount of sub-critical crack growth. They also studied the amplitude distribution of AE signals and found that low-amplitude and short duration events were generated when the fracture was characterised by grain boundary flow, but high amplitude events were the result of a catastrophic failure.

In this research, however, the results only indicate that an increase in percentage of surface fracture is accompanied by low-amplitude long-duration events which can be assumed as the characteristic of brittle mode grinding. This observation was confirmed by the SEM and the 3D observations. Higher AE spectral amplitude was found to be associated with smooth ground surface. However, sub-surface median cracks were found for this condition.

Cuthrell [65] suggested that a distinct peak at higher amplitude could be a characteristic curve shape for the fracture of the brittle material during low speed drilling and scratching tests of different hydrogen embrittled ceramics. Konsztowicz [66] reported that low energy initial cracking within the glass phase of both zirconia and alumina during thermal shock is of short duration.

Crack propagation under load will -after a certain length of time- lead to breakage of the component without prior warning as soon as the critical stress intensity

is exceeded. This phenomena was observed during the bending test carried out in this research. An acoustic emission sensor was attached on the ground ceramic specimens to monitor and study the signals before the specimens broke. For some specimens cracks propagated in a very short time 20 to 60 μs before fracture occurred.

High AE events indicated by high amplitudes represent high energy release. Therefore the AE of higher amplitude events could be related to the degree of workpiece cracking when a smooth ground surface was produced. Low AE spectral amplitude was found to be associated with a rough ground surface of silicon nitride material. This was observed when coarse and extremely sharp grains were used. The strength of the subsequent ground ceramic component was found to be low. This is due to the high percentage of the brittle grinding and considerable cracking when coarse grit sizes were used. Small grit sizes with different bonded grinding wheels produced higher ground strength compared with coarse grit sizes. This was due to the small crack sizes initiated on the ground ceramic component.

8.5. Evaluation of Surface and Sub-surface Micro Cracks of Ground Ceramic

Three basic types of cracks that can occur after the passage of an abrasive grain on the surface of ceramic materials. Only radial cracks and machining marks are visible on the surface, median and lateral cracks (parallel to the surface) are formed below the affected zone and thus not visible. The energy introduced in the layers close to the ground surface invariably leads to the formation of these cracks.

Small grit sizes produced smooth ground surface, however, sub-surface cracks were found to be very close to the ground surface. Median sub-surface cracks were found to be in a deeper locations from the ground surface. Lateral cracks were initiated and propagated by residual stresses only near base to the plastic deformation [44]. In this research, the lateral cracks were observed to be very close to the ground surface (2-4 μm) compared with the median cracks (2-15 μm). The depth of the lateral cracks from the ground surface was not found to be affected by increasing the depth of cut or the diamond grinding wheel grit size. However the sub-surface median cracks was

found to be at a deeper locations when the depth of cut was increased. This condition was observed when small or blunt diamond grinding wheel grit size were used.

The surface damage depth on the ground surface was found to be higher when coarse or the grits condition on the wheel surface were extremely sharp. The surface damage depths measured when D46, D76 and D126 used were found to be 9, 12.2 and 18.7 μm respectively. The sub-surface cracks were found at low depth beneath the ground surface for these conditions and found to be 2, 3 and 7 μm. Blunt grinding wheels (D46 and D126) produced low damage depth on the ground surface (5, 9 μm). The sub-surface median cracks beneath the ground surface were found at deeper locations (6.5 and 11 μm) for these cases.

At low table feed, higher damage depths were observed on the ground surfaces in most of the cases. These depths were found to be small when the table feed was increased. The sub-surface cracks beneath the ground surface was found at larger location when higher table feeds rate were used (see Figures 158 and 143). The location of these sub-surface cracks beneath the ground surface was found to increase when the depth of cut was increased. This was observed over all the table feeds and grit sizes used.

The amount of cracking observed on the sub-surface was less when resin bonded grinding wheel used compared with cast iron bond type. The grit size, bond type and surface condition of the wheel were found to be the most influential factors for cracks initiation and propagation on the surface as well as their dimensions and locations in the sub-surface layers of ground ceramic. Soft bonded and small grits size of the grinding wheel was found to improve the strength of ground ceramic.

The types of cracks formed in ground ceramic is, median cracks (longitudinal cracks) are running parallel to the grinding direction and perpendicular to the surface. These cracks result from the high tensile stresses at the bottom of the grinding groove. Radial cracks extend radially from the grinding groove. They are located perpendicular to the grinding direction and the surface.

Critical defect sizes in brittle materials are among the smallest of all materials of the order of 1 μm to 50 μm depending upon the application and the material. In silicon nitride structural materials, the critical defects are silicon inclusions around 25 μm in size, measured using ultrasonic by Evans et al [59]. This defect of silicon nitride was detected in this research for unground ceramic (sintering damage) using 100 MHz acoustic microscopy at a depth of 500 to 1000 μm from the unground surface of the silicon nitride material.

Sub-surface cracks can be a function of several factors including material properties, grinding conditions, grinding wheel parameter and grinding wheel truing and dressing conditions. Lawn [25] reported that the brittleness, which is defined as the ratio of hardness to toughness H/K_c of a material was a governing factor affecting the penetration depth of sub-surface damage.

An analytical model for the prediction of sub-surface damage of ceramics subjected to grinding was described by Zhang and Howes [27]. The model correlates sub-surface damage to the type of workpiece material and grinding parameters. The penetration depth of sub-surface damage δ was given by;

$$\delta = (200\, h_{max})^{1/\log(\lambda\,(H/Kc))}$$

Where; λ is constant (10^{-2} $m^{1/2}$) and h_{max} is the maximum grit depth of cut can be calculated from equation (2.5) given in the literature survey (chapter 2), (H) is the material hardness, (E) is the elastic modulus and (Kc) is fracture toughness of the material.

The theoretical calculation of the above formulas were found to be in agreement with the experimental results of the sub-surface cracks locations obtained in this research. However, the generalisation of this formula for conditions where grits becomes worn and blunt is doubtful. A much deeper location of median sub-surface cracks beneath the ground surface was measured at this condition. Median and lateral sub-surface micro cracks were found in a distance very close to the ground surface. The

size of these cracks and their distance from the ground surface were found to be affected by different levels of wheel and machine parameters. Lateral cracks are very close to the surface by 2-4 μm and median cracks 2-15 μm from the ground surface.

8.6. Grinding Ceramic Specimens with Artificial Cracks Initiated on their Surface

The use of v-shape disc to create a crack provided the advantage of having different crack depths. This advantage is difficult to simulate using single diamond. Artificial cracks were initiated with different depths by using v-shape discs have the same grit size as those used for the grinding wheels. These cracks were initiated on the ceramic surface in both longitudinal and transverse directions. The AE signals released during the artificial crack initiation on the surface of the specimens was monitored at different depths. The acoustic emission activity was found to increase with increasing the artificial crack depths.

The size of radial crack surrounding the groove surface and the deformed zone underneath the groove were found to increase when the depth of groove increased (see Figures 169 and 170). In particular, significant difference in AE signals occurs for smooth groove scratching as compared to rough groove. The groove generation mechanism when inspected using SEM was mostly brittle. When the depth of scratch increased the percentage of ductility in deformed area decreased or disappeared. The material removal on the deepest part of the grooves were observed in some areas to be in ductile mode (smooth) and in other areas to contain micro fractures, especially in the centre of the groove. At a larger groove depth, a deeper locations of sub-surface median cracks extended perpendicular to the surface. Shorter median cracks propagated when the depth of artificial cracks were small. When the grinding process was carried out on these cracks, lateral cracks were found to propagate in the sub-surface more or less parallel to the grinding and groove surface direction.

The grinding process was carried out on the artificial cracks at different levels of grinding wheel and machine parameters to investigate their propagation. The AE signals were stored and analysed for both specimens ground with and without artificial

cracks created on their surfaces. The AE spectral amplitude was found to be higher when specimens were ground with artificial cracks. The AE signals are affected by the depth of grinding cut whether it was smaller or larger than the depth of the artificial crack. These signals were then compared with the SEM observations for both surface and sub-surface section of ground specimens and 3D surface topography as shown in Figures 171, 172, 176 and 177.

The variations in the AE spectral amplitude recorded during grinding specimens with and without artificial cracks on the surface was due to the propagation of these cracks. Due to the hardness of silicon nitride materials only a thin surface layer was affected. When the depth of grinding cut was higher than the depth of artificial cracks, these cracks were found to disappear and they have less affect on the strength of ground specimens.

The depth of the artificial cracks on the ground surface was measured before and after the grinding process. The propagation distance of these cracks due to different levels of grinding wheel and machine tools parameters was investigated. The artificial crack was found to be "closed up" in some cases by a thin layer. This could be due to the influence of residual stresses (see Figure 171). It was found that the propagation distance of the artificial cracks on the ground surface increased when the table feed, grinding wheel bond type hardness and diamond grinding wheel grit sizes were increased. This was found to be associated with generation of higher AE amplitude from the grinding zone.

The depths of remaining artificial cracks after the grinding process were measured. The propagation distances of these cracks on the ground surface due to different diamond grinding wheel grit size used were then measured. The propagation depth was observed to be reduced when the depth of grinding cut increased. The influence of the remaining artificial cracks was found to affect the strength of ground ceramic. Remaining artificial cracks on the ground ceramic specimens with depths of 29, 22, 9 and 5.7 μm were found to affect the fracture strength of these specimens. These were found to be 249, 318, 352.3 and 387.1 MPa respectively (see Figures 186

and 188). Small grit size was found to produce high ground strength, which means small distance of cracks propagation occurred compared with coarse grit size. It was observed that the fracture strength of the ground specimens improved when the influence of artificial cracks propagation was absent.

The propagation distance on the ground surface was measured using 3D surface topography. The propagation distance of an artificial crack created by a depth of cut of 25 μm was found to be 11 μm. This was found when a cast iron bonded grinding wheel with D76 was used. This propagation distance was found to increase when the diamond wheel grit size was increased. A propagation distance of 13 μm was measured after grinding a ceramic specimen with an artificial crack depth of 140 μm. This was found when resin bonded grinding wheel with D126 grit size was used (see Figures 176 and 177).

Different grinding passes were carried out on the artificial cracks at different grinding cut directions. The AE spectral amplitude generated from the grinding zone was monitored (see Figures 173 and 174). It was found that the levels of AE spectral amplitude varied with respect to the grinding cut direction. A higher AE spectral amplitude was observed to generate during the down-cut compared with up-cut grinding pass. This could reflect a long propagation distance of the artificial crack.

The AE signals generated during the bending test of ground specimens with artificial cracks were monitored. The signals were found to give an indication of the crack propagation before the specimens were fractured. This situation occurred when the artificial cracks were larger than the actual depth of grinding cut. The signals represented a very short time propagation of these cracks before the specimens were broken. These very short periods could be due to the small distance of cracks propagation. The AE signals gave a slight indication before the ground specimen was fractured when the depth of cut was larger than the depth of artificial crack (see Figure 195).

Sub-surface cracks were initiated by grinding specimens with artificial cracks. Median and lateral sub-surface cracks were found underneath the ground surface with artificial cracks (see Figure 172). The sub-surface cracks were found to be at a deeper locations, 45 μm from the ground surface. However, these locations were found to vary in some areas to be in the range of 15 to 30 μm. The locations of these sub-surface cracks were found to be at a larger depth from the ground surface compared with those measured when ceramic specimens were ground without artificial cracks.

8.7. Experimental Verification of FE Model

An attempt was made to study the structural behaviour of ceramic materials during grinding process. The crack initiation and propagation and the residual stresses were also investigated. The diamond grits size and their variations during grinding is an important factor which affects the final strength of ground ceramic. The simulation model was carried out by dividing the ceramic specimen to elements according to the grit size of grinding wheel used. Each grit size was applied with different normal and tangential forces per grit. The grinding force per grit calculations was explained in appendix A1.

Grinding of ceramic was simulated by applying normal and tangential grinding forces per grit on the ceramic surface as shown in Figure 35. These forces resulted from the experimental work for different levels of wheel and machine parameters. The output results of the first set of forces solved at the edge of the ceramic specimen model was used as input to the next run. This was repeated to cover the grinding distance required as shown in Figure 36. This was made to simulate the process as it happens in real grinding situation. This figure also shows the stresses due to the material removal in the grinding zone. The stresses indicate that the behaviour of material removal started with compressive stresses flowed by tensile stresses. Figure 37 shows the ceramic specimen ground with and without crack initiated on the surface and the condition of the sub-surface.

Applying the forces per unit grits was simulated and the area just under one grit was observed. It is believed that this can explain how micro cracks are initiated in the

radial plane. Very fine elements size (0.5 μm) were created on the surface of the ceramic FE model. These fine elements are appropriate with the nature of micro-cracks initiated on both surface and sub-surface of ground ceramic. The distance of the sub-surface cracks from the ground surface are very small. This was measured using SEM in the experimental work to be 2-15 μm. Cracking is believed to be caused by loading and unloading of moving forces on the specimen and also by the elastic/plastic residual stress field left after grinding. This condition was observed in the animation of the FE model during active grits action.

The grinding forces applied on the surface of specimen were found to have an influence on the initiation of the cracks on the surface due to tensile forces and the initiation of sub-surface cracks due to the compressive behaviour of the grinding forces. The distance of sub-surface cracks from the ground surface due to the compressed ground surface was investigated. Figure 38 shows the initiation of surface cracks due to the tensile interface of the grit and the workpiece. Artificial cracks were initiated on the surface of the FE model of ceramic specimen. The grinding forces were then applied on the cracks to investigate the propagation of these cracks on the sub-surface as shown in Figure 39.

The removal of material through mechanical fracture was found to increase as grit size increased. The random nature of slight differences in grit sizes and orientations or sharpness during grinding was simulated by randomly increasing or decreasing the force per unit grit. Maximum normal force and minimum tangential force were used to simulate sharp grits. Different values of radial forces were investigated to evaluate crack development during loading.

The effect of tensile forces during grinding and its effect on crack initiation and propagation was investigated by applying radial forces from one element toward different elements on the specimen. The behaviour of these forces was to create a higher friction that generate tensile actions on the contact zone between the force source and the ceramic surface. This can be observed clearly in the animation of FE options. The effect of different force values can be clearly seen in Figure 40, where 40 mN per

active grit was applied. This figure shows the propagation of crack in depth as indicated by lines 6, 5, 4, 3 and 2. These lines represent the values of stresses which are to be expected around a crack growth. The crack tip lies at a zone of tensile residual stress surrounded by a zone of "crack opening forces" exerted by the radially expanded plastic zone.

The compressive layer on the surface was associated with the formation of sub-surface crack. This phenomenon was observed when D46 grit size of diamond grinding wheel used in the both experimental and simulation model. The higher compressive residual stress on the surface may greatly increase the resistance to the crack initiation on the ground surface. However, when a surface flaw is already present, the compressive stress effectively closes the mouth of the crack. Below this compressive layer, the cracks were observed on the sub-surface (see Figure 41). This may be due to that the crack tip is under a tensile stress condition that could initiate the sub-surface cracks.

Tensile stresses may initiate surface cracks on the ground surface and secondly sub-surface cracks. This phenomenon was observed with cast iron bond diamond with D126 grit size as shown in Figure 42. This figure shows that the crack started to propagate within the weaker grain boundaries. This was observed when the elements size of the ceramic model were not equal, which may create different grains resistance to the force applied. These observations obtained from the simulation model were found in agreement with the experimental results explained in section 8.5.

The effect of residual stresses type on the surface and sub-surface cracks were investigated at different depths from the ground surface. This was studied at different grinding forces and different grits condition from blunt to extremely sharp grits. The depth of residual stresses from the ground surface is shown in Figures 43 and 44. These figures show that the residual stresses were produced due to different wheel and machine parameters. These parameters were presented by the grinding forces resulted from the experimental work. From these figures, compressive residual stresses were found on the ground surface. These stresses were observed to change to tensile stresses

when the distance beneath the ground zone increased from 59 to 139 μm. Sub-surface micro-cracks were observed to initiate when the tensile residual stresses were increased. These FE observations were in agreement with the experimental results obtained by other researcher [113] using x-ray technique.

9. CONCLUSION AND RECOMMENDATION FOR FUTURE WORK

The main objective of this research was to understand the initiation and propagation of surface and sub-surface cracks during the grinding of advanced ceramic materials. In order to study this a comprehensive preliminary study was carried out to investigate parameters that may affect the mechanics of the grinding operation itself. These parameters are the wheel type, wheel surface topography and the effect of very high infeed grinding.

The main experimental work in this research was carried in two sections. Grinding specimens without artificial cracks on their surface and specimens ground with artificial cracks with different depths. The response of fracture strength, surface roughness, AE spectral amplitude, grinding forces, specific grinding energy, crack size, the depth of surface damage and location of sub-surface median cracks beneath the ground surface due to different levels of grinding wheel and machine parameters were investigated. Different levels of grinding wheel and machine tool parameters were investigated which are diamond grinding wheel grit size, bond type, grinding wheel condition, depth of cut, grinding wheel speed and table feed.

9.1. Effect of Grinding Wheel and Machine Tool Parameters on Ground Ceramic Component

The effect of different levels of grinding wheel and machine tool parameters on the ground ceramic were investigated. The strength of the ground ceramic was improved when small diamond grinding wheel grit sizes were used. The surface roughness produced due to different levels of grinding wheel and machine parameters was found to affect the strength of ground ceramic component. Small diamond grinding wheel grit size (D46) was found to produce smooth ground surfaces over all other machining parameters. These were found to be in the range of 0.5674 to 0.7596 μm. The fracture strength achieved was found in the range of 437.6 to 569.6 MPa. Median diamond grinding wheel grit size (D76) was found to produce ground surfaces in the range of 0.8296 to 1.1984 μm. The fracture strength achieved for this case was found in the range of 290 to 383.8 MPa. Coarse diamond grinding wheel grit size (D126) was

found to produce rough ground surfaces in the range of 1.179 - 1.596 μm. The fracture strength achieved here, was found in the range of 169.7 to 332 MPa.

The grains condition and their distribution on the wheel surface were varied to investigate their influence on surface and sub-surface cracks of ground ceramic. Different levels of grinding wheel/truing speed ratios produced different sharpness of the grains on the grinding wheel surface. The load of individual grit as well as its shape was found to have an influence on the crack initiation and its propagation. Higher damage depth on the ground surface was found when the grain is extremely sharp. This was found to be associated with low fracture strength when the depth of cut increased and low table feed was used. Blunt grits condition was found to be associated with sub-surface cracks when stiff grinding wheels were used. Resin bonded grinding wheel with small grit size was found to produce higher ground strength at low levels of depth of cut.

The fracture strength was found to decrease when the grits on the wheel surface were extremely sharp. At grinding wheel/truing speed ratios of +0.3, +0.4 and +0.6, the fracture strength of specimens ground using D126 wheel grit size was found to be 381.8, 196.7 and 169.71 MPa. The surface roughness of these specimens was found to be 1.179, 1.3616 and 1.596 μm. At the same speed ratios, the fracture strength of specimens ground using wheel with small grit size (D46) was found to be 342.7, 501.71 and 354.3 MPa. The surface roughness of these specimens was found to be 0.704, 0.5674 and 0.755 μm respectively.

The effect of diamond grinding wheel bond type with different grit size on the surface roughness was investigated. Resin diamond grinding wheel creates improved surface roughness values (0.7, 0.98, 1.3 μm) compared with vitrified (0.62, 1.17, 1.607 μm) and cast iron (0.65, 1.124, 1.509 μm). Resin bond produced higher fracture strength values (503.5, 335.7 and 315.86 MPa) compared with vitrified (438.9, 322.6 and 240.6 MPa) and cast iron bonded grinding wheels (419.85, 276.24 and 239.1 MPa). These results are averaged values at different machine tool parameters for D46, D76 and D126 grinding wheels grit size respectively. Small values of surface roughness

produced by cast iron and vitrified bonded wheels with D46 grit sizes was associated with lower fracture strength values compared with slightly higher surface roughness value of resin bonded wheel with the same grit size. This was due to the increase of sub-surface median cracks when harder bonded wheel was used.

The reduction in the strength of ground ceramic was found to be associated with an increase in both AE spectral amplitude ratio (151 to 299) and normal grinding forces from 4.4 to 9.75 N/mm. The specific grinding energy at the same machining parameters was found to decrease (586.5 to 72.5 J/mm^3) with increasing the depth of cut (25 to 443 μm). The reduction on the specific grinding energy and the increase in both AE spectral amplitude and grinding forces was found to be associated with an increase in the crack size (68.8 to 522 μm) when the depth of cut and the table feed were both increased. This could reflect a higher percentage of brittle grinding mode occurred at higher depth of cut at these conditions.

During the grinding process monitoring, it was observed that the AE signal has a much quicker response than grinding forces detection. AE technique is a good tool that can be used to trigger the grinding forces measurement channels, without losing data just prior to the trigger. The development of the normal and tangential grinding forces at the beginning of the cut were slow in comparison with the rise in AE amplitude. Recording the maximum values of grinding forces levels could be more accurate when they triggered by AE sensor together with dynamometer. This could be studied for further work.

The grinding forces were found to increase when the depth of cut was increase. The ratio of normal forces to tangential forces was found to increase from 31.8 % to 39.3 % when the depth of cut was increased from 25 to 443 μm. Low strength of ground ceramic component was found to be associated with larger grinding forces generated due to the grinding wheel surface condition when the depth of cut was increased. The reduction on the strength was due to the increase in the amount of cracking on the ground ceramic component. The load of individual grain as well as its shape were found to have an influence on the crack initiation and its propagation in

both surface and sub-surface of the ground ceramic. Higher damage depth on the ground surface was observed when the grain is extremely sharp. Blunt wheel surface condition was found to be associated with sub-surface median cracks. The increase in the grinding forces was found to be associated with an increase in the AE spectral amplitude averaged over different levels of table feed, grit size and bond type when the depth of cut increased. Higher values of grinding forces were observed when the table feed was increased and deeper location of sub-surface median cracks beneath the ground surface were observed.

The crack size of ground ceramic component was found to be affected by the grinding wheel and machining parameters. The diamond grinding wheel grit size and condition was found to be the most influential factors on the crack size of ground ceramic component. At +0.3 grinding wheel/truing speed ratio, crack sizes of 128 μm, 292.2 μm, 388.7 μm were estimated from the broken ground ceramic specimens when D46, D76 and D126 respectively used. Larger crack size of 522 μm at +0.6 speed ratio was found when coarse and sharp D126 grit size was used. At +0.4 speed ratio, small cracks size was observed over all the grit sizes used. The strength of ground ceramic was found to be reduced when the grit size sharpness was increased. The depth of cut and table feed were also found to have an influence, however the grinding wheel speed has a slight effect on the size of these cracks. This could be due to the range of the wheel speed used was not wide enough to have an influence on the crack size. Further work should attempt to study the effect of high grinding wheel speed on the surface damage depth, sub-surface crack dimensions and their depth from the ground surface.

9.2. Correlation of Acoustic Emission (AE), Scanning Electron Microscopy (SEM) and 3D Topography Data to Investigate the Ground Ceramic Condition

The main objective of this research was to look at the initiation and the propagation of cracks in ceramic grinding. The parameter chosen, were dictated by the limitations of the machine used. However, these parameters are realistic and represent ranges that are really available for use in industry. The most influential factors found that initiate the cracks on the ground surfaces were the grinding wheel condition and the

increasing of grinding wheel grit size (D46 to D126). The propagation distance of surface cracks were found to be larger when the wheel grit size increased at low table feed levels and small levels of depth of cut. A blunt grits and fine grit size were found to initiate sub-surface median cracks. The propagation of these median cracks were found to be of larger size when harder bonded grinding wheels were used. At higher table feeds, sub-surface median cracks were initiated at deeper depths beneath the ground surface. The propagation distance of these cracks in the sub-surface were found to increase when the depth of cut was increased.

The precision grinding of ceramic using diamond abrasive, always occurs with a combination of brittle and ductile deformations. The percentage of each of these modes can be affected by the diamond grinding wheel grit size, bond type and the grinding wheel condition as well as machine tool parameters. Rough ground surfaces were found to be associated with high surface damage. This was found when extremely sharp and a coarse diamond grit size (D126) were used. Long distance of cracks propagation depth on the ground surface of 11-18 μm were measured when cast iron bonded grinding wheel was used. Resin bonded grinding wheel with the same grit size initiated cracks on the ground surface with less propagation distance (11-13 μm). The surface roughness (Ra) produced in these specimens were in the range of 1.179 to 1.596 μm. Low ceramic strength was achieved in the range of 169.7 to 332 MPa.

Low AE spectral amplitude ratio (150) was generated during grinding these rough ceramic surfaces. This was observed to be in a frequency range of 0.3 to 0.7 MHz. Long period of time between each AE event were found that could reflect a long distance of crack propagation on these rough ground surfaces.

In contrast to the rough ground ceramic specimens achieved using coarse grit size (D126), Fine diamond grinding wheel grit size (D46) was used to produce smooth ground surfaces. Individual surface damage was found on the smooth ground surfaces to depth of 7-9 μm. The surface roughness (Ra) of smooth ground surfaces produced were in the range of 0.567 to 0.759 μm. This was associated with higher strength

specimens in the range of 437.6 to 569.6 MPa. Resin bonded grinding wheel with D46 grit size produced the highest ground strength.

Smooth ground surfaces observed by SEM were correlated with high AE spectral amplitude ratio (300-700). These amplitudes generated at a frequency range of 0.5-0.7 MHz. The time between each AE event was small, and could reflect that the small crack propagation distances were generated. A higher amount of sub-surface median cracks were found when blunt and cast iron bonded wheel with small grit size (D46) were used. The locations and dimensions of these cracks was found to increase when the depth of cut was increased.

Median sub-surface cracks were found underneath smooth ground surfaces produced by cast iron bonded wheel with small grit size (D46). These cracks were observed to start beneath solid (crack-free) layers of the ground surface at 7 to 13 μm. The dimension of these median sub-surface cracks was found to increased when their depths from the ground surface increase. This effect was due to the increase in the depth of grinding cut. For a 7 μm solid layer thickness, a median crack with a dimension of 20 μm x 14 μm was found. This was formed at an actual depth of cut of 6 μm. Increasing the depth of cut to 288 μm, the solid layer thickness was increased to 13 μm. The dimension of the sub-surface crack was also increased to 55 μm x 30 μm. The AE spectral amplitude generated at this two conditions was increased from 350 to 700.

The selected group of results of ceramic specimens ground with different grinding wheels and machine tool parameters were linked to AE signals, SEM and 3D surface topography. High AE spectral amplitude was generated due to the initiation of sub-surface cracks underneath a smooth ground surface produced when small grit sizes were used. The higher AE spectral amplitude could also be due to the high contact friction between the workpiece and small grit size of the grinding wheel. This was observed to be associated with higher tangential grinding forces when small grit size were used and the depth of cut was increased. The time between each AE event generated when small grit sizes were used is very small which could be due to small distance of crack propagation. Low AE spectral amplitude was observed when coarse grit sizes were used that produced a higher percentage of brittle grinding mode. The

time between each AE event is slightly bigger which could be due to larger distance of crack propagation. Further work should attempt to develop a system to monitor the amount of cracking on the workpiece. A complete AE monitoring system with multi-sensors will be more accurate to predict the grinding mode.

From SEM observations, it was observed that the most basic requirement for maintaining a ductile material removal regime is to ensure that the depth of cut made by an individual abrasive cutting grain does not exceed some threshold value (i.e. a critical depth of cut), otherwise fracture occurs beneath the abrasive edge (crack initiation). To achieve ductile-regime grinding of advanced ceramic material. Further work should concentrate on the two main factors which seem to be most influential. These are, wheel grit size and bond hardness.

9.3. Evaluation of Surface and Sub-Surface Micro-Cracks

Different crack types were found as a consequence of the grinding of advanced ceramic material. These cracks can be classified in two forms, visible radial cracks and machining marks found on the ground surface. The second type are median and lateral cracks and formed below the affected grinding zone and thus not visible. The locations of the sub-surface cracks beneath the ground surface were increased when blunt or fine grit size wheels were used.

The surface damage depth on the ground surface was found to be higher when coarse or extremely sharp grits were used. These depths were measured for D46, D76 and D126 to be 9, 12.2 and 18.7 μm respectively. The sub-surface cracks were found at low depth beneath the ground surface for these grit sizes to be 2, 3 and 7 μm. Blunt grinding wheels (D46 and D126) produced low damage depth on the ground surface (5, 9 μm). The location of these sub-surface cracks beneath the ground surface were found at deeper distance (6.5 and 11 μm) for these conditions.

Small grit size D46 initiated sub-surface cracks at deeper distance (5.2, 5.4, 6.7 and 6.2 μm) at grinding wheel/truing speed ratios levels (+0.3, +0.4, +0.5 and +0.6). These conditions were found to be associated with small values of surface damage. This

was due to the condition of this grit size was extremely blunt at these speed ratios. At -0.5 speed ratio, D46 resin grit size was extremely sharp. Low fracture strength of 508.8 MPa was obtain for this condition.

Median and lateral cracks were found to be initiated in the sub-surface at layers very close to the ground surface. The median cracks were observed to be at a deeper distance from the ground surface compared with the lateral cracks. The depth of the median cracks from the ground surface was observed to increase (2-15 μm) with increasing the depth of cut, table feed and when fine or blunt grits were used. Lateral cracks were found under a thin layer with a thickness of (2-4 μm). It is believed to be created due to residual stresses after grinding. The depth of the lateral cracks beneath the ground surface were not found to be affected by increasing the depth of cut.

The increase in the depth of cut for the same grinding wheel bond type and grit size used was found to increase the dimensions and the locations of the sub-surface median cracks. Soft bonded diamond grinding wheel type produced small sub-surface cracks dimensions and depth from the ground surface compared with hard bonded grinding wheel type. D76 resin bonded wheel was found to initiate sub-surface median crack with a dimension of 20 x 30 μm and at 6 μm beneath the ground surface. Blunt D126 resin bonded wheel was observed to increase the dimension and depth of median sub-surface micro cracks beneath the ground surface. The size was measured to be 40 μm in height parallel to the grinding direction and 22 μm perpendicular to the ground surface. The depth of this median crack beneath the ground surface was measured to be 11 μm.

9.4. Specimens Ground with Artificial Cracks on their Surface

Different levels of artificial crack depths were initiated on the surface of ceramic specimens using v-shape disc have the same grit size of those used in the grinding wheel. The author believes this method of crack production was more accurate in simulating the crack initiation due the grinding process compared with single diamond scratch method.

Using SEM, the groove generation mechanism was observed to be mostly brittle. When the depth of scratch increased, the percentage of plastically deformed area decreased or disappeared. Radial crack on the surrounding surface of the groove were found to increase when the depth of the groove was increased, the deformed area underneath the groove was also increased. The acoustic emission activity was found to increase with increasing artificial crack depths. At larger groove depths, a deeper location of sub-surface median cracks extended perpendicular to the surface. Shorter median cracks propagation was found when the depth of artificial cracks was small.

The average values of AE spectral amplitude generated from the grinding zone for different levels of grinding wheel and machine tool parameters were found to be higher when specimens were ground with artificial cracks (in the range of 210 to 440) These values can be compared with AE amplitude generated from specimens ground without artificial cracks (in the range of 150 to 300) on their surface. When the depth of grinding cut was larger than the depth of artificial cracks, little effect was observed and higher fracture strength of ground specimens was found. This was due to the less propagation distance of the artificial cracks. Decreasing the depth of damage on the ground surface (35.5, 22, 7.7 μm) was associated with increasing in the fracture strength of the ground ceramic specimens (251, 318, 387.1 MPa).

The increase in the levels of diamond grinding wheel grit size, wheel bond hardness and table feed were found to be the most influential factors that increase the propagation distance of the artificial cracks during grinding. The propagation distance of the artificial cracks after the grinding process was measured. When cast iron bonded grinding wheel with D76 grit size was used, the artificial crack in ground surface extended to 11 μm. The propagation distance of the artificial cracks measured using this grit size represents 44 % of its depth. In some areas, the cracks initiated were found after grinding to be "closed up" by a thin layer. This may be due to the influence of residual stresses. For large grit size D126 and soft bond (resin) wheel, the propagation distance was measured to be 13 μm. The propagation distance of the artificial cracks measured using this grit size represents 9.3 % of its depth.

Median and lateral sub-surface cracks were found underneath the ground surface with artificial cracks. The sub-surface cracks were found to be at a deeper locations from the ground surface (45 μm) and varied from 15 to 30 μm according to the wheel grit size used. The locations of these sub-surface cracks were found to be at a larger depth from the ground surface compared with those measured when ceramic specimens ground without artificial cracks (2-15 μm).

The AE signals generated during the three point bending test of specimens ground with artificial cracks were monitored. The signals were found to give an indication of the crack propagation before the specimens were fractured. This was observed when the artificial cracks were larger than the actual depth of grinding cut. These signals represent a very short time propagation of these cracks before the specimens were broken. These very short periods could be due to the small distance of cracks propagation. It was found that the AE signals did not give any indication before unground specimens were fractured.

9.5. Experimental Verification of FE Model

Crack initiation and propagation during grinding process of advanced ceramic materials have been investigated experimentally and theoretically. Experimental results were validated using FE model. The mechanical properties of silicon nitride material and the grinding forces obtained from the experimental work were used as input to the FE model.

Compressive and tensile forces were simulated. Tensile stresses on the surface due to tensile contact between the grain and the workpiece. This was associated with surface cracks on the ceramic model and secondly sub-surface cracks. This was carried out by applying radial forces from one element toward different elements on the specimen model. The behaviour of these forces was found to create a higher friction that generate tensile actions on the contact zone between the force source and the ceramic surface. This phenomenon was observed with cast iron bond diamond with D126 grit size. The crack started to propagate within the weaker grain boundaries. This

was observed when the elements size of the ceramic model were not equal, which may create different grains resistance to the force applied.

The distance of the sub-surface cracks from the ground surface were very small. This was measured using SEM in the experimental work to be 2-15 μm. These results in agreement with the observations obtained by FE simulation model. Cracking is believed to be caused by loading and unloading of moving forces on the specimen and also by the elastic/plastic residual stress field left after grinding. From the post-processing of the simulation model, the animation of the specimen during active grits action was observed. The surface crack depths were found to increase as grit size increased.

The cracks were observed to be initiated when the grinding wheel condition changes. This was simulated by varying both normal and tangential grinding forces. Surface cracks were initiated when the wheel condition is sharp. This was simulated by applying high values of normal forces and low values of tangential forces. Sub-surface cracks were observed to initiate when the values of tangential force increased compared with normal forces. The propagation of these cracks in depth was indicated by values of stresses which are expected around a crack growth. The crack tip lies at a zone of tensile residual stress.

The compressive layer on the ground surface was associated with the formation of sub-surface crack. This phenomenon was observed when D46 grit size of diamond grinding wheel was used in both experimental and simulation model. The higher compressive residual stress on the surface greatly increase the resistance to crack initiation on the ground surface. However, when a surface flaw is already present, the compressive stress effectively closes the mouth of the crack. Below this compressive layer, the cracks were observed on the sub-surface.

10. REFERENCES

[1] Boothroyd, G. and Kingth, W.A.,(1989) " Fundamentals of Machining and machine Tools", 2nd ed, Marcel Dekker Inc., New York, pp. 49-52.

[2] Metzger, J. L., (1989) " Wheel Performance in Superabrasive Grinding" Industrial Diamond Review, 49, pp. 116-117.

[3] Ernst, H. and Merchant, M. E. (1941) "Surface Treatment of Metals", American Society of Metals, New York, pp. 299-378.

[4] Spur, G., Stark, C., and Tio, T. H., 1985, "Grinding of non-oxide ceramics using diamond grinding wheels", ASME, PED-Vol. 17, Nov. 1985, pp. 33-44.

[5] Pai, D.M., Ratterman, E. and Shaw, M. C. (1988) "Grinding Forces and Energy for Brittle Materials" ASME Proceeding, International Society Symposium on Machining of Advanced Ceramic Materials and Components, pp. 99-111.

[6] Inasaki, I. (1986) "High-Efficiency Grinding of Advanced Ceramics", Annals of CIRP, Vol. 35, No. 1, pp. 211-214.

[7] Inasaki, I. (1987) "Grinding of Hard and Brittle Materials", Annals of the CIRP, Vol. 36, No. 2, pp. 463-471.

[8] Morgan, J. I. and Hooper, R. M. (1987) "Grinding PSSS Ceramic with Diamond Wheels " Industrial Diamond Review, Vol. 47, pp 262-264.

[9] Inasaki, I. (1988) "Speed-Stroke Grinding of Advanced Ceramics", Annals of the CIRP, Vol. 37, No. 1, pp. 299-302.

[10] Malkin, S., Ritter, J.E., (1989) "Grinding Mechanisms and Strength Degradation for Ceramics", Journal of Engineering for Industry, Vol. 111, pp. 167-174.

[11] Marshall, D. B., Lawn, D. B. and Cook, R. F., (1987) "Microstructural Effects on Grinding of Alumina and Glass Ceramics" Journal American Ceramic Society, 70 [6] pp. 139-140.

[12] Yui, A., Watanabe, T. and Yoshida, Y., (1988) "Effects of the Grinding Process upon Surface Grinding Accuracy of Advanced Ceramics" ASME Proceedings, International Society Symposium on Machining of Advanced Ceramic Materials and Components, pp. 47-56

[13] Subramanian, K. and Ramanath, S. (1992) "Mechanism of Material Removal in the Precision Grinding of Ceramics", ASME, Vol. 58, Precision Machining: Technology and Machine Development and Improvement, pp. 1-19.

[14] Lutz, G. , (1993) "Grinding of advanced ceramics", International ceramic, Vol. 42, No. 6. pp. 367-371.

[15] Kovach, J.A., Blau, P. J. and Malkin, S. (1993) "A Feasibility Investigation of High Speed, Low Damage Grinding for Advanced Ceramics" Proceeding of the 5th International Grinding Conference, October 26-28, 1993, Cincinnati, Ohio, MR93-352, pp. 1-16.

[16] Maksoud, T. M. A., Mokbel, A. A. (1995) "Very High Infeed Effects on the Grinding of Advanced Ceramic Materials" Proceeding of AL-Azhar Engineering Fourth International Conference, December 16-19, Vol. 7, pp. 283-295.

[17] Zhang, B. and Howes, T. D., (1994) "Material-removal mechanisms in grinding ceramics" Annals of the CIRP, Vol. 43, Part 1, pp. 305-308.

[18] Bifano, T. D., Dow, T. A. and Scattergood, R. O. (1991) "Ductile-regime grinding: a new technology for machining brittle materials" ASME, Journal of Engineering for Industry, Vol. 113, pp. 184-189.

[19] Nakagawa, T., Suzuki, K. and Uematsu, T. (1986) "High Efficiency Grinding of Ceramics and Hard Metals on Grinding Centre" Annals of the CIRP, Vol. 35, pp. 205-210.

[20] Akbari, J., Saito, Y., Hanaoka, T. and Enomoto, S., (1993), "Detection of cutting mode during scratching of ceramics using acoustic emission", International Journal of Society for Precision Engineering, Vol. 27, No. 1, pp. 35.

[21] Mayer, J.E. and Fang, G. P., (1994) "Effect of grit depth of cut on strength of ground ceramic" Annals of the CIRP, Vol. 43, Part 1, pp. 309-312.

[22] Mayer, J. R. and John E, (1993) "Efficient Improved Strength Grinding of Ceramics" Proceeding of the 5th International Grinding Conference, October 26-28, Cincinnati, Ohio, MR93-356, pp. 1-15.

[23] Takaki, J. and Liu, M., (1993) "Influence of Wheel Sharpness on the Strength of Ground Ceramics", Proceeding of the First International Abrasive Technology Conference", Seoul, Korea, 1-2 Nov., pp. 137-142.

[24] Tanaka, T., Isono, Y. and Ueda, S. (1995) "Influences of surface roughness and phase transformations induced by grinding of the strength of ZrO_2-Y_2O_3)" Journal of Precision Engineering, Vol. 17, No. 2, pp. 117-123.

[25] Lawn, B. R., (1993) "Fracture of Brittle Solid - Second Edition, Cambridge University Press, pp. 249-306.

[26] Lawn, B. R. and Evans, A. G. (1977) "A model for crack initiation in elastic/plastic indentation fields", Journal of Materials Science, Vol. 12, pp. 2195-2199.

[27] Zhang, B. and Howes, T. D., (1995) "Sub-surface Evaluation of Ground Ceramics" Annals of the CIRP Manufacturing Technology, Vol. 44, No. 1, pp. 263-266.

[28] Zhang, B., Tokura, H. and Yoshikawa, M. (1988) "Study on Surface Cracking of Alumina Scratching by Single-Point Diamonds" Journal of Material Science, Vol. 23, pp. 3214-3224.

[29] Maksoud T. and Howes T. (1989) "Effect of Hydrodynamic Pressure of high Viscosity Coolant on the Stability of Surface Grinding Process" ASME, International Conference, Grinding Symposium, San Francisco, CA. USA

[30] Brinksmeirer, E, Preub, W. and Riemer, O. (1995) "Form Friction to Chip Removal" An Experimental Investigation of Micro-cutting process. Part II: Ductile to Brittle Transition in Monocrystallline Silicon and Germanium, Proceeding of 8th International Precision Engineering Seminar, pp. 335-338, Compiegne, France.

[31] Thomas T. R. and Sayles R. S. (1977) "Stiffness of machine Tool Joints: A Random Process Approach ", Journal of Engineering for Industry, pp. 250-256.

[32] Conway, J. C., Kirchner, H. P., (1980) "The mechanics of crack initiation and propagation beneath a moving sharp indenter", Journal of Material Science, Vol. 15, pp. 2879-2883.

[33] Lawn, B. R. and Wilshaw, R. (1975), "Review, Indentation fracture: principles and applications", Journal of Material Science, Vol. 10, pp. 1044-1081.

[34] Shi, G. C. (1973) "Handbook of stress intensity factors" Lehigh University Press, Lehigh.

[35] Mecholsky, J. J., Freiman, S. W. and Rice, R. W. (1977)" Strength of Ground Glass" Eleventh International Congress on Glass, Prague, Czechoslovakia, pp. 167-173.

[36] Kirchner, H. P. (1984) "Damage Penetration at Elongated Machining Grooves in Hot-Pressed Si3N4", Journal of the American Ceramic Society, Vol. 67, No. 2, pp. 127-132.

[37] Marshall, D. B., Evans, A. G. and Khuri Yakub, B. T., (1983), "The Nature of Machining Damage in Brittle Materials", Proceeding of the Royal Society of London' pp. 385, 461-475.

[38] Hakulinen, M. (1985) "Residual strength of ground not isostatically pressed silicon nitride" Journal of material science, Vol. 20, 1049-1060.

[39] Rice, R. W., Mecholsky, J. J. and Baker, P. F., 1981 "The Effect of Grinding Direction on Flaw Character and Strength of Single and Polycrystalline Ceramics", Journal of Material. Science, Vol. 16, p. 853-858.

[40] Maksoud, T. M. A., Morgan, J and Scott, J. (1992) " Numerical Analysis of Heat Transfer through Wheels used for Ceramic Component" Proceeding of the Numerical Conference. Vol. VII, Part 2, pp. 1267-1279.

[41] Maksoud, T. M. A., Scott, J.E. and Mokbel, A. A. (1993) " Residual Stresses in the Grinding of Silicon Nitride Ceramics Materials". Proceeding of the Ninth National Conference on Manufacturing Research, University of Bath 7-9 September, pp 257-261.

[42] Lawn, B. R., Padture, N. P., Guiberteau, F. and Cai, H. (1994) "A model for micro crack initiation and propagation beneath hertzian contacts in polycrystalline ceramics" Acta metall. mater. Vol. 42, No. 5, pp. 1683-1693.

[43] Anstis, G. R., Chantikul, P., Lawn, B. R. and Marshall, D. B., (1981) "A Critical Evaluation of Indentation Techniques for Measuring Fracture Taoughness: I, Direct Crack Measurements", Journal of the American Ceramic Society, Vol. 64, No. 9, pp. 533-538.

[44] Marshall, D. B., Lawn, B. R. and Evans, A. G., (1982), " Elastic / Plastic Indentation Damage in Ceramics: The Lateral Crack System", Journal of the American Ceramic Society, Vol. 65, No. 11, pp. 561-566.

[45] Lawn, B. R. and Evans, A. G., (1980) "Elastic/Plastic Indentation Damage in Ceramics: The Median/Radial Crack System", Journal of the American Ceramic Society, Vol. 63, No. 9-10, pp. 574-581.

[46] Padture, N. P., (1993) "Postfailure subsidiary cracking from indentation flaws in brittle materials", Journal of Material Research, Vol. 8, No. 6, pp. 1411-1417.

[47] Tonshoff, H. K. Brinksmeier, E. and Hetz, F., (1987) "Detection of Micro cracks" , Annals of CIRP, Vol. 36, No. 2, pp. 545-552.

[48] Kanai, H., Chubachi, N. and Sannomiya T., (1992) "Non Contact Measurement of Acoustic Emission Signals in the 100 MHz Frequency Range Using an Acoustical Microscope", Acustica, Vol. 76, 1992, pp. 199-204.

[49] Somekh, M. G., Liu, M and See, C. W. (1995) "An accurate non-contacting laser based system for surface wave velocity measurement", Measurement Science Technology, UK, Vol. 6, pp. 1329-1337.

[50] Inasaki, I (1991) "Monitoring and Optimisation of Internal Grinding Process", Annals of CIRP, Vol. 44, pp. 359-362.

[51] Inasaki, I. (1985) "Monitoring of Dressing and Grinding Processes with Acoustic Emission Signals", Annals of CIRP, Vol. 34/1, pp. 233-239.

[52] Dornfeld, D. and Blum, T. (1990) "Grinding Process Feedback Using Acoustic Emission", MR90, SEM, pp. 525-230.

[53] Koenig, W. and Klumpen, T., (1993) "Monitoring and Sensor Concepts of Higher Process Reliability", SME 5th International Grinding Conference, Cincinnati, Ohio, MR93-352.

[54] Bifano, T. G. and Yi, Y. (1992) "Acoustic Emission as an Indicator of Material Removal Regime in Glass Micro machining", Journal of Precision Engineering, Vol. 14, October, pp. 219-228.

[55] Hundt, W., Leuenberger, D. and Rehsteiner, F., (1994) "An Approach to Monitoring of the Grinding Process Using Acoustic Emission Technique" Annals of CIRP Vol. 43, pp. 295-298.

[56] Webster, J., Marinescu, I. and Bennett, R., (1994), "Acoustic Emission for Process Control and Monitoring of Surface Integrity During Grinding" Annals of CIRP Vol. 43, pp 299-304.

[57] Liu, J. J. (1991) "Monitoring the Precision Machining Process", Sensors, Signal Processing and Information Analysis", PhD Theses, University of California, Berkely, pp. 171-177.

[58] Dornfeld, D. and Chang, P., (1993) "Chatter and Surface Pattern Detection for Cylindrical Grinding Using a Fluid Coupled Acoustic Emission Sensor", International Conference on Machining of Advanced Materials, Nist, July , pp. 159-167.

[59] Evans, A. G., Kino, G. S., Khuri-Yakub and Tittmann, B. R. (1977) "Failure Prediction in Structural Ceramics" Materials Evaluation, pp. 85-96.

[60] Eda, H., Kakino, Y., Fujiwara, A. and Kishi, K. (1984) "In-Process Detection of Grinding Cracks by the Use of Acoustic Emission" Proceeding of the 5th International Conference of Production Engineering, Tokyo, pp. 306-313.

[61] Malen, K. and Bolin, L. (1974) "A theoretical Estimate of Acoustic Emission Stress Amplitudes" Physical Statistical Society Vol. 61, pp. 637-643.

[62] Diei, E. N. and Dornfeld, D. A., (1987) "A Model of Tool Fracture Generated Acoustic Emission During Machining" ASME, Journal of Engineering for Industry, Vol. 109, pp. 227-232.

[63] Desai, J. D. and Gerberich, W. W., (1975) "Analysis of Incremental Cracking by the Stress Wave Emission Technique" Engineering Fracture Mechanics, Vol. 7, No. 1. pp. 153-158.

[64] Dalgleish, B. J., Fakhr, A., Pratt, P. L. and Rawlings, R. D. (1979) "The Temperature Dependence of the Fracture Toughness and Acoustic Emission of Polycrystalline Alumina" Journal of Material Science, Vol. 14, pp. 2605-2612.

[65] Cuthrell, R. E., (1979) "The Influence of Hydrogen on the Deformation and Fracture of the Near Surface Region of Solids: Proposed Origin of the Rebinder-Westwood Effect" Journal of Material Science, Vol. 14, p. 612-618.

[66] Konsztowicz, K. J., (1990) "Crack Growth and Acoustic Emission in Ceramics During Thermal Shock" Journal of American Ceramic Society, Vol. 73, No. 3, pp. 502-510.

[67] Eitzen, D. and Breckenridge, F. R., (1987) "Acoustic Emission Sensors and Their Calibration", NDT Handbook - Acoustic Emission Testing, Vol. 5, Edited by Paul McIntire, pp 121-134.

[68] Harris, D. O., Telelman, A. S. and Darwish, F. A., (1972) "Acoustic Emission", ASTM STP 505, American Society for Testing and Materials, Philadelphia, PA, pp. 243-246.

[69] Evans, A. G. and Lintzer, M., (1977) "Annual Review of Material Science", Vol. 7, pp. 179-185.

[70] Pollock, A. A. (1973) "Fundamental of Acoustic Emission" Non-destructive Testing, Vol. 6, pp. 264-276.

[71] Ono K., Stem, R. and Long, M., (1972) "Acoustic Emission", ASTM-STP-505, American Society of Testing and Material, Philadelphia, USA, pp. 125-134.

[72] Bendat, J. S. and Piersol, A. G., (1971) "Random Data Analysis and Measurement Procedures", John Wiley & Sons Inc., NY.

[73] McEachron, R. W. and Lorence, S. C. (1988) " Superabrasives and Structural Ceramics in Creep Feed Grinding". American Ceramic Society Bulletin. Vol. 67/6, pp. 1031-1036.

[74] Wortendyke, P. R. , (1989) "An Introduction to Structural Ceramics" General Electric Superabrasives, Worthington, Ohio, USA.

[75] MATSUI Seiki and TAMAKI Jun'ichi, (1986)" Effect of Dresser Type on Surface Topography of grinding wheel" Japan Society of precision Engineering, Vol. 20, No. 2, pp. 135-137.

[76] Shafto, G. R. and Notter, A. T., (1979) "Truing and dressing of Resin Bonded Peripheral Wheels", De Beers Diamond and ABN Abrasive in Grinding - A Selection of Papers Presented at the DE Beers Dusseldorf Conference, pp. 1510-1519.

[77] Inasaki, I., (1989) " Dressing of Resin Diamond Grinding Wheels", Annals of CIRP, Vol. 38, No. 1, pp. 315-318.

[78] Taketo, N., Kohzo, A. and Kubo, H., (1989) "Newly development dressing technology for cutting off Sialon Ceramics", Annals of CIRP, Vol. 38, No. 1, pp 327-330.

[79] Notter, A. T. and Bailey, M. M, (1977) "Truing and dressing diamond and CBN grinding wheels", Industrial diamond review, May, pp. 163-168.

[80] Rezaei, S. M., (1987) "Investigation of In-process dressing in creep feed grinding". PhD Thesis, University of Bristol.

[81] Maksoud, T. M. A and Mokbel, A. A. (1996) "New Cooltip Dresser for Alumna Wheels" Presented in the IMEC conference, 7-9 August, University of Connecticut, USA, pp. 61-64.

[82] Syoji, K., Zhou, L. and Matsui, S., (1990) "Studies on Truing and Dressing of Diamond Wheels", Japanies Society of Precision Engineering, Vol. 24, No. 2, pp. 124-129.

[83] King, R. I. and Hahn, R. S, (1986) "Handbook of Modern Grinding Technology", Pub: Chapman and Hall Advanced Industrial Technology Series, pp. 88-97.

[84] Scott, W. and Baul, R. M. ,(1976) "Identification of grinding wheel wear using random process analysis" Wera, Vol. 39, pp. 361-375.

[85] Tonshoff, H. K., (1993) "Fast Sensor Systems for the Diagnosis of Grinding Wheel and Workpiece" Proceeding of the 5th International Grinding Conference, October 26-28, 1993, Cincinnati, Ohio, MR93-369, pp. 1-15.

[86] Thomas, T. R., (1975), "Recent Advances In the Measurement and Analysis of Surface Microgeometry", Wear, Vol. 33, pp. 205-233.

[87] Bhateja, C. P., (1975) "The Intrinsic Characteristics of Ground Surface" Proceedings of the Abrasive Engineering Society's International Technical Conference, pp. 139-147.

[88] Davies, C. E., (1974) "The Dependence of Grinding Wheel Performance on Dressing Procedure" International Journal of Machine Tool Design Research, Vol. 14, pp.44-52.

[89] Maksoud, T. M. A., Dean, C., Jones, T. D. and Howes, T. D. (1988), "Theoretical and Experimental Investigation into the Effect of Lateral Oscillation in Cylindrical Grinding" Proceedings of the Third International Grinding Conference, October 4-6, Fontana, Wisconsin, SME, MR88-601, pp. 1-17.

[90] Verkerk, J. (1977) , "Final Report Concerning CIRP Co-operative Work on the Characterisation of Grinding Wheel Topography" Annals of the CIRP, Vol. 26 No. 2, pp. 385-392.

[91] Dornfeld, D. and Cai, H. G. (1984) "An Investigation of Grinding and Wheel Loading Using Acoustic Emission" Trans. ASME, Journal of Engineering for Industry, Vol. 106, pp. 28-33.

[92] Evans, A. G. and Marshall, D. B., (1981) "Wear Mechanisms in Ceramics", Fundamentals of Friction and Wear of Materials, Editor by D. A. Rigney, ASME, pp. 439-447.

[93] Kingdom, R. (1992) " A Guide to the Monitor and Control (MAC) program", Version 1.2c, Faculty of Technology Studied, University of Glamorgan.

[94] Acoustic emission sensors, suppliers Physical acoustic Corporation. Cambridge, Cambridgeshire, UK.

[95] Talysurf 5, Rank-Taylor-Hobson, Mechanical Engineering, University of Glamorgan.

[96] STEREOSCAN 260, Scanning Electron Microscopy (SEM), Chemical Engineering Department, University of Glamorgan.

[97] New View 100 system -Zygo- Lambda Photometric Limited, Harpenden, England.

[98] J. J. Instruments, Model MK30, Bending Machine, Civil Engineering Department, University of Glamorgan.

[99] Van Moppes-IDP, Diamond grinding wheel supplier, Gloucester, England.

[100] Taguchi, G. and Konishi, S., "Taguchi Method, orthogonal arrays and linear graphs - Tool for Quality Engineering", Editor, American Supplier Institute Inc., 1987.

[101] High frequency imaging and characterisation system, Ultrasonic Science Ltd., Fleet, Hants, UK.

[102] Integrated Design Engineering Analysis Software I-DEAS, User Manual -Finite Element Modelling- Mechanical Engineering Department, University of Glamorgan.

[103] Matsumoto, T., Inasaki, I. and Ogawa, K., (1993) "Monitoring of Grinding Process with a Sensor Integrated CBN Wheel" Proceedings 5th International Grinding Conference October 26-28, Cincinnati, Ohio MR93-367, pp. 1-14.

[104] Konig, W. and Klumpen, T., (1993) "Monitoring and Sensor Concepts for Higher Process Reliability" Proceedings 5th International Grinding Conference October 26-28, Cincinnati, Ohio, MR93-358, pp. 1-23.

[105] Tonshoff, H. K. and Heuer, W., (1991) "Methods of Contact Detection of Dressing of Superabrasive Grinding Wheels" Proceedings - Superabrasive 91- CIRP Conference, Chicago, June, 1991, pp. 7.39-7.55.

[106] Tonshoff, H. K., Trumpold, H., Brinksmeier, E. and Wobker, H. G., (1989) "Evaluation of Surface Layers of Machined Ceramics", Annals of the CIRP, Vol. 38, No. 2, pp. 699-708.

[107] Gordon, R. "ITTI Finite Element Training Project", Plate and Shell Analysis, MCC, UMIST Support Unit.

[108] Pung, R., (1993) "Guide Lines For Diamond Wheel Selection For Grinding Ceramic" Proceedings - Advance Ceramic Conference- Cincinnati, Ohio, May 20-21, 1993, EM93-162, pp. 1-12.

[109] Samuel, R., Chandrasekar, S., Farris, T. N. and Lich, R. H., (1989) "Effect of Residual Stresses on the Fracture of Ground Ceramics", Journal of the American Ceramic Society Vol. 72, No. 10, pp. 1960-1966.

[110] Raj, B. and Jha, B. B. (1994) "Fundamentals of Acoustic Emission", British Journal of Non-destructive Test, Vol. 36, No 1, January 1994, pp. 16-23.

[111] Dornfeld, D. and Cai, H. G., (1984) "An Investigation of Grinding and Wheel Loading using Acoustic Emission", ASME, Journal of Engineering for Industry, Vol. 106, No. 1, pp. 28-33.

[112] Johnson-Walls, D., Evans. A. G., Marshall, D. B. and James, M. R. (1986) "Residual Stresses in Machined Ceramic Surfaces", Journal of the American Ceramic Society, Vol. 69, No. 1, pp. 44-47.

[113] Scott, J. I., (1992) " Plan Form Grinding of Silicon Nitride Ceramic Materials", PhD thesis, Department of mechanical engineering, University of Bristol.

LIST OF THE AUTHOR'S RELEVANT PUBLISHED PAPERS

1. Maksoud, T. M. A., Demille, J. J. and Mokbel, A. A. (1993) " Optimum Selection of Diamond Grinding Wheel in Relation to Ceramic Materials" Proceeding of the Tenth Conference of the Irish Manufacturing Committee, 8-10 September, pp 400 - 410.

2. Maksoud, T. M. A., Mokbel, A. A. and Morgan, J. E. (1994) " Finite Element Simulation Model for the Mechanics of Grinding of Ceramic Material " Proceeding in the 2nd International Conference of Sheet Metal, University of Ulster 12-13 April. pp 429-439.

3. Maksoud, T. M. A., Mokbel, A. A. (1995) "Very High Infeed Effects on the Grinding of Advanced Ceramic Materials" Proceeding of AL-Azhar Engineering Fourth International Conference, December 16-19, Vol. 7, pp. 283-295.

4. Maksoud, T. M., Mokbel, A. A. and AL-Ismaily, S. L. (1994) "Effect of Stiffness on the Grinding of Ceramics", Proceeding of Eleventh Conference of the Irish Manufacturing Committee, The Queens University of Belfast, 31 August-2 September, pp. 141-151.

5. Maksoud, T. M. A., Scott, J. E. and Mokbel, A. A. (1993) " Residual Stresses in the Grinding of Silicon Nitride Ceramics Materials, "Proceeding of the Ninth National Conference on Manufacturing Research, University of Bath 7-9 September, pp 257-261.

6. Maksoud, T. M. , Mokbel, A. A. and Morgan, J. E. (1995) "In-process Detection of Grinding Wheel Truing and Dressing Conditions using Flapper Nozzle Arrangement" accepted to be published in IMechE.

7. Maksoud, T. M. A and Mokbel, A. A. (1996) "New Cooltip Dresser for Alumna Wheels" Presented in the IMEC Conference, 7-9 August, University of Connecticut, USA, pp. 61-64.

WORK TO BE PUBLISHED

1. Correlation of Acoustic Emission (AE), Scanning Electron Microscopy (SEM) and 3D Topography Data to Investigate the Ground Ceramic Condition.

2. Artificial Cracks Creation on Ceramic Specimens and their Propagation during Grinding Process.

3. Evaluation of Surface and Sub-Surface Cracks of Ground Ceramic.

4. Diamond Grinding Wheel Condition Monitoring by Using AE Technique.

5. Improving the strength of ground advanced ceramic material.

APPENDICES

Appendix A1: Finite Element Theoretical Background

A1.1. Estimating the Grinding Forces per Grit

The grinding forces per grit were calculated according to the grinding zone width and the concentration of the diamond grits on the grinding wheel surface. If the normal force measured in the experimental section is F_n , then normal force applied per grit F_{ng} can be calculated as [13];

$$F_{ng} = F_n / N_s . A_c \qquad \text{(A1.1)}$$

Where A_c the contact area and can be calculated from;

$$A_c = w\,(a\,d_s)^{1/2} \qquad \text{(A1.2)}$$

Where; w = Width of the grinding wheel
a = Depth of cut
d_s = Equivalent diameter of the wheel

The number of grits per cm^2 N_s can be calculated as;

$$N_s = (N_{ccw})^{2/3}$$

N_{ccw} = Number of grits/cubic centemeter of wheel volume (A1.3)

$= (N_{cc} \times \text{Concentration})/ 4*100$ (A1.4)

N_{cc} = Number of grit/cc (A1.5)

$= N_c \times 5 \times \text{Density of diamond}$ (A1.6)

Where; N_c = Number of grit per carat
One carat = 0.2 gms
Density of diamond = 3.51 gms/cc

A1.2. Theoretical Background

Finite element modelling divides the structure into a grit of elements which form a model of the real structure. Each of the elements is a simple shape (such as square or triangle) for which the finite element program has information to write the governing equations in the form of a stiffness matrix. The unknowns for each element are the displacements at the node points, which are the points at which the elements are connected. The finite element program will assemble the stiffness matrices for these simple elements together to form a global stiffness matrix for the enter model. This stiffness matrix is solved for unknown displacements at the nodes, the stresses in each element can then be calculated.

A finite element is divided by assuming a form of the equation for the internal strains. Some elements are defined to assume that the strain is a constant throughout the element, while others use higher-order functions. Using these equations and the actual geometry of a given element, the equilibrium equations between the external forces and the nodal displacements can be written. There will be one equation for each degree of freedom for each node of the element. These equations are most conveniently written in matrix form for use in a computer algorithm. The matrix of the coefficients becomes a "stiffness matrix" that relates forces {F} to displacements {d}.

$$\{F\} = [K] * \{d\} \qquad \text{(A1.7)}$$

The theory of total minimum potential energy can be employed to drive the finite element equations. The total potential energy is given by the difference between the work done and the strain energy. The work done on the four node quadrilateral element, shown in the Figure A1.1 is given by;

$$W = w_1 P_{zI} + \theta_{x1} M_{x1} + \theta_{y1} M_{y1} + \ldots\ldots\ldots + w_4 P_{z4} + \theta_{x4} M_{x4} + \theta_{y4} M_{y4} \qquad \text{(A1.8)}$$

This is generally written in matrix form as,

$$W = \{a\}^t \{f\}^t \tag{A1.9}$$

Where;

$$\{a\}^t = [w_1\ \theta_{x1}\ \theta_{y1} \quad \ldots\ldots\ldots\ w_4\ \theta_{x4}\ \theta_{y4}] \tag{A1.10}$$

$$\{f\}^t = [F_{Z1}\ M_{X1}\ M_{Y1} \ldots\ldots\ P_{Z4}\ M_{X4}\ M_{Y4}] \tag{A1.11}$$

The strain energy for a structure is given by,

$$U = \int_{Vol} \frac{\{\sigma\}^t \{\varepsilon\}^t}{2} dVol \tag{A1.12}$$

Where;

$$\{\sigma\}^t = [\sigma_x\ \sigma_y\ \tau_{xy}\ \tau_{yz}\ \tau_{zx}] \tag{A1.13}$$

$$\{\varepsilon\}^t = [\varepsilon_x\ \varepsilon_y\ \gamma_{xy}\ \gamma_{yz}\ \gamma_{zx}] \tag{A1.14}$$

The stresses and stains are related by Hook's law for linear elastic homogeneous materials. The direct stresses are related to the direct strain given by,

$$\varepsilon_x = \frac{1}{E(\sigma_x - \nu\sigma_y)} \tag{A1.15}$$

$$\varepsilon_y = \frac{1}{E(\sigma_y - \nu\sigma_x)} \tag{A1.16}$$

These equations can be re-written in matrix form and re-arranged to give,

$$\begin{pmatrix} \sigma_x \\ \sigma_y \end{pmatrix} = \frac{E}{1-\nu^2} \begin{pmatrix} 1 & \nu & \varepsilon_x \\ \nu & 1 & \varepsilon_y \end{pmatrix} \tag{A1.17}$$

The shear strains are related to the shear stresses,

$$\gamma_{zx} = \frac{\tau_{zx}}{G} \tag{A1.18}$$

$$\gamma_{yz} = \frac{\tau_{yz}}{G} \tag{A1.19}$$

$$\gamma_{zx} = \frac{\tau_{zx}}{G} \tag{A1.20}$$

Where,

$$G = \frac{E}{2(1-\nu)} \tag{A1.21}$$

The strain term γ_{xy} is due to the bending while the terms γ_{yz} and γ_{zx}, are due to the shear. The bending shear stress is included with the direction bending stress to give,

$$\begin{bmatrix} \sigma_x \\ \sigma_y \\ \tau_{xy} \end{bmatrix} = \frac{E}{1-\nu^2} \begin{bmatrix} 1 & \nu & 0 \\ \nu & 1 & 0 \\ 0 & 0 & \frac{1-\nu}{2} \end{bmatrix} \begin{bmatrix} \varepsilon_x \\ \varepsilon_y \\ \gamma_{xy} \end{bmatrix} \tag{A1.22}$$

This is generally written as,

$$\{\sigma\}_b = [D]_b \{\varepsilon\}_b \tag{A1.23}$$

The shear stress-strain relationship is given by,

$$\begin{pmatrix} \tau_{yz} \\ \tau_{xx} \end{pmatrix} = \frac{E}{2(1-\nu)} \begin{pmatrix} 1 & 0 \\ 0 & 1 \end{pmatrix} \begin{pmatrix} \gamma_{yz} \\ \gamma_{zx} \end{pmatrix} \tag{A1.24}$$

Which is generally written as,

$$\{\sigma\}_s = [D]_s \{\varepsilon\}_s \tag{A1.25}$$

The strain-displacement relationships for small deflections are;

$$\varepsilon_x = \frac{\delta u}{\delta x} \tag{A1.26}$$

$$\varepsilon_y = \frac{\delta v}{\delta y} \tag{A1.27}$$

$$\gamma_{xy} = \frac{\delta u}{\delta y} + \frac{\delta v}{\delta x} \tag{A1.28}$$

$$\gamma_{yz} = \frac{\delta v}{\delta z} + \frac{\delta w}{\delta y} \tag{A1.29}$$

$$\gamma_{zx} = \frac{\delta u}{\delta z} + \frac{\delta w}{\delta x} \tag{A1.30}$$

The elastic matrices due to bending $[D_b]$ and shear $[B_s]$ are given by;

$$D_b = \frac{Eh^3}{12(1-\nu)} \begin{bmatrix} 1 & \nu & 0 \\ \nu & 1 & 0 \\ 0 & 0 & \frac{1-\nu}{2} \end{bmatrix} \tag{A1.31}$$

$$D_s = \frac{\alpha Eh}{2(1+\nu)} \begin{pmatrix} 1 & 0 \\ 0 & 1 \end{pmatrix} \tag{A1.32}$$

Where α is a correction factor introduced to take account of the non-uniform shear strain distribution and warping. For isotropic materials, $\alpha = 5/6$.

Where; θ = Cylindrical polar co-ordinate
E = Young's modulus of elasticity
G = Modulus of rigidity
α = Coefficient of assumed solution polynomial
γ = Shear strain component
σ = Direct stress component
ε = Direct strain component
ν = Poisons ratio
τ = Shear stress component
U = Strain energy
W = Work done by external load
P = Nodal load component
t = Element thickness
v = Displacement component in y direction
w = Displacement component in z direction
u = Displacement component in x direction

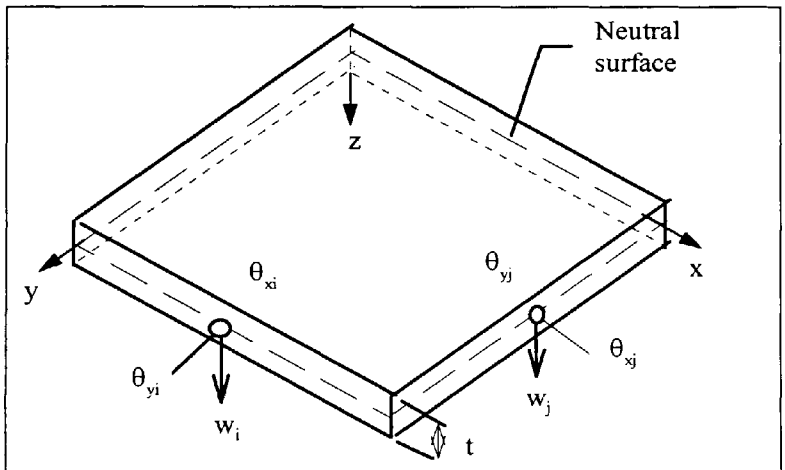

Thin Plate Element with Thickness, t.

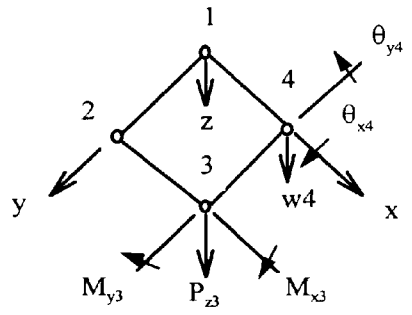

Figure A1.1: Nodal work done by a four node quadrilateral element.

Appendix A2: Ceramic Strength Testing

The reduction in the strength of ceramic material caused by the grinding process was investigated by calculating the fracture strength of the ground specimens. Three point bending test equipment was used to perform this part. This test is conducted by loading the centre of the ground specimen as shown in Figure A2.1. The load is applied gradually at a constant rate until the specimen fails. The fracture strength of the ground specimens can then be calculated. A simple theory of bending was used for the calculation;

$$\frac{M}{I} = \frac{\sigma}{y} = \frac{E}{R} \qquad \text{(A2.1)}$$

Where;
M = The applied bending moment of a transverse section.
I = The second moment of area of the beam cross-section about the neutral axis.
σ = The stress at distance Y from the neutral axis of the beam material.
E = Young's modulus of elasticity for the beam material.
R = The radius of curvature of the neutral axis at the section.

The ground ceramic specimen can be considered as a simply supported beam carrying a single concentrated load as shown in Figure A2.1. The maximum bending moment M_{max} is given by;

$$M_{max} = \frac{W}{2} \cdot \frac{L}{2} = \frac{WL}{4} \qquad \text{(A2.2)}$$

$$I = \frac{bd}{12} \qquad \text{(A2.3)}$$

$$y = \frac{d}{2} \qquad \text{(A2.4)}$$

Where;
W = The fracture load
L = The distance between two edges.
b = The sample width
d = The sample depth

From equation (A2.1)

$$\sigma = \frac{My}{I} \tag{A2.5}$$

By substituting equations ((A2.2), (A2.3), (A2.4) into equation (A2.5). The nominal stress can be given as,

$$\sigma = \frac{3WL}{2bd^2} \tag{A2.6}$$

Substituting the load of sample fracture in the above equation, the fracture strength of the sample can be calculated. Since at that point the nominal stress of the sample was exceeded, its value can be taken as the fracture strength.

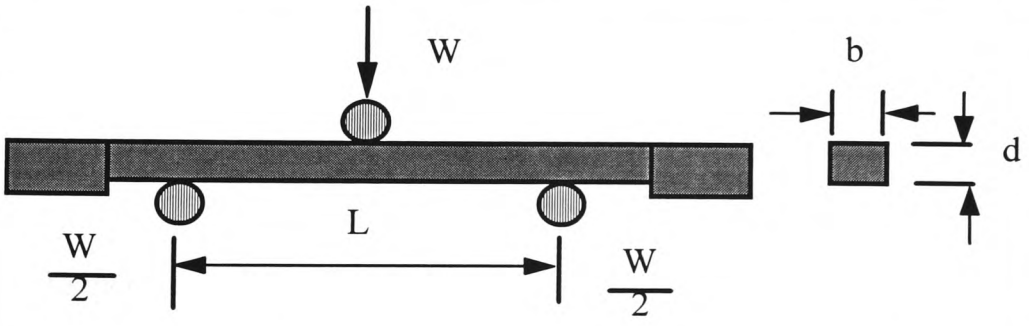

Figure A2.1: Layout of the ground specimen during the three point bending test.

Appendix A3: Experimental Design and Analysis

A3.1. Orthogonal Array

Orthogonal arrays have been in use for many years, but their application by Taguchi [100] has some special characteristics. At first glance, Taguchi method seems to be nothing more than an application of fractional factorials. In his approach to quality engineering, however, the primary goal is the optimisation of product/process design for minimal sensitivity to "noise" ratio. Quality engineering, according to Taguchi method, focuses on the contribution of factor levels to robustness. In contrast with pure research, quality engineering applications in industry do not look for cause and effect relationships. Such a detailed approach is usually not cost-effective. Rather, good engineers should be able to involve their skills and experience in designing experiments by selecting characteristics with minimal interactions in order to focus pure main effects.

Orthogonal arrays can have factors with many levels as shown in Figure A3.1. The convention for naming arrays is $L_a(b^c)$ where;

a = Number of experimental runs

b = Number of levels of each factor

c = Number of columns in the array

Dr. Taguchi recommends that experiments be designed with emphasis on main effects, to the extent possible. Because there will be situations in which interactions must be analysed. This method has devised specific triangular tables for certain arrays to help practitioners assign factors and interactions in a non-arbitrary method to avoid possible confounding.

A3.2. Linear Graphs

One of Taguchi's contribution to the use of orthogonal arrays in the design of experiments is the linear graph. These graphs are pictorial equivalents of triangular

tables or matrices that represent the assignment of interactions between all columns of an array. Linear graphs are, thus, a graphic tool to facilitate the often complicated assignment of factors and interactions, factors with different numbers of levels, or complicated experiments such as pseudo factor design to an orthogonal array.

A linear graph shown in Figure A3.2 is used as follows:

- Factors are assigned to points of the graph.
- An interaction between two factors is assigned to the line segment connecting the two resprctive points.

A3.3. The basic steps in designing the experiments

1. Define the problem
- A clear statement of the problem to be solved
2. Determine the objective
- Identify output characteristics
3. Brainstorm
- Group factors into control factors and noise factors
- Determine levels and values for factors
4. Design the experiment
- Select the appropriate orthogonal array for control factors
- Assign control factors and interaction to orthogonal array columns
- Select an outer array for noise factors and assign factors to columns
5. Conduct the experiment and collect data
6. Analysis the data by:
- Regular analysis
- Average response tables
- Average response graphs
- ANOVA
7. Interpret results
- Select optimum levels of control factors
- Predict results for the optimum condition

A3.4 Experimental Requirements and Design

An experimental design must be able to perform the following tasks;

1) Validity: The conclusions drawn from the experimental results must be free from bias or symmetrical errors.

2) Precision: If the absence of systematical error is achieved by randomisation, the estimated effect of a parameter differ from its true value random variation only. A precise experiment is one which gives a measure of this variation. This is achieved by reproducing or replicating an experiment.

3) Coverage. The range of experiments performed must be representative of the range of possible results.

Full factorial experimental design is the most widely used. The parameters under investigation, known as 'factors', are tested at all possible factor levels. For a full factorial array experiment design (L_{27}) requires 3^3x7^3 or 9,261 experiments plus replications. A fractional factorial design keep judgement of the main effects, but reduces the total number of experiments required by combining or 'aliasing' interactive effects with these main effect. A publication listing the available orthogonal arrays is given by Taguchi [100], and L_{27} orthogonal array example is shown in Figure A3.1. The first column indicates the number of experiments which must be performed to complete the fractional factorial design i.e. 27. The first row indicates the number of factors or main effects which can be tested i.e. 13. The other columns represent the levels of each factor 1 to 3 which may used. For example, experiment number 1 requires all 13 factors to be at level 1, indicated in the second row. Similarly, experiment 2 requires factors 1 to 4 to be at level 1 in row 3, whilst factors 5 to 13 are at level 3 in row 3.

The degree of freedom associated with a complete orthogonal array is defined as on less than the total number of experiment. For example, the L_{27} array has 26 degrees of freedom available. The sum of the degree of freedom associated with the factors and

their interactions must be less or equal to the degree of freedom associated with orthogonal array.

Analysis of an orthogonal array is performed by averaging the response variable (X) associated with each factor and level. A typical response variable could be fracture strength or surface roughness. For example, in the L_{27} array shown in Figure A3.1 The effect of factor A assigned to column 1 is the average of response variable associated with experiments 1 to 9 for level 1. the effect of factor A at level 2 is the average of experiments 10 to 18 and the effect of factor A at level 3 is the average of response variable (X) resulting from experiments 19 to 27. Plotting these averages in response variable (X) against the level of factor A gives an indication of the effect of A on Y. Also, analysis of variance technique can be applied to orthogonal arrays to give an indication of the significance changing factor A on response variable X.

A3.5. Method of creating different level column for a three-level system

It is possible to create a column of nine levels by using segment in a linear graph for a three-level system; in such system each interaction occupies two column. For example, we represent levels 1, 2, 3, 4, 5, 6, 7, 8, 9 by combinations of levels 1, 2 ,3 of column, *viz.*, 11, 12, 13, 21, 22, 23, 31, 32, and 33, of column 2 and column 5 at both ends of a single segment in L_{27} shown in Figure A3.1, and we erase columns 2, 5 ,8 and 11 from the array. In effect, one column of eight degrees of freedom at nine levels has been formed instead of the four columns at three levels, each of two degrees of freedom, 2, 5, 8 and 11. The new orthogonal array is as shown in Figure A3.3. A similar techniques was used by Scott [113] are applied to column 5 and 8 using columns 6, 7, 9 and 10 respectively, then the L_{27} orthogonal array has three 7-levels factors and three 3-level factors. This method is known as the idle column technique and column 1, used in three 7-levels assignments, is known as idle column. The new resulting orthogonal array is shown in Figure A3.5. This array was used in this research to investigate different levels of grinding wheel/truing speed ratios, grinding wheel speed, depth of cut, table feed grinding wheel grit size and grinding wheel bond type shown in Table [5].

A3.6 Analysis of Variance

Analysis of variance (ANOVA) technique was used to division the total variation within an experiment due to:

1. Attribute causes effect due to main factors such as grit size, on their interaction
2. Unattribute causes which are assumed and described as error variation.

In applying ANOVA technique to experimental data, three assumptions are made:

A) Error variation in normally distributed

B) Different measurement are independent

C) The relative size of errors are unrelated

The standard method for expressing analysis of variance results is in tabular form:

Source of Variance	Degree of Freedom	Sum of Squares	Mean Square	F-Ratio	$F_{0.05}$	$F_{0.01}$
Treatments	k-1	SSTr	MS(Tr) = SSTr/(k-1)	$\frac{MS(Tr)}{MSE}$	y/n	y/n
Error	k(n-1)	SSE	MSE = SSE/k(n-1)			
Total	nk-1	SST				

If we assume k treatment or experimental factors exist, denoted by subscript I, each with n observations, denoted by subscript j, then the first step in constructing an analysis of variance table is to calculate the total sum of square (SST) of all k treatments and n observations. This is given by the following formula;

$$SST = \sum_{i=1}^{k} \sum_{j=1}^{n} (Y_{ij})^2 - C \qquad \text{A3.1}$$

Where; Y_{ij} = Response variable for the jth observations of the ith treatment.

and C = Correction term, given by;

$$C = \frac{\sum_{i=1}^{k} (Y_{ij})^2}{kn} \qquad \text{A3.2}$$

Testing the significance of a particular factor, the total sum of square (SST) must be separated into sum of squares for individual factors or treatments (SSTr), and the error sum of squares (SSE). The treatment sum of squares (SSTr) is given by;

$$SSTr = \frac{\sum_{i=1}^{k} (\sum_{j=1}^{n} Y_j)^2}{n} - C \qquad \text{A3.3}$$

From ANOVA analysis, it allows the effect of individual factors such as grit size for example to be tested for significance and the response of results obtained (i.e.fracture strength).due to the wheel grit size.

No.	1	2 3 4	5 6 7	8 9 10	11 12 13
1	1	1 1 1	1 1 1	1 1 1	1 1 1
2	1	1 1 1	2 2 2	2 2 2	2 2 2
3	1	1 1 1	3 3 3	3 3 3	3 3 3
4	1	2 2 2	1 1 1	2 2 2	3 3 3
5	1	2 2 2	2 2 2	3 3 3	1 1 1
6	1	2 2 2	3 3 3	1 1 1	2 2 2
7	1	3 3 3	1 1 1	3 3 3	2 2 2
8	1	3 3 3	2 2 2	1 1 1	3 3 3
9	1	3 3 3	3 3 3	2 2 2	1 1 1
10	2	1 2 3	1 2 3	1 2 3	1 2 3
11	2	1 2 3	2 3 1	2 3 1	2 3 1
12	2	1 2 3	3 1 2	3 1 2	3 1 2
13	2	2 3 1	1 2 3	2 3 1	3 1 2
14	2	2 3 1	2 3 1	3 1 2	1 2 3
15	2	2 3 1	3 1 2	1 2 3	2 3 1
16	2	3 1 2	1 2 3	3 1 2	2 3 1
17	2	3 1 2	2 3 1	1 2 3	3 1 2
18	2	3 1 2	3 1 2	2 3 1	1 2 3
19	3	1 3 2	1 3 2	1 3 2	1 3 2
20	3	1 3 2	2 1 3	2 1 3	2 1 3
21	3	1 3 2	3 2 1	3 2 1	3 2 1
22	3	2 1 3	1 3 2	2 1 3	3 2 1
23	3	2 1 3	2 1 3	3 2 1	1 3 2
24	3	2 1 3	3 2 1	1 3 2	2 1 3
25	3	3 2 1	1 3 2	3 2 1	2 1 3
26	3	3 2 1	2 1 3	1 3 2	3 2 1
27	3	3 2 1	3 2 1	2 1 3	1 3 2
	a	b b a b b^2	c a a c c^2	b a a c b b^2 c c^2	b a a c^2 b^2 b c c^2
Group	1	2	3		

Figure A3.1: L_{27} Orthogonal array used for fractional factorial experimental design [100]

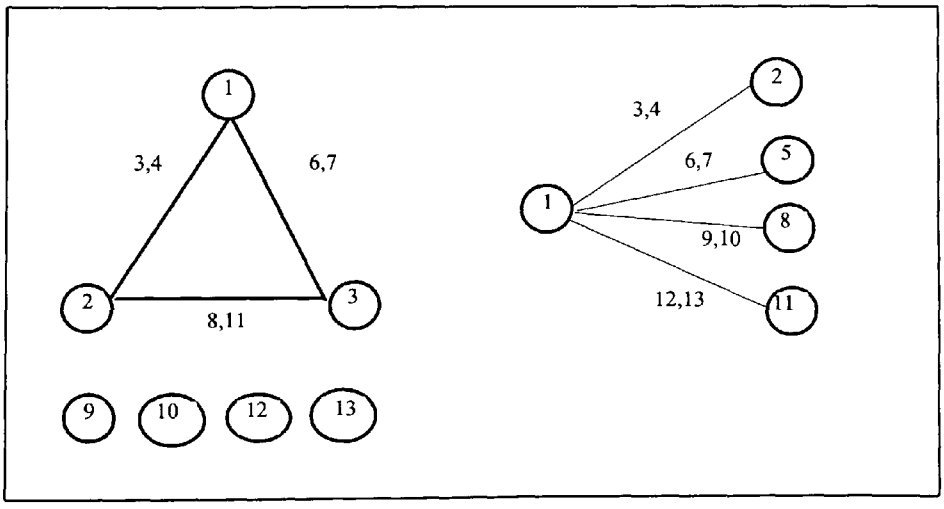

Figure A3.2: Various linear graphs used to manipulate the L_{27} orthogonal array [100]

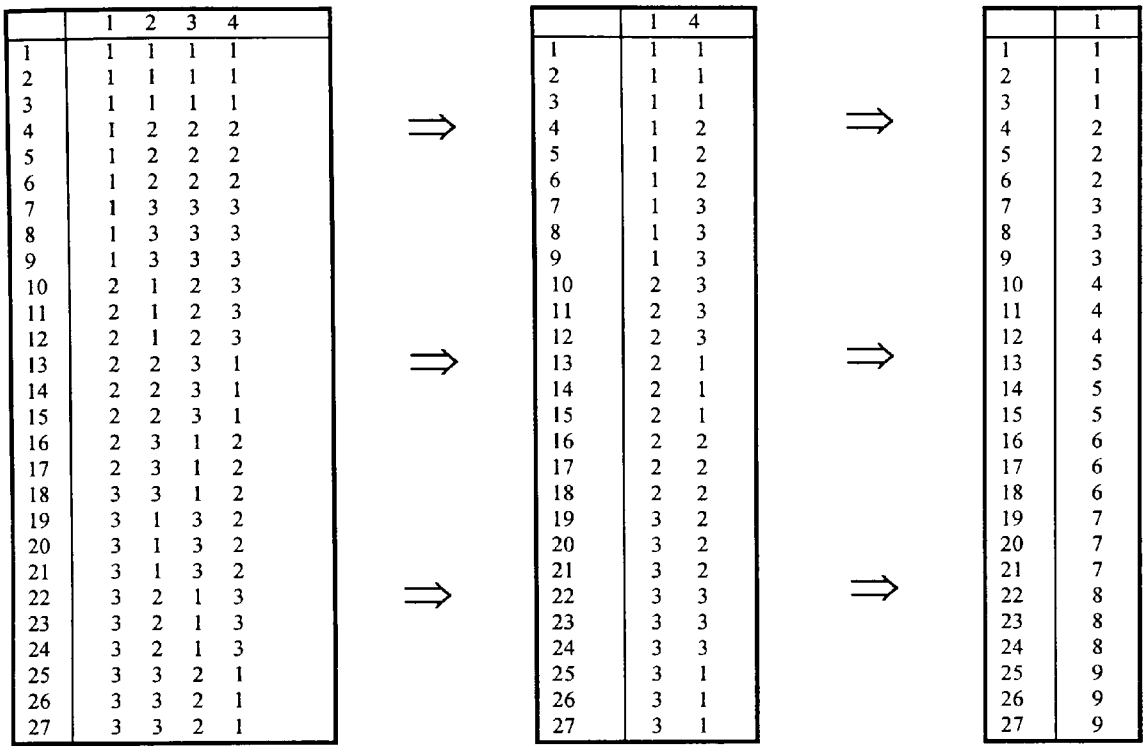

	1	2	3	4
1	1	1	1	1
2	1	1	1	1
3	1	1	1	1
4	1	2	2	2
5	1	2	2	2
6	1	2	2	2
7	1	3	3	3
8	1	3	3	3
9	1	3	3	3
10	2	1	2	3
11	2	1	2	3
12	2	1	2	3
13	2	2	3	1
14	2	2	3	1
15	2	2	3	1
16	2	3	1	2
17	2	3	1	2
18	3	3	1	2
19	3	1	3	2
20	3	1	3	2
21	3	1	3	2
22	3	2	1	3
23	3	2	1	3
24	3	2	1	3
25	3	3	2	1
26	3	3	2	1
27	3	3	2	1

	1	4
1	1	1
2	1	1
3	1	1
4	1	2
5	1	2
6	1	2
7	1	3
8	1	3
9	1	3
10	2	3
11	2	3
12	2	3
13	2	1
14	2	1
15	2	1
16	2	2
17	2	2
18	2	2
19	3	2
20	3	2
21	3	2
22	3	3
23	3	3
24	3	3
25	3	1
26	3	1
27	3	1

	1
1	1
2	1
3	1
4	2
5	2
6	2
7	3
8	3
9	3
10	4
11	4
12	4
13	5
14	5
15	5
16	6
17	6
18	6
19	7
20	7
21	7
22	8
23	8
24	8
25	9
26	9
27	9

Figure A3.3: Modification to the L_{27} orthogonal array to generate a single 9-level factor

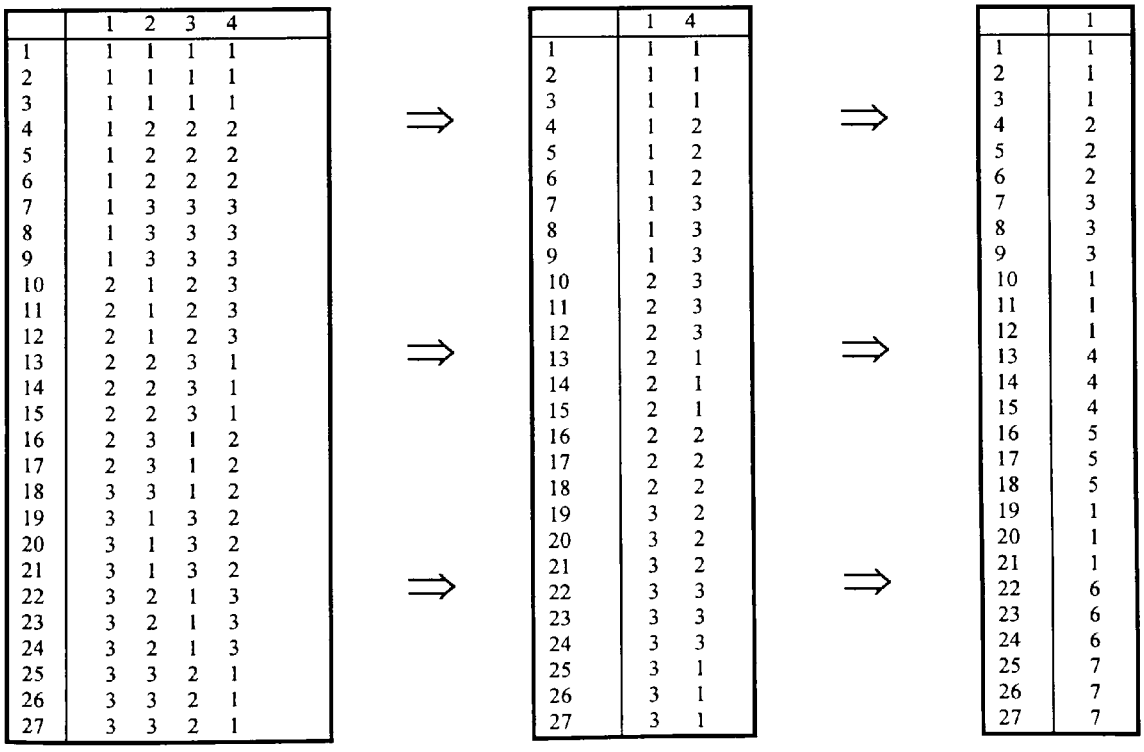

	1	2	3	4
1	1	1	1	1
2	1	1	1	1
3	1	1	1	1
4	1	2	2	2
5	1	2	2	2
6	1	2	2	2
7	1	3	3	3
8	1	3	3	3
9	1	3	3	3
10	2	1	2	3
11	2	1	2	3
12	2	1	2	3
13	2	2	3	1
14	2	2	3	1
15	2	2	3	1
16	2	3	1	2
17	2	3	1	2
18	3	3	1	2
19	3	1	3	2
20	3	1	3	2
21	3	1	3	2
22	3	2	1	3
23	3	2	1	3
24	3	2	1	3
25	3	3	2	1
26	3	3	2	1
27	3	3	2	1

	1	4
1	1	1
2	1	1
3	1	1
4	1	2
5	1	2
6	1	2
7	1	3
8	1	3
9	1	3
10	2	3
11	2	3
12	2	3
13	2	1
14	2	1
15	2	1
16	2	2
17	2	2
18	2	2
19	3	2
20	3	2
21	3	2
22	3	3
23	3	3
24	3	3
25	3	1
26	3	1
27	3	1

	1
1	1
2	1
3	1
4	2
5	2
6	2
7	3
8	3
9	3
10	1
11	1
12	1
13	4
14	4
15	4
16	5
17	5
18	5
19	1
20	1
21	1
22	6
23	6
24	6
25	7
26	7
27	7

Figure A3.4: Modification to the L_{27} orthogonal array to generate a single 7-level factor

	1	5	8	11	12	13
1	1	1	1	1	1	1
2	1	2	2	2	2	2
3	1	3	3	3	3	3
4	2	1	2	3	3	3
5	2	2	3	1	1	1
6	2	3	1	2	2	2
7	3	1	3	2	2	2
8	3	2	1	3	3	3
9	3	3	2	1	1	1
10	1	1	1	1	2	3
11	1	4	4	2	3	1
12	1	5	5	3	1	2
13	4	1	4	3	1	2
14	4	4	5	1	2	3
15	4	5	1	2	3	1
16	5	2	5	2	3	1
17	5	4	1	3	1	2
18	5	5	4	1	2	3
19	1	1	1	1	3	2
20	1	6	6	2	1	3
21	1	7	7	3	2	1
22	6	1	6	3	2	1
23	6	6	7	1	3	2
24	6	7	1	2	1	3
25	7	1	7	3	1	3
26	7	6	1	2	2	1
27	7	7	6	1	3	2

Figure A3.5: Modified L_{27} orthogonal array showing three levels of three 7-levels factors and three 3-levels factors.

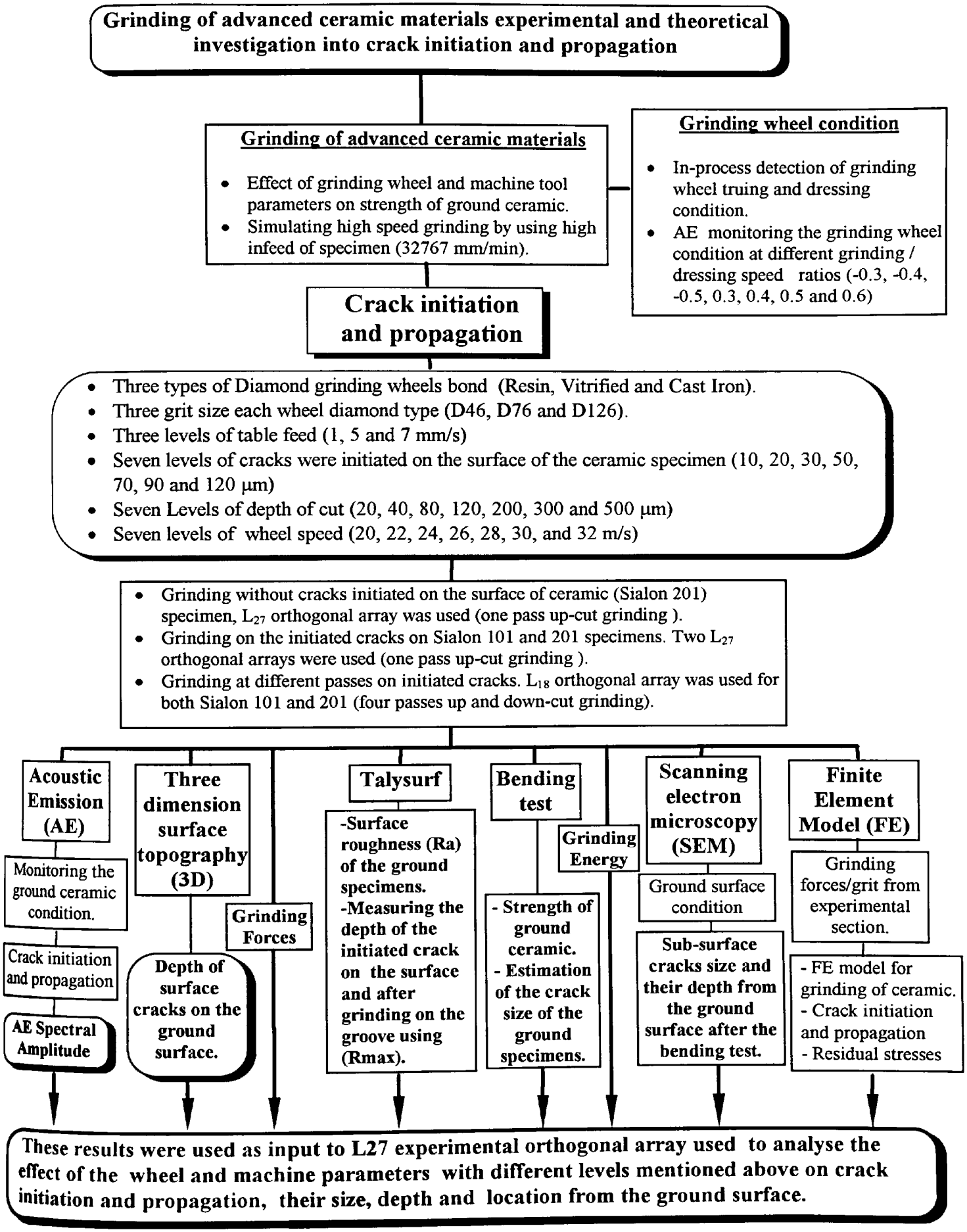

Figure 1: Chart showing the areas investigated during this research

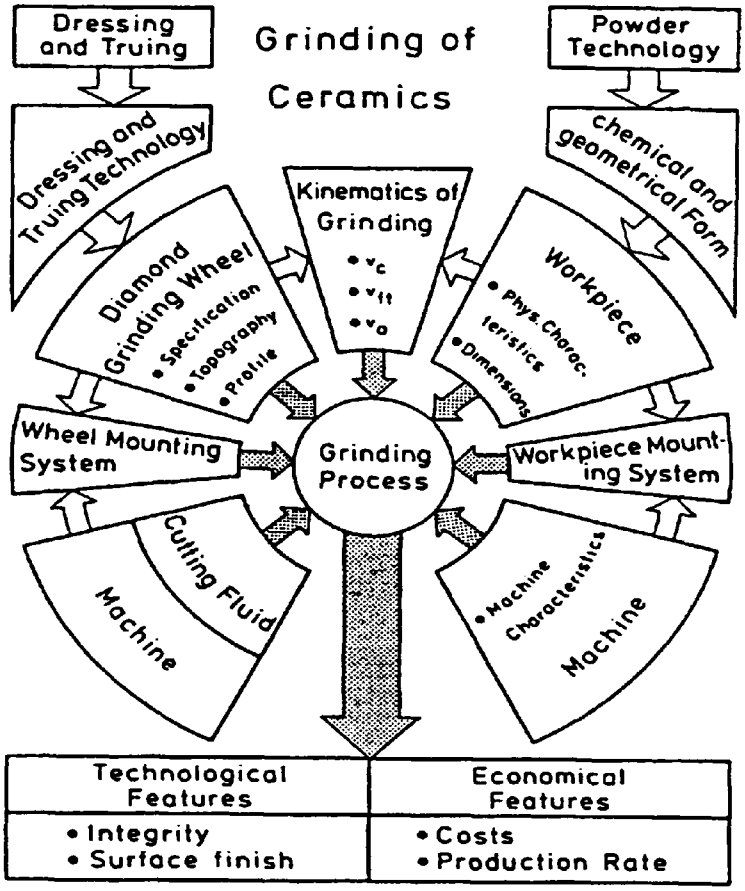

Figure 2 : Parameters influencing the grinding process [4]

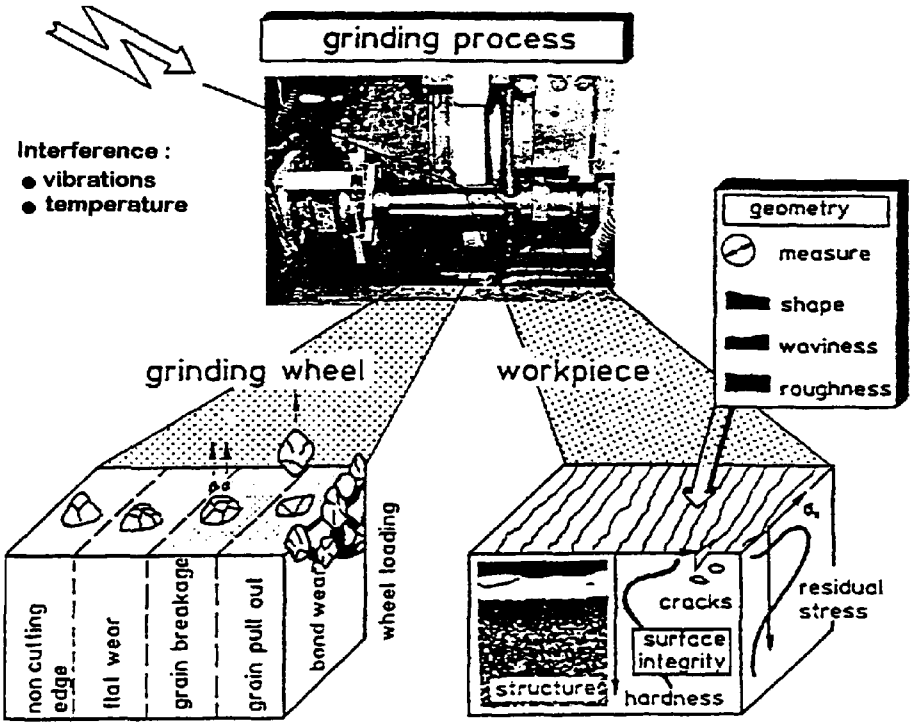

Figure 3 : Influence of the grinding process on workpiece and grinding wheel [85]

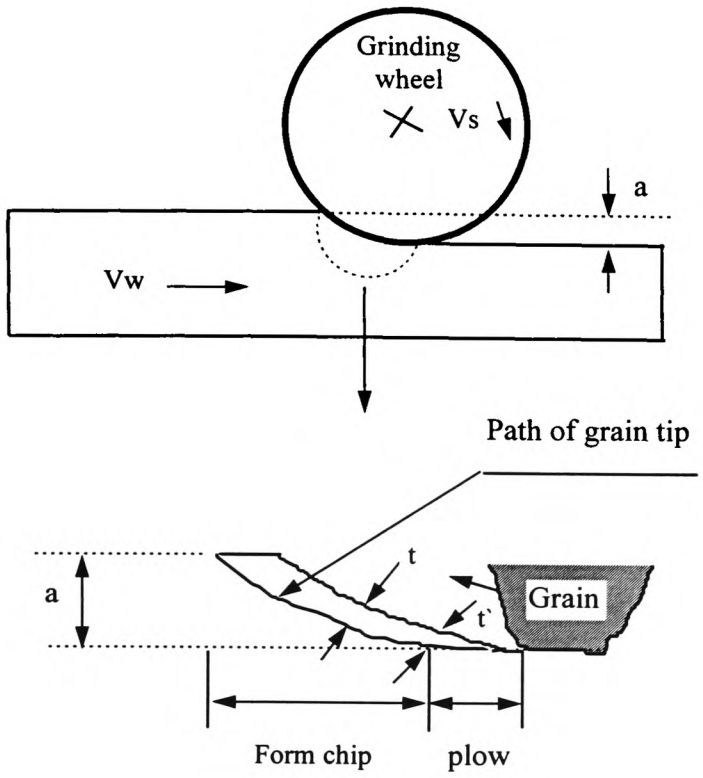

Figure 4: Illustration showing path of grain tip through grinding zone and transition

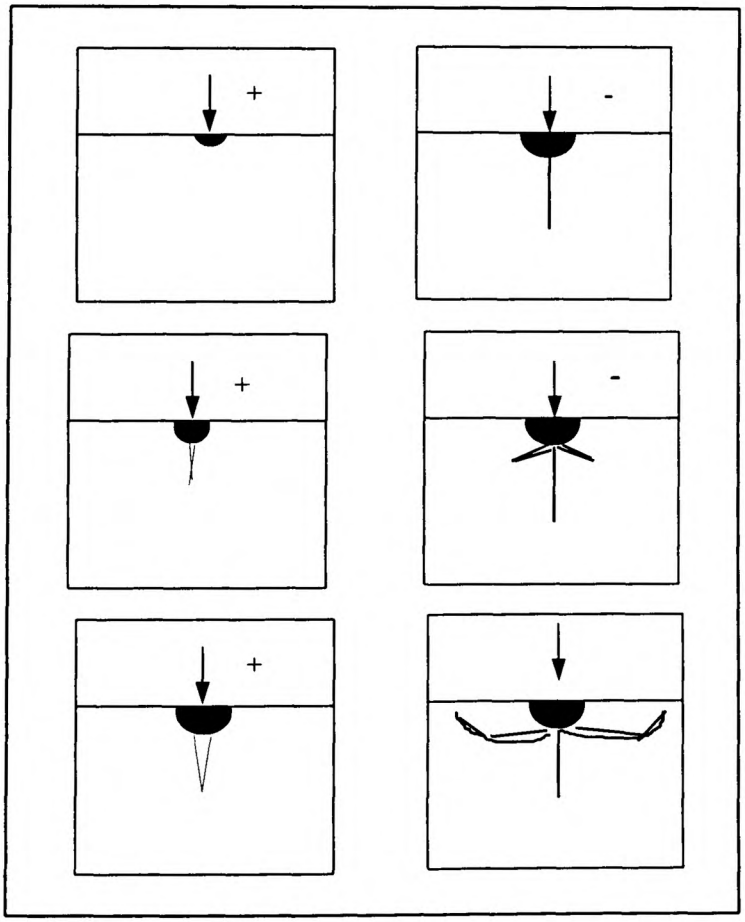

Figure 5: Schematic of vent crack formation under point indentation [33]

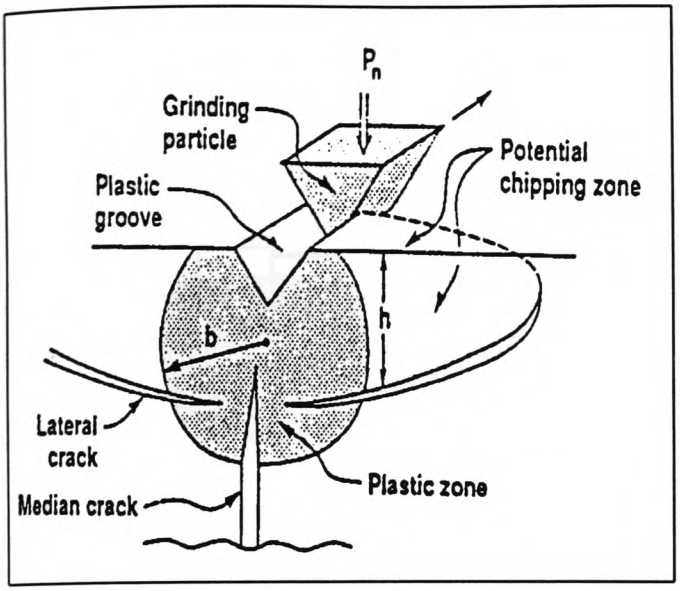

Figure 6 : Illustration of plastic zone, medium cracks, and radial cracks due to scratching by an abrasive point under a normal load Pn [92].

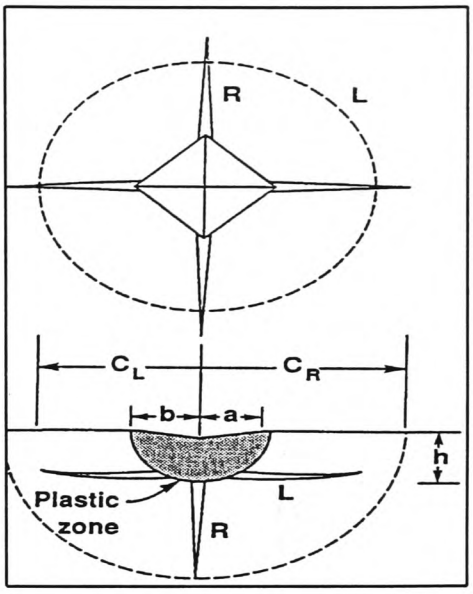

Figure 7: Illustration of plastic zone and crack formed by Vickers indentation in brittle material: R = radial cracks of dimension Cr; and L = lateral cracks of dimension Cl

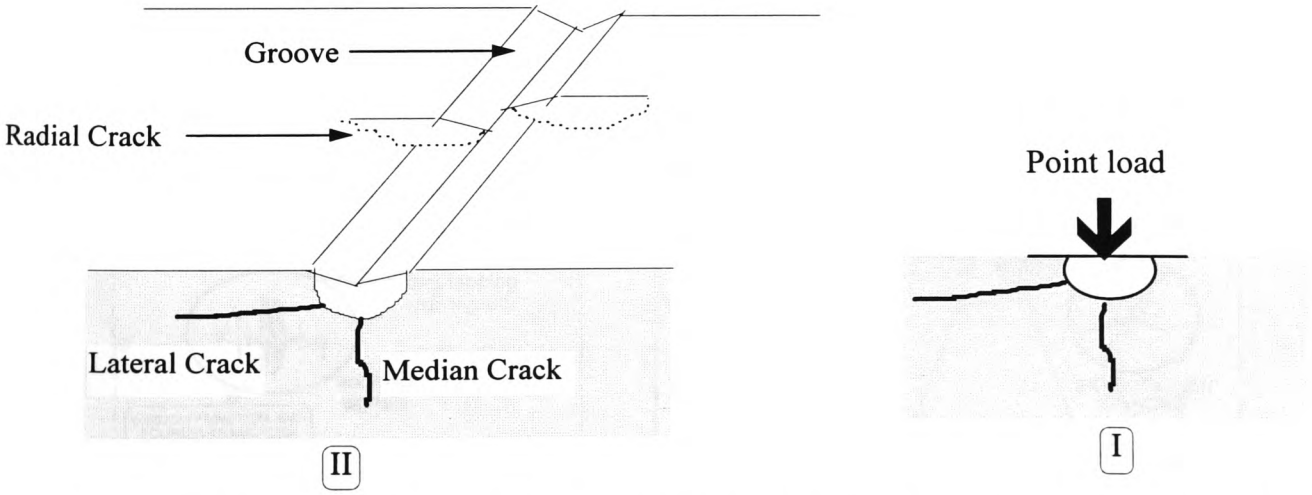

Figure 8: Diagrammatic view of the types of cracks when static point load is applied (I) and after the passage of an abrasive grain (II) with regard to chop formation through brittle fractures

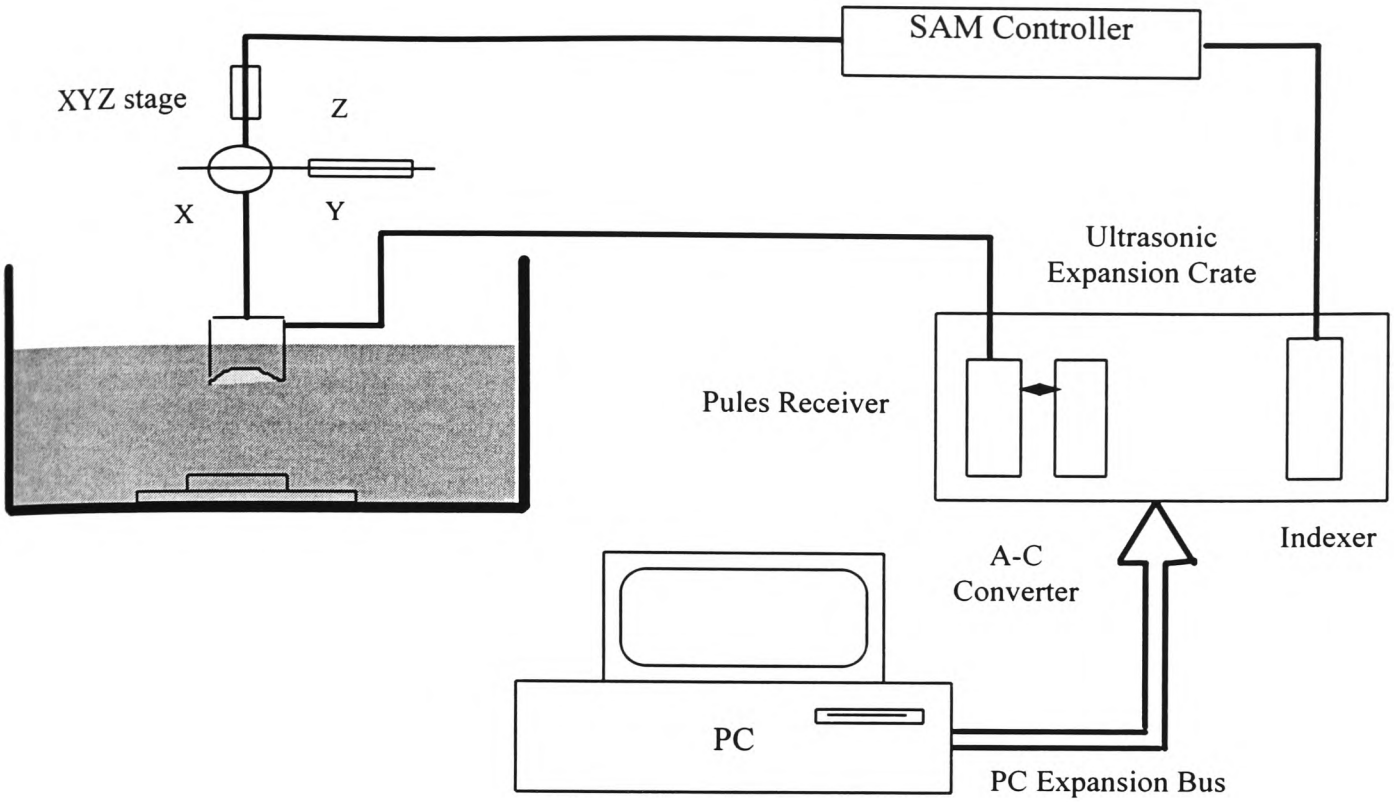

Figure 9: Block schematic diagram of scanning acoustic microscope

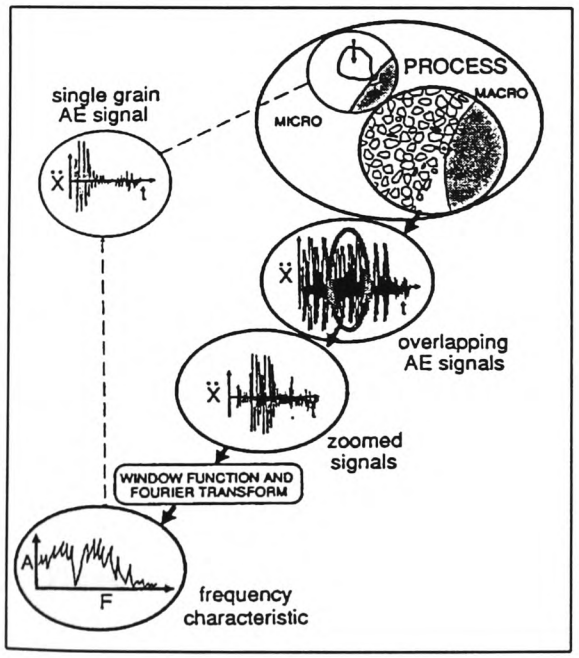

Figure 10: AE Measurement Chain [55]

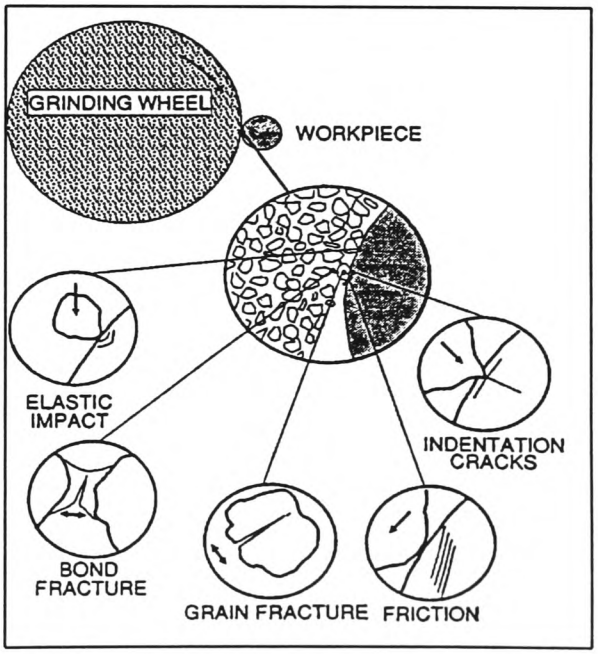

Figure 11: Strategy for the extract of a single grain AE from grinding [55]

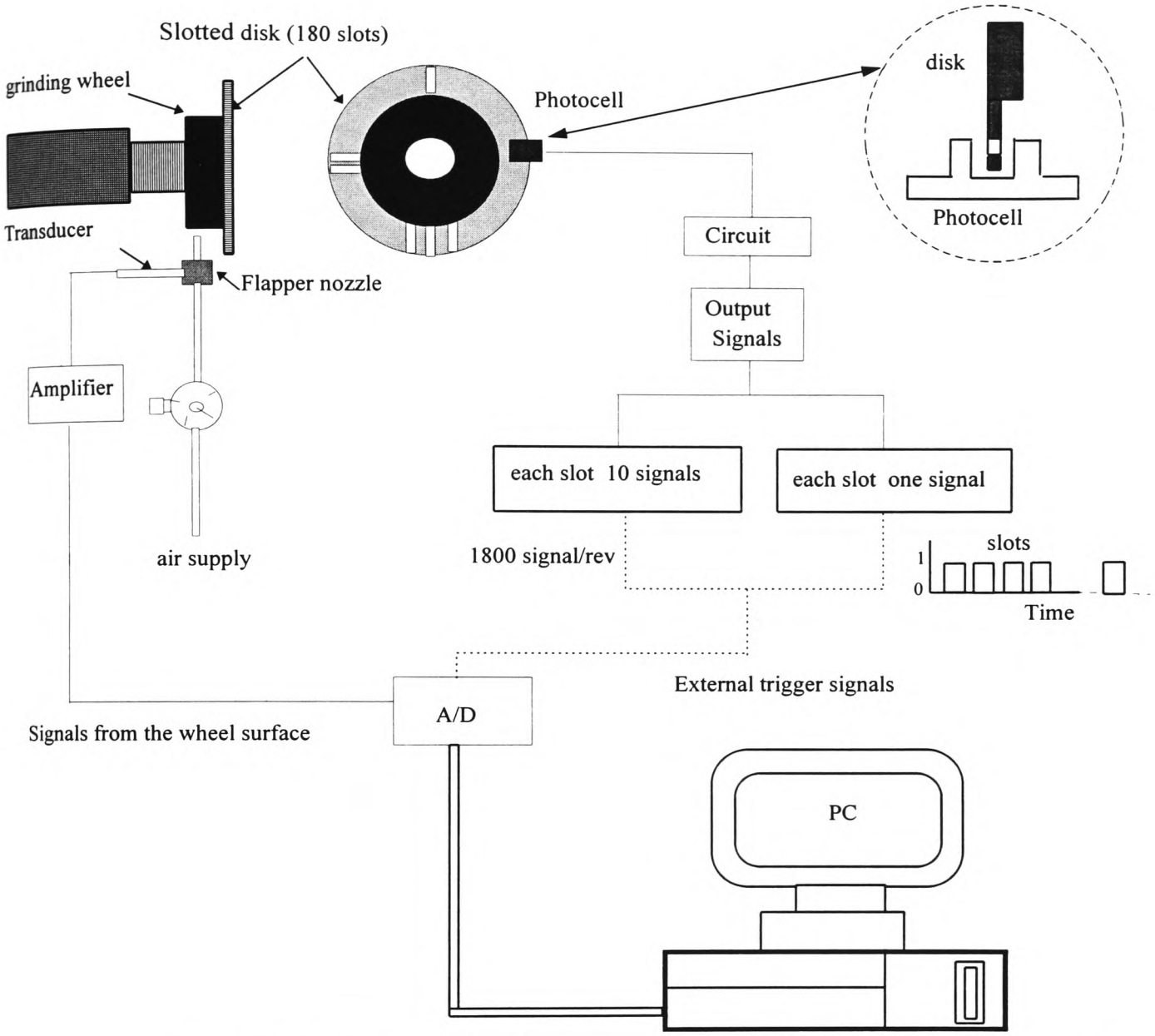

Figure 12: Diagram showing instrument layout used for grinding wheel topography measurement and analysis.

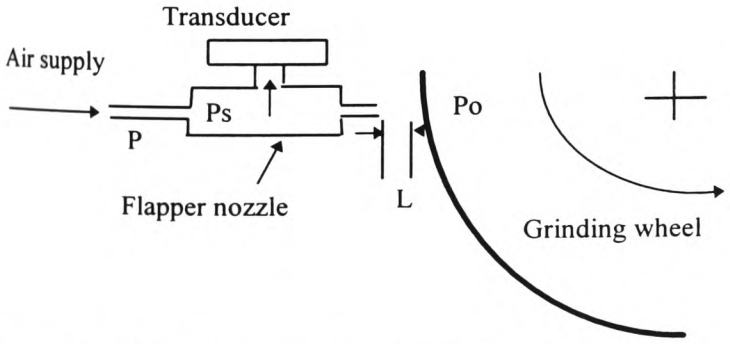

Figure 13: Variable residual pressure Po coming from the variation of the distance between the wheel surface structure and the flapper nozzle.

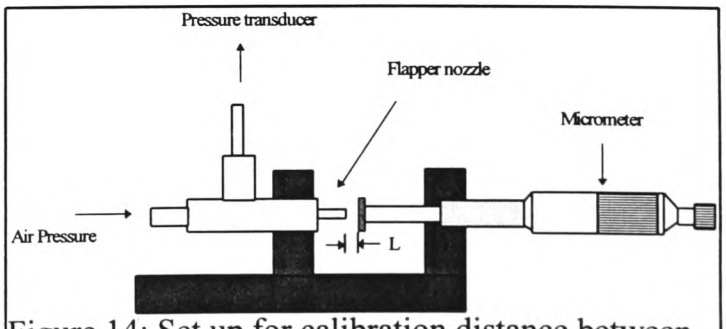

Figure 14: Set up for calibration distance between the flapper nozzle and the wheel surface.

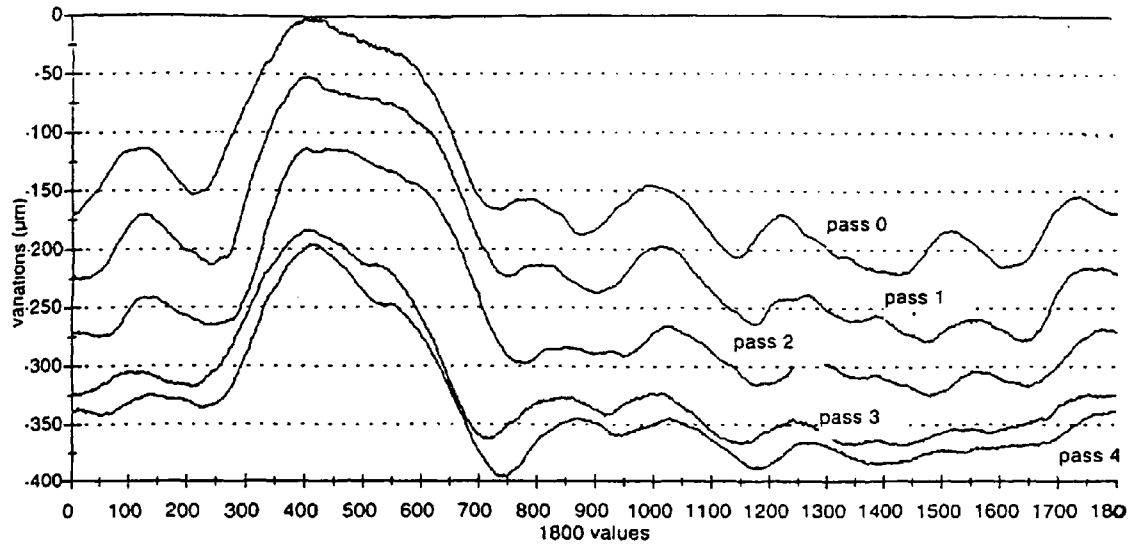

Figure 15: Grinding wheel condition at different pass numbers which gives an indication of dressing depth

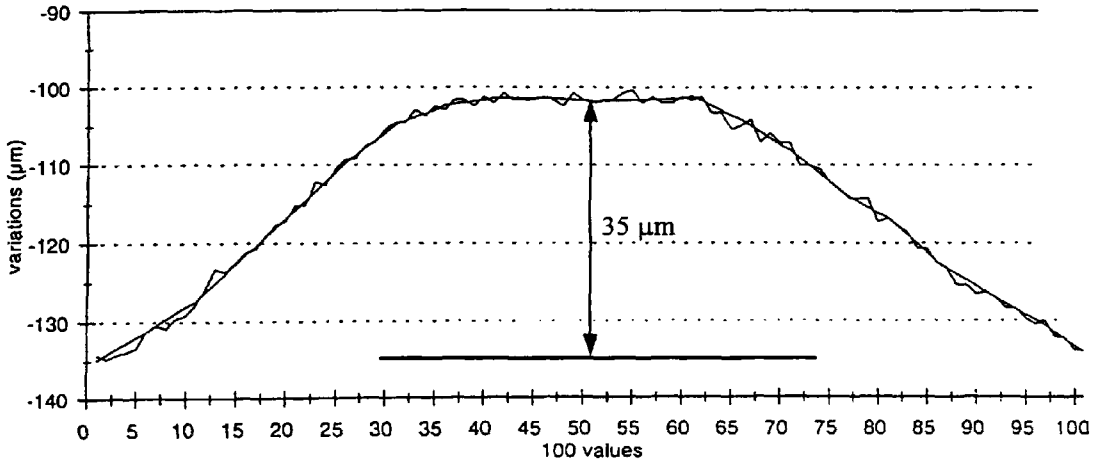

Figure 16: Raw signals from flapper nozzle converted into spatial distance

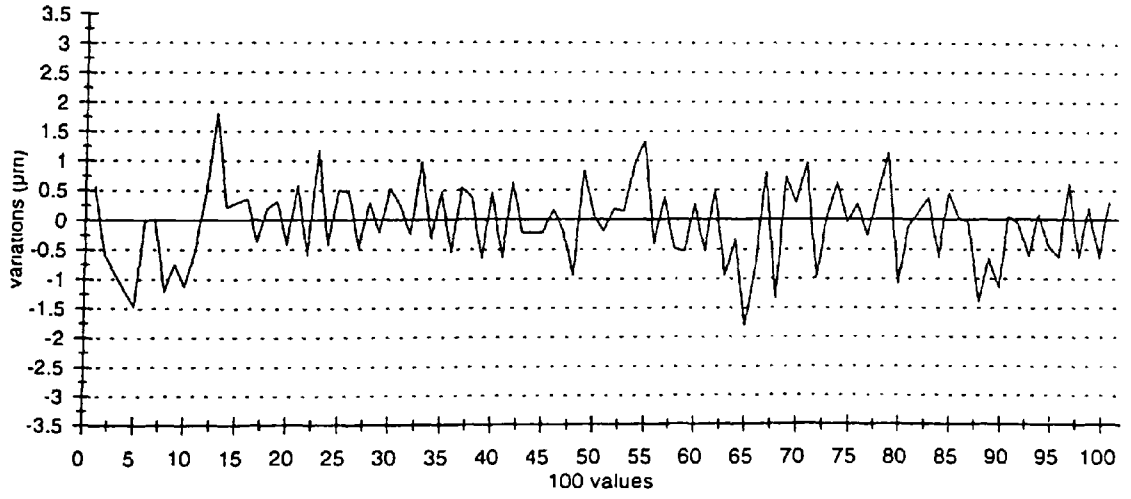

Figure 17: The separated high frequency signal from figure (16) taken to indicate surface wheel condition

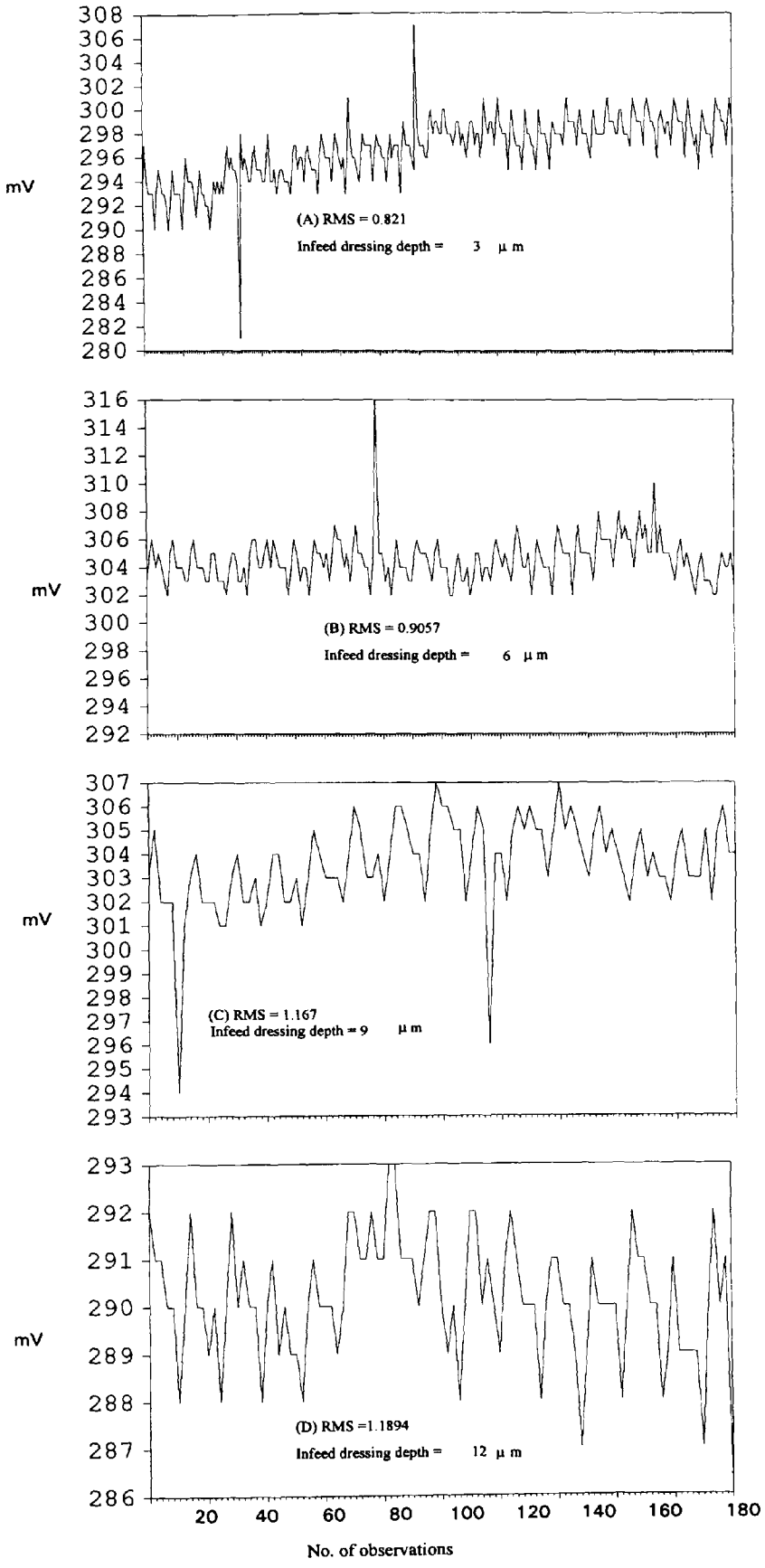

Figure 18: Variation of RMS values with changes of dressing depths (3 - 12 μm)

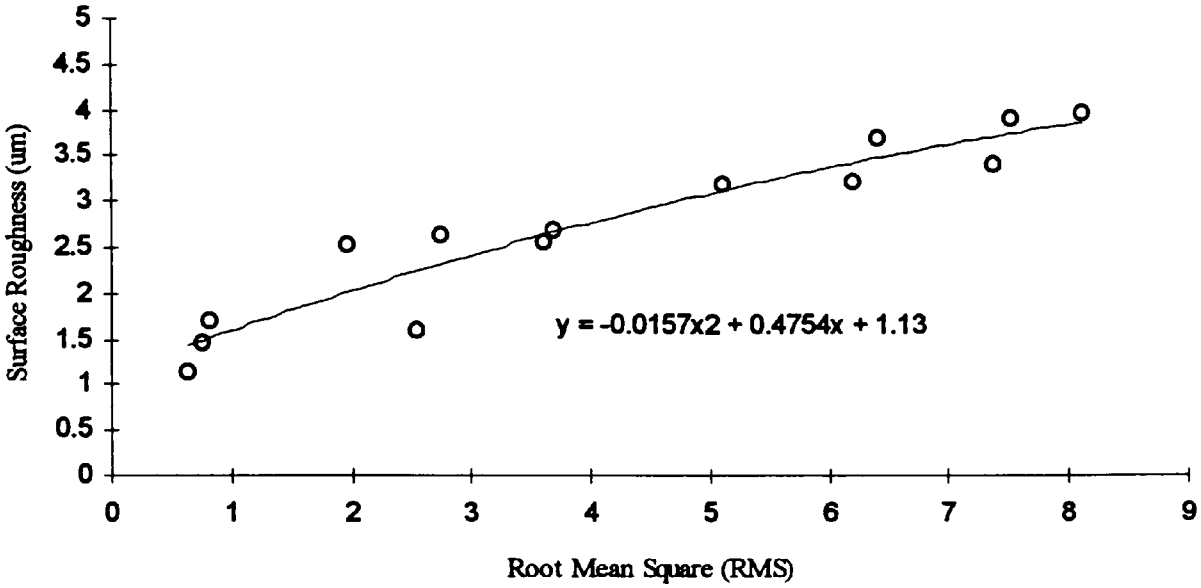

Figure 19: Surface roughness compared with root mean square of the high frequency content of the flapper nozzle raw signal at different dressing conditions and different wheels grit size.

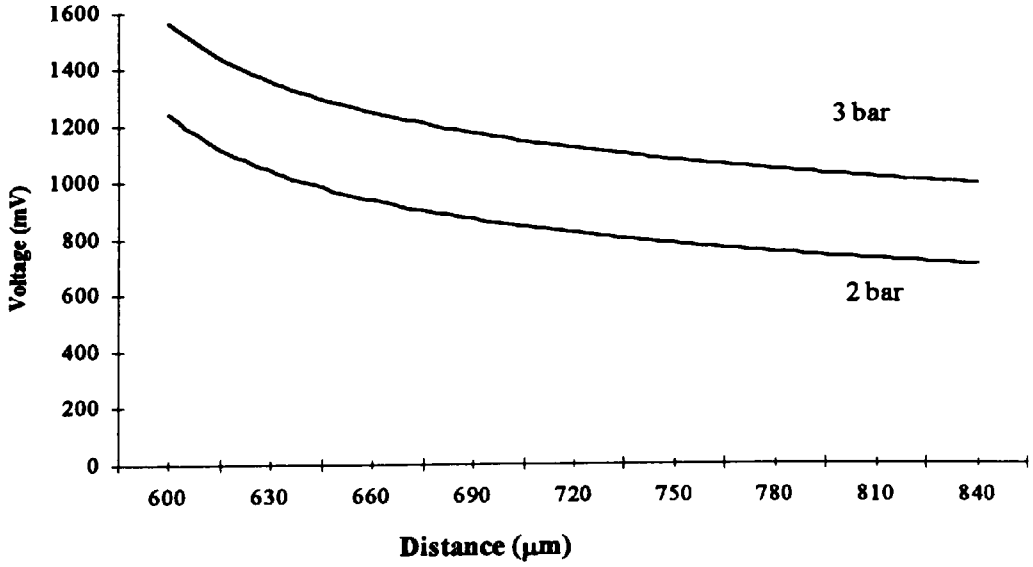

Figure 20: The variation response of the transducer at different distance from the wheel surface at different air pressure.

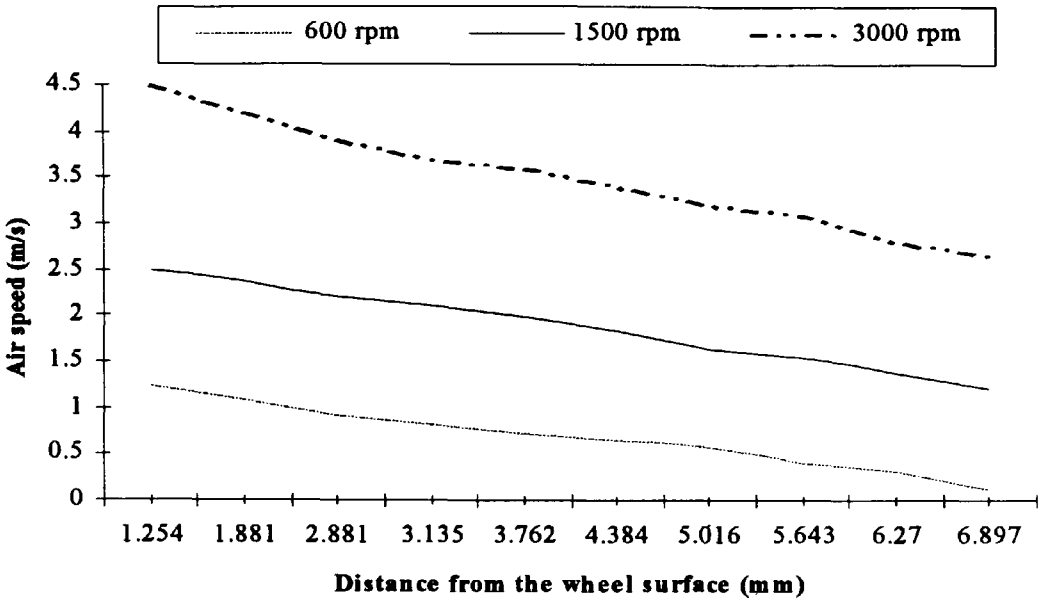

Figure 21: Variation of air speed with distance from the wheel surface at different wheel speed for low porosity grinding wheel.

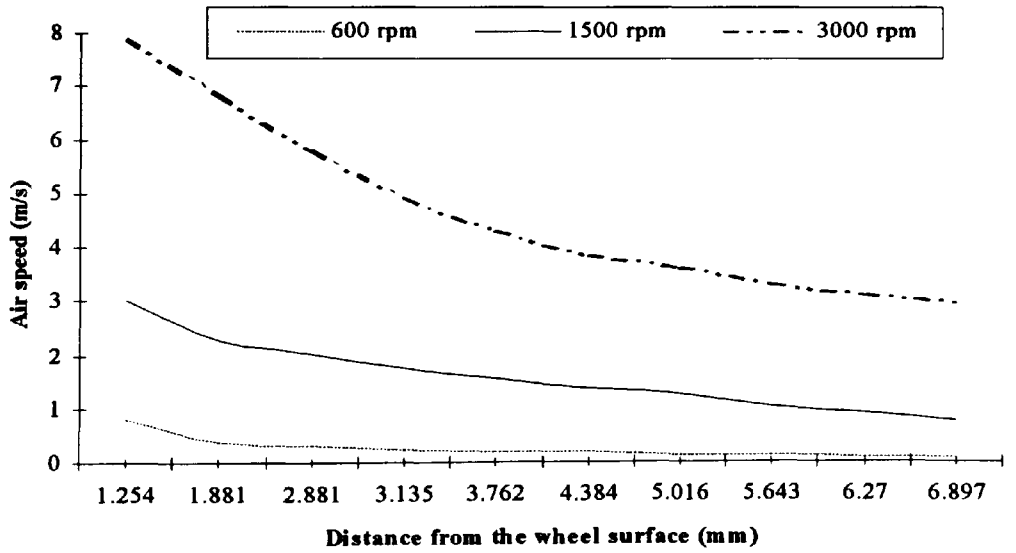

Figure 22: Variation of air speed with distance from the wheel surface at different wheel speed for high porosity grinding wheel.

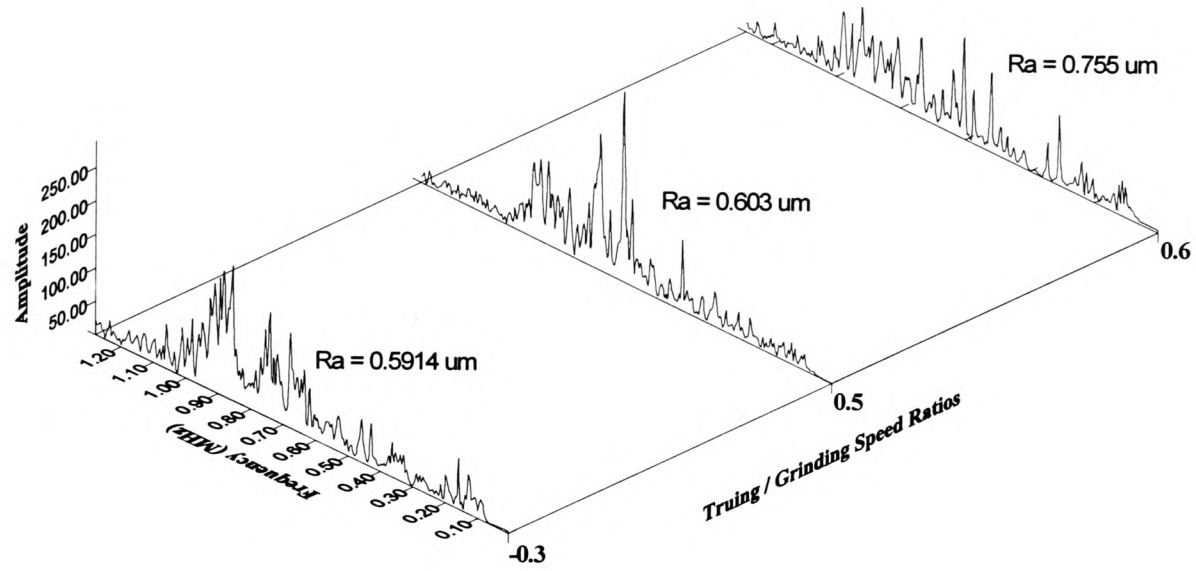

Figure 23: AE spectral amplitude and frequency for different grinding/truing wheel speed ratios for cast iron diamond wheel with D46 grit size.

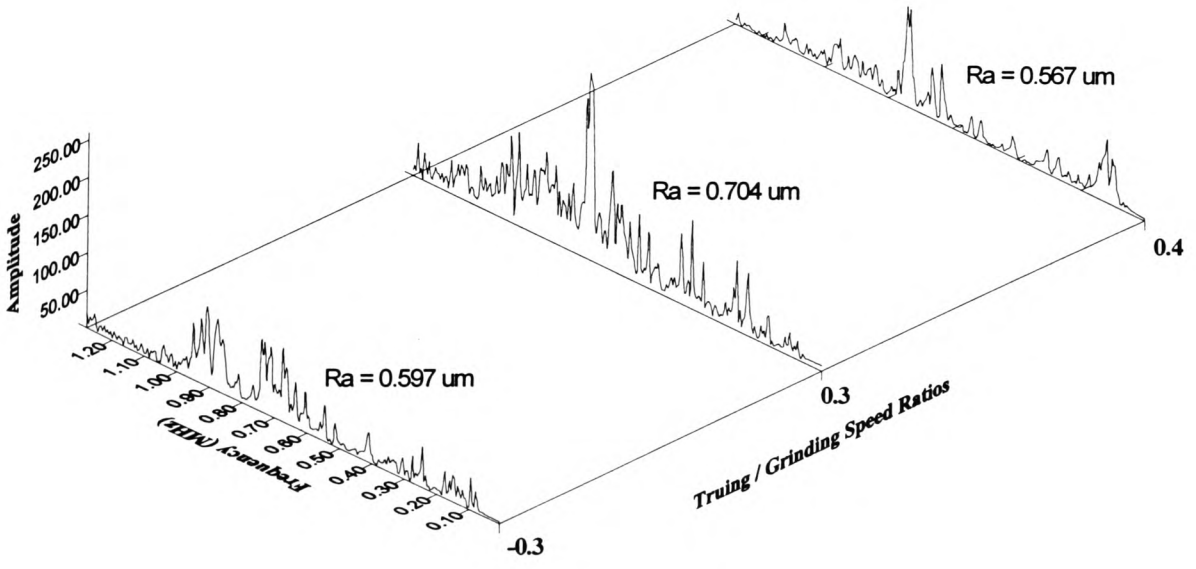

Figure 24: AE spectral amplitude and frequency for different grinding/truing wheel speed ratios for vitrified diamond wheel with D46 grit size.

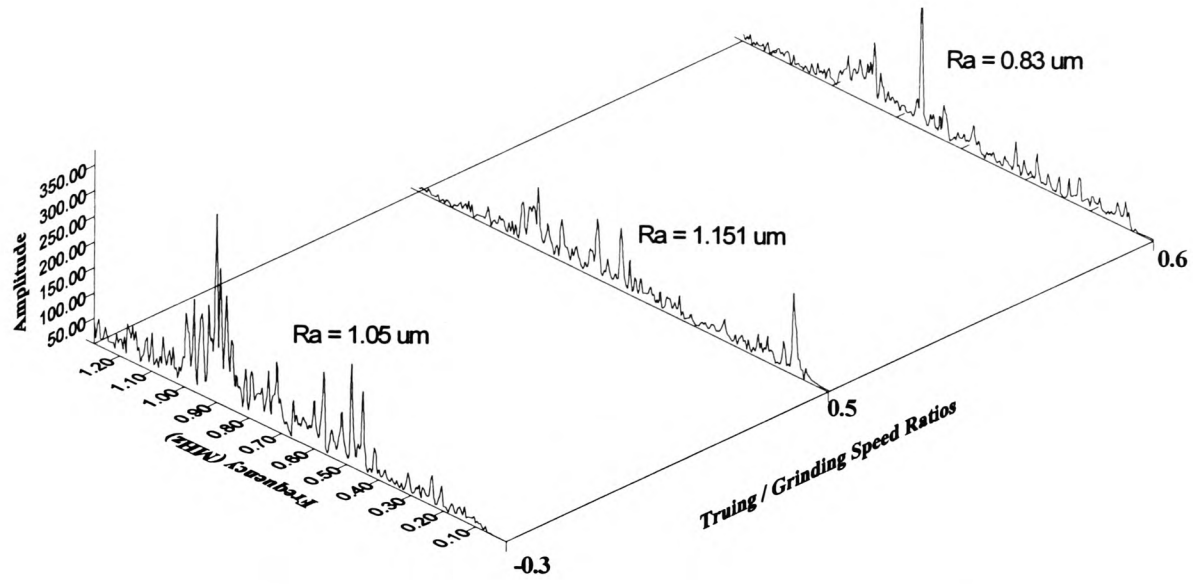

Figure 25: AE spectral amplitude and frequency for different grinding/truing wheel speed ratios for resin diamond wheel with D76 grit size.

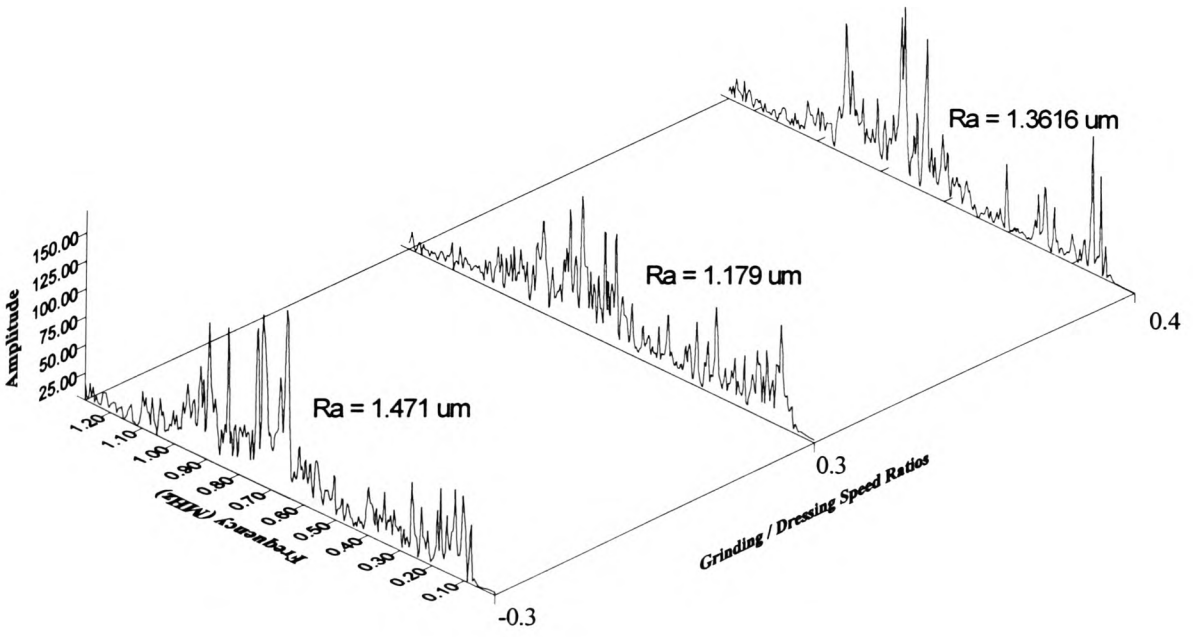

Figure 26: AE spectral amplitude and frequency for different grinding/truing wheel speed ratios for resin diamond wheel with D126 grit size.

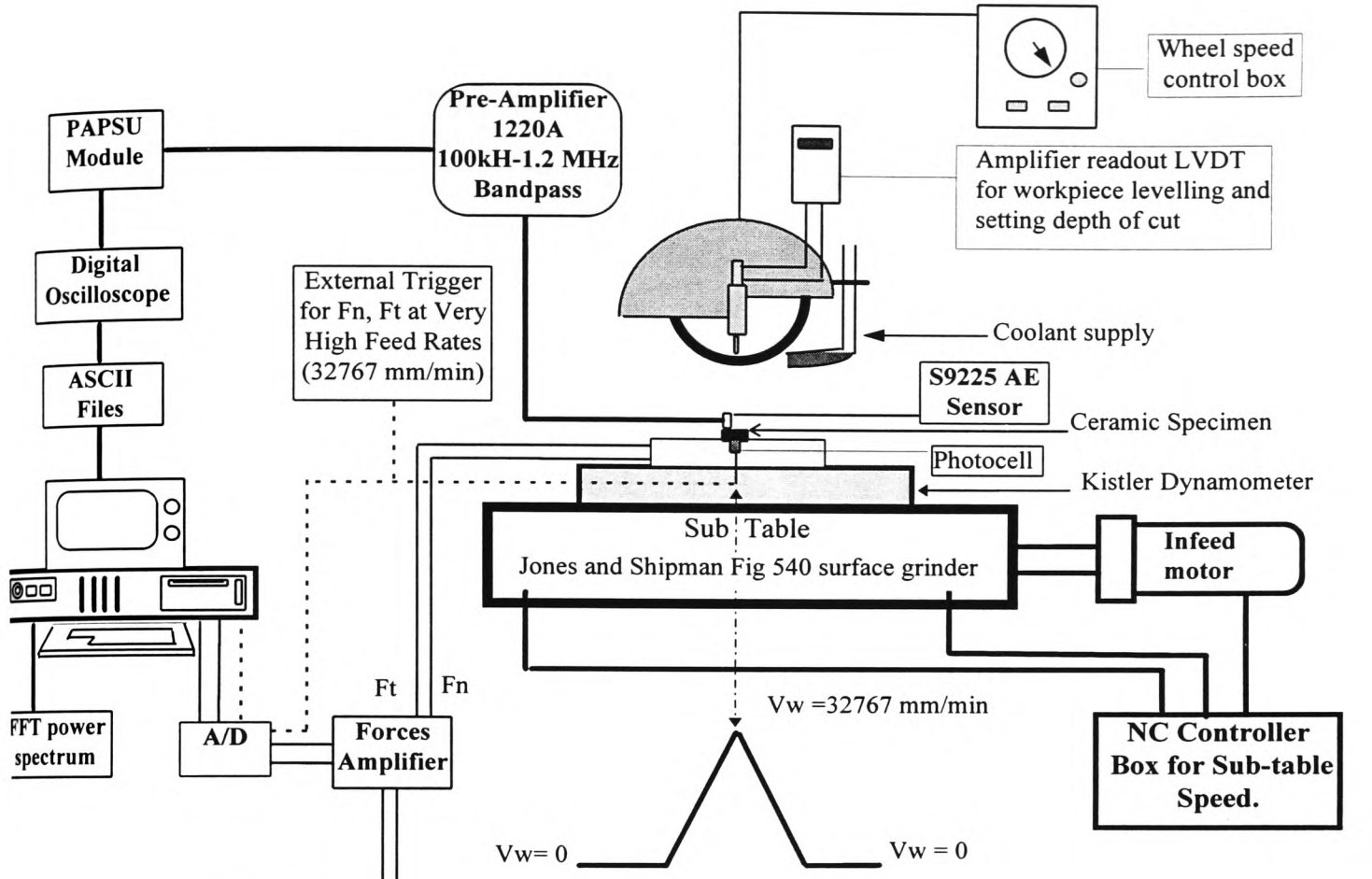

Figure 27: A schematic of grinding machine and instrumentation used

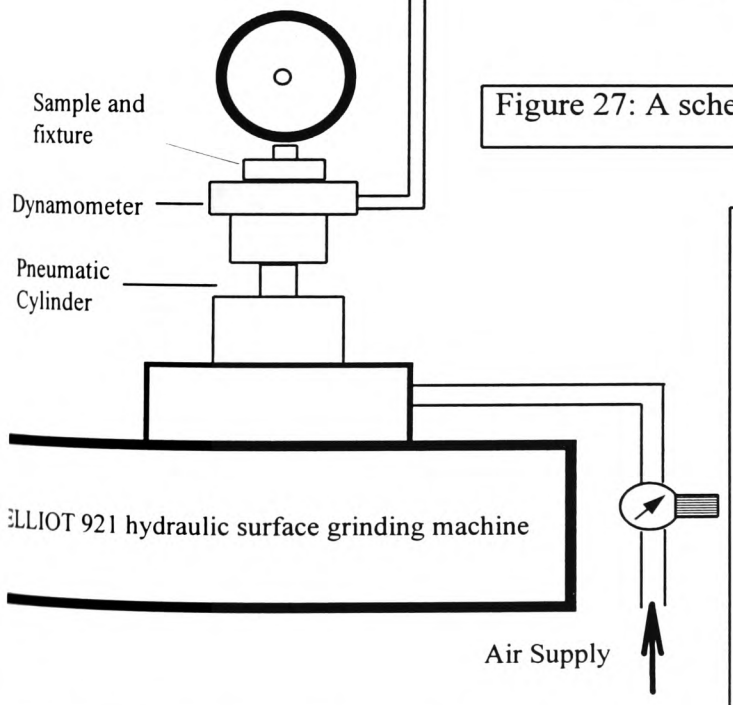

Figure 28: Experimental set-up for wheel/ workpiece stiffness

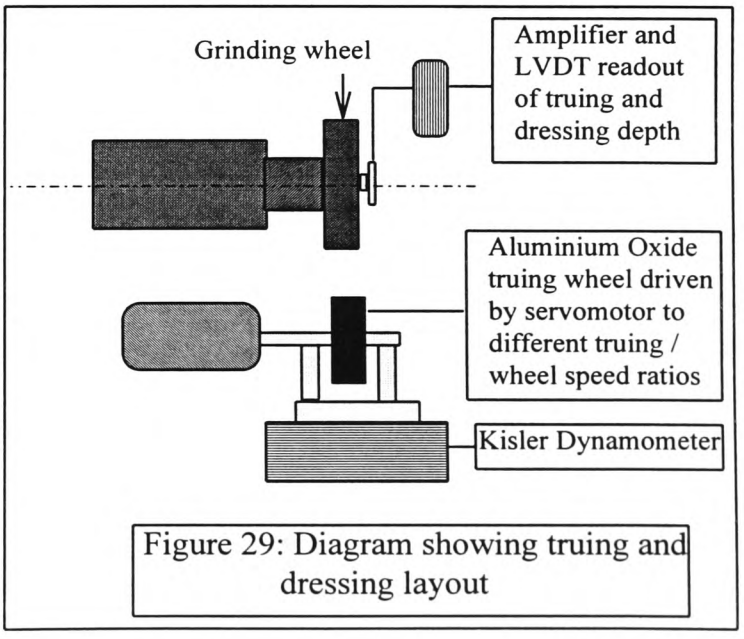

Figure 29: Diagram showing truing and dressing layout

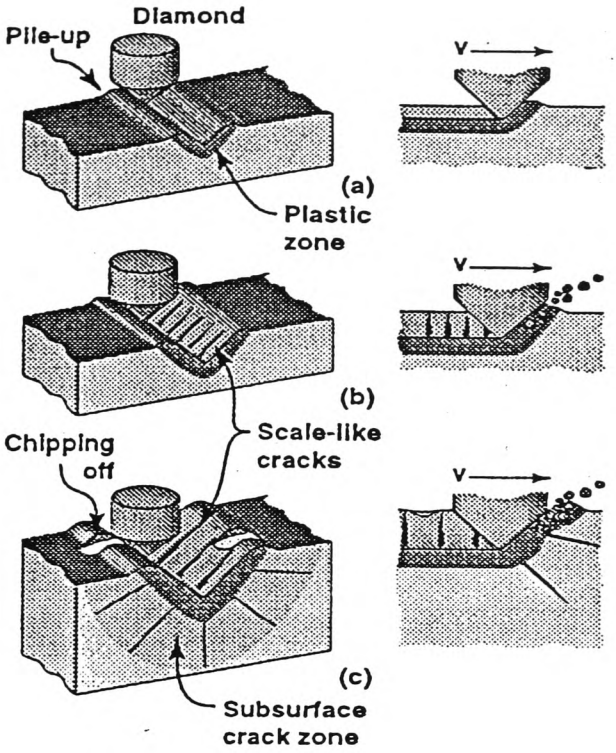

Figure 30: Illustration of Scratching Mechanisms using single diamond [28]

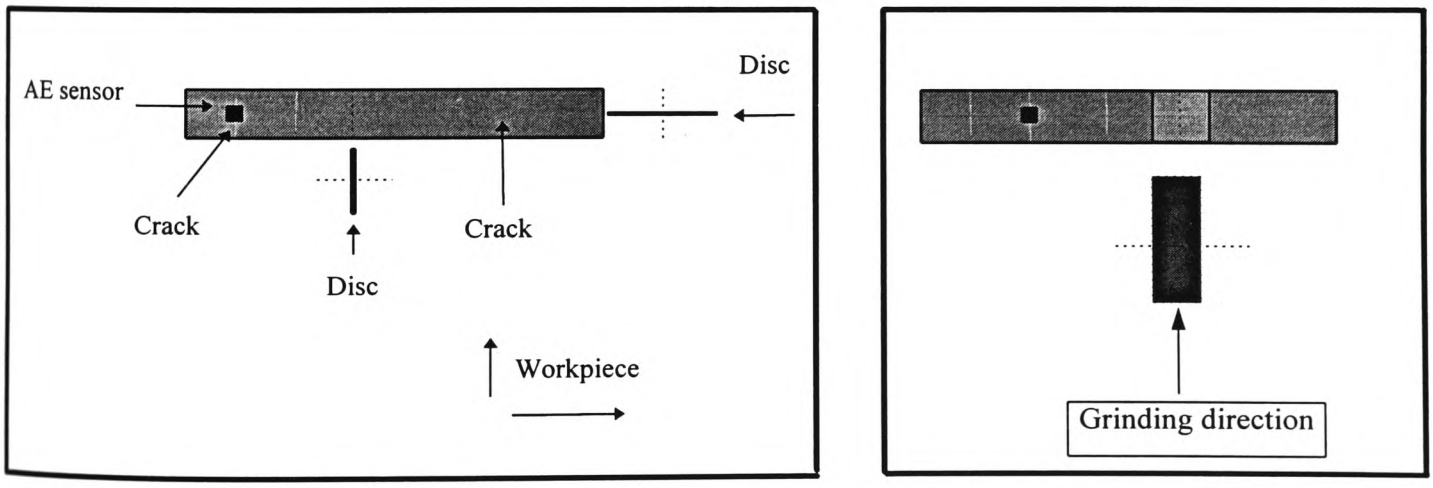

I II

Figure 31: Illustration shows the artificial cracks initiated by v-shaped disc on the ceramic surface specimens (I) and grinding on the cracks initiated on the surface of ceramic specimens (II).

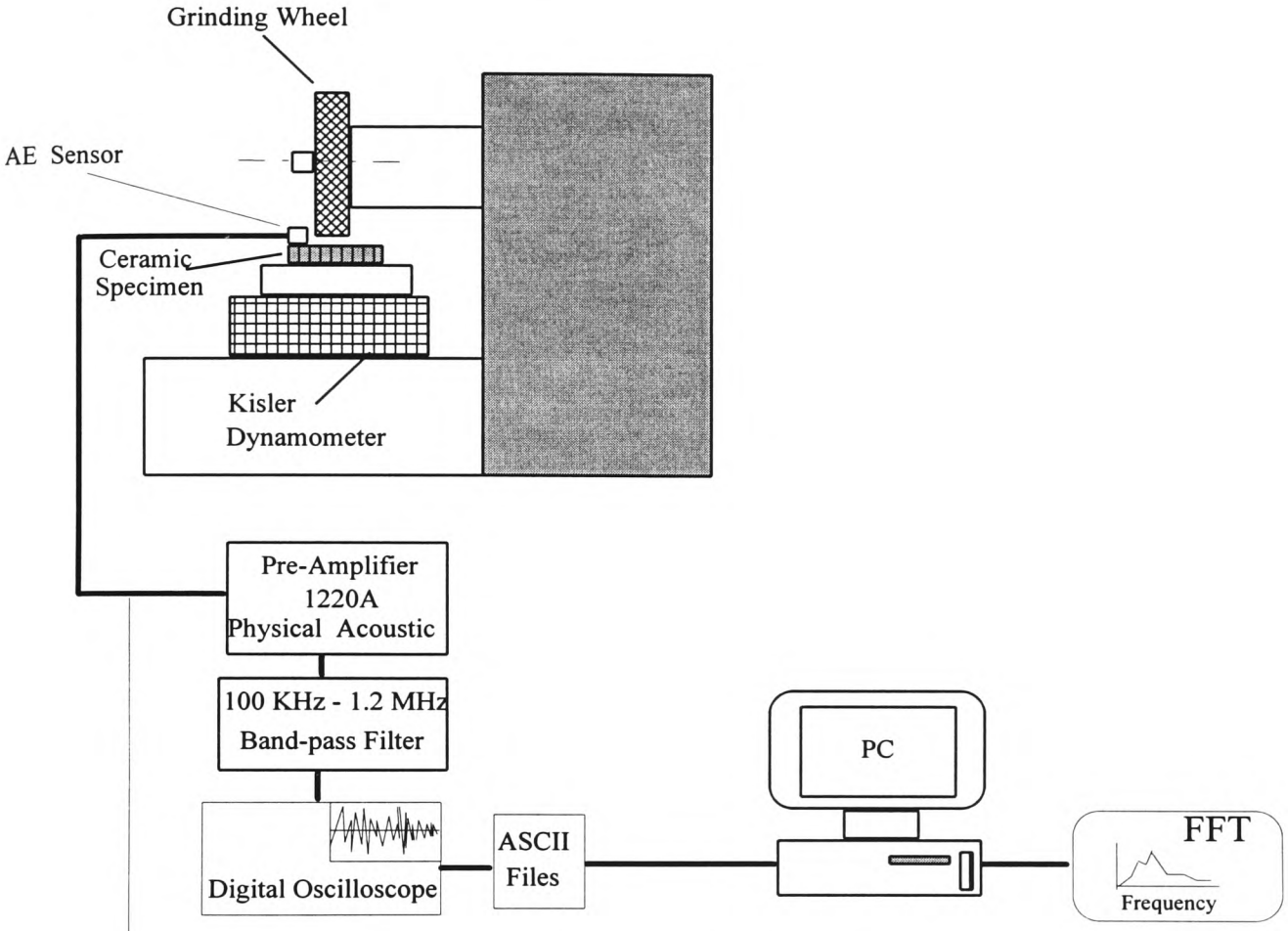

Figure 32: Acoustic emission measurement chain used to study the material remova mode and crack initiation and propagation during grinding of ceramic.

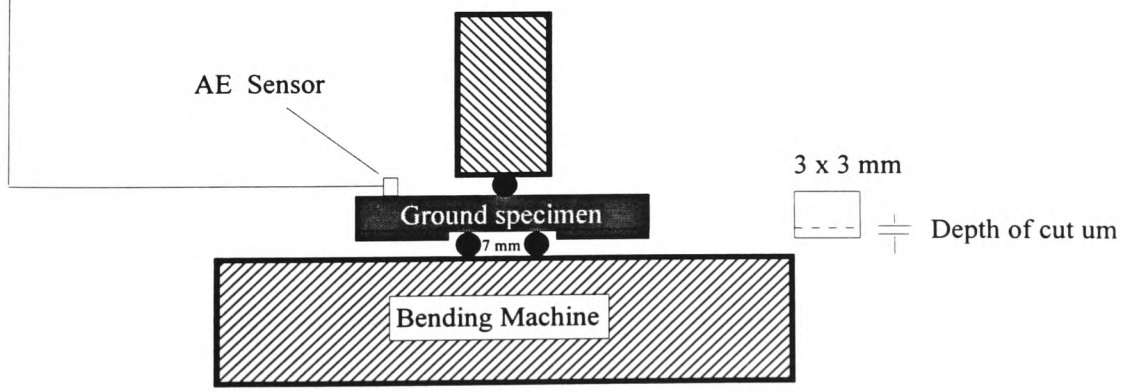

Figure 33: Three point bending test setting for ground ceramic specimens

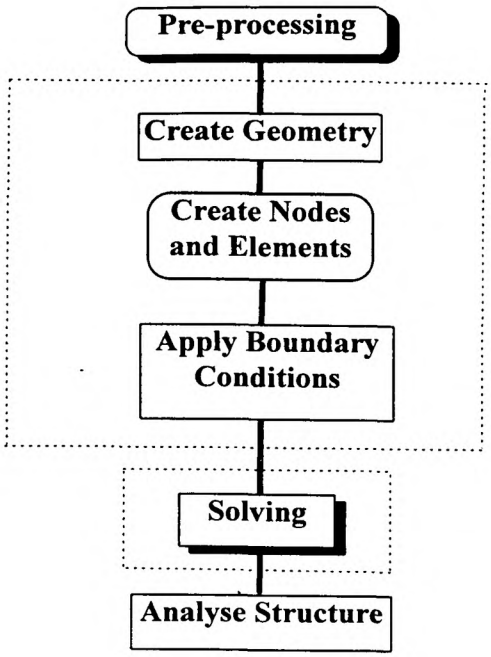

Figure 34: The three stages of finite element model FE.

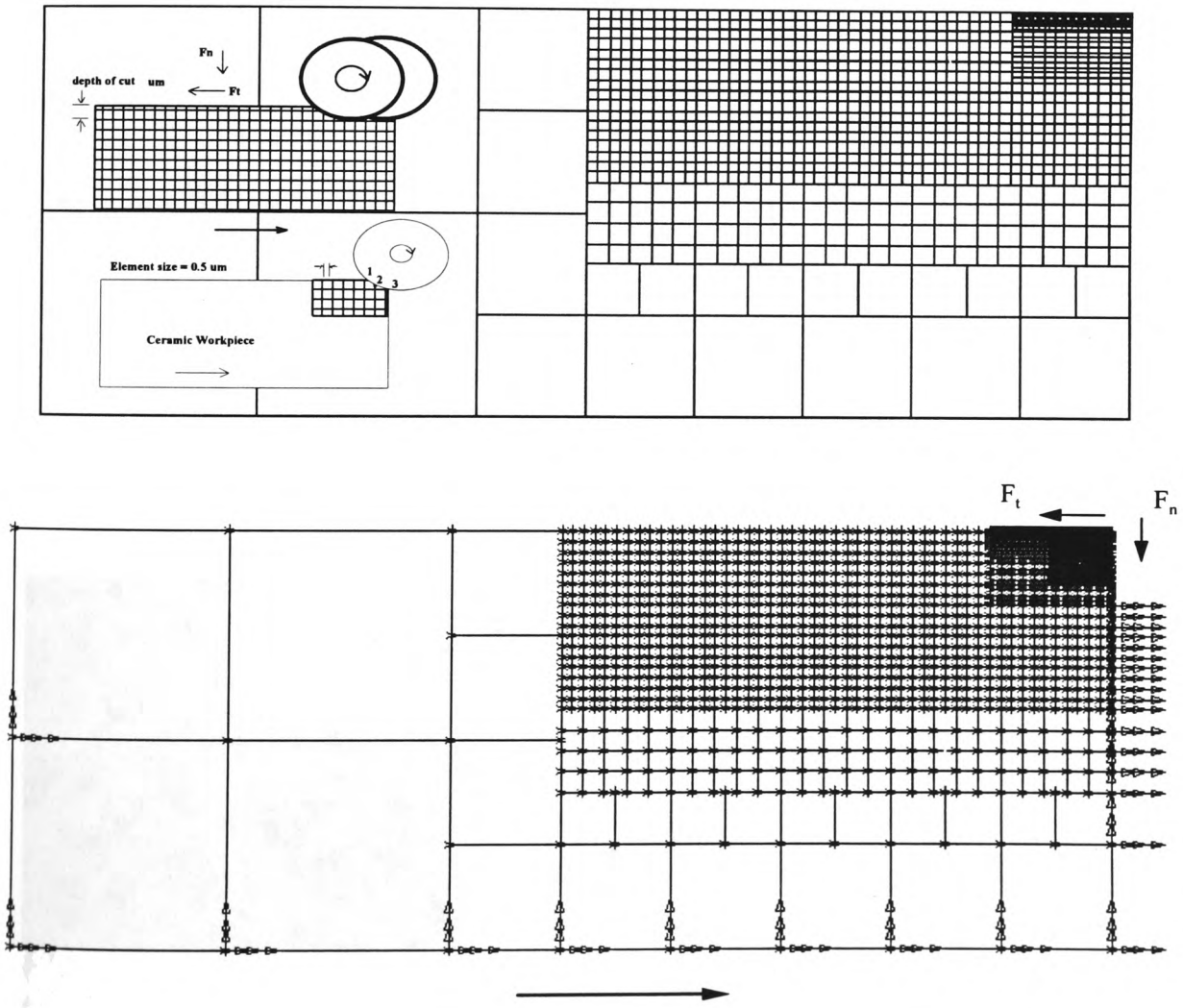

Figure 35: The physical model of grinding of ceramic.

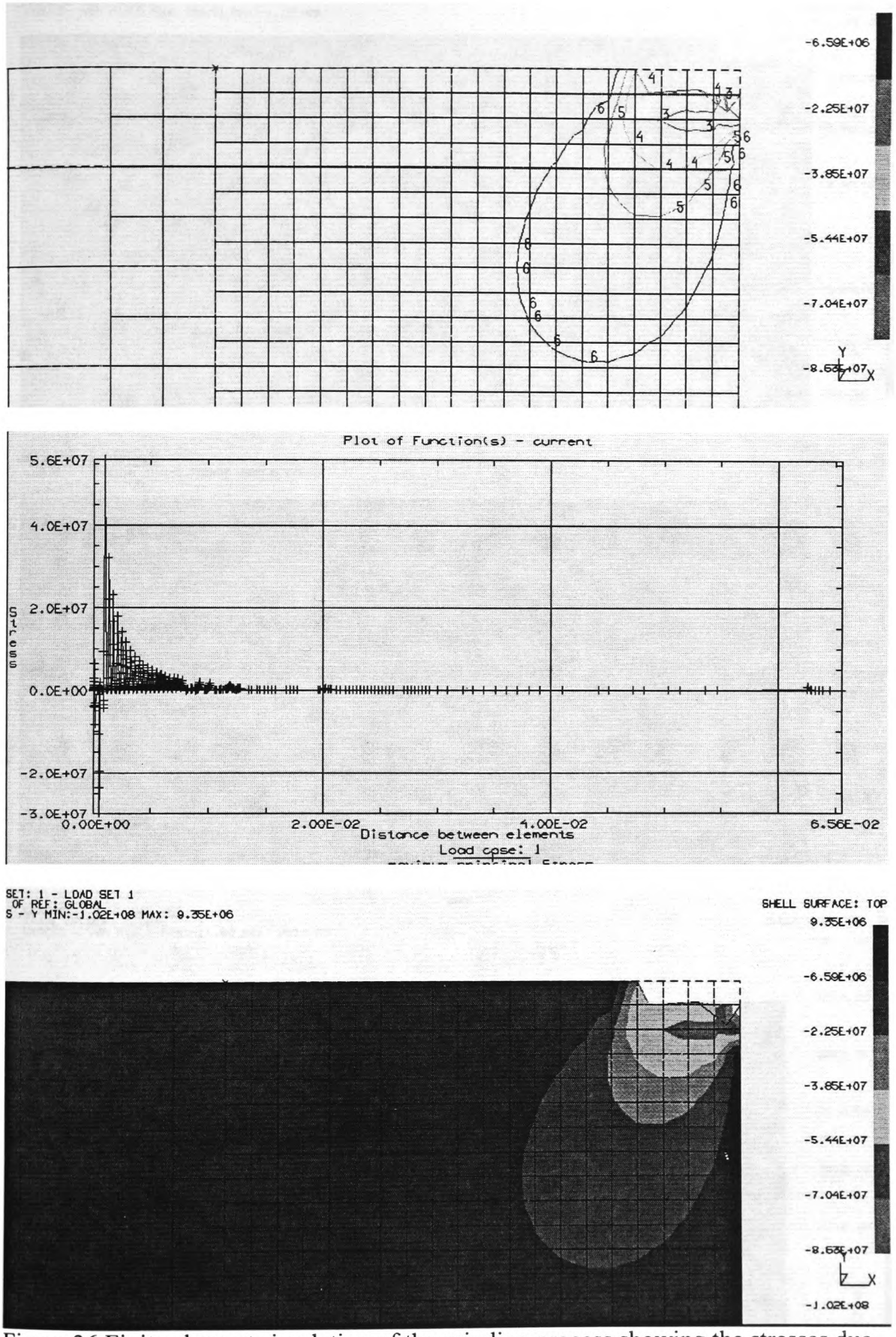

Figure 36 Finite element simulation of the grinding process showing the stresses due to the material removal.

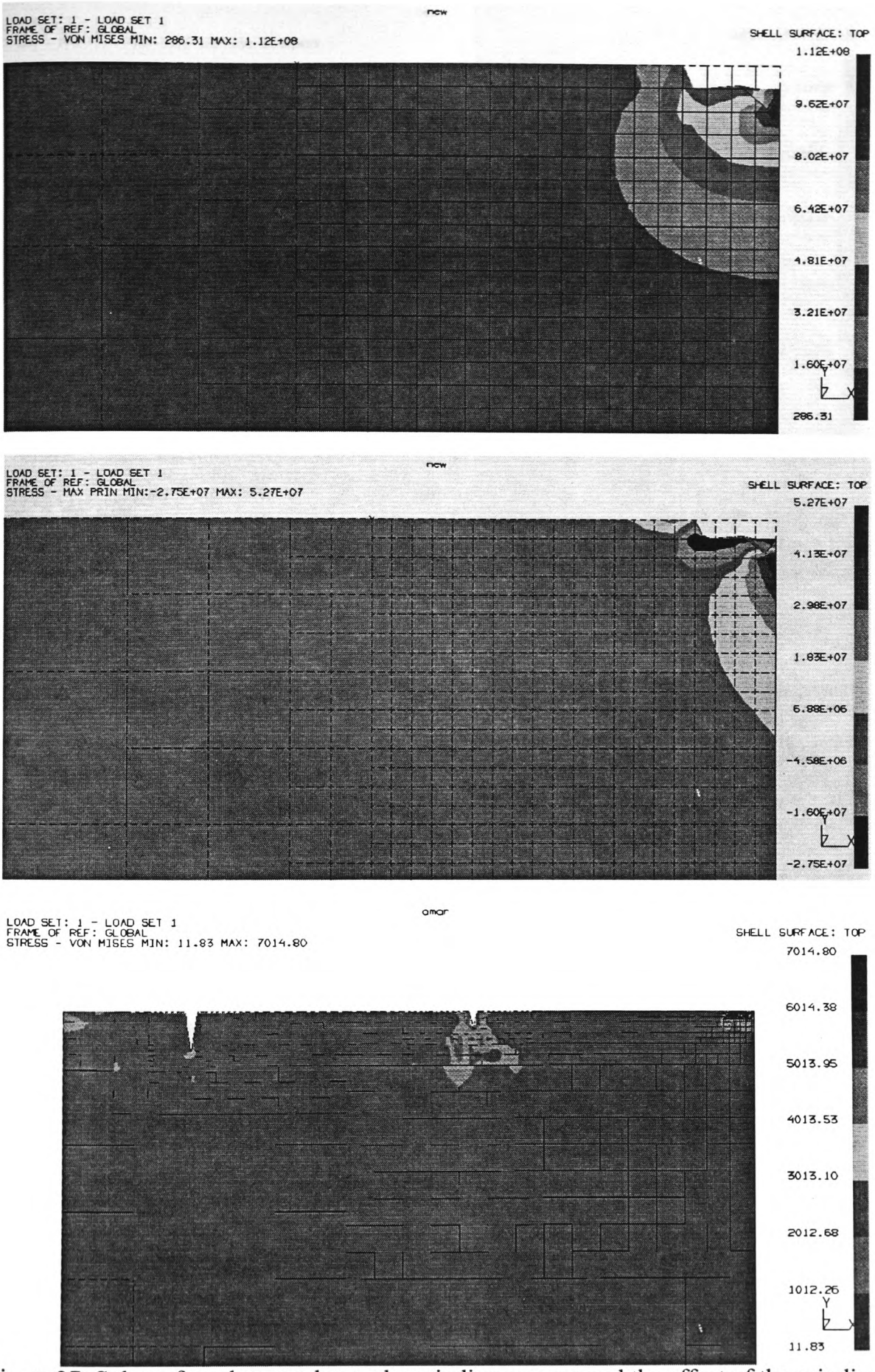

Figure 37: Sub-surface damage due to the grinding process and the effect of the grinding process on the artificial cracks on the ceramic surface (below).

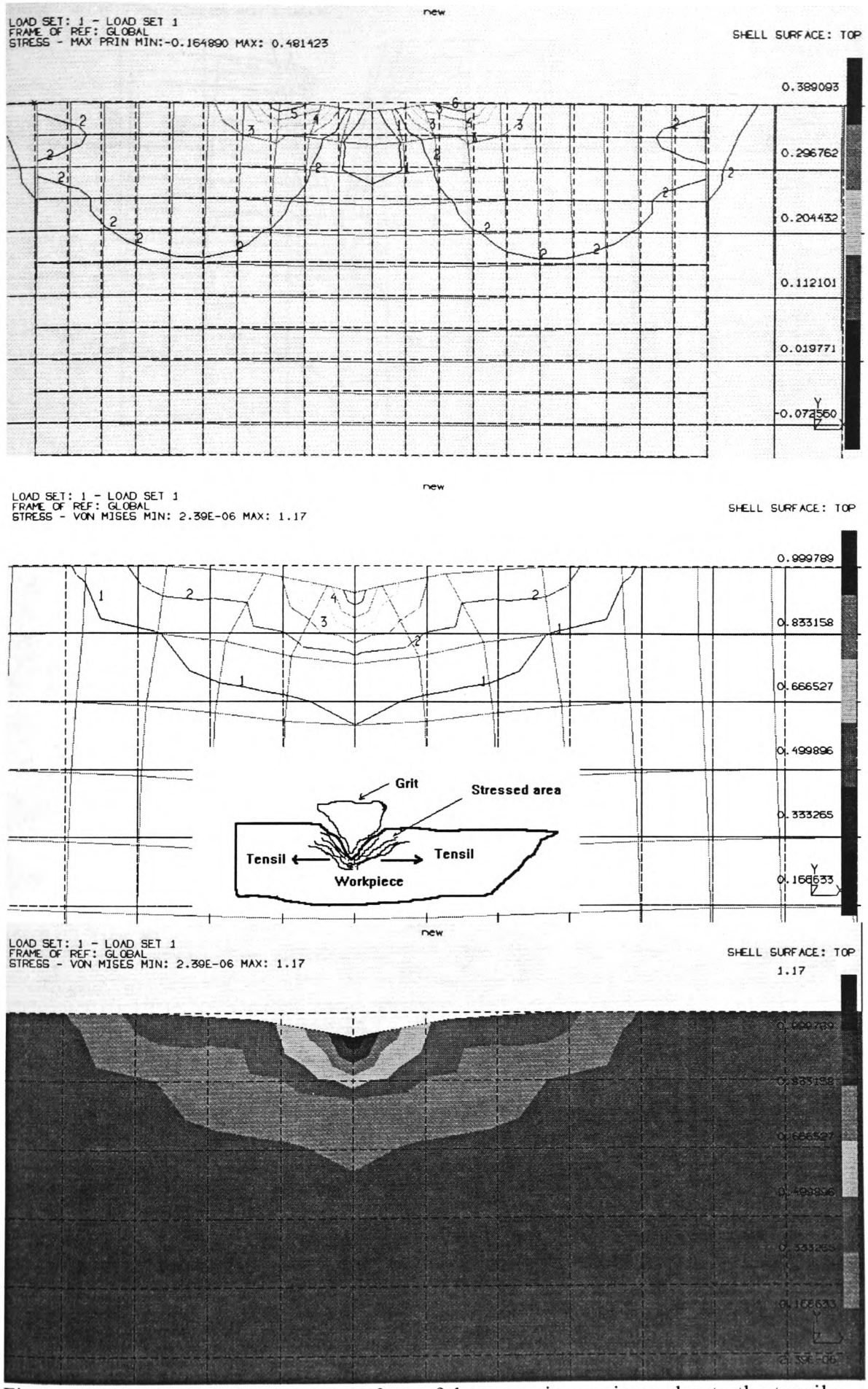

Figure 38: Crack initiation on the surface of the ceramic specimen due to the tensile grit action on the surface.

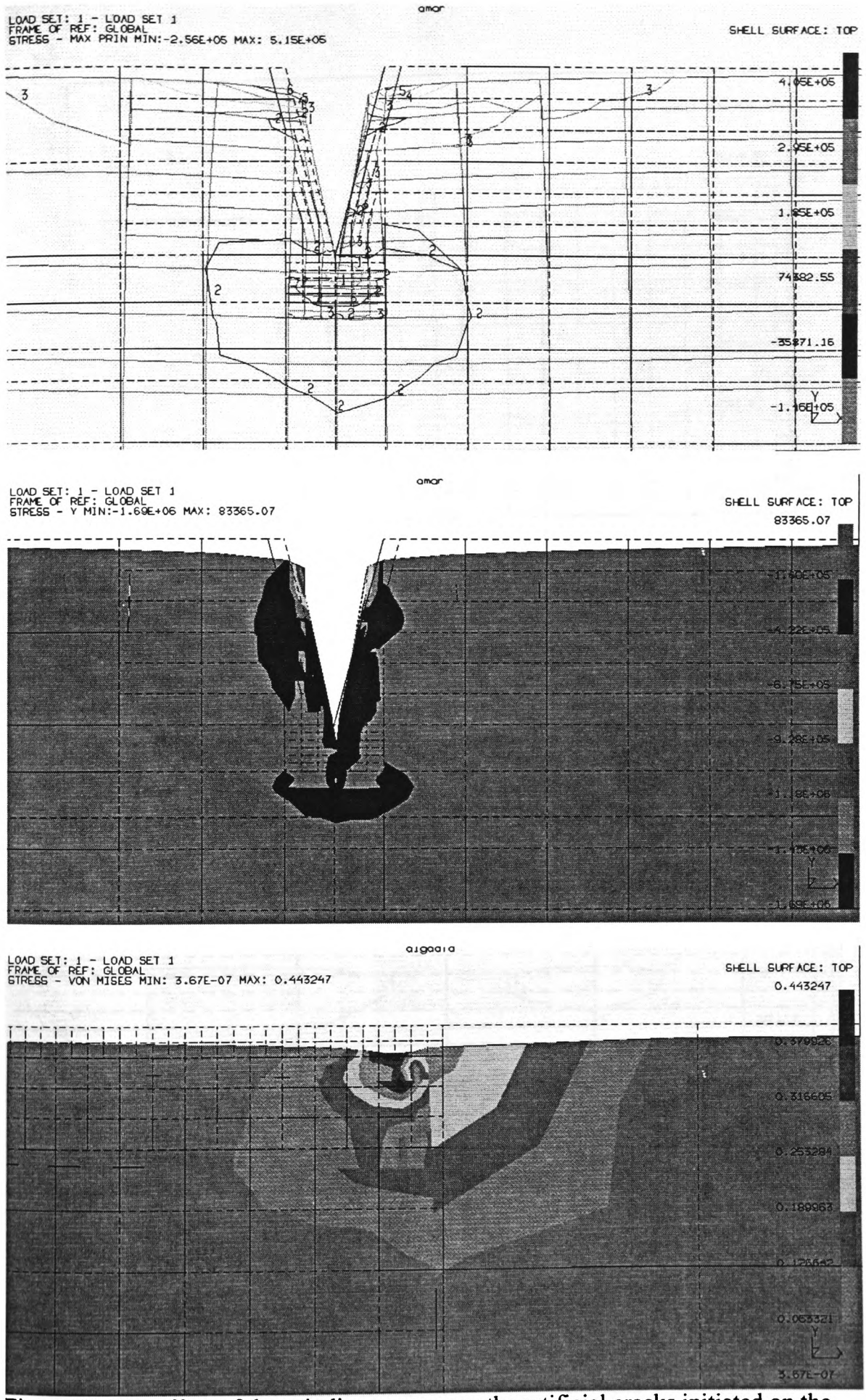

Figure 39: The effect of the grinding process on the artificial cracks initiated on the ceramic surface and their propagation in the sub-surface.

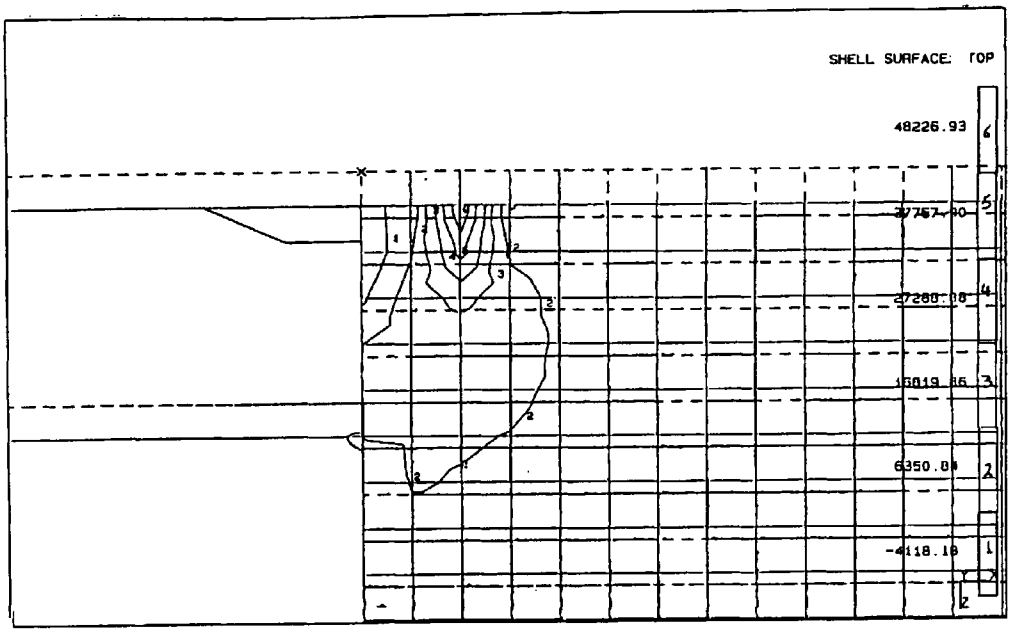

Figure 40: The effect of tensile grinding force on crack initiation and propagation at 40 mN per grit.

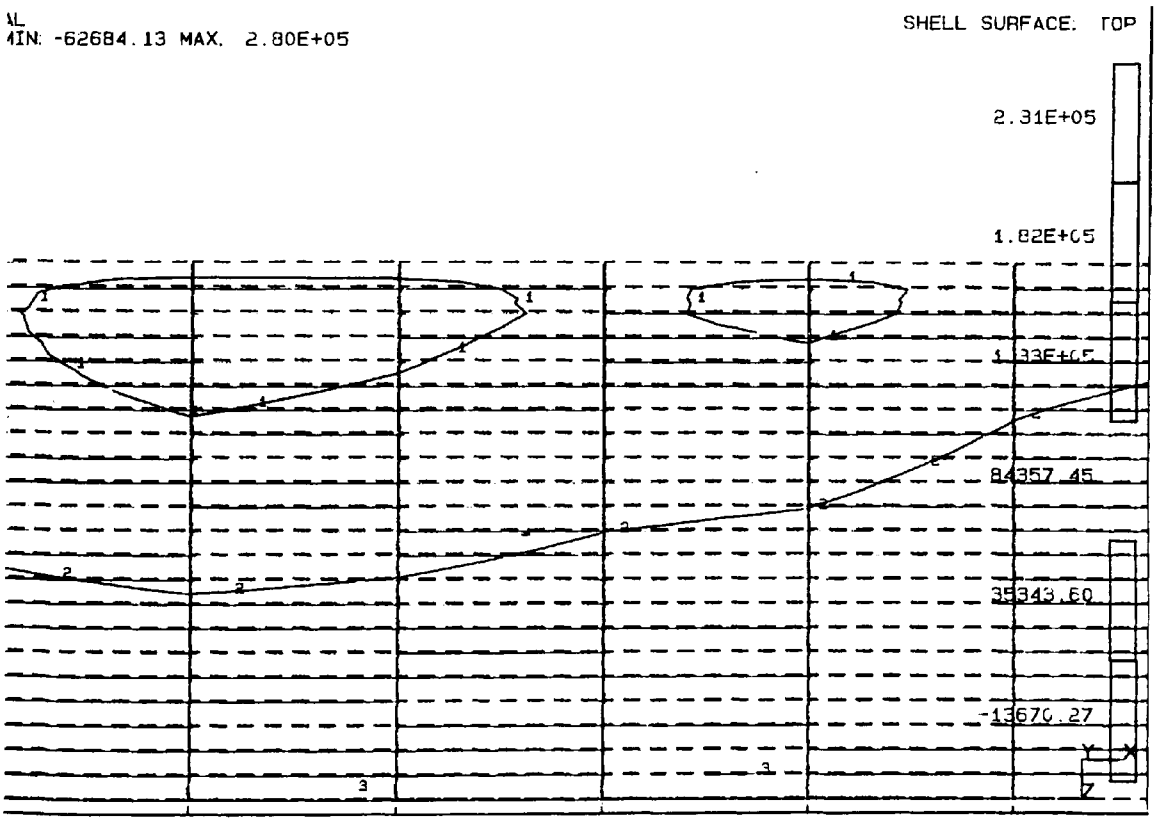

Figure 41: Sub surface crack under the compressive layer of the ground surface.

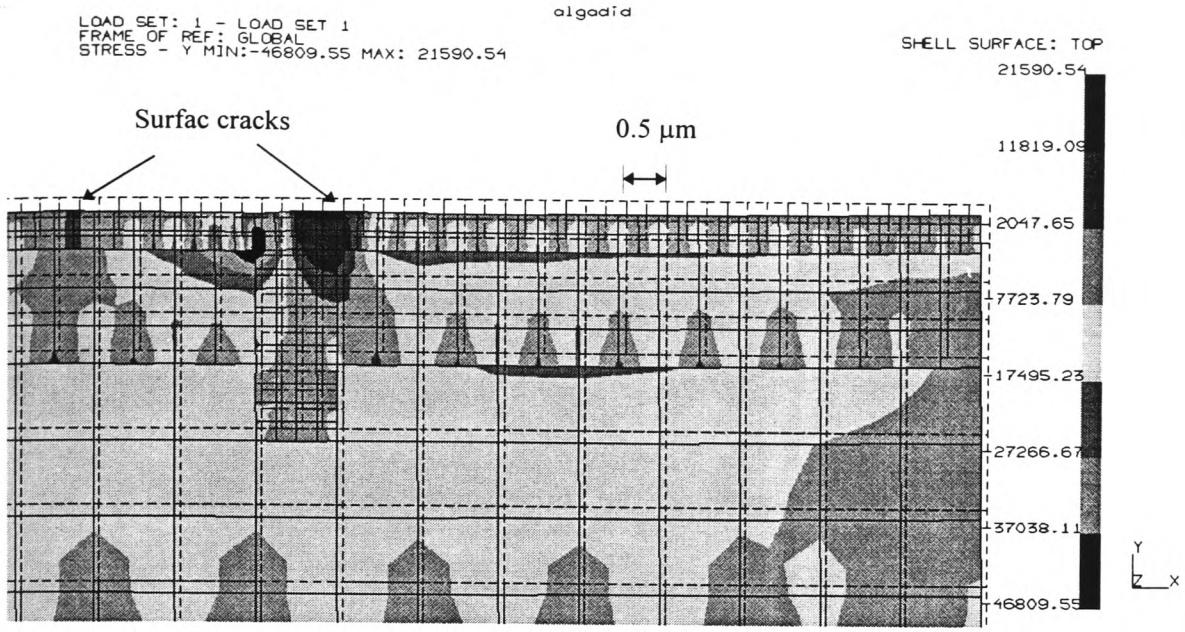

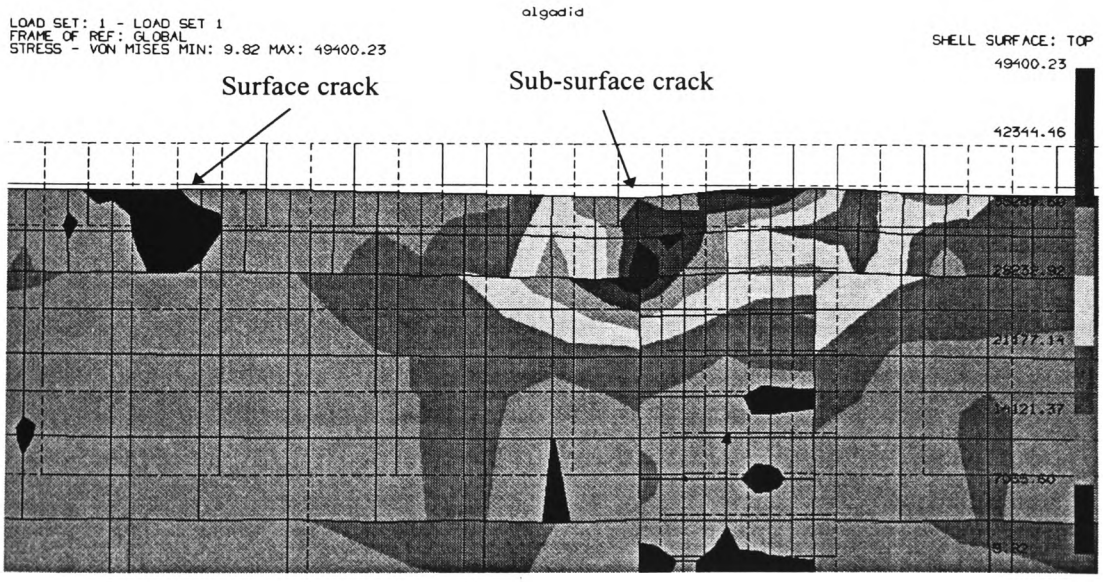

Figure 42: Surface and sub-surface cracks initiated due the grinding process.

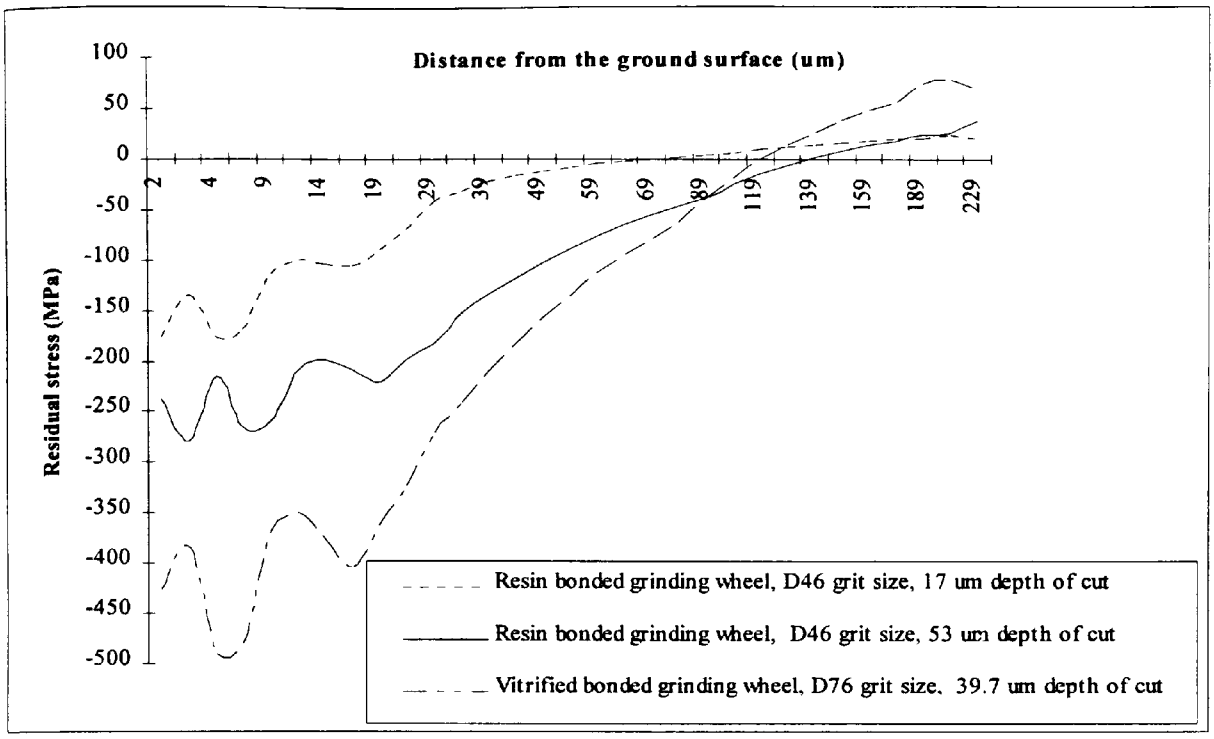

Figure 43: Residual stresses and their depth from the ground surface for D46 resin and D76 vitrified diamond grinding wheels at different depth of cut

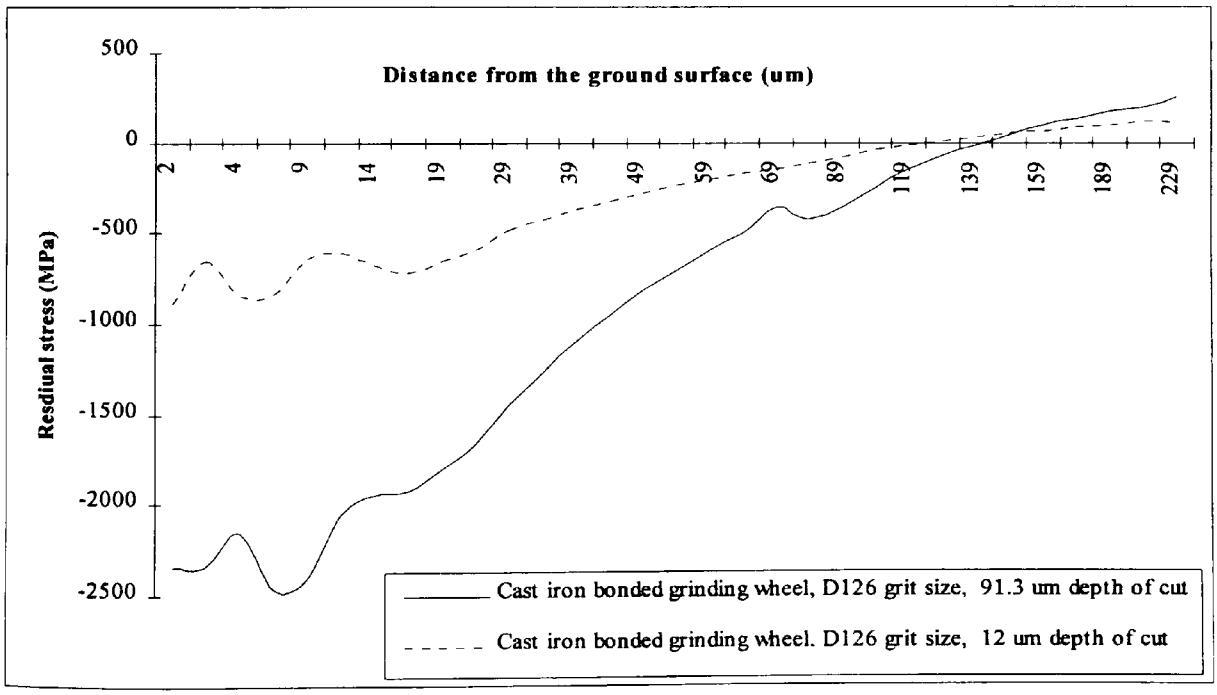

Figure 44: Residual stresses and their depth from the ground surface for D126 cast iron diamond grinding wheels at different depth of cut

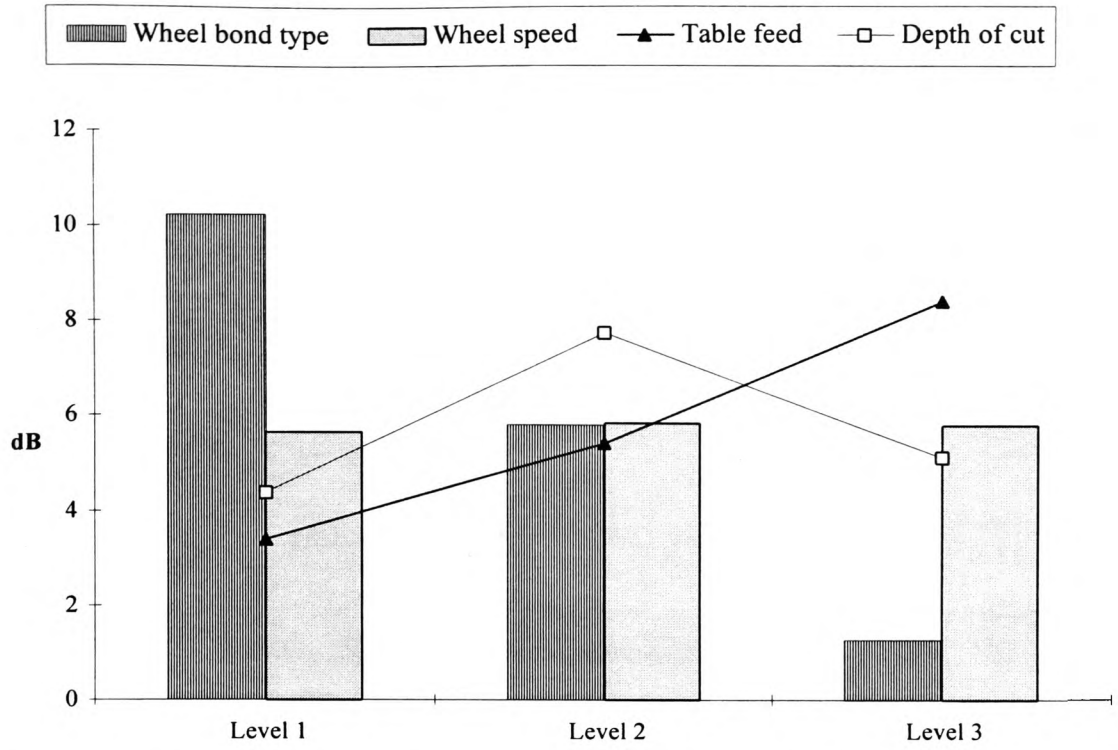

Figure 45: Response characteristics of control factors at varying levels on surface roughness

Level	Wheel Type	Wheel Speed m/s	Feed Rate mm/s	Depth of Cut μm
1	Metal	20	1	100
2	vitrified	30	3.5	250
3	Resin	40	6	500

Wheel / Machine parameters levels used in L_9 experimental design.

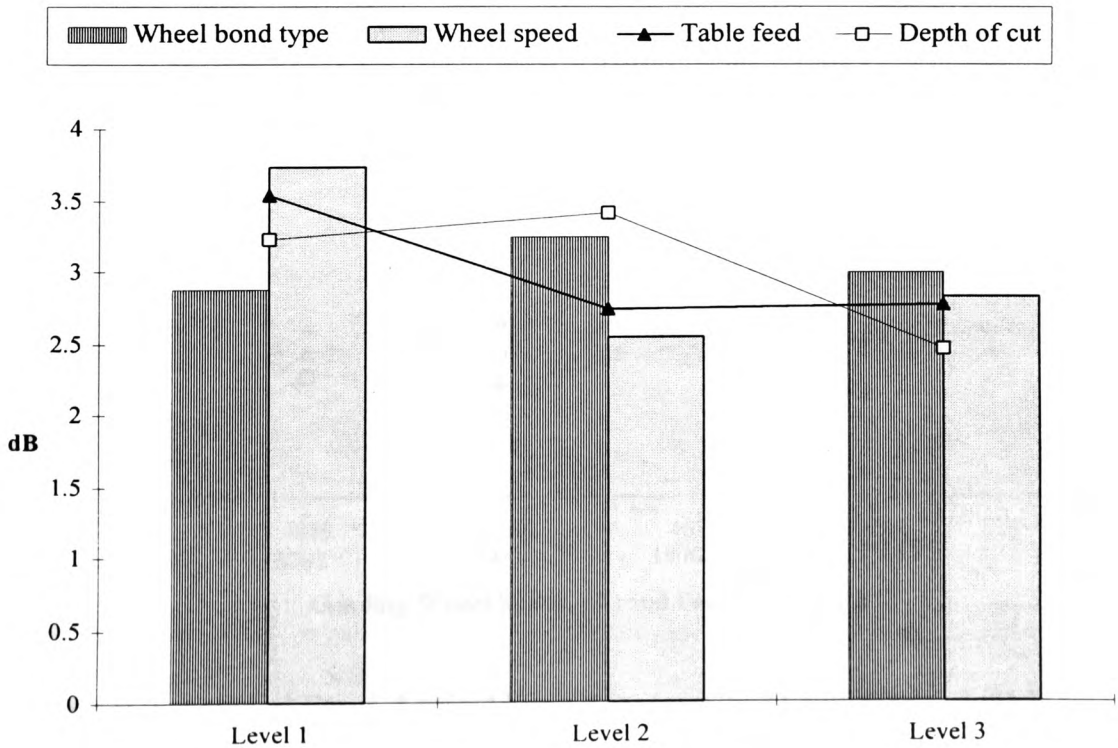

Figure 46: Response characteristics of control factors at varying levels on material strength properties

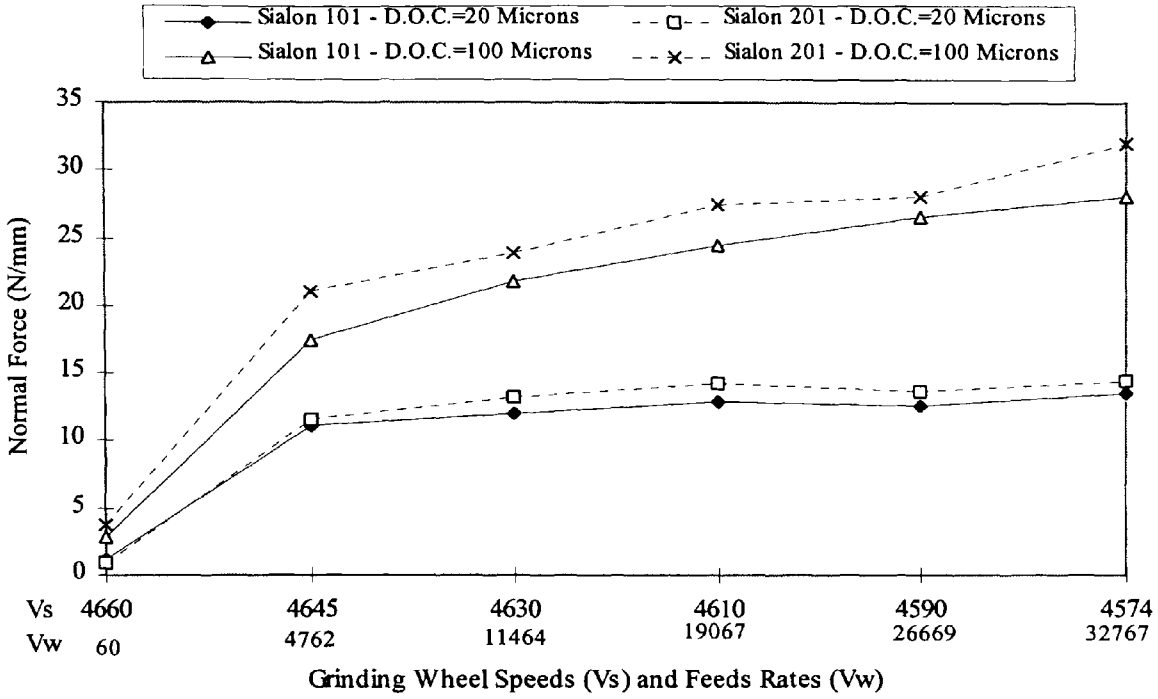

Figure 47: Normal Force Against Feed Rates (mm/min) and Wheel Speed (rpm)

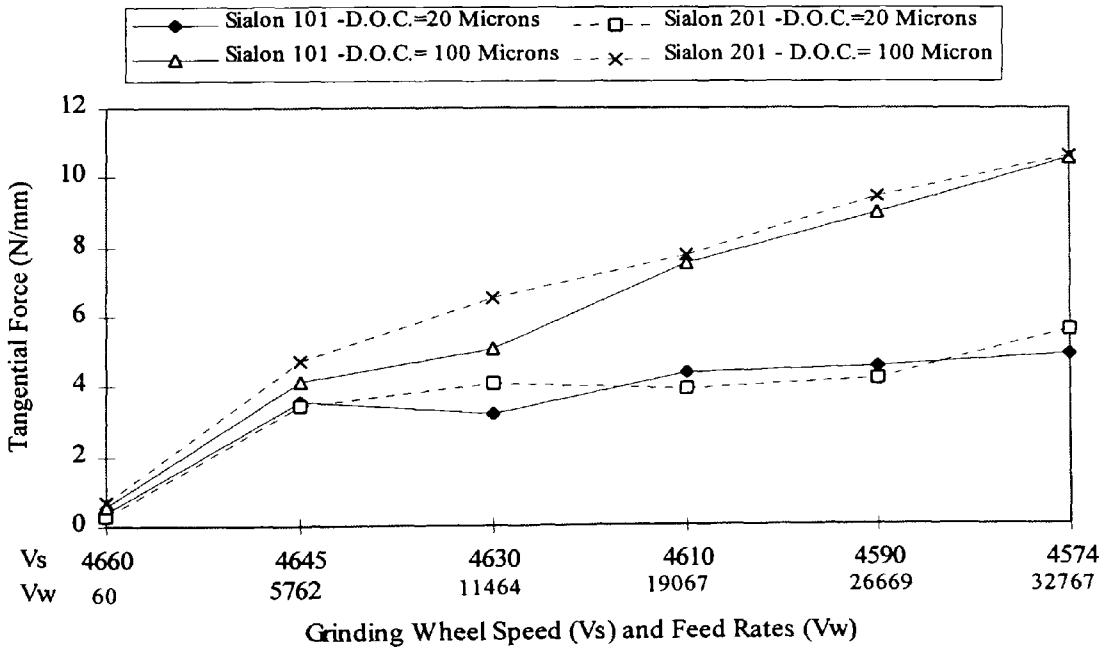

Figure 48: Tangential Force Against Feed Rate (mm/min) and Wheel Speed (rpm)

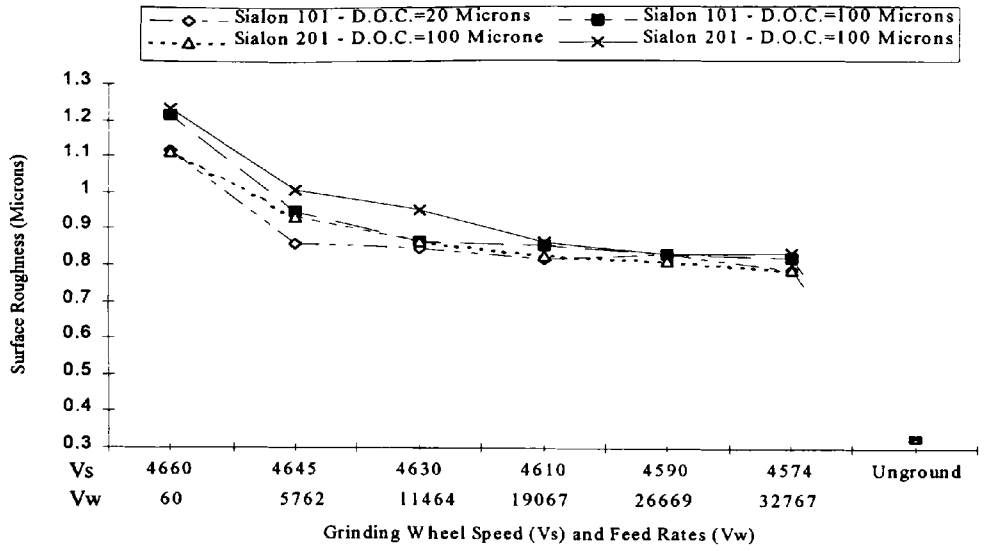

Figure 49: Surface Roughness Against Feed Rate (mm/min) and Wheel Speed (rpm)

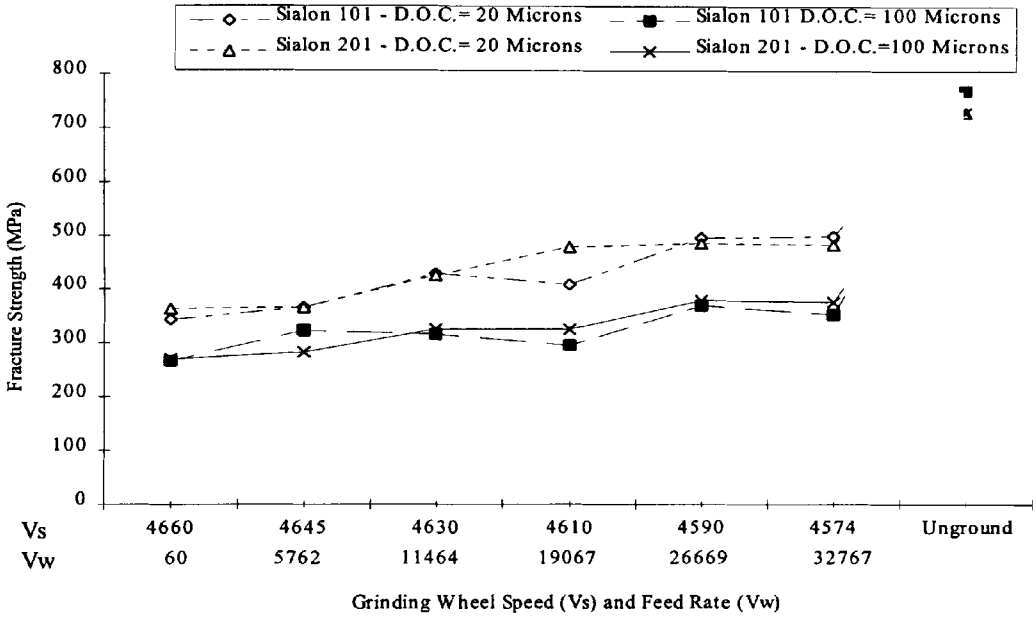

Figure 50: Fracture Strength Against Feed Rate (mm/min) and Wheel Speed (rpm)

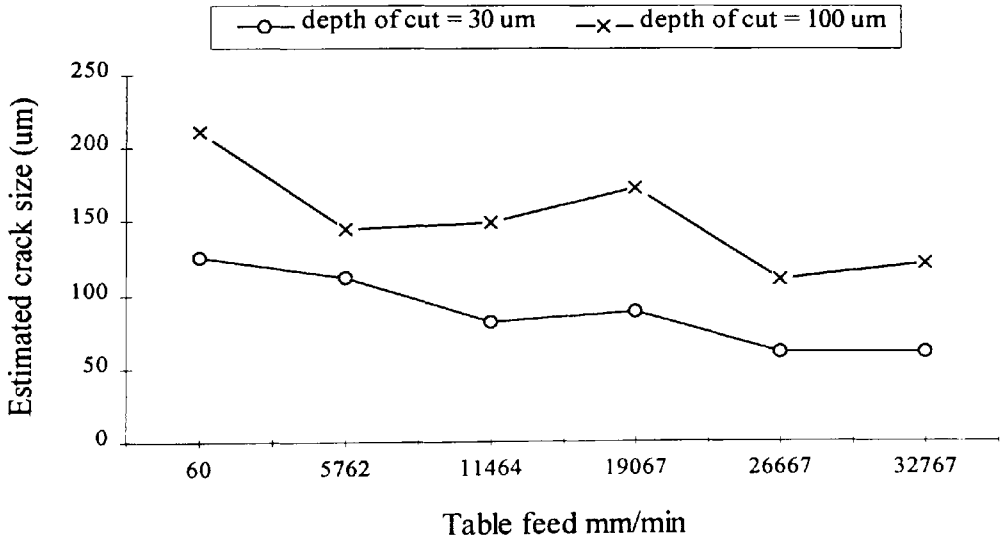

Figure 51: Estimated crack size against table feed at different depth of cut.

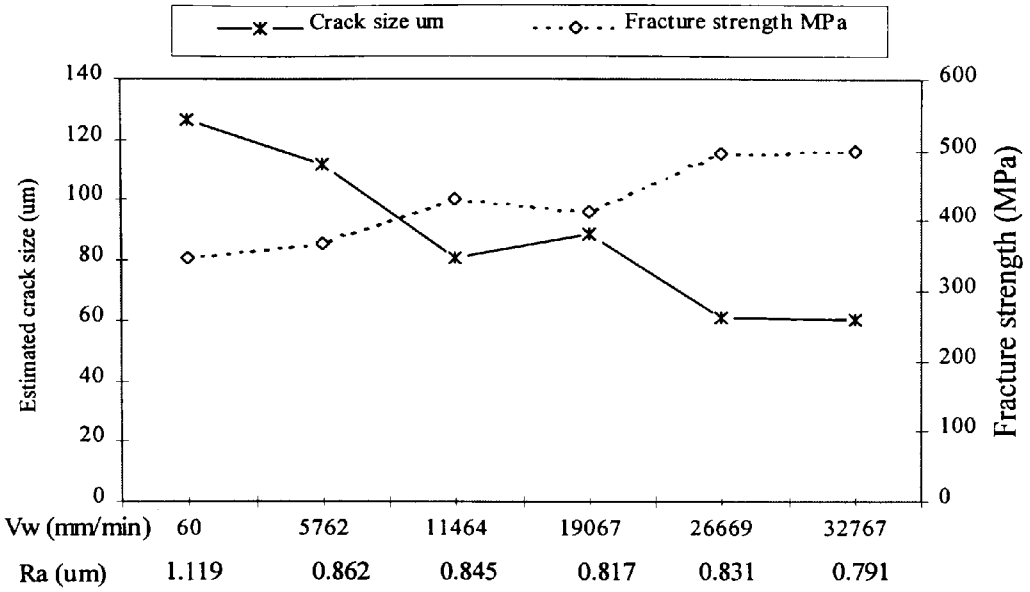

Figure 52: Fracture strength and estimated crack size against surface roughness and table feed (Vw) at 30 μm depth of cut.

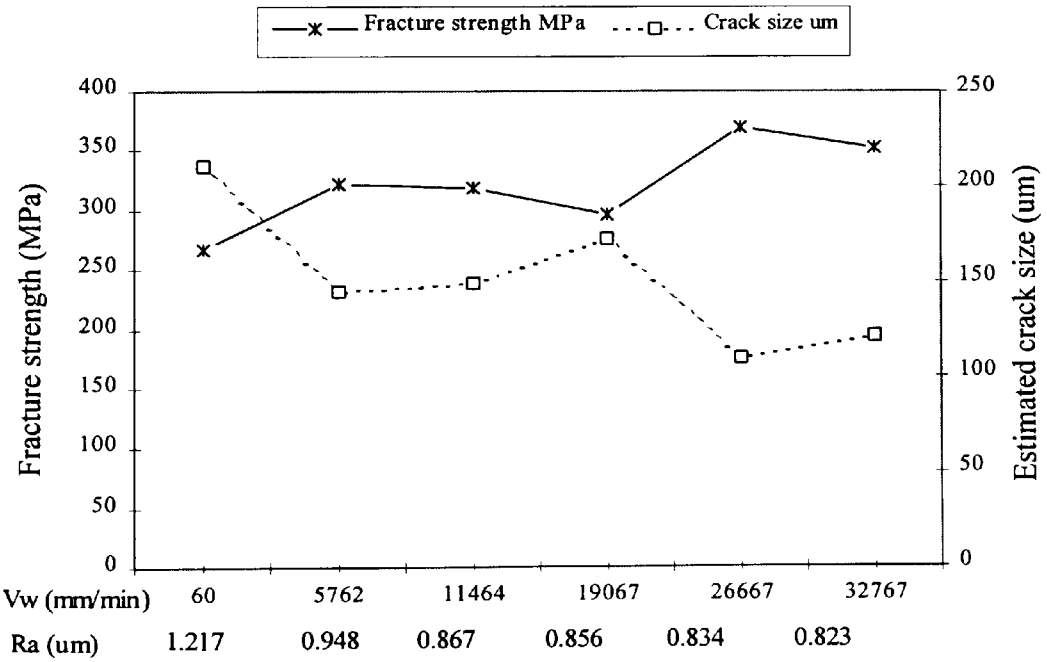

Figure 53: Fracture strength and estimated crack size against surface roughness and table feed (Vw) at 100 μm depth of cut.

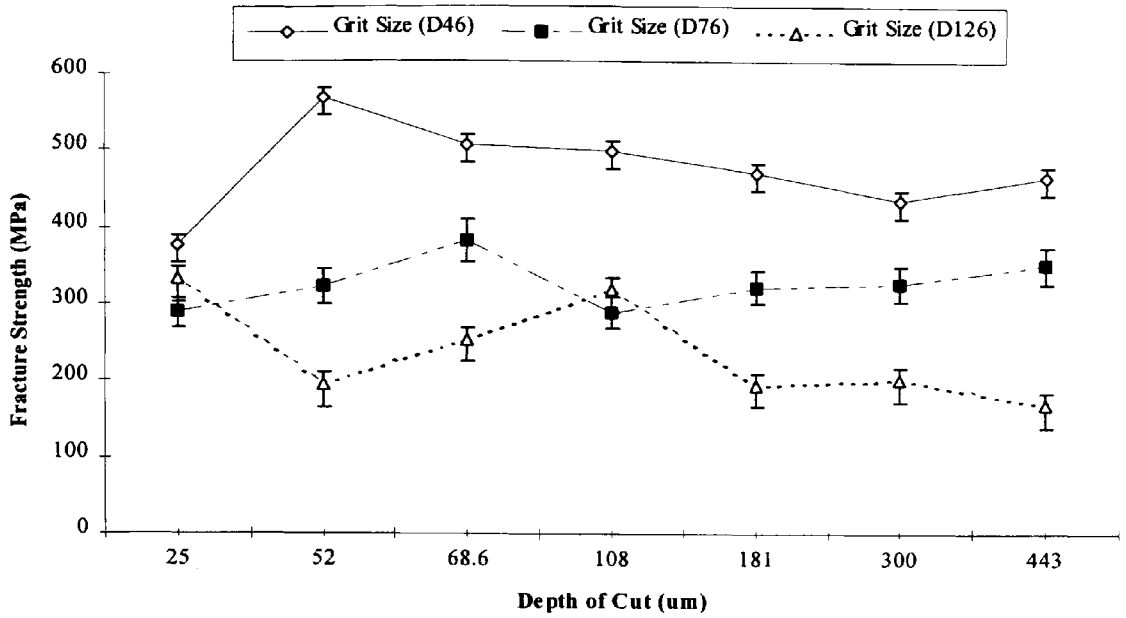

Figure 54: Fracture strength against depth of cut for different levels of grit size.

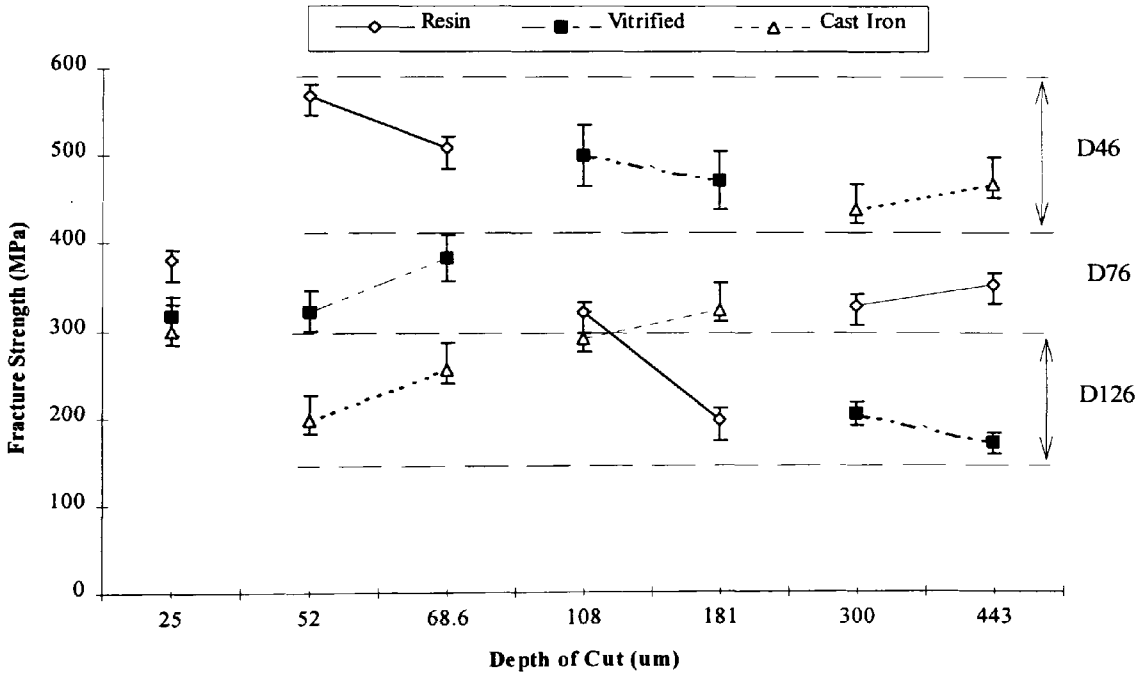

Figure 55: Fracture strength against depth of cut for different levels of bond type.

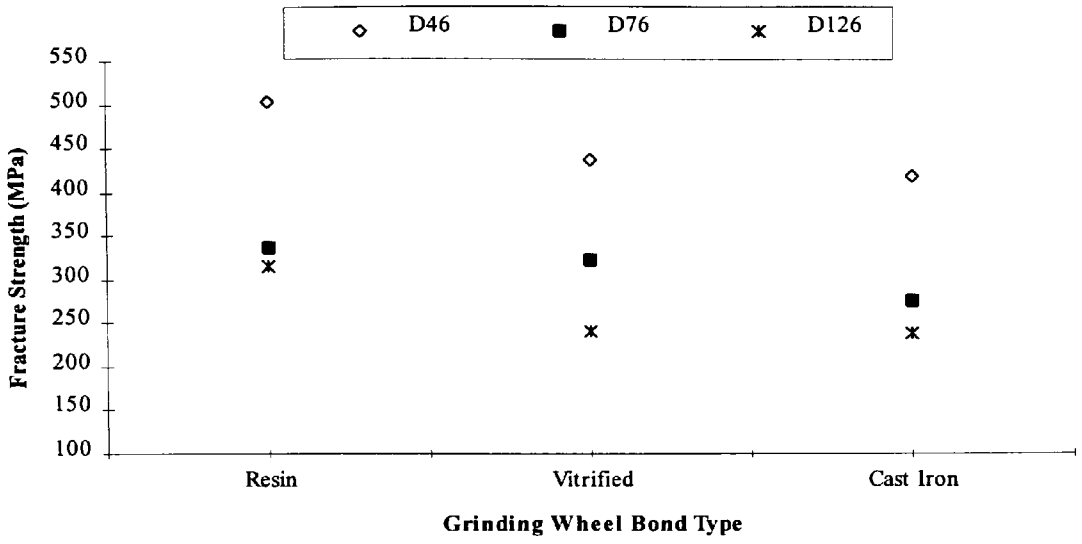

Figure 56: Fracture strength against grinding wheel bond type for different levels of grit size.

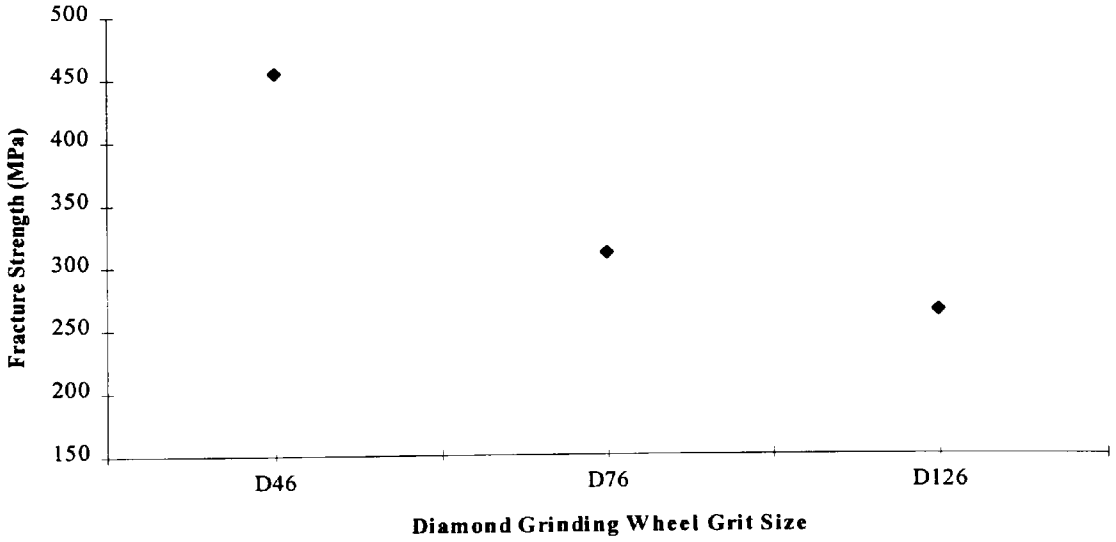

Figure 57: Fracture strength against grit size averaged over different levels of bond type.

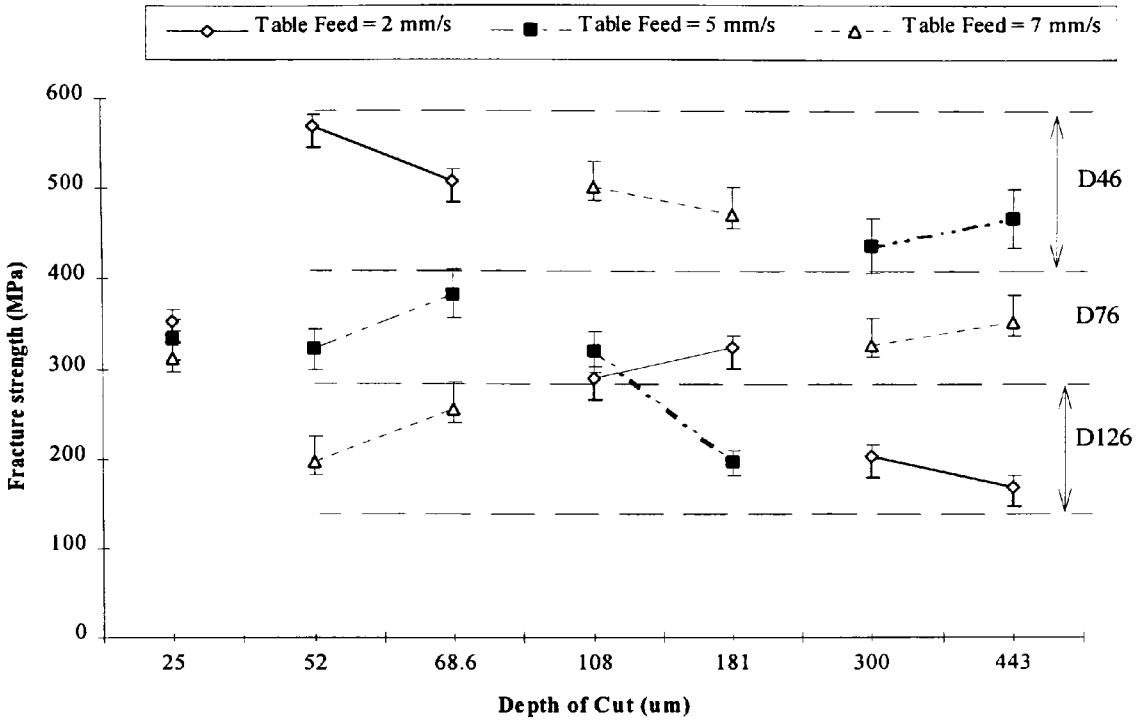

Figure 58: Fracture strength against depth of cut for different levels of table feed.

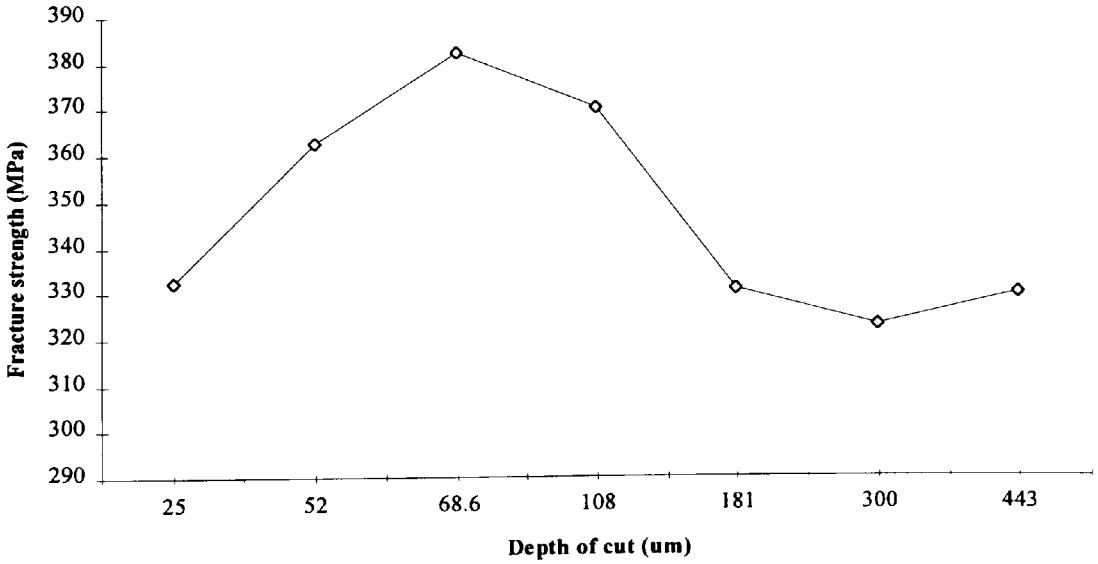

Figure 59: Fracture strength against depth of cut averaged over different levels of table feed.

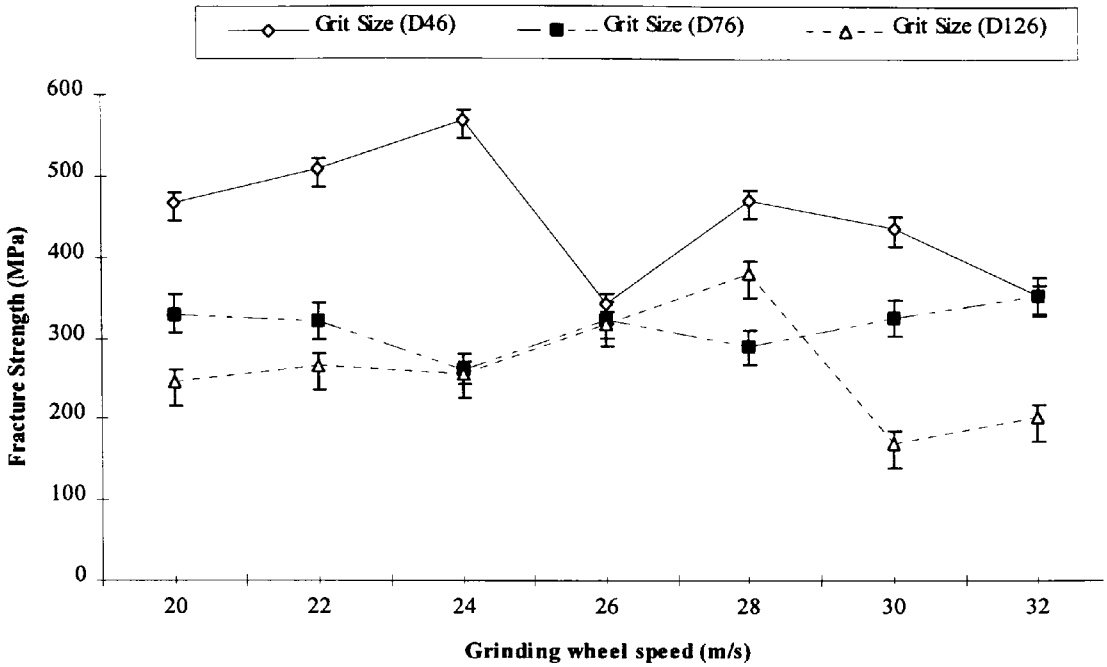

Figure 60: Fracture strength against grinding wheel speed for different levels of grit size.

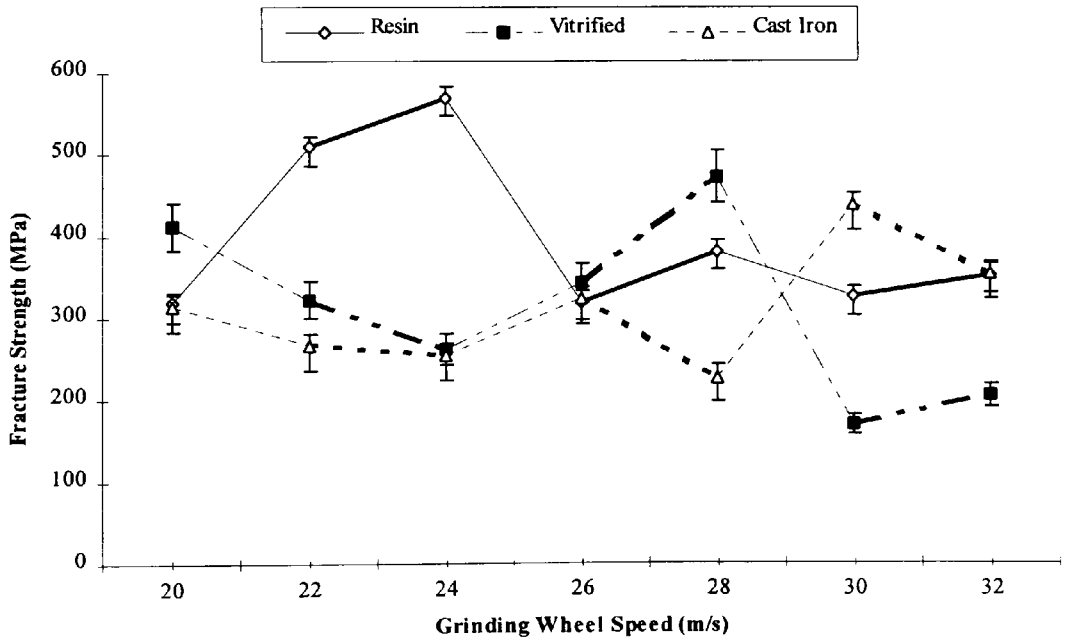

Figure 61: Fracture strength against grinding wheel speed for different levels of bond type.

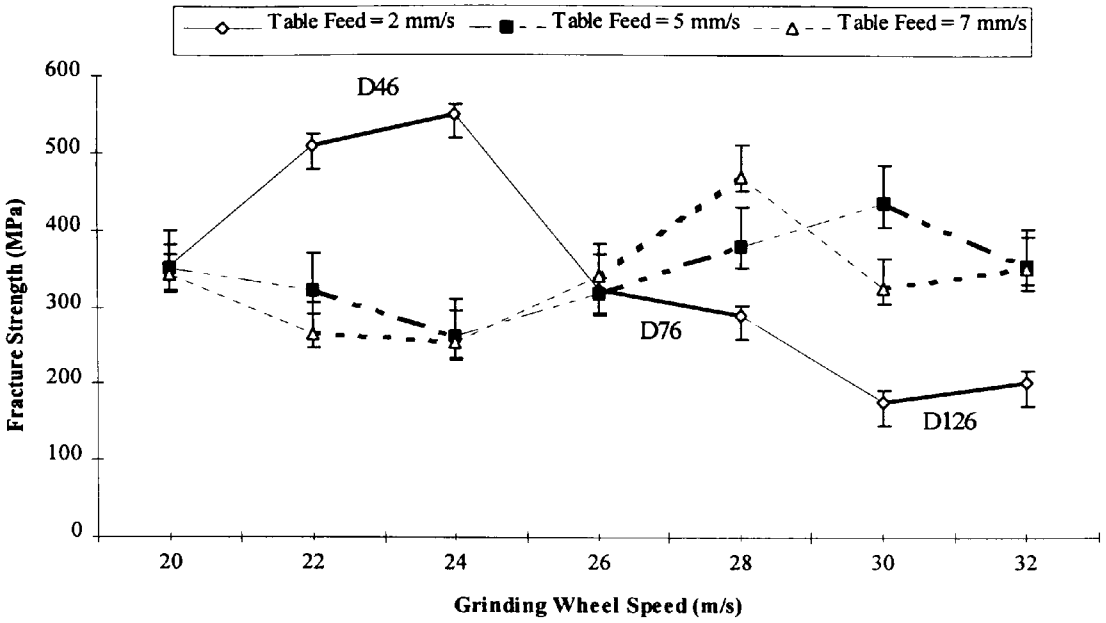

Figure 62: Fracture strength against grinding wheel speed for different levels of table feed.

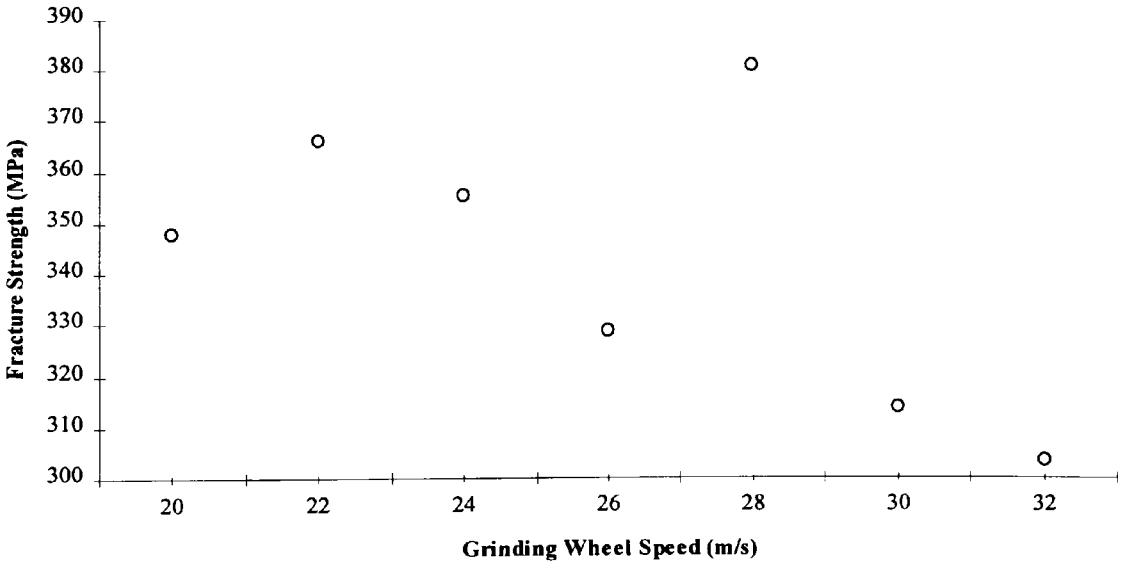

Figure 63: Fracture strength against grinding wheel speed averaged over different levels of table feed.

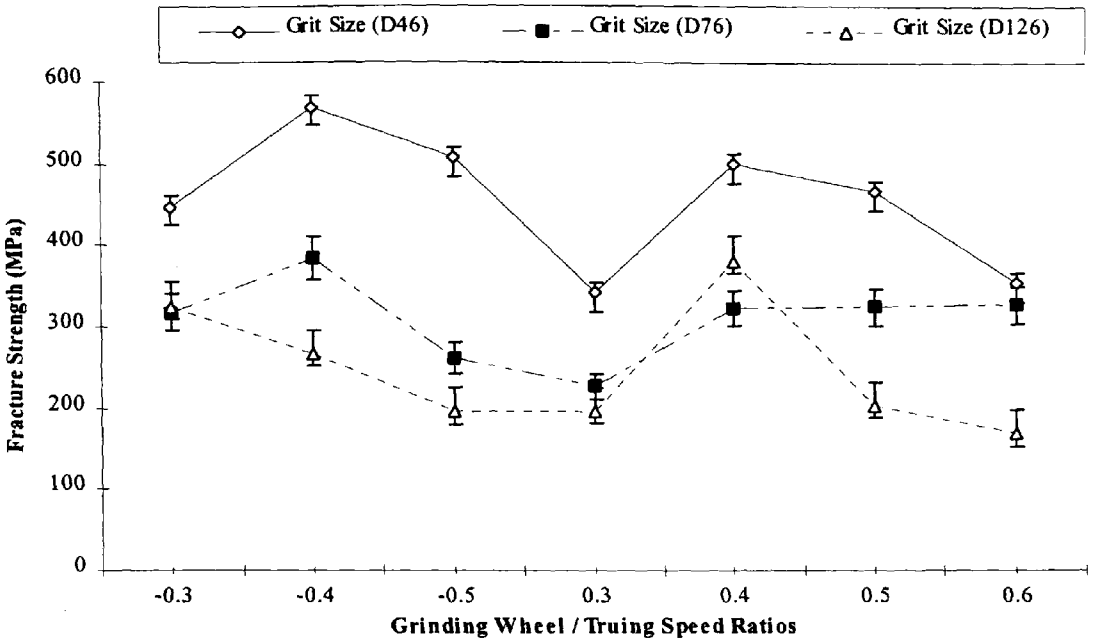

Figure 64: Fracture strength against grinding wheel/truing speed ratios for different levels of grit size.

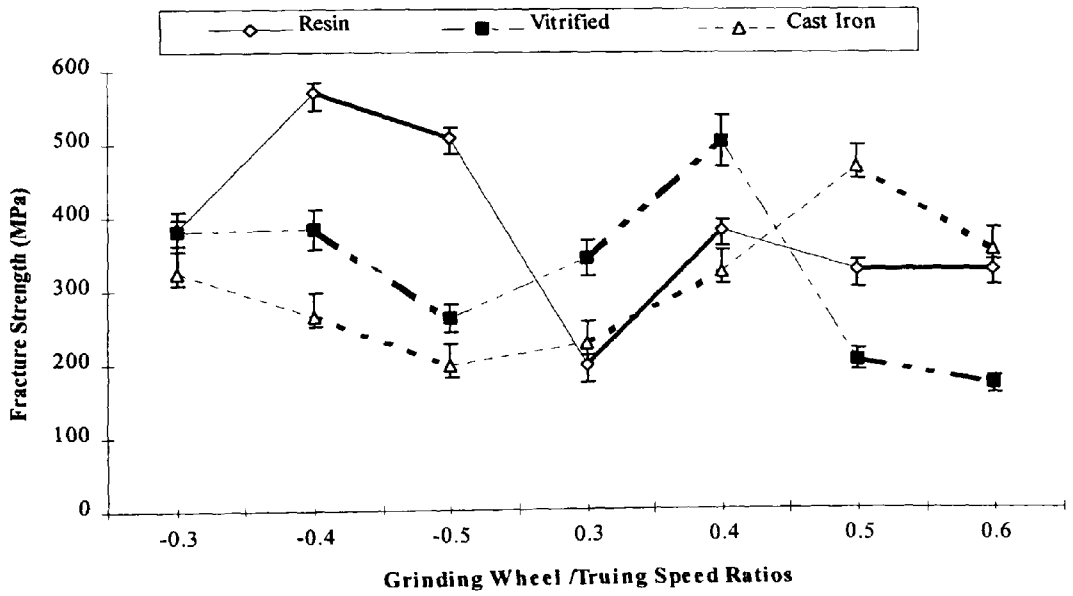

Figure 65: Fracture strength against grinding wheel/truing speed ratios for different levels of bond type.

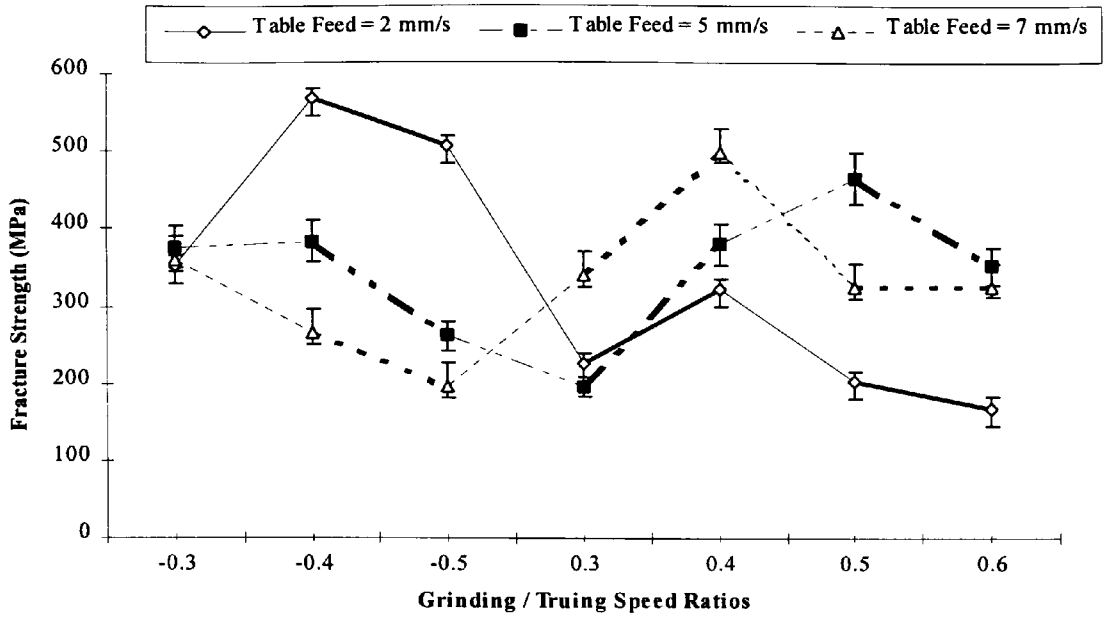

Figure 66: Fracture strength against grinding wheel/truing speed ratios for different levels of table feed.

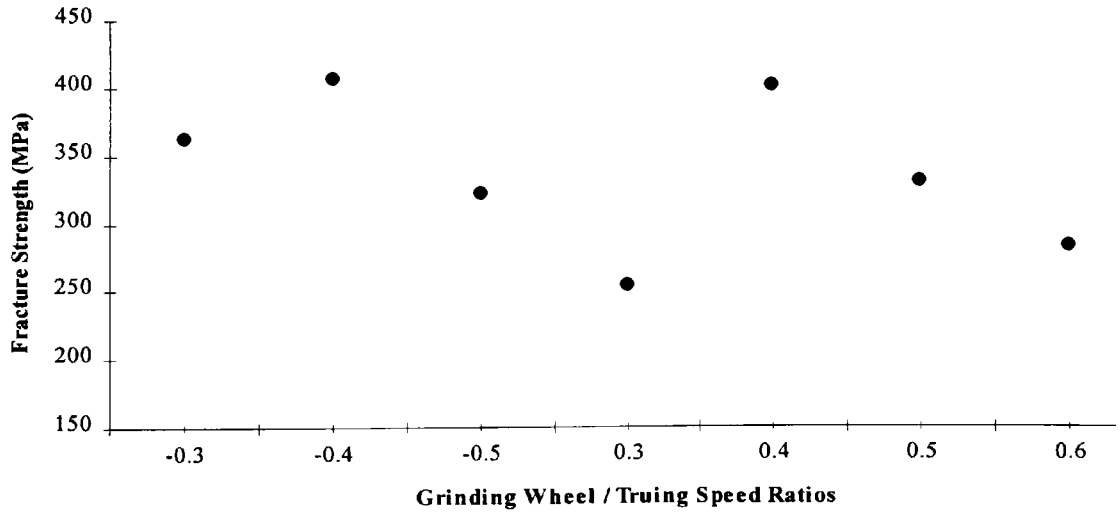

Figure 67: Fracture strength against grinding wheel/truing speed ratios averaged over different levels of table feed.

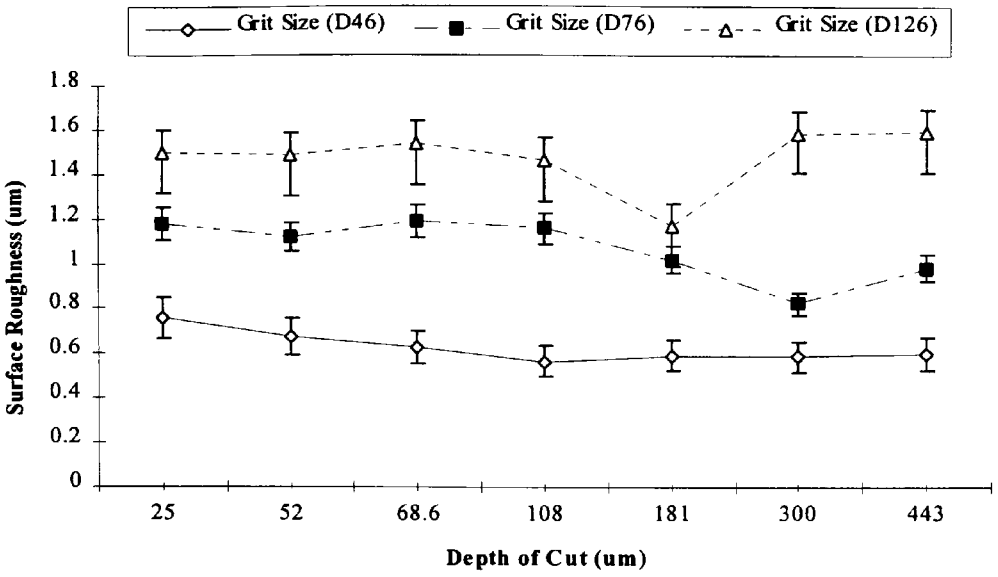

Figure 68: Surface roughness against depth of cut for different levels of grit size.

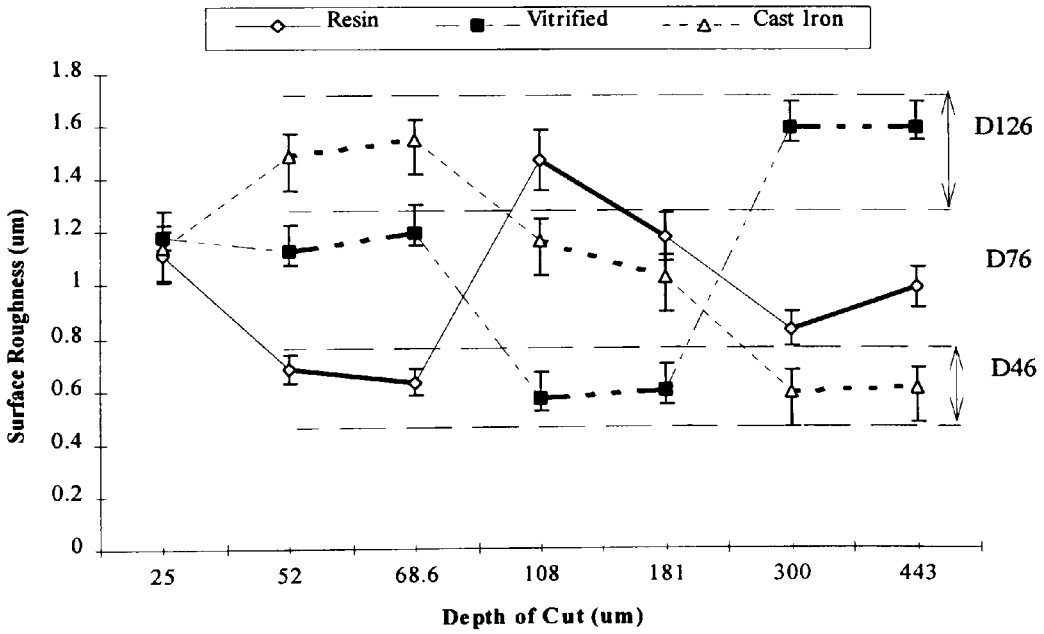

Figure 69: Surface roughness against depth of cut for different levels of bond type.

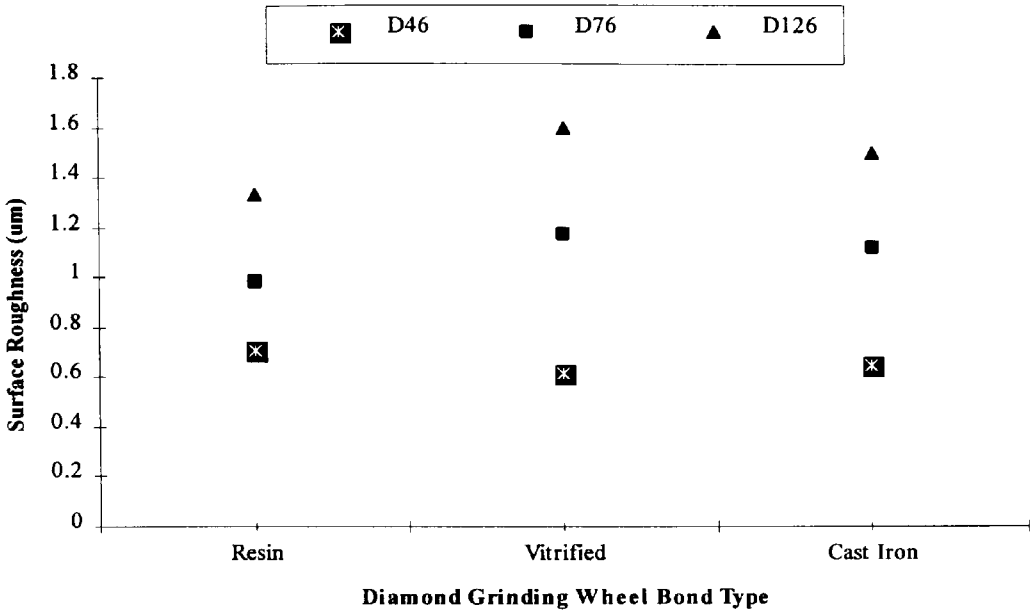

Figure 70: Surface roughness against grinding wheel bond type for different levels of grit size.

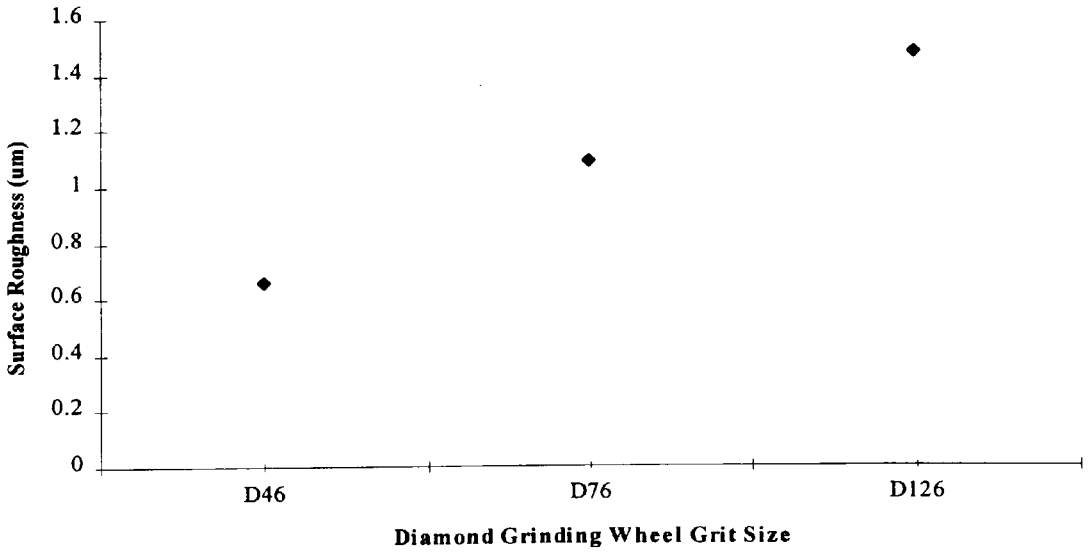

Figure 71: Surface roughness against grit size averaged over different levels of bond type.

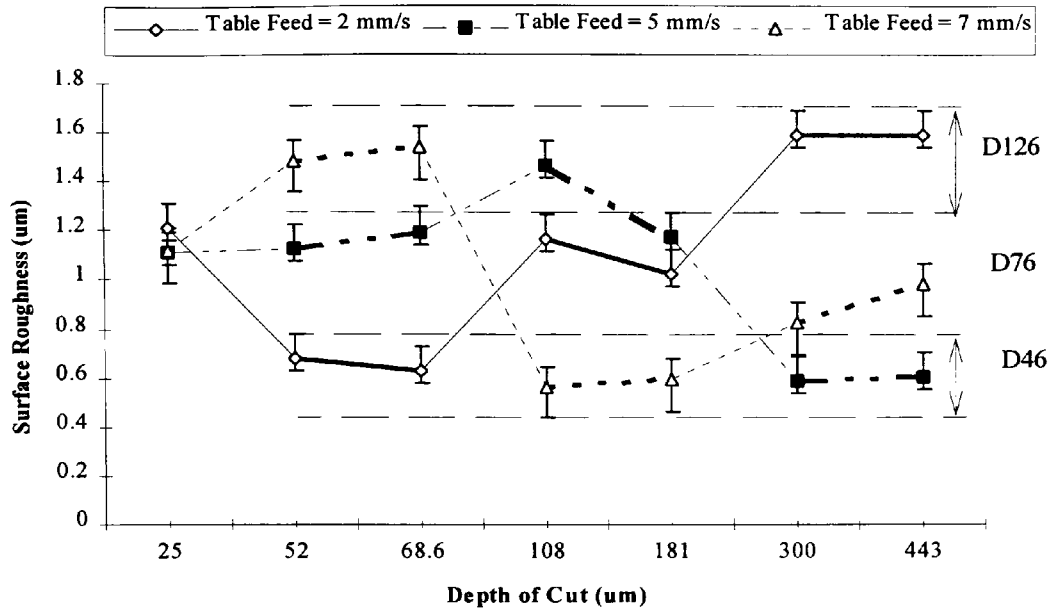

Figure 72: Surface roughness against depth of cut for different levels of table feed.

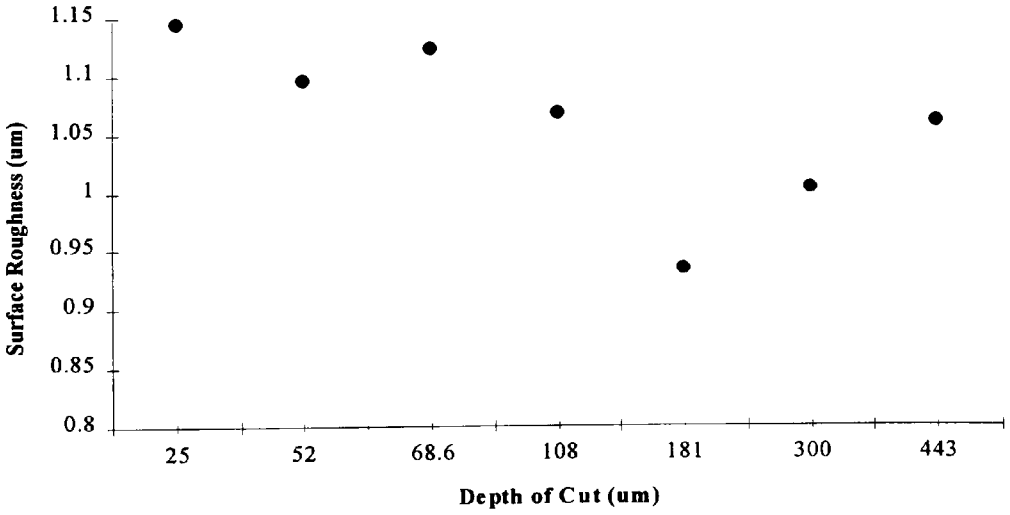

Figure 73: Surface roughness against depth of cut averaged over different levels of table feed.

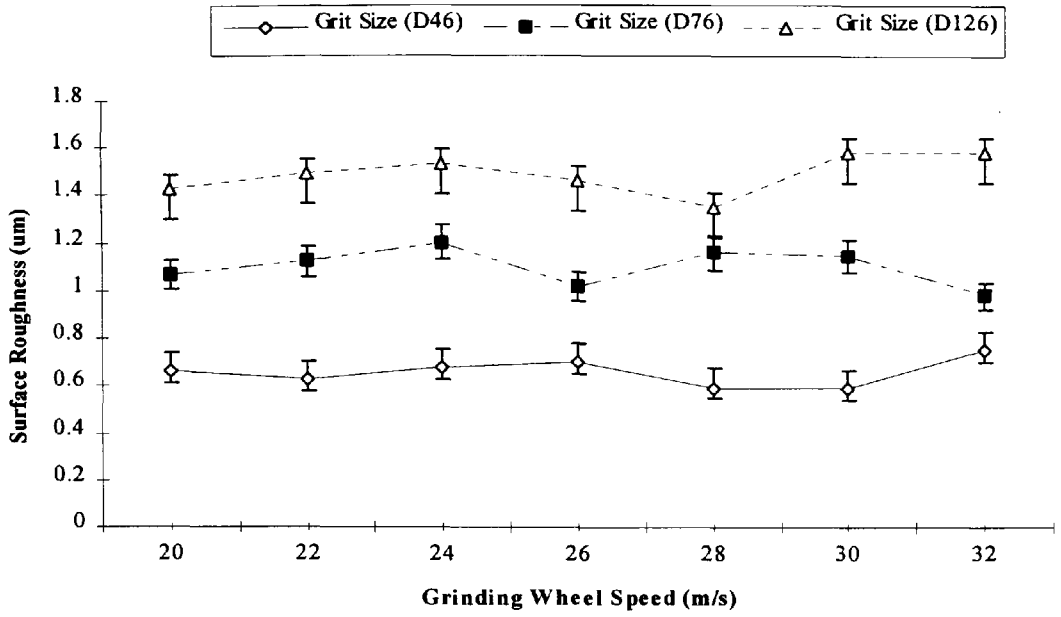

Figure 74: Surface roughness against grinding wheel speed for different levels of grit size.

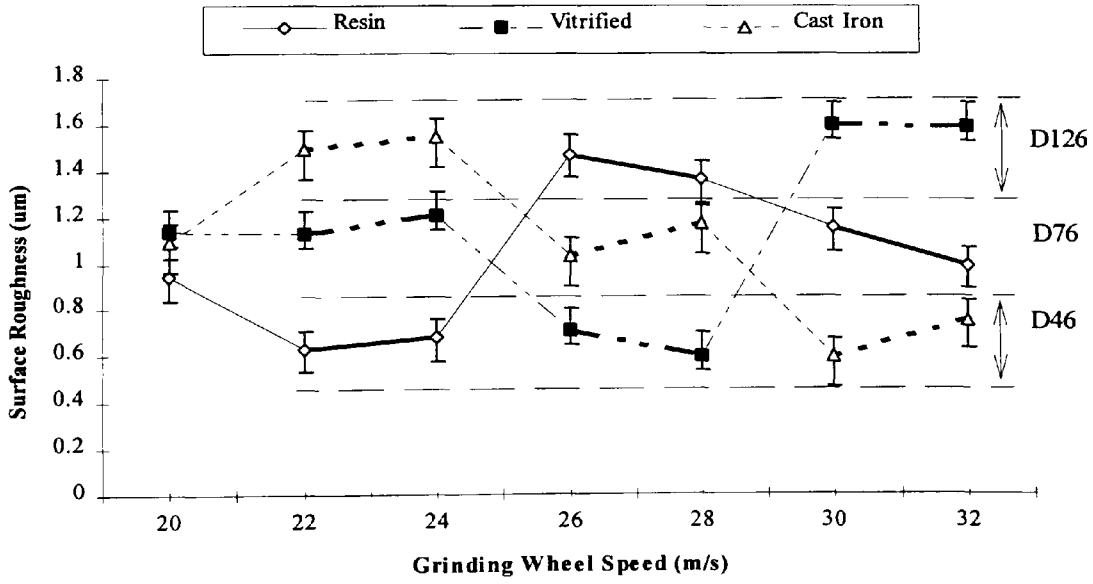

Figure 75: Surface roughness against grinding wheel speed for different levels of bond type.

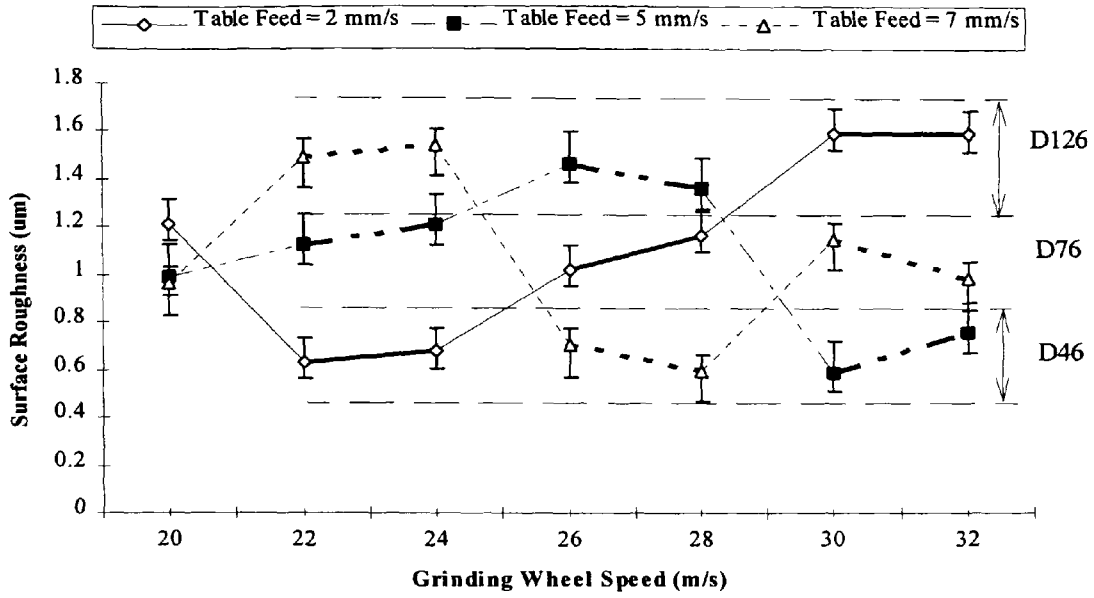

Figure 76: Surface roughness against grinding wheel speed for different levels of table feed.

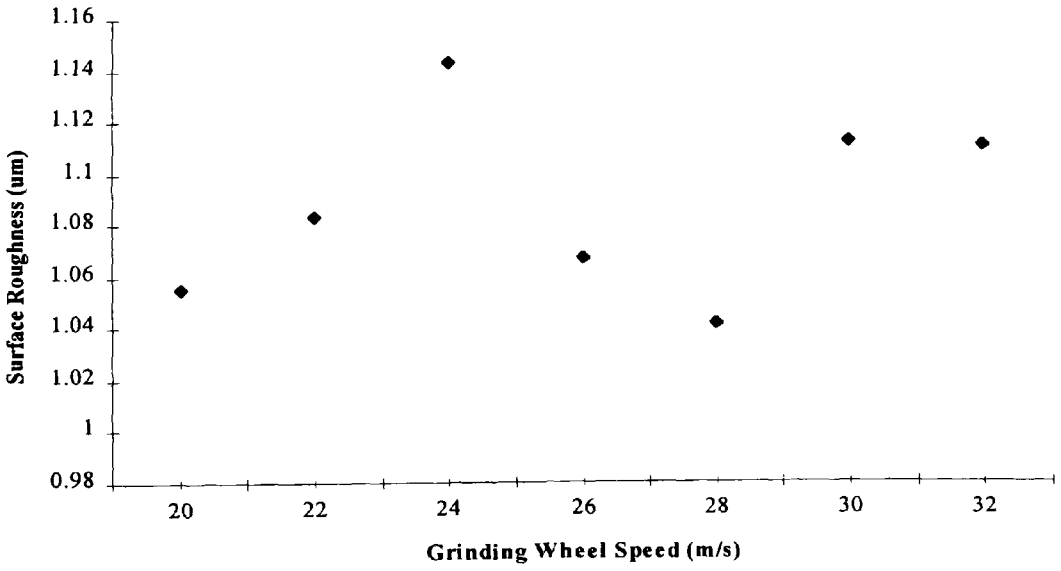

Figure 77: Surface roughness against grinding wheel speed averaged over different levels of table feed.

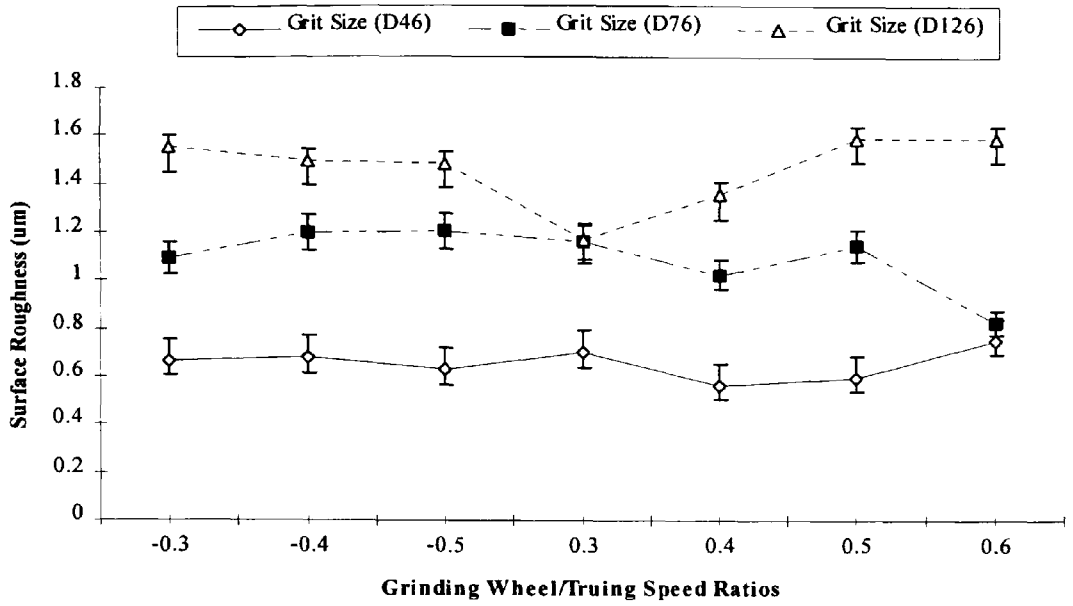

Figure 78: Surface roughness against grinding wheel/truing speed ratios for different levels of grit size.

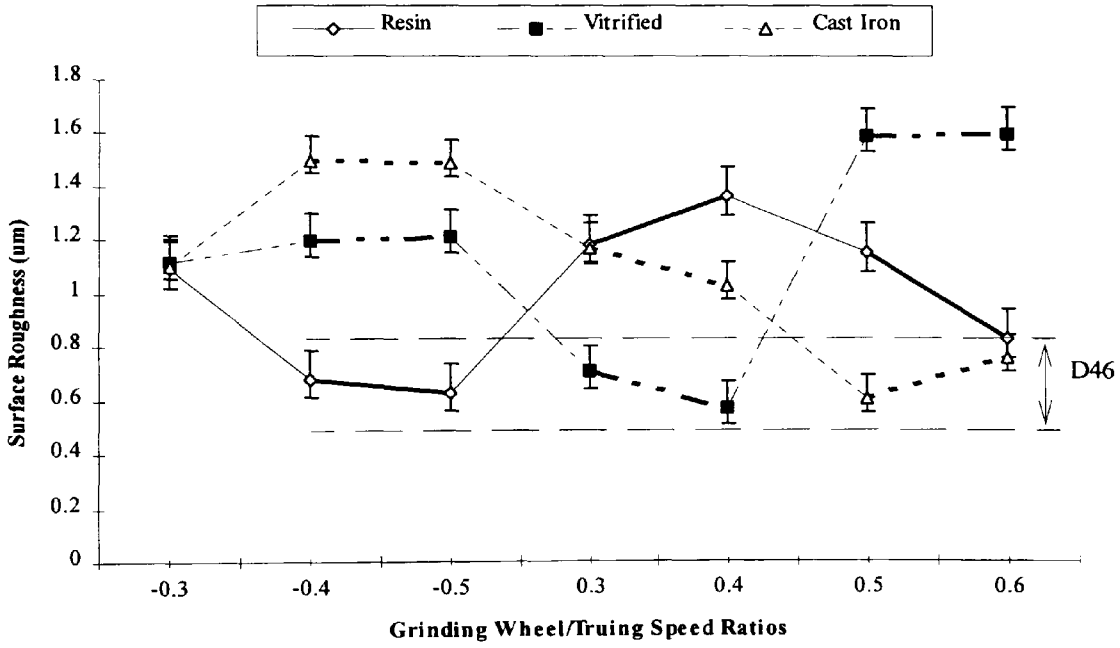

Figure 79: Surface roughness against grinding wheel/truing speed ratios for different levels of bond type.

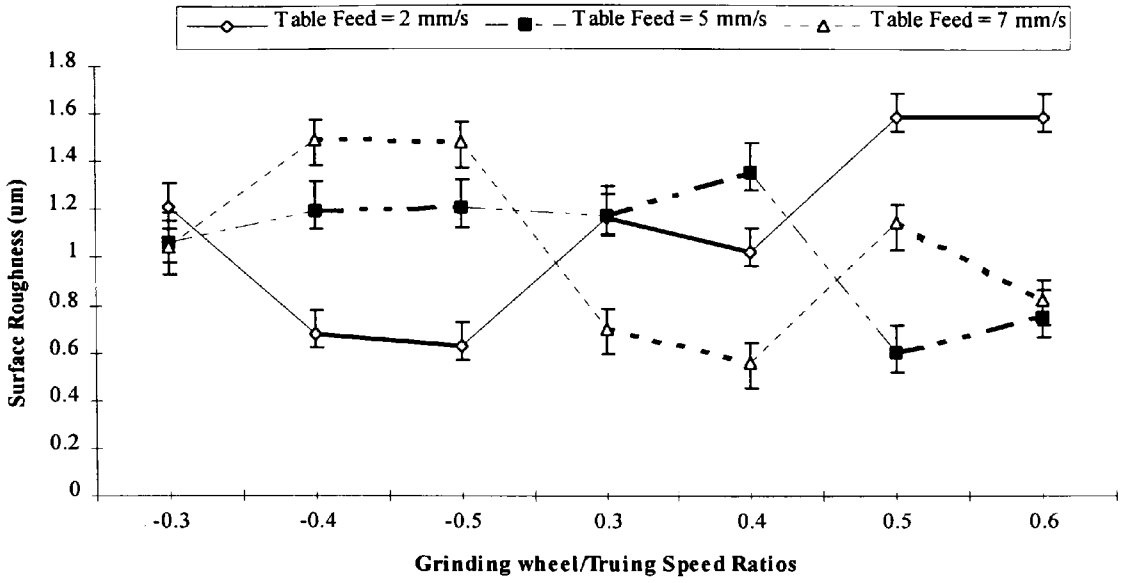

Figure 80: Surface roughness against grinding wheel/truing speed ratios for different levels of table feed.

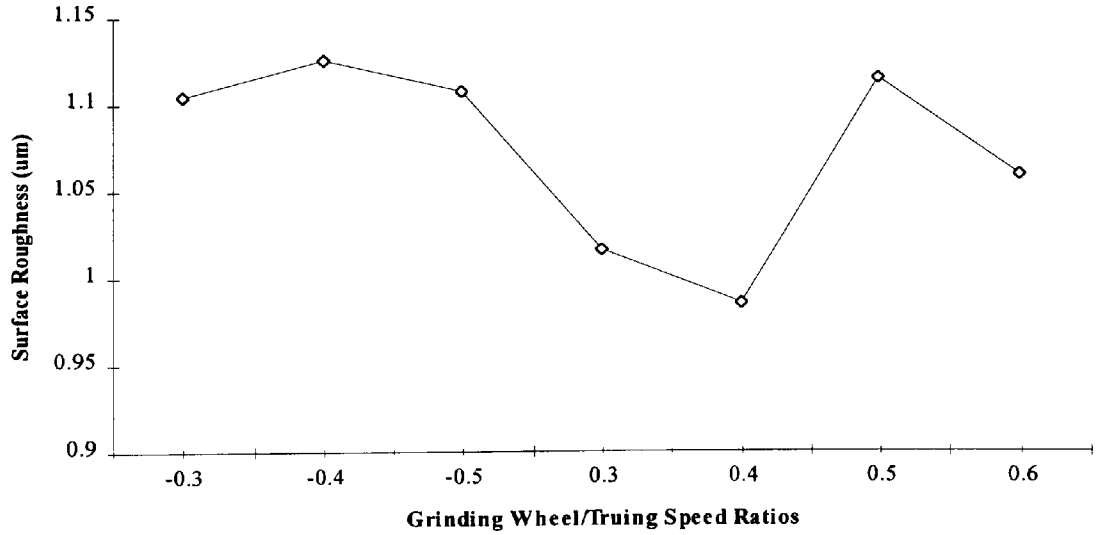

Figure 81: Surface roughness against grinding wheel/truing speed ratios averaged over different levels of table feed.

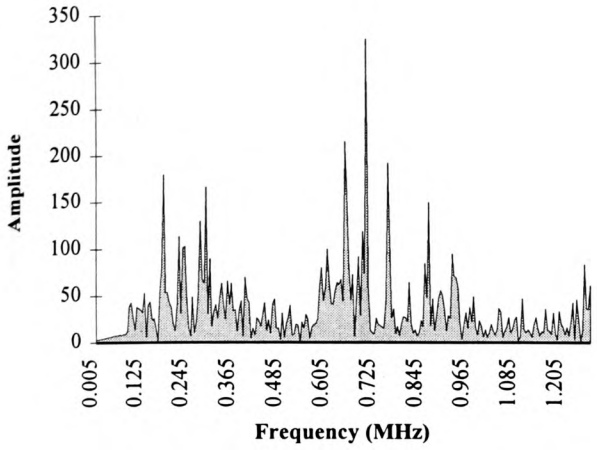

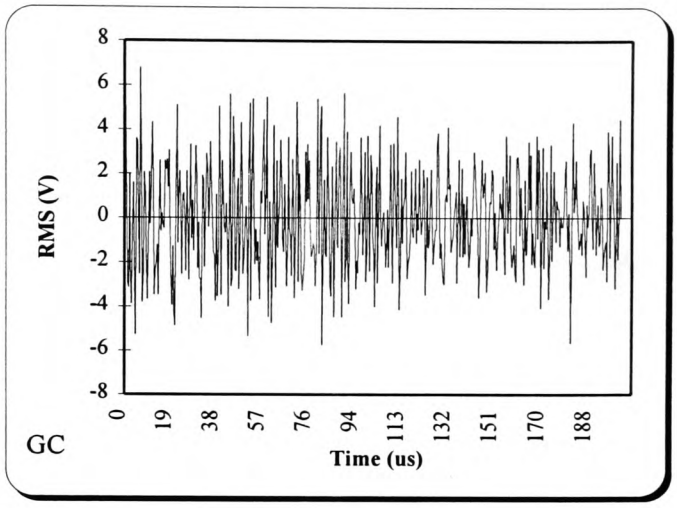

Grit size	Bond type	Table feed mm/s	Wheel speed m/s	Depth of cut (um)		Crack depth um	Gri./Tru. speed
				GC	GN		
D76	Resin	5	20	301.5	310	120	0.6

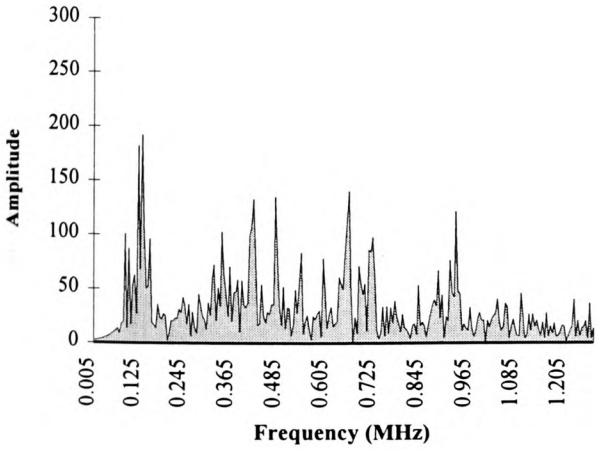

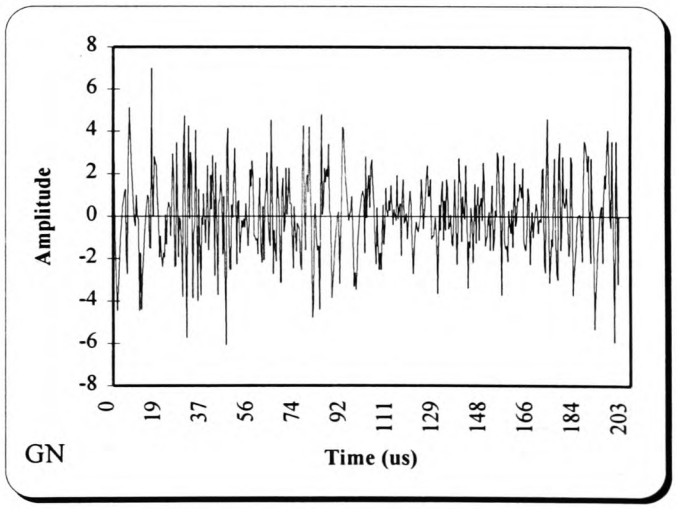

Figure 82: AE spectral amplitude of ground specimens with (GC) and without (GN) cracks initiated on the surface at grinding wheel and machine parameters mentioned above.

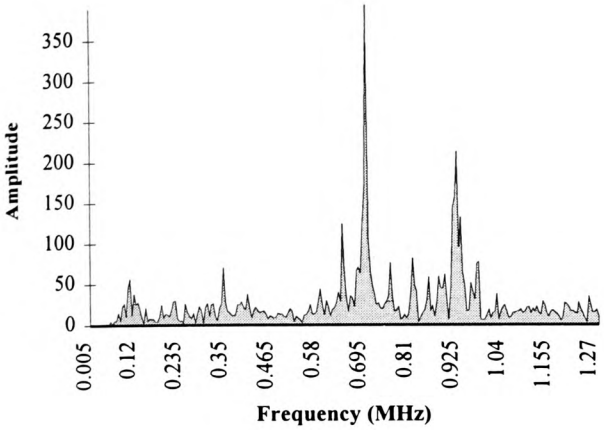

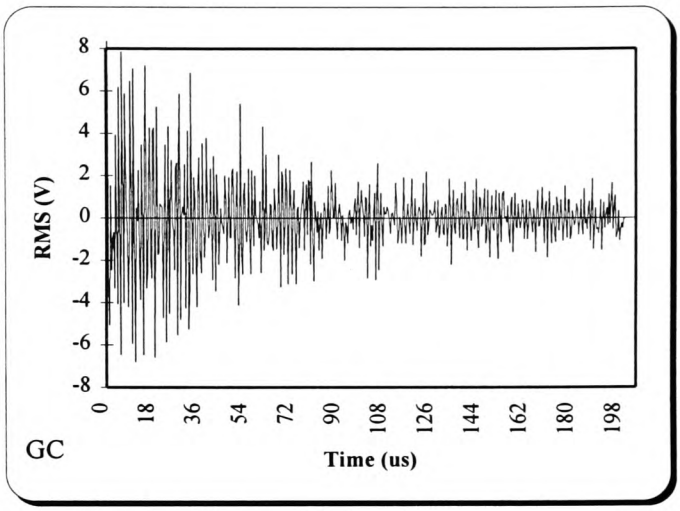

Grit size	Bond type	Table feed mm/s	Wheel speed m/s	Depth of cut (um)		Crack depth um	Gri./Tru. speed
				GC	GN		
D126	Resin	5	28	19.5	30.5	70	0.4

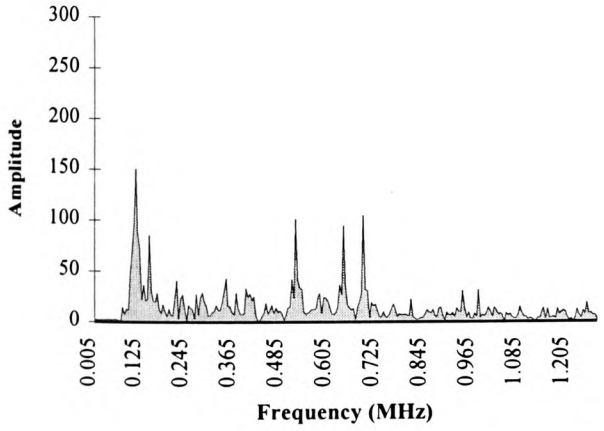

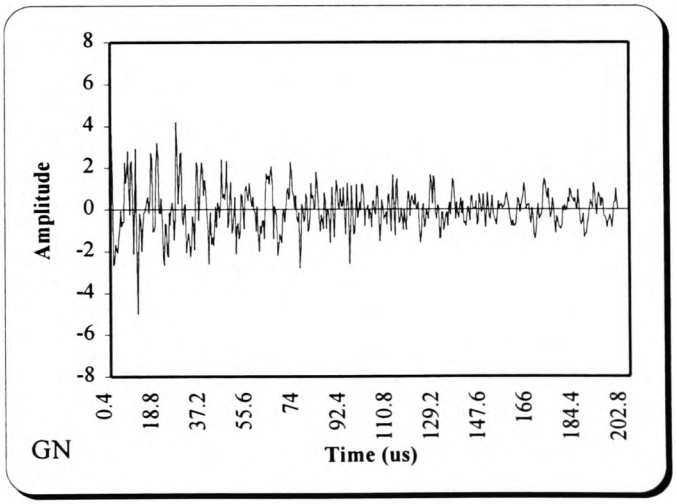

Figure 83: AE spectral amplitude of ground specimens with (GC) and without (GN) cracks initiated on the surface at grinding wheel and machine parameters mentioned above.

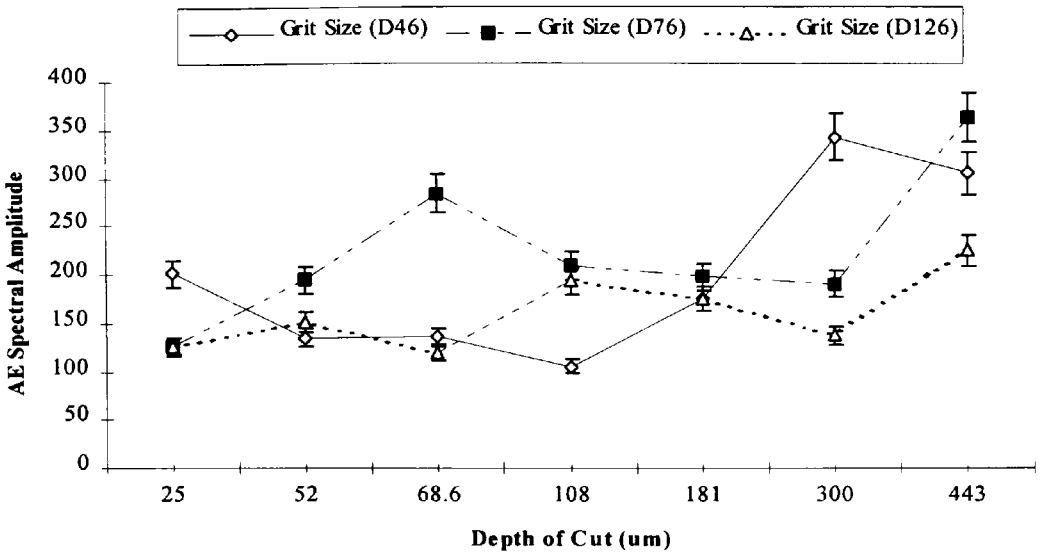

Figure 84: AE Spectral Amplitude against depth of cut for different levels of grit size.

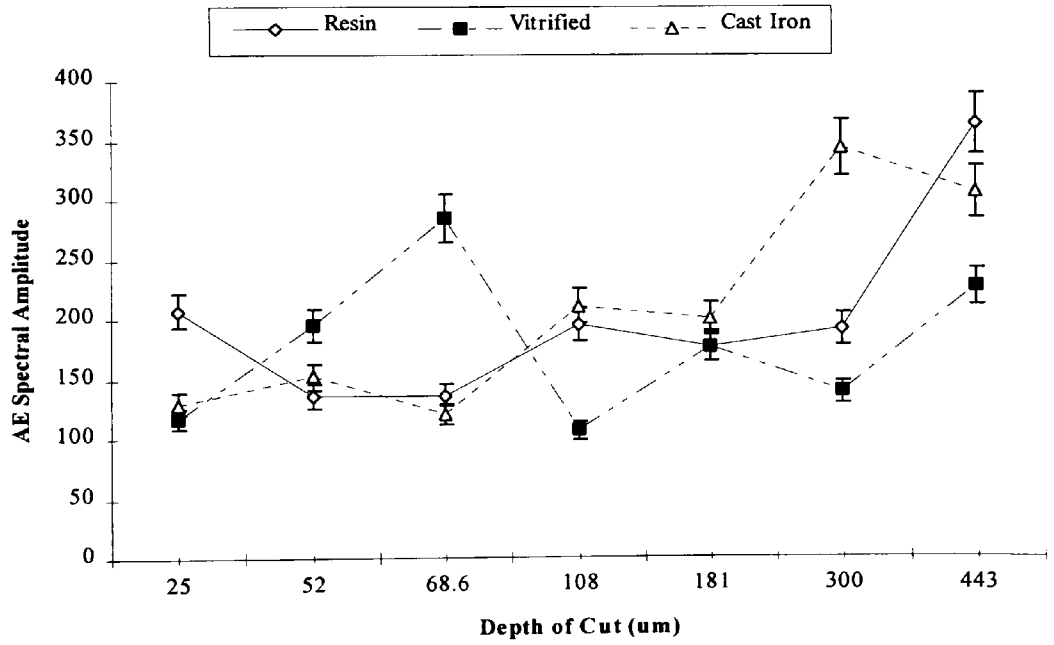

Figure 85: AE Spectral Amplitude against depth of cut for different levels of bond type.

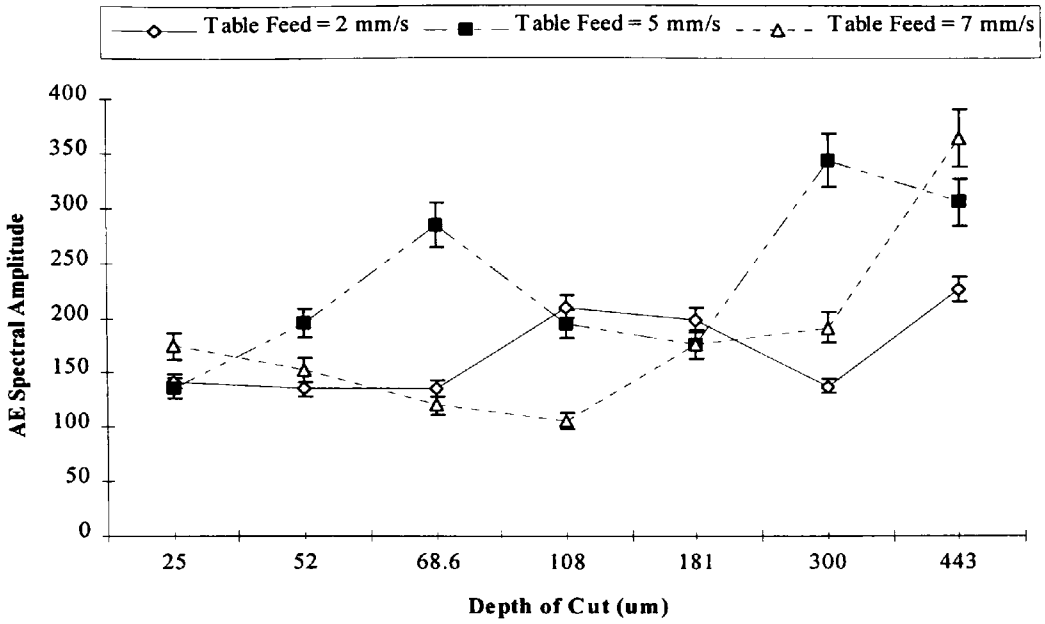

Figure 86: AE Spectral Amplitude against depth of cut for different levels of table feed.

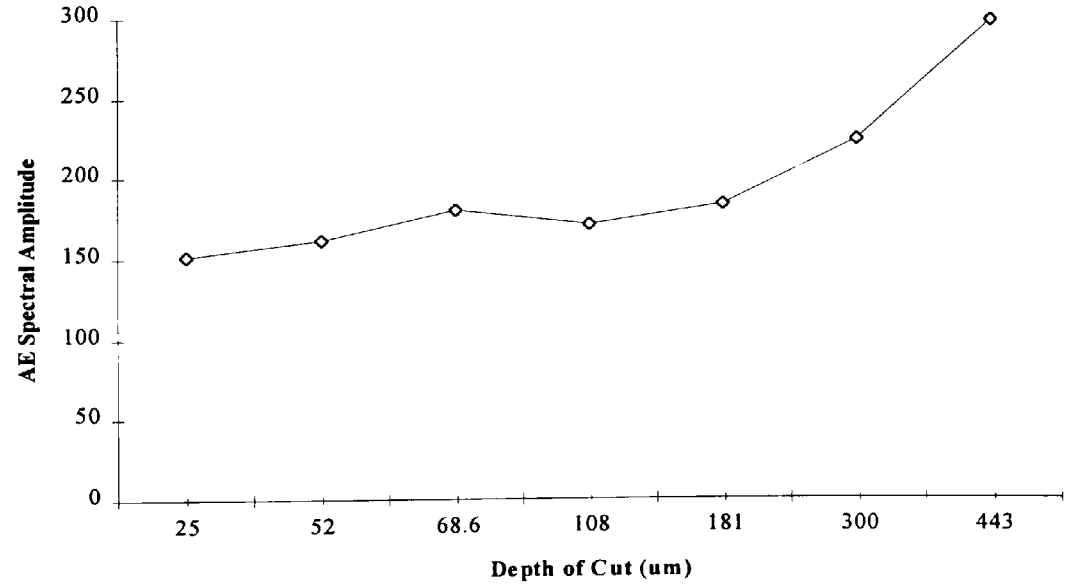

Figure 87: AE Spectral Amplitude against depth of cut averaged over different levels of table feed.

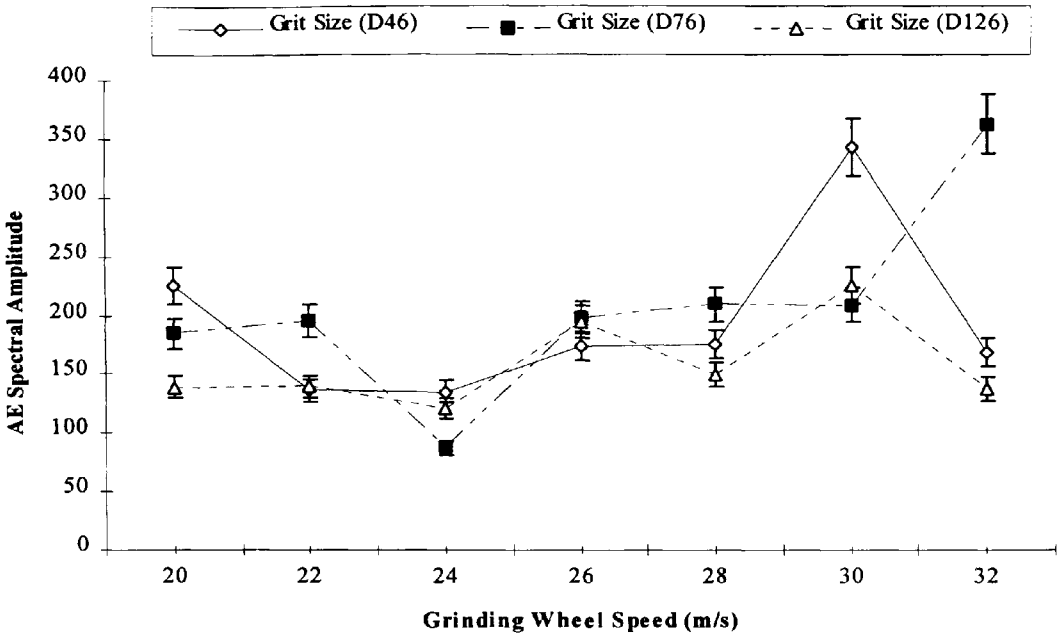

Figure 88: AE Spectral Amplitude against grinding wheel speed for different levels of grit size.

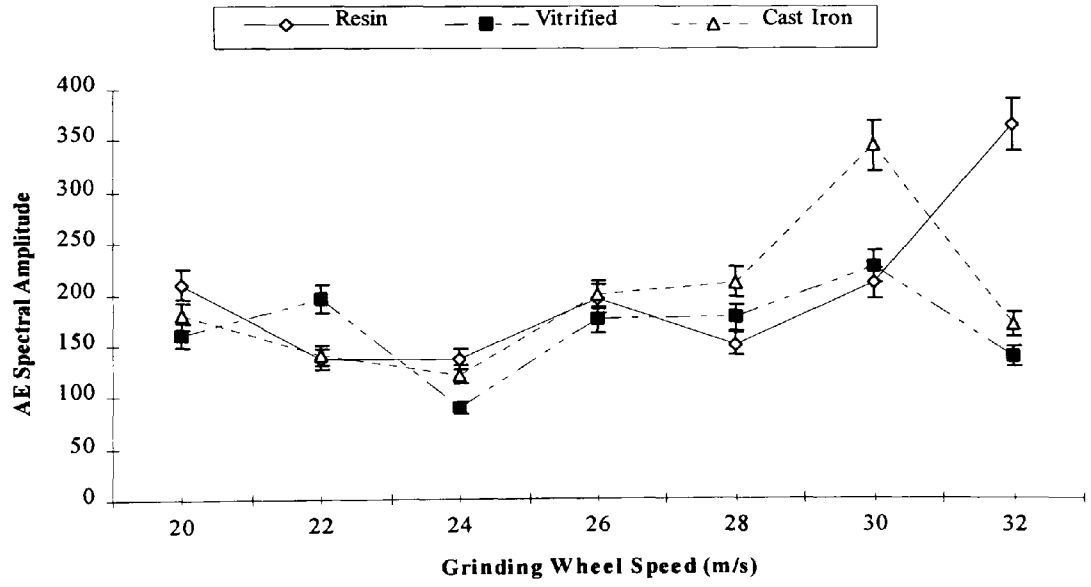

Figure 89: AE Spectral Amplitude against grinding wheel speed for different levels of bond type.

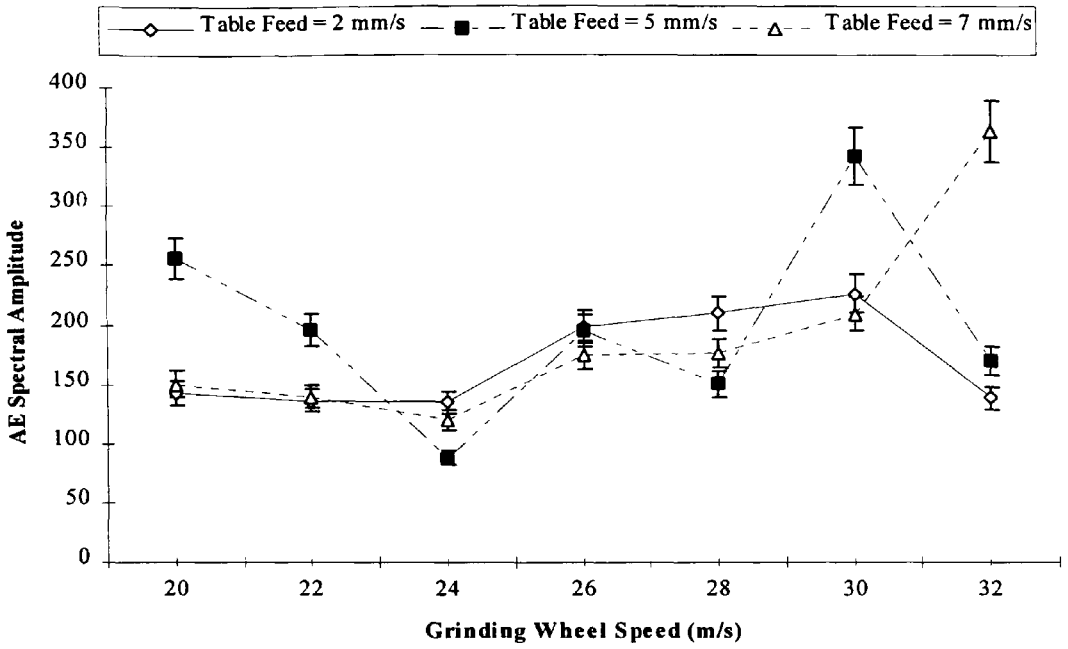

Figure 90: AE Spectral Amplitude against grinding wheel speed for different levels of table feed.

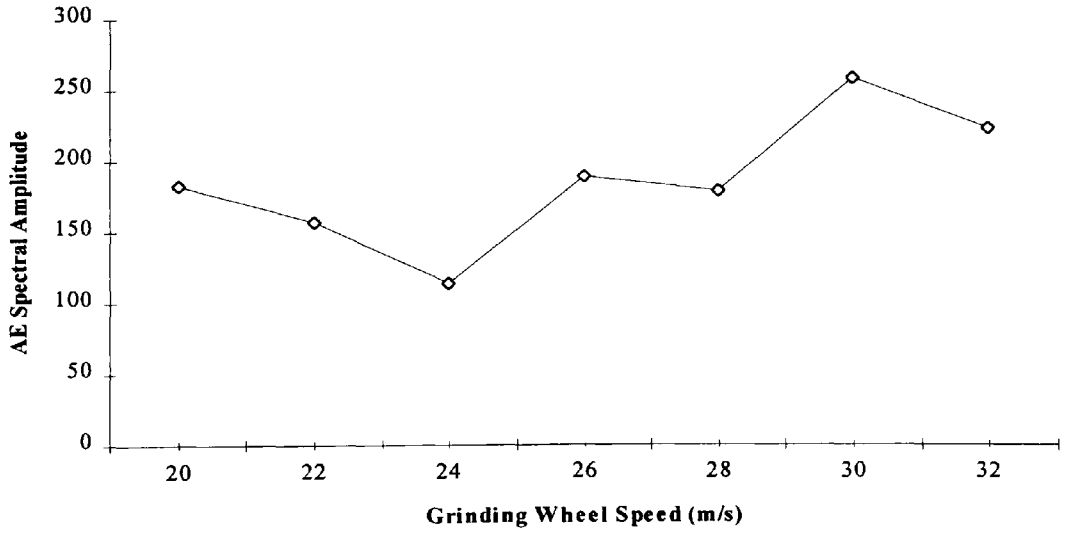

Figure 91: AE Spectral Amplitude against grinding wheel speed averaged over different levels of table feed.

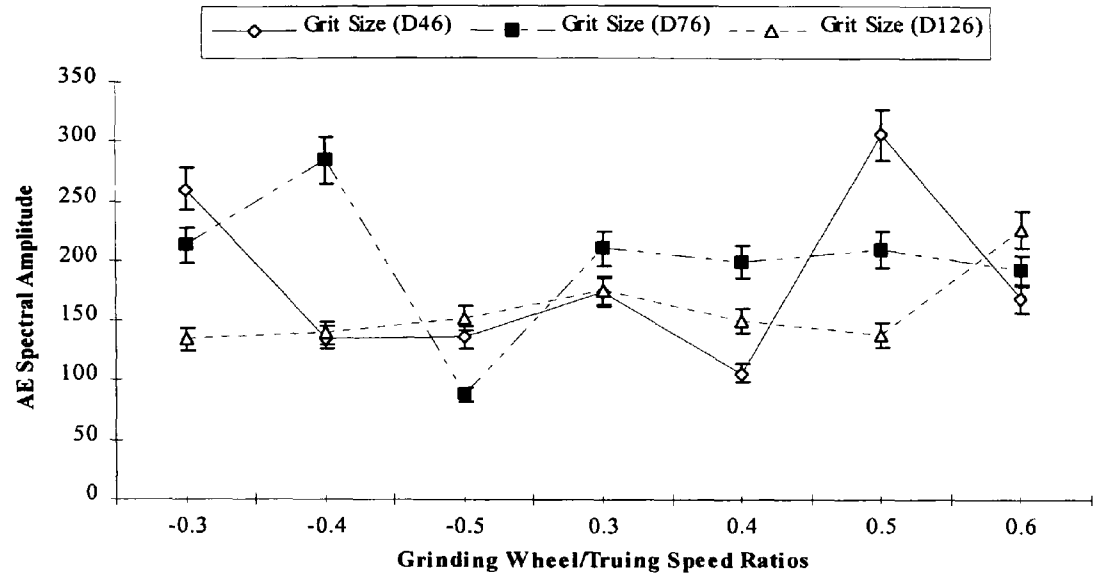

Figure 92: AE Spectral Amplitude against grinding wheel/truing speed ratios for different levels of grit size.

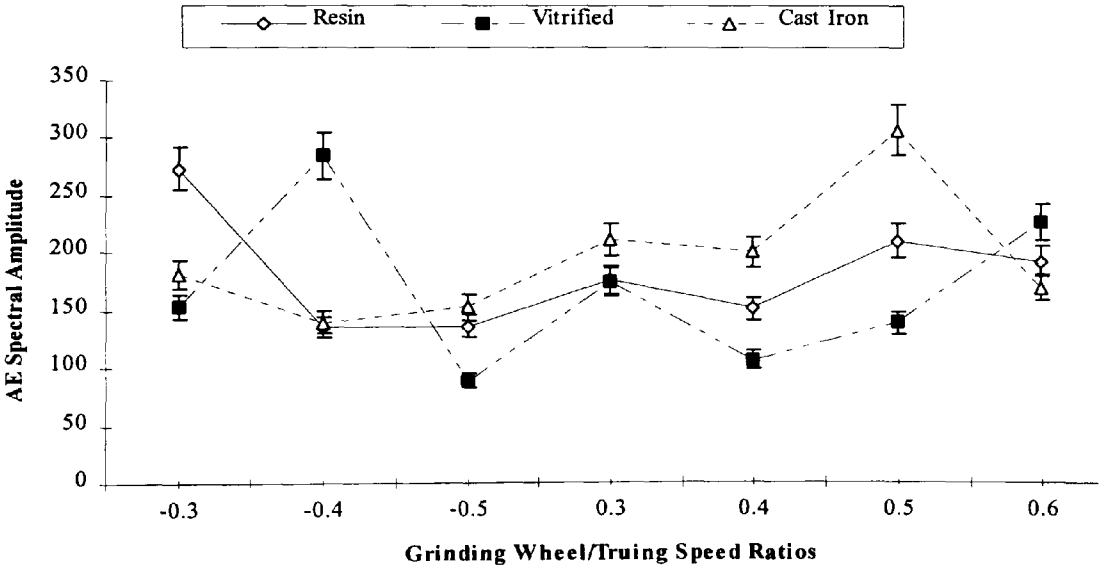

Figure 93: AE Spectral Amplitude against grinding wheel/truing speed ratios for different levels of bond type.

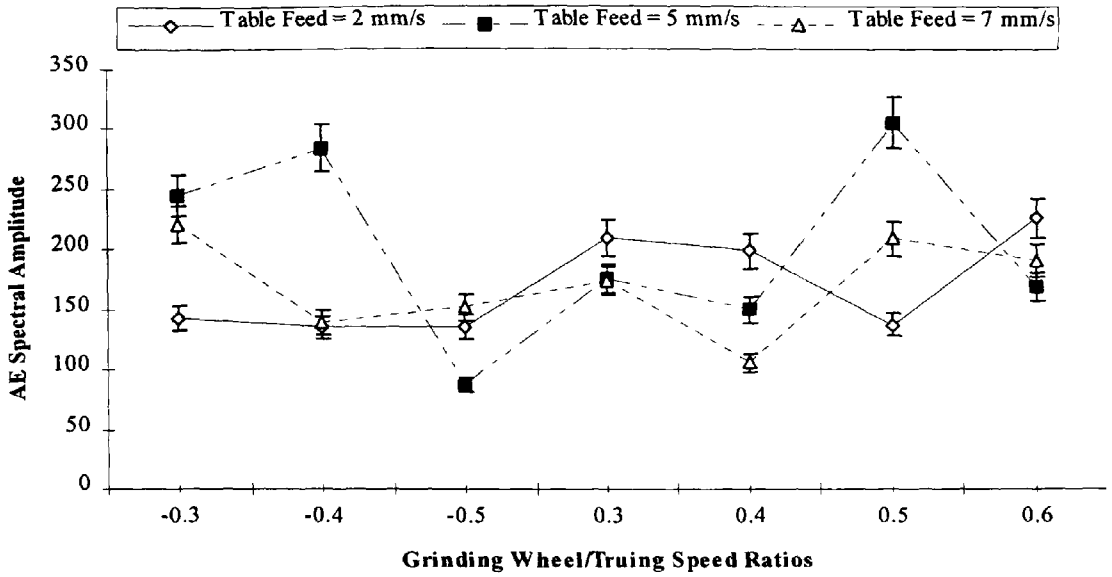

Figure 94: AE Spectral Amplitude against grinding wheel/truing speed ratios for different levels of table feed.

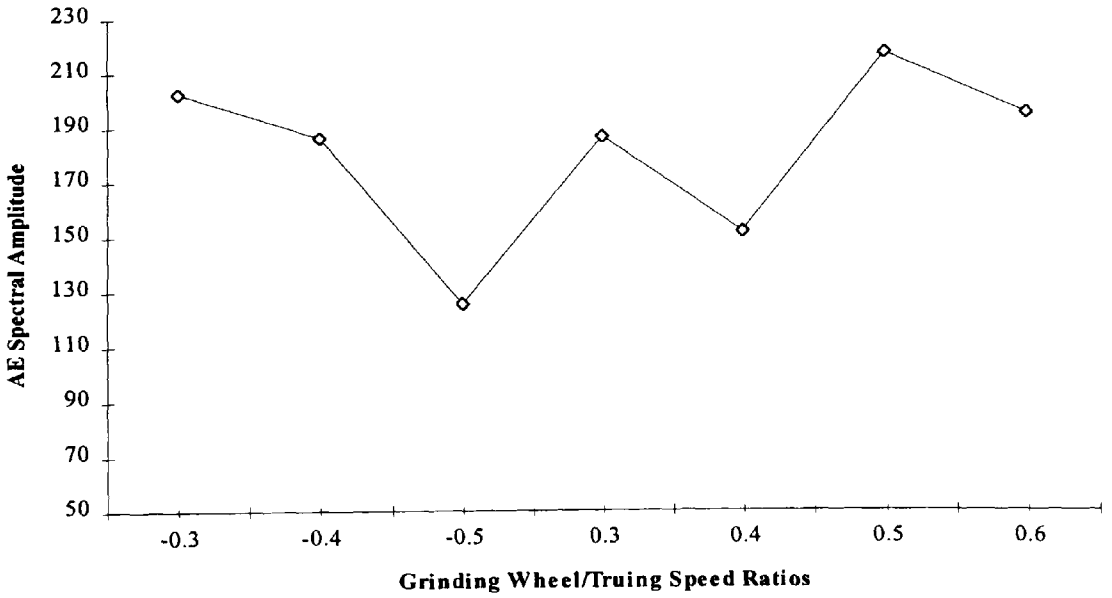

Figure 95: AE Spectral Amplitude against grinding wheel /truing speed ratios averaged over different levels of table feed.

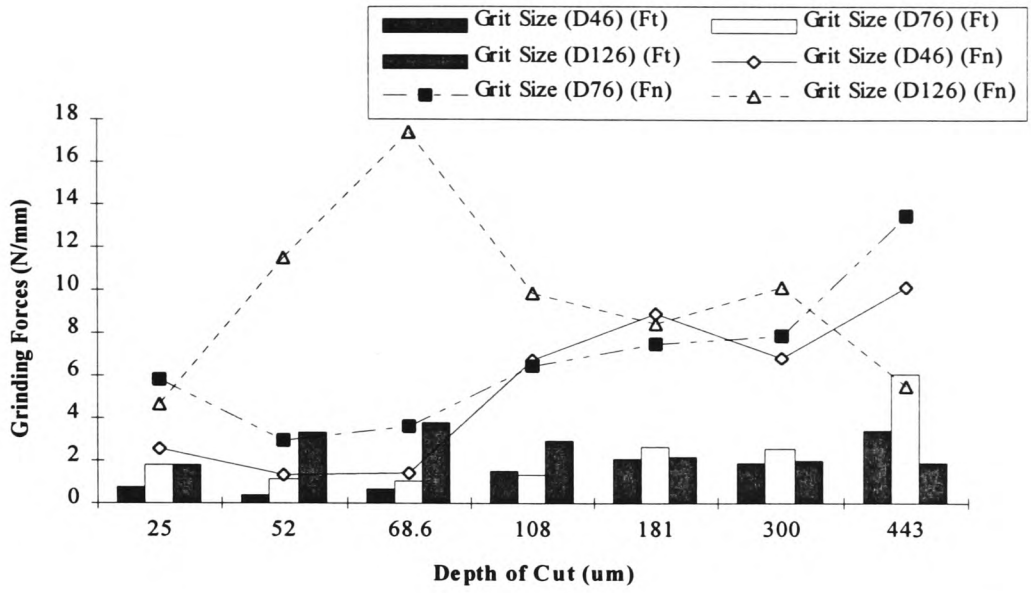

Figure 96: Grinding forces against depth of cut for different levels of grit size.

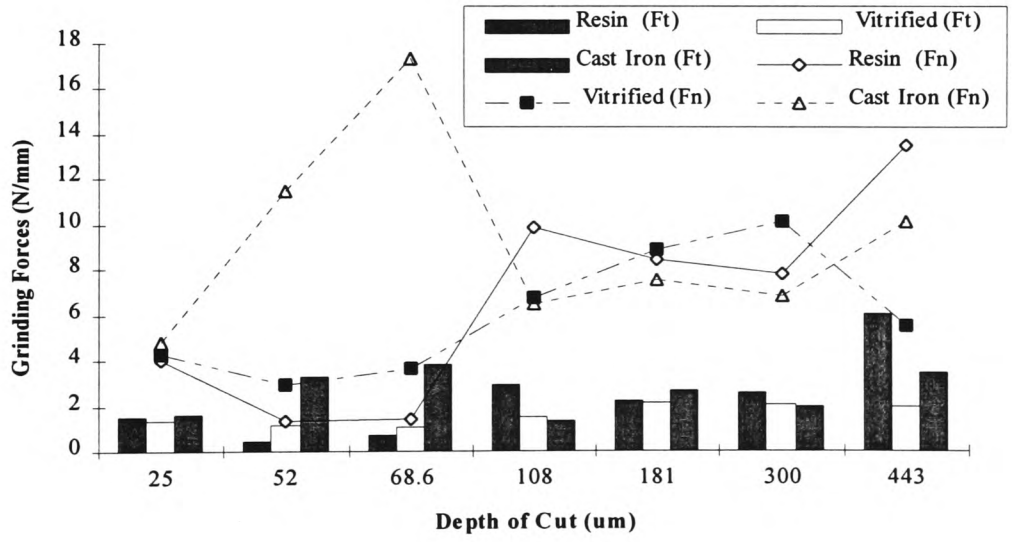

Figure 97: Grinding forces against depth of cut for different levels of bond type.

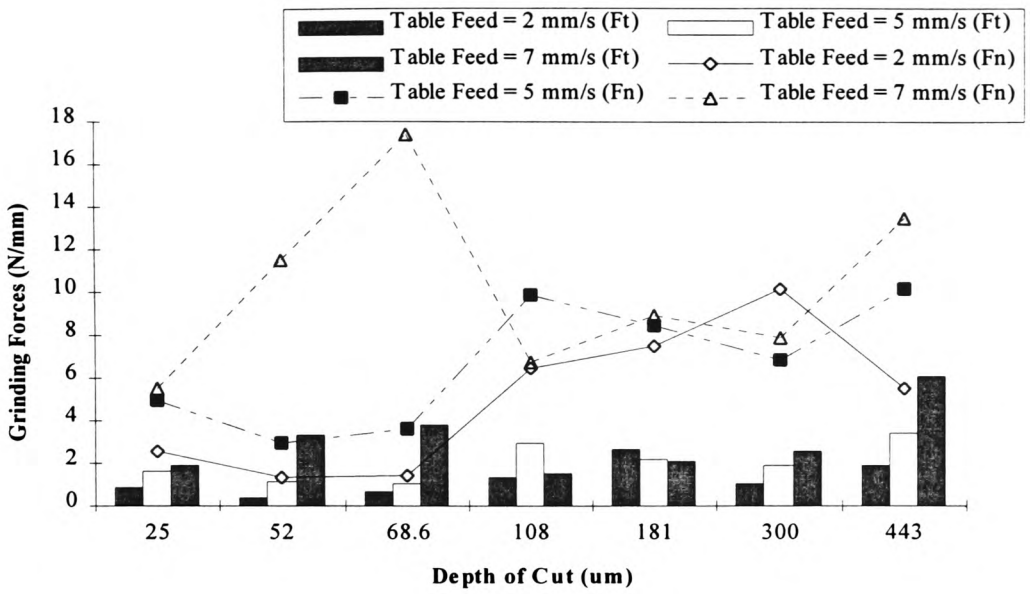

Figure 98: Grinding forces against depth of cut for different levels of table feed.

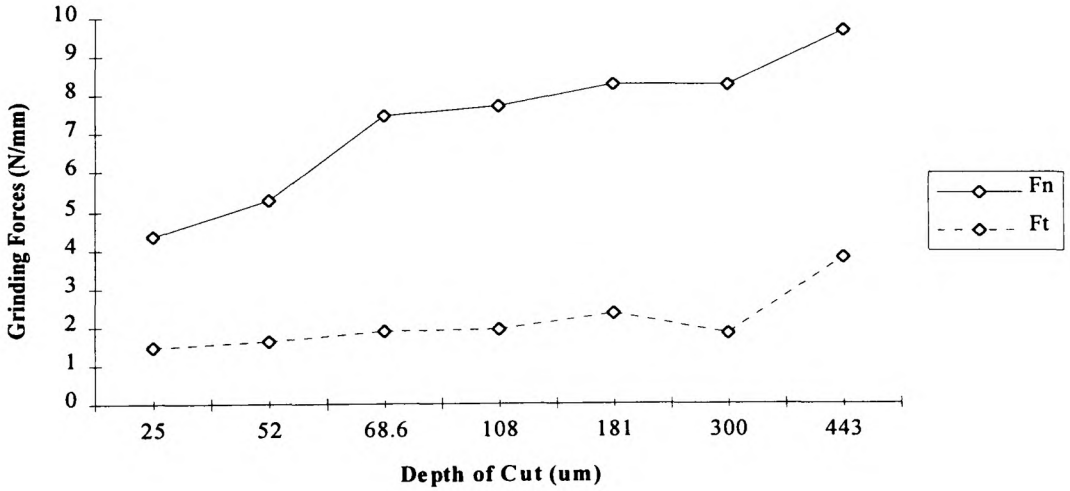

Figure 99: Grinding forces against depth of cut averaged over different levels of table feed.

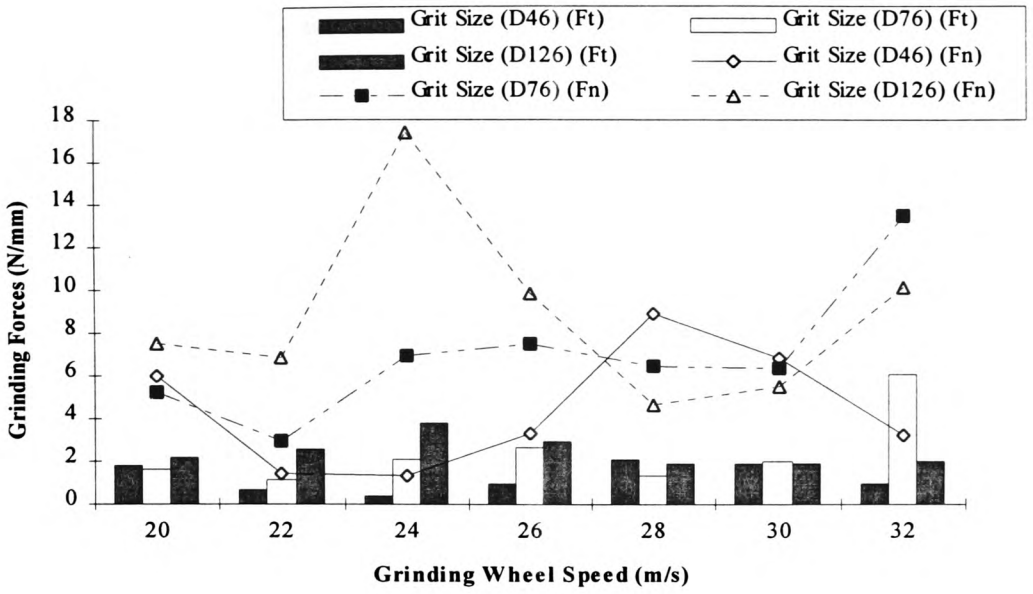

Figure 100: Grinding forces against grinding wheel speed for different levels of grit size.

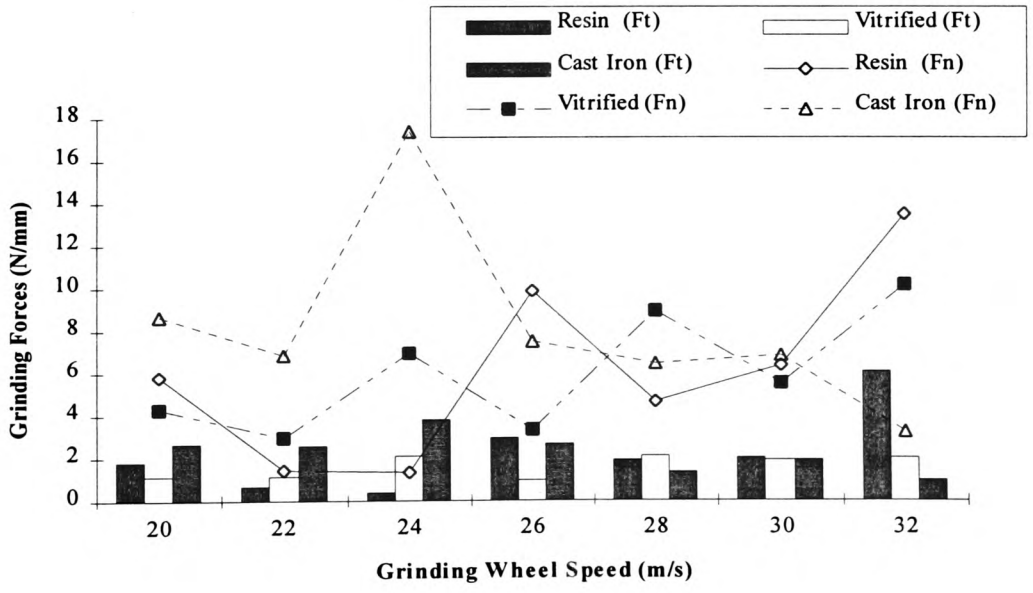

Figure 101: Grinding forces against grinding wheel speed for different levels of bond type.

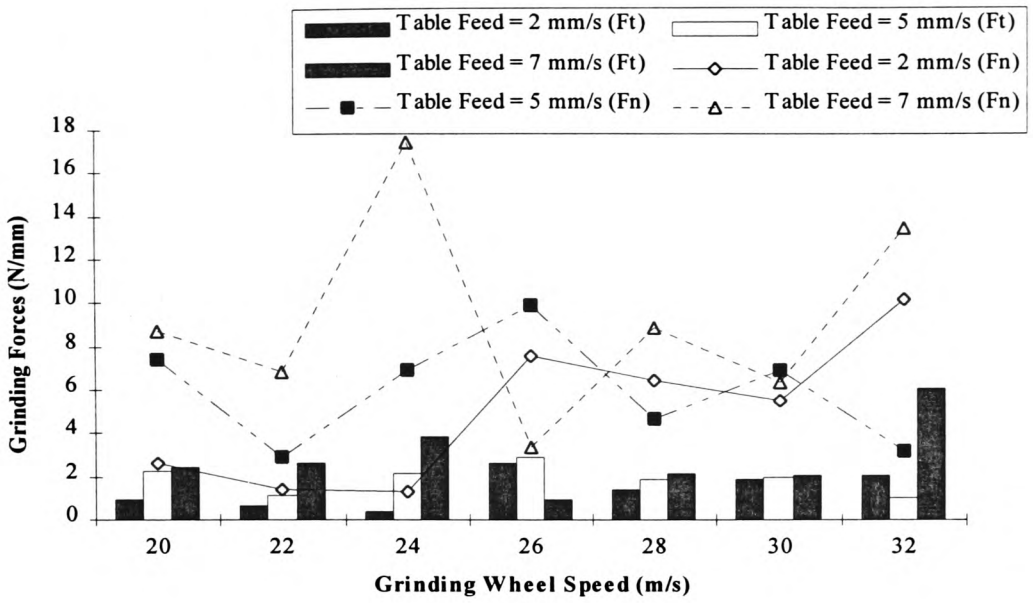

Figure 102: Grinding forces against grinding wheel speed for different levels of table feed.

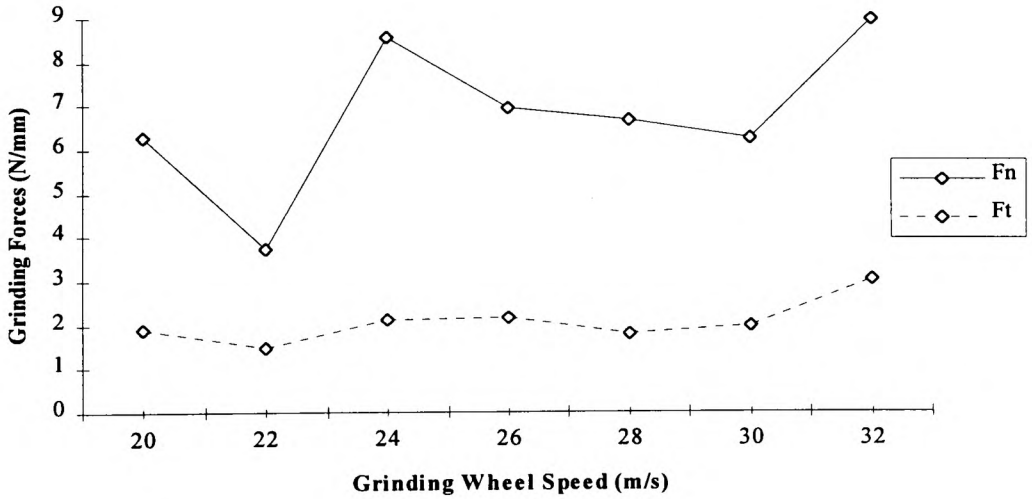

Figure 103: Grinding forces against grinding wheel speed averaged over different levels of table feed.

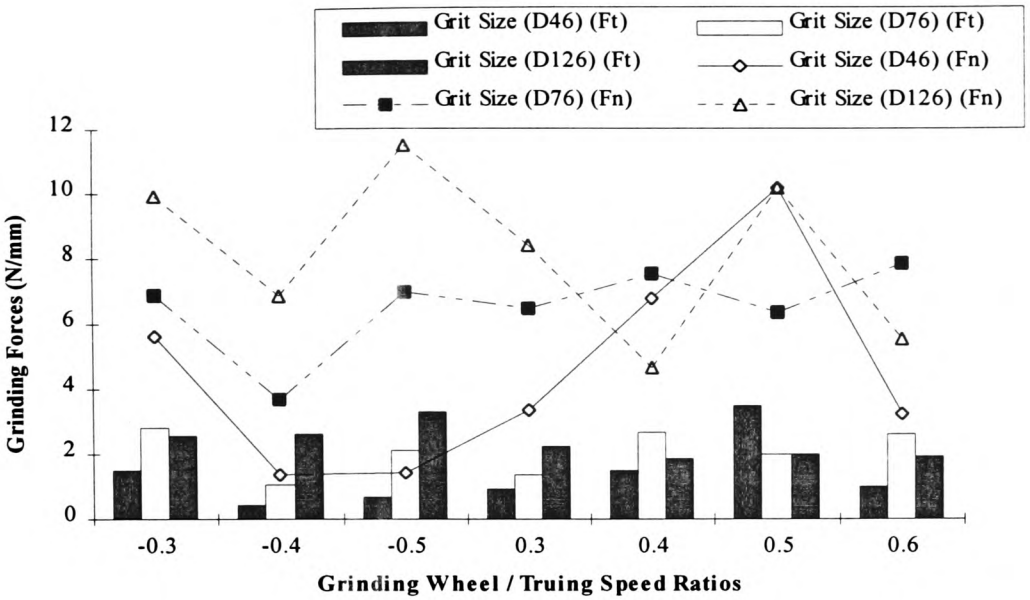

Figure 104: Grinding forces against grinding wheel/truing speed ratios for different levels of grit size.

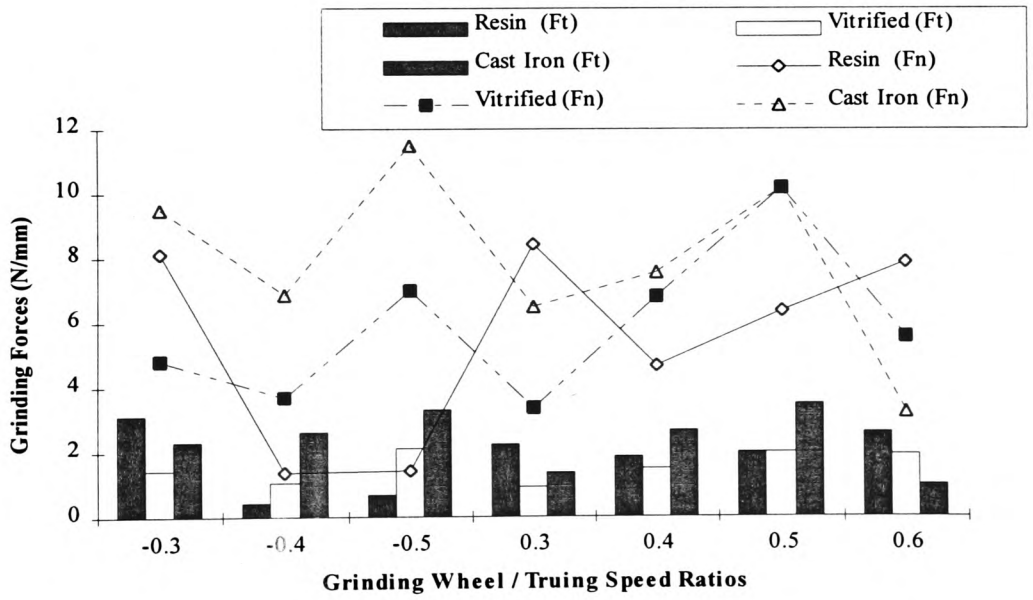

Figure 105: Grinding forces against grinding wheel/truing speed ratios for different levels of bond type.

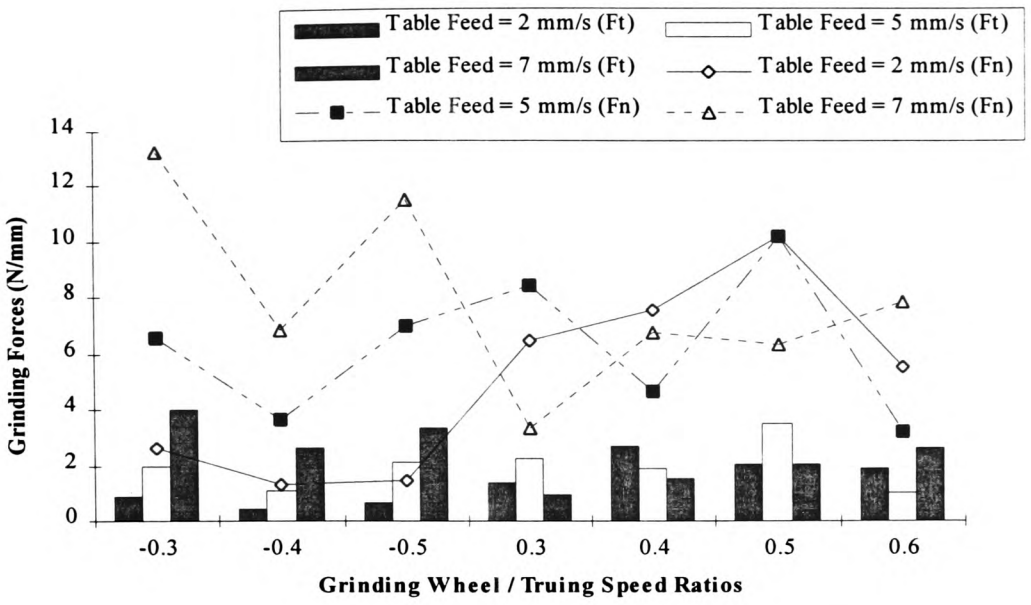

Figure 106: Grinding forces against grinding wheel/truing speed ratios for different levels of table feed.

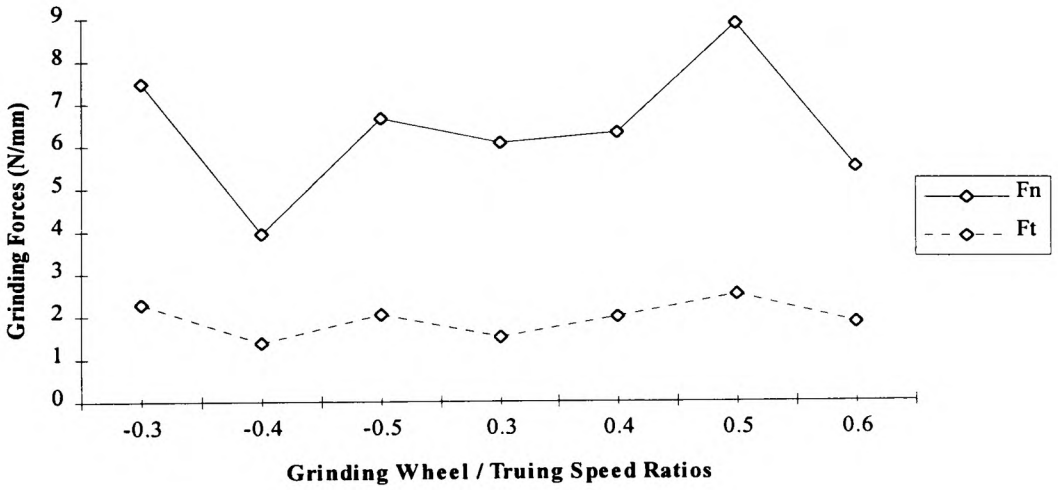

Figure 107: Grinding forces against grinding wheel/truing speed ratios averaged over different levels of table feed.

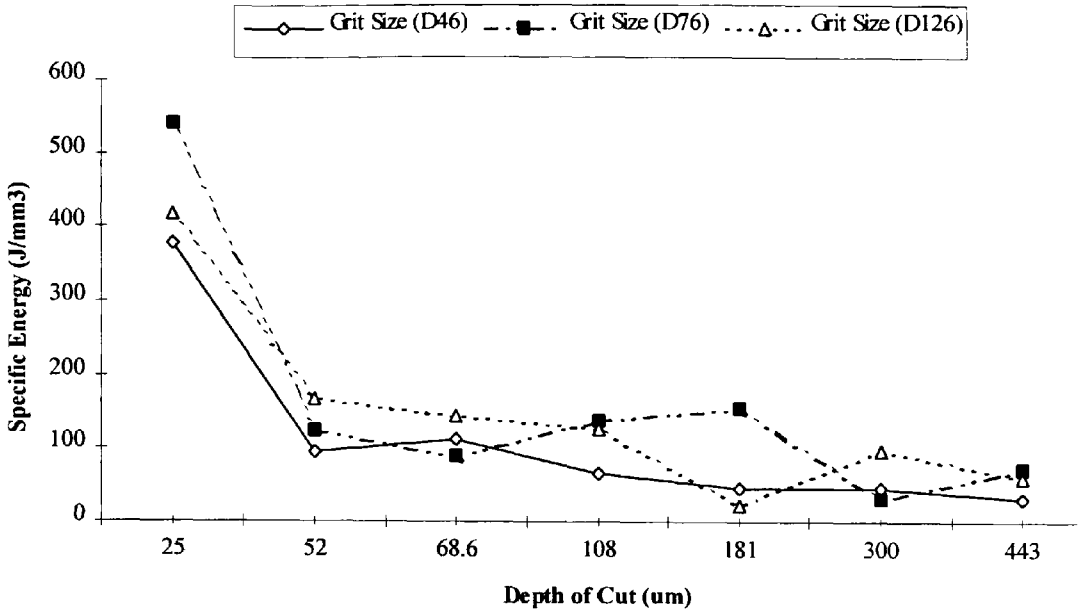

Figure 108: Specific energy against depth of cut for different levels of grit size.

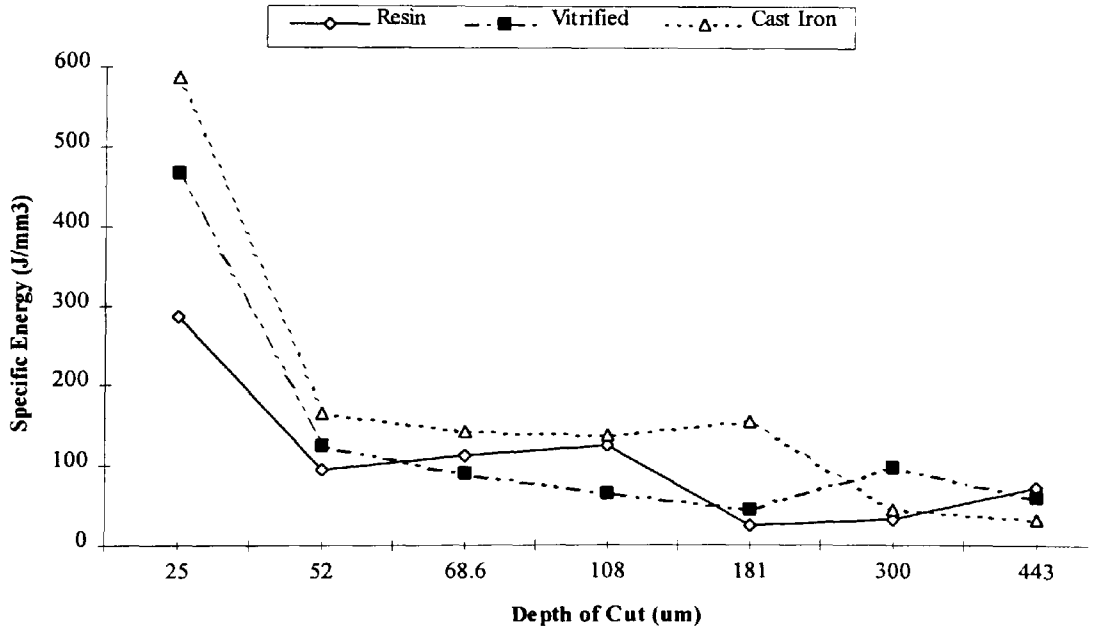

Figure 109: Specific energy against depth of cut for different levels of bond type.

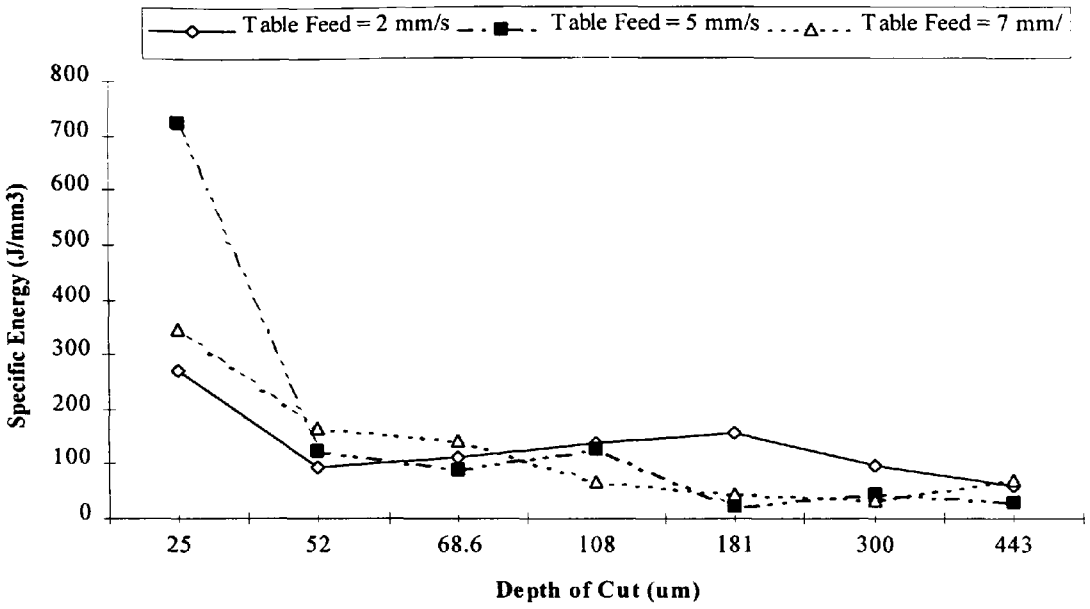

Figure 110: Specific energy against depth of cut for different levels of table feed.

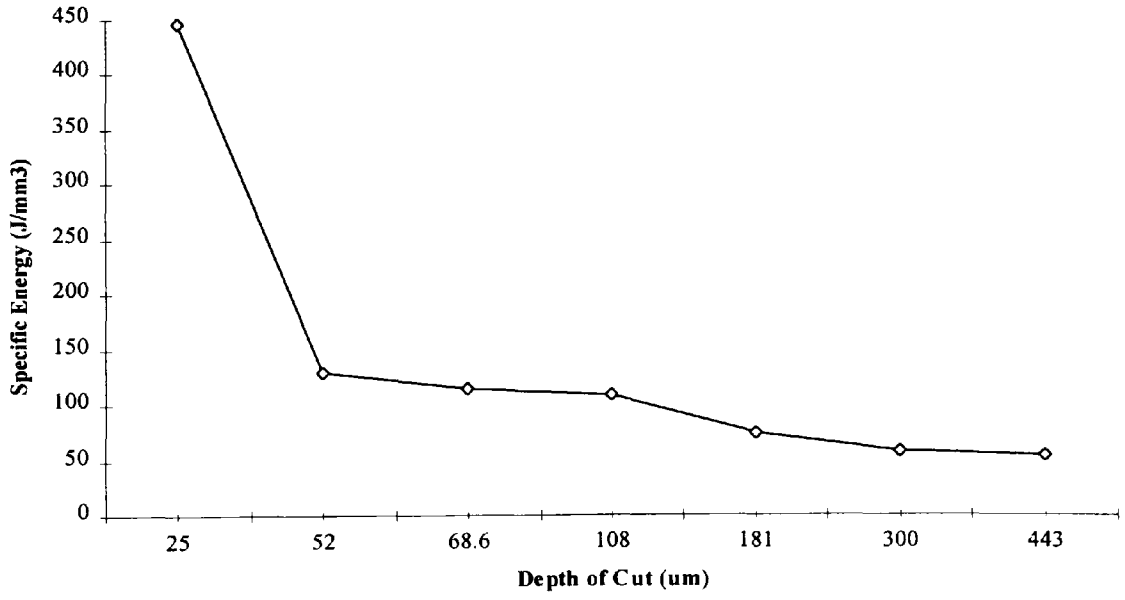

Figure 111: Specific energy against depth of cut averaged over different levels of table feed.

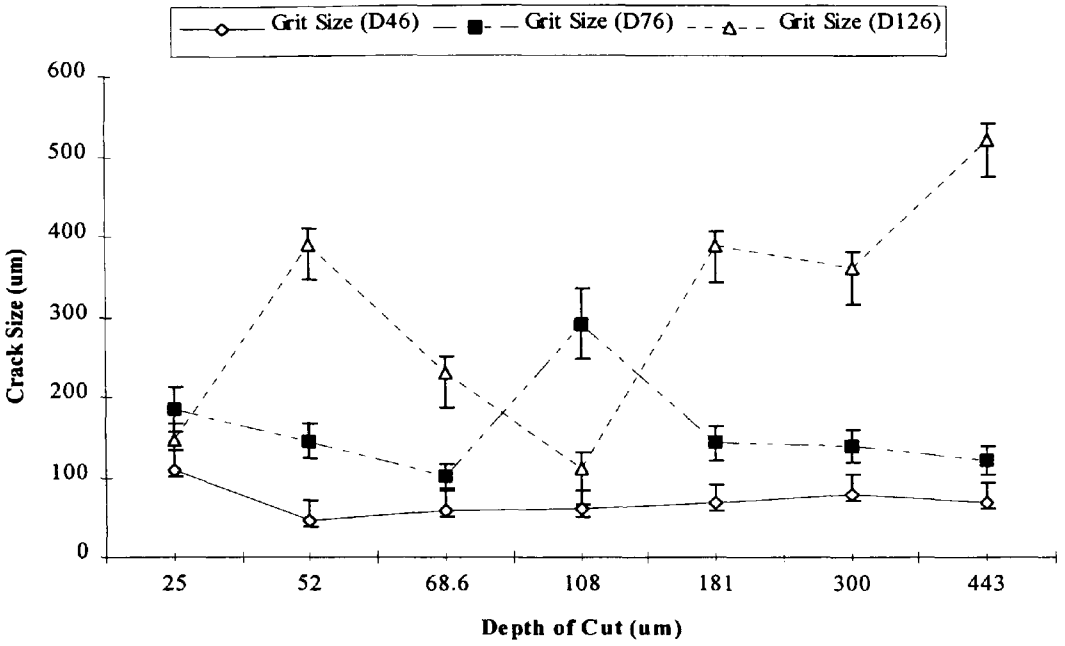

Figure 112: Estimated crack size against depth of cut for different levels of grit size.

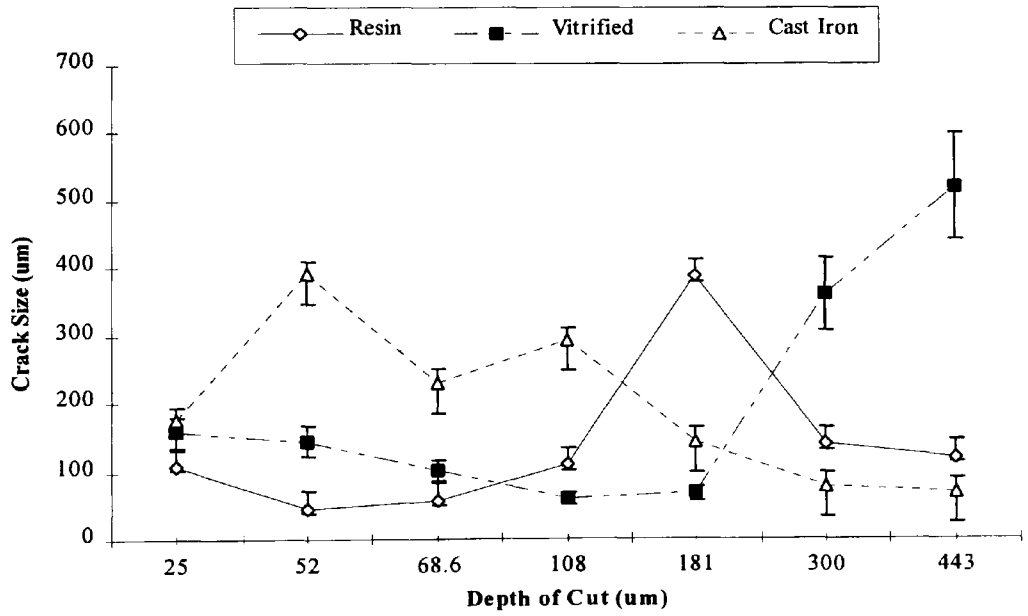

Figure 113: Estimated crack size against depth of cut for different levels of bond type.

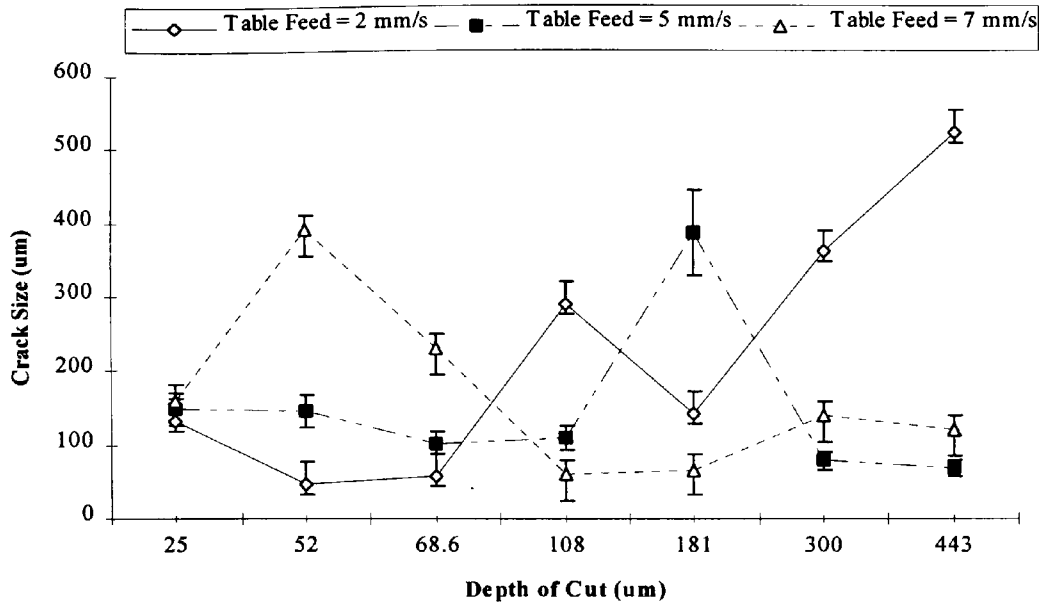

Figure 114: Estimated crack size against depth of cut for different levels of table feed.

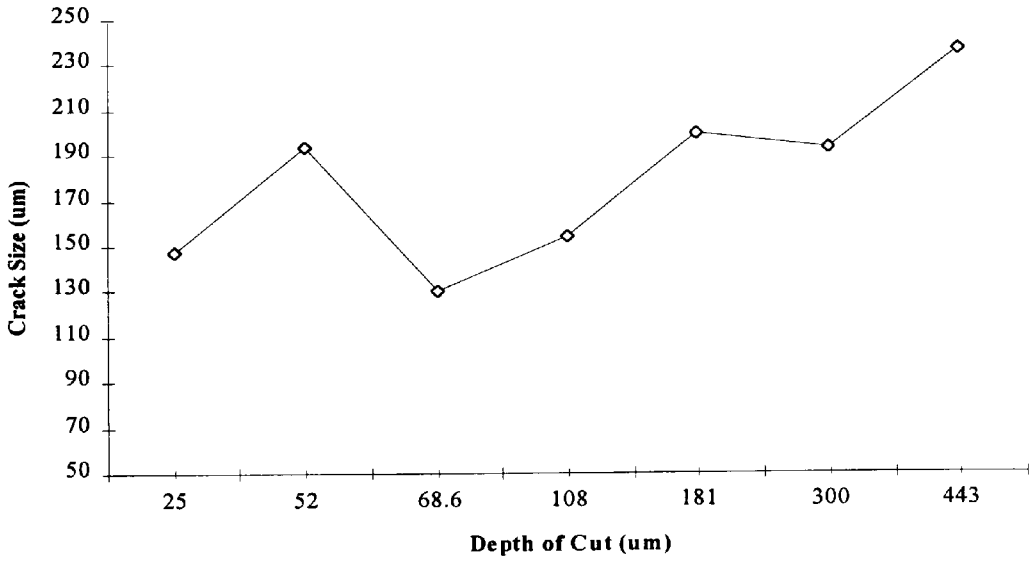

Figure 115: Estimated crack size against depth of cut averaged over different levels of table feed.

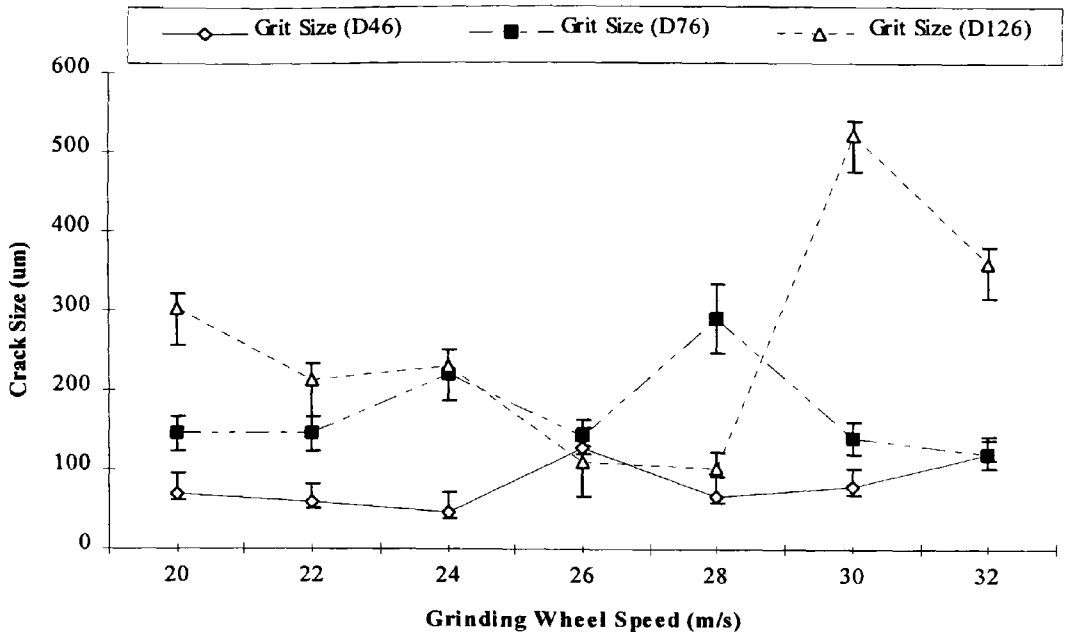

Figure 116: Estimated crack size against grinding wheel speed for different levels of grit size.

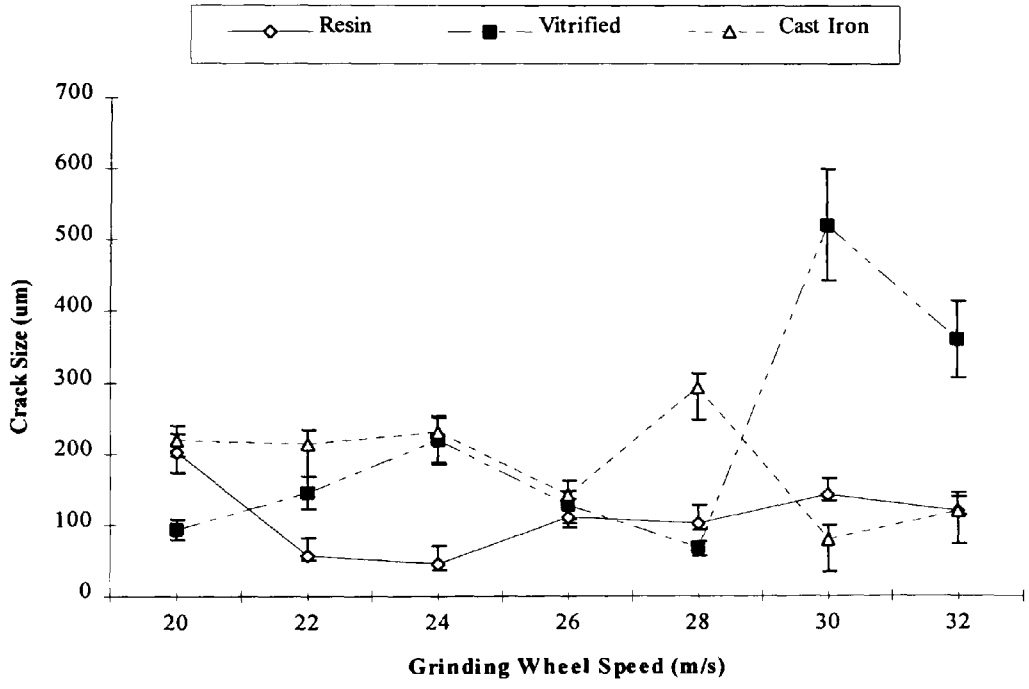

Figure 117: Estimated crack size against grinding wheel speed for different levels of bond type.

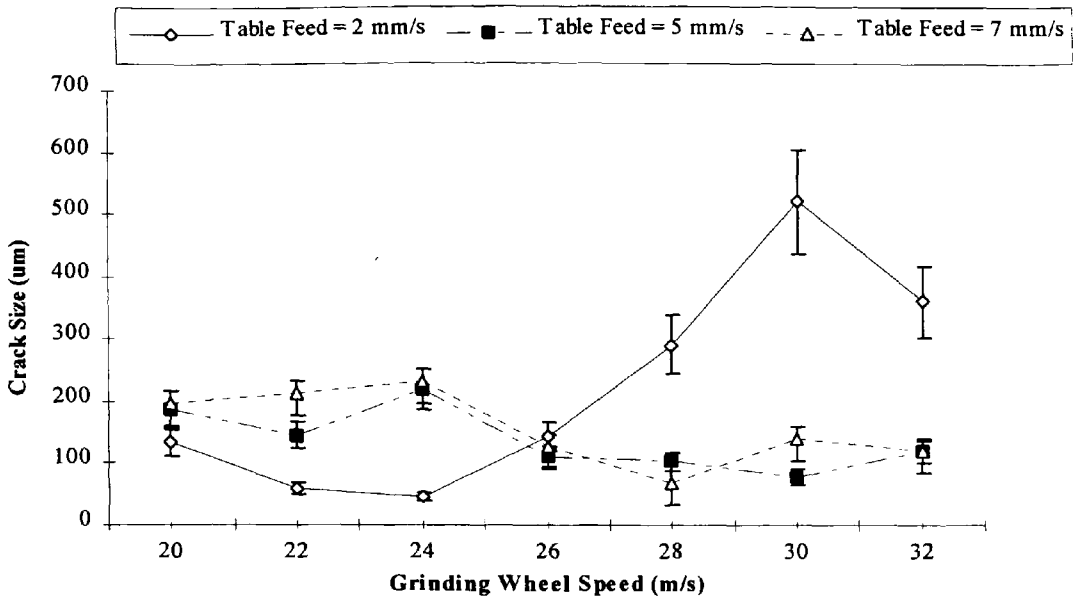

Figure 118: Estimated crack size against grinding wheel speed for different levels of table feed.

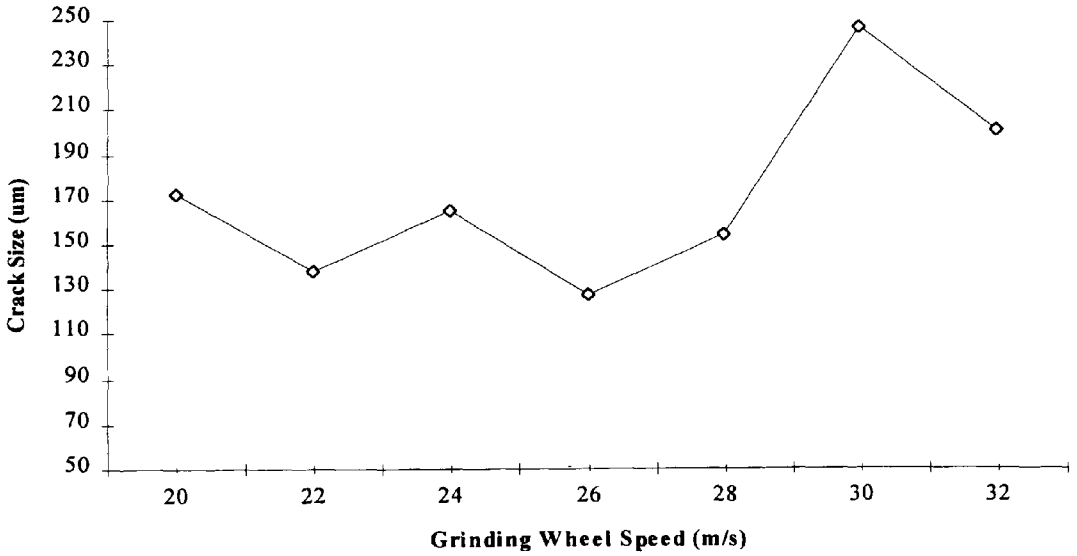

Figure 119: Estimated crack size against grinding wheel speed averaged over different levels of table feed.

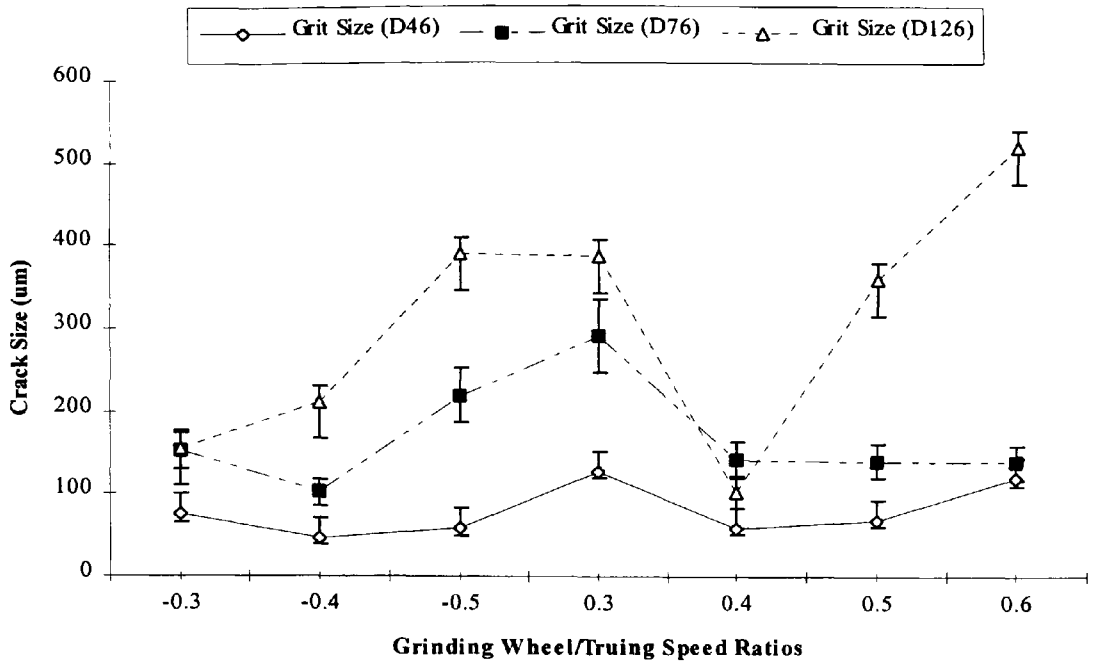

Figure 120: Estimated crack size against grinding wheel/truing speed ratios for different levels of grit size.

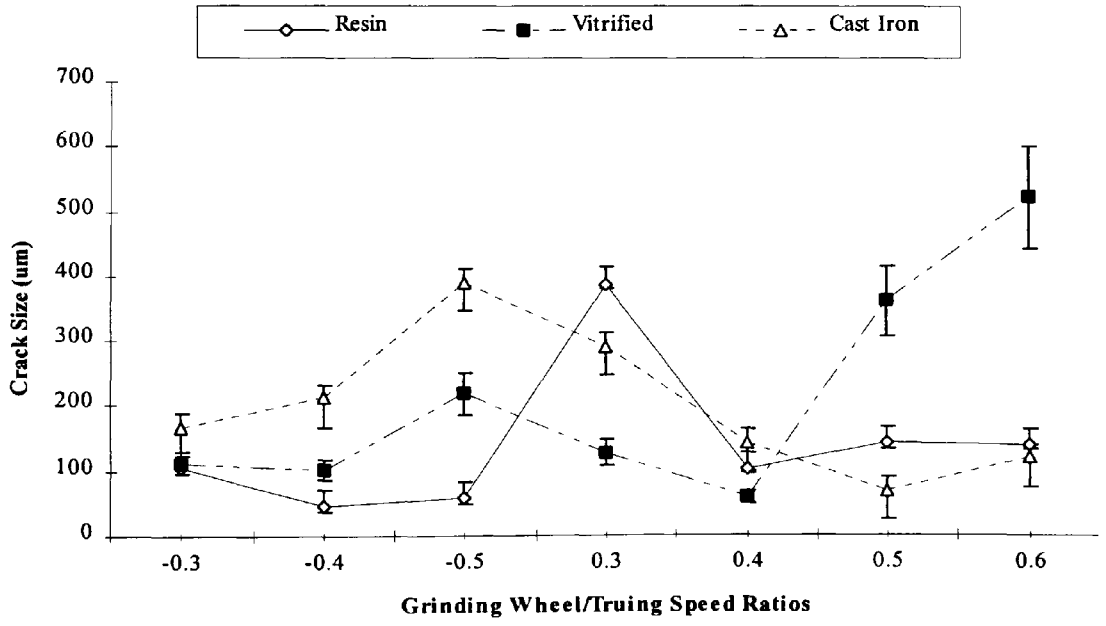

Figure 121: Estimated crack size against grinding wheel/truing speed ratios for different levels of bond type.

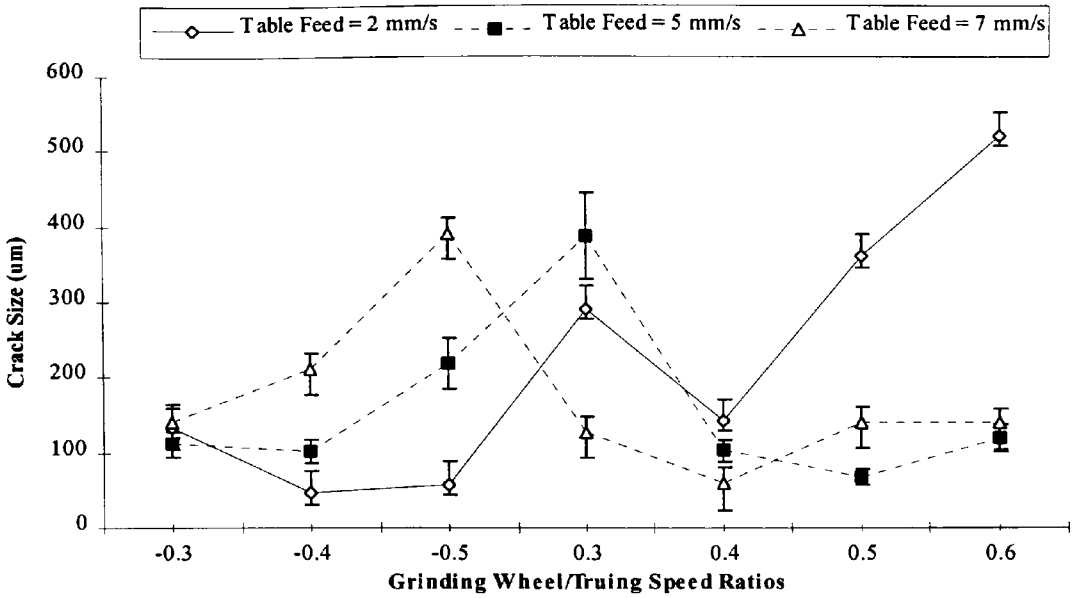

Figure 122: Estimated crack size against grinding wheel/truing speed ratios for different levels of table feed.

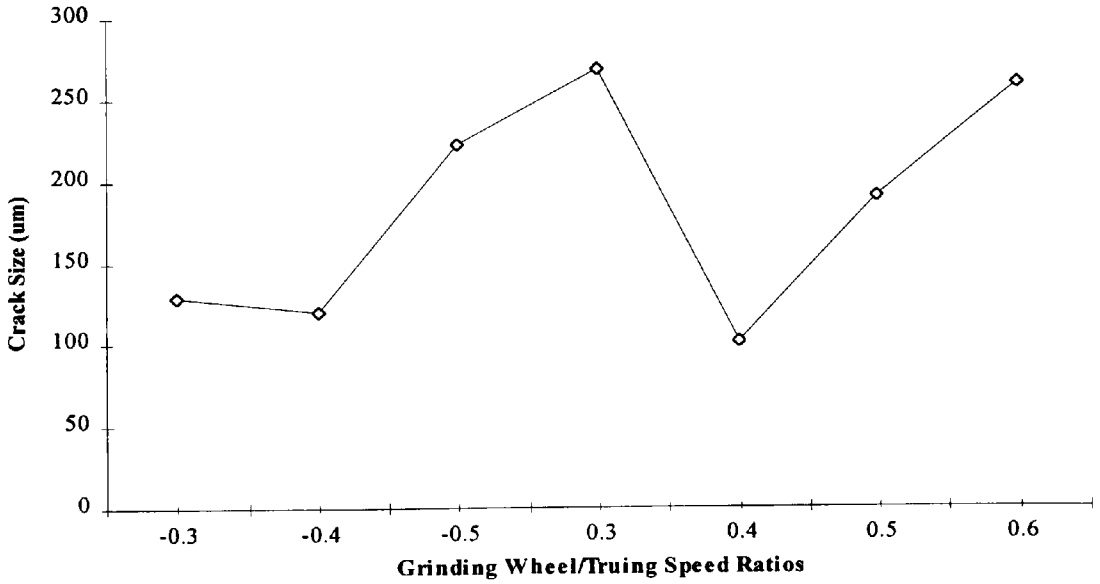

Figure 123: Estimated crack size against grinding wheel/truing speed ratios averaged over different levels of table feed.

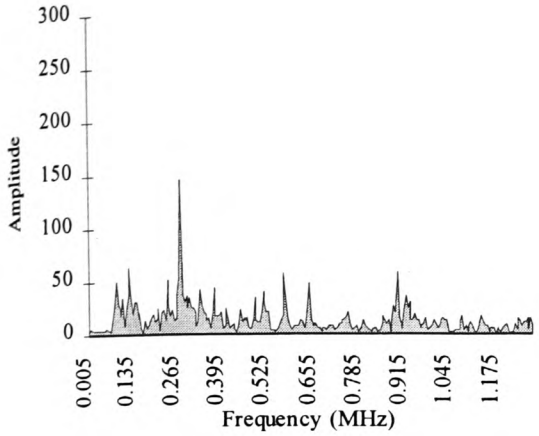

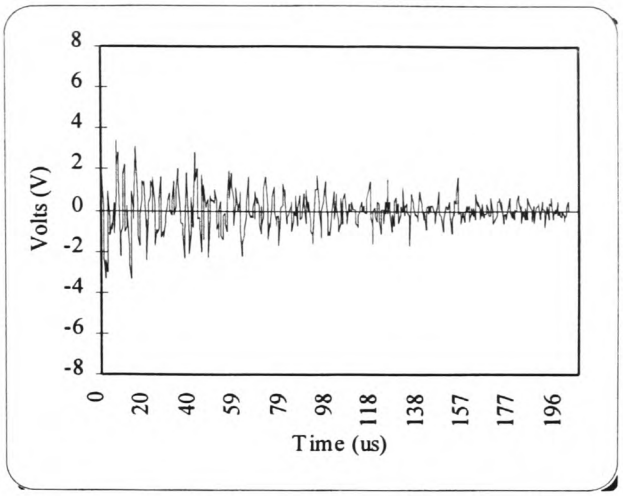

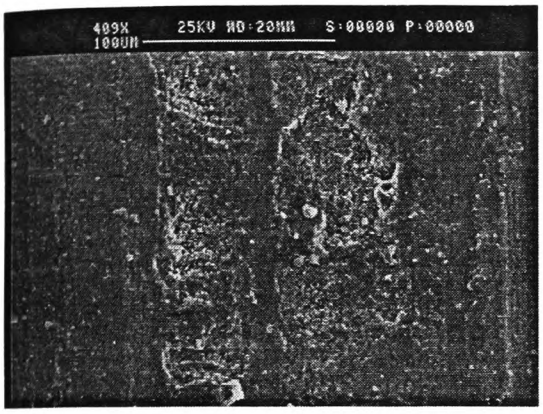

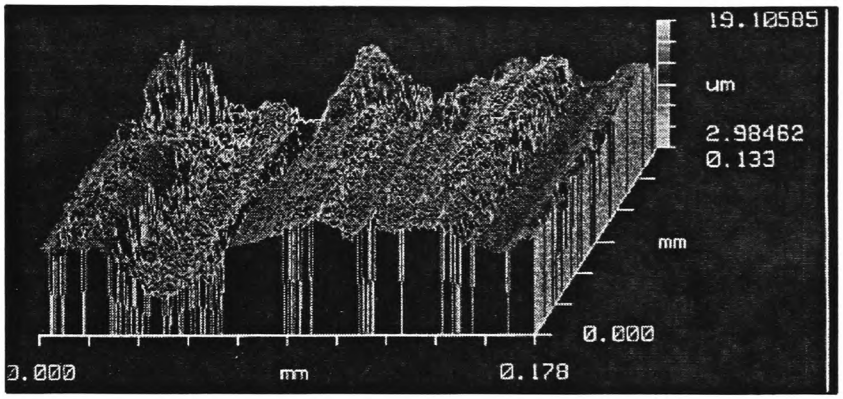

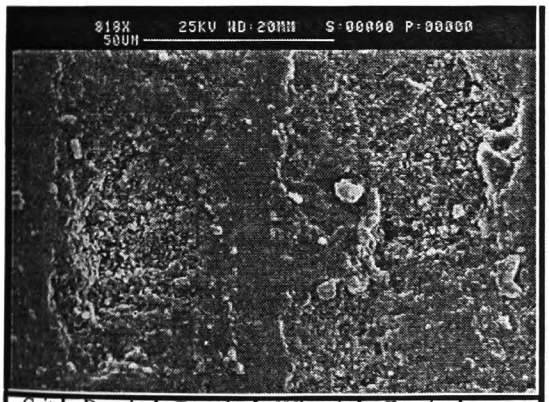

Grit size	Bond type	Depth of cut µm	Wheel speed m/s	Feed rate mm/s	G/D
D126	Cast iron	91.3	24	7	-0.3

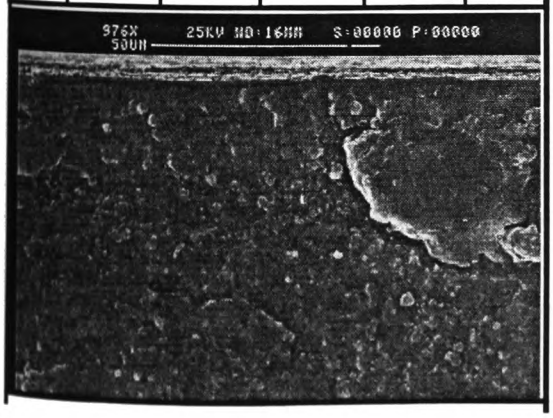

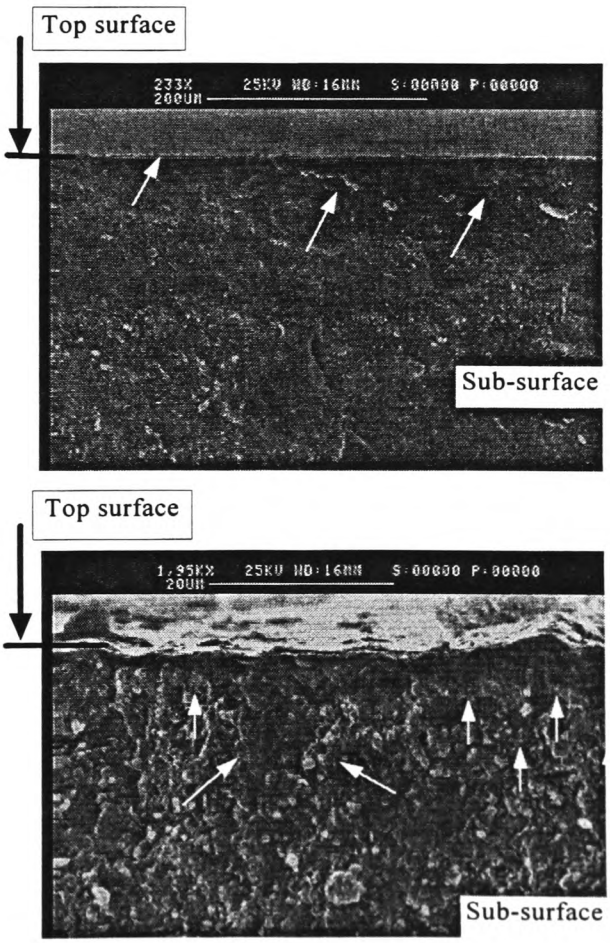

Figure 124: Correlation of AE, SEM and 3D topography for rough ground ceramic condition at the parameters mentioned above.

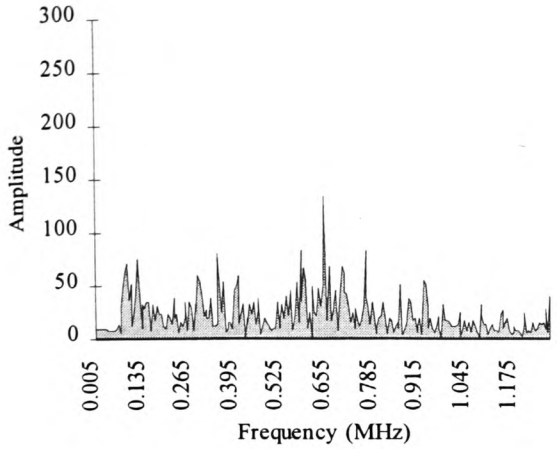

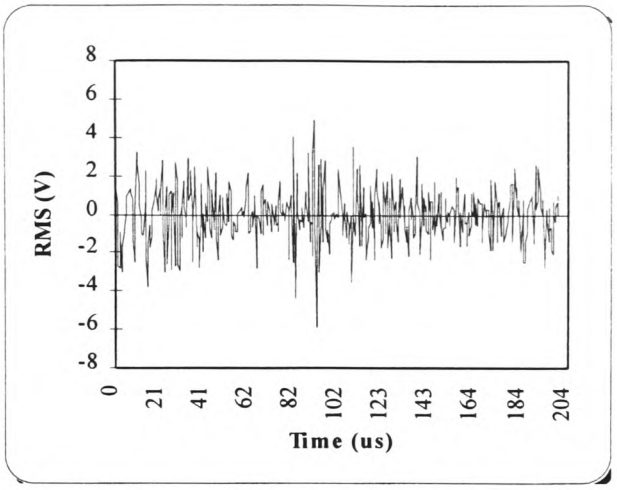

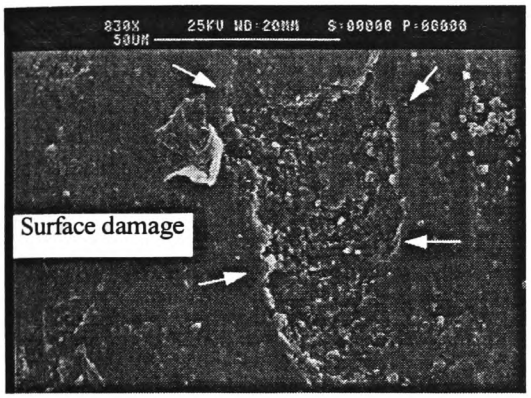

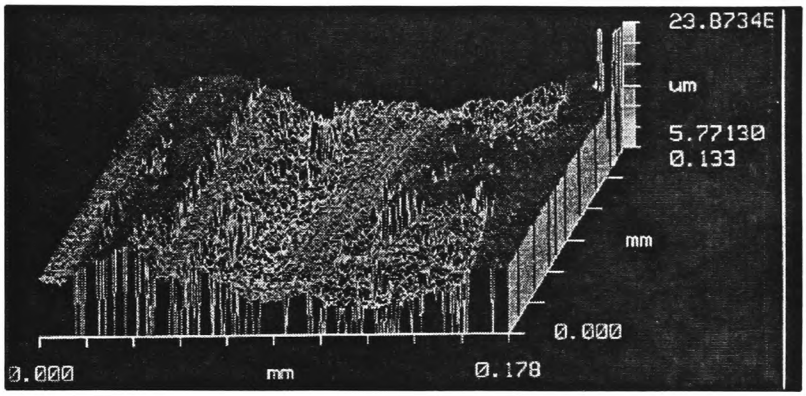

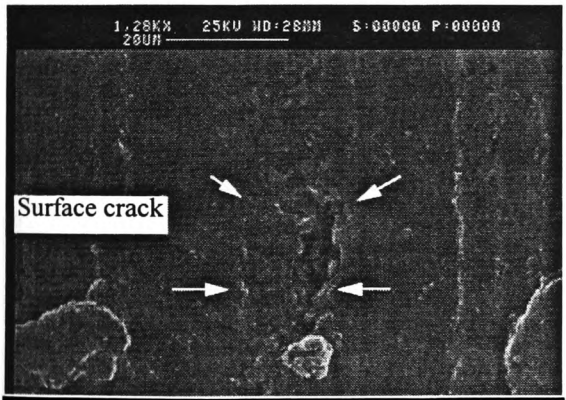

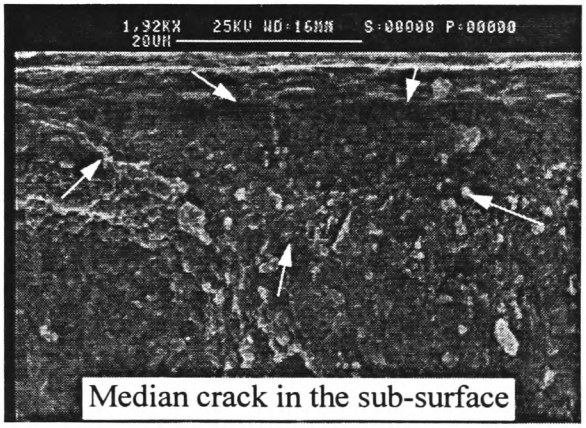

Grit size	Bond type	Depth of cut µm	Wheel speed m/s	Feed rate mm/s	G/D
D126	Cast iron	57	20	7	-0. 5

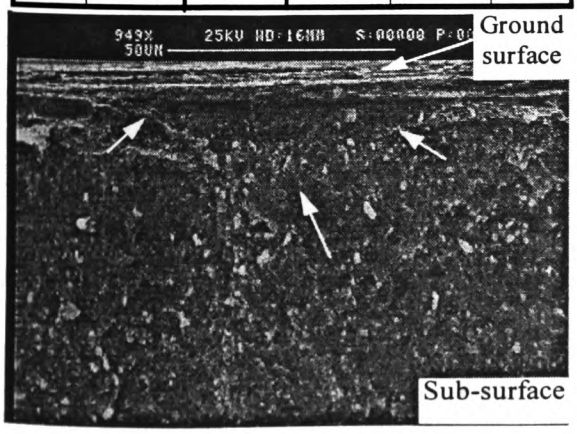

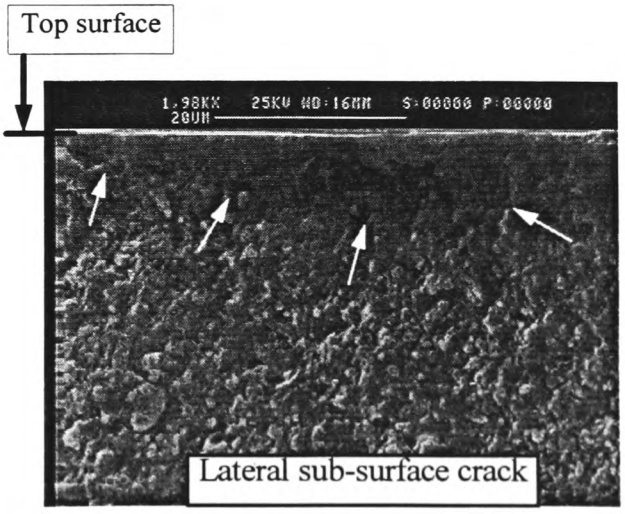

Figure 125: Correlation of AE, SEM and 3D topography for rough ground ceramic condition at the parameters mentioned above.

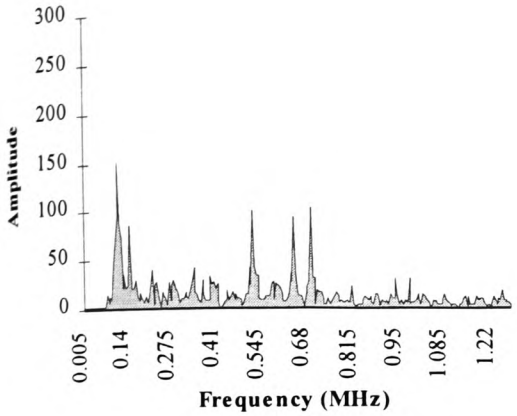

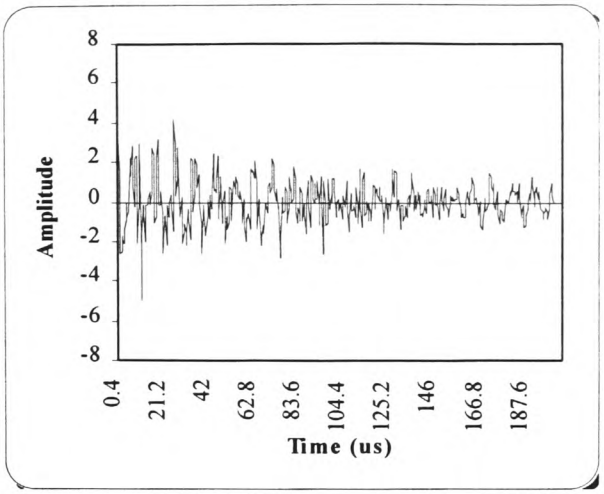

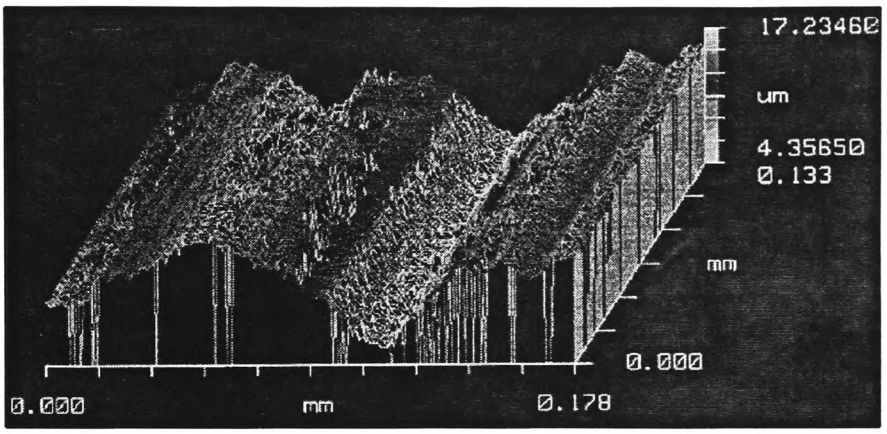

Surface damage on the ground surface

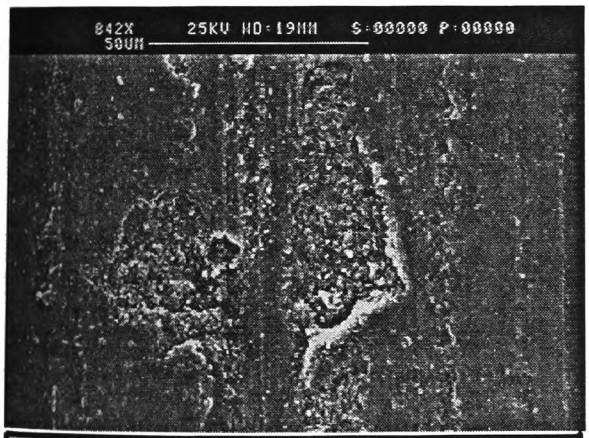

Grit size	Bond type	Depth of cut µm	Wheel speed m/s	Feed rate mm/s	G/D
D126	Resin	19.5	28	5	0.4

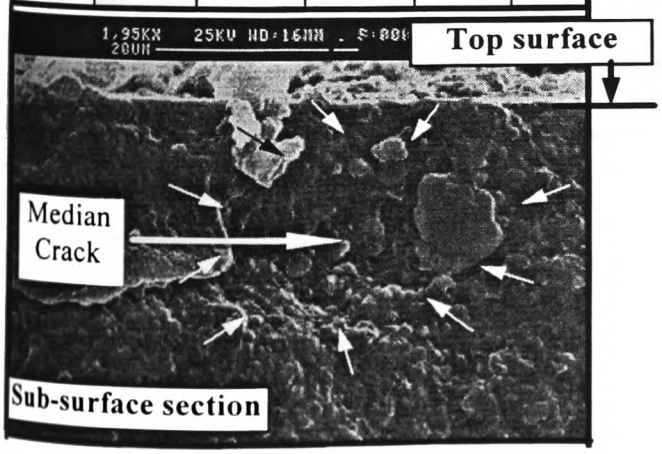

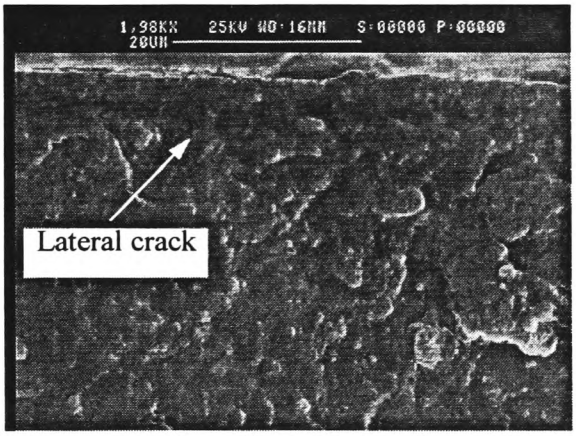

Lateral and median sub-surafce carcks located in a distance very close to the ground surface.

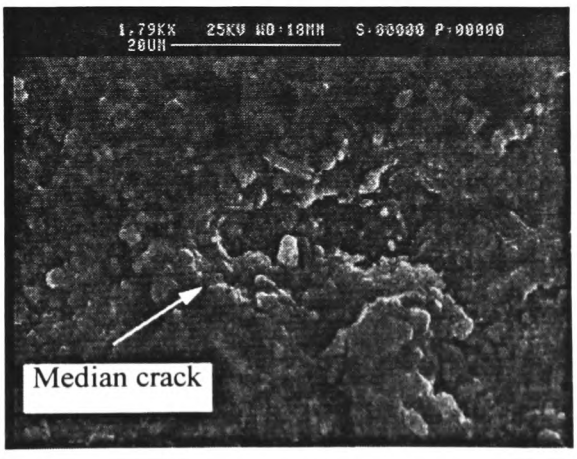

Figure 126: Correlation of AE, SEM and 3D topography for rough ground ceramic condition at the parameters mentioned above.

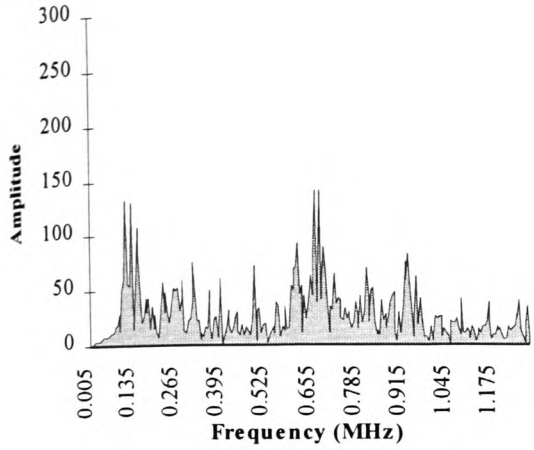

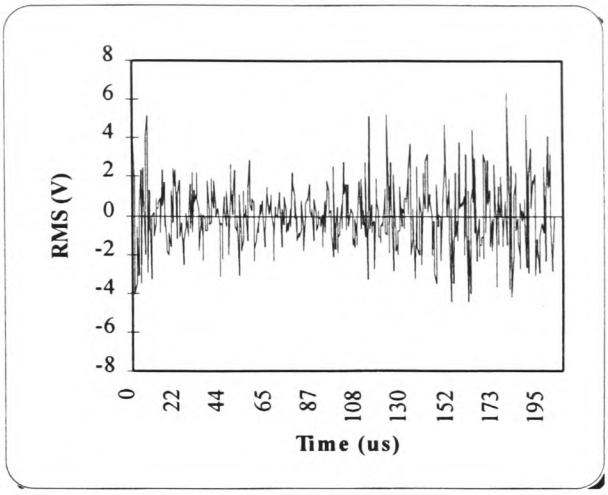

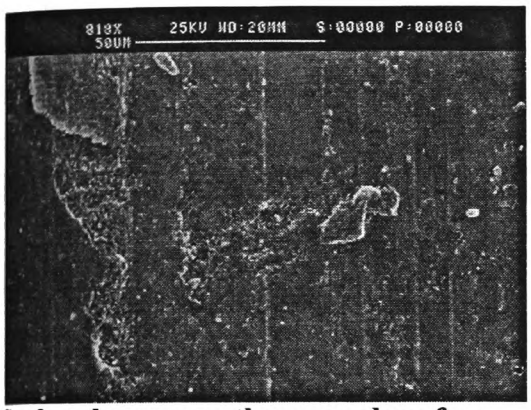

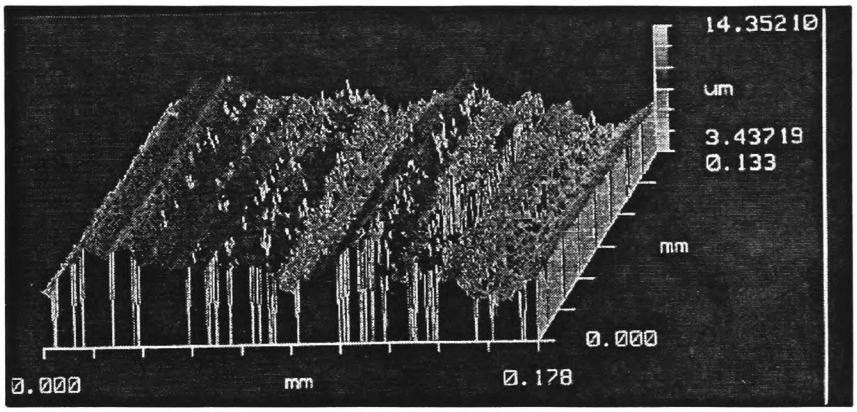

Surface damage on the ground surface

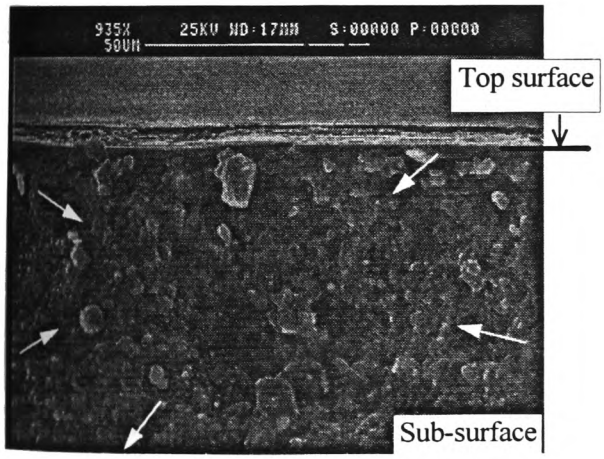

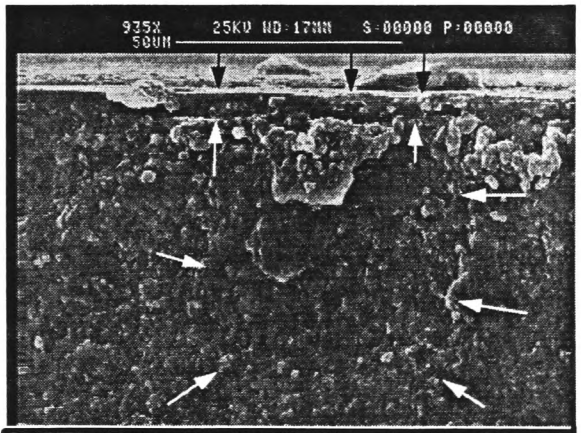

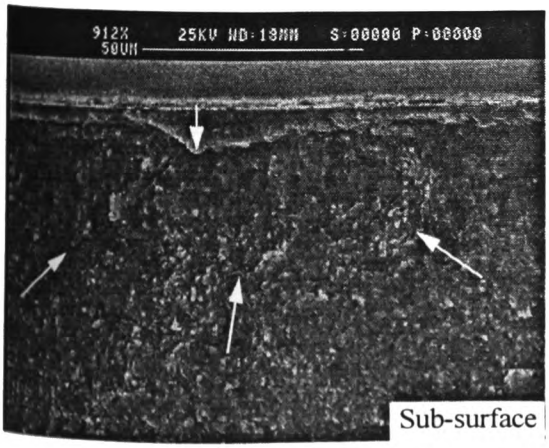

Grit size	Bond type	Depth of cut µm	Wheel speed m/s	Feed rate mm/s	G/D
D126	Resin	186	20	5	0.3

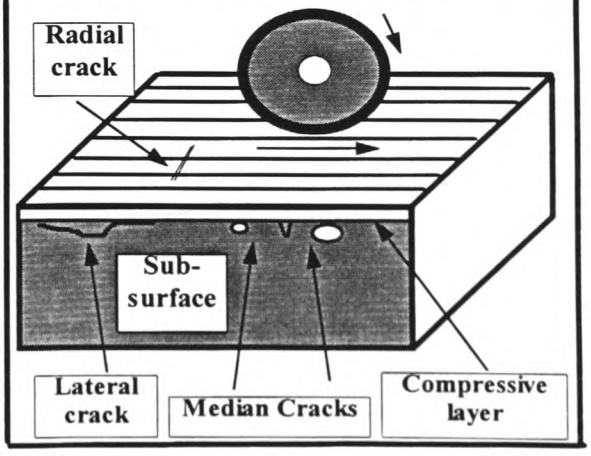

Figure 127: Correlation of AE, SEM and 3D topography for rough ground ceramic condition at the parameters mentioned above.

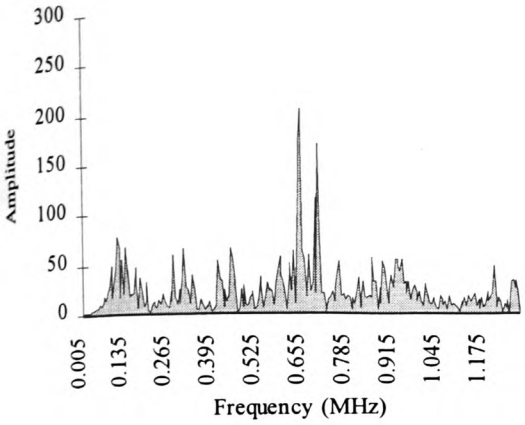

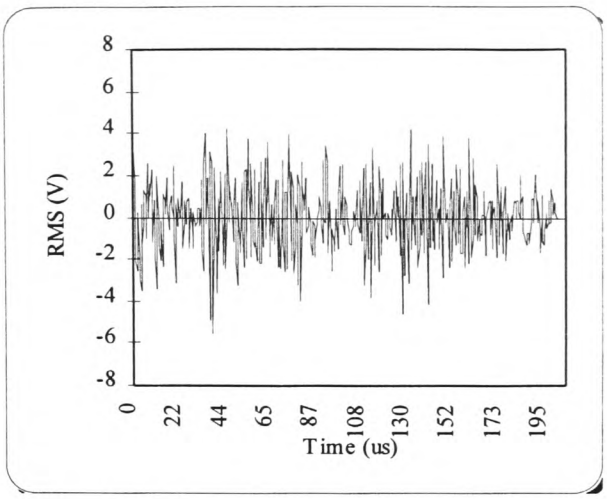

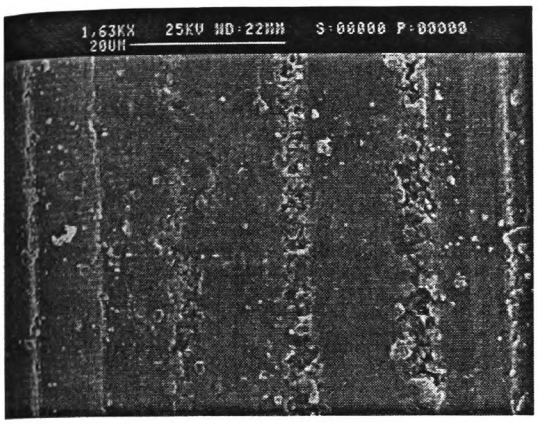

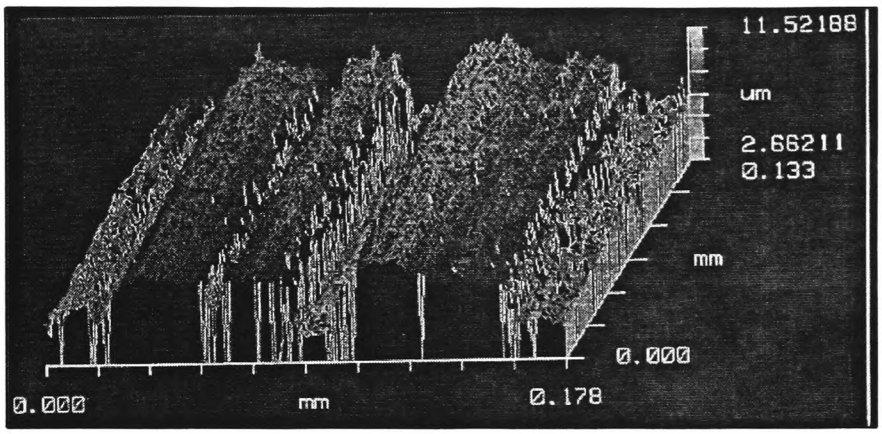

Surface damage on the ground surface

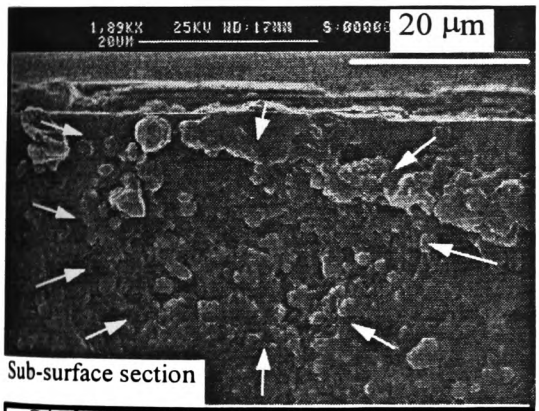

Grit size	Bond type	Depth of cut µm	Wheel speed m/s	Feed rate mm/s	G/D
D126	Resin	120	26	5	-0.3

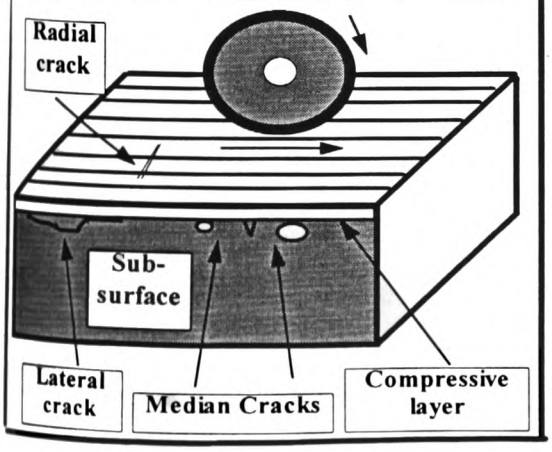

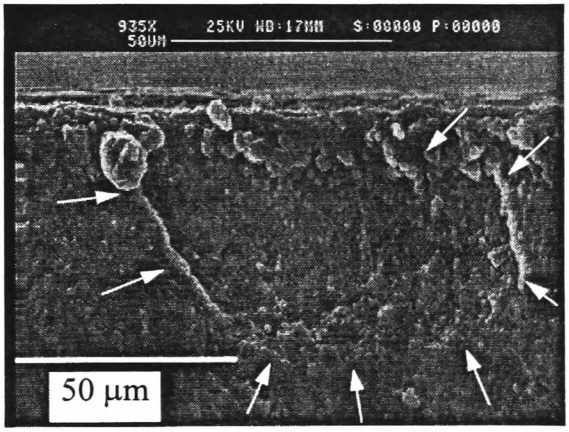

Top surface at breakage point

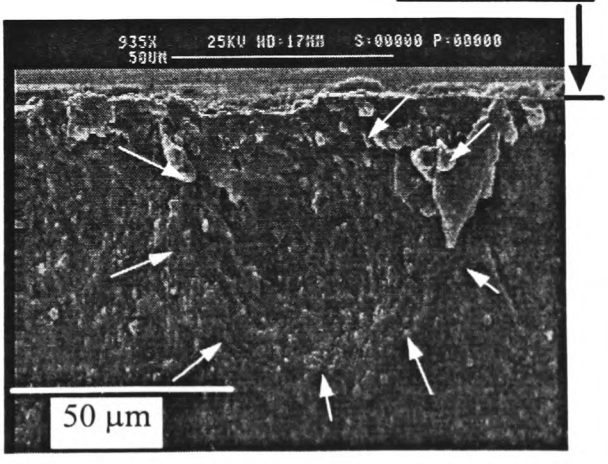

Figure 128: Correlation of AE, SEM and 3D topography for rough ground ceramic condition at the parameters mentioned above.

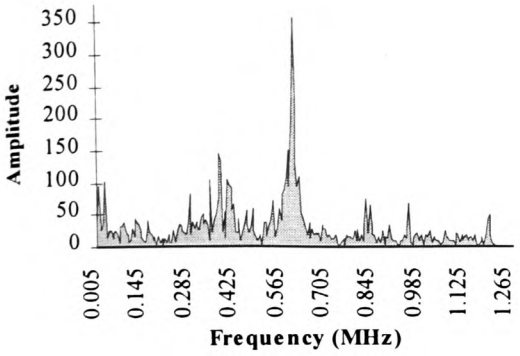

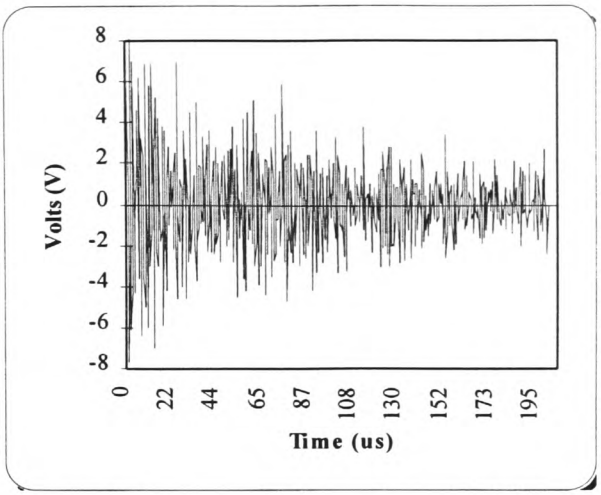

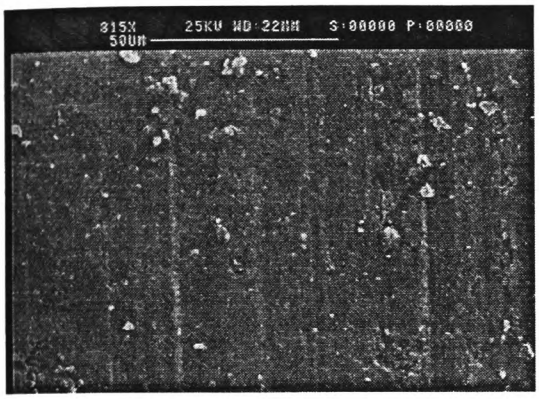

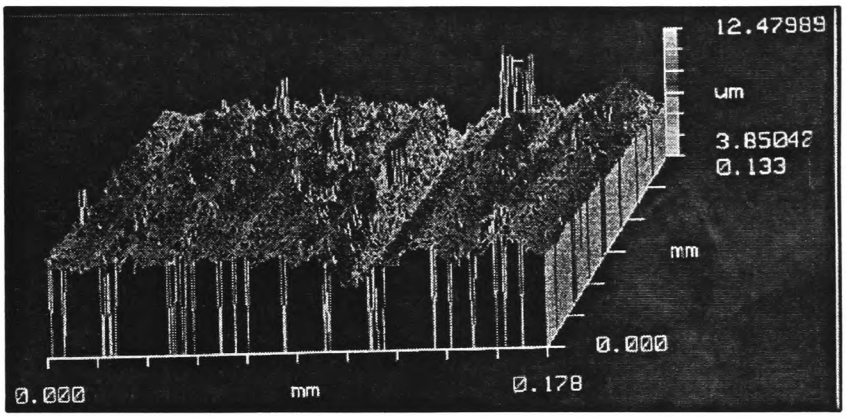

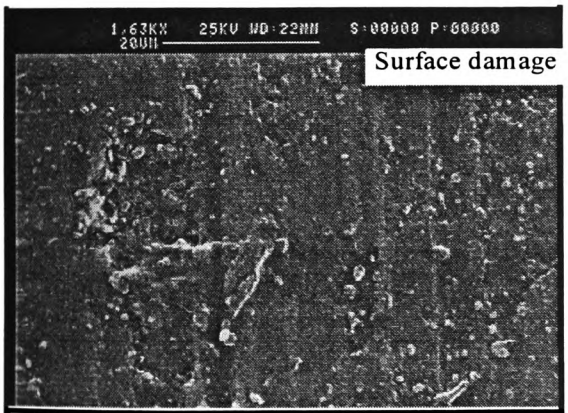

Grit size	Bond type	Depth of cut µm	Wheel speed m/s	Feed rate mm/s	G/D
D46	Cast iron	6	32	7	0.6

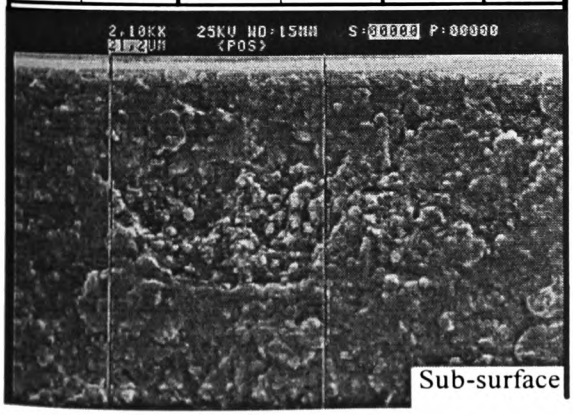

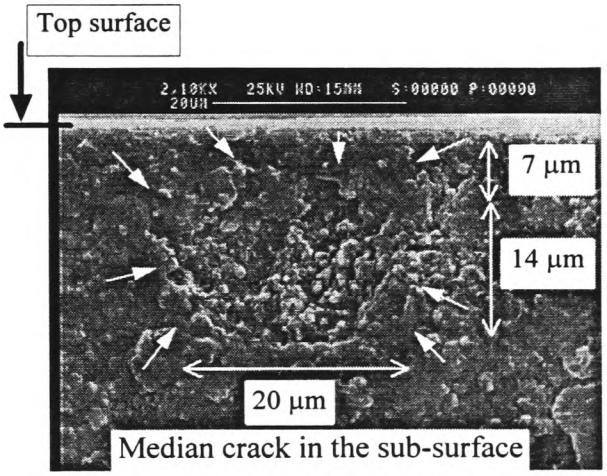

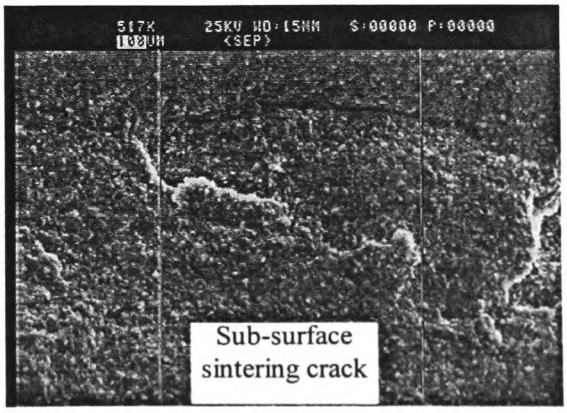

Figure 129: Correlation of AE, SEM and 3D topography for smooth ground ceramic condition at the parameters mentioned above.

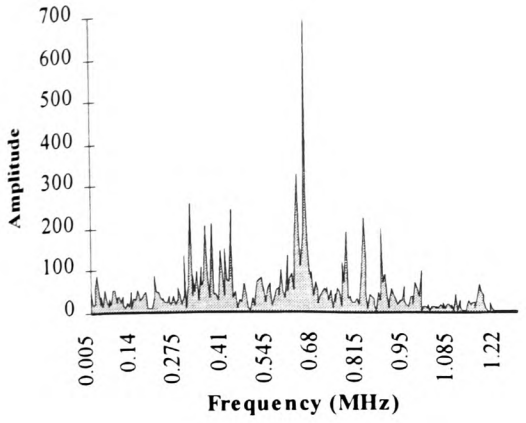

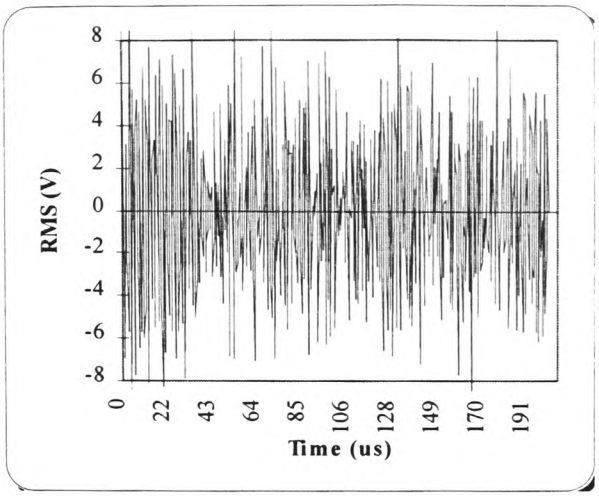

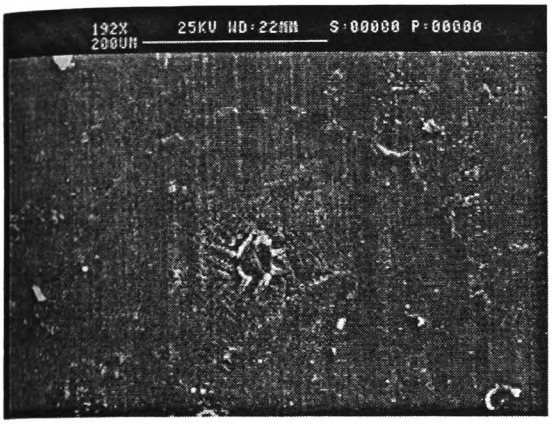

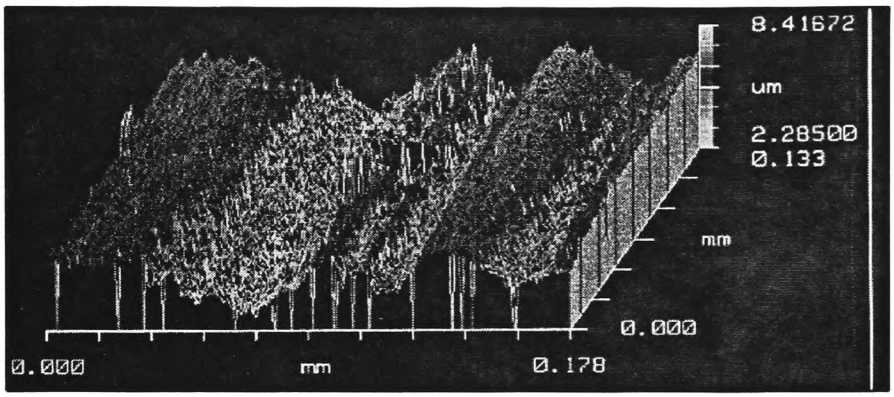

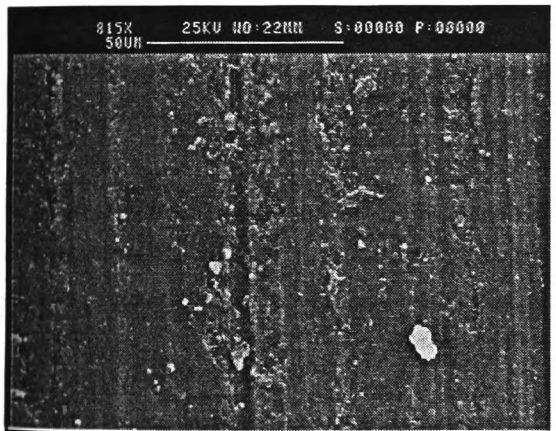

Grit size	Bond type	Depth of cut µm	Wheel speed m/s	Feed rate mm/s	G/D
D46	Cast iron	288	30	5	-0.3

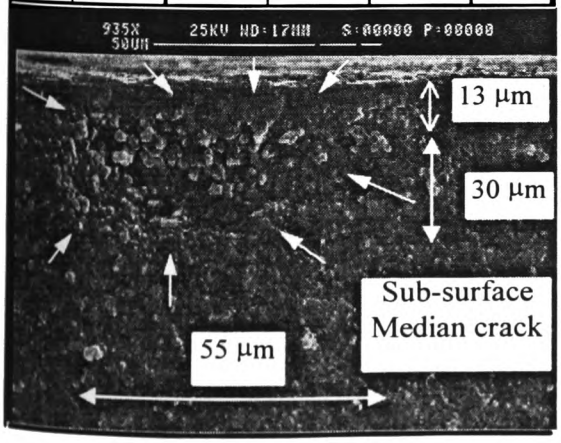

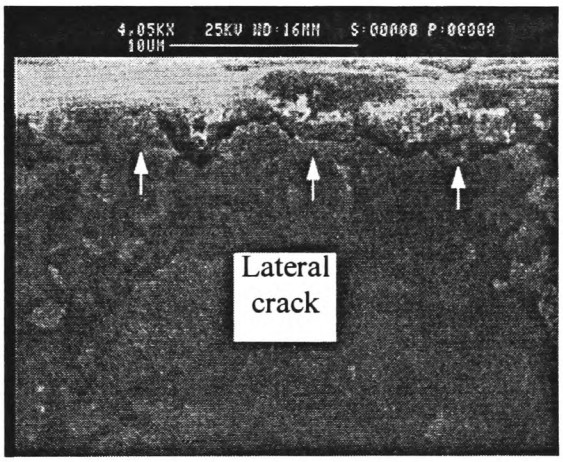

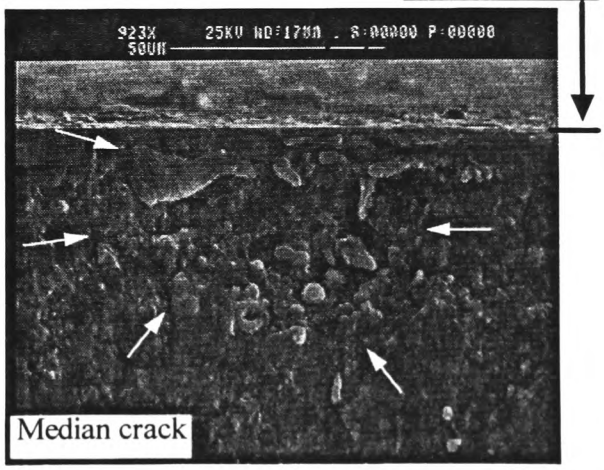

Figure 130: Correlation of AE, SEM and 3D topography for smooth ground ceramic condition at the parameters mentioned above.

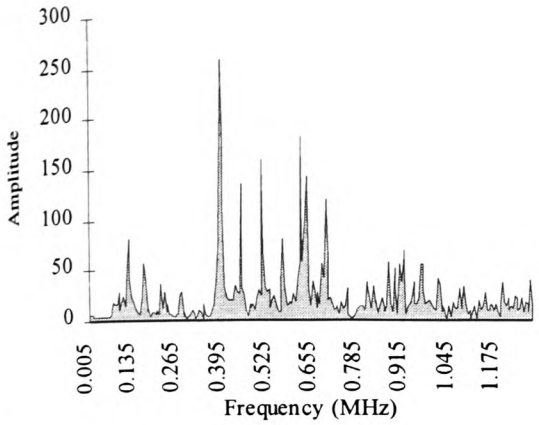

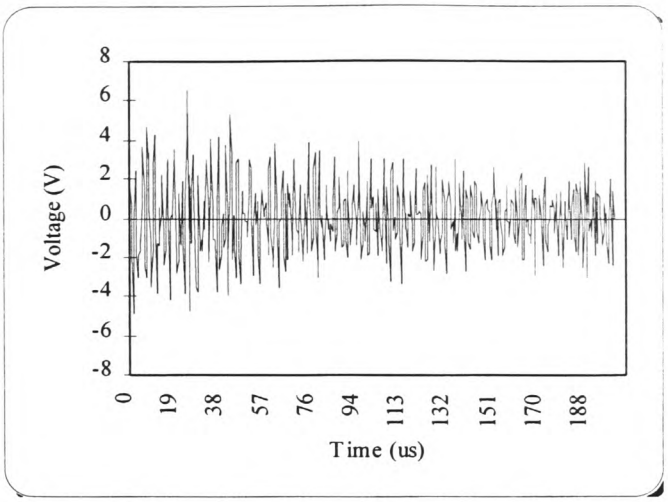

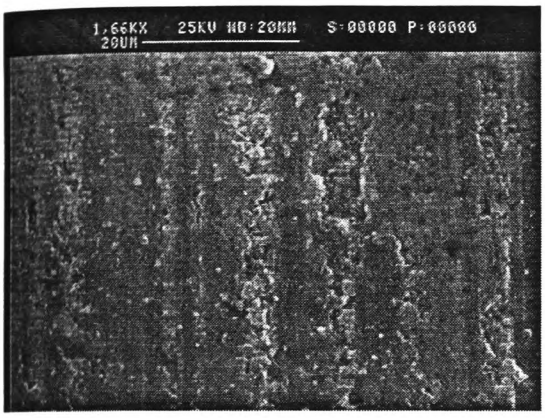

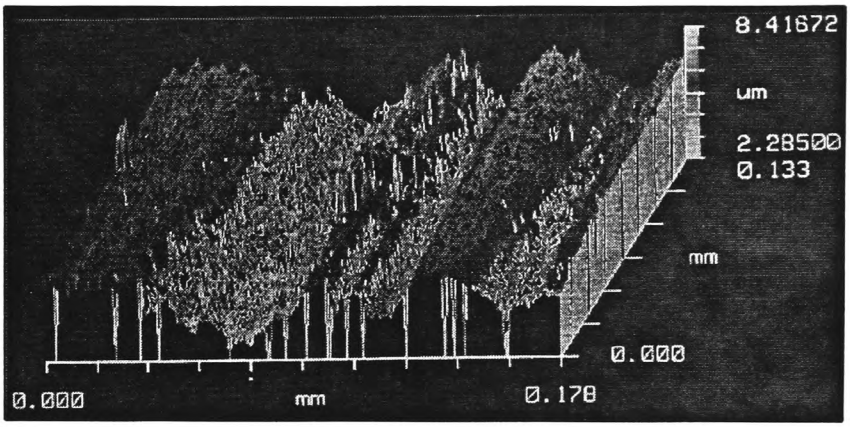

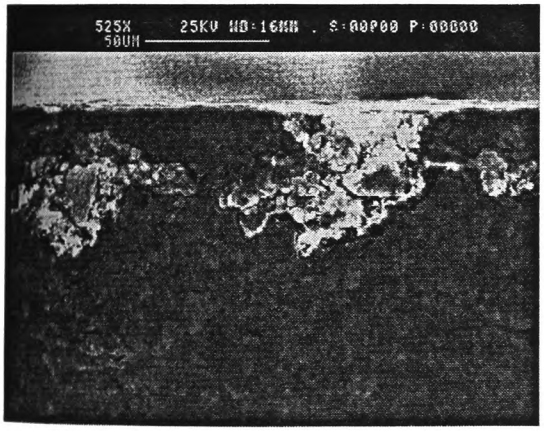

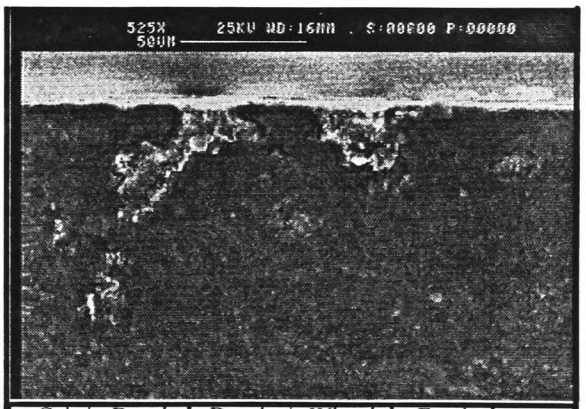

Grit size	Bond type	Depth of cut µm	Wheel speed m/s	Feed rate mm/s	G/D
D46	Resin	17	20	2	-0.3

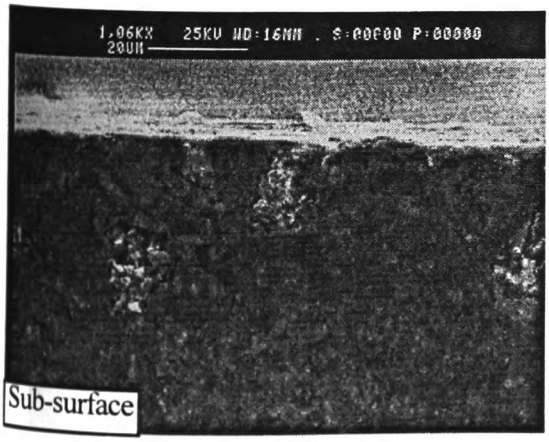

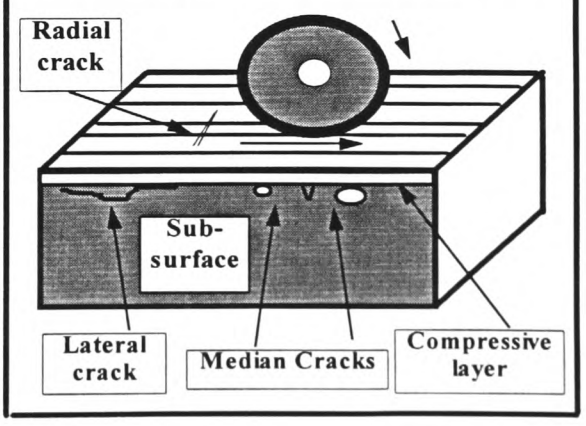

Figure 131: Correlation of AE, SEM and 3D topography for smooth ground ceramic condition at the parameters mentioned above.

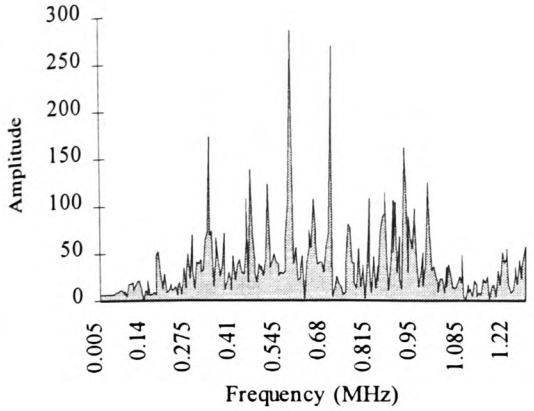

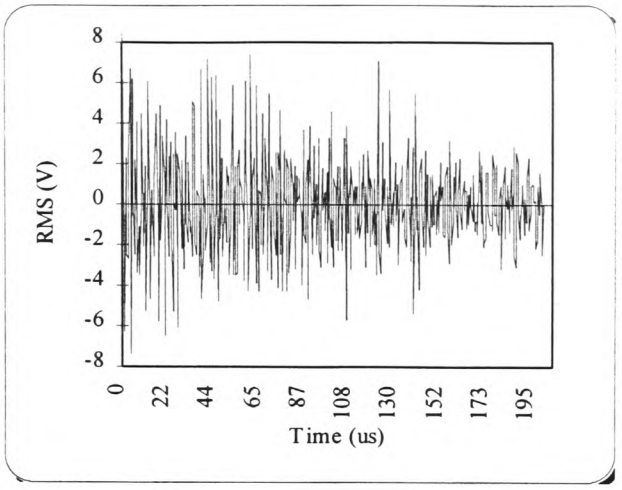

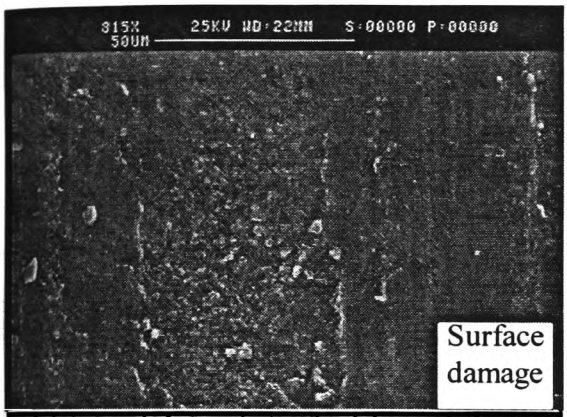

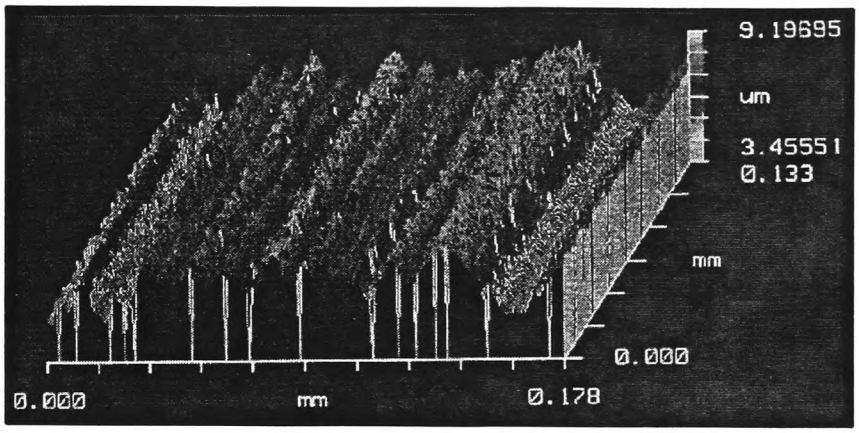

Grit size	Bond type	Depth of cut μm	Wheel speed m/s	Feed rate mm/s	G/D
D46	Vitrified	185	28	7	-0.3

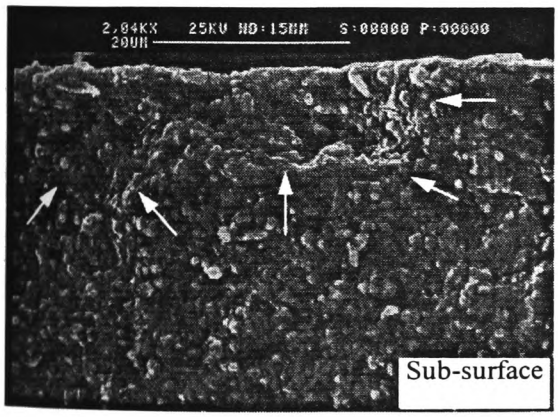

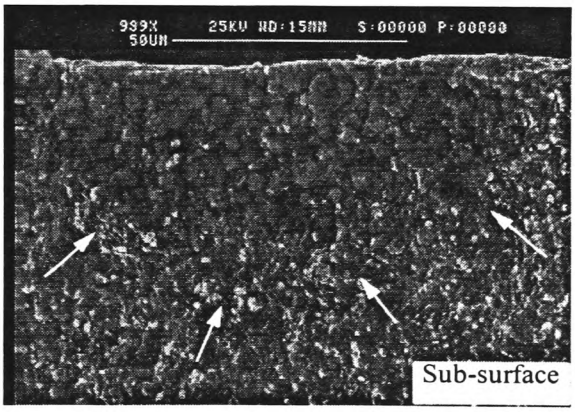

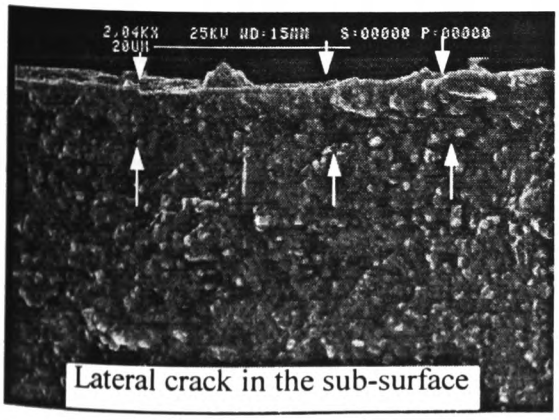

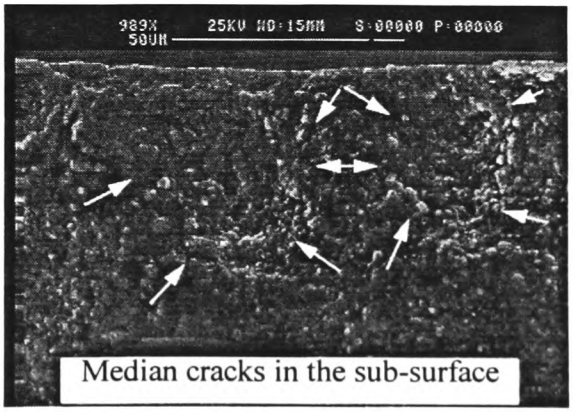

Figure 132: Correlation of AE, SEM and 3D topography for smooth ground ceramic condition at the parameters mentioned above.

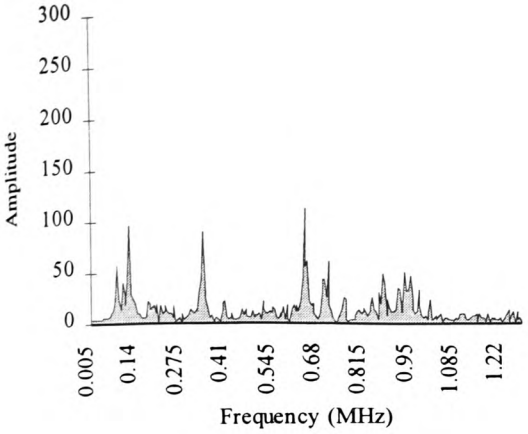

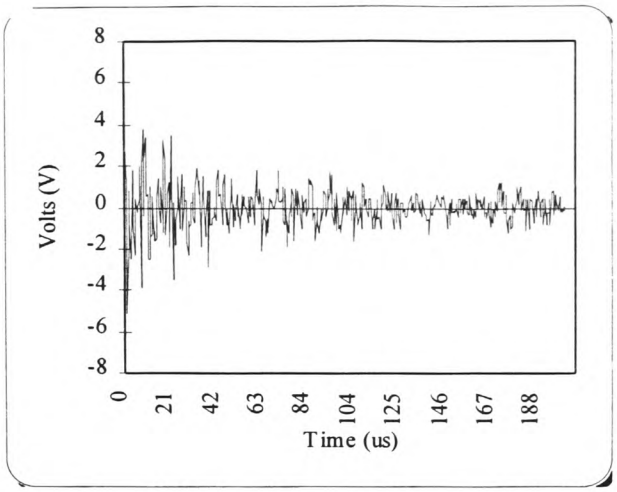

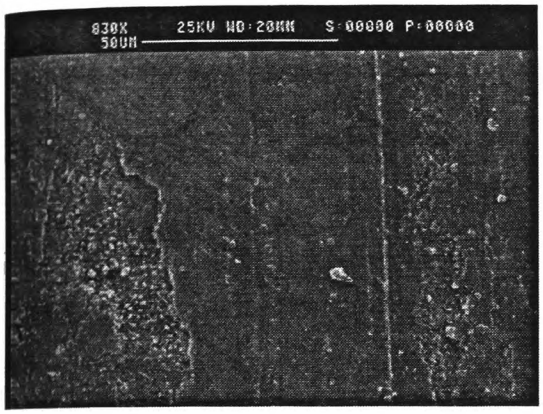

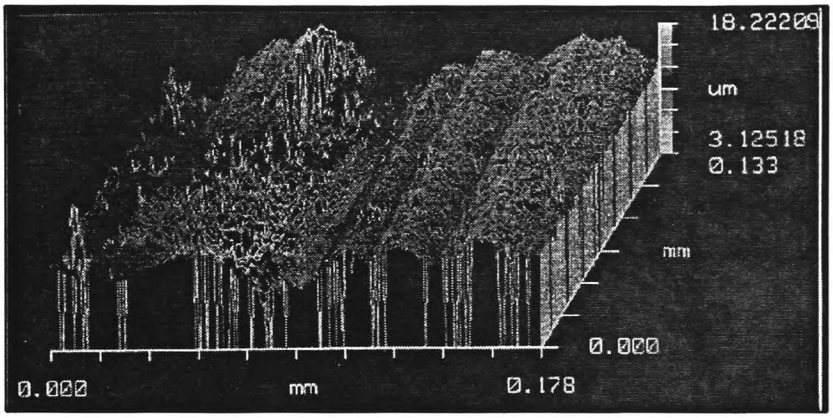

Surface damage on the ground surface

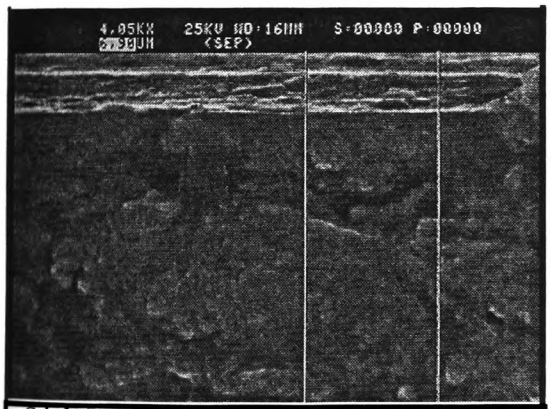

Grit size	Bond type	Depth of cut µm	Wheel speed m/s	Feed rate mm/s	G/D
D76	Cast iron	39.3	20	2	-0.3

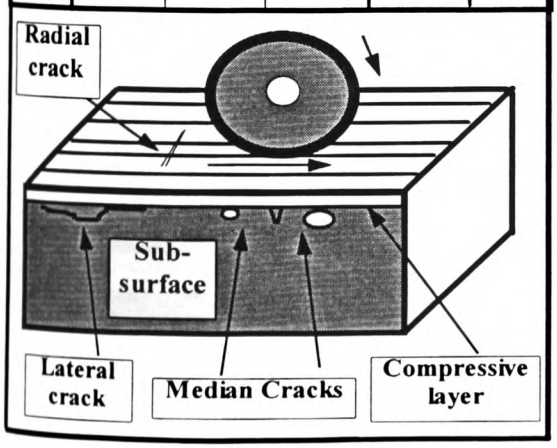

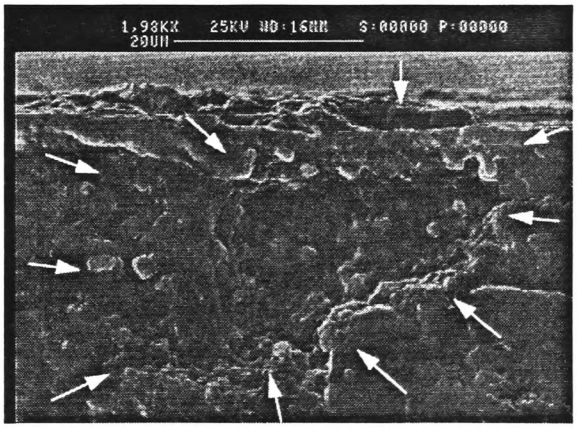

Sub-surface cracks underneath the ground surface

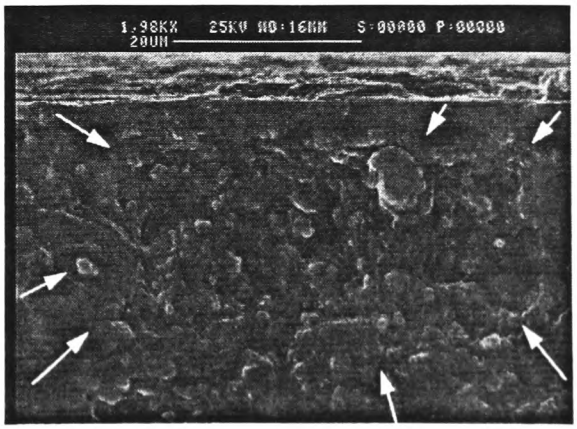

Figure 133: Correlation of AE, SEM and 3D topography for ground ceramic condition at the parameters mentioned above.

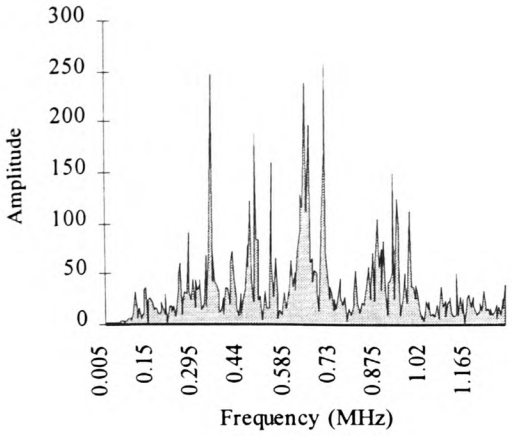

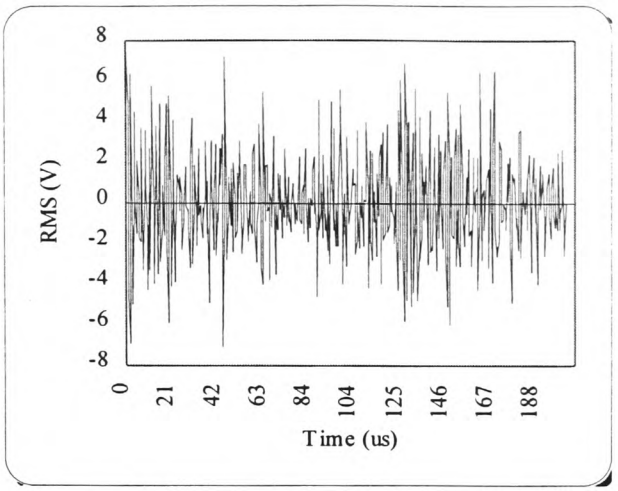

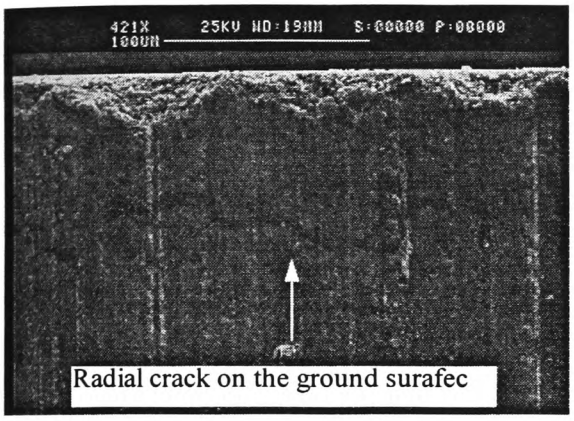

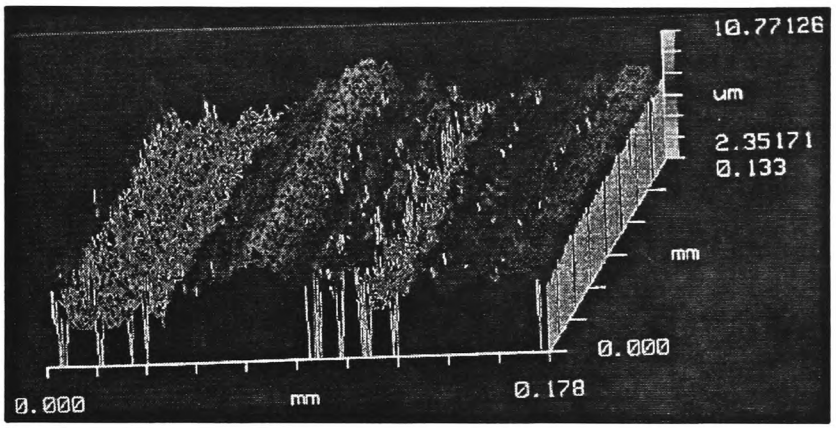

Surface damage on the ground surface

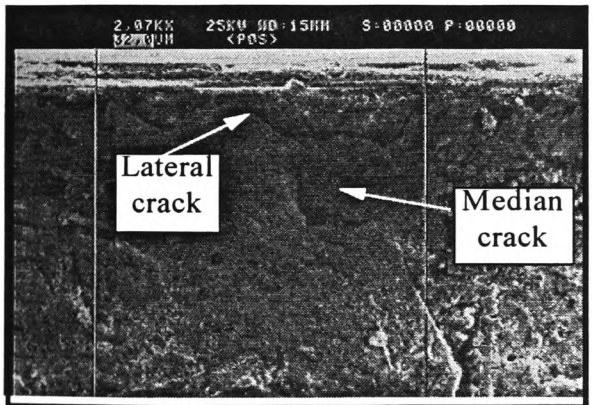

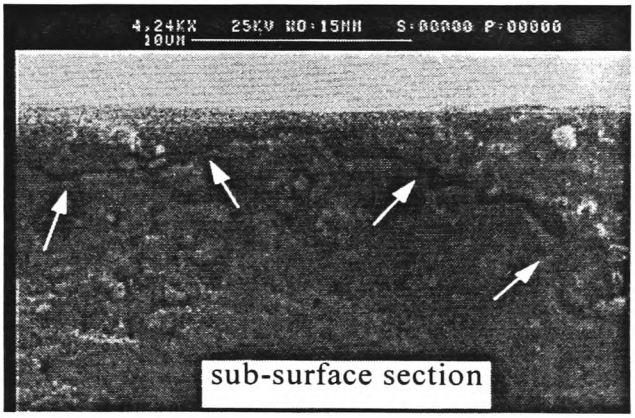

Grit size	Bond type	Depth of cut µm	Wheel speed m/s	Feed rate mm/s	G/D
D76	Cast iron	137.7	28	2	0.3

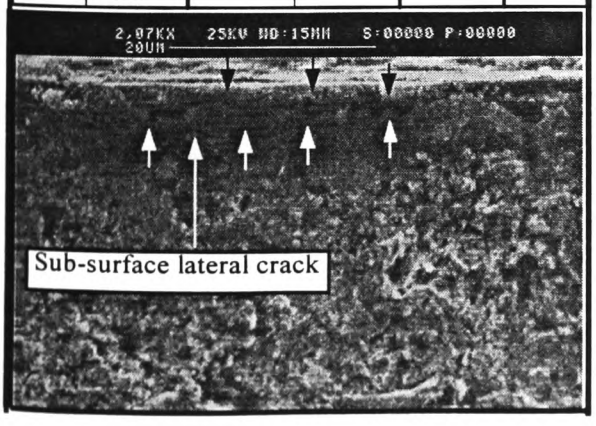

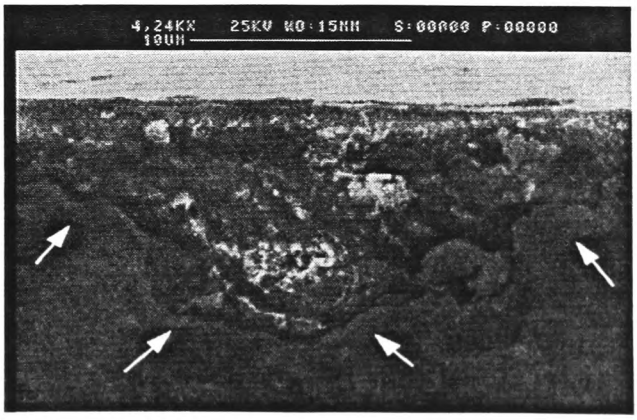

Figure 134: Correlation of AE, SEM and 3D topography for ground ceramic condition at the parameters mentioned above.

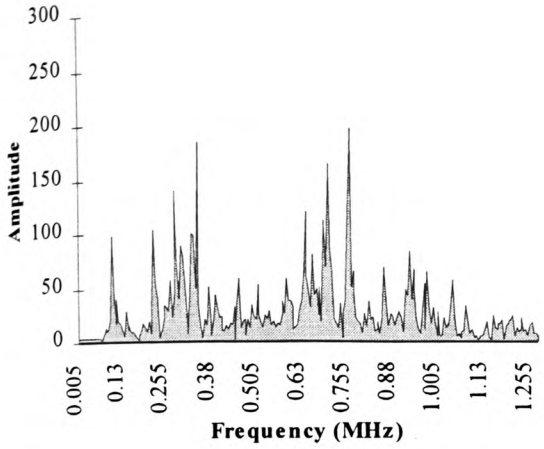

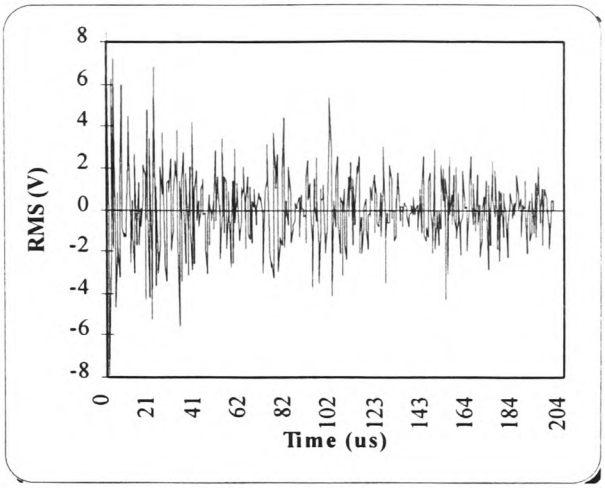

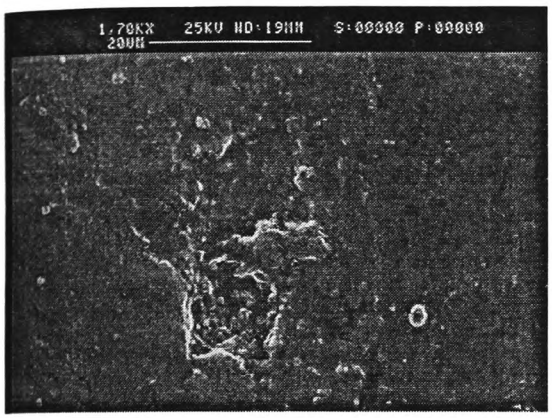

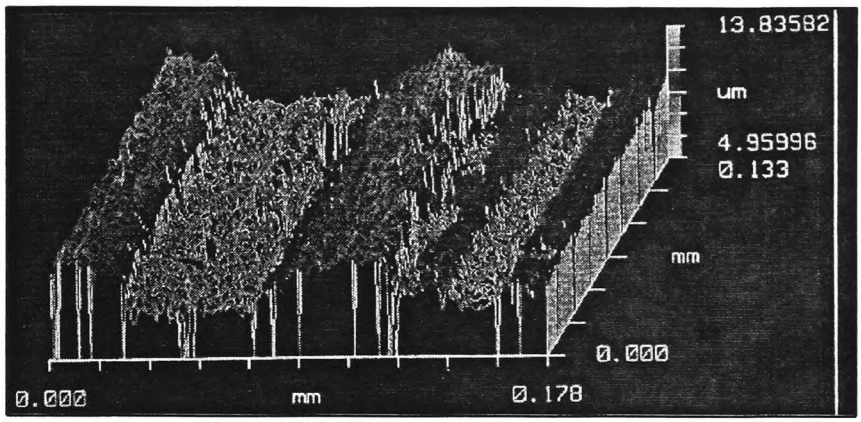

Surface damage on the ground surface

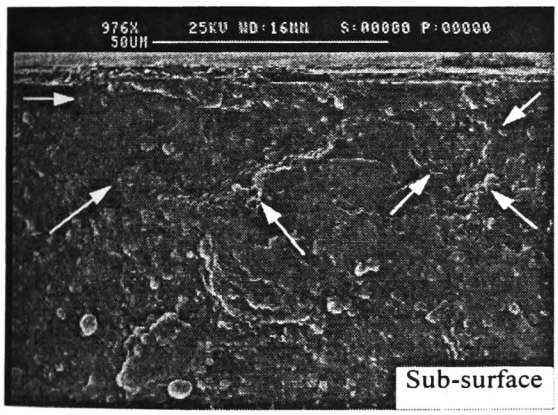

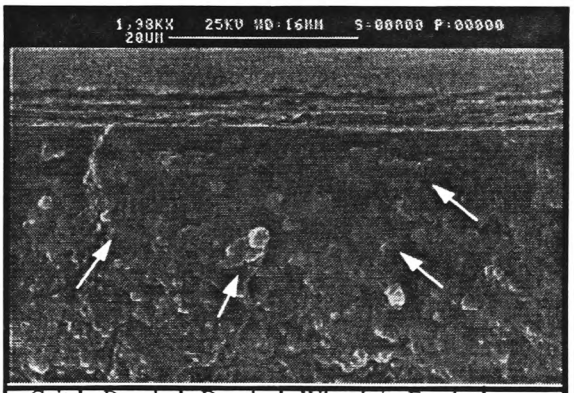

Grit size	Bond type	Depth of cut µm	Wheel speed m/s	Feed rate mm/s	G/D
D76	Cast iron	222.5	26	2	0.4

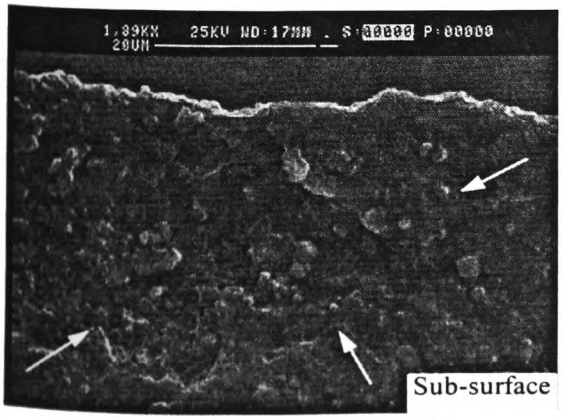

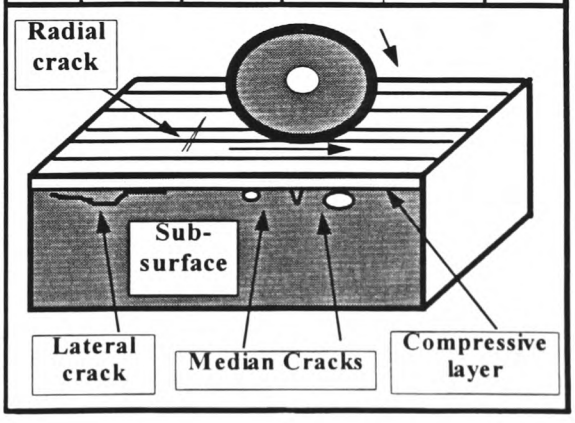

Figure 135: Correlation of AE, SEM and 3D topography for ground ceramic condition at the parameters mentioned above.

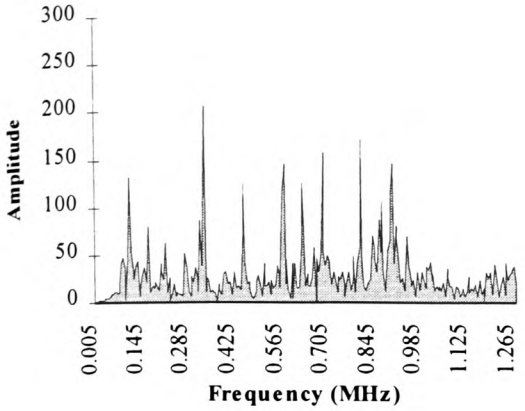

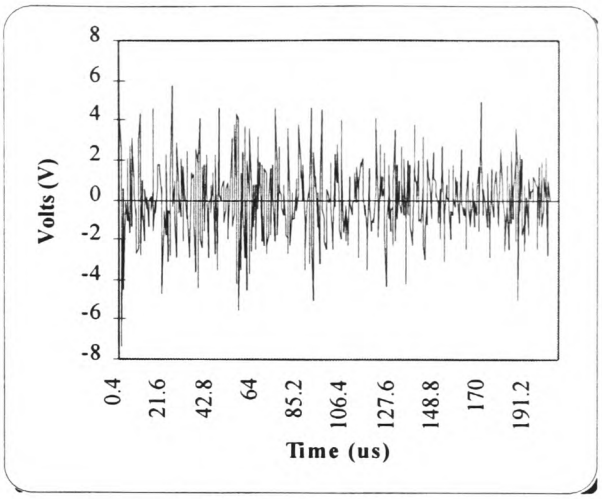

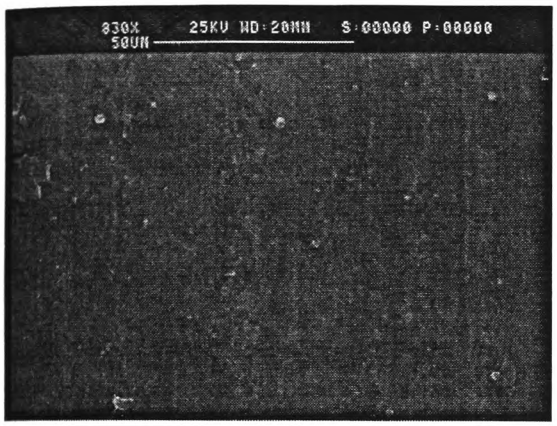

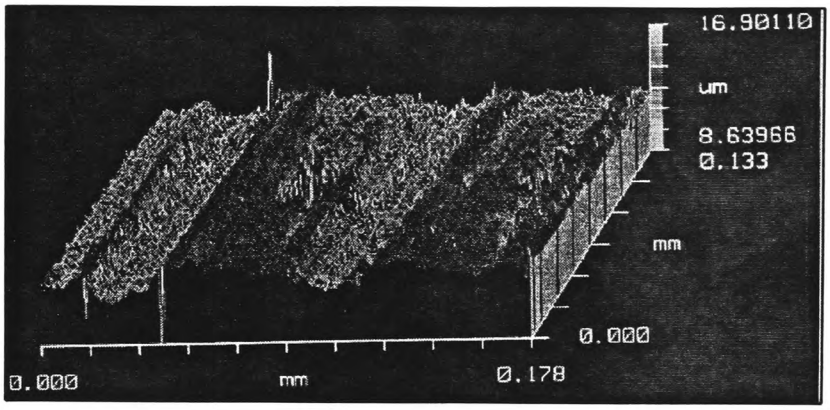

Grit size	Bond type	Depth of cut µm	Wheel speed m/s	Feed rate mm/s	G/D
D76	Resin	35	30	7	0.5

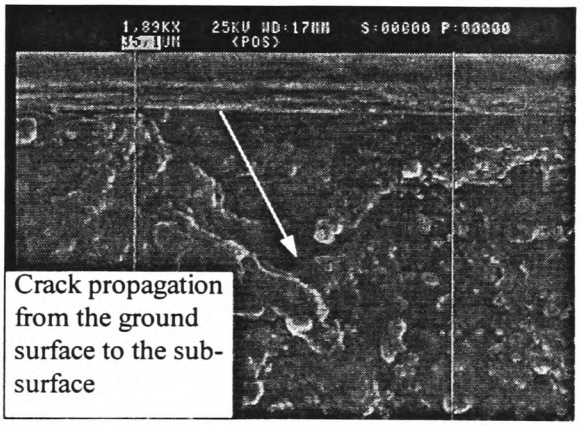

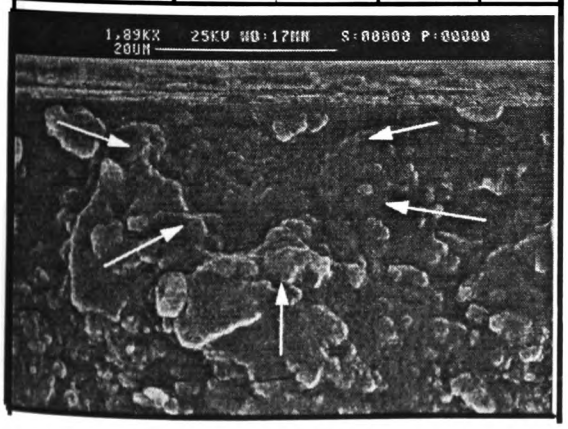

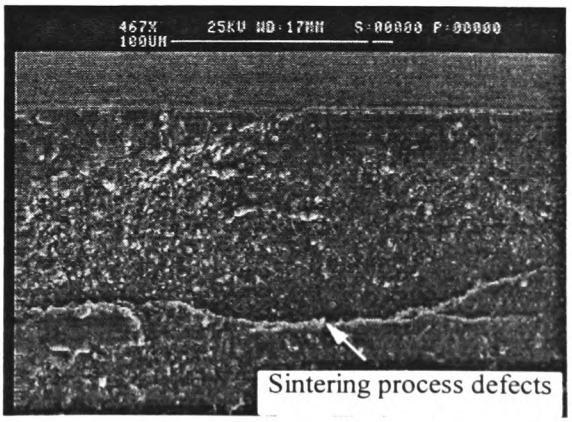

Figure 136: Correlation of AE, SEM and 3D topography for ground ceramic condition at the parameters mentioned above.

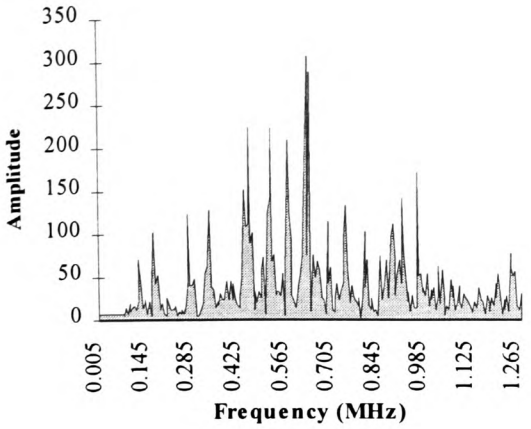

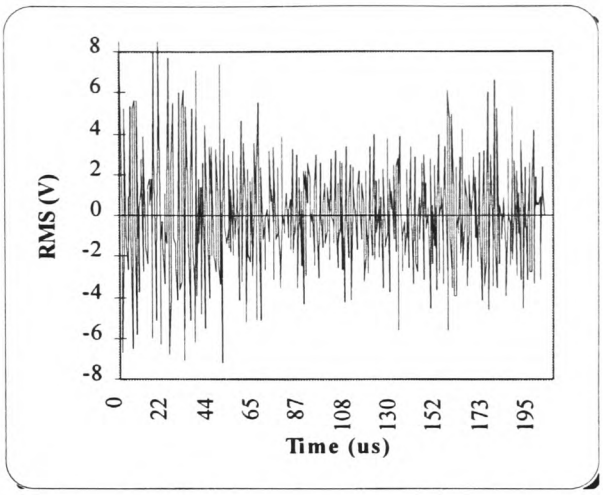

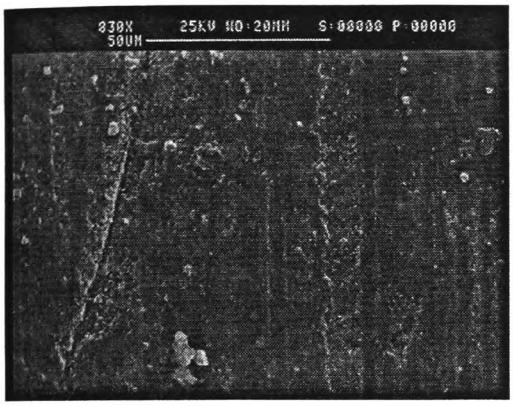

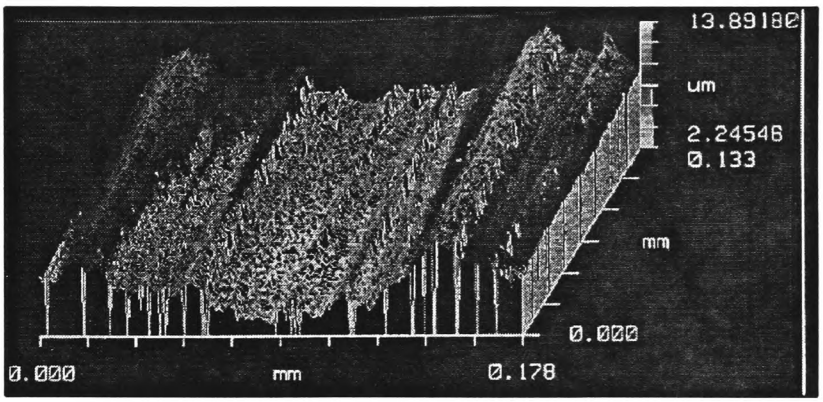

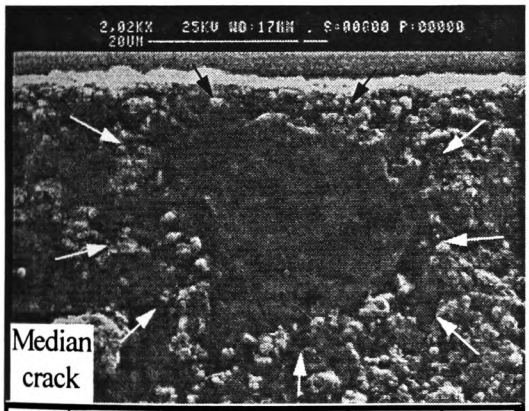

Grit size	Bond type	Depth of cut µm	Wheel speed m/s	Feed rate mm/s	G/D
D76	Resin	383.5	32	7	-0.3

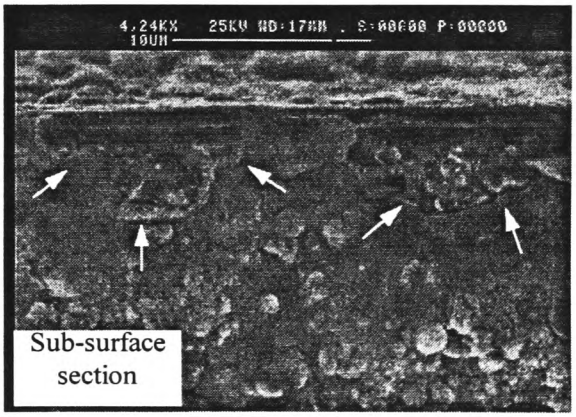

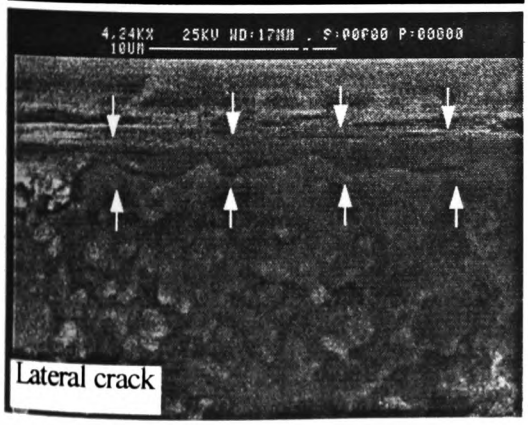

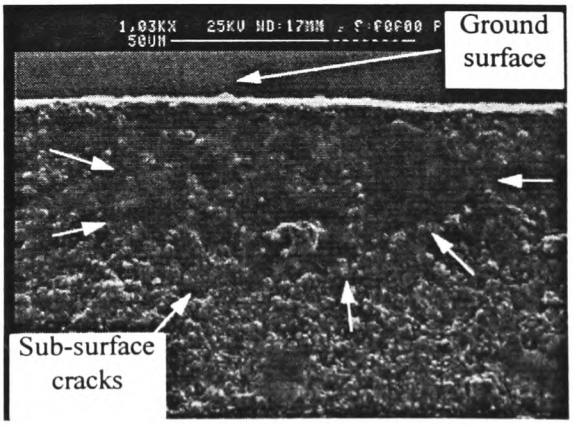

Figure 137: Correlation of AE, SEM and 3D topography for ground ceramic condition at the parameters mentioned above.

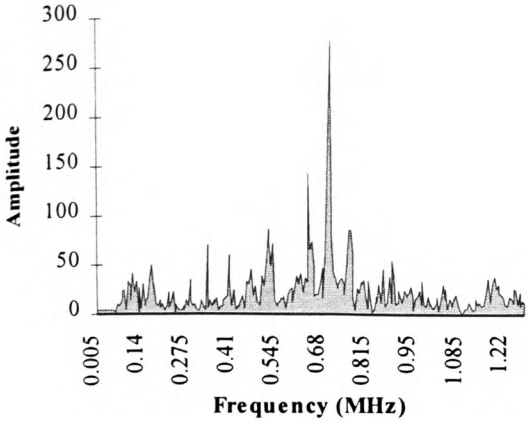

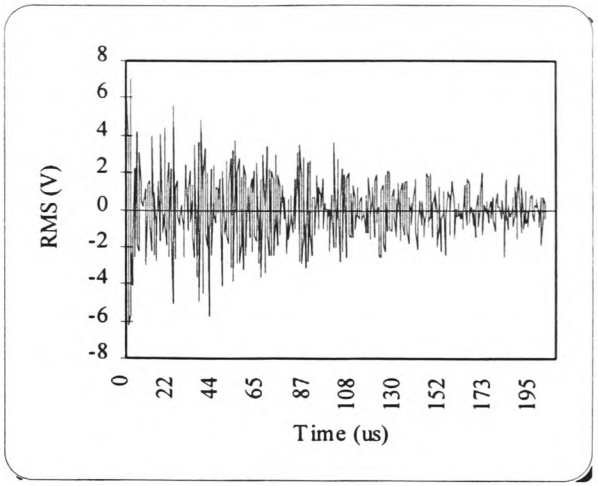

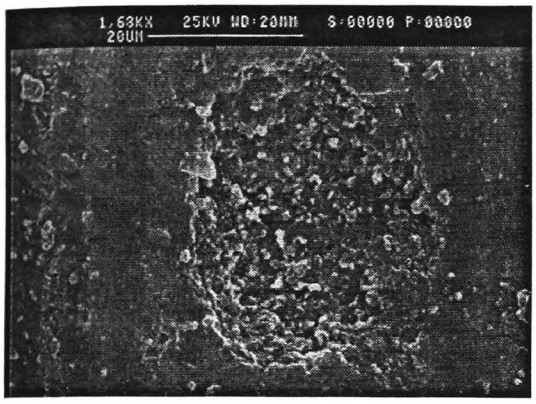

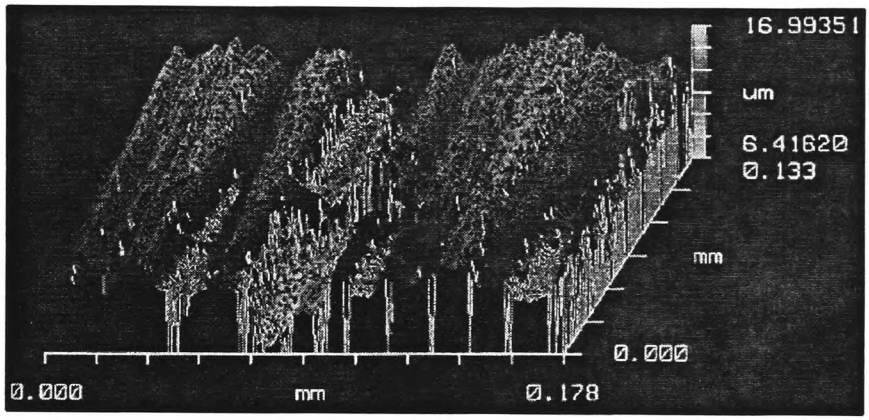

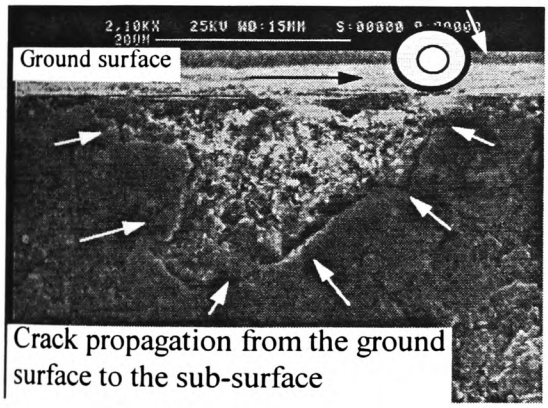

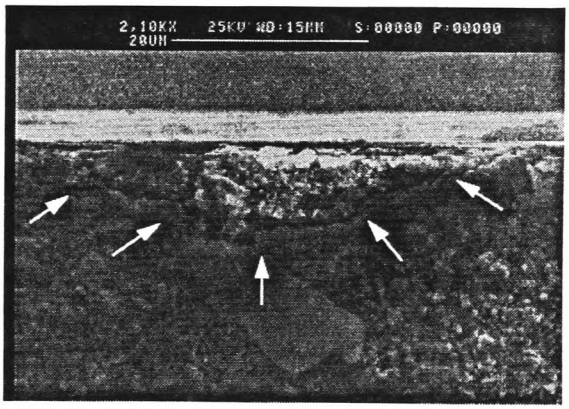

Grit size	Bond type	Depth of cut µm	Wheel speed m/s	Feed rate mm/s	G/D
D76	Vitrified	47.5	20	5	-0.4

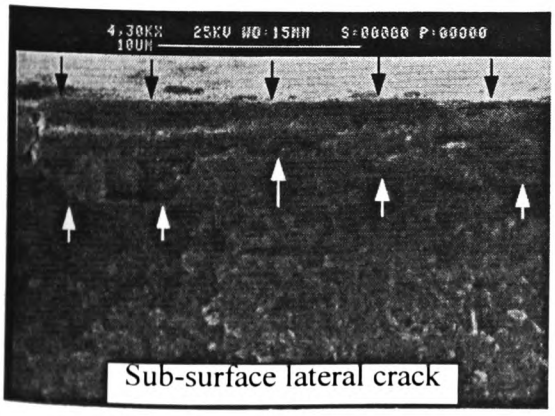

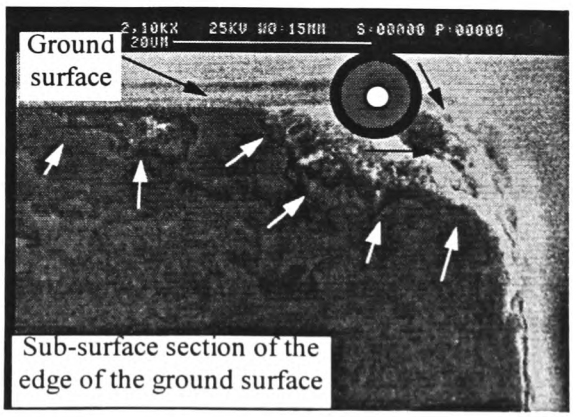

Figure 138: Correlation of AE, SEM and 3D topography for ground ceramic condition at the parameters mentioned above.

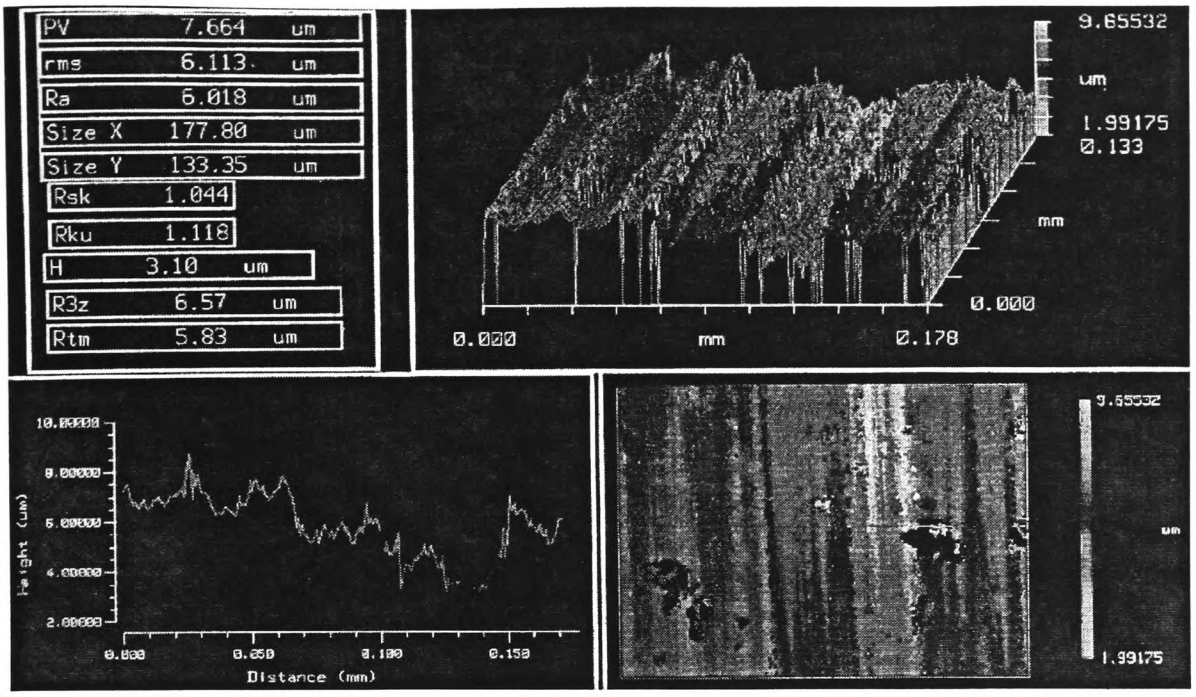

Figure 139: Depth of surface crack and machine marks on the ground surface at 53 μm depth of cut, 24 m/s wheel speed, 2 mm/s table feed, D46 grit size resin bond wheel and -0.4 grinding wheel/truing speed ratio.

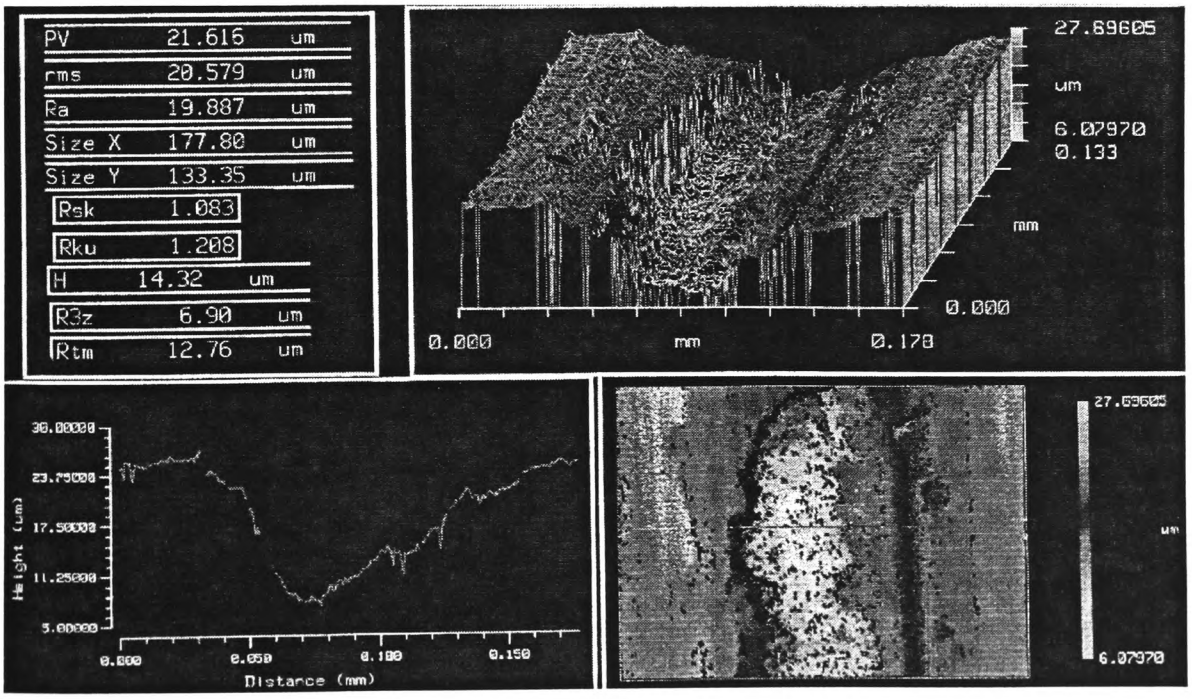

Figure 140: Depth of surface crack and machine marks on the ground surface at 91 μm depth of cut, 24 m/s wheel speed, 7 mm/s table feed, D126 grit size cast iron bond wheel and -0.3 grinding wheel/truing speed ratio.

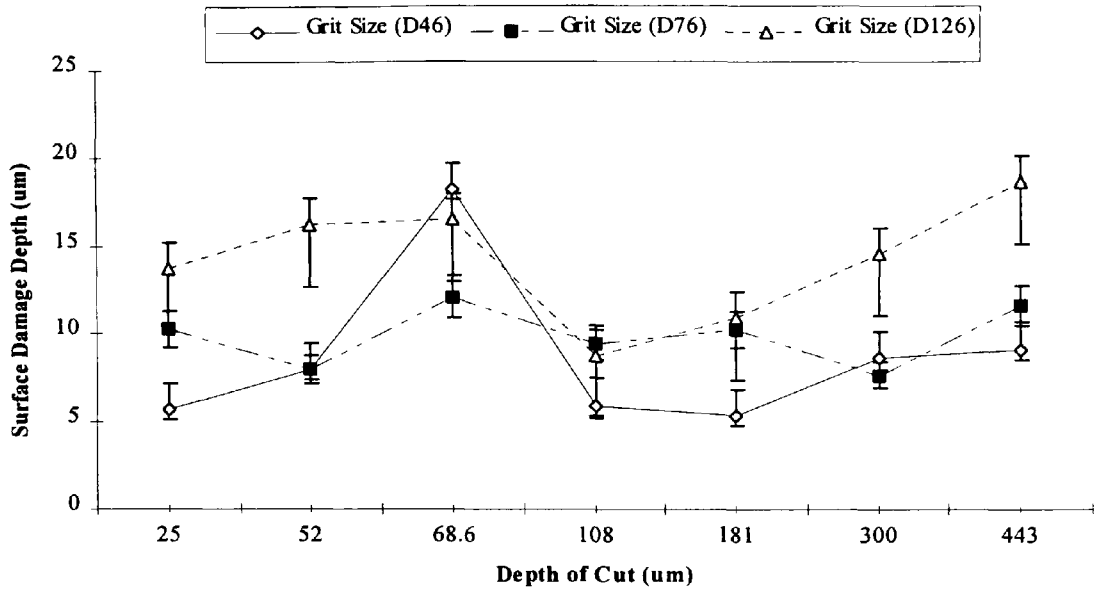

Figure 141: Surface damage depth of the ground surface measured by 3D surface topography method against depth of cut for different levels of grit size.

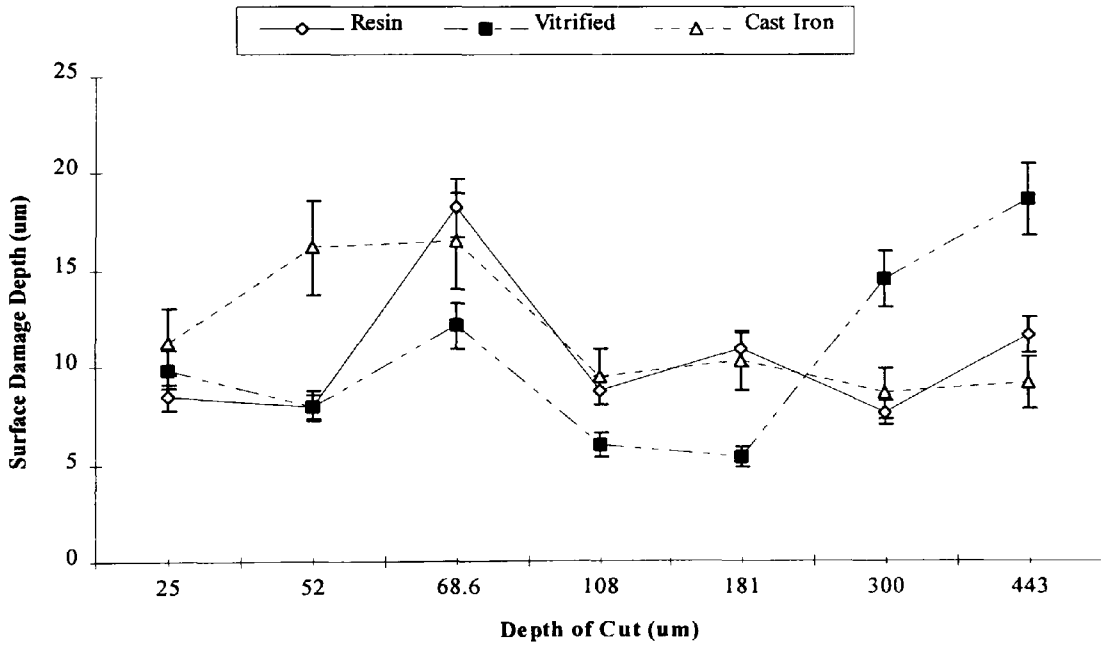

Figure 142: Surface damage depth of the ground surface measured by 3D surface topography method against depth of cut for different levels of bond type.

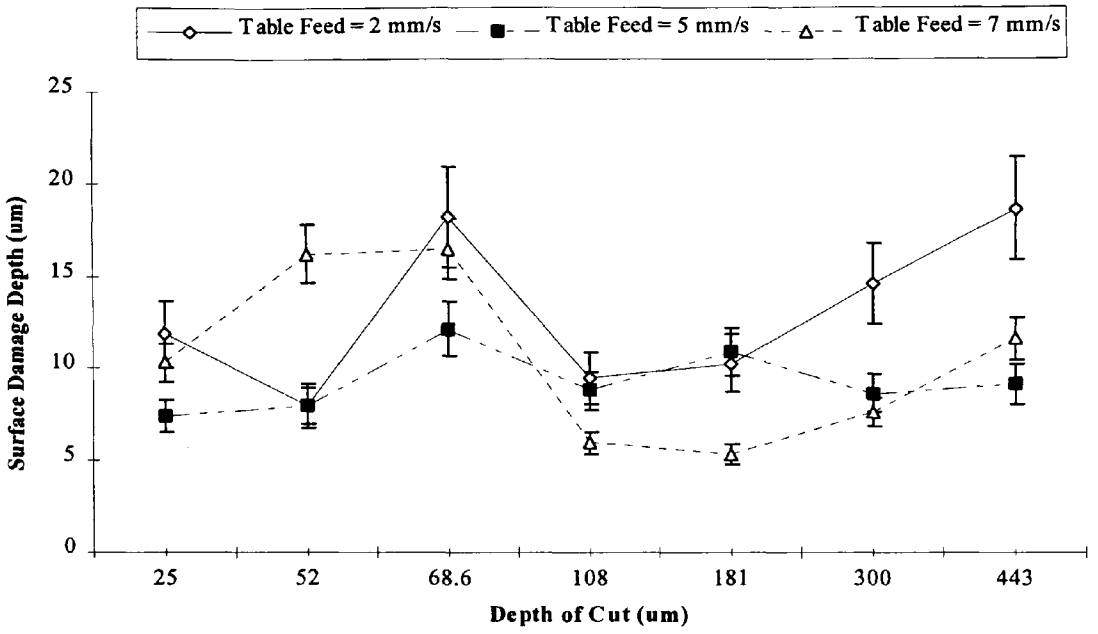

Figure 143: Surface damage depth of the ground surface measured by 3D surface topography method against depth of cut for different levels of table feed.

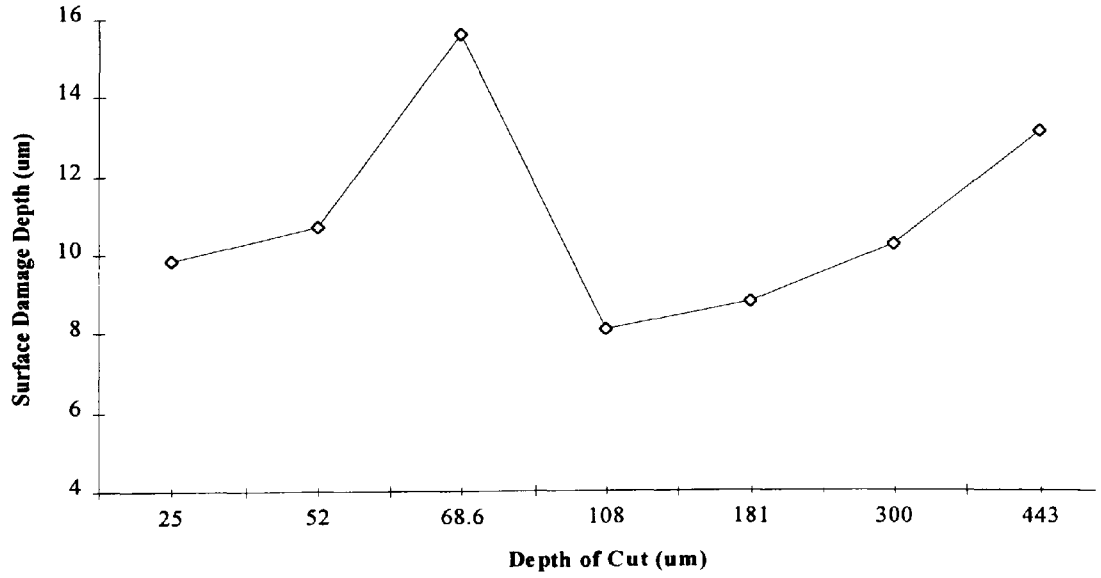

Figure 144: Surface damage depth of the ground surface measured by 3D surface topography method against depth of cut averaged over different levels of table feed.

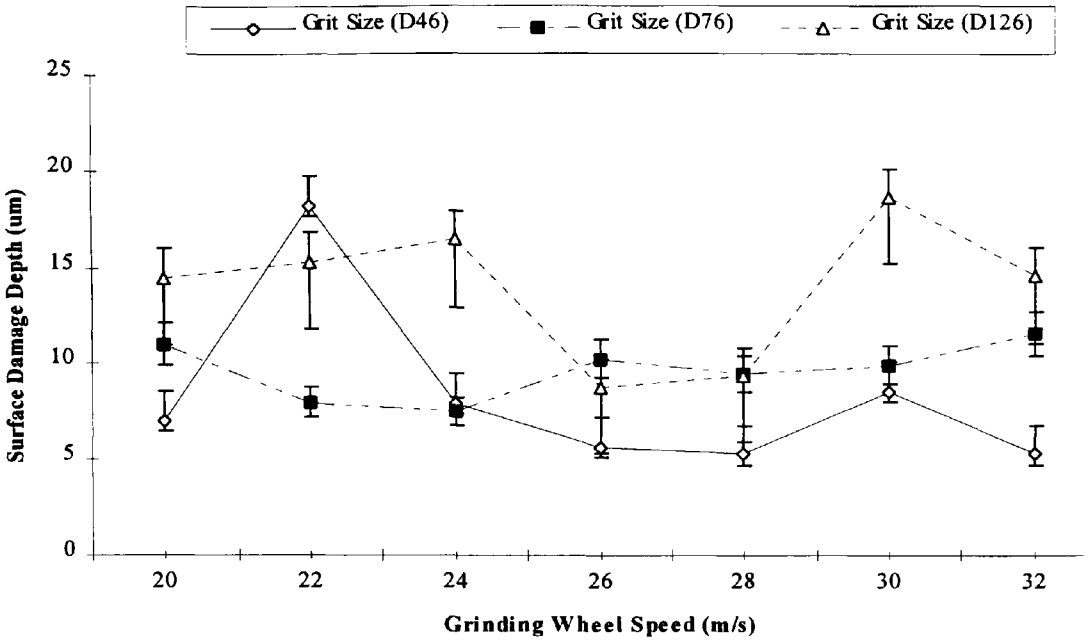

Figure 145: Surface damage depth of the ground surface measured by 3D surface topography method against grinding wheel speed for different levels of grit size.

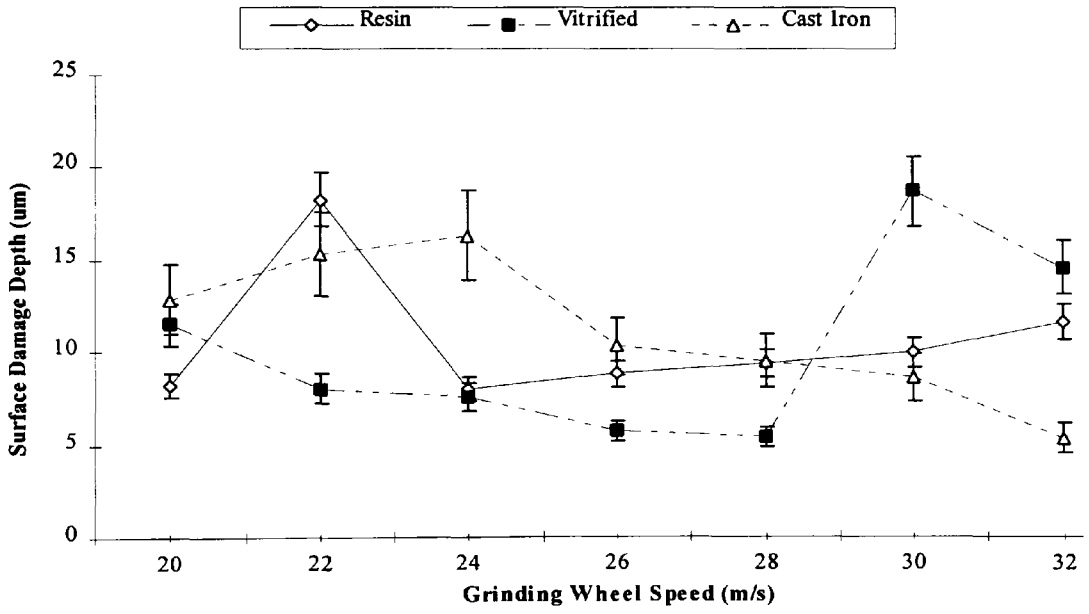

Figure 146: Surface damage depth of the ground surface measured by 3D surface topography method against grinding wheel speed for different levels of bond.

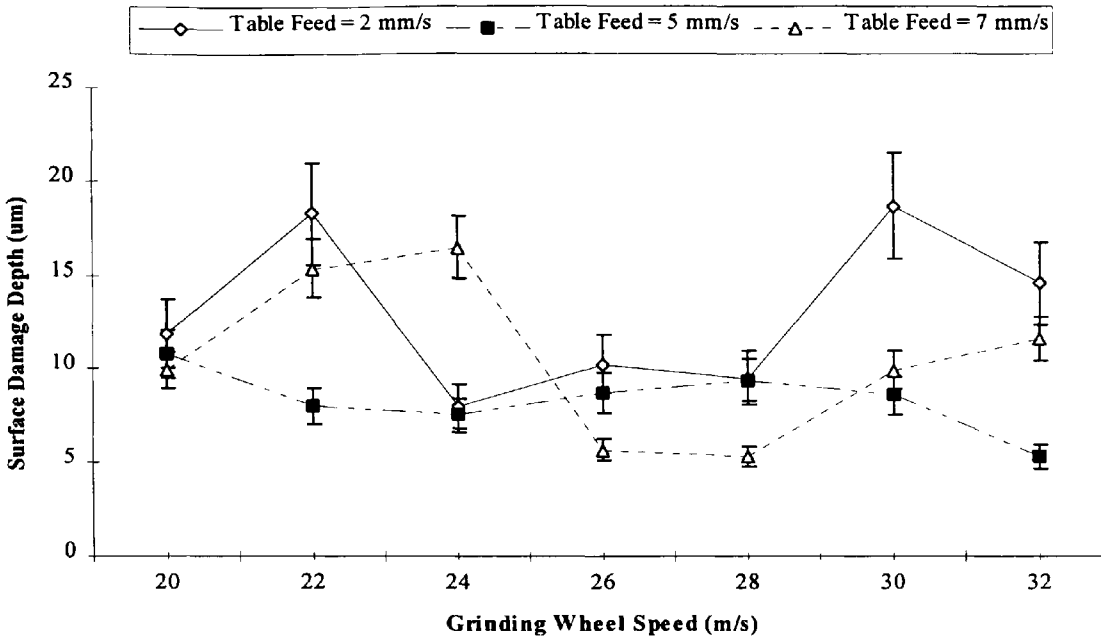

Figure 147: Surface damage depth of the ground surface measured by 3D surface topography method against grinding wheel speed for different levels of table feed.

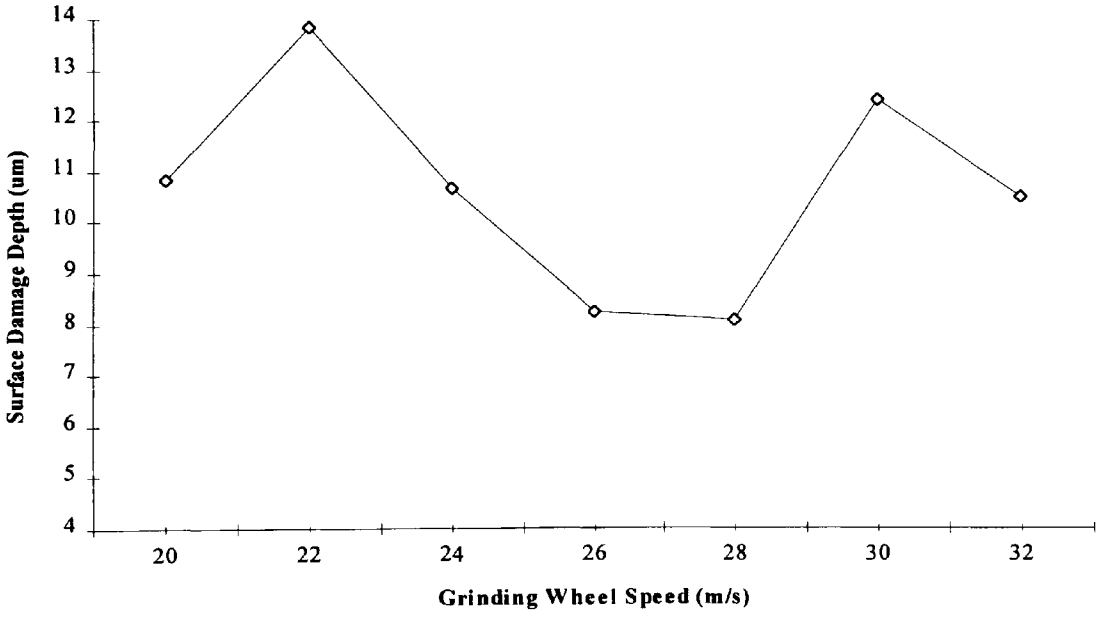

Figure 148: Surface damage depth of the ground surface measured by 3D surface topography method against grinding wheel speed averaged over different levels of table feed.

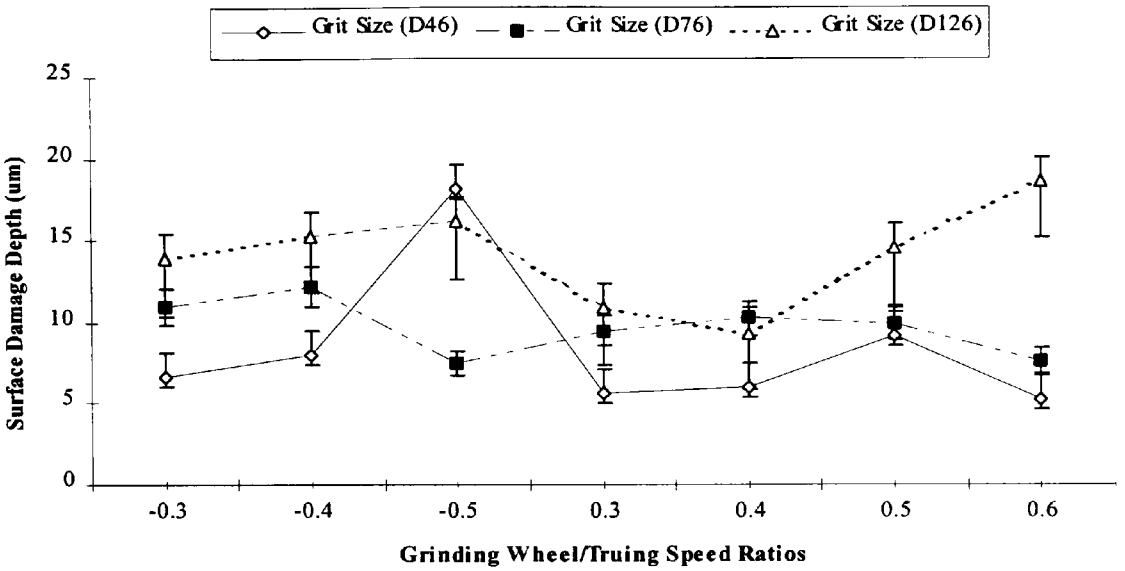

Figure 149: Surface damage depth of the ground surface measured by 3D surface topography method against grinding wheel/truing speed ratios for different levels of grit size.

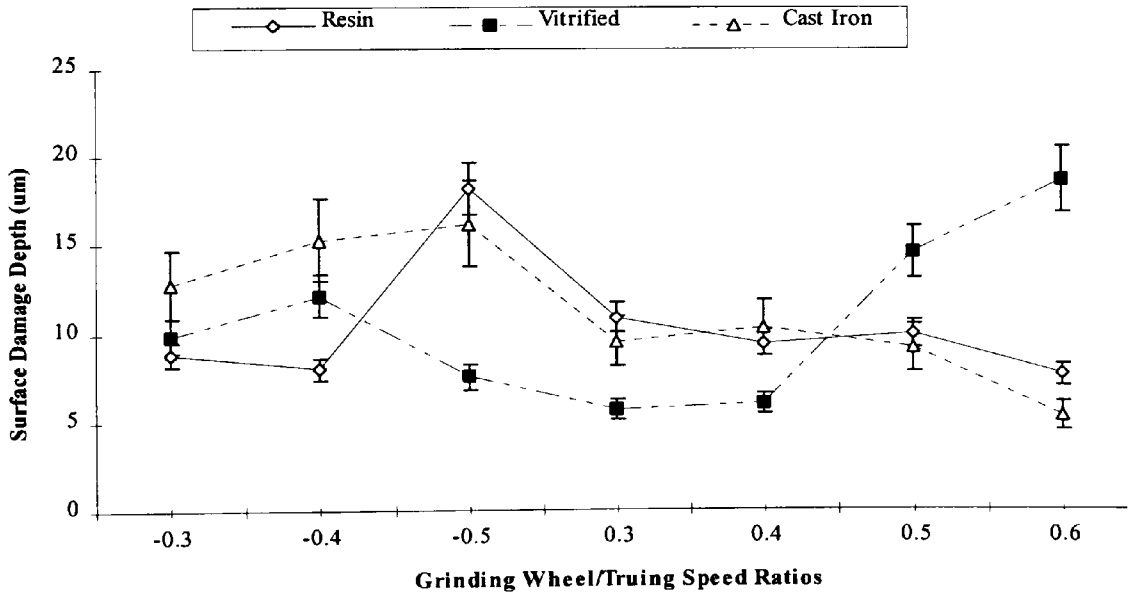

Figure 150: Surface damage depth of the ground surface measured by 3D surface topography method against grinding wheel/truing speed ratios for different levels of bond type.

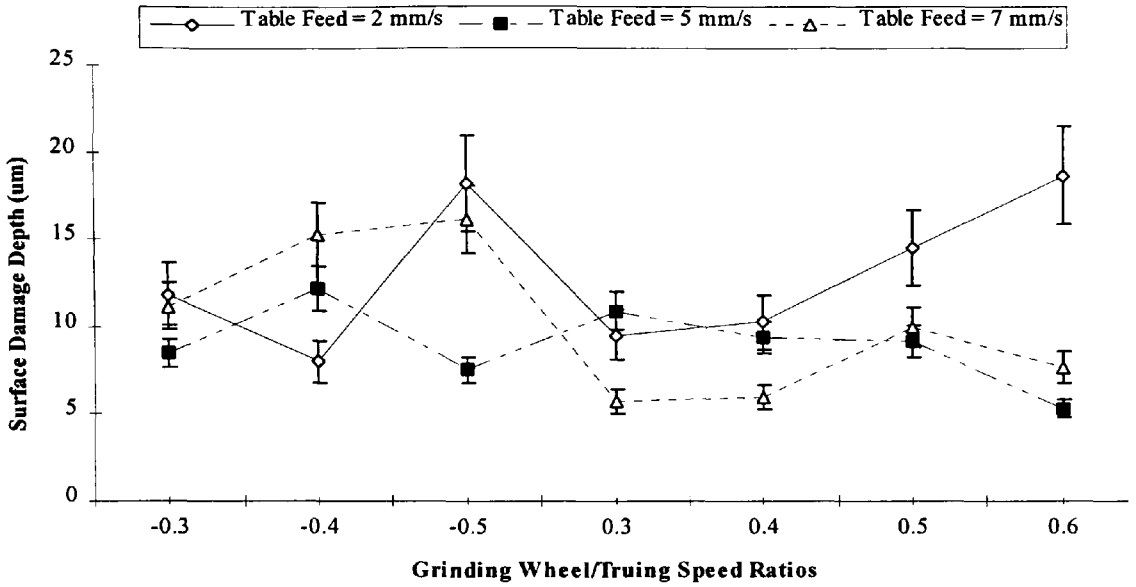

Figure 151: Surface damage depth of the ground surface measured by 3D surface topography method against grinding wheel/truing speed ratios for different levels of table feed.

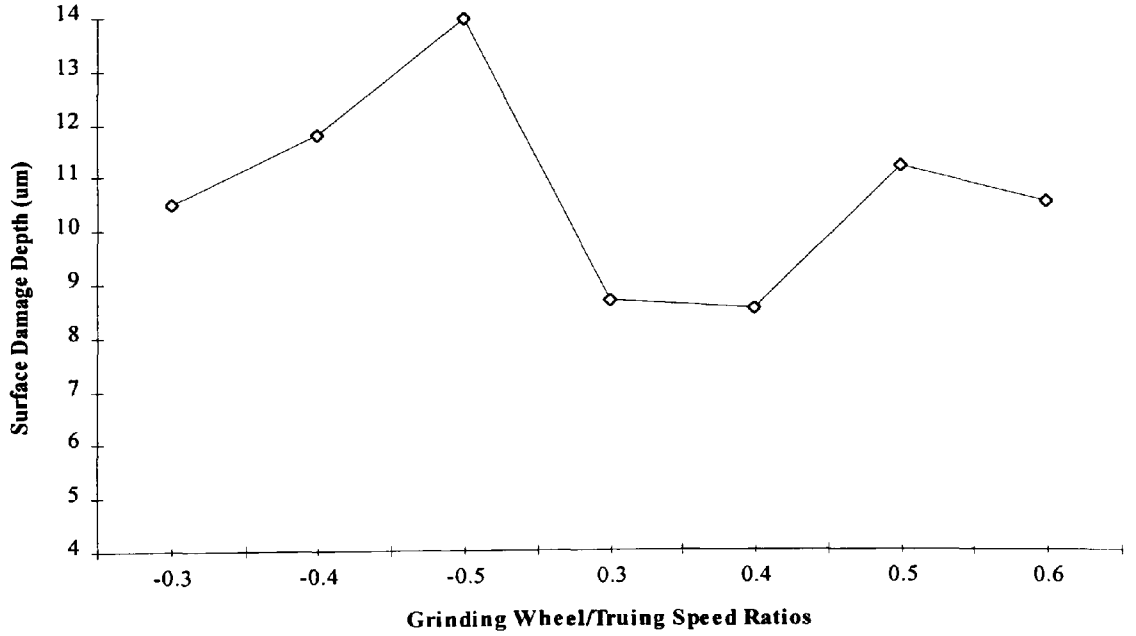

Figure 152: Surface damage depth of the ground surface measured by 3D surface topography method against grinding wheel/truing speed ratios averaged over different levels of table feed.

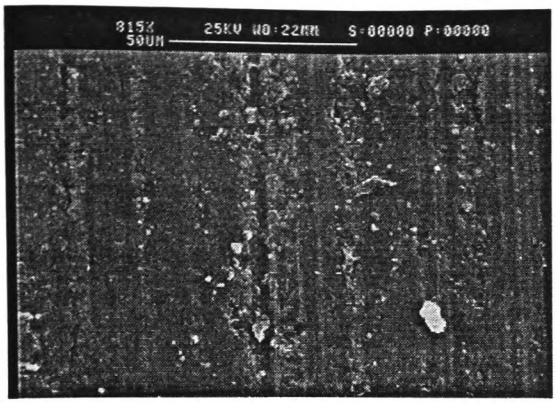

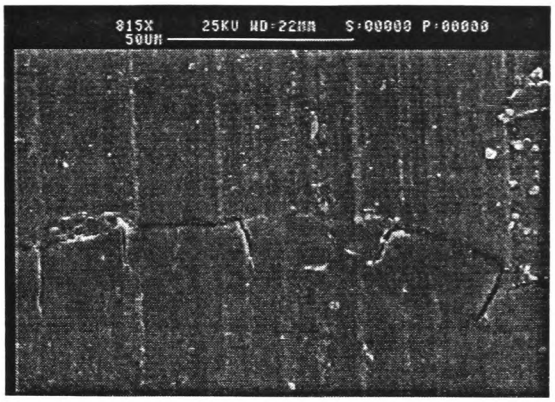

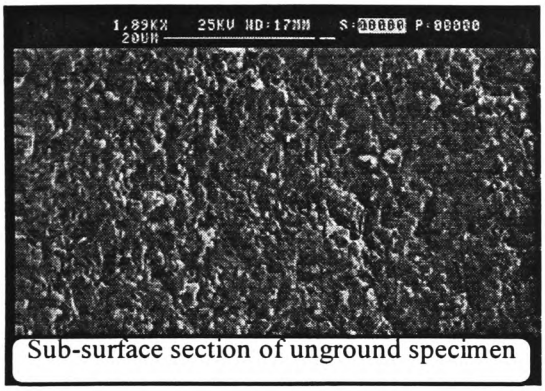

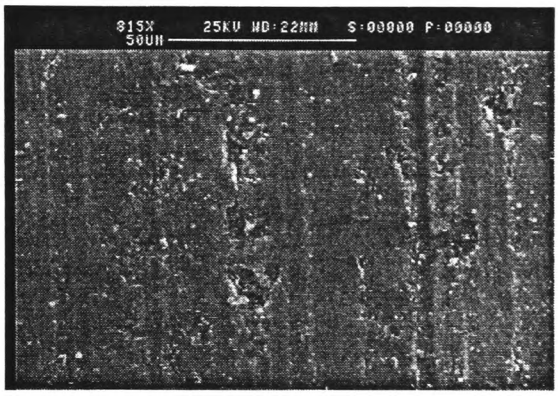

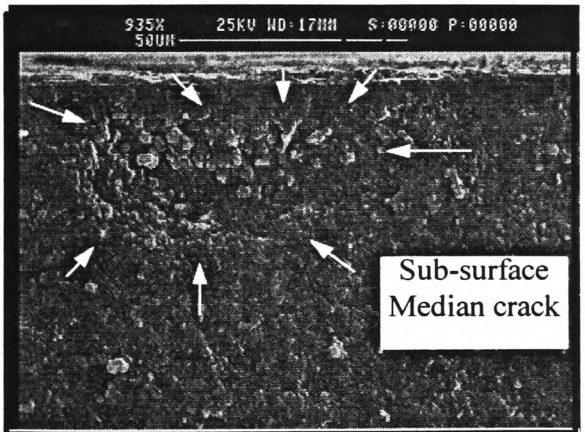

Grit size	Bond type	Depth of cut µm	Wheel speed m/s	Feed rate mm/s	G/D
D46	Cast iron	288	30	5	-0.3

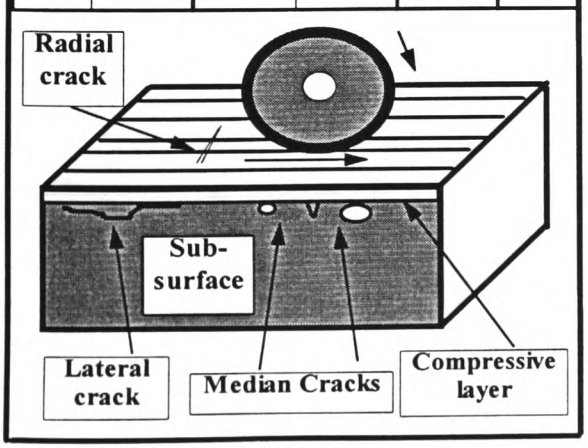

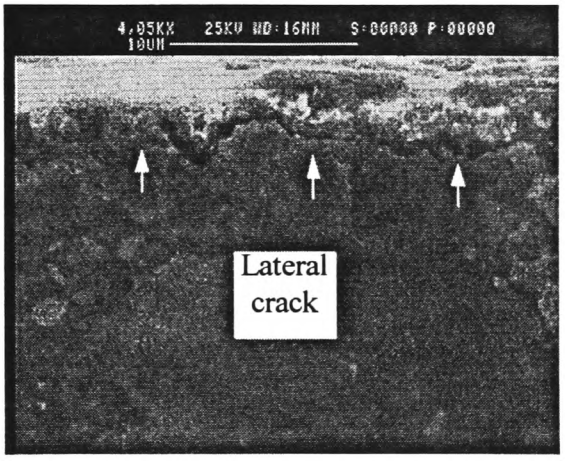

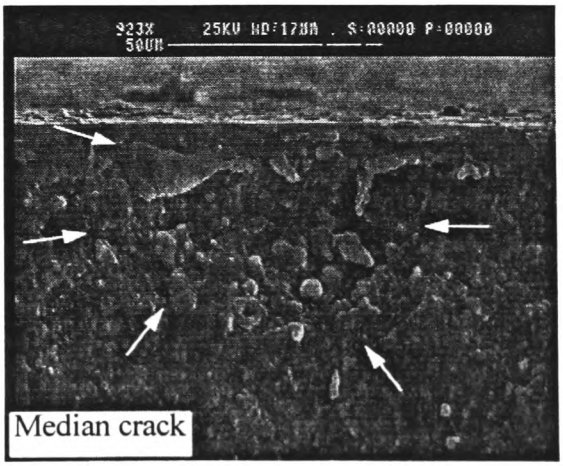

Figure 153: The effect of grinding wheel and machine parameters mentioned above on the surface and sub-surface cracks and their distance from the ground surface.

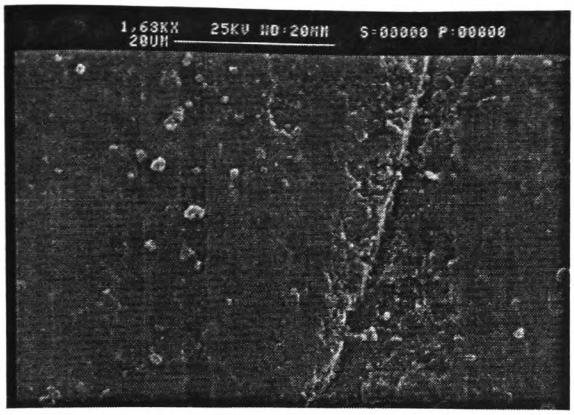

Surface cracks on the ground surface

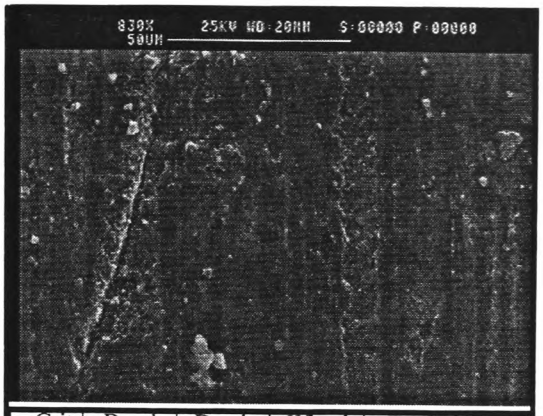

Grit size	Bond type	Depth of cut µm	Wheel speed m/s	Feed rate mm/s	G/D
D76	Resin	383.5	32	7	-0.3

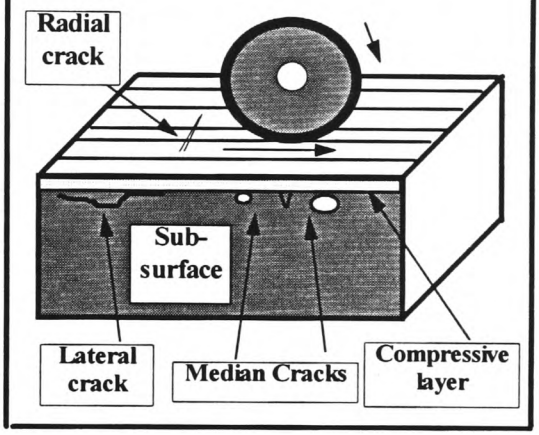

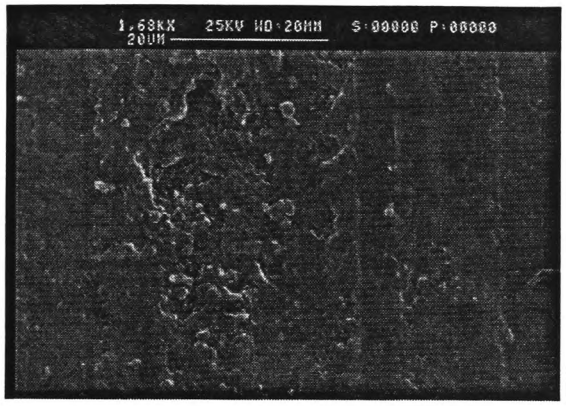

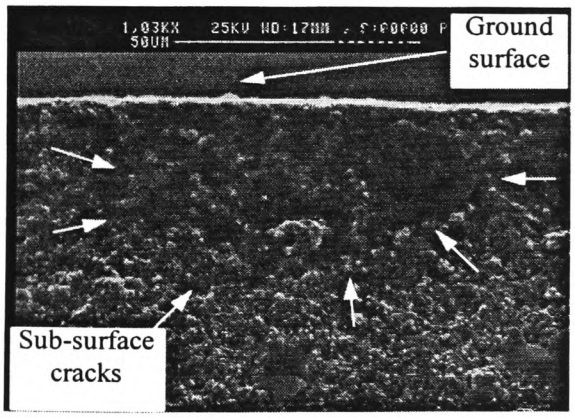

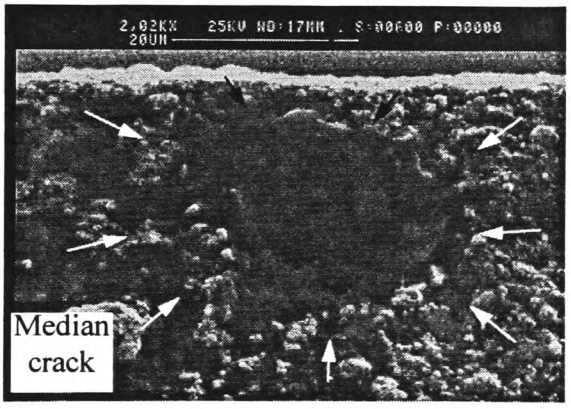

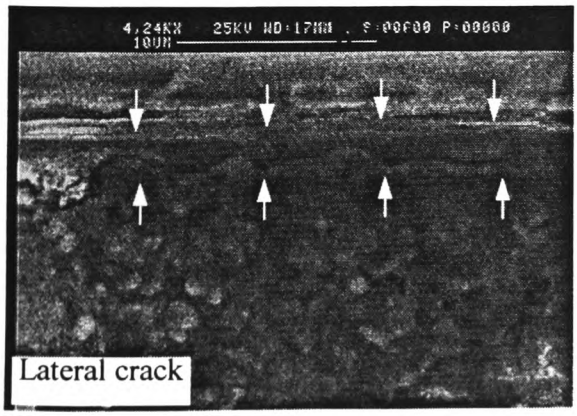

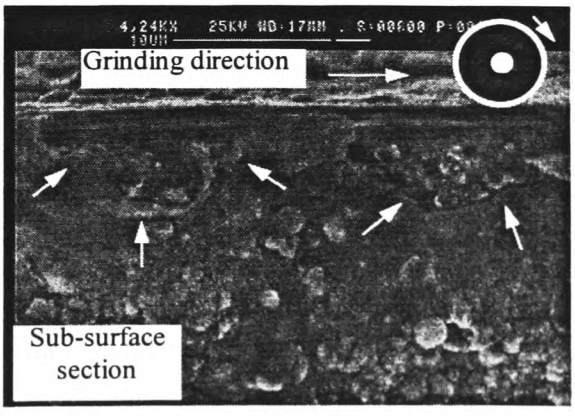

Figure 154: The effect of grinding wheel and machine parameters mentioned above on the surface and sub-surface cracks and their distance from the ground surface.

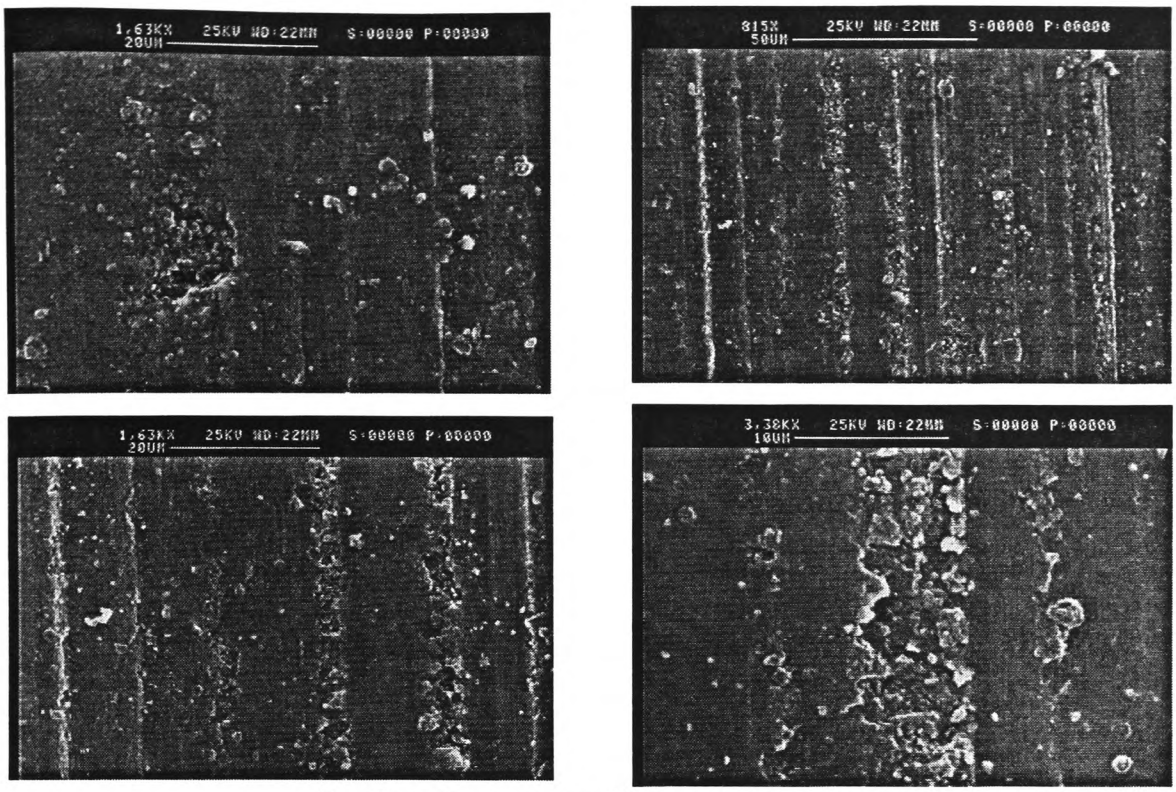

Surface damage on the ground surface

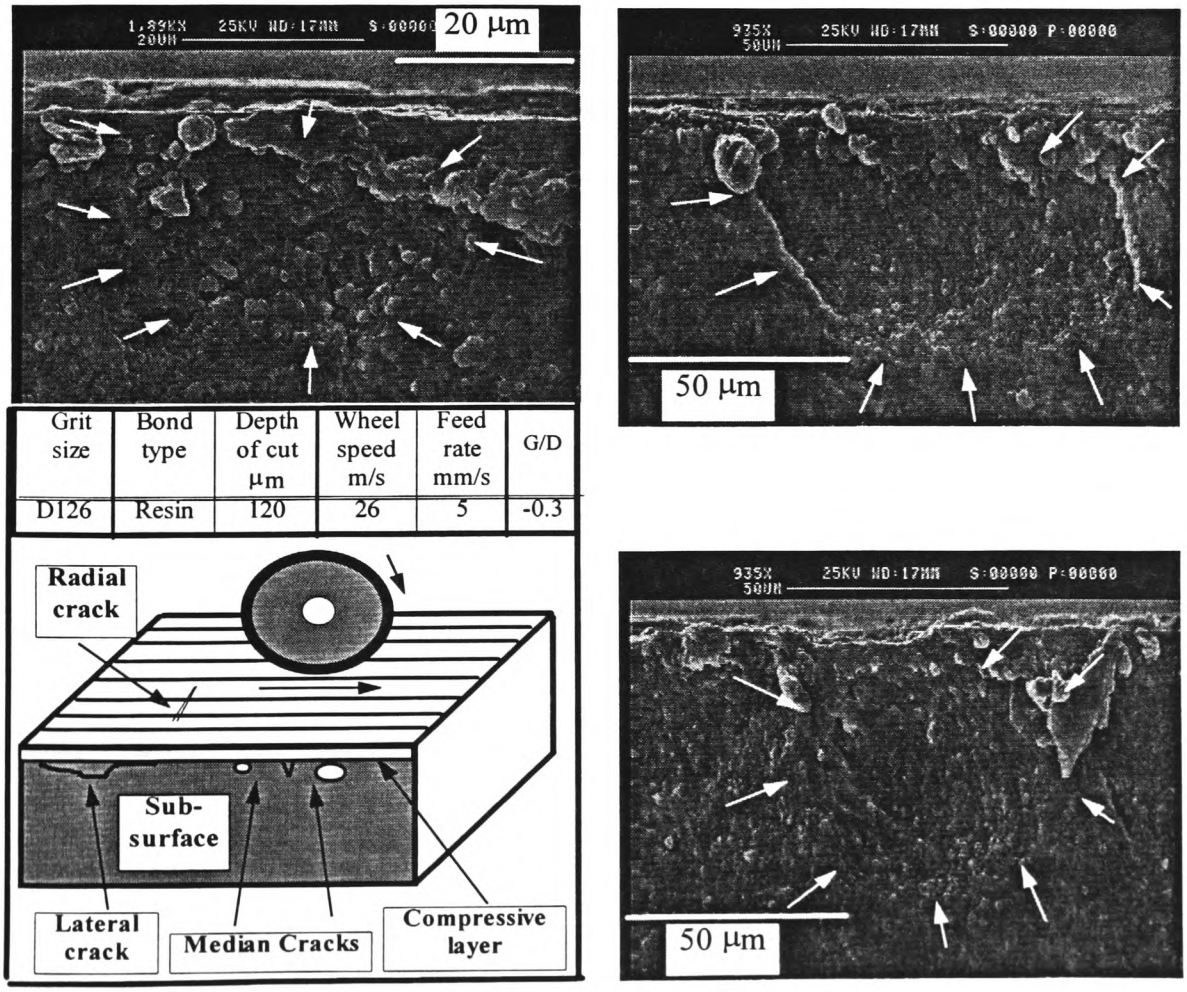

Grit size	Bond type	Depth of cut µm	Wheel speed m/s	Feed rate mm/s	G/D
D126	Resin	120	26	5	-0.3

Figure 155: The effect of grinding wheel and machine parameters mentioned above on the surface and sub-surface cracks and their distance from the ground surface.

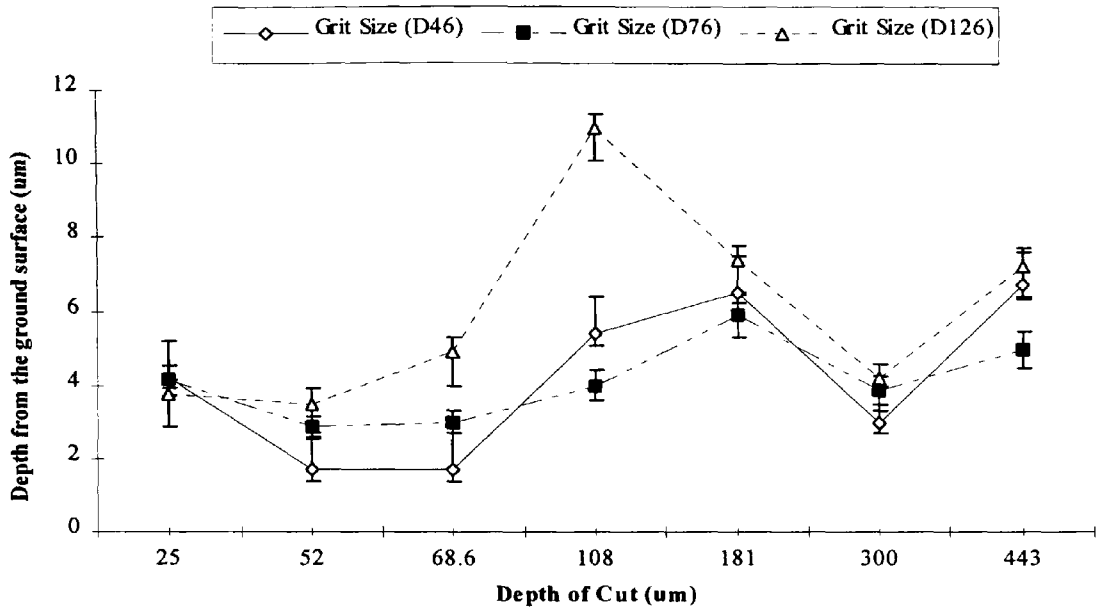

Figure 156: Subsurface crack distance from the ground surface against depth of cut for different levels of grit size.

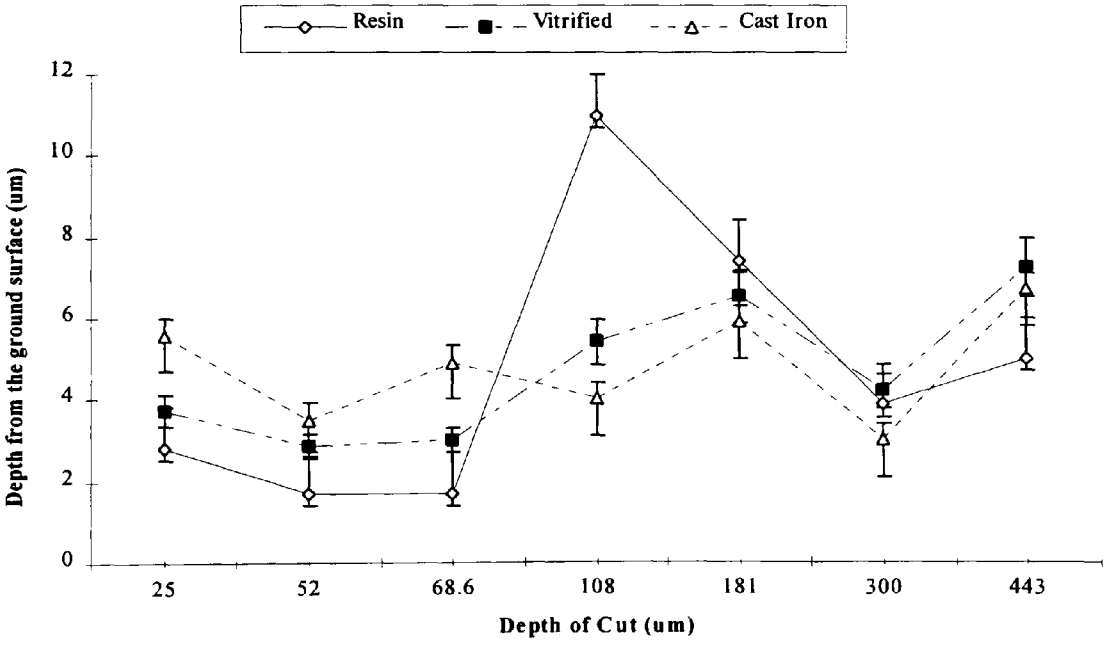

Figure 157: Subsurface crack distance from the ground surface against depth of cut for different levels of bond type.

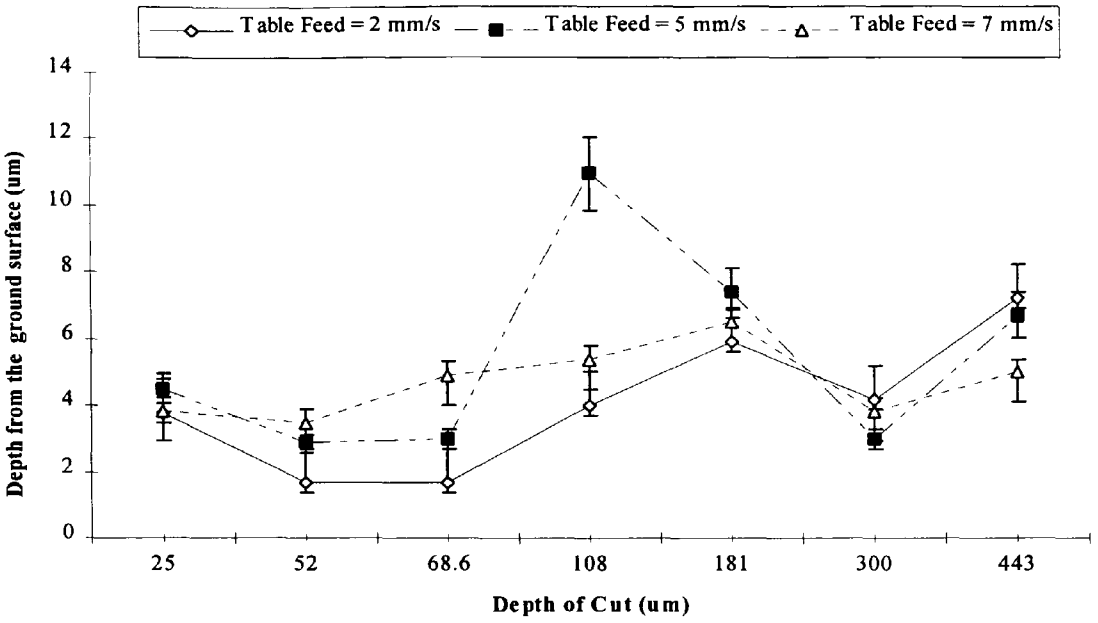

Figure 158: Subsurface crack distance from the ground surface against depth of cut for different levels of table feed.

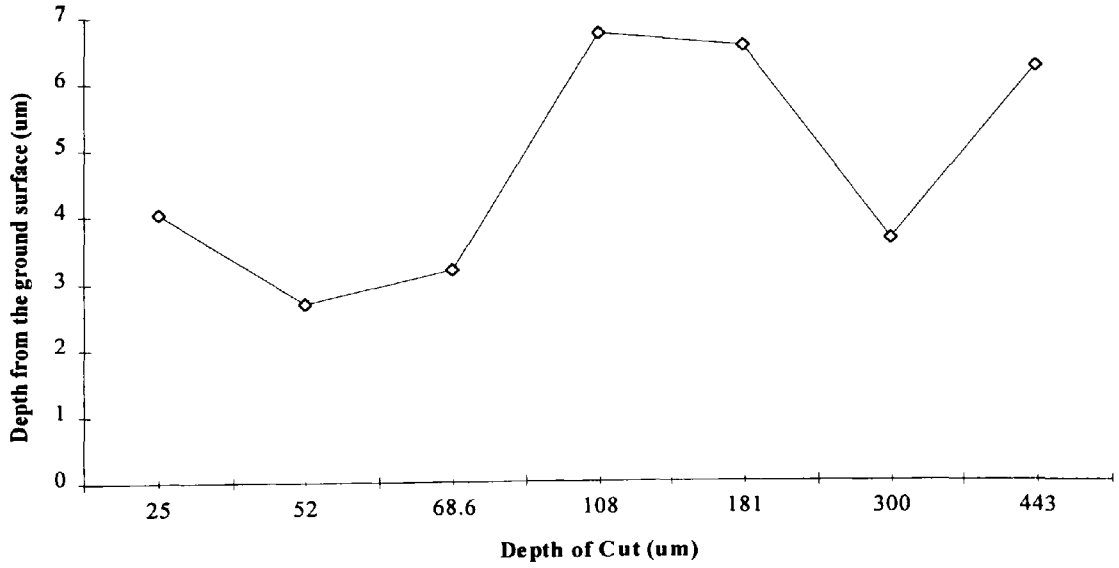

Figure 159: Subsurface crack distance from the ground surface against depth of cut averaged over different levels of table feed.

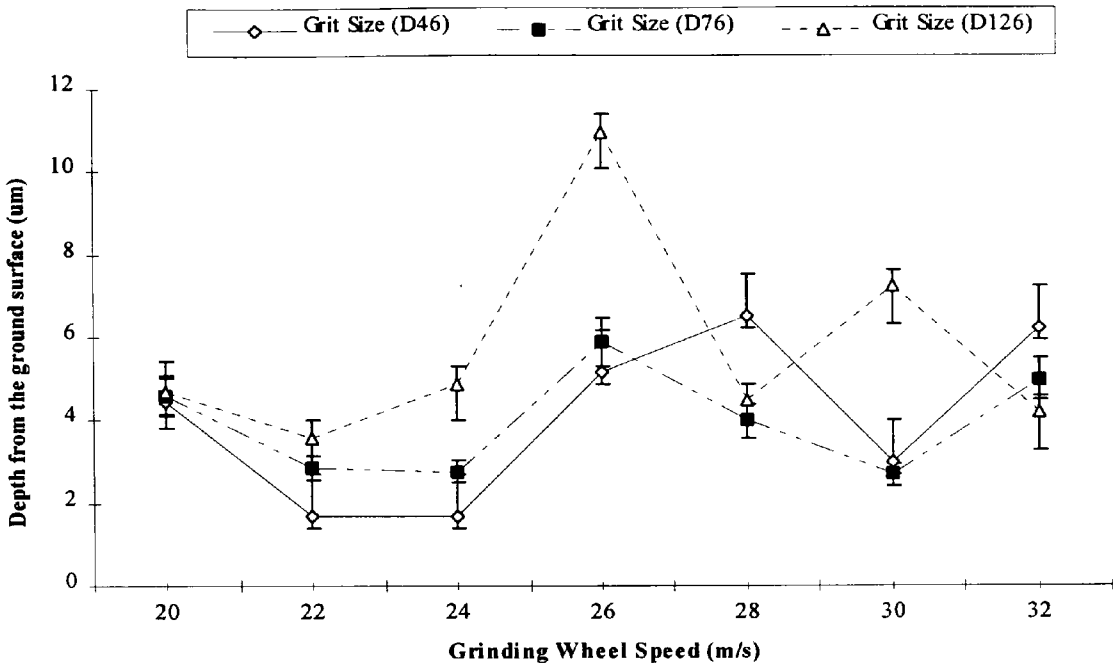

Figure 160: Subsurface crack distance from the ground surface against grinding wheel speed for different levels of grit size.

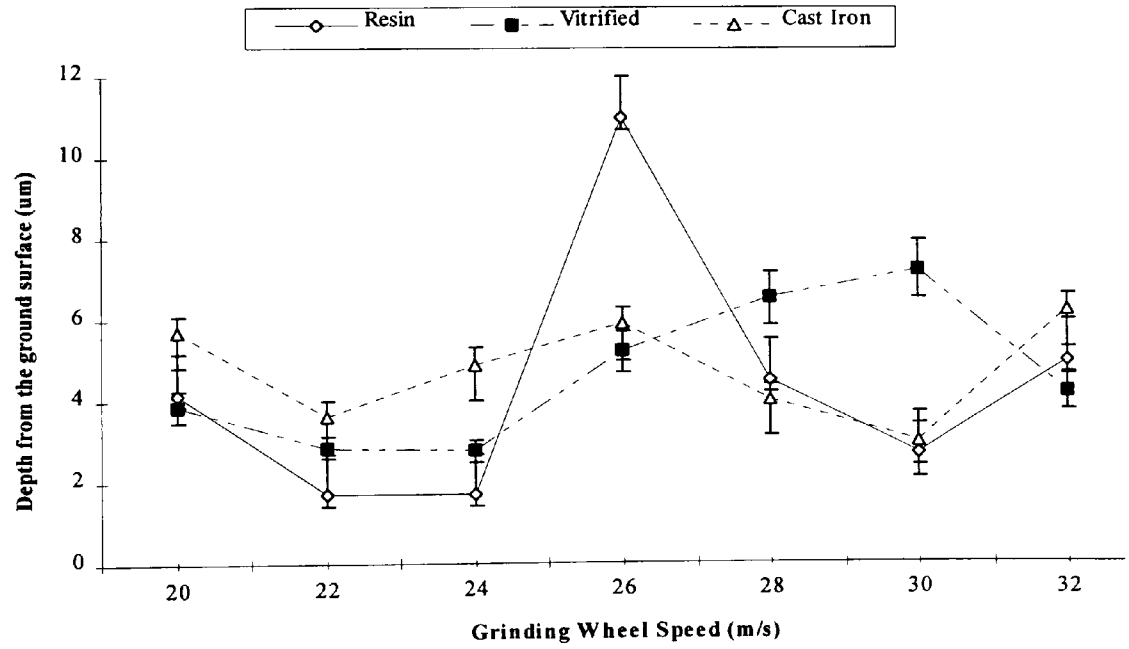

Figure 161: Subsurface crack distance from the ground surface against grinding wheel speed for different levels of bond type.

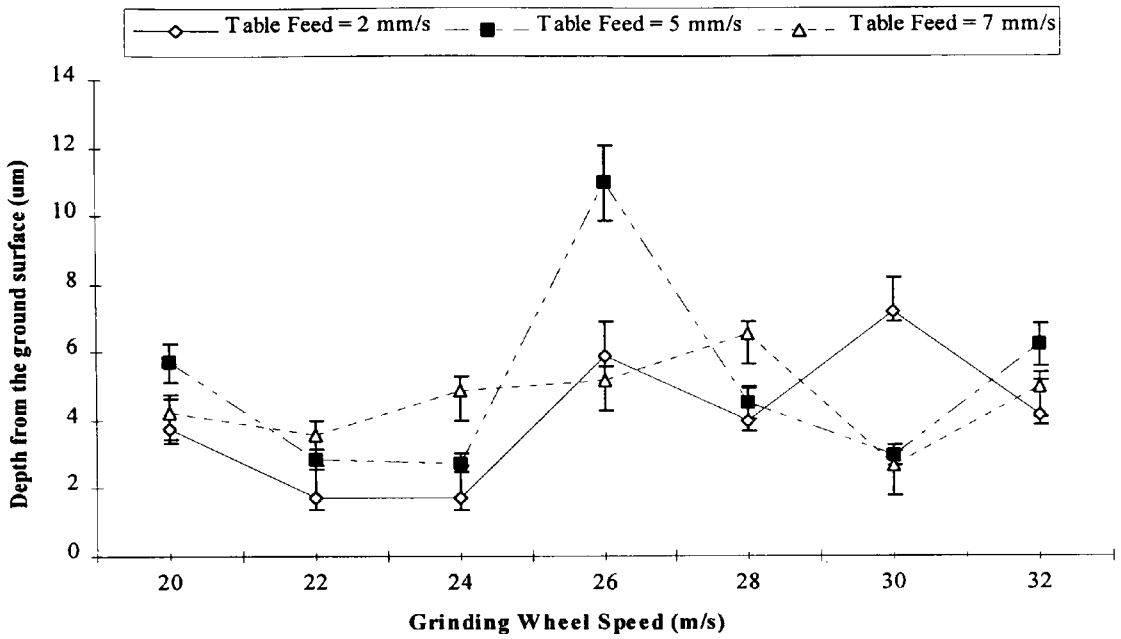

Figure 162: Subsurface crack distance from the ground surface against grinding wheel speed for different levels of table feed.

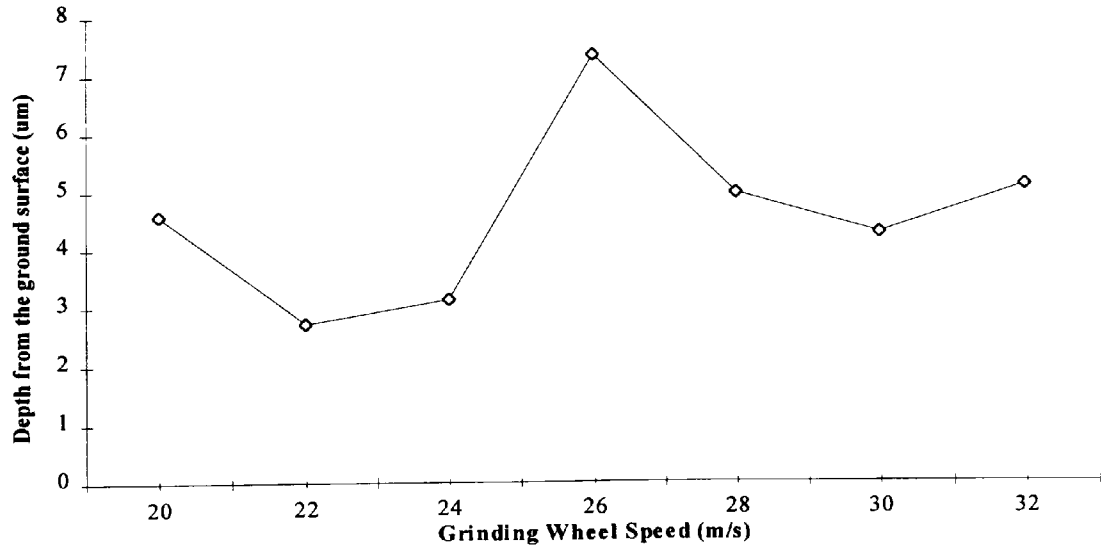

Figure 163: Subsurface crack distance from the ground surface against grinding wheel speed averaged over different levels of table feed.

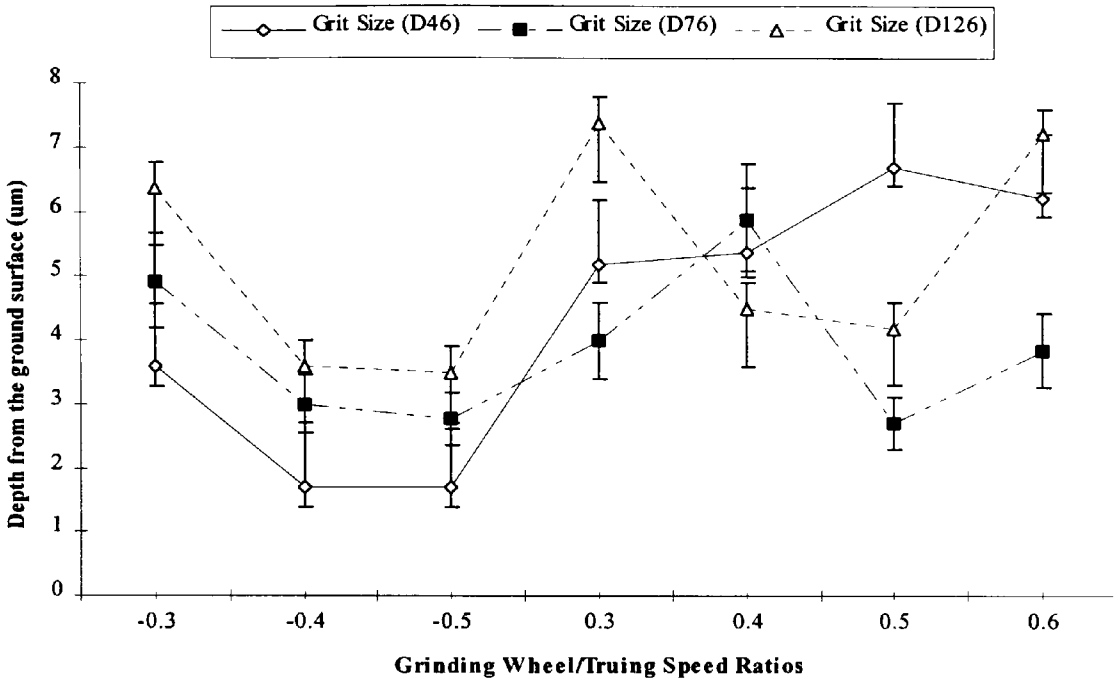

Figure 164: Subsurface crack distance from the ground surface against grinding wheel/truing speed ratios for different levels of grit size.

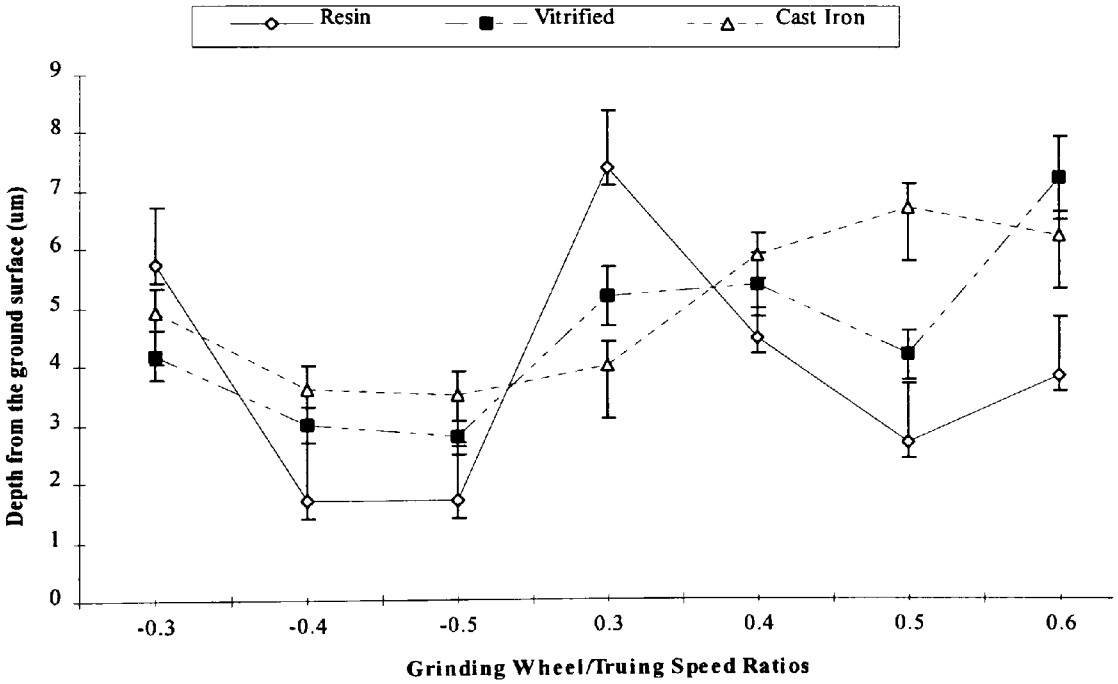

Figure 165: Subsurface crack distance from the ground surface against grinding wheel/truing speed ratios for different levels of grinding wheel bond type.

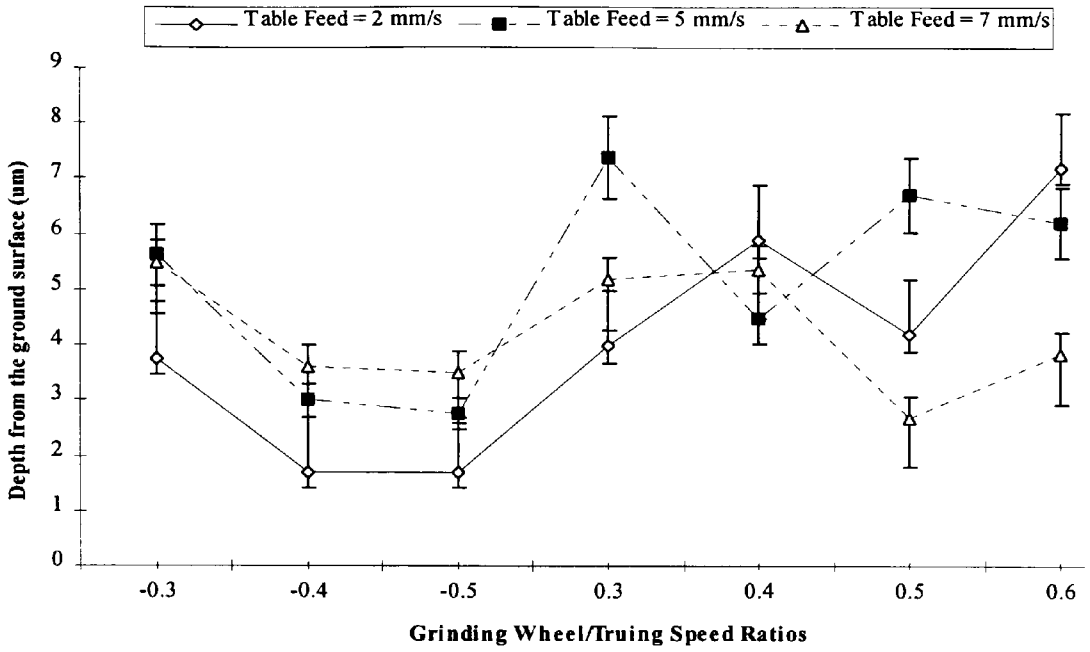

Figure 166: Subsurface crack distance from the ground surface against grinding wheel/truing speed ratios for different levels of table feed.

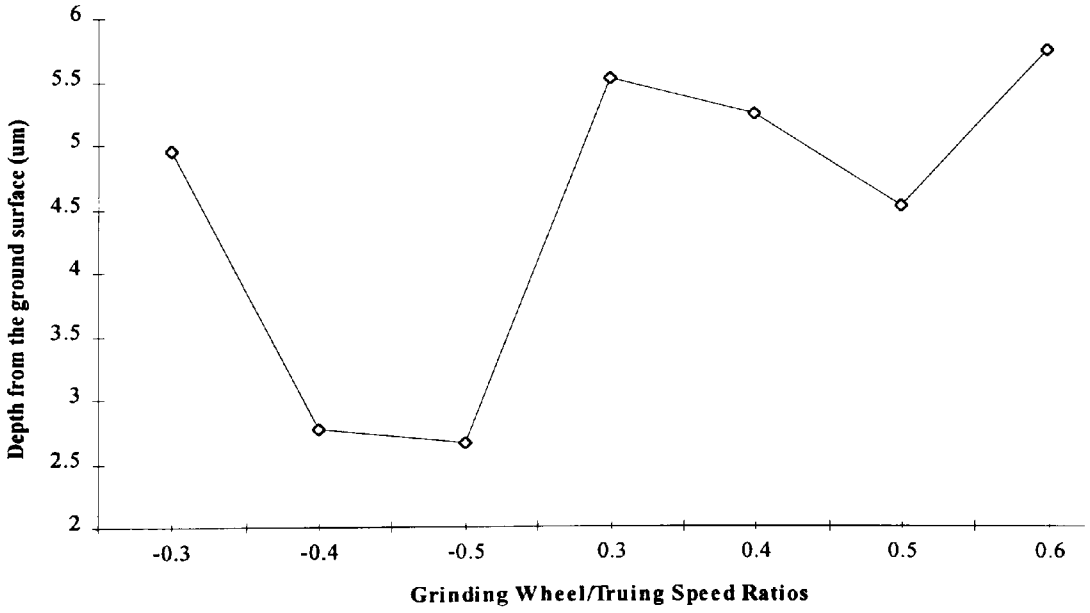

Figure 167: Subsurface crack distance from the ground surface against grinding wheel/truing speed ratios averaged over different levels of table feed.

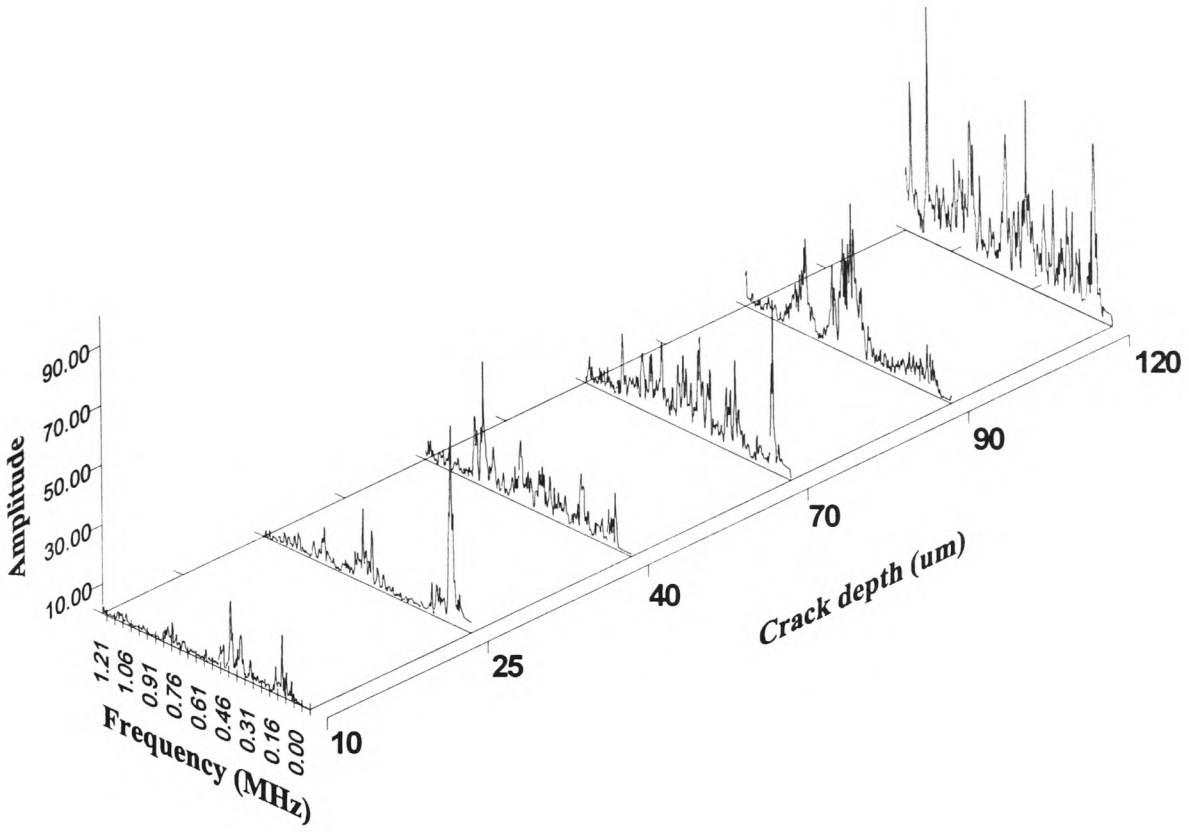

Figure 168: AE spectral amplitude against frequency generated from different groove depths.

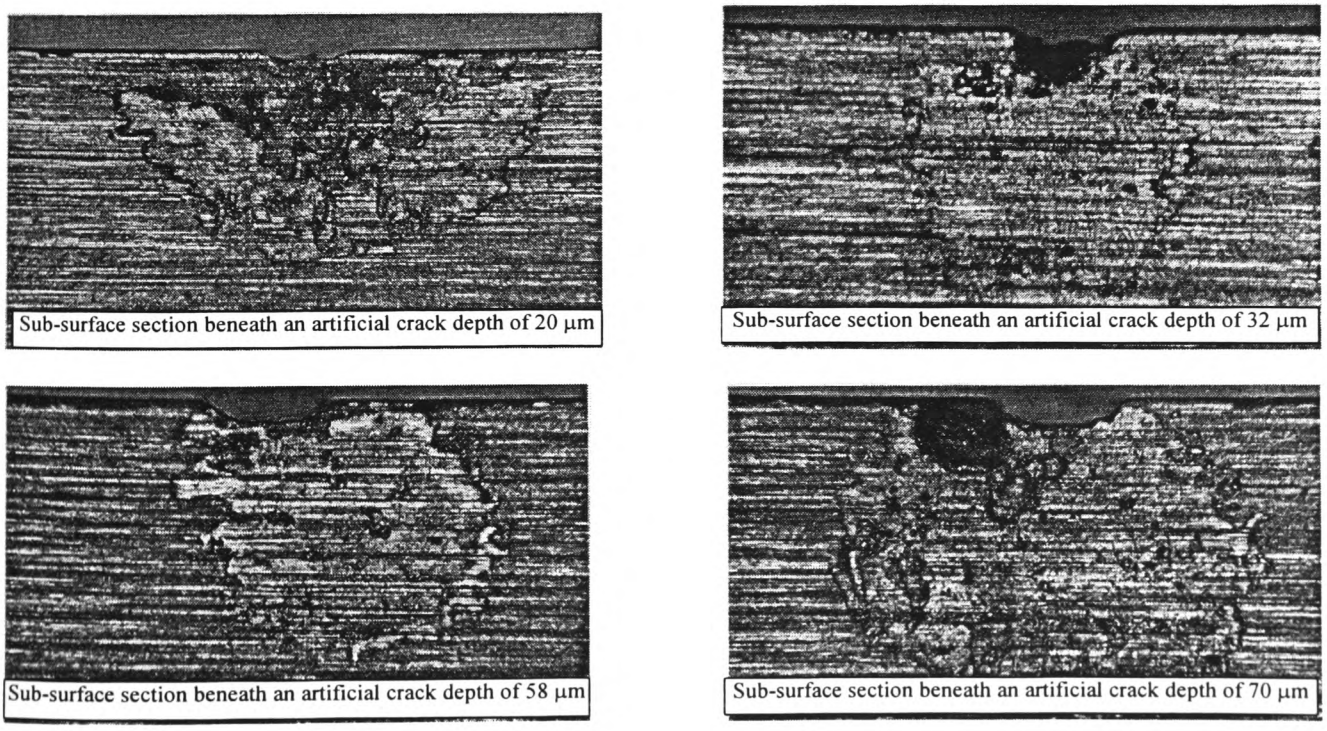

Figure 169: Microscopy observations of the affected zone underneath the groove created by v-shape disc.

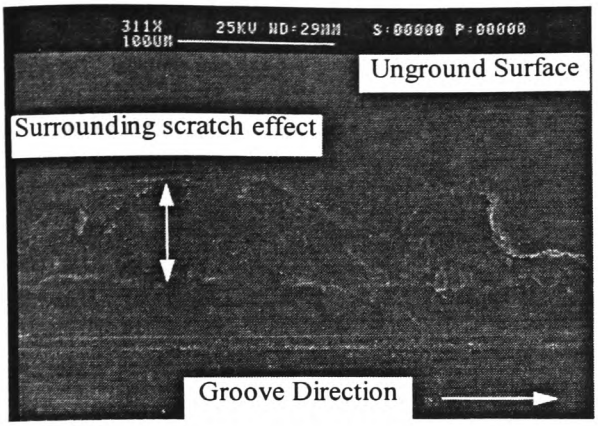

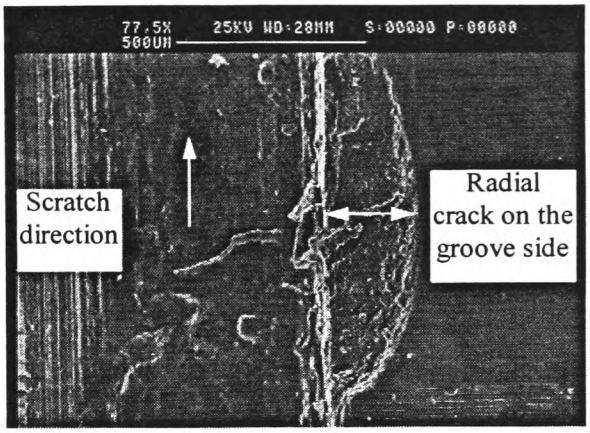

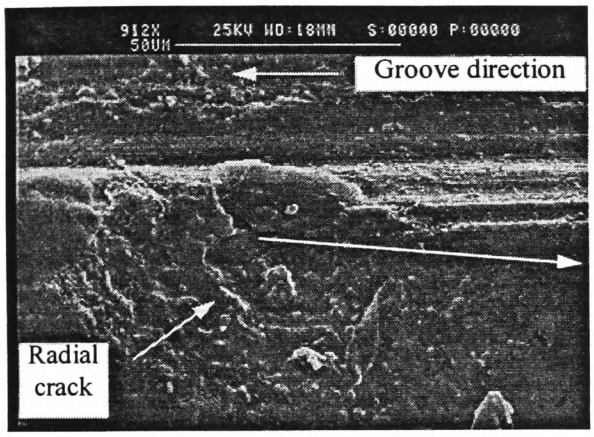

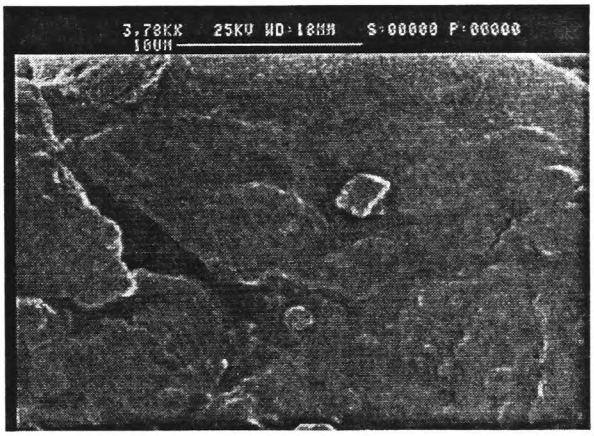

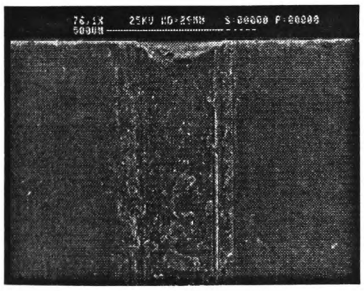

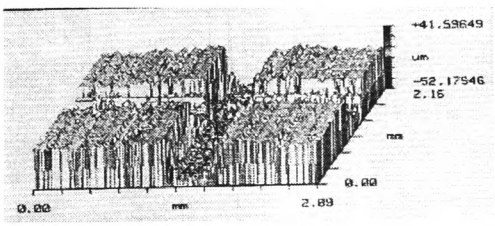

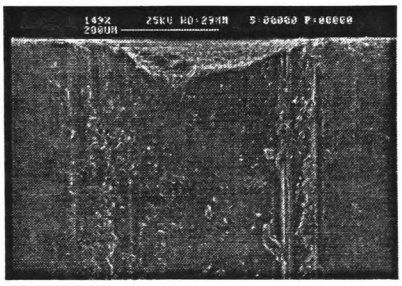

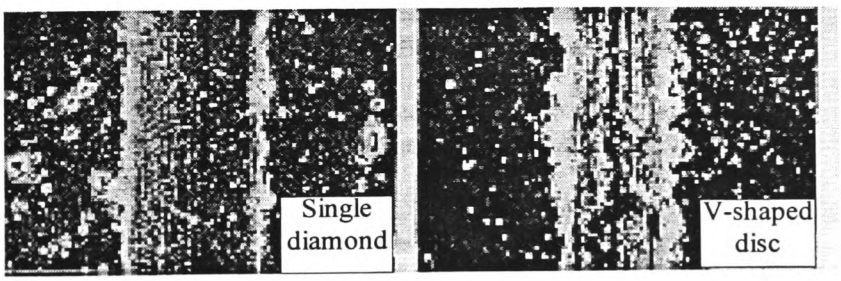

Figure 170: Effect of v-shape scratch on the surrounding area of the groove compared with a single diamond scratch test.

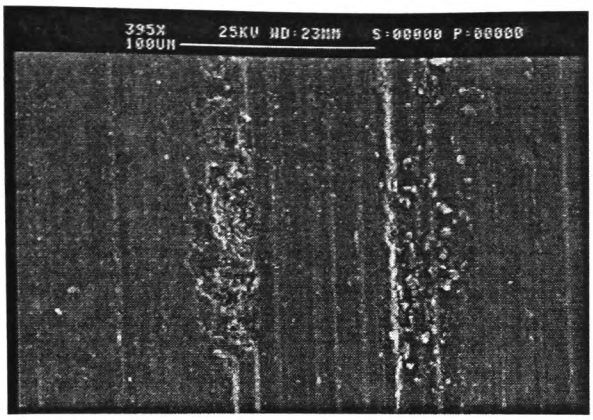

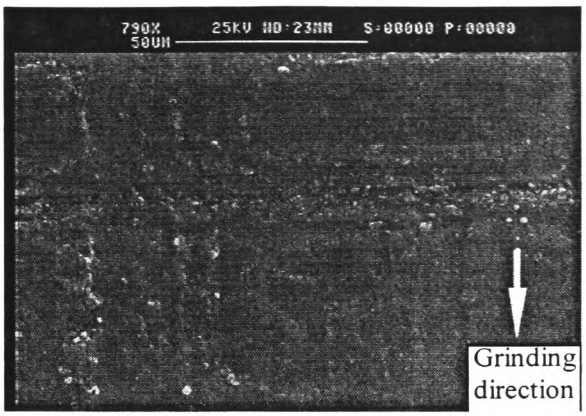

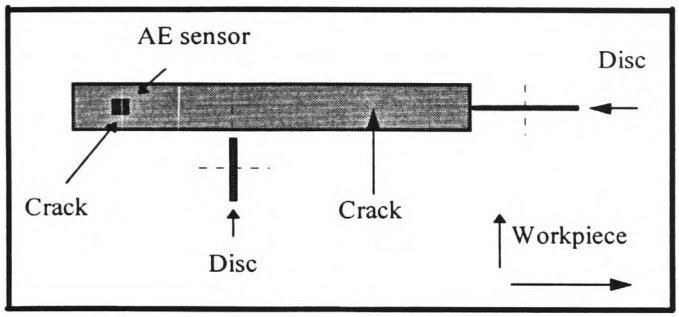

I

Crack initiation on the ceramic surface specimens

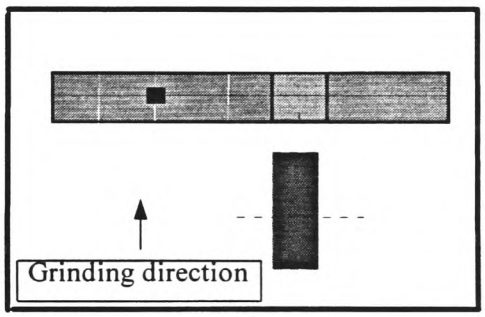

II

Grinding on the cracks initiated on the surface of ceramic specimens

Grit size	Bond type	Depth of cut µm	Wheel speed m/s	Feed rate mm/s	crack depth µm	G/D
D76	Cast iron	13.5	20	2	25	-0. 3

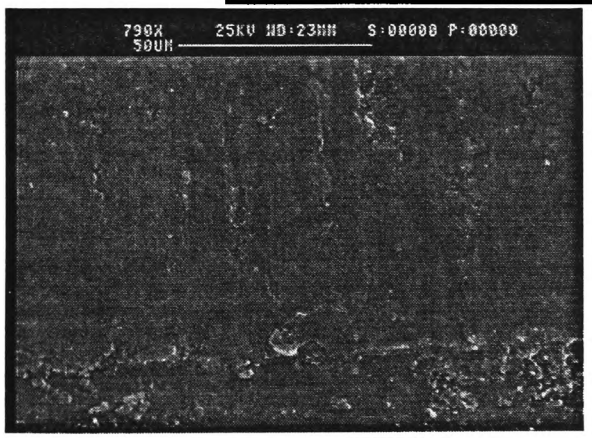

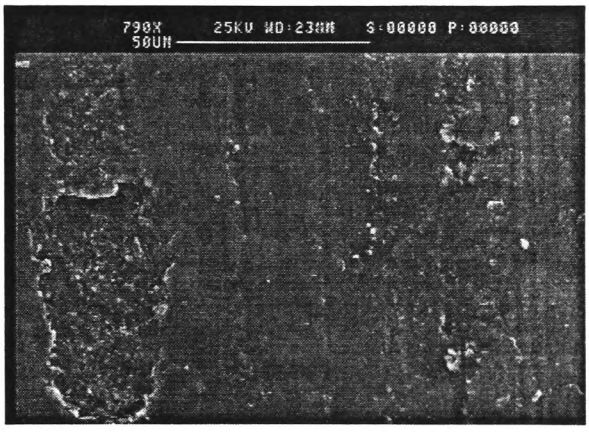

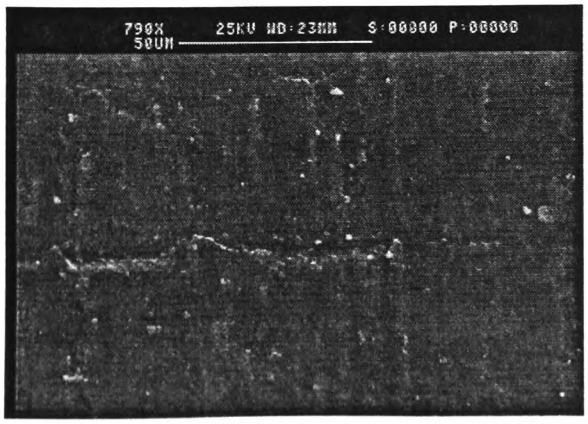

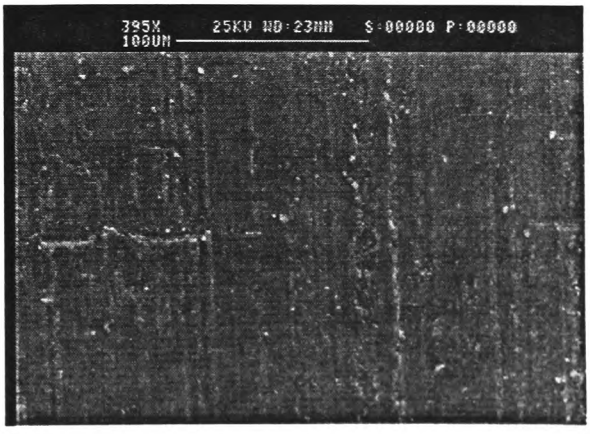

Figure 171: Grinding on the specimen with crack initiated on the surface at grinding wheel and machine parameters mentioned above.

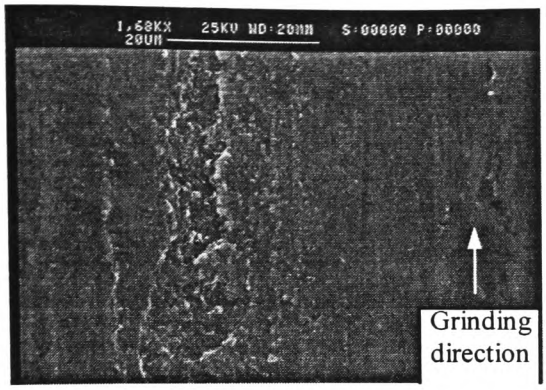

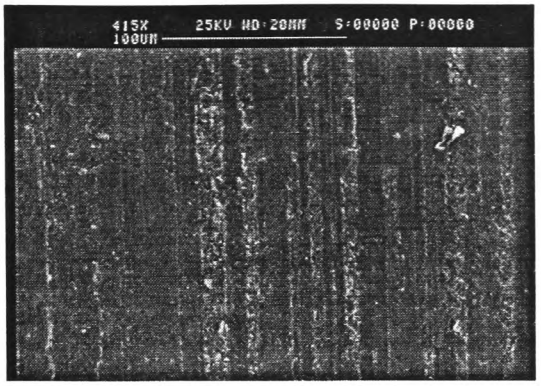

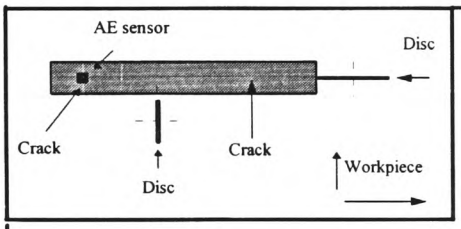

I

Crack initiation on the ceramic surface specimens

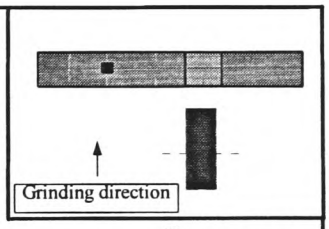

II

Grinding on the cracks initiated on the surface of ceramic specimens

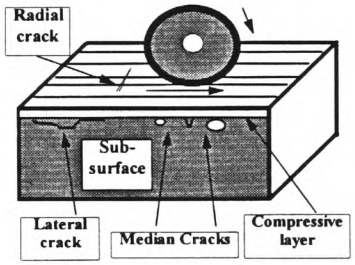

Grit size	Bond type	Depth of cut µm	Wheel speed m/s	Feed rate mm/s	Crack depth µm	G/D
D46	Vitri fied	12.5	26	7	30	0. 3

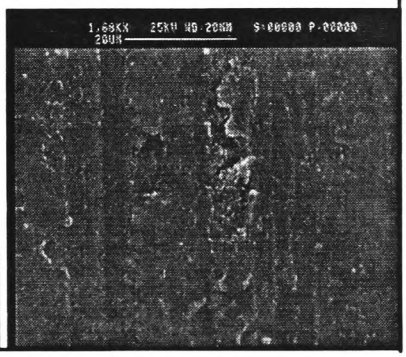

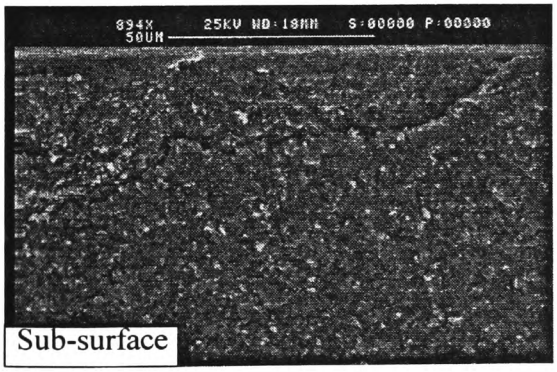

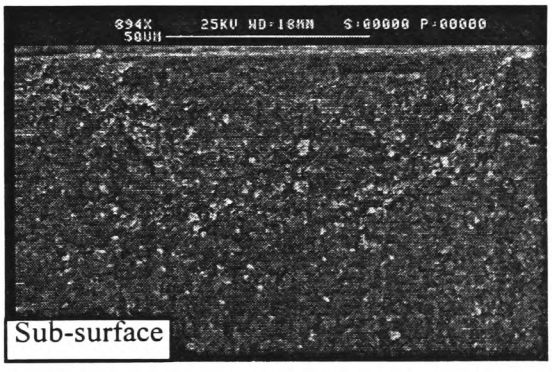

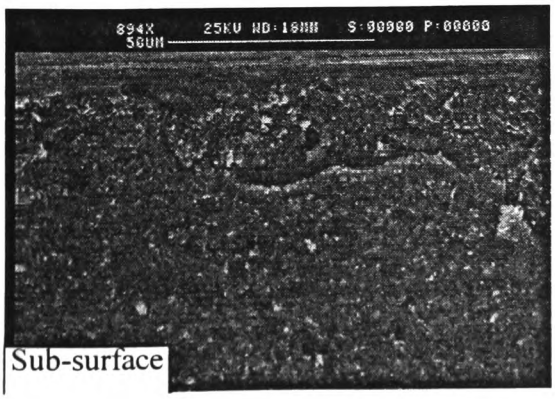

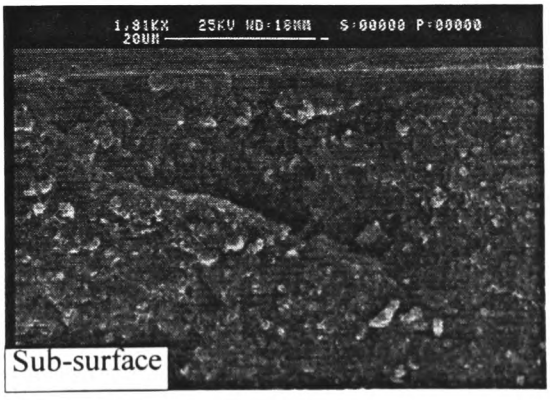

Figure 172: Grinding on the specimen with crack initiated on the surface at grinding wheel and machine parameters mentioned above.

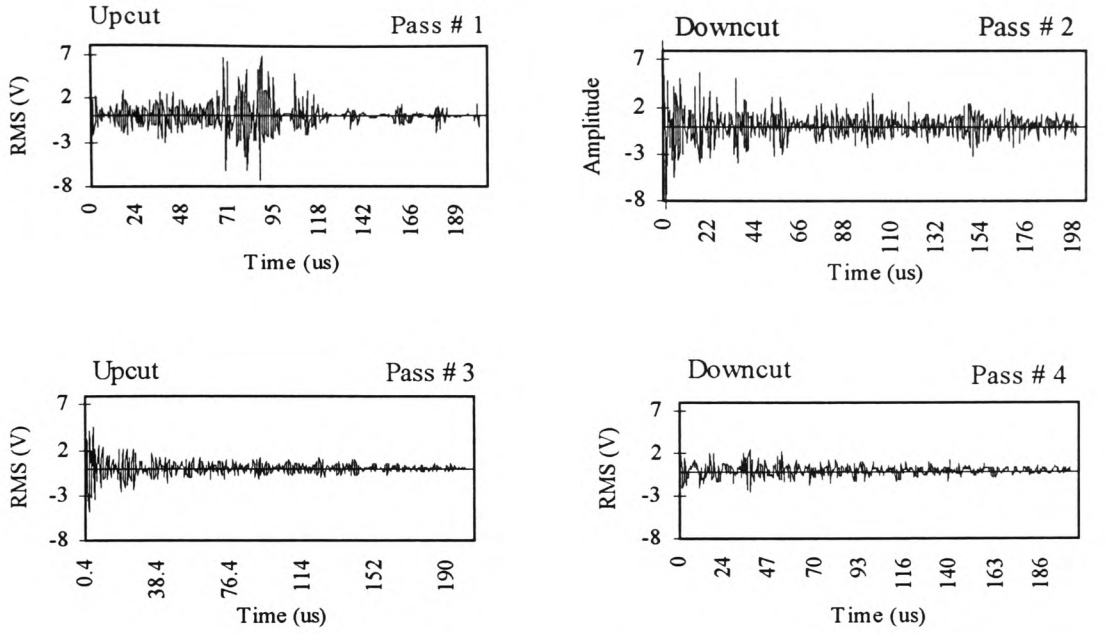

Sialon Type	Crack Depth µm	Depth of Cut µm	Table Feed mm/s	Wheel Speed m/s	Gri./Tru. Speed ratio	Grit Size	Wheel bond Type
201	30	50	1	32	0.3	D76	Cast Iron

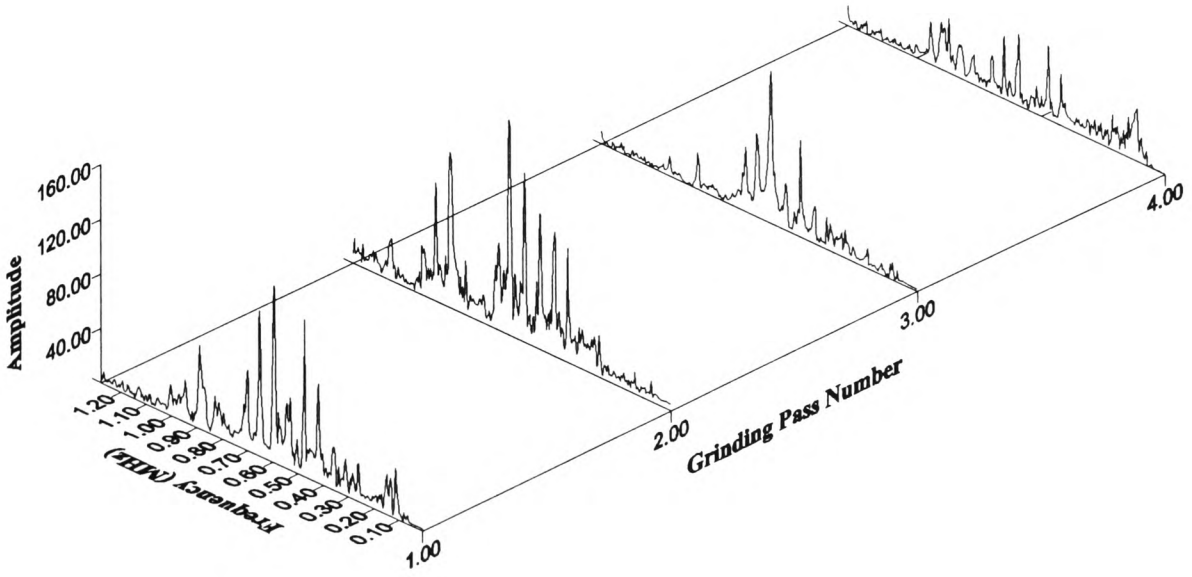

Figure 173: AE spectral amplitude generated during different grinding passes with cracks initiated on the ceramic surface specimens at grinding wheel and machine parameters mentioned above.

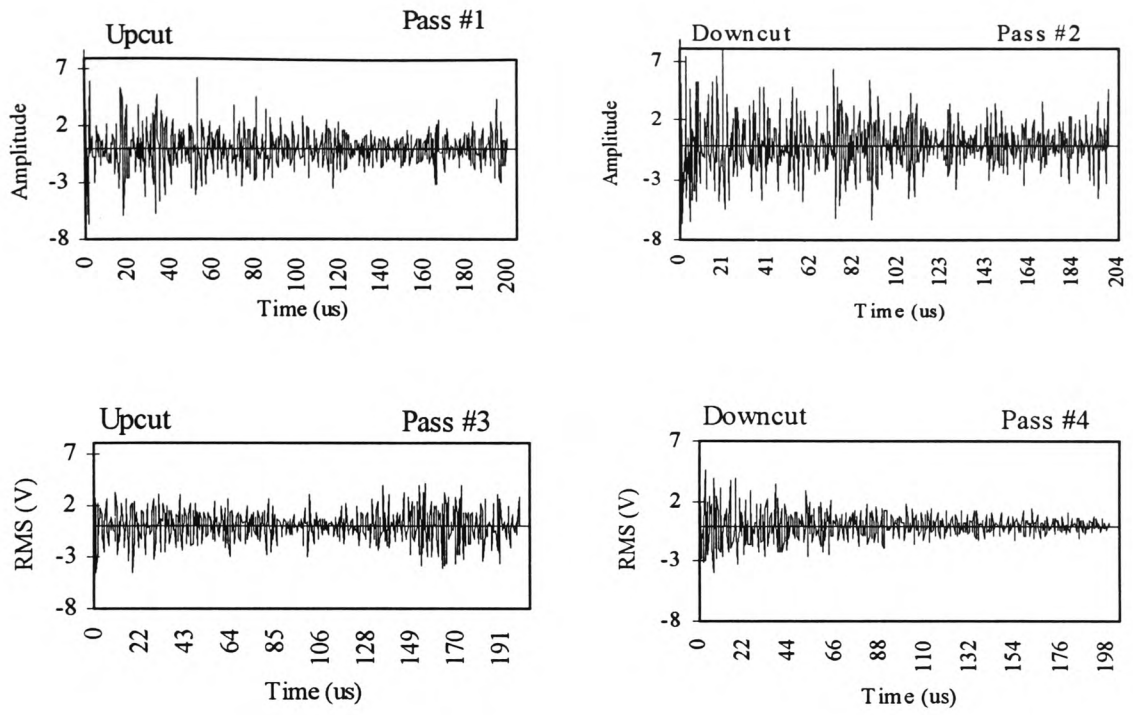

Sialon Type	Crack Depth µm	Depth of Cut µm	Table Feed mm/s	Wheel Speed m/s	Gri./Tru. Speed ratio	Grit Size	Wheel bond Type
101	70	150	1	32	-0.3	D46	Vitrified

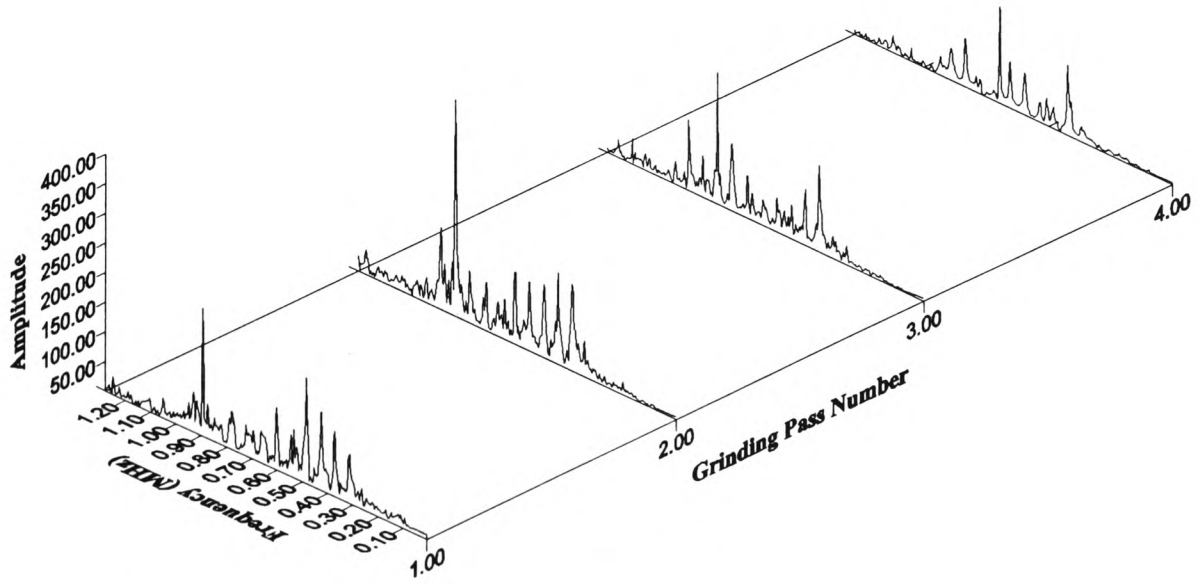

Figure 174: AE spectral amplitude generated during different grinding passes with cracks initiated on the ceramic surface specimens at grinding wheel and machine parameters mentioned above.

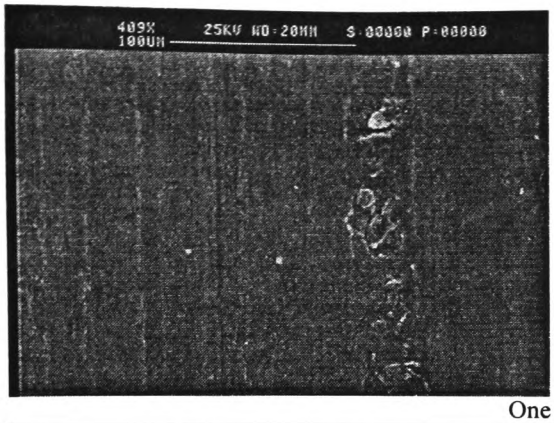
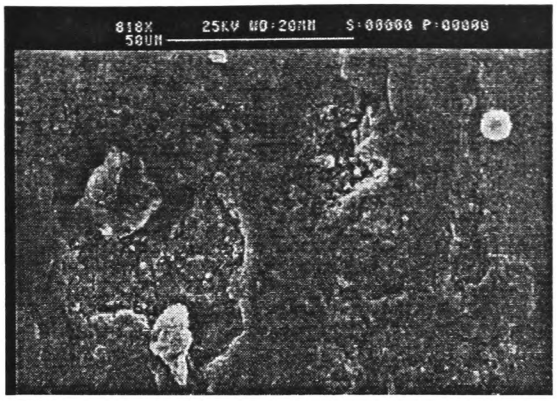

One grinding pass

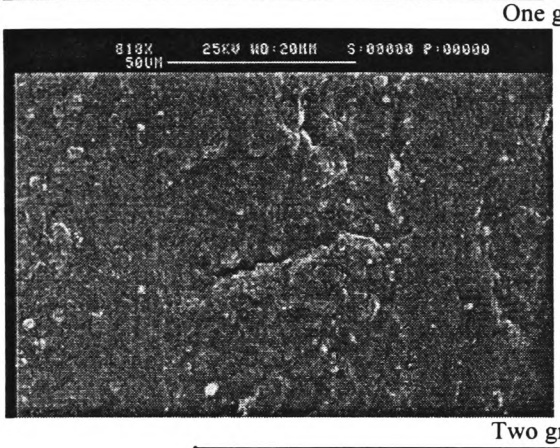
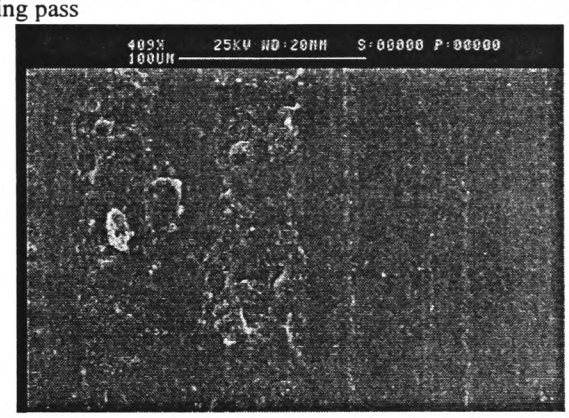

Two grinding passes

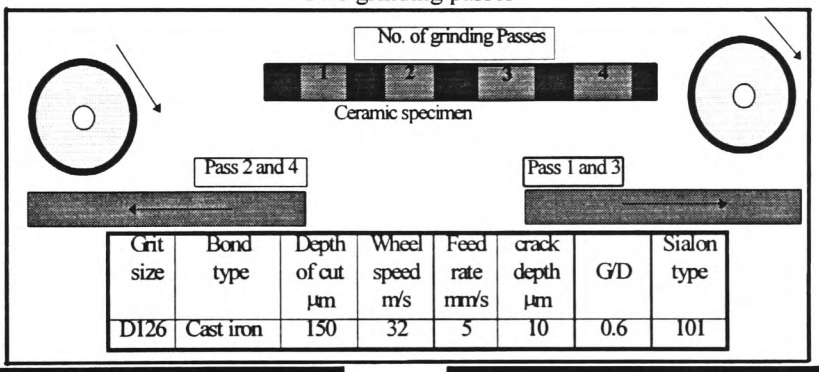

Grit size	Bond type	Depth of cut µm	Wheel speed m/s	Feed rate mm/s	crack depth µm	G/D	Sialon type
D126	Cast iron	150	32	5	10	0.6	101

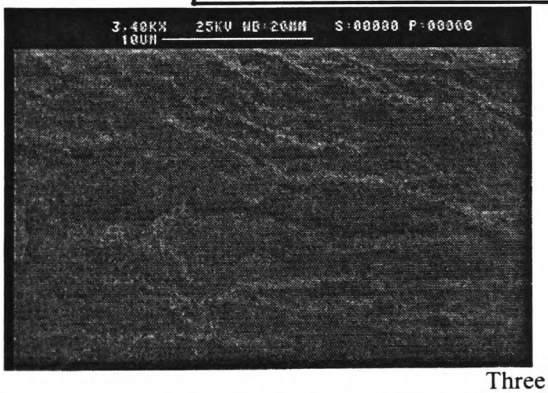
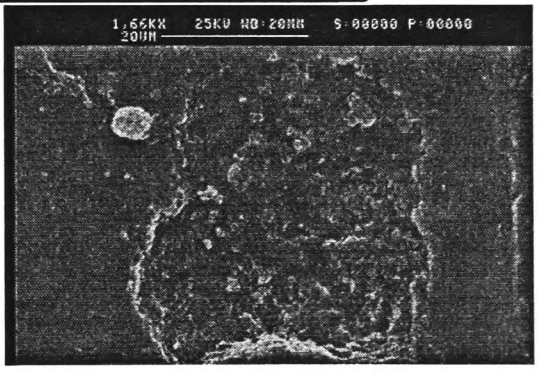

Three grinding passes

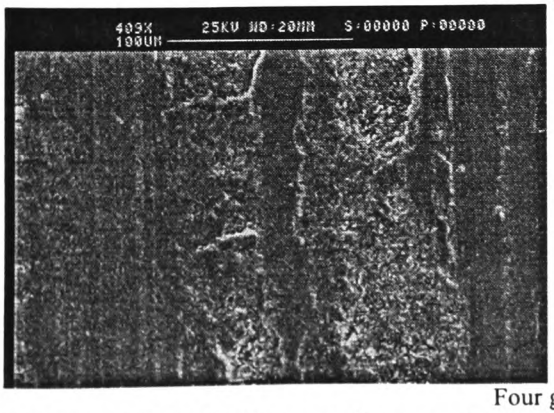
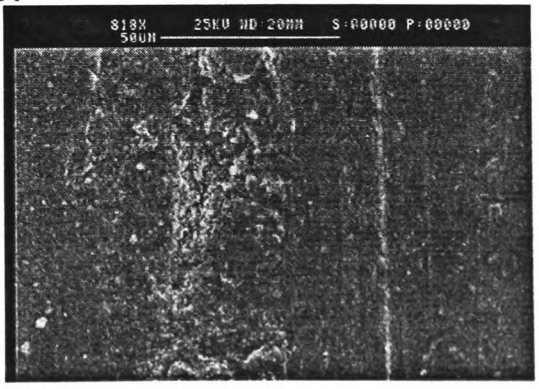

Four grinding passes

Figure 175: Grinding on the specimen with crack initiated on the surface at different grinding passes and grinding wheel and machine parameters mentioned above.

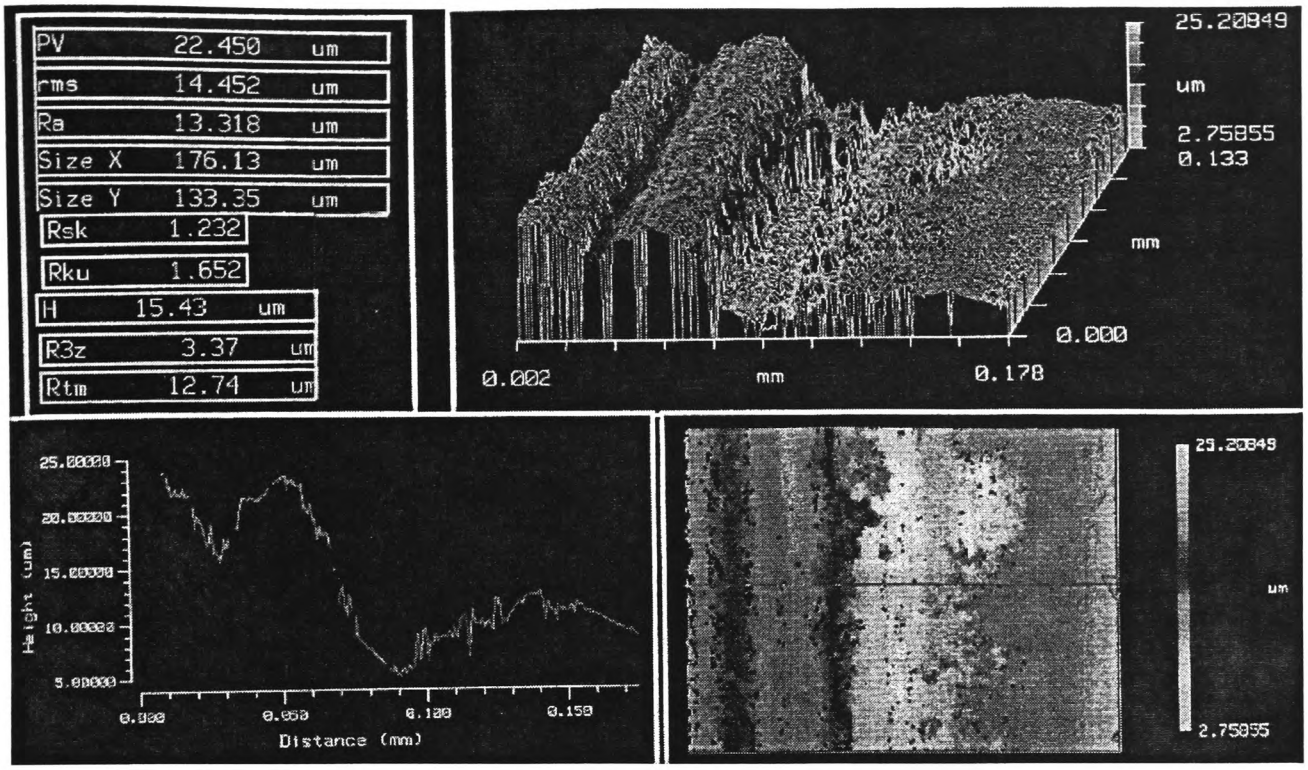

Figure 176: Depth of surface damage on the ground surface at 13 μm depth of cut, 20 m/s wheel speed, 2 mm/s table feed, D76 grit size cast iron bonded wheel and -0.3 grinding wheel/truing speed ratio. Grinding with artificial crack initiated on the surface.

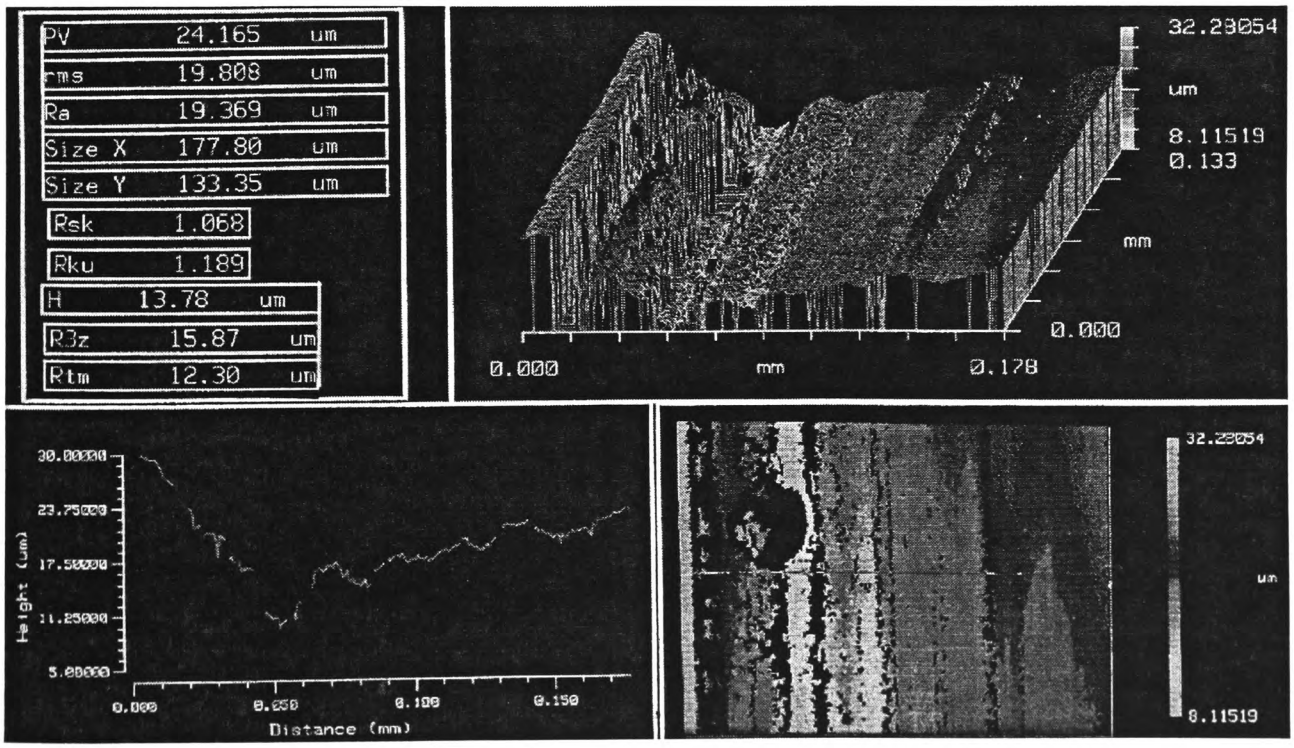

Figure 177: Depth of surface damage on the ground surface at 128.7 μm depth of cut, 26 m/s wheel speed, 5 mm/s table feed, D126 grit size resin bonded wheel and -0.3 grinding wheel/truing speed ratio. Grinding with artificial crack on the surface.

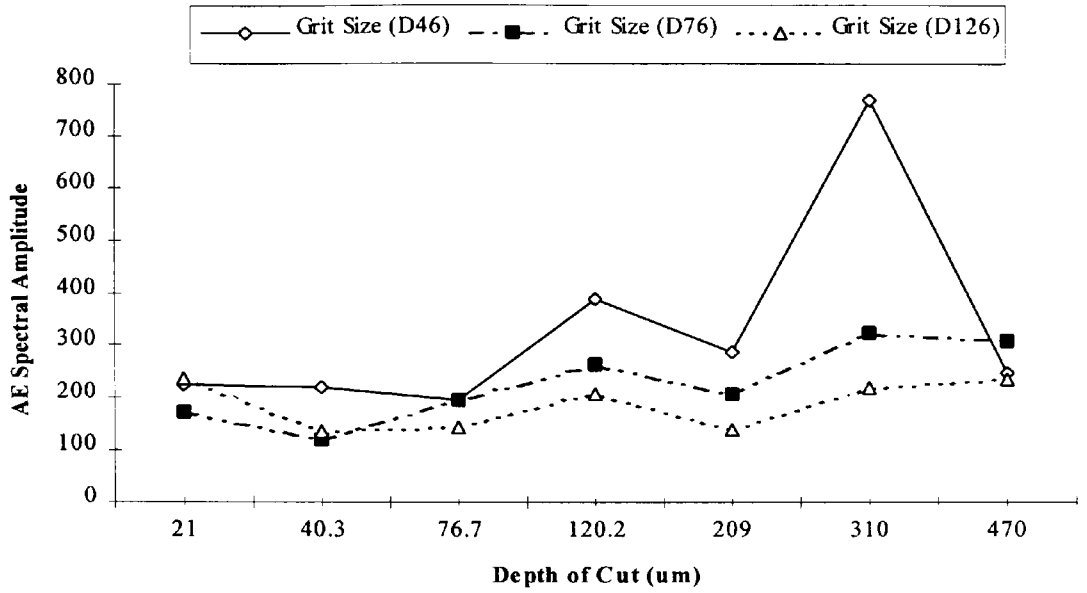

Figure 178: AE Spectral Amplitude against depth of cut for different levels of grit size for the specimens ground with cracks initiated on the surface.

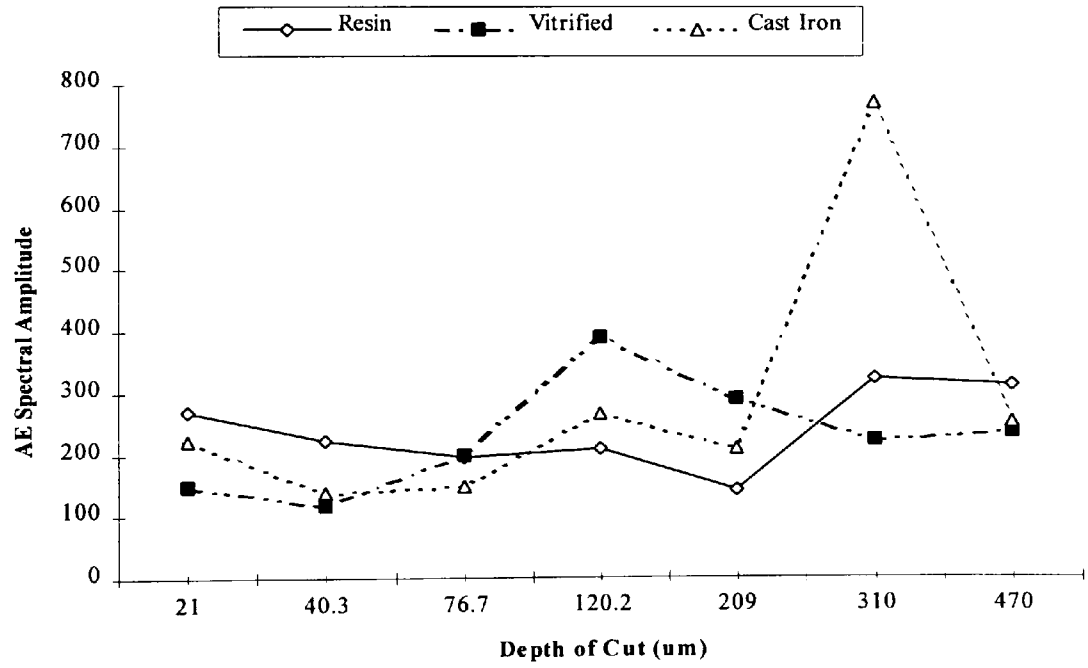

Figure 179: AE Spectral Amplitude against depth of cut for different levels of bond type for the specimens ground with cracks initiated on the surface.

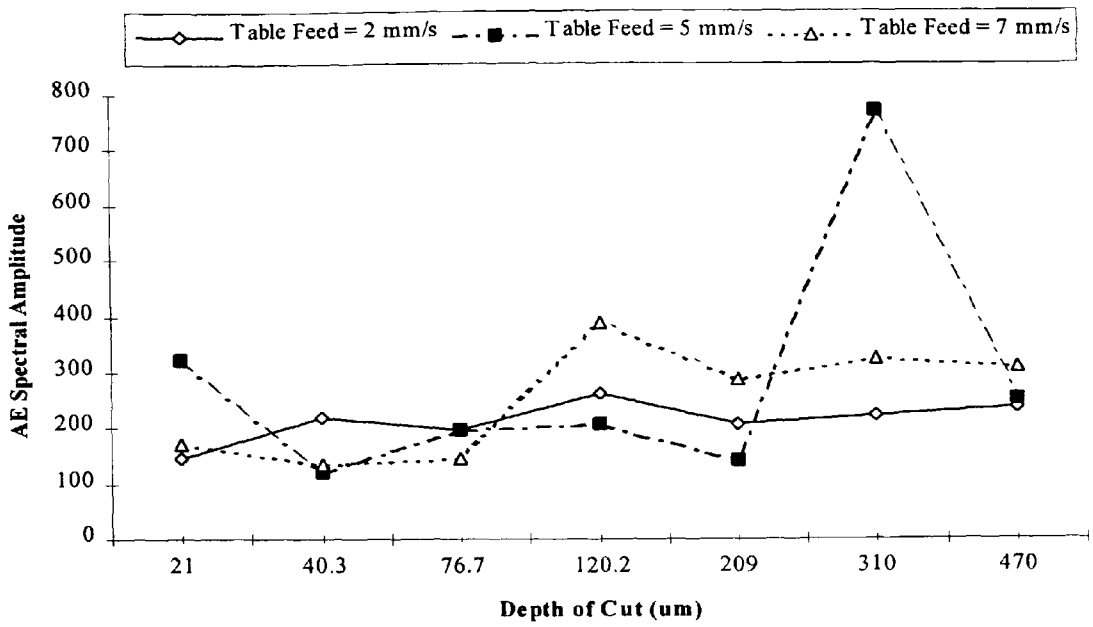

Figure 180: AE Spectral Amplitude against depth of cut for different levels of table feed for the specimens ground with cracks initiated on the surface.

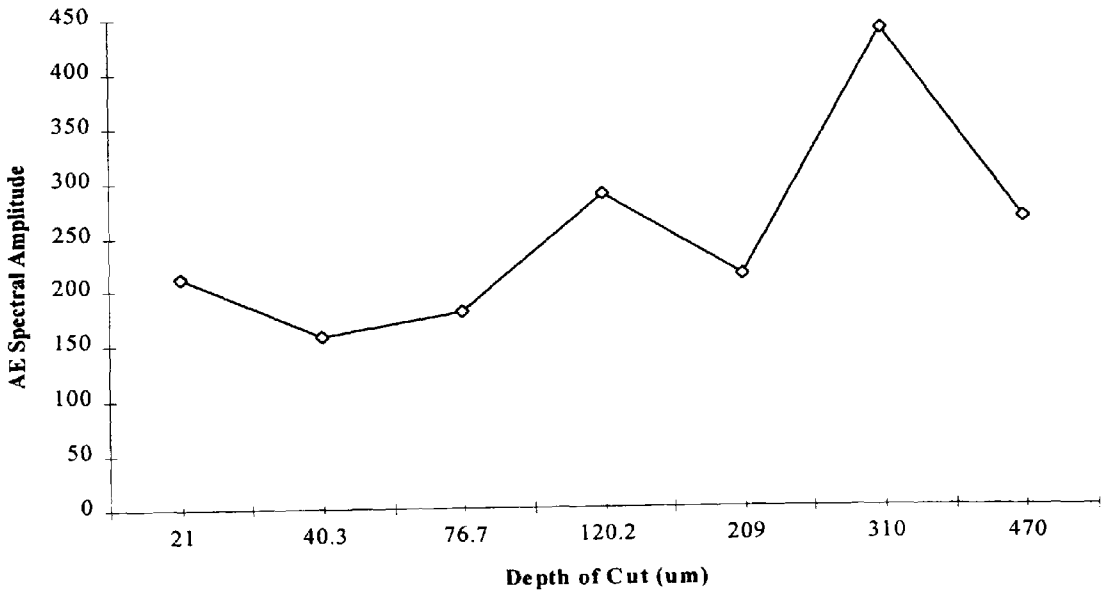

Figure 181: AE Spectral Amplitude against depth of cut averaged over different levels of table feed for the specimens ground with cracks initiated on the surface.

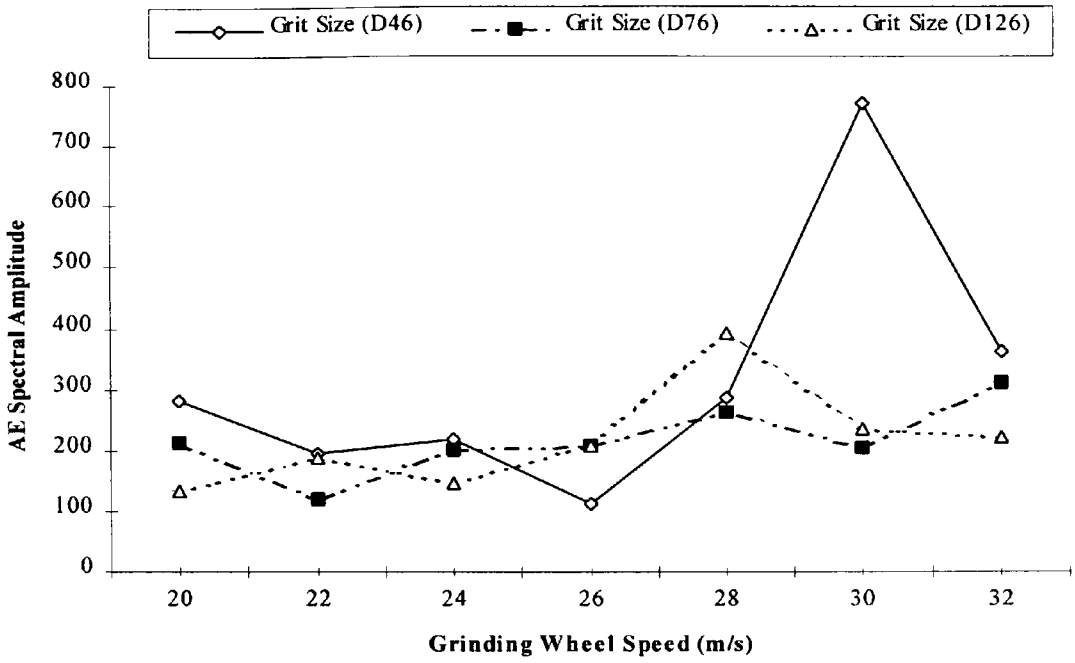

Figure 182: AE Spectral Amplitude against grinding wheel speed for different levels of grit size for the specimens ground with cracks initiated on the surface.

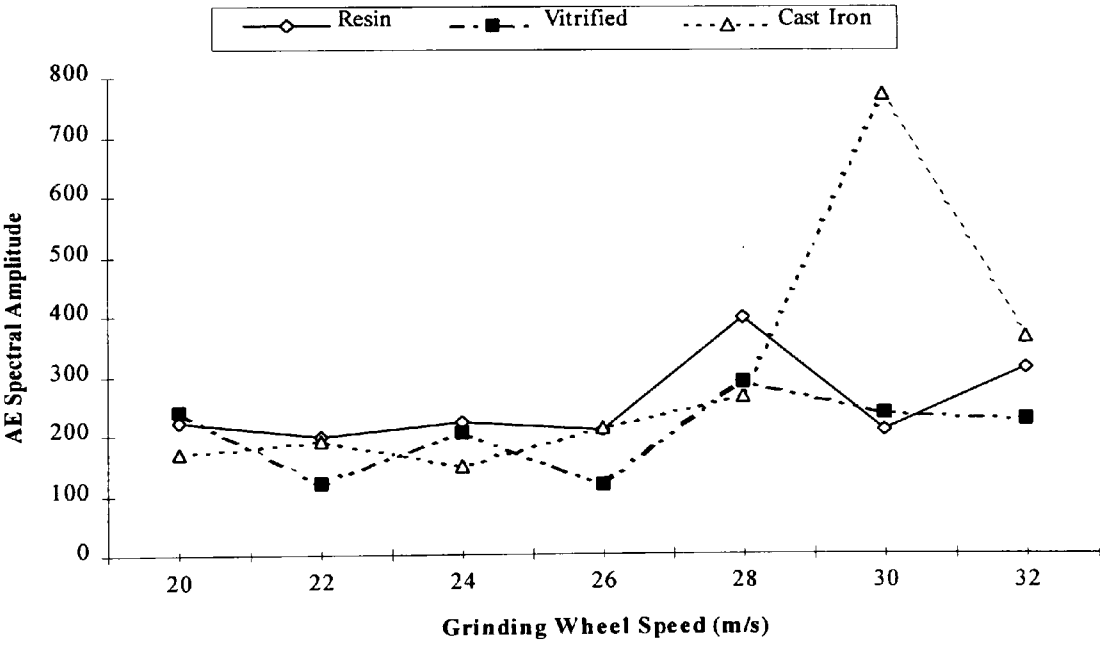

Figure 183: AE Spectral Amplitude against grinding wheel speed for different levels of bond type for the specimens ground with cracks initiated on the surface.

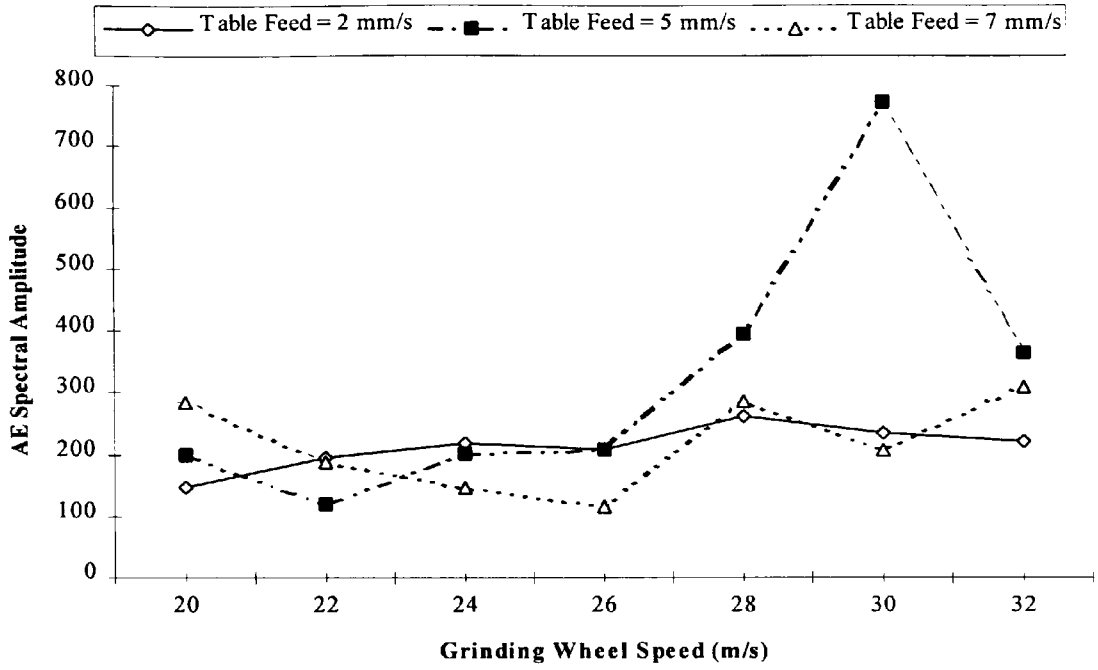

Figure 184: AE Spectral Amplitude against grinding wheel speed for different levels of table feed for the specimens ground with cracks initiated on the surface.

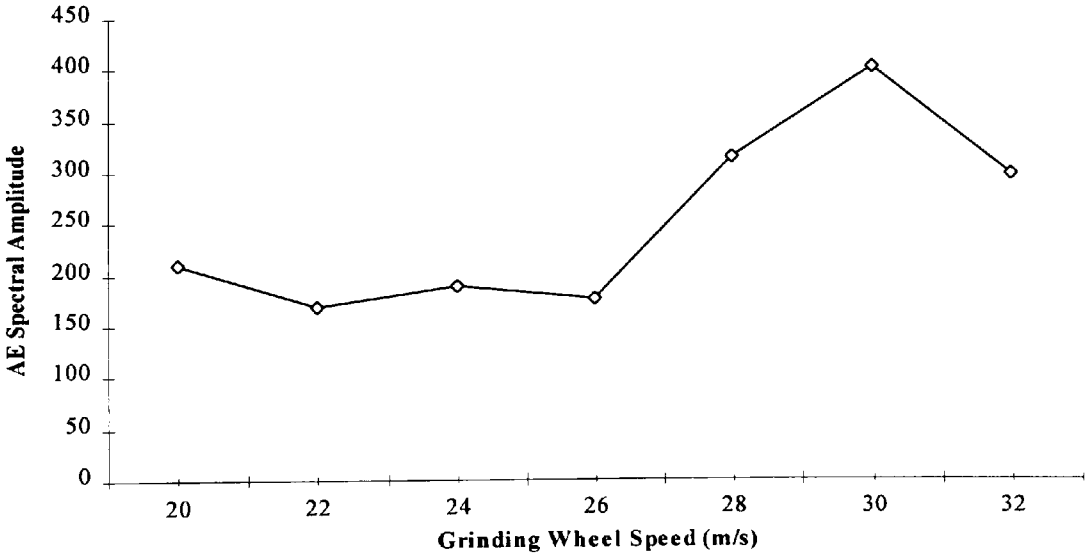

Figure 185: AE Spectral Amplitude against grinding wheel speed averaged over different levels of table feed for the specimens ground with cracks initiated on the surface.

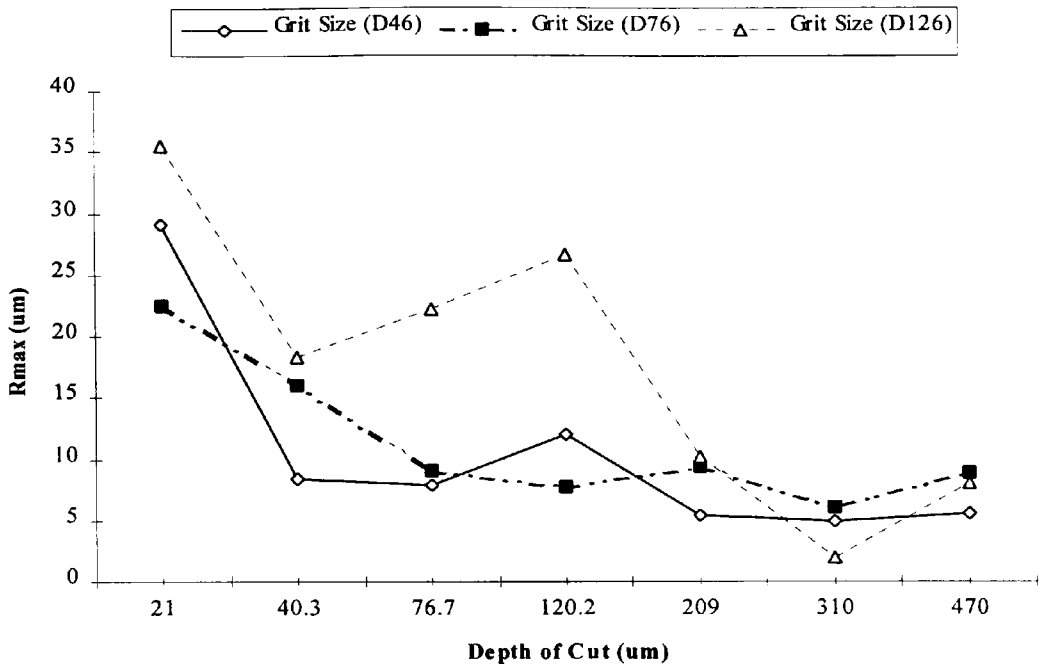

Figure 186: Depth of surface damage (Rmax) against depth of cut for different levels of grit size for the specimens ground with cracks initiated on the surface.

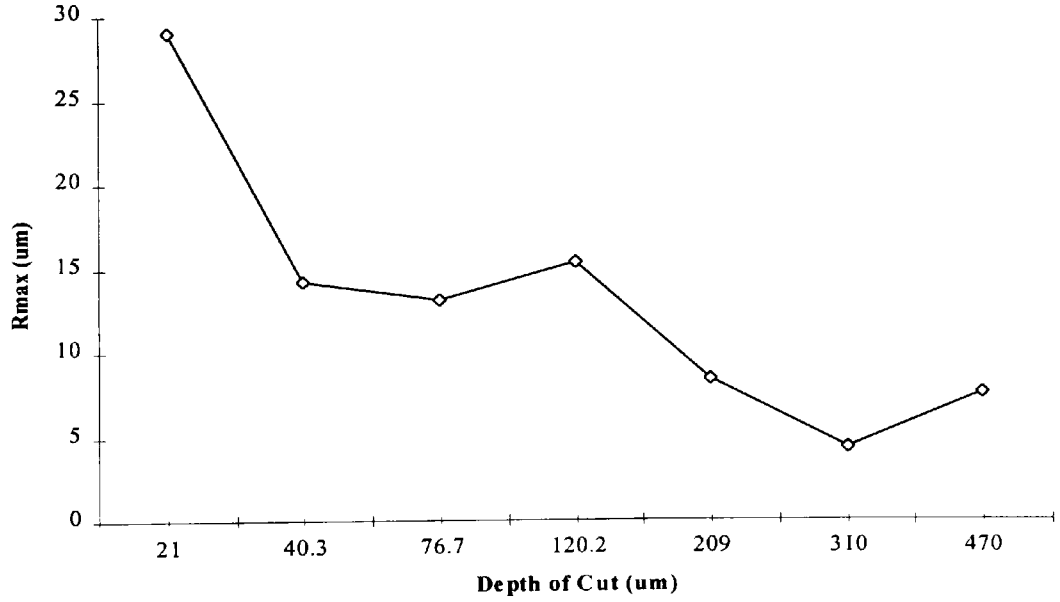

Figure 187: Depth of surface damage (Rmax) against depth of cut averaged over different levels of grit size for the specimens ground with cracks initiated on the surface.

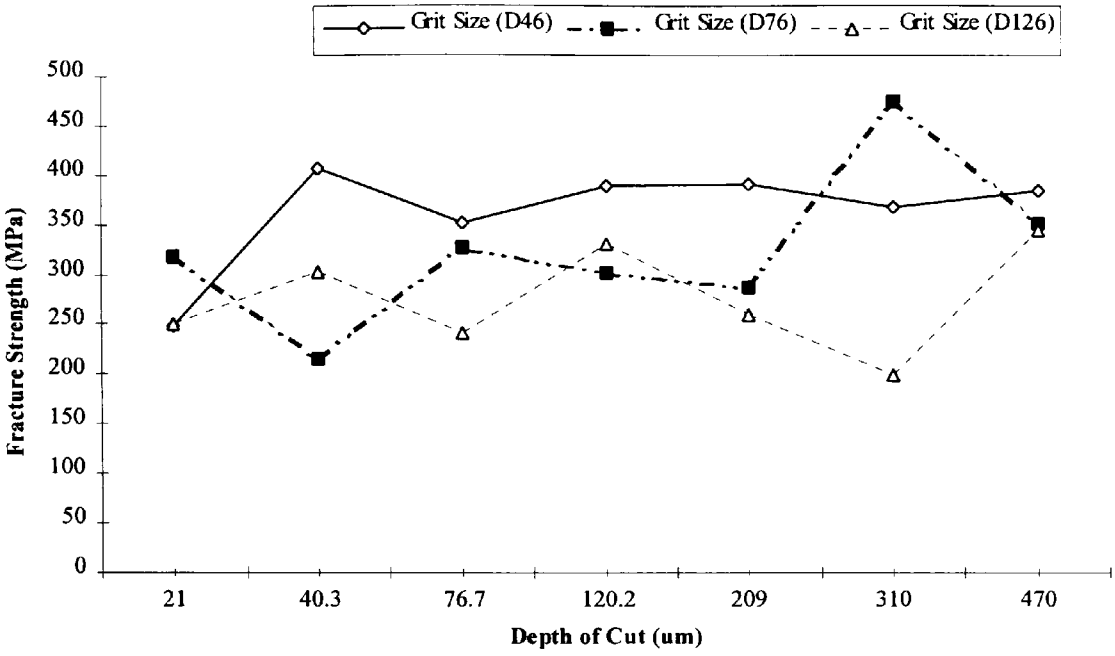

Figure 188: Fracture strength against depth of cut for different levels of grit size for the specimens ground with cracks initiated on the surface.

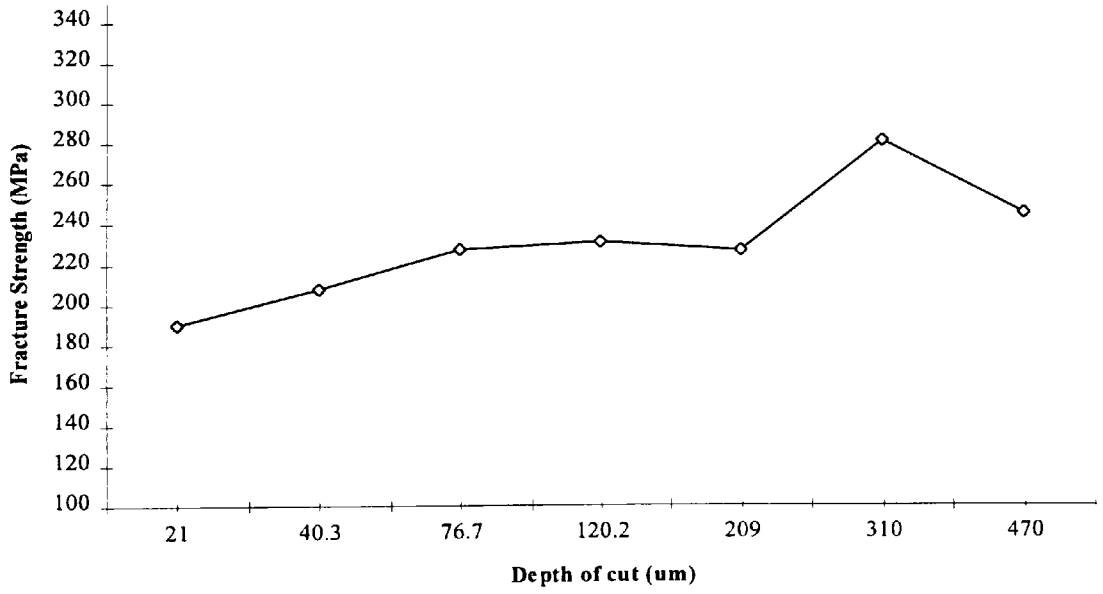

Figure 189: Fracture strength against depth of cut averaged over different levels of grit size for the specimens ground with cracks initiated on the surface.

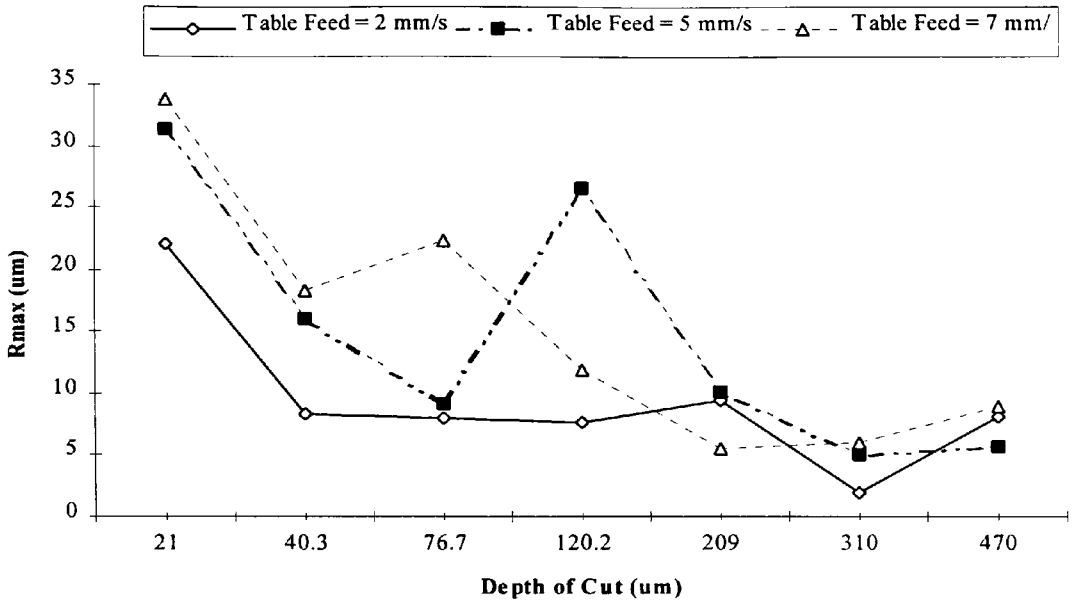

Figure 190: Depth of surface damage (Rmax) against depth of cut for different levels of table feed for the specimens ground with cracks initiated on the surface.

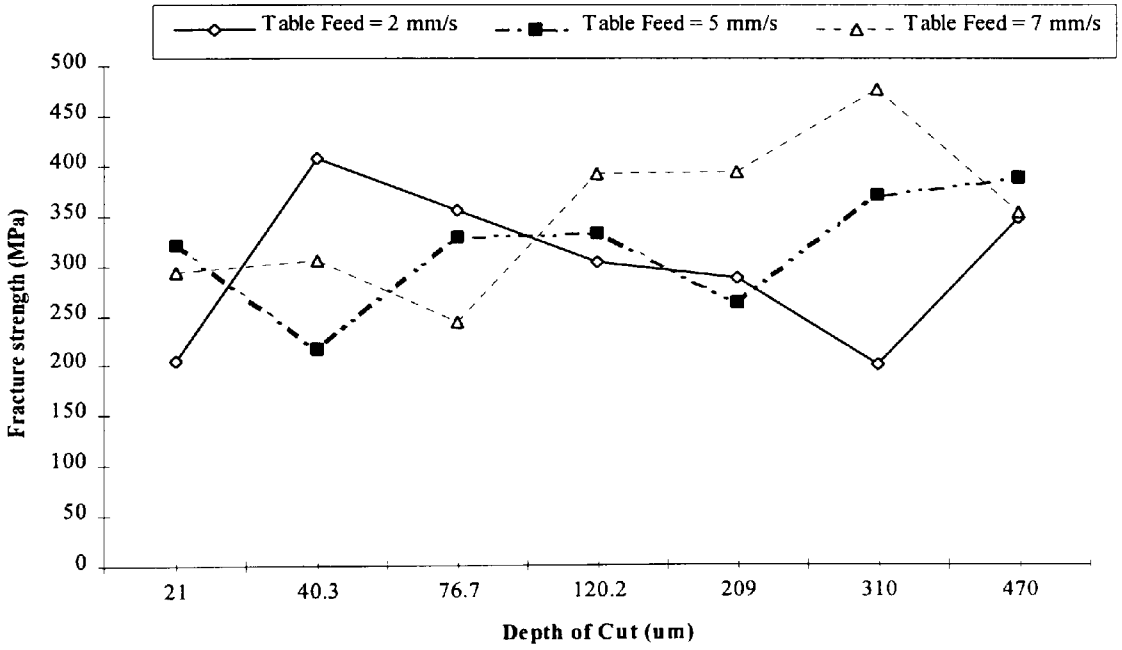

Figure 191: Fracture strength against depth of cut for different levels of table feed for the specimens ground with cracks initiated on the surface.

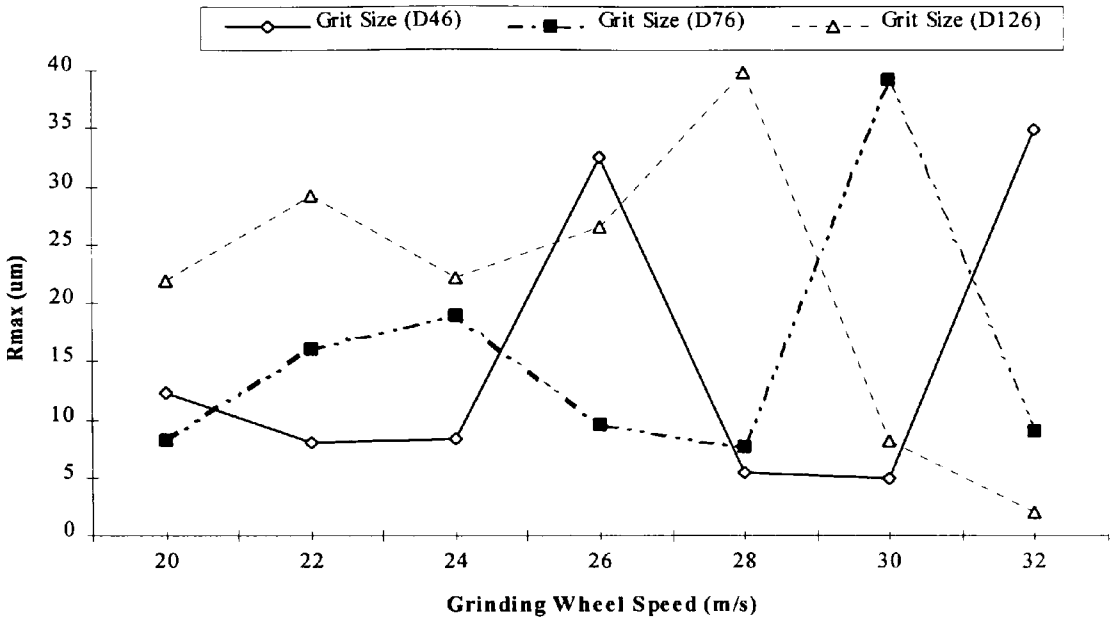

Figure 192: Depth of surface damage (Rmax) against grinding wheel speed for different levels of grit size for the specimens ground with cracks initiated on the surface.

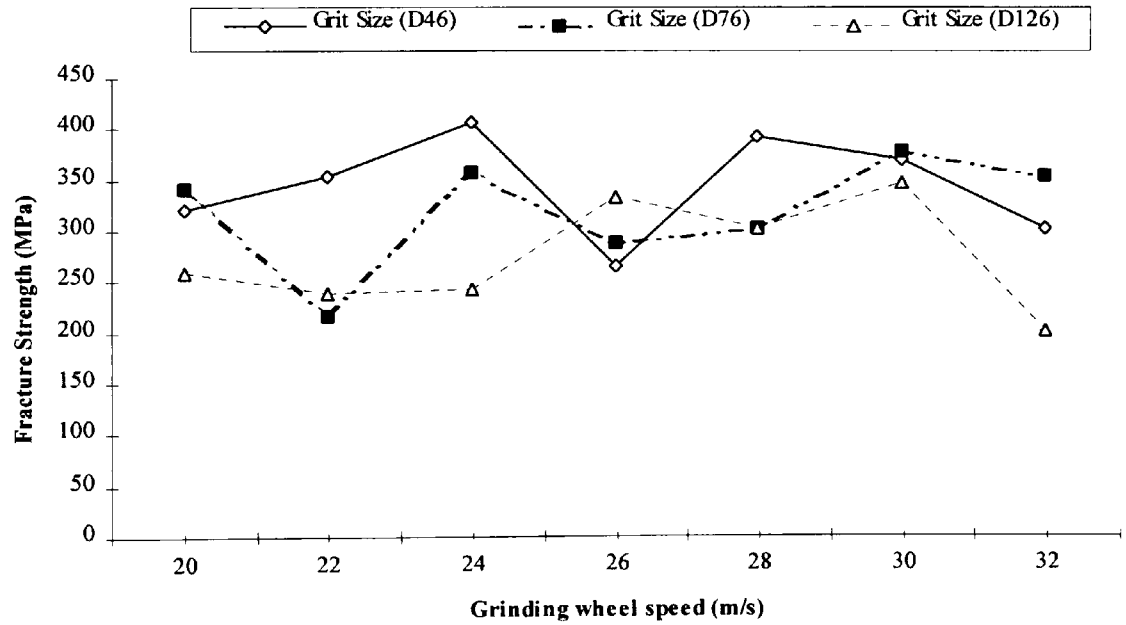

Figure 193: Fracture strength against wheel speed for different levels of grit size for the specimens ground with cracks initiated on the surface.

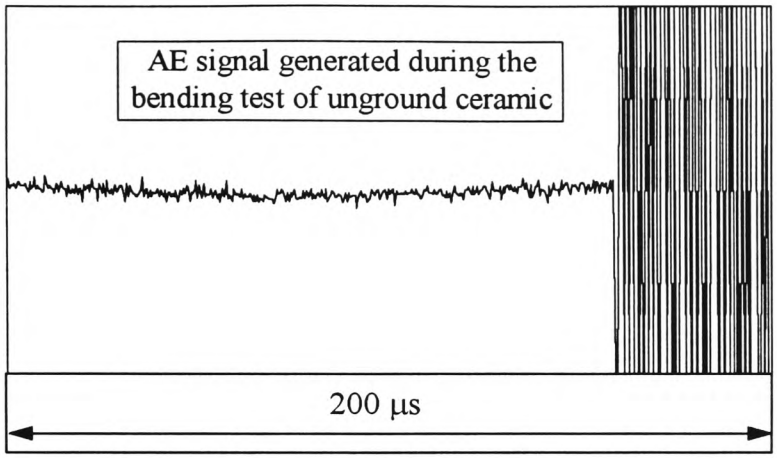

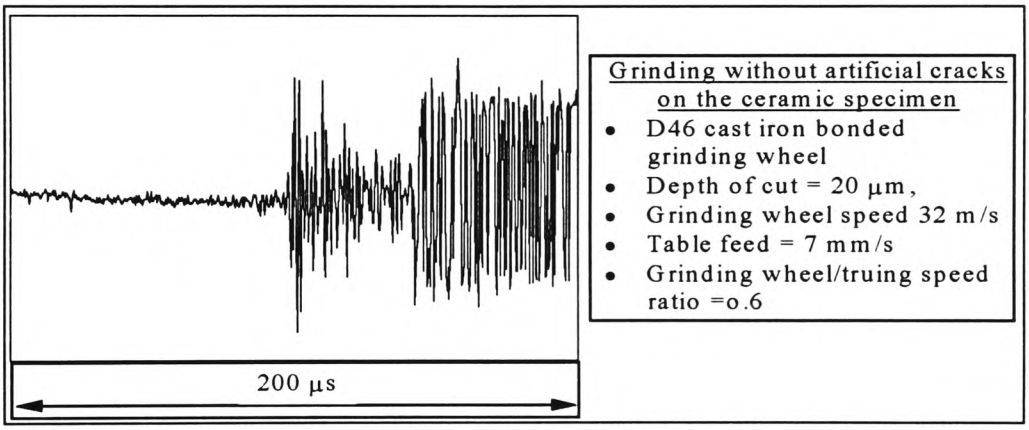

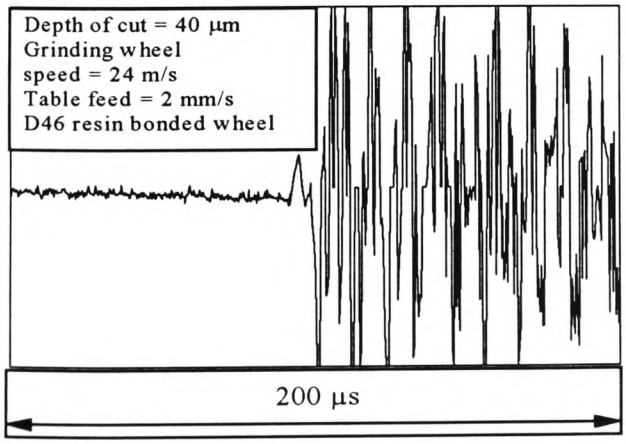

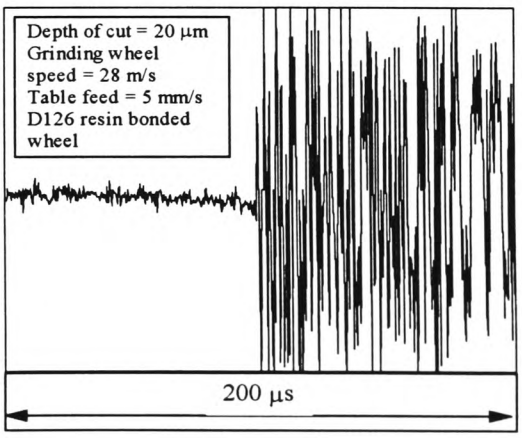

Figure 194: AE signals of ground ceramic specimens recorded during the bending test

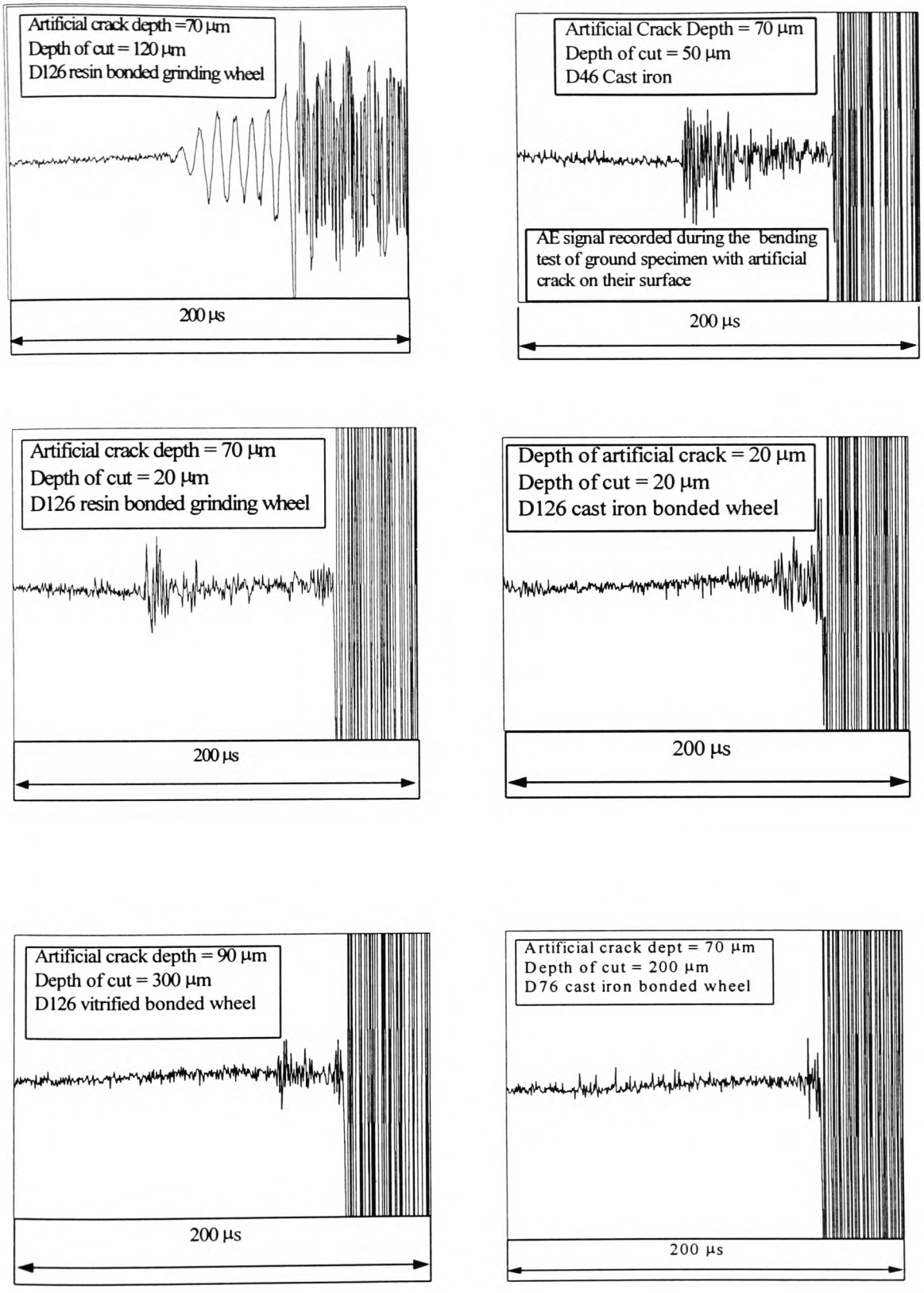

Figure 195: AE signals during the three point bending test of specimens ground with artificial cracks

Grinding wheel type	Resin diamond wheel 140/170 grit size
Truing type	Aluminium oxide truing wheel
Grinding revolution	1131 - 1920 rpm
Dresser revolution	1536 - 2829 rpm
Truing/grinding speed ratio	0.4 & 0.8
Dressing depth	10 - 50 μm

Table 1: Dressing Condition

Grinding wheel condition	rough	fine
Material used for GWEP	mild steel	mild steel
Depth of cut (μm)	50	30
Depth of dress (μm)	40 - 60	10 - 30
Distance between the wheel and the nozzle L (mm)	3	3
Air pressure (bar)	2	2

Table 2: Flapper nozzle setting parameters used to measure the grinding wheel envelop profile (GWEP).

Pass No.	RMS μm	Skewness	Kurtosis	Mean μm	Variance	St. dev. μm	Max. value μm	Min. value μm
0	1.97	0.34	1.68	-0.08	0.74	0.86	3.93	-3.18
1	1.22	0.13	0.0511	-0.0319	0.704	0.839	2.65	-2.57
2	5.68	0.038	-0.212	-2.91	0.7213	0.849	2.69	-3.36
3	6.39	0.076	-0.377	-0.209	0.88	0.939	2.57	-2.99
4	6.47	0.17	-0.287	-0.0879	0.93	0.964	2.82	-2.78

Table 3: Rough wheel parameters at different grinding passes using the flapper nozzle arrangement

Hardware	
AE Sensor	Physical acoustics model S9225
Preamplifier	Physical acoustic model 1220A
Band - pass filter	100 KHz - 1.2 MHz
Sensor peak sensitivity	250 v/(m/s) (output voltage/surface velocity)
Sensor sensitivity range	(100 KHz - 1 MHz) ± 13 dB
Data	**collection procedure**
gould 450 digital storage oscilloscope	It has the ability to sample at a rate of 100 megasamples/sec
Sampling rate	2.5 MHz
Oscilloscope record length	500 point
Data transferred	ASCII files to PC using procomm package
Furrier transform	512 point FFT using excel package
Averaging	

Table 4: AE system description and data collection procedure

Exp. No.	Dres. / Gri. speed ratio	Depth of Cut (μm)	Wheel Speed (m/s)	Table Feed mm/s	Grit Size	Wheel Type	Depth of Crack (μm)
1	-0.3	20	20	2	D46	Resin	10
2	-0.3	40	22	5	D76	Vitrified	10
3	-0.3	80	24	7	D126	Cast Iron	10
4	-0.4	20	22	7	D126	Cast Iron	20
5	-0.4	40	24	2	D46	Resin	20
6	-0.4	80	20	5	D76	Vitrified	20
7	-0.5	20	24	5	D76	Vitrified	30
8	-0.5	40	20	7	D126	Cast Iron	30
9	-0.5	80	22	2	D46	Resin	30
10	-0.3	20	20	2	D76	Cast Iron	10
11	-0.3	120	26	5	D126	Resin	10
12	-0.3	200	28	7	D46	Vitrified	10
13	0.3	20	26	7	D46	Vitrified	50
14	0.3	120	28	2	D76	Cast Iron	50
15	0.3	200	20	5	D126	Resin	50
16	0.4	20	28	5	D126	Resin	70
17	0.4	120	20	7	D46	Vitrified	70
18	0.4	200	26	2	D76	Cast Iron	70
19	-0.3	20	20	2	D126	Vitrified	10
20	-0.3	300	30	5	D46	Cast Iron	10
21	-0.3	500	32	7	D76	Resin	10
22	0.5	20	30	7	D76	Resin	90
23	0.5	300	32	2	D126	Vitrified	90
24	0.5	500	20	5	D46	Cast Iron	90
25	0.6	20	32	7	D46	Cast Iron	120
26	0.6	300	20	5	D76	Resin	120
27	0.6	500	30	2	D126	Vitrified	120

Table 5: Fractional Factorial Experimental Array Showing Different Levels of Grinding Wheel and Machine Parameters

Factors and Error	Degree of Freedom	Sum of Square	Mean Square	F-Ratio	$F_{0.05}$	$F_{0.01}$
Grinding Wheel condition	6	61,386.865	10,231.14	4.5	NO	NO
Depth of Cut	6	10,543.764	1,757.294	0.77	NO	NO
Grinding Wheel Speed	6	11,450.046	1,908.341	0.84	NO	NO
Feed Rate	2	1,158.251	579.1256	0.255	NO	NO
Grit Size	2	174,410.65	87,205.32	38.38	YES	NO
Bond Type	2	25,354.465	12,677.23	5.58	NO	NO
Error	2	4,544.39	2,272.195			
Total	26	288,848.43	11,109.55			

Table 6: Analysis of variance table showing the significant grinding wheel and machine parameters on the fracture strength of ground ceramic component

Factors and Error	Degree of Freedom	Sum of Square	Mean Square	F-Ratio	$F_{0.05}$	$F_{0.01}$
Grinding Wheel condition	6	0.28886	0.04814	11.28	YES	YES
Depth of Cut	6	0.63427	0.10571	24.78	YES	YES
Grinding Wheel Speed	6	0.14463	0.0241	5.65	YES	YES
Feed Rate	2	0.30064	0.15032	35.24	YES	YES
Grit Size	2	15.28519	7.64259	1791.62	YES	YES
Bond Type	2	0.3566	0.1783	41.8	YES	YES
Error	110	0.46923	0.004265			
Total	134	17.47943	0.13044			

Table 7: Analysis of variance table showing the significant grinding wheel and machine parameters on the surface roughness of ground ceramic component

Factors and Error	Degree of Freedom	Sum of Square	Mean Square	F-Ratio	$F_{0.05}$	$F_{0.01}$
Grinding Wheel condition	6	306,087.39	51,014.56	5.783	NO	NO
Depth of Cut	6	775,467.24	129,244.5	14.65	YES	NO
Grinding Wheel Speed	6	311,866.4	51,977.73	5.892	NO	NO
Feed Rate	2	91,092.805	45,546.4	51.63	YES	YES
Grit Size	2	28,299.972	14,149.98	1.6	NO	NO
Bond Type	2	70,028.131	35,014.06	3.969	NO	NO
Error	3	26,464.62	8,821.54			
Total	27					

Table 8: Analysis of variance table showing the significant grinding wheel and machine parameters on the specific grinding energy of ground ceramic component

Exp. No.	Sialon Type	Crack Depth μm	Depth of Cut μm	Table Feed mm/s	Wheel Speed m/s	Gri./Dre. Speed Ratios	Grit Size	Wheel bond Type	Grinding Passes			
1	101	10	20	1	20	-0.3	D46	Resin	1	2	3	4
2	101	10	50	3	26	0.3	D76	Vitrified	1	2	3	4
3	101	10	150	5	32	0.6	D126	Cast Iron	1	2	3	4
4	101	30	20	1	26	0.6	D126	Cast Iron	1	2	3	4
5	101	30	50	3	32	-0.3	D46	Resin	1	2	3	4
6	101	30	150	5	20	0.3	D76	Vitrified	1	2	3	4
7	101	70	20	3	20	0.3	D76	Cast Iron	1	2	3	4
8	101	70	50	5	26	0.6	D126	Resin	1	2	3	4
9	101	70	150	1	32	-0.3	D46	Vitrified	1	2	3	4
10	201	10	20	5	32	0.3	D76	Resin	1	2	3	4
11	201	10	50	1	20	0.6	D126	Vitrified	1	2	3	4
12	201	10	150	3	26	-0.3	D46	Cast Iron	1	2	3	4
13	201	30	20	3	32	0.6	D126	Vitrified	1	2	3	4
14	201	30	50	5	20	-0.3	D46	Cast Iron	1	2	3	4
15	201	30	150	1	26	0.3	D76	Resin	1	2	3	4
16	201	70	20	5	26	-0.3	D46	Vitrified	1	2	3	4
17	201	70	50	1	32	0.3	D76	Cast Iron	1	2	3	4
18	201	70	150	3	20	0.6	D126	Resin	1	2	3	4

Table 9: Fractional Factorial Experimental Array Showing Different Levels of Grinding Wheel and Machine Parameters used to Investigate the Changes on the AE Signals due to Different Grinding Passes of Specimens Ground with Artificial Cracks on Their Surface.

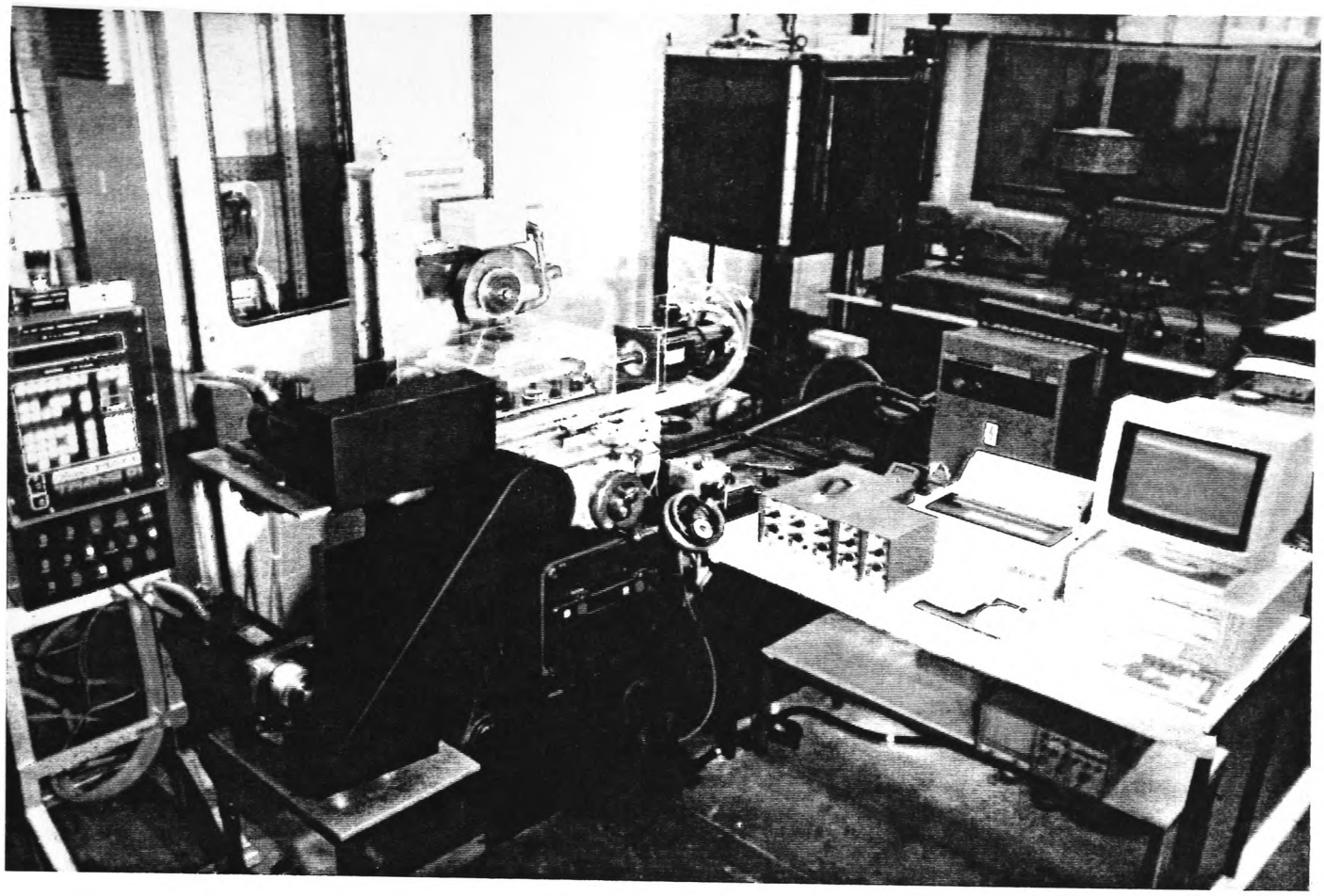

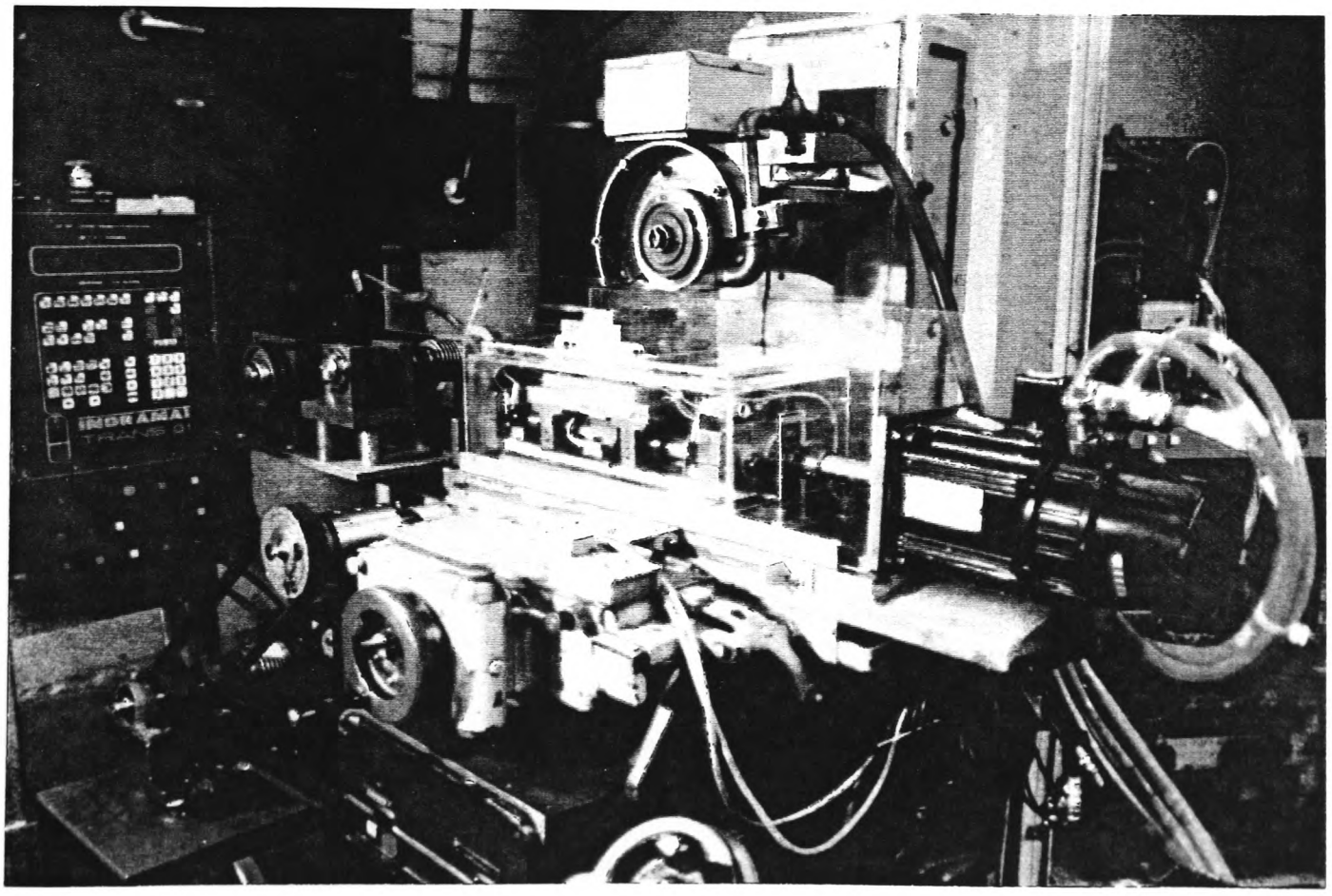

Plate 1: Photograph of modified Jones and Shipman fig 540 surface grinder used in this research.